THE THEORY OF TURBULENT FLOW WITH COMPLEX CHEMICAL KINETICS

By

Luen Tong Tam

BSc (Eng), MSc, DIC

THESIS SUBMITTED FOR THE DEGREE OF

DOCTOR OF PHILOSOPHY

IN THE FACULTY OF ENGINEERING

UNIVERSITY OF LONDON

AND

FOR THE DIPLOMA OF MEMBERSHIP

OF IMPERIAL COLLEGE

Heat Transfer Section
Mechanical Engineering Department
Imperial College of Science and Technology
Exhibition Road
London SW7

FEBRUARY 1981

TO MY PARENTS

ABSTRACT

A new theory of turbulent flow with complex chemical kinetics (Spalding,1976d), "ESCIMO" (Engulfment, Stretching, Coherence, Inter-diffusion, Moving Observer) is presented, applied and evaluated. The ESCIMO theory has both biographical and demographical aspects. Much of this work is focussed on the fold biographic studies. A numerical solution procedure for solving the chemical-kinetic equations is incorporated into the theory.

Attention is given to the burning process in a single "fold" composed initially of a layer of fresh gaseous premixed-mixture of hydrogen+oxygen+nitrogen system and a layer of the corresponding hot products. Three different burning regimes are observed: (1) laminar flame propagation, (2) internal flame propagation, and (3) spontaneous ignition. The predictions made are compared with available analytical solutions to assess their accuracy.

In order to validate the "non-mixed" model of the fold biographic theory, predictions are compared extensively with laboratory experimental data on the "idealised" stretching folds in a converging channel. The agreement is good. The numerical solution procedure for solving chemical kinetic equations is shown to be a valuable tool for evaluating turbulent reacting flows.

Finally, the complete theory of the ESCIMO approach is applied to a pre-mixed, steady-flow, well-stirred reactor under fully turbulent conditions. The performance is calculated as a function of three independent dimensionless ratios; the chemical loading, the Reynolds number and the mixing rate. The following are considered:

- the influence of fold-formation (i.e. the effect of mass fraction of fresh gas in a newly formed fold, M_o) on the performance of the well-stirred reactor;
- the corresponding blow-out limit;
- the population-average reaction rate; and
- the probability-density functions.

Results have been expressed as first and second moments of the corresponding probability-density functions. It is argued that the pdf of concentration fluctuations must be calculated from the theory rather than the presumed-pdf procedure.

It is observed that the ESCIMO theory has promising prospects of fulfilling the need for a general means of prediction.

P R E F A C E

The work presented here covers most of my research activities in the Department of Mechanical Engineering, Imperial College, London, during the period October 1976 to October 1980.

The objectives of the work were to develop, verify and test the ESCIMO theory (Engulfment, Stretching, Coherence, Inter-diffusion, Moving Observer), (Spalding 1976d). The main emphasis was on the application of the biographical part of the above theory to turbulent combustion for a hydrogen-oxygen-system, thereby demonstrating its ability to handle multiple-reaction systems.

During the first six months of my research, I had the opportunity of working with Drs D Tatchell, S K Srivatsa and N C Markatos of CHAM Limited, and Dr I K Jennions at Imperial College.

This early work provided me with a basic understanding of the numerical turbulent combustion modelling and the finite-difference procedures.

For the last three and a half years, my research was directed towards the development and verification of a numerical procedure for solving chemical-kinetic equations, and conducting experimental investigations to study the fold biographic theory. The former allows us,

for the first time, to extend the ESCIMO approach to multiple-reaction systems.

During the first stage of this research, it was recognised that application of the TDMA (Tri-Diagonal Matrix Algorithm) procedure alone, for solving the chemical-kinetic equations, would require excessive computer times. Therefore, the standard point-by-point simultaneous adjustment of SENECKS (Solver for Equilibrium and Non-Equilibrium Chemical-Kinetics Systems) algorithm, originated in the CREK (Pratt 1976) computer code, was incorporated into the present complex chemical kinetic solution package.

Since the convergence was still rather slow, my attention was directed towards improving the speeds and accuracy of the solution procedure for these 'stiff' chemical kinetic problems.

I studied the particular numerical characteristics of the problem, and I introduced some modifications and improvements into the solution procedure. It was concluded that a hybrid type of chemical kinetic solvers, which combined two well-documented algorithms, namely, TDMA and SENECKS together, led to a rapid solution of problems associated with turbulent reacting flows (Ref 140). This successful solution procedure, mainly based on Professor Spalding's ideas, directed me to

a further study on the ESCIMO theory.

At the next stage, I concentrated on studying the inter-diffusion and chemical reaction processes in a stretching laminar layer. By making use of the existing GENMIX code, and the above mentioned improvement in the solution procedures, I succeeded in predicting the influences of initial conditions, stretching time, diffusion time, and reaction time on the layer composition, with chemical reaction relating to hydrogen-oxygen combustion type. This provided some useful information for the fold biographic theory.

In order to demonstrate further the potential of the ESCIMO approach (i.e. its extension to multiple reaction systems), the complete theory, combining the demographic and biographic aspects, was applied to a well-stirred reactor. The demographic aspect of such a problem was originally developed by Spalding (1979a).

During the final stage of work, I focussed attention on providing some experimental data for the verification of the fold biography of ESCIMO theory. I performed some experiments on the 'idealised' stretching layers in a converging channel with different inclined angles.

The experiments consisted of two parts, namely, the measurement of the concentrations of a tracer-gas in

cold flows, and the temperature measurement of a hydrogen-air laminar diffusion stretched flame. Both parts were investigated on the same apparatus.

Comparisons were made of the fold biographic theory with the experimental data. This led me to extend the development and modification of the solution procedure, to predict the laminar diffusion stretched flame for which buoyancy effect can be taken into consideration.

These activities are described, in detail, in this thesis.

A C K N O W L E D G E M E N T S

I must express my sincere gratitude to all those who provided help and cooperation in various ways, at different stages of my research study. First, I am deeply grateful to my supervisor, Professor D Brian Spalding, for his patient guidance and constant encouragement throughout this work. Most of what is presented here is based on his ideas. I must also thank him for his constructive criticisms of my technical writing and research methods. I have benefited a great deal from working under his supervision.

I also thank Dr A S C Ma for discussions and encouragement during the conduct of the experiments.

Discussions with Drs Pun and Przekwas and the staff of CHAM Limited, have been very useful in overcoming various technical difficulties encountered during my research work.

My thanks also go to Mr M B Tung for his helpful discussion concerning the combustion rig, particularly regarding the safety aspect in the design.

I am indebted to all those colleagues with whom I participated in both academic and social discussions, especially, G W Carroll, M A Nosier, R L T Sun,

A H A Baghdadi, S Parameswaran, W C Fan, Y X Ding and H Q Qin.

I wish to thank Mr Bob King for his help in designing, assembling and building my experimental rig and in processing the photographic material.

Thanks are due to Colleen King, Sue Farmiloe, Maggie Dean and Frith Oliver for their assistance in administrative matters; Peter Dale who helped in solving many computing problems, and Miss E M Archer and Mrs S Boot for providing excellent library services.

I must thank Dr N C Markatos for his technical assistance and his sincere collaboration in the work.

I am grateful to Alana Anthony for her excellent typing of this thesis.

Finally, I wish to acknowledge Concentration Heat and Momentum Limited, London, and the Science Research Council for providing financial support during the period of my studies.

LUEN TONG TAM

London, February 1981

TABLE OF CONTENTS PAGE NO.

ABSTRACT		1
PREFACE		3
ACKNOWLEDGEMENTS		7
TABLE OF CONTENTS		9
NOMENCLATURE		16
CHAPTER 1 -	INTRODUCTION	24
1.1	The Problem Considered	24
1.2	Desirability of the ESCIMO Approach	25
1.2.1	The biographic theory	26
1.2.2	The demographic theory	28
1.2.3	The complete ESCIMO theory	29
1.3	Practical Relevance	30
1.4	Objective of the Research	32
1.5	Review of Chemical Kinetics	34
1.6	Review of Previous Theoretical Work	36
1.6.1	Earlier concepts of turbulent flame propagation	36
1.6.2	Current modelling of turbulent reacting flows	38
1.7	Layout of the Thesis	47
CHAPTER 2 -	MATHEMATICAL STRUCTURE OF THE BIOGRAPHIC THEORY	49
2.1	Introduction	49
2.2	Necessary Assumptions	49
2.2.1	Folds at birth	49
2.2.2	Stretching rate	50
2.2.3	The inter-diffusion model	50
2.2.4	Molecular transport	52
2.2.5	Chemical kinetics	54
2.3	The Characteristic Time Scales of a Fold	57
2.4	Governing Equations	59
2.5	Auxiliary Relations	60
2.5.1	Thermodynamic properties	60
2.5.2	The calculation of laminar-transport properties	62
2.5.3	The reaction-kinetic data	65

TABLE OF CONTENTS PAGE NO.

2.6	Closure	66
CHAPTER 3 -	METHOD OF COMPUTING FOLD BIOGRAPHY	68
3.1	Introduction	68
3.1.1	Preliminary remarks	68
3.1.2	Layout of the chapter	68
3.2	The General Form of the Differential Equations	69
3.2.1	The coordinate system	71
3.2.2	Description of the control volume and the flame-following-grid system	72
3.3	Finite-Difference Form Expressions	76
3.4	The Line-by-Line Procedure	78
3.4.1	Source term linearisation	79
3.4.2	The tri-diagonal matrix algorithm (TDMA)	81
3.5	Review of the Line-by-Line Procedure	83
3.6	The Nature of the Difficulties	83
3.7	The Alternatives	84
3.8	Review of the Point-by-Point Procedure	85
3.8.1	The two-operators splitting methods	86
3.8.2	The super-iteration method	87
3.9	Criticism of the Existing Methods	88
3.10	The Method Employed	90
3.11	Description of the "SENECKS Solution Procedure	93
3.11.1	The solution of chemical equilibrium equations	94
3.11.2	The solution of chemical kinetic equations	99
3.11.3	Under-relaxation and convergence criterion	102
3.12	Auxiliary Information	103
3.12.1	Initial conditions	103
3.12.2	Boundary conditions	105
3.12.3	Entrainment formulae	106
3.12.4	Calculation of the mixture temperatures	109
3.13	Closure	110

TABLE OF CONTENTS PAGE NO.

CHAPTER 4 - RESULTS OF COMPUTATION OF FOLD BIOGRAPHY 111

4.1 Introduction 111
4.2 Review of Earlier Results by ESCIMO Approach 112
4.3 Theoretical Approach 113
4.4 Analytical Solutions 115
4.4.1 Laminar flame speed idealisation 115
4.4.2 Classification of the fold burning regimes 120
4.5 Numerical Investigation 125
4.6 Presentation of Results 132
4.6.1 Burn-out and mixing times of a fold 132
4.6.2 Flame speed calculations 137
4.6.3 Predictions for comparison with analytical results 141
4.6.4 Other features of the fold biography 144
4.7 Closure 183

CHAPTER 5 - EXPERIMENTAL WORKS 186

5.1 Introduction 186
5.2 Objectives 190
5.3 Experimental Apparatus 190
5.3.1 Gas supply system 190
5.3.2 The reactor 192
5.3.3 The test section 193
5.3.4 Measured quantity 195
5.3.5 The coordinate and the measuring locations 195
5.3.6 The traversing mechanism 196
5.3.7 The measuring equipment 197
5.4 Experimental Procedure 200
5.5 Experimental Conditions 201
5.6 Experimental Results 203
5.6.1 Interpretation of results 203
5.6.2 Presentation of results 204

TABLE OF CONTENTS PAGE NO.

5.7	Discussion of Results	206
5.7.1	Error analysis	206
5.7.2	Three-dimensional effect	212
5.7.3	Degree of reproducibility	216
5.8	Remarks	216
5.9	Introductory Remarks	220
5.9.1	The problem considered	220
5.10	Objectives of the Experiment	220
5.11	Experimental Apparatus	221
5.11.1	The gas supply system	223
5.11.2	The ignition system	224
5.11.3	The cooling water system	225
5.11.4	Flame stabilisation	227
5.12	The Configuration of the Test Section	227
5.13	The Measured Quantities	227
5.14	The Measured Locations	228
5.15	The Wall Temperature	228
5.16	Temperature Measuring Equipment	228
5.17	Experimental Conditions	232
5.18	Experimental Procedure	232
5.19	Measurement Details	234
5.20	Calculation of the gas temperature from the emf readings	236
5.21	Experimental Results	241
5.22	Discussion	245
5.22.1	Error analysis	245
5.22.2	Degree of reproducibility of the measurements	248
5.23	Concluding Remarks	253
5.24	Closure	253
CHAPTER 6	- COMPARISON OF PREDICTIONS WITH EXPERIMENTAL RESULTS	255
6.1	Introduction	255
6.2	Outline of the Chapter	255
6.3	The Cold-Flow Prediction	256
6.3.1	Description of the problem	256

TABLE OF CONTENTS PAGE NO.

6.3.2	Experimental coordinate system	257
6.3.3	Mathematical statement	260
6.3.4	Governing differential equations	262
6.3.5	Computational details	263
6.3.6	Comparison of the predicted with measured quantities	263
6.3.7	Results	264
6.3.8	Discussion	272
6.3.9	Lagrangian approach	274
6.3.10	The extension of the fold biographic study	276
6.3.11	Presentation of results	277
6.3.12	Discussion	280
6.3.13	Probability-density function	280
6.3.14	Summary	282
6.4	The Hot-Flow Prediction	282
6.4.1	Introduction	282
6.4.2	The problem	283
6.4.3	Objectives	285
6.4.4	Mathematical statement	285
6.4.5	The governing equations	286
6.4.6	Solution procedure	288
6.4.7	Computational details	292
6.4.8	Grid-independent tests	297
6.4.9	Comparison between the predicted and measured quantities	300
6.4.10	Further predictions	308
6.4.11	Discussion	312
6.4.12	Probability-density function of the fold	322
6.5	Closure	326

TABLE OF CONTENTS (Continued) PAGE NO.

CHAPTER 7 - APPLICATION OF ESCIMO TO THE WELL-STIRRED REACTOR 328

7.1 Introduction 328

7.1.1 The problem considered 328

7.1.2 Previous work 328

7.1.3 Review of earlier results by the ESCIMO approach 333

7.1.4 Purpose of the present study 333

7.2 Mathematical Description 334

7.2.1 Method of analysis 334

7.2.2 Assumptions for macro-scale aspect 334

7.2.3 Demographic analysis 335

7.2.4 Assumptions for micro-scale aspect 339

7.2.5 Biographic analysis 340

7.2.6 The coupling of demography and biography 340

7.2.7 Dimensional analysis 343

7.3 Presentation of Results 345

7.3.1 Typical results of fold biography 346

7.3.2 The performance of a well-stirred reactor 352

7.3.3 Population-average quantities 360

7.4 Connexion with the Presumed-pdf Procedure 382

7.4.1 Purpose 382

TABLE OF CONTENTS PAGE NO.

7.4.2 Criticism of the "presumed-pdf" procedure 382

7.4.3 Criticism of the fragment-coalescence procedure 384

7.4.4 The alternative 384

7.4.5 Results of the ESCIMO approach 388

7.5 Closure 402

CHAPTER 8 - CONCLUDING REMARKS 404

8.1 Achievements of the Present Work 404

8.1.1 Theoretical achievements 404

8.1.2 Experimental achievements 406

8.2 Suggestions for Future Work 407

REFERENCES 409

APPENDICES

Appendix A: THE LEAST-SQUARE LINEAR REGRESSION ANALYSIS 439

Appendix B LINEARISATION OF THE CHEMICAL REACTION SCHEMES 442

NOMENCLATURE

SYMBOL	MEANING	LOCATION OF FIRST APPEARANCE
a	Age of the fold, i.e. time since its formation.	eqn (2.2-1)
$a^L_{e\ell,j}$	The number of kg-atoms of element $e\ell$ per kg-mole of species j.	eqn (3.4-6)
A,B,C	Coefficients of the generalised partial-differential equation.	eqn (3.2-2)
A_1, A_2	Entrainment constants.	eqns (3.12-6) (3.12-7)
A_i, B_i, C_i, D_i	Coefficients in finite-difference equation.	eqn (3.4-1)
A_j, A_{-j}	Arrhenius pre-exponential factors.	eqns (2.2-6) (2.2-7)
B_j, B_{-j}	Exponent-on-temperature of modified Arrhenius pre-exponential factor.	eqns (2.2-6) (2.2-7)
C	Burning-time constant.	
C_1	Dimensionless number signifying "chemical loading".	
C_2	Dimensionless number representing "Reynolds number".	
C_3	Dimensionless number representing "mixing rate".	
C_{p_j}	Heat capacity of ideal gas species j.	eqn (2.5-1)
C_p	Heat capacity of mixture.	eqn (2.3-1)
D	Source term of the generalised partial-differential equation.	eqn (3.2-2)
D_{el}	Diffusion coefficient of elemental species.	eqn (2.4-1)
D_{ij}	Binary diffusion coefficient.	eqn (2.2-2)
D_i	Diffusion coefficient of species i.	eqn (2.2-2)

SYMBOL	MEANING	LOCATION OF FIRST APPEARANCE
e	DVM reading.	eqn (5.6-1)
E_i	Coefficient in finite-difference equation.	eqn (3.11-16)
f_ϕ	Newton-Raphson correction function.	eqn (3.11-1)
F_E, F_I	Factors in entrainment-adjustment formulae.	eqns (3.12-12) (3.12-14)
g	The root-mean-square concentration fluctuation.	
g	Gravitational acceleration.	eqn (6.4-1)
G	Gibbs function.	eqn (3.11-3)
h	Enthalpy of mixture.	eqn (2.4-3)
h_j	Ideal-gas enthalpy of species j.	eqn (2.4-3)
$\tilde{h}$	Stagnation enthalpy.	eqn (6.4-5)
h_c	Heat transfer coefficient.	eqn (5.20-1)
JJ	Number of distinct forward reactions considered in reaction mechanism.	
K	Multiple-factor.	eqn (2.3-4)
K_j, K_{-j}	Forward and reverse reaction rates.	eqns (2.2-4) (2.2-5)
K_j^P	The equilibrium constant for reaction j.	eqn (2.2-8)
M	A third body involved in reaction j.	Sec (2.2-5)
M_i, M_j	Molecular weights of species i and j.	eqn (2.5-7)
M_o	Mass fraction of fresh gas in a newly-formed fold.	
$m_{el,i}$	Element concentration at grid I.	eqn (3.4-6)
$m_{inert,i}$	Inert concentration at grid I.	eqn (3.4-7)

SYMBOL	MEANING	LOCATION OF FIRST APPEARANCE
$m_{j,b}$	Mass fraction of species j at burned layer.	eqn (3.12-1)
$m_{j,u}$	Mass fraction of species j at unburned layer.	eqn (3.12-1)
$\dot{m}$	Mass flow rate through the well-sitrred reactor.	
$\dot{m}''_{ch}$	The mean mass flow rate across a grid boundary, due to the chemical reaction.	eqn (3.12-10)
$\dot{m}''_{diff}$	The mean mass flow rate across a grid boundary, due to the molecular diffusion.	eqn (3.12-11)
$\dot{m}''_I, \dot{m}''_E$	Entrainment rates at I, E boundaries.	eqns (3.12-12) (3.12-16)
N_D	Damköhler number.	
NLM	The number of distinct elements present in reacting species.	eqn (3.11-5)
NS	Number of species.	eqn (3.11-3)
n'_j, n''_j	Molecularity of forward and reverse reaction j, dimensionless.	eqn (2.2-8)
p	Pressure.	eqn (2.3-2)
P	$\equiv p + \int \rho_{ref} g dz$.	eqn (6.4-2)
P_a	Population distribution function.	eqn (1.2-1)
$\dot{P}_a$	Source term of P_a.	eqn (1.2-1)
$\tilde{P}, \bar{P}$	Probability-density functions.	
R	Universal gas constant.	eqn (2.2-8)
R	Stretching rate.	eqn (2.2-1)
R^*_{ref}	Reference reaction rate.	eqn (2.3-2)
R_j, R_{-j}	Rate of forward and reverse reaction j, respectively.	eqns (2.2-4) (2.2-5)

SYMBOL	MEANING	LOCATION OF FIRST APPEARANCE
$\tilde{r}_f\langle T,\sigma_1,\ldots\sigma_i,\ldots\sigma_N\rangle$	The fold-average reaction rate.	
$r_f\langle\tilde{T},\tilde{\sigma}_1,\ldots\tilde{\sigma}_i,\ldots\tilde{\sigma}_N\rangle$	Reaction rate which would result from inserting fold-average concentration and temperature into the Arrhenius expression.	
$\tilde{\tilde{r}}$	Reaction rate correlation.	
$\bar{r}_\phi$	Space-average reaction rate of species ϕ.	
S_j^o	One-atmosphere ideal gas specific entropy of species j.	eqn (2.5-3)
S_u, S_p	Source term linearised, i.e. $S_\phi = S_u + S_p\phi$.	eqn (3.4-3)
S_u	Speed of flame propagation.	eqn (3.12-17)
S_ϕ	Source term of dependent variable ϕ.	eqn (3.2-1)
T	Temperature.	eqn (2.2-6)
T_b	Temperature at burned layer.	eqn (2.3-2)
T_g	Gas temperature.	eqn (5.20-1)
T_j, T_{-j}	Activation temperature (activation energy divided by gas constant).	eqns (2.2-6) (2.2-7)
T_j	Hot junction temperature.	eqn (5.20-1)
T_u	Temperature at unburned layer.	eqn (5.20-1)
T_w	Wall temperature.	
t_b	Burn-out time of the fold.	
t_{diff}	Diffusion time.	eqn (2.3-1)
t_f	Linear flame-propagation time across the fold.	
t_m	Mixing time.	

SYMBOL	MEANING	LOCATION OF FIRST APPEARANCE
t_{react}	Chemical reaction time.	eqn (2.3-4)
t_{res}	Residence time.	
t_{str}	Stretching time.	Sec (2.3)
u	Longitudinal velocity.	eqn (6.3-1)
u'	Root-mean-square value of the velocity fluctuation.	eqn (1.6-1)
V	Reactor volume.	
$\bar{W}$	Molecular weight of mixture.	eqn (6.4-6)
X_j	Molar fraction of species j.	eqn (2.2-2)
Y	Fold thickness.	eqn (2.2-1)
Y_o	Initial fold thickness.	eqn (2.3-1)
$Z_1..,Z_7$	Coefficients of thermodynamic properties.	eqns (2.5-1) (2.5-3)

GREEK SYMBOL		
$\alpha'_{k_j}, \alpha''_{k_j}$	Stoichiometric coefficients for species k, i.e. number of (kg-mole) k in reaction j as a reactant or as a product, respectively.	eqns (2.2-4) (2.2-5)
$\bar{\alpha}_j$	Third-body stoichiometric coefficient in reaction j; either 0 or 1.	eqn (2.2-4)
ε	Emmisivity of the thermocouple junction.	eqn (5.20-1)
$\varepsilon_{ij/k}$	The Lennard-Jones force constant.	Table (2.2)
Γ_ϕ	Transport of coefficient ϕ.	eqn (3.2-1)
η	Relaxation factor for recovering the temperature and species.	eqn (3.11-12)
λ_j	Species thermal conductivity in the modified Eucken correction form.	eqn (2.2-3)

GREEK SYMBOL	MEANING	LOCATION OF FIRST APPEARANCE
λ_j^o	Thermal conductivity of pure-gas.	eqn (2.5-12)
λ	Thermal conductivity of mixture.	eqn (2.2-3)
θ	Inclined angle.	
μ_j	Viscosity of species j.	eqn (2.5-8)
ν	Kinematic viscosity.	eqn (1.6-2)
ρ	Density.	eqn (1.2-1)
σ	Stefan-Boltzman constant.	eqn (5.20-1)
σ_i	Mole number of species i in mixture.	eqn (2.3-2)
σ_{ij}	The collision diameter of the molecule in angstroms.	eqn (2.5-7)
σ_m	Reciprocal of mixture mean molecular weight.	eqn (2.2-4)
τ	Reactedness.	
$\tilde{\tau}$	Fold-averaged reactedness.	
$\bar{\tau}$	Space-average reactedness.	
$\dot{\bar{\tau}}$	Space-average burning rate.	
ϕ	Dependent variable in finite-difference equation.	eqn (3.2-1)
ϕ_i^*	Weight-average value of ϕ at adjacent nodes.	eqn (3.11-1)
$\overline{\phi'^2}$	The variance of concentration.	
π_i	Lagrangian multiplier.	eqn (3.11-7)
ψ	$\equiv \int_o^Y \rho dy$, stream function.	eqn (2.4-4)
ξ	$\equiv \int_o^Y \rho u dy$, stream function.	eqn (6.3-1)

GREEK SYMBOL	MEANING	LOCATION OF FIRST APPEARANCE
ω	Dimensionless stream function.	eqn (3.2-2)
$\Omega_{D_{ij}}^{(1,1)*}$	The mass diffusivity collision integral.	eqn (2.5-7)
$\Omega_{\mu_j}^{(2,2)*}$	The thermal conductivity collision integral.	eqn (2.5-8)

SUBSCRIPTS

b	Burned state.
C	Cold stream.
diff	Diffusion.
E	Condition at the E boundary of the finite-difference grid.
H	Hot stream.
I	Condition at the I boundary of the finite-difference grid.
K	Number of iterations.
max	Maximum.
min	Minimum.
P	Located at point P.
react	Reaction.
ref	Reference.
res	Residence.
str	Stretching.
u	Unburned.

SUPERSCRIPTS	MEANING
'	Fluctuating component of a property.
"	Per unit area.
·	Per unit time.
—	Population-(space-) average value, or time average value.
∿	Fold-average value.

CHAPTER 1 - INTRODUCTION

1.1 The Problem Considered

The prediction of turbulent flows with complex reaction schemes has long been a very complicated problem. The difficulty arises in describing the interaction of many reacting chemical species with the fluctuating temperature and velocity fields which characterise such flows.

In considering the chemical kinetics of the combustion processes for a number of elementary reactions, it is important to note that they involve a number of intermediate species in addition to the reactants and products. These intermediate species are essential for controlling the progress of the reaction. The rate of reaction in each elementary reaction step can be expressed mathematically (equation 2.2-4) as suggested by Arrhenius (1889). This expression implies that the rate of reaction depends on the collisions of reactants and the temperature at which the reaction takes place.

For laminar flows, the rate constant and the activation energy can be determined from experiment and the flow can be accurately predicted numerically, as will be explained later (Chapter 3).

However, most of the practical combustion processes are turbulent. A theoretical analysis based on the classical Eulerian approach assumes that all species concentrations, temperature and velocity components fluctuate around their time-average values.

Since the approach is based on Eulerian viewpoint, attention is focussed on space rather than on matter. In this circumstance, the fluid properties which are composed of time-average and fluctuating components need be calculated at each point of the flow. Consequently, there are too many differential equations to be solved, and too many empirical constants and correlations to be specified. Furthermore, those approaches lead to difficulties in understanding the chemical kinetics and molecular interdiffusion phenomena of turbulence∿chemistry interaction. In addition, it is difficult to predict the time-average reaction rate accurately. The latter aspect constitutes a major problem in turbulent reacting flows.

1.2 Desirability of the ESCIMO Approach

In order to avoid the difficulties, the ESCIMO theory has been proposed by Spalding (1976d). The acronymn ESCIMO stands for Engulfment, Stretching, Coherence, Inter-Diffusion, Moving Observer. The important

feature of the ESCIMO approach is that it consists of both the Lagrangian and Eulerian aspects which are correspondingly related with the biographic and demographic theories. The combination of these approaches can deduce the influences of hydrodynamics, molecular diffusion, and chemical kinetics on turbulent combustion from the physical laws rather than making any 'guess' of the probability-density functions. This enables the ESCIMO theory to predict the turbulent combustion in a more realistic and economic way.

1.2.1 The biographic theory

In the Lagrangian aspect (Spalding, 1976d), attention is focussed on the coherent 'lumps' of fluid which are created in the turbulent motion by turbulent mixing and entrainment of burned and fresh gases at different locations. The moment two parent-gas bodies come together due to engulfment (i.e., the birthplace of folds) they form a fold. Once the folds are formed, they retain their identity and their sizes are small in comparison with the large turbulent eddies. This means that the scale of the folds is comparable with the molecular scale.

Due to the turbulent mean motion and random fluctuations, folds are subjected to a stretching process. During the stretching process, inter-diffusion and chemical reactions take place in the normal direction

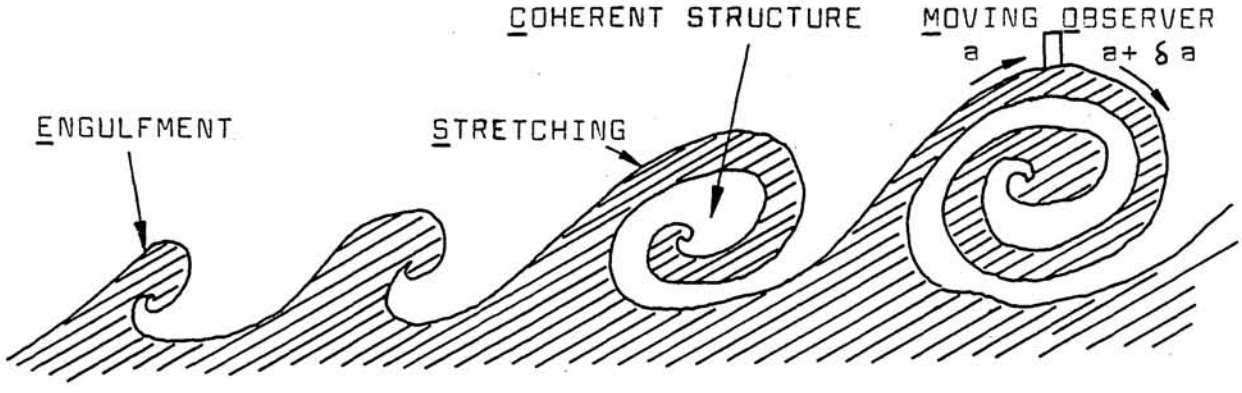

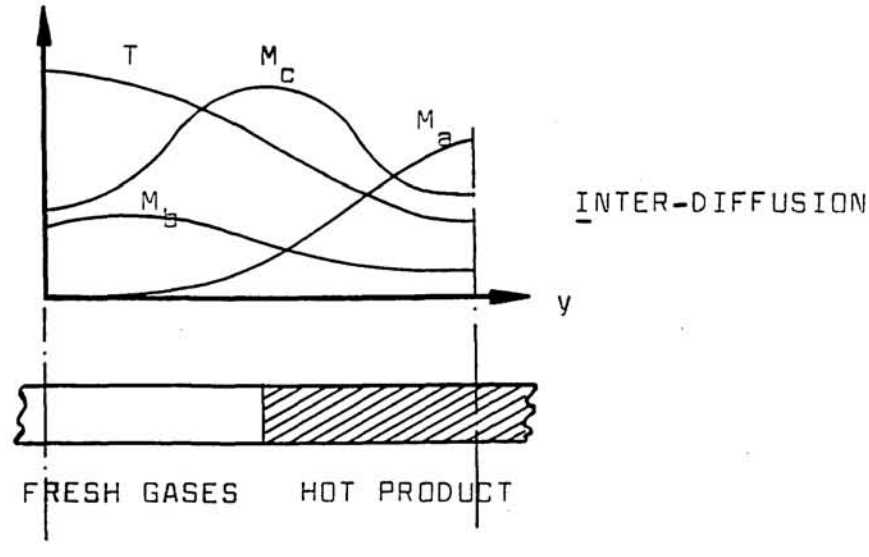

PROPERTY DISTRIBUTIONS ACROSS A FOLD AT ANY SUCCESSIVE AGE, 'a' .

FIGURE 1.1 PROCESS OF ENGULFMENT AND STRETCHING.

to the interface of the layer-pairs of the folds. Furthermore, the folds retain their identities while being stretched and squashed in their ageing paths and simultaneously diminished in thickness until the stretching process is completed. Finally, they will lose their identities ('death' of folds) by way of re-engulfment or removal from the system by outflow.

A simplified illustration of this process is shown in Figure 1.1.

The moving observer is another important feature in ESCIMO, for it provides a great simplification in analysing the stretched-fold. Since the fold biography is analysed in a reference frame which moves with the fold during its lifetime, the inter-diffusion and chemical reaction processes can be described as a set of one-dimensional, transient, parabolic equations and are governed by the laminar laws.

1.2.2 The demographic theory

The Eulerian aspect of ESCIMO is concerned with the analysis of the population of coherent fluid folds in space. It involves the solution of differential equations of the population of a given group of fluid folds, having the initial size, age and composition within a given range (Spalding 1979d).

$$\rho \frac{D\, p_a}{Dt} = \mathrm{Div}(\Gamma_{eff}\ \mathrm{grad}\ p_a) + \rho\ \dot{p}_a, \qquad (1.2\text{-}1)$$

where p_a represents the probability of finding, at any location, folds which have originated in a certain birthplace, having an age between a and a+δa, whereas $\dot{p}_a$ represents the source term.

In association with the engulfment process, the source term $\dot{p}_a$ can be determined by the fold-formation rate (engulfment) and re-engulfment rate.

The simple case of the demographic theory is that of the well-stirred reactor problem, for populations of coherent fluid folds are under the local equilibrium conditions. Under this circumstance, equation (1.2.1) is therefore reduced to $\dot{p}_a=0$.

Consequently, p_a can be expressed in terms of an analytical formula, as will be discussed in Chapter 7.

1.2.3 The complete ESCIMO theory

As already mentioned, the main advantage of the ESCIMO approach is that it allows for a reacting system of arbitrary complexity for which it can be separated from the calculation of fold population distribution.

When both of the biographic and demographic parts of ESCIMO have been solved, their combination provides complete information about the flow field properties (namely, the time-average quantities and the statistical representations of space probability density

functions) at any location in the turbulent reacting flow field.

1.3 Practical Relevance

The main reasons for developing such a general turbulent reacting flow theory are:

(1) To assist the design engineer in improving performance and operation of combustion equipment in industrial engineering.

(2) To provide the necessary information for air pollution control in environmental engineering.

(3) To introduce a possible technique of fire prevention and reduce the risk of explosion in engineering equipment.

Typical examples of combustion systems are:

- The well-stirred reactor.
- Two-dimensional steady axisymmetrical flame in converging duct.
- Two-dimensional steady axisymmetrical turbulent combustion chamber.
- Two-dimensional steady rocket-exhaust plume.
- Three-dimensional steady gas-turbine chambers.
- Three-dimensional unsteady spark-ignition engine and reciprocating engine.

- Three-dimensional unsteady gas and duct explosion.
- Two-dimensional steady turbulence buoyant flame near an adiabatic wall.

A trial-and-error experimental study of the above combustion systems and designs will involve very high costs of the relevant combustion equipment. Thus, it is important to discuss further the desirability of such a general theoretical approach to practical problems. Some examples are in:

(1) Industrial engineering

From the engineering point of view, the designer of combustion equipment requires a high heat-release rate and a wide range of flame stability limits. For instance, good performance of a turbo-jet combustor requires extremely high volumetric heat release rates, low emissions and low pressure drops. Of course, a high combustion efficiency and stability over a wide range of fuel-air ratios are also desirable. These can mainly be achieved in turbulent combustion processes.

(2) Environmental engineering

The pollution control is an important feature in combustion processes for environmental engineering research. Usually, air pollution is created by the formation and emission of combustible solids, hydrocarbon, sulphur and nitrogen oxides from the combustion equipment.

A design engineer should always maximise the combustion efficiency and minimise the formation of pollutants. To optimise both requires knowledge of the chemical kinetics related to the reaction of oxidation of soot and the formation of nitrogen oxide in turbulent flames.

1.4 Objective of the Research

The main objective of the present study was to develop, validate, refine and test the ESCIMO theory. The emphasis was on the application of the biographical part of the ESCIMO theory to turbulent combustion in the hydrogen-oxygen- system, thereby, demonstrating its ability to handle multiple reaction systems. Experimental investigations were carried out to supplement the data on converging channel flows for validating the fold biographic theory.

The work was performed in five main stages as described below.

(1) Development of the prediction procedure

A numerical solution procedure for calculating chemical-kinetic equations which combined two numerical algorithms, namely, the TDMA (Tri-Diagonal Matrix Algorithm) and the SENECKS (Solver for Equilibrium and Non-Equilibrium Chemical-Kinetics Systems) was employed and this provided

a rapid solution to problems associated with turbulent combustion. This solution procedure has been successfully incorporated into the ESCIMO approach.

(2) Investigation of the fold biographic theory

The fold biographic theory was investigated by studying the influences of initial conditions, stretching time, diffusion time and chemical reaction time on a stretched fold with reactions related to the hydrogen-oxygen combustion system.

(3) Application

The complete ESCIMO theory was extended to multiple reaction on the hydrogen-oxygen-nitrogen-system and was applied to the well-stirred reactor. It was shown that the influences of hydrodynamics, laminar-transport and chemical kinetics on the performance of the well-stirred reactor can be taken into account by the established theory. It is thus suggested that the ESCIMO approach is capable of predicting the multiple chemical reactions in turbulent flows.

(4) Experimental investigation

Two types of experiments were performed, namely: (a) a cold-flow experiment, in which distributions of concentrations of a tracer-gas across the stretched-folds were measured; and (b) a combustion experiment,

in which the temperature profiles across the laminar diffusion hydrogen-air stretched flame were measured.

The objective of the experiment was to provide experimental data for the verification of the fold biographic theory.

(5) Comparisons

A numerical solution procedure adopting the above laminar stretched flame under the influence of buoyancy was developed. This procedure was shown to be approximately 50 times faster than Kee and Miller's (1978) two splitted-operators method.

Comparisons of the predictions with cold-flow measurements as well as combustion measurements from above experiments were made.

1.5 Review of Chemical Kinetics

This thesis is concerned primarily with the chemical kinetics of gas-phase reactions in combustion processes.

Reactions can be classified into two types. The first includes those bimolecular reactions which have been studied in flame structure studies. The techniques range from the high-temperature flame (Fenimore and

Jones, 1959) through intermediate temperature studies of the fuel-oxygen explosion limit (Baldwin and Coure, 1962), to low-temperature measurements of the reverse reaction (Kaufman, 1963; Clyne and Thrush, 1963). Therefore, the data available covers a wide range with reasonable accuracy for the specification of the kinetic constants.

The second group consists of the 'third-body' radical recombination reactions, applicable to common flame systems. The only type of termolecular reaction of importance is that in which two atoms combine to form a stable molecule by collision with a 'third-body'* (some other molecule or a solid surface).

Many of the kinetic data for high temperatures are available only for shock-tube studies of the reverse (dissociation) reaction (Schott, 1958; Strehlow, 1962).

In addition, detailed knowledge of the elementary reactions for the hydrocarbon fuel requires more elaborate studies by chemists (Dixon-Lewis, 1967). However, the main features of the hydrogen-oxygen

---

* This third-body (M) is required to remove the energy released when the composition bond is formed. If this energy is not removed by collisions or radiation within a few vibrational periods (10^{-13} seconds), the molecule will redissociate.

system have been studied by Baldwin, Doran and Mayor, (1960); Clyne and Thrush (1963): Jenkins and Spalding (1967) and Dixon-Lewis (1970b) and are fairly well-understood. For this reason, the reaction mechanism for the H_2-O_2 system was chosen for the study presented in this thesis.

1.6 Review of Previous Theoretical Work

1.6.1 Earlier concepts of turbulent flame propagation

The wrinkled flame concept

The first attempt to investigate the effect of turbulence on flame propagation was made by Damköhler (1940). His first assumption of the model was that the scale of turbulence was large compared to the reaction zone thickness. Hence, the turbulent flame was regarded as a continuous laminar flame-front wrinkled by turbulence. It could be shown that the burning velocity of turbulence S_T could be related to the laminar flame speed S_L in accordance with:

$$S_T = S_L + u' \quad , \qquad (1.6\text{-}1)$$

where u' is the root mean-square fluctuation velocity.

Effect of turbulent transfer process

Damköhler et al (1947) also proposed that when the stirring turbulent eddies were smaller than, or at least comparable with, the reaction zone thickness, the ratio S_T/S_L could be written as:

$$S_T/S_L = \left(\frac{\varepsilon}{\nu}\right)^{\frac{1}{2}} \quad , \qquad (1.6\text{-}2)$$

where ν is the kinematic viscosity of fluid;

ε is defined by the product of the turbulent scale and the root mean-square fluctuation velocity, $\varepsilon \equiv \ell u'$.

A more elaborate treatment of this model had been done by Shchelkin (1943) on the assumption that the wrinkled front was distorted into cones. He then proposed the following relations:

$$S_T = S_L \left| 1 + B\,(u'^2/S_L^{\,2}) \right|^{\frac{1}{2}} \qquad (1.6\text{-}3)$$

where B is a constant close to unity.

From the above expression, it may be seen that when the turbulent intensity reaches very high values, equations (1.6-1) and (1.6-3) become

$$S_T \sim u' \quad . \qquad (1.6\text{-}4)$$

Flame stretching

The above original ideas of the turbulent flame propagation, can be summed up to the fact that the turbulent structure consists of a number of small-scale eddies at which the laminar flame surfaces are continuously distorted and stretched by the turbulent mean motion.

Damköhler (1947) studied the effect of turbulence on the flame velocity in gas mixtures and defined the Damköhler number as the ratio of the chemical reaction rate to the rate of strain*, i.e. $N_D \equiv \frac{R}{\gamma}$.

The influence of rates of strain on the stretched laminar diffusion flamelets was studied by Kent and William et al (1976). More details will be given in Chapter 5.

1.6.2 Current modelling of turbulent reacting flows

The 'naive' approach

Since 1960 the theory of laminar flames has been well understood. During the 1970's the advent of the digital computer provided means of predicting successfully, the hydrodynamics of the non-reacting turbulent flows

---

* The number N_D indicates how the rate of strain and the chemical reaction can affect the turbulent flame.

with the aid of the turbulence models, developed by Kolomogorov (1942), Prandtl (1945), Harlow and Nakayama (1967) and Launder and Spalding (1972).

These models have been employed by many authors to analyse the chemical reactions in turbulent flows. However, most of them ignored the difficulty of fluctuation correlations. The above works assumed that the time-average reaction rates depend only on the local time-average concentrations.

Jones and Prothero (1968) were the first to apply the above approach to a perfectly stirred reactor theory. Jenkins and Spalding (1969) also considered a similar problem using the knowledge of multiple reaction mechanism (which has been discussed in Section 1.5). The authors set up a solution procedure for such reactants and obtained satisfactory results. However, this can be applied only when turbulent combustion is kinetically controlled (Spalding, 1976c).

There is evidence (see Spalding 1976c) that when the reaction is controlled by hydrodynamics, the predicted quantities behave similarly to a laminar flame rather than a turbulent one. Particularly, results of the 'Naive' approach show that the predictions for the flame width and the species concentrations are unrealistic in turbulent flame propagation in ducts. The reason given by Donaldson (1972) was that the concentration

and temperature fluctuations have a considerable effect on the reaction rate because of the non-linear dependence of the Arrhenius term on species and temperature.

Eddy-break-up model

Spalding (1959) proposed an "entrained-is-burned" model which was concerned with a theory for the rate of spread of the confined turbulent flame propagation. Two assumptions were used, namely:

- That the flame from the centre bluff-body entrains fluid from its surroundings just as in a non-reacting turbulent jet.

- That the rate of entrainment at high stream-velocities controls the rate of burning.

Later, Spalding (1971c) suggested that the local rate of reaction should depend upon the rate of "eddy-break-up" (EBU). That suggestion was based on the arguments that:

- The decay of turbulent energy comes about by the breaking of large lumps of fluid into successively smaller ones.

- The rate of energy decay is approximately equal to $0.35\rho\left|\frac{\partial\bar{u}}{\partial y}\right|$ times the local energy, where $\frac{\partial\bar{u}}{\partial y}$ is the local velocity gradient.

However, at the interfaces between the hot and cold lumps of fluid, there is a gas of intermediate reactedness, τ; and this may have a reaction rate controlled by chemical kinetic process. The actual time-average reaction rate is therefore presumed to be controlled simultaneously by chemical kinetics and eddy-break-up.

Together with the turbulent mixing-length hypothesis, the above model was applied to turbulent,pre-mixed, confined flames. The results were in better agreement with experiments than those of the Naive approach.

Motivated by this initial success, Manson and Spalding (1973) employed the k-ε-g turbulence model (where $g=\overline{m_{fu}'^2}$, the mean-square fluctuation of concentration) to extend further the EBU model for the confined-premixed-flame situation. The time-average reaction rate by the "eddy-break-up" process is given by:

$$\bar{R} = C_{EBU}\ \rho\ g^{\frac{1}{2}}\ \frac{\varepsilon}{k}\ , \qquad (1.6\text{-}5)$$

where C_{EBU} is a Universal constant. However, only limited success was achieved (see Spalding, 1976c).

Coherent structure models

The concepts of "coherent large scale structure" in turbulent shear flows were widely established by considerable experimental evidence. Brown and Roshko (1974) showed that large eddies were formed by engulfment in non-reacting free shear layers. Roshko (1976) argued that it is necessary to separate the turbulent and the non-turbulent processes.

Large coherent structures usually exist where they are created by turbulence. Small scale eddies must decay quickly when they become comparable in size with the molecular size.

Figure (1.2) represents Roshko's study (1976) of a plane turbulent mixing layer. He observed those motions developing at the mixing layer between a high-speed flow of nitrogen and a slower flow of a helium/oxygen mixture of the same density. The visible vortices are of large coherent structures.

Witte (1975) proposed an analytical concept of a turbulent flame consisting of a distribution of coherent laminar flame elements. The thickness of the diffusion flame was supposed to be small in comparison with the wave length of prominent disturbances in the gas. Owing

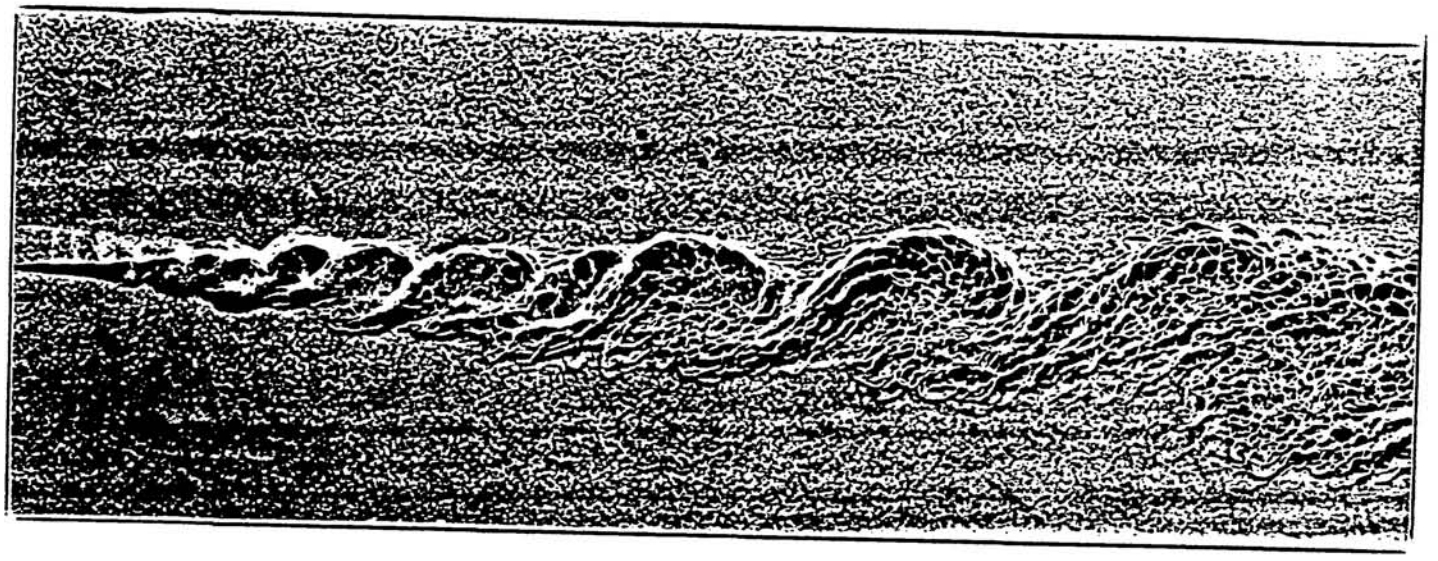

FIGURE 1.2 SPARK SHADOWGRAPH OF MIXING LAYER BETWEEN NITROGEN (UPPER) WITH U_1 = 880 cm/sec AND HELIUM (LOWER) WITH U_2 = 330 cm/sec. PRESSURE = 4 atm (ROSHKO, 1976).

to the characteristics of coherent structures, the local flame elements were stretched and distorted by the local gas rotation in their own planes.

Marble and Broadwell, (1977) extended this coherent flame model to predict fuel consumption rates for strained laminar mixing layers and also for turbulent fuel jets.

The presumed 'probability-density function' approach

Spalding (1971b) proposed a differential equation for the root-mean-square fluctuating concentration, g, which involves a balance of convection, diffusion, generation and dissipation. This equation was solved numerically, together with the usual time-average equations for momentum, energy, concentration and turbulent quantities. To use such a theory for the prediction of turbulent reacting flows, it is necessary, in addition, to presume a probability distribution function (pdf) for a fluctuation concentration where pdf is the probability of finding a concentration, f, lying in the interval f to f+df.

Many forms of pdf's have been proposed for the reacting flow calculations. For instance, Spalding (1971b), proposed a square wave form of species-time variation,

which compared to two delta functions for a free diffusion flame and used by Elghobashi (1974) for confined diffusion flames. Bilger and Kent (1972) proposed a Gaussian pdf for solving the diffusion flame.

Alternatively, Borghi et al (1977) postulated a rectangle flanked by a delta function which was applied to the well-stirred reactor theory.

Since all the proposals for pdf presumptions are doubtful, it appears that "guesses" of the flame shapes were made before the solutions were given.

Dopazo and O'Brien (1976) and Pope (1976) formulated a turbulent transport equation for solving the probability distribution function of a scalar embedded in a simple turbulent flow. However, this approach has three defects.

(1) The importance of the molecular diffusion has not been taken into account.

(2) The turbulent convection and the molecular action terms require too many correlation assumptions.

(3) It seems to be very difficult to establish the chemical kinetic solution by this approach.

The Fragment-Coalescence approach

Curl (1963), Evangelista et al (1969) and Pratt (1976) applied a 'Fragment-Coalescence' model to the well-stirred reactor. The general assumptions of this approach were given as:

- Turbulence breaks injected gases into fragments and rate and size are determined hydrodynamically.
- Fragments coalesce and mix instantly.
- Chemical reaction proceeds by chemical kinetics control.

The advantage of this kind of approach is that the full knowledge of complex chemical kinetics can be incorporated.

Disadvantages of this kind of approach are:

(1) Since the molecular transport is regarded as being so rapid as to allow the fragments to coalesce and to mix instantly, the influence of the laminar transport terms on the turbulent flame prediction is absent.

(2) This approach requires an additional integro-differential equation for the rate of change of the concentration probability-density function. Again, this equation appears to have the same defects as the presumed pdf approaches.

1.7 Layout of the Thesis

The thesis so far contains only the introductory materials. The remainder of the thesis is presented in seven chapters.

Chapter 2 contains the mathematical structure of the biographic theory.

Chapter 3 is concerned with the method of computing fold biography. The differential equations are reduced to finite-difference equations by integration over small control volumes surrounding each grid node. As mentioned earlier, the solution methods of chemical kinetic equations (TDMA and SENECKS) have been employed and optimised in the present work. This is described in detail in this chapter.

In Chapter 4, the results of computations of fold biography are presented.

Chapter 5 describes the experimental methods on fold biographic investigations. These were carried out on both non-reacting flow and reacting flow under different stretching conditions. The experimental situation is that of a vertical converging channel.

In Chapter 6, comparisons are made between predictions and experiments. In addition, the effect of buoyancy force on the diffusion laminar stretched flame is taken into consideration in the prediction procedure.

The application of the ESCIMO to a well-stirred reactor is described in Chapter 7.

Finally, Chapter 8 summarises the main contributions of the present study and the conclusions made thereon, together with recommendations for future work.

In addition to the eight chapters, the thesis also includes a list of references and appendices that provide supplementary details regarding the mathematical formulation.

CHAPTER 2 - MATHEMATICAL STRUCTURE OF THE BIOGRAPHIC THEORY

2.1 Introduction

This chapter describes the mathematical formulation of the Lagrangian aspect in the ESCIMO theory for considering the small-scale folds of turbulent combustion in the hydrogen-oxygen systems.

The assumptions for folds at birth, such as the interdiffusion model, the details of laminar transport and the chemical reaction mechanism employed, are given in Section 2.2.

The characteristic time scales for a fold are specified in Section 2.3.

The governing equations are given in Section 2.4. These equations include the balance of atomic elements, the balance of species and the balance of energy. The addition of auxiliary relations completes the mathematical basis of the biographic theory of ESCIMO.

2.2 Necessary Assumptions

2.2.1 Folds at birth

Due to random motions and the turbulent mixing process, large-scale eddies are broken down into

small-scale eddies (Spalding, 1978b).

As illustrated in Figure 2.1, folds are formed by the engulfment of one stream by another and the consequent formation of interleaved layers of different initial sizes and compositions. The initial thickness of a fold, Y_o, is supposed to be of the order of mixing length (Spalding, 1976d). Since all fold sizes are at molecular levels, and since the Moving Observer is used, the governing equations are subject to laminar flows.

It is supposed that the folds do not communicate with one another, the analysis is regarded as being by precisely similar folds (Spalding, 1978b). Consequently, the analysis can be focussed on a single fold.

2.2.2 Stretching rate

As a consequence of both shear in the mean motion and of turbulent fluctuations, the thickness of a newly-formed fold continuously diminishes in accordance with, (Spalding, 1976d, 1979a).

$$R = - \frac{d}{da} \ln \int_o^Y \rho dy \quad , \qquad (2.2\text{-}1)$$

where R is the stretching rate, presumed uniform throughout the fold biography.

2.2.3 The inter-diffusion model

The inter-diffusion model chosen here is appropriate to the pre-mixing of hydrogen-oxygen gases. The following assumptions are made:

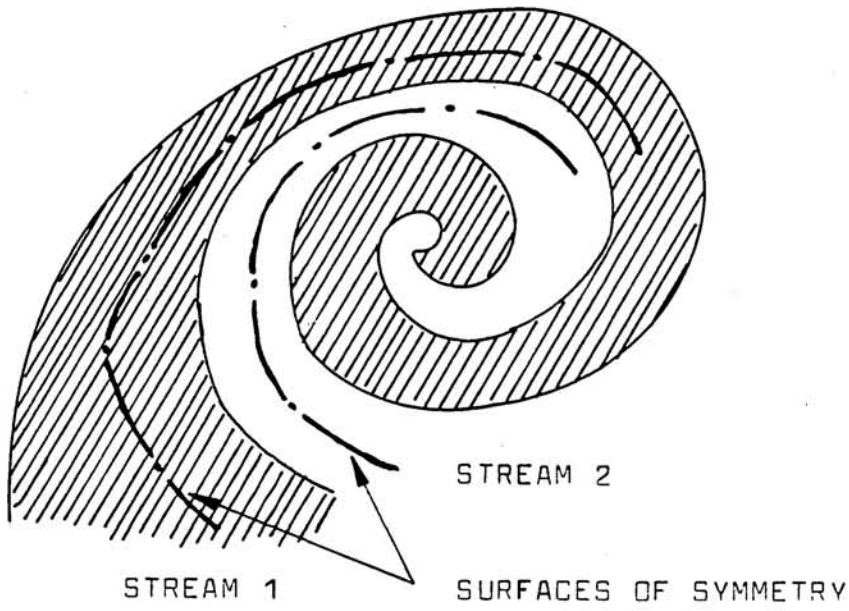

FIGURE 2.1 ILLUSTRATION OF THE FORMATION OF A SINGLE FOLD.

- The initially-formed fold consists of two 'parent' layers which have the same elemental composition; the 'fresh' layer containing the unburned gases and the 'hot' layer containing equilibrium combustion products of the 'fresh' one.

- The two 'parent' layers come into contact initially in a very thin zone, hence, the initial spatial profiles are step-like.

- It is supposed that the mass fraction of the fresh layer in a newly-formed fold is 0.5.

2.2.4 Molecular transport

The diffusion law proposed by Hirschfelder and Curties (1954) is employed for the present study. The assumptions are as follows:

- The thermal diffusion and the reciprocal thermal diffusion (i.e. the Dufour effect) are negligible.

- The diffusion model of binary mixtures is applied to any diffusional flux of species i in the mixture.

- The local diffusion coefficients of all the atomic elements and the inert species, are supposed to be the same.

Diffusion coefficient

The diffusion coefficient of species i, D_i, is given by the following equation:

$$\frac{1-X_i}{D_i} = \sum_{j \neq i} \frac{X_j}{D_{ij}} \quad , \qquad (2.2\text{-}2)$$

where X_j's and D_{ij}'s are the molar fraction of species j and the binary diffusion coefficient for species i in species j, respectively.

The calculation of various D_{ij}'s is shown in sub-section 2.5.2.

Thermal conductivity of mixture

The thermal conductivity of the mixture, λ, is obtained by weighting the conductivities of species, according to the mass fraction, m_j:

$$\lambda = \sum_j m_j \lambda_j \quad , \qquad (2.2\text{-}3)$$

where λ_j is the thermal conductivity of species j, described in sub-section 2.5.2.

2.2.5 Chemical kinetics

The gas-phase reaction mechanism of hydrogen-oxygen-nitrogen, including reactions of hydroproxyl reported by Dixon - Lewis (1970b), is employed here and is tabulated in Table 2.1. It contains 7 elementary reactions with 8 species where nitrogen is considered to be inert. In the reactions 4 and 7, M refers to a third-body.

Reaction steps	Elementary reaction	Type of reaction
1	$OH+H_2 \underset{K_{-1}}{\overset{K_1}{\rightleftharpoons}} H_2O+H$	Chain propagation
2	$H+O_2 \underset{K_{-2}}{\overset{K_2}{\rightleftharpoons}} OH+O$	" branching
3	$O+H_2 \underset{K_{-3}}{\overset{K_3}{\rightleftharpoons}} OH+H$	" branching
4	$M+H+O_2 \underset{K_{-4}}{\overset{K_4}{\rightleftharpoons}} HO_2+M$	" propagation
5	$H+HO_2 \underset{K_{-5}}{\overset{K_5}{\rightleftharpoons}} OH+OH$	Quadratic branching
6	$H+HO_2 \underset{K_{-6}}{\overset{K_6}{\rightleftharpoons}} H_2+O_2$	Chaintermination
7	$M+H+H \underset{K_{-7}}{\overset{K_7}{\rightleftharpoons}} H_2+M$	Chain termination

TABLE 2.1: THE CHEMICAL REACTION MECHANISM

Forward and reverse reaction rates

For a reacting mixture composed of NS species taking part in all reversible reactions, the forward and reverse rates of the jth reaction step are given as:

$$R_j = K_j (\rho\sigma_m)^{\bar{\alpha}_j} \{ \prod_{\text{all } k} (\rho\sigma_k)^{\alpha'_{k_j}} \} \text{ kg-moles } m^{-3} sec^{-1}; \tag{2.2-4}$$

and,

$$R_{-j} = K_{-j} (\rho\sigma_m)^{\bar{\alpha}_j} \{ \prod_{\text{all } k} (\rho\sigma_k)^{\alpha''_{k_j}} \} \text{ kg-moles } m^{-3} sec^{-1}; \tag{2.2-5}$$

where K_j and K_{-j} ≡ the forward and reverse reaction-rate constant, respectively;

σ_k ≡ the mole number of species k;

σ_m ≡ the reciprocal of the mixture mean molecular weight;

$\bar{\alpha}_j$ ≡ $\begin{cases} 1, & \text{if the reaction involves a third body,} \\ 0, & \text{otherwise;} \end{cases}$

α'_{k_j}, α''_{k_j} ≡ stoichiometric coefficients for species σ_k; i.e. number of (kg-mole) σ_k in reaction j as a reactant and a product, respectively.

The symbol π denotes the product of all quantities of the kind immediately following it; thus, to evaluate the contents of the curly brackets of equation (2.2-4). it is necessary to inspect the jth reaction and to multiply the $(\rho\sigma_k)^{\alpha'_{kj}}$ values appropriate to each of the chemical species appearing on the right-hand side of the equation (2.2-4).

Reaction rate constants

The forward and reverse reaction rate constants are both of Arrhenius type, i.e.

$$K_j = A_j T^{B_j} \text{ Exp } (- \frac{T_j}{T}) \quad ; \qquad (2.2\text{-}6)$$

and, $$K_{-j} = A_{-j} T^{B_{-j}} \text{ Exp } (- \frac{T_{-j}}{T}) \quad ; \qquad (2.2\text{-}7)$$

where the constants A_j's, B_j's and T_j's are supplied for each reaction step, according to the 'standard' reaction-kinetic data reported by Dixon-Lewis (1970b). Further details are given in Section 2.5.3. In addition, the values of K_j and K_{-j} for an elementary reaction obey the relations:

$$K_{-j} = \frac{K_j \ (RT)^{n''_j - n'_j}}{K_j^{\ P}} \quad ; \qquad (2.2\text{-}8)$$

where $K_j^{\ P}$ is the equilibrium constant.

2.3 The Characteristic Time Scales of a Fold

Diffusion time

To indicate the molecular diffusion of the fold, the following time-scale will be used (Spalding, 1979a):

$$t_{diff} \equiv \frac{\rho_u Y_o^2}{(\lambda/C_p)_u} \quad , \qquad (2.3\text{-}1)$$

where Y_o, ρ λ and C_p are the newly-formed fold thickness, density, thermal conductivity and heat capacity of the mixture, respectively; the subscript u indicates unburned condition.

Stretching time

The stretching time, t_{str}, is defined as equal to the reciprocal of the stretching rate which has been discussed in sub-section 2.2.2.

Chemical-reaction time

The reaction time differs for each elementary reaction step. It is therefore necessary to specify a characteristic time (an arbitrarily-chosen reference) to measure the reactiveness of the mixture in the fold. The present hydrogen-oxygen mechanism shows that the reaction time-scale is

dominated by the slow-branching reaction, $H+O_2 \rightarrow OH+O$ (Dixon-Lewis, 1970b). Consequently, this time-scale is chosen as the chemical reaction characteristic time. The following method is adopted:

- The reference reaction rate of this reaction step is first calculated by inserting the maximum values of variables described in equation 2.2-4, appropriate to all chemical species appearing on the burned or unburned layer. i.e.

$$R^*_{ref}=R^*_{ref}\left(T_b,\ \sigma_i,\ \rho_u,\ W_u,\ p\right) \quad , \quad (2.3\text{-}2)$$

  where T_b is the temperature at the burned layer; σ_i is the molar number of species i corresponding to the burned or unburned layer, accordingly; W_u is the molecular weight of the fresh mixture; and p is the pressure.

- The reference reaction time-scale is therefore given by:

$$t^*_{react} = \frac{\frac{\rho_u}{W_u}}{R^*_{ref}} \quad , \quad (2.3\text{-}3)$$

  This reference reaction has a dominant effect on the whole reaction scheme; as it allows the effect of pressure to be fully meaning incorporated.

In the fold biographic study, all the reaction rate constants of the forward and reverse reaction steps (K_j's and K_{-j}'s) must be allowed to change simultaneously by multiplying by the same factor K for each investigation (see Chapter 4). Once the parameter t_{diff}/t_{react} is selected, the factor K is determined by the following relations:

$$t_{react} = \frac{t^*_{react}}{K} \quad . \qquad (2.3\text{-}4)$$

2.4 Governing Equations

Suppose an observer is moving with the fold, then the behaviour of the chemical reaction and the inter-diffusion processes in the fold can be described by a set of one-dimensional, unsteady, differential equations as follows:

Balance of atomic elements

$$\frac{\partial m_{el}}{\partial a} = \frac{\partial}{\partial \psi} \left(\rho^2 D_{el} \frac{\partial m_{el}}{\partial \psi}\right) \quad . \qquad (2.4\text{-}1)$$

Balance of species

$$\frac{\partial \phi_j}{\partial a} = \frac{\partial}{\partial \psi} \left(\rho^2 D_j \frac{\partial \phi_j}{\partial \psi}\right) + \frac{S_{\phi_j}}{\rho} \quad . \qquad (2.4\text{-}2)$$

Conservation of energy

$$\frac{\partial h}{\partial a} = \frac{\partial}{\partial \psi} \left(\rho \frac{\lambda}{C_p} \frac{\partial h}{\partial \psi}\right) + \frac{\partial}{\partial \psi} \left\{\sum_j \left(\rho^2 D_j - \rho \frac{\lambda}{C_p}\right) h_j \frac{\partial \phi_j}{\partial \psi}\right\} \quad , \qquad (2.4\text{-}3)$$

where ψ stands for a kind of stream function, defined by:

$$\psi \equiv \int_o^Y \rho dy \quad , \qquad (2.4\text{-}4)$$

and varies with age, as a consequence of equation (2.2-1), in accordance with:

$$\psi \equiv \psi_o \text{ Exp } (-a/t_{str}) \quad . \qquad (2.4\text{-}5)$$

2.5 Auxiliary Relations

2.5.1 Thermodynamic properties

The dimensionless values of constant pressure heat capacities, enthalpies and entropies of chemical species have been expressed as polynomials in temperature (see Pratt, 1976 and Spalding and Srivatsa et al, 1977).

$$\frac{C_{p_j}}{R} = Z_1+Z_2T+Z_3T^2+Z_4T^3+Z_5T^4; \qquad (2.5\text{-}1)$$

$$\frac{h_j}{RT} = Z_1+ \frac{Z_2T}{2} + \frac{Z_3T^2}{3} + \frac{Z_4T^3}{4} + \frac{Z_5T^4}{5} + \frac{Z_6}{T} ; \qquad (2.5\text{-}2)$$

$$\frac{S_j^{\,o}}{R} = Z_1 \log T +Z_2T+ \frac{Z_3T^2}{2} + \frac{Z_4T^3}{3} + \frac{Z_5T^4}{4} + Z_7 ; \qquad (2.5\text{-}3)$$

There are thus seven coefficients $Z_1,\ldots,Z_7$ corresponding to each chemical species for each of the two temperature ranges, 300^oK to 1000^oK and 1000^oK to 5000^oK. The coefficients are the same as those used in reference (150).

The enthalpy equation (2.5-2) includes both the sensible enthalpy and the standard-state enthalpy of formation. The entropy $S_j^{\,o}$ in equation (2.5-3) includes the low-temperature enthalpy of formation and also the chemical and sensible contributions. The entropy S_j at any arbitrary pressure is given by:

$$S_j = S_j^{\,o} - RT \log \frac{p}{p_o} \quad , \qquad (2.5\text{-}4)$$

where $p_o \equiv$ standard atmospheric pressure.

Here, the enthalpy and the specific heat capacity of mixture are respectively given by:

$$h = \sum_j \sigma_j h_j \quad , \qquad (2.5\text{-}5)$$

$$C_p = \sum_j \sigma_j C_{p_j} \quad , \qquad (2.5\text{-}6)$$

where σ_j is the molar number of species j.

2.5.2 The calculation of laminar-transport properties

Binary diffusion coefficients and species viscosities

Lennard-Jones' (12-6) potential model was adopted for calculating the binary diffusion coefficient and for the species viscosity. The method was based on Chapman-Enskog' theory,(see Fristrom and Westenberg, 1965).

The binary diffusion coefficient, D_{ij}, the absolute viscosity for all species except H_2O, μ_j, and the viscosity of the species H_2O, μ_{H_2O} (see Croom and Leyhe, 1966), are respectively given as:

$$D_{ij} = \frac{1.86\text{x}10^{-7} \left[(M_i+M_j)/M_iM_j\right]^{\frac{1}{2}} T^{3/2}}{p.\ \sigma_{ij}^{2}\ \Omega_{D_{ij}}(1,1)^*} \quad . \qquad (2.5\text{-}7)$$

$$\mu_j = \frac{2.6693\text{x}10^{-6}\ \sqrt{M_jT}}{\sigma_{ij}^{2}\ \Omega_{\mu_j}(2,2)^*} \quad ;$$

$$j \neq H_2O \quad . \qquad (2.5\text{-}8)$$

$$\mu_{H_2O} = \begin{cases} \dfrac{2.5639\ \sqrt{T}}{1+\dfrac{1371}{T} \times 10^{-37.4/T}} \times 10^{-6}; & T \leq 1300^{o}K \\ \\ \dfrac{1.498\ \sqrt{T}}{1+\dfrac{24.51 \times 10^{-6}}{T^2}} & ; T > 1300^{o}K \end{cases}$$

; (2.5-9)

where D_{ij} is the binary diffusion coefficient in $m^2 sec^{-1}$; p is pressure in atm σ_{ij} is the collision diameter of the molecule in angstroms; $\Omega_{D_{ij}}^{(1,1)*}$, the mass-diffusivity collision integral (which is a function of $\frac{k}{\varepsilon_{ij}}$ T); $\Omega_{\mu_j}^{(2,2)*}$, the thermal-conductivity collision integral (which is a function of $\frac{k}{\varepsilon_{jj}}$ T); $\frac{\varepsilon_{jj}}{k}$, the Lennard-Jones force constant in K^o; T is the absolute temperature in K^o; and M_i, M_j are molecular weights.

For bimolecular collisions between unlike molecules, the following approximations are used:

$$\varepsilon_{ij} = \sqrt{\varepsilon_{ii}\ \varepsilon_{jj}} \quad ; \qquad (2.5\text{-}10)$$

$$\sigma_{ij} = \tfrac{1}{2}\ (\sigma_{ii} + \sigma_{jj}) \quad . \qquad (2.5\text{-}11)$$

The collision integral data

Strictly speaking, quantities like ε_{ij}/k, σ_{ij} etc, are characteristic of a particular pair of molecules i and j. The collision diameters σ_{jj} and Lennard-Jones constant ε_{jj}/k are listed in Table 2.2

Species	σ_{jj}, angstroms	ε_{jj}/k ^{o}K	Reference
N_2	3.681	91.5	29
H	2.497	99.8	29
O	3.068	102.2	29
HO_2	4.2	289.0	52
H_2O	2.64	209.0	52
OH	3.11	93.8	29
O_2	3.433	113.0	29
H_2	2.968	33.3	29

TABLE 2.2: THE COLLISION DIAMETERS AND LENNARD-JONES FORCE CONSTANTS

Curve-fitting technique

For the sake of economy, all the binary diffusion coefficients, D_{ij}'s and species viscosities, μ_j's described in equations (2.5-7 - 2.5-9) have been further expressed in the form of AT^B. The corresponding constants of A's and B's were thus obtained

from the least-square linear regression analysis. Further details are given in Appendix A.

The thermal conductivity of species

Thermal conductivity for a pure gas is obtained from the viscosity (see Hirschfelder et al, 1954), i.e.

$$\lambda_j^{o} = \frac{15}{4} \frac{R\ \mu_j}{M_j} \quad . \qquad (2.5\text{-}12)$$

With the aid of the modified Eucken correction (Fristrom and Westenberg, 1965), the species thermal conductivity is expressed as:

$$\lambda_j = (0.115 + 0.178\ C_{p_j})\ \lambda_j^{o} \quad . \qquad (2.5\text{-}13)$$

2.5.3 The reaction-kinetic data

The forward and reverse rate constants of an elementary reaction step described in equations (2.2-4 and 2.2-5) are respectively written in Arrhenius form, e.g.

$$K_j = A_j T^{B_j} \operatorname{Exp}(-T_j/T) \quad ; \qquad (2.5\text{-}14)$$

and $$K_{-j} = A_{-j} T^{B_{-j}} \operatorname{Exp}(-T_{-j}/T) \quad . \qquad (2.5\text{-}15)$$

Standard values of A_j's, B_j's and T_j's for forward and reverse reactions given by Dixon-Lewis (1970b) are listed in Table 2.3.

Reaction j	A_j	B_j	T_j	A_{-j}	B_{-j}	T_{-j}
1	3.303×10^{10}	0	2.7×10^{3}	1.561×10^{11}	0	1.04×10^{4}
2	2.460×10^{11}	0	8.25×10^{3}	1.325×10^{10}	0	-2.203×10^{12}
3	1.798×10^{10}	0	4.7×10^{3}	8.131×10^{9}	0	3.712×10^{3}
4	5.400×10^{9}	0	-7.5×10^{2}	7.701×10^{12}	0	2.278×10^{4}
5	6.996×10^{10}	0	0	3.668×10^{9}	0	1.927×10^{4}
6	1.297×10^{10}	0	0	2.791×10^{10}	0	2.873×10^{4}
7	4.497×10^{9}	0	0	1.378×10^{13}	0	5.227×10^{4}

TABLE 2.3: STANDARD VALUES OF A_j, B_j AND T_j FOR FORWARD AND REVERSE REACTIONS

2.6 Closure

The assumptions made in modifying the diffusion model of binary mixtures for the laminar transport calculation have been presented.

The seven-step mechanism of hydrogen-oxygen-nitrogen system has been incorporated in the theory.

The characteristic times of diffusion, stretching and chemical reaction for the fold have been specified.

The stretching and inter-diffusion processes of the fold have been presented as a set of one-dimensional, unsteady, balance equations.

The thermodynamic properties and the chemical kinetic data have been given.

The method of computing fold is presented in the next chapter.

CHAPTER 3 - METHOD OF COMPUTING FOLD BIOGRAPHY

3.1 Introduction

3.1.1 Preliminary remarks

The governing equations of the fold biography have already been given in the previous chapter. The main task of this chapter is to present the numerical solution procedures for the chemical reaction species concentrations.

Two finite-difference solution methods (TDMA and SENECKS) have been assembled together, providing a rapid solution to problems associated with turbulent combustion.

3.1.2 Layout of the chapter

This chapter comprises of twelve sections. Section 3.2 presents the derivation of the finite-difference equations. With the aid of the source term linearisation, the algorithm, TDMA,is described in Section 3.4. The second algorithm SENECKS is presented in Section 3.11.

The aim is to utilise the advantages of both the TDMA and the SENECKS numerical algorithms for providing an efficient and accurate solution procedure for solving the chemical-kinetic equations. First, the line-by-line solution and the point-by-point adjustment

methods are reviewed in Sections 3.5 and 3.8, respectively. Thereby, an explanation of the new numerical algorithm employed in this thesis is given in Section 3.10.

With the insertion of the appropriate initial and boundary conditions, the method of computing fold biography is completed by the auxiliary information given in Section 3.12.

3.2 The General Form of the Differential Equations Solved

A set of one-dimensional, unsteady, parabolic-type differential equations govern the fold biography. Their general form is given by:

$$\frac{\partial \phi}{\partial a} = \frac{\partial}{\partial \psi} \left(\rho \Gamma_{\phi} \frac{\partial \phi}{\partial \psi} \right) + \frac{S_{\phi}}{\rho} \quad , \qquad (3.2\text{-}1)$$

where ϕ represents atomic element, species or enthalpy;

ρ is the local gas density;

Γ_{ϕ} is the exchange coefficient of entity ϕ ($\equiv$ diffusion coefficient times density, or thermal conductivity divided by specific heat);

S_ϕ is the source term of entity ϕ per unit volume described in Table 3.1;

and, ψ is a kind of stream function described in equation (2.4-5).

ϕ	S_ϕ
concentration of atomic element, m_{el}	0
species concentration $n_j = \frac{m_j}{w_j}$	$\sum_{k=1}^{JJ} (\alpha'_{jk}-\alpha''_{jk})(R_k-R_k)/\rho$
enthalpy, h	$\frac{\partial}{\partial\psi} \{\sum_j (\rho^2 D_j - \rho \frac{\lambda}{C_p}) h_j \frac{\partial n_j}{\partial\psi}\}$

TABLE 3.1: EXPRESSION FOR THE SOURCE TERM S_ϕ FOR THE DEPENDENT VARIABLE ϕ

In practice, the finite-difference technique seems to be the best method for numerical calculations in this type, because it is economic with regard to computer time and storage. Therefore, the above partial-differential equations are reduced to a set of algebraic equations relating the value of a dependent variable at each node in the finite-difference mesh to values at neighbouring nodes.

The resulting equations are then solved numerically.

3.2.1 The coordinate system

The GENMIX computer program (Spalding, 1978a) is especially useful for the present study. In order to use it for this purpose, the Patankar-Spalding coordinate system, $a \sim \omega$ is employed to transform equation (3.2-1) to the following general form:

$$\frac{\partial \phi}{\partial a} + (A+B\omega)\frac{\partial \phi}{\partial \omega} = \frac{\partial}{\partial \omega}\left(C\frac{\partial \phi}{\partial \omega}\right) + D \quad , \qquad (3.2\text{-}2)$$

I		II		III		IV
Variation of with age	+	Lateral convection in w-direction	=	Molecular diffusion of ϕ	+	Creation or destruction source

where ω is the dimensionless stream function defined as:

$$\omega \equiv \frac{\psi-\psi_I}{\psi_E-\psi_I} \quad ;$$

$$A = \frac{\dot{m}''_I}{\psi_E-\psi_I} \quad ;$$

$$B = \frac{\dot{m}''_E-\dot{m}''_I}{\psi_E-\psi_I} \quad ;$$

$$C = \frac{\rho\,\Gamma_\phi}{(\psi_E-\psi_I)^2} \quad ;$$

$$D = \frac{S_\phi}{\rho}$$

The present coordinate system is such that the grid is made up of lines of constant age, intersecting lines of constant non-dimensional stream function ω. On a grid line of constant age, the whole computation is therefore concerned with nodes which lie in the range: $0 \leq \omega \leq 1.0$.

3.2.2 Description of the control volume and the flame-following-grid system

(a) The control volume

The finite-difference equations described in Section 3.4 are derived by integrating the differential equations over small control volumes surrounding each grid node. Figure 3.1 shows the manner in which the dependent variables are stored on the finite-difference grid. It may be noted that the cell boundaries of constant ω lines for dependent variables are lying midway between the two neighbouring nodes at a constant age line. A slightly different practice is adopted for locating dependent variables near the boundaries of the solution domain. This modification is to enable the control volume to coincide with the boundary itself.

Attention is focussed on the cluster of grid nodes shown in Figure 3.2. The value of a dependent variable, $\phi_{i,D}$ at a 'late' age node i, with the values at the

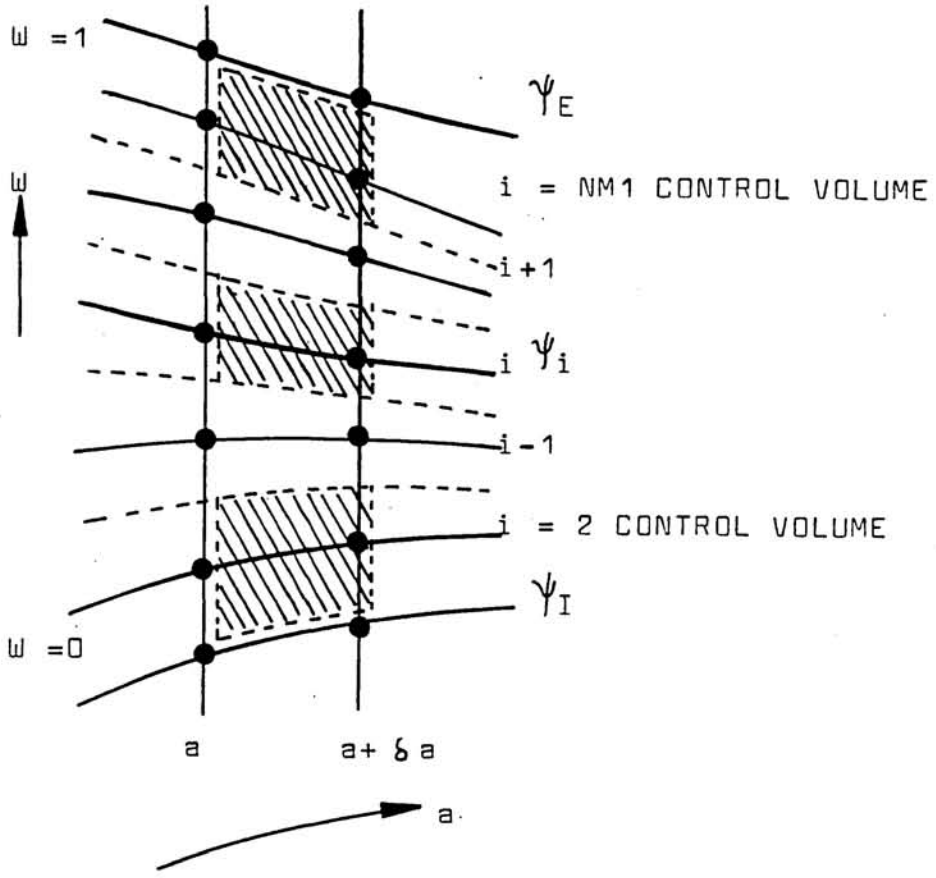

FIGURE 3.1 DEFINITION OF CONTROL VOLUMES.

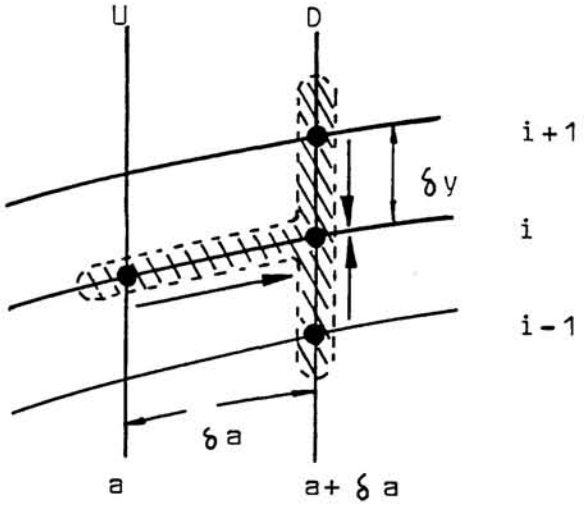

FIGURE 3.2 ILLUSTRATION OF THE FOUR-NODE FORMULA FOR MARCHING INTEGRATION.

two neighbouring nodes at the same age, $\phi_{i-1,D}$ and $\phi_{i+1,D}$, and with the central value at the 'early' age node $\phi_{i,u}$ are connected by a four-node cluster. Therefore, the finite-difference formula for determination of the dependent value at the central 'late' age point is connected with two unknowns ($\phi_{i-1,D}$ and $\phi_{i+1,D}$).

(b) The flame-following-grid system

Since the two 'parent' layers of the fold were initially into contact at a very thin zone, it is desirable, in view of economy, to concentrate the grid nodes only in the reaction zone region.

The grid system, which was originally proposed by Spalding and Stephenson (1971a), moves with the direction of the propagating flame, and the entrainment and de-entrainment adjustments are employed here. Further details will be discussed in sub-section 3.12.3. This kind of grid system is defined as the flame-following-grid system.

As illustrated in Figure 3.3, the domain of integration covers only the reaction zone. As a consequence of the choice of the grid system, the hot and cold boundaries are located at the edges of the region where significant physical and chemical variations occur within the calculation domain.

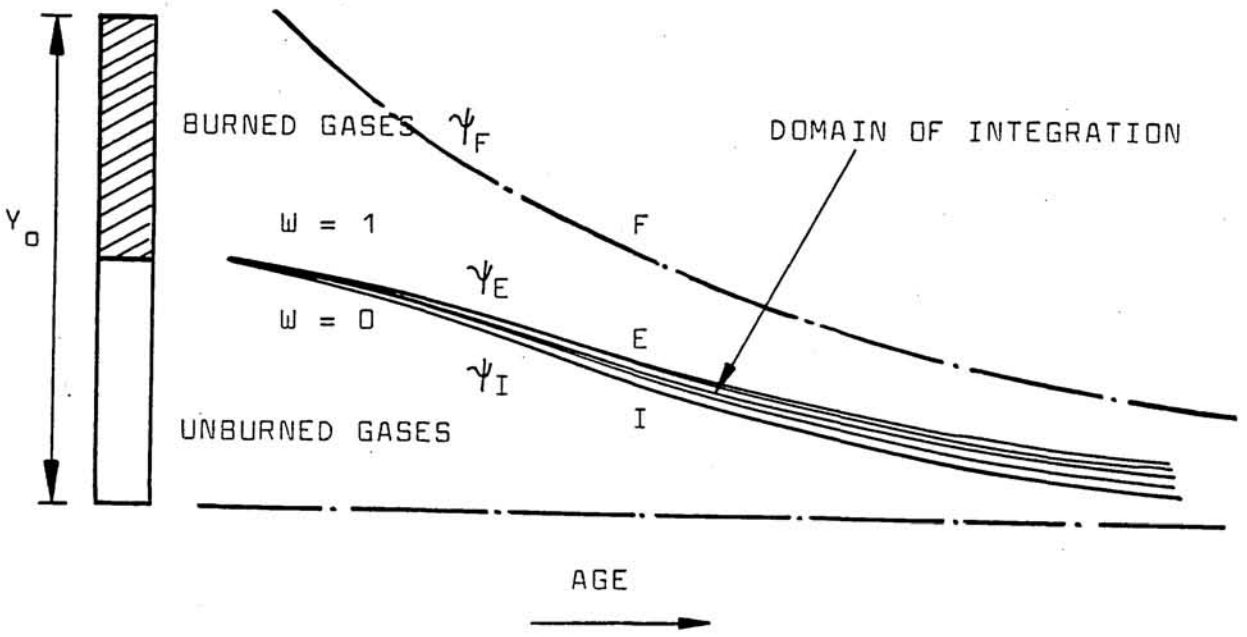

FIGURE 3.3 ILLUSTRATION OF THE FLAME-FOLLOWING-GRID TECHNIQUE.

3.3 The Finite-Difference Form Expressions

There are three different expressions which can be used to express the chemical kinetic equations in the finite-difference form, namely, the fully explicit scheme, the Crank-Nicholson scheme and the fully-implicit scheme.

When the fully explicit scheme is chosen to solve the transient problem, the finite-difference equations, except for the time-dependent term are expressed explicitly in terms of 'early' time values. Hence, all dependent variables ϕ's at the 'late' time are very easy to obtain. However, instability problems arise when the marching time step is large. This time-step limitation causes excessive computer time for any computation.

In the Crank-Nicholson finite-difference scheme, all dependent variables ϕ's at the node point P are expressed as: $\frac{1}{2}(\phi_P^u + \phi_P^D)$; where the superscripts 'u' and 'D' refer to the 'early' time and the 'late' time, respectively. The equations are therefore simultaneous. The advantage of this method is that an arbitrarily longer time step can be chosen in comparison with the fully explicit expression. This method is often called semi-implicit.

When the fully implicit scheme is considered, all the space derivatives are expressed at the 'late' time. The general finite-difference equation is therefore more implicit and stable. This gives a set of simultaneous algebraic equations which are usually solved by either of the following methods:

- The line-by-line solution procedure.
- The point-by-point adjustment procedure.
- The inversion of large matrices.

The large matrix inversion methods are seldom used because of large computer storage and time required. For this reason, only the line-by-line procedure and simultaneous point-by-point adjustment are employed here. The solution procedures will be discussed in turn.

3.4 The Line-by-Line Procedure

Integration of equation (3.2-2) for ϕ over an appropriate control volume yields:

$$D_i \phi_{i,D} = A_i \phi_{i+1,D} + B_i \phi_{i-1,D} + C_i$$

$$+ \frac{S_{\phi_i}}{\rho} (\omega_{i+\frac{1}{2}} - \omega_{i-\frac{1}{2}}) \, \delta a \quad , \qquad (3.4\text{-}1)$$

where $\phi_{i,D}$ is the value of a dependent variable at a downstream (i.e. late age) node i; $\phi_{i+1,D}$; $\phi_{i-1,D}$ are values of the dependent variable at nodes i+1 and i-1 respectively; A_i, B_i, C_i, D_i are coefficients containing the effects of convection and diffusion; and S_{ϕ_i} is the source term.

Now, the solution algorithm for solving the chemical kinetic equations is focussed on the fully-implicit scheme. In solving NS number of reacting species in addition to one more enthalpy balance equations, this algorithm preserves a tri-diagonal matrix structure of a set of (NS+1) linear equations. Of course, the solution procedure requires the source term linearisation technique. This technique is described in subsection 3.4.1 below. Each dependent variable along a grid line is therefore solved by a simple recurrence formula (equation 3.4-5).

3.4.1 Source term linearisation

The forward and reverse reaction rates of any elementary reaction steps have already been described in Section 2.2.5. The total reaction sources of any species ϕ appearing in all reaction steps are therefore given by:

$$S_\phi = \sum_{j=1}^{JJ} (\alpha'_{\phi_j} - \alpha''_{\phi_j}) (R_j - R_{-j}) \quad , \qquad (3.4\text{-}2)$$

where JJ is the number of distinct reaction steps considered in the reaction mechanism; α'_{ϕ_j} and α''_{ϕ_j} are the total stoichiometric coefficients of a reactant and product, respectively in reaction j of species ϕ.

A species not taking part in any of the reactions, i.e. $S_\phi=0$, is said to be inert.

Now, the task is to linearise the chemical sources. The source term in equation (3.4-2) is usually expressed as follows:

$$S_\phi = S_\phi^* + \frac{\partial S_\phi}{\partial \phi_P} (\phi_P - \phi_P^*)$$

$$= (S_\phi^* - \frac{\partial S_\phi}{\partial \phi_P} \phi_P^*) + \frac{\partial S_\phi}{\partial \phi_P} \phi_P$$

$$= S_u + S_P \phi_P \quad , \qquad (3.4\text{-}3)$$

where ϕ_P^* is the value of species ϕ_P at 'old-time'; and

S_ϕ^* is the corresponding source term of ϕ_P^*.

The $\frac{\partial S_\phi}{\partial \phi_P}$ term can be obtained by first differentiating the total S_ϕ term with respect to the reacting species ϕ, then taking the total derivative over all those elementary reaction steps, in which species ϕ is involved.

$$\frac{\partial S_\phi}{\partial \phi_P} = \sum_{j=1}^{JJ} \{(\alpha'_{\phi_j} - \alpha''_{\phi_j})(\Sigma \frac{\partial R_j}{\partial \sigma'_{\phi_j}} - \Sigma \frac{\partial R_{-j}}{\partial \sigma''_{\phi_j}})\} \quad ;(3.4\text{-}4)$$

where σ_{ϕ_j} = species ϕ appears in reaction step j;

σ_{ij} = species i appears in reaction step j;

$$\frac{\partial \sigma_{ij}'}{\partial \sigma_{\phi_j}'} = \begin{cases} 1, & \text{if } \sigma_{\phi_j}' = \sigma_{ij}' \\ 0, & \text{otherwise} \end{cases} ;$$

$$\frac{\partial \sigma_{ij}''}{\partial \sigma_{\phi_j}''} = \begin{cases} 1, & \text{if } \sigma_{\phi_j}'' = \sigma_{ij}'' \\ 0, & \text{otherwise;} \end{cases}$$

the superscripts '′' and '″' refer to the forward reaction and reverse reaction, respectively.

Further details of the treatment of S_u's and S_p's are described in Appendix B.

3.4.2 The Tri-Diagonal Matrix Algorithm (TDMA)

With the aid of the source term linearisation, the general finite-difference equation (3.4-1) is rewritten as:

$$\phi_i = A_i' \, \phi_{i+1} + B_i' \quad , \qquad (3.4\text{-}5)$$

where $A_i' = A_i/(D_i - B_i A_{i-1}')$;

$$B_i' = (B_i B_{i-1}' + C_i)/(D_i - B_i A_{i-1}').$$

With the insertion of the appropriate initial and boundary conditions, TDMA provides a means of solving the equation by direct substitution.

3.4.3 The balance of the atomic element equations

The atomic element, $m_{el,i}$, at the local grid node i is defined by:

$$m_{el,i} = \sum_{j=1}^{NS} a_{el,j}^{L} \, \sigma_j$$

$$el=1,\ldots,NLM \quad , \qquad (3.4\text{-}6)$$

in which σ_j stands for local molar number of species j; $a_{el,j}^{L}$ stands for the number of kg-atoms of element el per kg-mole of species j.

The inert species and the elements constituting the reacting species are both governed by a source-free differential equation. Since the local diffusion coefficients of all the elements and the inert species are supposed to be the same, the concentrations of the elements and the inert species at any point are linearly related, i.e.

$$\frac{m_{el,I} - m^*_{el,I}}{m^*_{el,E} - m^*_{el,I}} = \frac{m_{inert,i} - m^*_{inert,I}}{m^*_{inert,E} - m^*_{inert,I}} , \qquad (3.4\text{-}7)$$

where I and E refer to the two boundaries; the superscript '*' denotes the initial conditions; and $m_{el,i}$, $m_{inert,i}$ are local values of the concentrations of the element and the inert gas respectively.

The number of differential equations for the species concentrations can therefore be reduced from NS to NS-NLM, while the rest of the species concentrations are obtained by algebraic substitution, in accordance with:

$$\sigma_k = \{m_{el} - \sum_{j \neq k} a^L_{el,j}\, \sigma_j\} / a_{el,k} ,$$

$$k = NS-NLM+1, \ldots, NS$$

$$el = 1, \ldots\ldots, NLM \qquad . \qquad (3.4\text{-}8)$$

3.5 Review of the Line-by-Line Procedure

Spalding and Stephson (1971a) applied the fully-implicit form of the finite-difference equation to calculate the unsteady, laminar, plane-flame propagation problem. Tsatsaronis (1978) used the same method to solve a similar problem. Golvichev et al (1976) applied a modified version of the Crank-Nicholson semi-implicit scheme to solve the chemical kinetic processes in two-dimensional turbulent reactive gas flows.

Because of each finite-difference equation being automatically satisfied line-by-line, iteration procedure is not necessary. However, the stability of the computations is sensitive to the solution order of the NS+1 equations. Furthermore, the marching time step size is determined by the fastest reaction step while the global reaction scheme is dominated by the slowest one. Therefore, in order to obtain a satisfactory result, excessive computer time is usually required.

3.6 The Nature of the Difficulties

The finite-difference method for solving the chemical kinetic equations in turbulent reacting flows described above. suffers from a number of associated difficulties. The fact is that the reaction rates are non-linear and coupled together in the production term of chemical species equations. The computational procedures

become difficult because many reactions including the free radical species are involved and in disparate time scales. In some regions of the flow field, some of the reaction rates change very rapidly while the rest are hardly changed at all.

The stiffness and disparate time scales of the chemical-kinetic equations are the important features of numerical analysis for turbulent combustion processes.

3.7 The Alternatives

To cope with the 'stiffness' problems, it has been suggested that the above set of simultaneous equations (3.4-1) should be solved by a Gauss-Seidel point-by-point iteration procedure (McBride 1971 and Pratt 1976). That is, the solution of the algebraic equations is simultaneously adjusted at a given 'cell' until the residual error is reduced to zero. Obviously, this error will spread in the neighbouring cells. However, the residual error can be eliminated by employing an explicit sweep along the line of grid nodes until convergence is achieved.

The choice of point-by-point adjustment methods for solving the stiff chemical kinetic equations is

due to two reasons: (a) the non-linearity of the Arrhenius source terms causes the line-by-line procedure to fail unless the grid sizes are sufficiently small; and (b) the methods of simultaneous iteration procedure are generally satisfied point-by-point, hence it is easier to obtain satisfactory convergence.

3.8 Review of the Point-By-Point Procedure

Gordon and McBride (1971) used this numerical algorithm to calculate the complex chemical equilibrium processes in rocket performance. The improvement of the accuracy of one-dimensional chemical kinetic calculation was discussed by Liniger and Willoughby (1967) and Lapidus and Seinfeld (1971). With the aid of the point-by-point procedure, they suggested employing either a trapezoidal approximation, or an exponential function to fit the non-linearity of the net reaction rates over an integral time interval. This method was also employed by Pratt (1976).

On the other hand, Hindmarsh (1972) used the stiffly stable, linear multiple methods of Nordsieck and Gear to solve a system of ordinary differential equations. With the aid of these methods, the marching time steps were restricted to only small values. Accuracy was achieved by optimising both step size and the solution order.

Since the chemical kinetic reactions normally change much faster than the hydrodynamic ones, the corresponding conservation equations must be solved separately. The special feature of the solution method is that two different numerical algorithms should be employed, each appropriate to the nature of the particular conservation equation being solved. The numerical solution procedure for this kind of problem can be divided generally into two categories, namely, (a) the two-operators splitting method; and (b) the super-iteration method. These methods are discussed below.

3.8.1 The two-operators splitting methods

The operator-splitting methods were employed to handle the fluid mechanical problems in association with combustion processes. The theoretical basis was described by Yanenko (1971). There are two classes of numerical splitting, namely, Alternating Direction Implicit Splitting and Majorant Splitting.

ADI Splitting

When the method of ADI Splitting is chosen, each marching time step is divided into many fractional steps. During a fractional step, some source terms in the finite-difference equations are expressed implicitly, then, in the next fractional step, another

set of terms are taken implicitly and an explicit combination of the remaining term is used. This type of splitting is claimed to have absolute consistency.

Majorant Splitting

On the other hand, the method of Majorant splitting allows some terms of the finite-difference equations during each fractional step to be considered, while the remaining terms are ignored. It produces consistency only after all fractional steps are completely computed.

Rizzi and Bailey (1975) employed this method to solve a three-dimensional supersonic inviscid, reacting flow. Thomas and Wilson (1975) applied the same method to solve the chemically reacting flow in turbulent free jets. Kee and Miller (1978) used a symmetric splitting-operator to calculate two-dimensional axisymmetric laminar-jet diffusion flames.

3.8.2 The super-iteration method

This method enables the hydrodynamic equations to be solved by TDMA while the conservation of chemical species and energy is solved point-by-point by the standard Newton-Raphson iteration procedure. Wormeck and Pratt (1976) applied this method to calculate two-dimensional steady parabolic turbulent flows.

A complete cycle of 'super-iteration' for solving the parabolic reacting flow is outlined:-

(1) Solve the hydrodynamic equations by TDMA.

(2) Set all reaction sources to zero and obtain the first 'guess' values of all reacting species along a grid line.

(3) Express the finite-difference equations of chemical species in a point-by-point scheme.

(4) Establish an adiabatic chemical equilibrium solution.

(5) Approach the solution from equilibrium to kinetic state.

(6) Repeat step 5, until the chemical kinetic equations are satisfied point-by-point.

(7) Adjust the hydrodynamic field.

3.9 Criticism of the Existing Methods

When the two-operators method is used, most of the overall computer time is spent on the chemistry step. Since the procedure is iterative in nature, convergence can only be achieved over a very fine fractional step. Therefore, the method developed by Kee and Miller (1978) required long execution time.

Alternatively, the super-iteration method has been proved successful and shown to be moderately accurate and stable (Pratt and Wormeck 1975 and 1977; Spalding and Srivatsa 1978). However, this still requires excessive computer time for comparable accuracy. Since the iteration procedure from step 5 to step 6 described in sub-section 3.8.2 is inefficient, convergence can only be achieved in an extremely slow manner. Table 3.2 illustrates the computer times which are cited from the above references.

Reference	Computer code	Grid	Computer	Execution time	Time/Grid node
77	Two operators method	50x1000	CDC6600	4 hrs	0.288sec
150	CREK	1x114	UNIVAC* 1108	15 secs	0.053sec
25	GCKP	1x704	UNIVAC 1108	76 secs	0.043sec
	ESCIMO (The present computer code)	60x1000	CDC6600	327 secs	0.005sec

TABLE 3.2: COMPARISON ON THE COMPUTER TIMES OF DIFFERENT CHEMICAL KINETIC SOLVERS

*

relative machine speed	
UNIVAC 1108	0.4
CDC6600	1

One of the objectives of the present work was to develop a new solution procedure which employs two successful algorithms (TDMA and SENECKS) for solving the complex chemical kinetic processes. This solution procedure provides an efficient and accurate solution of problems associated with chemically reacting gas mixtures and will be discussed in the next section and employed throughout this thesis.

Comparison of the above methods with the present solution procedure shows that the present computer code is about 50 times faster than the two-operators splitting method (Kee and Miller, 1978) and about 10 times faster than the CREK code which was originally developed by Wormeck and Pratt (1976). Further verification will be described in Chapter 6.

3.10 The Method Employed

The solution procedure was of a 'hybrid' type, because it combined the desirable portions of two numerical algorithms, namely, TDMA and SENECKS. The TDMA algorithm has been already described. The SENECKS procedure will be described in Section 3.11.

The overall solution procedure is summarised below. When the reactions are stiff, the chemical kinetic equations are first solved by the TDMA traverses. An

iterative point-by-point adjustment is adopted after the TDMA has been traversed in order to yield satisfactory convergence.

However, if the chemical reactions are not considered stiff, the TDMA traverse alone is sufficient to solve the problem. In this circumstance, the point-by-point adjustment of SENECKS is not required, because the reaction rates are so low that the non-linearity of the Arrhenius terms is relatively weak.

The solution procedure is outlined briefly in the following steps.

(1)
- Set up the initial conditions.
- Assign the boundary conditions, appropriately.

(2)
- Store the 'early' age species values.

(3)
- Linearise the reaction source.
- An inert species, a (NS-NLM-1) number of reacting species and one enthalpy equation are solved along a grid line by the TDMA traverse.
- The rest of NLM reacting species are computed by the element balance algebraic equations.
- Compute the local temperature and density.

(4) • When the local reaction rate is high*, then all reacting species require further treatment with the SENECKS procedure.

(5) • If the point-by-point adjustment is necessary, the value of ϕ_i^* appearing in equation (3.11-2) must be provided initially by the TDMA traverse (because this gives the best initial estimate).

• A set of Newton-Raphson correction equations is further solved simultaneously and iteratively at the grid node until all the Newton-Raphson correction variables are negligibly small. Hence, all the reacting species and the enthalpy equations are satisfied point-by-point.

• Recalculate the corresponding temperature and density.

---

* For any species, if any of these 'late' age values obtained by TDMA are larger or smaller than 25% of their corresponding 'early' age values, the local reaction rate is said to be high.

(6) • Adjust the hydrodynamic field, if necessary.
• Calculate the cross-stream distance.
• Calculate the cross-stream profiles.

(7) • Advance in age, until the domain of integration is achieved.

3.11 Description of the "SENECKS" Solution Procedure

(Solver for Equilibrium and Non-Equilibrium Chemical-Kinetic Systems)

The task is to describe the point-by-point adjustment method. This will be presented in two parts: (a) the method of equilibrium solution; and (b) the method of finite-rate solution.

In view of point-by-point adjustment, the solution of the simultaneous, algebraic finite-difference equations is obtained iteratively. It is therefore important to formulate the equations in a way which will ensure the convergence of the iterative scheme.

The general finite-difference equation for the point-by-point adjustment can be rewritten from equation (3.4-1) as:

$$f_\phi = D_i\ (\phi_i - \phi_i^*) - \frac{S_{\phi_i}}{\rho}\ (\omega_{i+\frac{1}{2}} - \omega_{i-\frac{1}{2}})\ \delta a, \quad (3.11\text{-}1)$$

where f_ϕ is a Newton-Raphson function of species concentration or enthalpy (see McBride 1971);

$$\phi_i^* = \frac{A_i}{D_i}\ \phi_{i+1} + \frac{B_i}{D_i}\ \phi_{i-1} + \frac{C_i}{D_i}\ , \quad (3.11\text{-}2)$$

and S_{ϕ_i} is the total source term of ϕ_i.

In addition, the C_i's and D_i's in equation (3.11-2) do not include any contributions from the source term.

3.11.1 The solution of chemical equilibrium equations

When the reaction rate is infinite, the combustion process will approach equilibrium. Since the overall chemical reaction is so fast in both directions, it can be supposed that equilibrium does exist. Therefore, the residence time approaches infinity. Under these circumstances,the reaction free energy is minimised. The composition of the gas can be determined by either one of the following methods:-

(1) Gibbs function minimisation.

(2) Equilibrium constant formulation.

(3) Equating forward and reverse rates at specified temperature and pressure.

The method of minimisation of Gibbs function for solving the gas-phase of the chemical-equilibrium equations is employed here. (See McBride 1971; Pratt 1976, and Spalding and Srivatsa 1977), i.e.

$$dG = \sum_{k=1}^{NS} g_k \, d\,\sigma_k = 0 \quad , \qquad (3.11\text{-}3)$$

where g_k is the partial molar Gibbs function defined by:

$$g_k = h_k - TS_k = h_k^o - TS_k^o + RT \log \left(\frac{\sigma_k}{\sigma_m}\right)$$

$$+ RT \log \left(\frac{p}{p_o}\right) \quad , \qquad (3.11.4)$$

σ_k is the molar number of species k; and σ_m is the reciprocal mixture molecular weight.

In addition, the NLM number of the atomic balance equations must also be satisfied, for instance,

$$\sum_{k=1}^{NS} a_{ik}^L \sigma_k - \sum_{k=1}^{NS} a_{ik}^L \sigma_k^* = 0$$

$$i=1, \text{NLM} \quad , \qquad (3.11\text{-}5)$$

where a_{ik}^L stands for the number of kg-atoms of element i per kg-mole of species k.

The method of Lagrangian undetermined multipliers is adopted for searching the condition of minimisation. Therefore, equations (3.11-3) and (3.11-5) can be

replaced by a set of equations given by:-

$$g_k + \sum_{i=1}^{NLM} \lambda_i \, a_{ik}^L = 0$$

$$k=1, NS \qquad ; \qquad (3.11\text{-}6)$$

in addition to the NLM constraint equations,

$$\pi_i = - \frac{\lambda_i}{RT} \qquad , \qquad (3.11\text{-}7)$$

where NS is the number of species and π_i represents the non-dimensional Lagrangian multiplier.

The details of the mathematical formulations can be found in reference (150).

A set of Newton-Raphson correction equations are thus given by:

$$\sum_{i=1}^{N} \left(\frac{\partial f_x}{\partial x_i}\right) \Delta x_i = - f_x \qquad , \qquad (3.11\text{-}8)$$

where f_x represents the correction function;

x_i is the correction variable; and

N is the number of choices of the correction variables.

The number of choices for the correction variables can be reduced further from (NLM+NS+2) to (NLM+2) by eliminating the correction variables $\Delta\log\sigma_k$'s, (Gordon and McBride, 1971). Subsequently, the solution matrix only involves NLM of the non-dimensionalised Lagrangian multipliers, π_i; a reciprocal of the mixture molecular weight, $\Delta\log\sigma_m$; and the temperature $\Delta\log T$.

The correction equations for the Lagrangian multiplers π_i's are:

$$\sum_{i=1}^{NLM} \left| \sum_{k=1}^{NS} a_{ik}^{L} \, a_{jk}^{L} \, \sigma_k \right| \pi_i + \left| \sum_{k=1}^{NS} a_{jk}^{L} \, \sigma_k \right| \Delta\log\sigma_m$$

$$+ \left| \sum_{k=1}^{NS} a_{jk}^{L} \, \sigma_k \left(\frac{h_k}{RT}\right) \right| \Delta\log T = \sum_{k=1}^{NS} a_{jk}^{L} \, \sigma_k^{*} - \sum_{k=1}^{NS} a_{jk}^{L} \, \sigma_k$$

$$+ \sum_{k=1}^{NS} a_{jk}^{L} \, \sigma_k \left(\frac{g_k}{RT}\right) \quad , \; j = 1,NLM \; . \qquad (3.11\text{-}9)$$

The correction equation for the reciprocal mixture molecular weight σ_m is:

$$\sum_{i=1}^{NLM} \left| \sum_{k=1}^{NS} a_{ik}^{L} \, \sigma_k \right| \pi_i + \left| \sum_{k=1}^{NS} \sigma_k - \sigma_m \right| \Delta\log\sigma_m$$

$$+ \left| \sum_{k=1}^{NS} \sigma_k \left(\frac{h_k}{RT}\right) \right| \Delta\log T = \sigma_m - \sum_{k=1}^{NS} \sigma_k + \sum_{k=1}^{NS} \sigma_k \left(\frac{g_k}{RT}\right)$$

(3.11-10)

The correction equation for the temperature is:

$$\sum_{i=1}^{NLM} \left| \sum_{k=1}^{NS} a_{ik}^{L} \sigma_k \left(\frac{h_k}{RT}\right) \right| \pi_i + \left| \sum_{k=1}^{NS} \sigma_k \left(\frac{h_k}{RT}\right) \right| \Delta\log\sigma_m$$

$$+ \left| \sum_{k=1}^{NS} \sigma_k \left(\frac{C_{p_k}}{R}\right) + \sum_{k=1}^{NS} \sigma_k \left(\frac{h_k}{RT}\right)^2 + \frac{1}{RT} \frac{\partial Q}{\partial \log T} \right| \Delta\log T$$

$$= \sum_{k=1}^{NS} \sigma_k^* \frac{h_k^*}{RT} - \sum_{k=1}^{NS} \sigma_k \left(\frac{h_k}{RT}\right) - \frac{Q}{RT}$$

$$+ \sum_{k=1}^{NS} \sigma_k \left(\frac{h_k}{RT}\right) \left(\frac{g_k}{RT}\right) \quad . \qquad (3.11\text{-}11)$$

With the aid of an initial estimation of σ_j^*, j=1,NS and T^* (which has already been obtained by TDMA in the first sweep), the above equations are simultaneously solved point-by-point by a standard Gaussian elimination procedure. During the computation, the coefficient of $\Delta\log\sigma_m$ in equation (3.11-10) could be reduced to zero and the above correction matrix will then become singular. It is therefore necessary to interchange between the row involving the zero coefficient of $\Delta\log\sigma_m$ and the row with the largest coefficient of $\Delta\log\sigma_m$'s. Since all the other diagonal elements are positive, the occurence of the singular matrix can be avoided.

The new values of such variables, are then calculated by:

$$\log\sigma_i^{(k+1)} = \log\sigma_i^{(k)} + \eta\ \Delta\log\sigma_i^{(k)}$$

$$i=1,NS \qquad ;(3.11\text{-}12)$$

$$\log\sigma_m^{(k+1)} = \log\sigma_m^{(k)} + \eta\ \Delta\log\sigma_m^{(k)} \qquad ;(3.11\text{-}13)$$

$$\log T^{(k+1)} = \log T^{(k)} + \eta\ \Delta\log T^{(k)} \qquad ;(3.11\text{-}14)$$

where the superscript 'k' indicates the iteration number, and η is an under-relaxation factor ($0<\eta<1$).

The convergence criterion and the under-relaxation factor will be discussed in sub-section 3.11.3.

3.11.2 The solution of chemical kinetic equations

When the reaction rates are finite, the Newton-Raphson correction equations are given by:-

Species balance equation

$$f_k = E_i\ (\sigma_k-\sigma_k^*) + \sum_{j=1}^{JJ} \{(\alpha'_{k_j}-\alpha''_{k_j})(R_j-R_j)\}$$

$$k=1,NS \qquad , \qquad (3.11\text{-}15)$$

where E_i is the coefficient of the grid cell, and is defined by:

$$E_i \equiv \frac{D_i \rho_i}{(\omega_{i+\frac{1}{2}} - \omega_{i-\frac{1}{2}})\ \delta a} \quad . \tag{3.11-16}$$

<u>The reciprocal mixture molecular weight</u>

$$f_M = \sum_{k=1}^{NS} \sigma_k - \sigma_m \quad . \tag{3.11-17}$$

<u>Enthalpy</u>

$$f_T = -\frac{h^*}{RT} + \sum_{k=1}^{NS} \frac{\sigma_k\ h_k}{RT} + \frac{Q}{RT} \quad , \tag{3.11-18}$$

where Q stands for the total source term of the mixture enthalpy.

The following matrix represents the formulated equations:

$$A\vec{X} = \vec{B} \quad , \tag{3.11-19}$$

where $\vec{X}$ and $\vec{B}$ are column vectors with elements,

$$X_i = \begin{cases} \Delta \log \sigma_k & , \ k=1,NS \\ \Delta \log \sigma_m & \\ \Delta \log T & . \end{cases} \tag{3.11-20}$$

$$B_i = \begin{cases} -f_k & , \ k=1,NS \\ -f_M & \\ -f_T & . \end{cases} \tag{3.11-21}$$

The coefficient matrix A is a square matrix, with elements,

$$A_{ij} = \begin{cases} \dfrac{\partial f_i}{\Delta \log\sigma_k} & , \quad k=1,NS \\[2ex] \dfrac{\partial f_i}{\Delta \log\sigma_m} & \\[2ex] \dfrac{\partial f_i}{\Delta \log T} & , \quad i=1,NS+2 \end{cases} \quad . \qquad (3.11\text{-}22)$$

The above equations are also solved iteratively by the standard Gaussian elimination technique. The new values of the variables are:

$$\log\sigma_i^{(k+1)} = \log\sigma_i^{(k)} + \eta\ (\Delta\log\sigma_i)^{(k)}$$

$$i=1,NS \qquad . \qquad (3.11\text{-}23)$$

$$\log\sigma_m^{(k+1)} = \log\sigma_m^{(k)} + \eta\ (\Delta\log\sigma_m)^{(k)} \quad .(3.11\text{-}24)$$

$$\log T^{(k+1)} = \log T^{(k)} + \eta\ (\Delta\log T)^{(k)} \quad .(3.11\text{-}25)$$

The determination of η and the convergence criterion will be discussed below.

3.11.3 Under-relaxation and convergence criterion

The under-relaxation parameter η is determined at each iteration from:

$$\eta = \text{minimum of } (1,\ \eta_1,\ \eta_2) \quad , \qquad (3.11\text{-}26)$$

where η_1 and η_2 are quantities which are defined below:

(a) For T, σ_m and species with $\frac{\sigma_j}{\sigma_m} > 10^{-8}$ and $\Delta\log\sigma_j > 0$, η_1 is defined as:

$$\eta_1 = \frac{2}{\text{maximum}\left|\,|\Delta\log T|, |\Delta\log\sigma_m|, |\Delta\log\sigma_j|\,\right|} \quad . \qquad (3.11\text{-}27)$$

This causes the correction variables T, σ_m and σ_j to be scaled so that none of the variables is increased by more than a factor of 7.39 |=Exp(2)| on any one iteration.

(b) For species with $(\frac{\sigma_j}{\sigma_m}) < 10^{-8}$ and $\Delta\log\sigma_j > 0$, η_2 is defined as:

$$\eta_2 = \frac{\log(10^{-4}) - \log\frac{\sigma_j}{\sigma_m}}{\Delta\log\sigma_j - \Delta\log\sigma_m} \quad . \qquad (3.11\text{-}28)$$

This scales all the corrections so that the species with σ_j initially less than 10^{-8}, increases to no more than 10^{-4}.

A convergence criterion of the σ_j's is given below:

$$\left(\frac{\sigma_j}{\sigma_m}\right) \left|\Delta \log \sigma_j\right| \leq 1.0 \times 10^{-10}$$

$$j=1,NS \qquad , \qquad (3.11\text{-}29)$$

3.12 Auxiliary Information

Attention is concentrated here on auxiliary information of the flame-following-grid technique for calculating the stretched-fold. These include: the initial profile prescriptions, the boundary conditions and the entrainment adjustment.

3.12.1 Initial Conditions

A single fold which contains two layers of equal masses of cold pre-mixed hydrogen-oxygen fuel and the equilibrium hot product is considered.

The unburned layer

The presumptions on the composition, the equivalence ratio, the temperature at the unburned layer and the initial fold thickness will be shown in Chapter 4.

The burned-layer

The concentrations of the hot products, which are supposed to be at equilibrium, are obtained from known concentrations of the fresh layer by utilising the mixture enthalpy and the minimisation of Gibbs energy described in sub-section 3.11.1.

Thickness of the reaction zone

The thickness of the reaction zone initially is assumed to be less than 3% of the newly-formed fold thickness. Thereby, the assumptions of concentrations distribution within the zone have a negligible effect upon the numerical results.

The structure of the reaction zone

Species concentration

The concentration distribution in this region is supposed to be linearly dependent on the dimensionless stream function ω, i.e.

$$m_{j.o}\{\omega\} = (m_{j,b}-m_{j,u})\ \omega + m_{j,u} \quad , \qquad (3.12\text{-}1)$$

where $m_{j,o}\{\omega\}$ is the mass fraction of species j at ω; the subscript 'o' indicates the initial conditions; $m_{j,b}$ and $m_{j,u}$ are the mass fractions of species j at the burned layer and the unburned layer, respectively.

Temperature

The enthalpy of the mixture is supposed initially to be uniform in the fold. Since the unburned temperature and concentrations at the unburned layer are known, an iterative procedure is employed to calculate the temperature at every grid point ensuring the uniformity of mixture enthalpy. The details of the procedure are given in sub-section 3.12.4.

3.12.2 Boundary Conditions

The flame-following-grid system ensures that the significant physical and chemical changes occur only in the integration domain. Consequently, all the conservation equations have zero diffusive flux on the I, E boundaries.

At I boundary

Species

$$\frac{\partial \sigma_I}{\partial a} = \frac{\partial \sigma_c}{\partial a} = \frac{S_{\phi_I}}{\rho_c} \quad . \qquad (3.12\text{-}2)$$

Enthalpy

$$h_I = (\sum_j \sigma_j h_j)_I \quad . \qquad (3.12\text{-}3)$$

At E boundary

Species

$$\frac{\partial \sigma_E}{\partial a} = \frac{\partial \sigma_H}{\partial a} = \frac{S_{\phi_E}}{\rho_H} \quad . \qquad (3.12\text{-}4)$$

Enthalpy

$$h_E = (\sum_j \sigma_j h_j)_E \quad . \qquad (3.12\text{-}5)$$

The above balance equations of species and enthalpy at I and E boundaries, are computed simultaneously, by the SENECKS procedure described in Section 3.11.

3.12.3 Entrainment formulae

The mass flow rates $\dot{m}''_I$ and $\dot{m}''_E$, across the cold and hot boundaries respectively, are determined by

the following entrainment formulae:

At I boundary

$$A_1 = \frac{t_{str}}{t_{str}+t_{react}} \quad , \qquad (3.12\text{-}6)$$

$$A_2 = \frac{t_{react}}{t_{str}+t_{react}} \quad , \qquad (3.12\text{-}7)$$

$$R_I = \frac{1}{0.01} \left| \frac{T_2-T_1}{T_{max}-T_{min}} \right| \quad , \qquad (3.12\text{-}8)$$

$$F_I = F_{I,p} \; R_I^{0.1} \quad , \qquad (3.12\text{-}9)$$

$$\dot{m}''_{ch} = \psi_{FOLD} \cdot \frac{d\tilde{\tau}}{da} \quad , \qquad (3.12\text{-}10)$$

$$\dot{m}''_{I,diff} = \frac{2 \; \Gamma_{\phi,NI} \; R_I}{(\delta y)_{NI}(1+R_I)} \quad . \qquad (3.12\text{-}11)$$

Entrainment rate at I boundary

$$\dot{m}''_I = F_I \; (A_1 \; \dot{m}''_{ch} + A_2 \; \dot{m}''_{I,diff}) \quad , \qquad (3.12\text{-}12)$$

At E boundary

$$R_E = \frac{1}{0.01} \left| \frac{T_N - T_{NM1}}{T_{max} - T_{min}} \right| \quad , \qquad (3.12\text{-}13)$$

$$F_E = F_{E,p} \; R_E^{0.1} \quad , \qquad (3.12\text{-}14)$$

$$\dot{m}_{E,diff} = \frac{2 \; \Gamma_{\phi,NE} \; R_E}{(\delta y)_{NE} \; (1+R_E)} \quad . \qquad (3.12\text{-}15)$$

Entrainment rate at E boundary

$$\dot{m}''_E = F_E \; (A_1 \; \dot{m}''_{ch} - A_2 \; \dot{m}''_{E,diff}) \quad , \qquad (3.12\text{-}16)$$

where, F_I and F_E are the factors which ensure that the change in temperature near each boundary is less than 1% of the maximum difference in each forward step; $\dot{m}''_{ch}$ is the part of the mean mass flow rate due to the chemical reaction; and $\dot{m}''_{diff}$ is the part of the mean mass flow rate due to the molecular diffusion.

In association with stretching, these expressions are significant when the chemical-kinetic time is much shorter than the time of diffusion, and the eddy-stretching rate is moderate, the factors A_1 and A_2 ensure that the entrainment rate is nearly proportional to the burning rate of the fold, $\frac{d\tilde{\tau}}{da}$;

therefore, the above entrainment adjustments will be the same as the entrainment formulae given by Spalding and Stephson (1971a). Consequently, the reaction zone is thin and the flame propagates. As the flame approaches steady propagation, the entrainment rate, $\dot{m}''_{ch}$ will tend to a constant given by:

$$\dot{m}''_{ch} \rightarrow \rho_u S_u \quad , \qquad (3.12\text{-}17)$$

where S_u is the speed of flame propagation.

On the other hand, when the reaction rate is low or the stretching rate is high, the factors A_1 and A_2 ensure that the entrainments are governed by the molecular diffusion. Hence, the reaction zone expands rapidly until the two boundaries coincide with two symmetry planes.

3.12.4 Calculation of the mixture temperatures

The local temperature is obtained by an iteration procedure until the following equation is satisfied,

$$h = \sum_{j=1}^{NS} \sigma_j h_j \quad , \qquad (3.12\text{-}18)$$

i.e.

$$h - \sum_{j=1}^{NS} \sigma_j h_j(T_k) = \sum_{j=1}^{NS} C_{p_j}(T_k)\sigma_j \, \Delta T_k \quad , \qquad (3.12\text{-}19)$$

$$T_{k+1} = T_k + \Delta T_k \quad , \qquad (3.12\text{-}20)$$

where $T_k \equiv$ the temperature at the kth iteration.

$h_j(T_k) \equiv$ the enthalpy of species j at temperature T_k.

$C_{p_j}(T_k) \equiv$ the constant pressure specific heat of species j at temperature T_k.

Convergence is monitored by computing $\frac{\Delta T_k}{T_{k+1}}$ at each iteration; and iteration is terminated when the ratio falls below a pre-specific limit (10^{-3} is chosen).

3.13 Closure

The details of the numerical solution procedure of the chemical kinetic equations have been presented. The results of computation of fold biography will be given in the next chapter.

CHAPTER 4 - RESULTS OF COMPUTATION OF FOLD BIOGRAPHY

4.1 Introduction

The present chapter is devoted to the presentation of fold biographic study of a stretched-fold.

The inter-diffusion model chosen here is appropriate to pre-mixed combustion of hydrogen-oxygen gases. The numerical algorithm for solving the complex reacting flow, described in Chapter 3, has been incorporated. In association with a range of conditions, it has been solved for a number of different stretching times, diffusion times, reaction times and initial fold sizes.

The main objectives of this study are:-

(1) To show that the ESCIMO approach applied to a stretched-fold by means of numerical investigation, allows investigation of complex reactions.

(2) To provide qualitative and quantitative understanding of the interaction between turbulence and chemistry.

The remainder of the chapter is made up of six sections and is arranged as follows:

Review of some earlier results obtained by the ESCIMO approach is presented in Section 4.2. Section 4.3

provides the theoretical approach concerning the defining variables and the dimensional analysis of a stretched-fold. Section 4.4 presents some analytical solutions for the verification of the biographic theory. Section 4.5 gives the numerical investigation of the grid-independence test. Presentations of computational results are in Section 4.6; which contains:

(a) a table with a wide range of a stretched-fold behaviour;

(b) the flame speed calculations;

(c) a comparison of analytical solutions which embodied some idealised assumptions; and

(d) a further presentation of fold biography.

Finally, Section 4.7 contains the closing remarks of the chapter as a whole.

4.2 Review of Earlier Results by ESCIMO Approach

The interaction of turbulence∿chemistry in a single fold in a well-stirred reactor was first discussed by Spalding (1979a). He selected a one-step exothermic chemical reaction between pre-mixed methane and air combustion model to investigate the fold biography. Noseir (1980) applied the same simple chemically reacting system to demonstrate the different burning

regimes of a stretched-fold by numerical calculation for many inter-diffusion and reaction phenomena within the fold.

However, the above results are strictly valid only for single-step reactions. Anyhow, these fruitful results allow further understanding of turbulent combustion processes.

The next step is to introduce the knowledge of the complex chemical-kinetic system into the present theory. Reference 134 contains some preliminary results of the extension to multiple chemical reaction of hydrogen-oxygen flame within a stretched-fold.

Details of computational results of fold biography will be presented and discussed.

4.3 Theoretical Approach

Dimensional analysis

For a more systematic study, the behaviour of a single fold is characterised by the ratios of characteristic times, age, a; diffusion, t_{diff}; stretching, t_{str}; and reaction, t_{react}.

Three dimensionless time ratios are thus grouped together and are employed to express the results of fold

biography. These governing parameters are given by:-

$$t_{diff}/t_{react};\ t_{diff}/t_{str};\ a/t_{react}.$$

Defining variable

A progress variable of a single stretched-fold is introduced here. The extent to which the fold has reached the equilibrium hot product condition is characterised by the "reactedness". τ; this variable varies with temperature and has a value of zero for the unburned gases and unity for fully burned gases, hence,

$$\tau = \frac{T - T_u}{T_{b,eq} - T_u} \quad ; \qquad (4.3\text{-}1)$$

where T_u is the unburned temperature; and

$T_{b,eq}$ is the temperature at equilibrium.

This variable, τ, can further be expressed as a function of age, properties of hydrodynamic, laminar transport and chemical kinetics.

$$\tau = \tau\ \{a, R, \rho, Y_o, M_o, \Gamma, R_{ref}\} \quad , \qquad (4.3\text{-}2)$$

where, 'a' represents the age of the fold;

R the stretching rate;

ρ the density of mixture;

Y_o the initial fold thickness;

M_o the mass fraction of fresh gas in a newly-formed fold;

Γ the transport coefficient of enthalpy; and

R_{ref} the reference reaction rate.

4.4 Analytical Solutions

It is of interest to discuss the analytical approach to a stretched-fold under three distinct burning regimes, namely, laminar-flame-speed control, stretching control and chemical kinetic control. This will provide useful information about the performance of fold biography. In addition, it is useful for the verification and the comparison between numerical predictions and analytical results. To clarify the situation, some idealisations for the flame propagation are first discussed.

4.4.1 Laminar flame speed idealisation

When the chemical reaction time is much shorter than the diffusion time and the stretching rate is moderate, it has already been shown that the burning process of a single fold proceeds by way of propagation into the unburned gas of a very thin flame-front at a

uniform velocity S_u (Spalding 1978b).

In this circumstance, the fold-average burning rate (the rate of change of $\tilde{\tau}$ with age) can be expressed through the laminar flame speed idealisation,

$$\frac{d\tilde{\tau}}{da} = \frac{\rho_u S_u}{\psi} \quad , \qquad (4.4\text{-}1)$$

where $\tilde{\tau}$ is the fold-average reactedness;

ρ_u is the unburned density; and

ψ as defined in the nomenclature, is a measure of total thickness of the fold.

During the burning process of a single fold, the fold-average reactedness $\tilde{\tau}$, rises as the age increases. This process will continue until the time required for completion of the possible reaction has been reached. At this point, the burn-out time of the fold is therefore defined as t_b at which $\tilde{\tau}$ has just reached unity. The derivation of these relations is given below:

Combining equations (4.4-1) and (2.4-5) yields,

$$\frac{d\tilde{\tau}}{da} = \frac{\rho_u S_u}{\psi_o \, \mathrm{Exp}\,(-a/t_{str})} \quad . \qquad (4.4\text{-}2)$$

As the flame propagation proceeds, the above equation indicates that the rate of burning increases with

the stretching rate. Integration of equation (4.4-2) gives:

$$\tilde{\tau} = \tilde{\tau}_o + \frac{t_{str}\,\rho_u S_u}{\psi_o}\left|\mathrm{Exp}(a/t_{str}) - 1\right| \quad , \quad (4.4\text{-}3)$$

where $\tilde{\tau}_o$ is the initial fold-average reactedness.

Discussion of this equation will further be presented in sub-section 4.4.2.

Speed of flame propagation

Now, attention is focussed on the determination of the flame speed (i.e. the burning velocity). It has been recognised that the speed of flame propagation is proportional to the square root of the product of the diffusion coefficient and the reaction rate (Spalding, 1979a):

$$\rho_u S_u \quad \alpha\sqrt{\Gamma R_{ref}} \quad . \qquad (4.4\text{-}4)$$

Owing to the fact that ψ_o and ρ_u are dependent upon the properties of a newly-formed fold, the above relationship can easily be connected with the diffusion time and reaction time as:

$$\frac{\psi_o}{\rho_u S_u} \quad \alpha(t_{diff}\ t_{react})^{\frac{1}{2}} \quad . \qquad (4.4\text{-}5)$$

The implication of this formula involves two parameters:

(1) the flame speed S_u; and

(2) the proportional constant C, defined as a burning constant of a stretched-fold.

For the sake of generalisation, it is necessary to formulate these two quantities. It is clear that once the mass proportion of fresh gases in a newly-formed fold is specified (i.e. M_o is fixed), the value of $\frac{\psi_o}{\rho_u \sqrt{t_{diff}}}$ must remain unchanged. In this circumstance, for a given combustible mixture in a fold, the flame speed parameter, S_u, is bound to be inversely proportional to the square root of the chemical reaction time only,

$$S_u \ \alpha \ \frac{1}{\sqrt{t_{react}}} \quad . \qquad (4.4\text{-}6)$$

In order to investigate the influences of the characteristic time ratios on the fold biography, times of reaction and stretching have been varied. Therefore, S_u could be described as a function of the dimensionless parameter, t_{diff}/t_{react} in the fold biographic studies.

Since the flame speed can be regarded as a property of gas, it is therefore easy to determine its value by experimental and theoretical approaches. From the physicochemical point of view, the flame speed (or burning velocity), S_u^* is a unique function of the initial combustible mixture.

Suppose that S_u^* is obtained from experimental findingsin which the reference reaction time is t^*_{react}. If the composition of the combustible gases in a newly-formed fold remain fixed, while the reaction parameter t_{diff}/t_{react} is changeable, then the flame speed of the stretched-fold which is governed by the internal flame propagation regime, is related by:

$$\frac{S_u}{S_u^*} = \sqrt{\frac{t^*_{react}}{t_{react}}} \quad . \qquad (4.4\text{-}7)$$

Equations (4.4-5 and 4.4-7) are very significant.

- Since the value of S_u^* can be obtained from experimental findings, the burning constant C (equation 4.4-5) can be deduced analytically.

- The left-hand side of equation (4.4-7) gives the normalised expression of flame speed on the internal flame propagation regime under the influence of reaction times.

On the other hand, the numerical prediction procedure of the ESCIMO approach does provide values of flame speeds which will be presented in Section 4.6.

The burning constant

The remaining task is to determine the burning constant, C. For a given combustible mixture, this constant which is defined by equation (4.4-5), can simply be expressed as:

$$C = \frac{\psi_o}{\rho_u S_u \sqrt{t_{diff}\, t_{react}}} \quad . \qquad (4.4\text{-}8)$$

Insertion of equation (4.4-7) into equation (4.4-8) yields,

$$C = \frac{\psi_o}{\rho_u \sqrt{t_{diff}}} \cdot \frac{1}{S_u^* \sqrt{t_{react}^*}} \quad . \qquad (4.4\text{-}9)$$

This analytical solution indicates that the burning constant, C, is a unique function of the initial mixture of a newly-formed fold.

4.4.2 Classification of the fold burning regimes

As already mentioned in the beginning of this section, the combustion process of a fold can be classified in

three different burning regimes. The laminar flame speed idealisation of a fold has already been described. It is now desirable to analyse the individual burning regimes so as to facilitate understanding of the fold biographic theory.

Laminar flame speed control regime

When the stretching rate is negligibly small and the reaction time is much shorter than the diffusion time, the fold-average reactedness $\tilde{\tau}$ versus age can be derived from the laminar-flame theory. With the absence of stretching, equation (4.4-2) becomes,

$$\frac{d\tilde{\tau}}{da} = \frac{\rho_u S_u}{\psi_o} \quad . \qquad (4.4\text{-}10)$$

Substitution of the burning constant and integration of the resulting equation yields,

$$\tilde{\tau}\langle a\rangle = \tilde{\tau}_o + \frac{1}{C\sqrt{t_{diff}\, t_{react}}} \; . \; a \; . \qquad (4.4\text{-}11)$$

Inspection of the above result shows that the relationship between $\tilde{\tau}$ and age is linear. The slope is inversely proportional to the square root of the product of diffusion time and reaction time, that is:

$$\alpha = \tan^{-1} \left(\frac{1}{C \sqrt{t_{diff}\, t_{react}}} \right) \quad . \qquad (4.4\text{-}12)$$

Under these circumstances, the burning process consists primarily of that of linear-propagation of a thin flame at uniform speed through the fold. The linear-burn-out time of the fold, t_f (corresponding to $\tilde{\tau}$ equal to unity), is proportional to the square root of the diffusion time and the reaction time, i.e.

$$t_f = (1 - \tilde{\tau}_o)\, C \sqrt{t_{diff}\, t_{react}} \; . \qquad (4.4\text{-}13)$$

<u>The stretching control regime</u>

When the stretching rate is moderate, and the reaction time is much shorter than the diffusion time, the thin reaction zone travels across the fold, which is subjected to a stretching process. The fold-average reactedness versus age is given by:

$$\tilde{\tau}\langle a \rangle = \tilde{\tau}_o + \frac{t_{str}}{C\sqrt{t_{diff}\, t_{react}}} \left| \mathrm{Exp}(a/t_{str}) - 1 \right| \; , \qquad (4.4\text{-}14)$$

Owing to the exponential term a/t_{str} in the formula, the influence of stretching on the burning process of this regime becomes more significant than other influences. To clarify this, the burn-out time of a stretched-fold, t_b, is thus deduced from the above relations.

$$t_b = t_{str} \ln \left|1+t_f/t_{str}\right| \quad , \qquad (4.4\text{-}15)$$

where t_f is the linear flame-propagation time across the fold, as described in equation 4.4-13.

When the value of t_f/t_{str} in this burn-out time formula is large enough, the argument of the logarithm is also large; the logarithm itself changes slowly, hence, the process is entirely controlled by the stretching time. This burning process often appears in the problem of premixed, confined baffle-stabilised flames. The phenomena of this burning process have been classified as the eddy-break-up type (Spalding, 1978c ; Noseir 1980).

The extreme of this regime is when the value of t_f/t_{str} tends to zero (when the stretching time is sufficiently large); then,

$$\ln \left|1+t_f/t_{str}\right| \rightarrow t_f/t_{str} \quad .$$

Subsequently, the burn-out time of the fold, t_b, will approach t_f, and the burning regime approach that of laminar flame speed control.

The above two burning processes are also classified as internal flame propagation regime.

Chemical kinetic control regime

When the stretching time is very short and the chemical reaction time is long, the high stretching rate forces all the concentration profiles to become uniformly distributed across the fold before the significant reactions takes place. In this circumstance, the burning process is entirely controlled by chemical kinetics. The fold burning rate of this regime is given by:

$$\dot{\tilde{\tau}} = \frac{d\tilde{\tau}}{da} \quad . \qquad (4.4\text{-}16)$$

As a consequence of rapid-diffusion, the properties in the fold are evened out and the burning rate is dependent upon the chemical kinetics alone. Therefore, the burn-out time of the fold is proportional to the reaction time only.

$$t_b = \int_{\tilde{\tau}_o}^{1} \frac{d\tilde{\tau}}{\dot{\tilde{\tau}}} \; \alpha \; t_{react} \quad . \qquad (4.4\text{-}17)$$

This burning process often appears in the problem of the well-stirred reactor of the Longwell-bomb type. (This will be discussed further in Chapter 7). The phenomena of this burning process have been classified as the spontaneous ignition regime (Spalding, 1978c).

4.5 Numerical Investigation

All the computations have been performed for a fuel-rich mixture of hydrogen+oxygen+nitrogen stretched fold at one atmospheric pressure. The initial composition at the fresh-layer is given in Table 4.1. The hot product at the burned layer is initially supposed to be at equilibrium.

(mass fraction)	N_2	H	O	HO_2	H_2O	OH	O_2	H_2
Fresh-layer	0.92066	0	0	0	0	0	0.06317	0.01617
Burned-layer	0.92066	1.23×10^{-5}	5×10^{-6}	2×10^{-5}	0.0707	8.4×10^{-7}	3×10^{-4}	0.008301

$p=1atm$, $T_u=336^oK$, $T_{b,eq}=1078^oK$, $M_o=0.5$.

TABLE 4.1: THE INITIAL COMPOSITION OF A FOLD

Grid-independence test

In order to test the grid-independence of numerical calculations, two different series of runs have been performed, namely:

(1) effect of the age interval; and

(2) effect of the number of grid nodes.

All these computations were performed to the same specifications of the stretched-fold ($\frac{t_{diff}}{t_{react}} = 10^6$, $\frac{t_{diff}}{t_{str}} = 10^3$). The initial composition of the fold is given in Table 4.1. Comparisons for the predicted fold-average quantities at a given age for different runs were also made.

Effect of the age interval

The effects of the age interval, δa, on the numerical solution were studied by varying the dimensionless time ratios,

$$\frac{\delta a}{t_{diff}} \left(\frac{Y}{Y_o}\right)^2 ; \frac{\delta a}{t_{str}} ; \frac{\delta a}{t_{react}} ;$$

while the number of grid nodes in the cross-fold direction was kept constant.

In order to ensure the numerical stability, the step size (age interval) must be less than any of the time scales of diffusion, stretching and chemical reaction. In addition, this step size should be small enough to yield the grid-independent solution. Therefore, it is necessary to determine the optimum step size at each age interval in accordance with:

$$\delta a = \text{FRA. Minimum} \left\{ t_{diff} \left(\frac{Y}{Y_o}\right)^2 , t_{str}, t_{react} \right\} \quad ; \qquad (4.5\text{-}1)$$

where FRA is the incremental factor.

Computations were performed with various values of FRA and with 40 grid nodes in the cross-stream direction. The predictions of fold-average quantities at a given age were compared for each run, as given in Table 4.2.

Inspection of Table 4.2 shows that the solution obtained from the coarser step size in runs 5 and 6 has strongly influenced the intermediate species calculations. On the other hand, it is observed that there are not many significant differences in the solutions of runs 1 and 2; this shows that the step size independence is being approached with this grid refinement.

Figure 4.1 shows the results of the grid-dependence

Number of cross-grid N=40, computer used: CDC 6600.

Run No.	1	2	3	4	5	6
FRA	0.01	0.02	0.03	0.05	0.075	0.1
a/t_{str}	0.1702	0.17	0.169	0.1701	0.1685	0.169
$\tilde{\tau}$	0.772	0.772	0.772	0.763	0.733	0.675
$\bar{T}$	911	911	910	903	881	838
$\tilde{H}x10^6$	2.05	2.08	2.09	2.02	1.83	1.46
$\tilde{O}x10^7$	5.78	5.8	6.07	5.87	5.25	4.04
$\tilde{HO}_2x10^5$	2.78	2.8	3.03	2.93	2.6	1.98
$\tilde{H_2O}x10^2$	5.47	5.47	5.47	5.41	5.2	4.79
$\tilde{OH}x10^7$	7.75	7.76	8.54	8.37	7.74	6.43
$\tilde{O}_2x10^2$	1.45	1.45	1.45	1.51	1.7	2.06
$\tilde{H}_2x10^2$	1.	1.	1.	1.01	1.04	1.08
Reaction rate						
$\tilde{R}_{H_2}$	-3.61	-3.6	-4.37	-6.23	-5.73	-4.68
$\tilde{R}_{H_2O}$	6.13	6.12	6.25	6.44	5.94	4.87
Computer time (secs)	210.1	120.	85.2	51.5	42.4	32.1

TABLE 4.2: GRID INDEPENDENCE TESTS -

EFFECT OF STEP SIZES

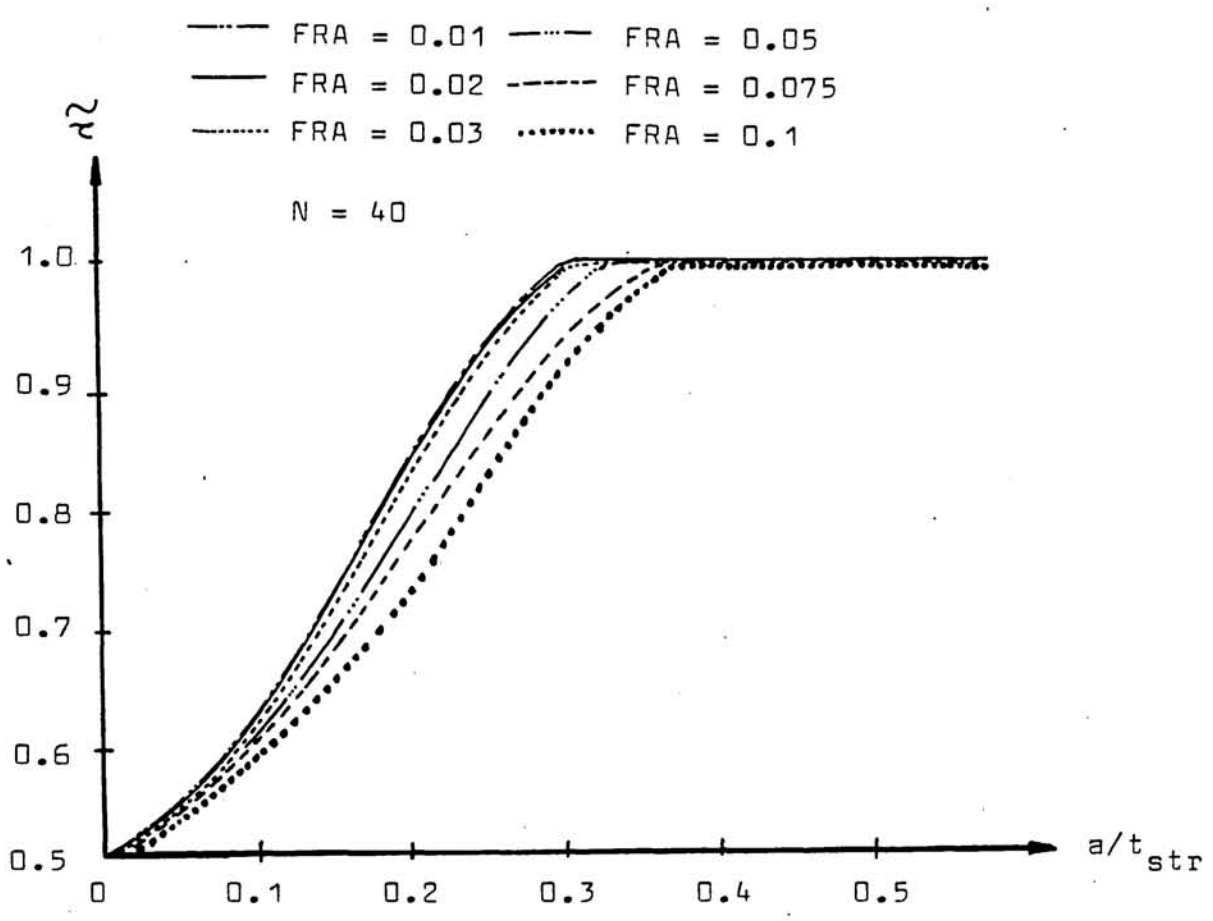

FIGURE 4.1 GRID-INDEPENDENCE TESTS (1)
EFFECT OF FRA.

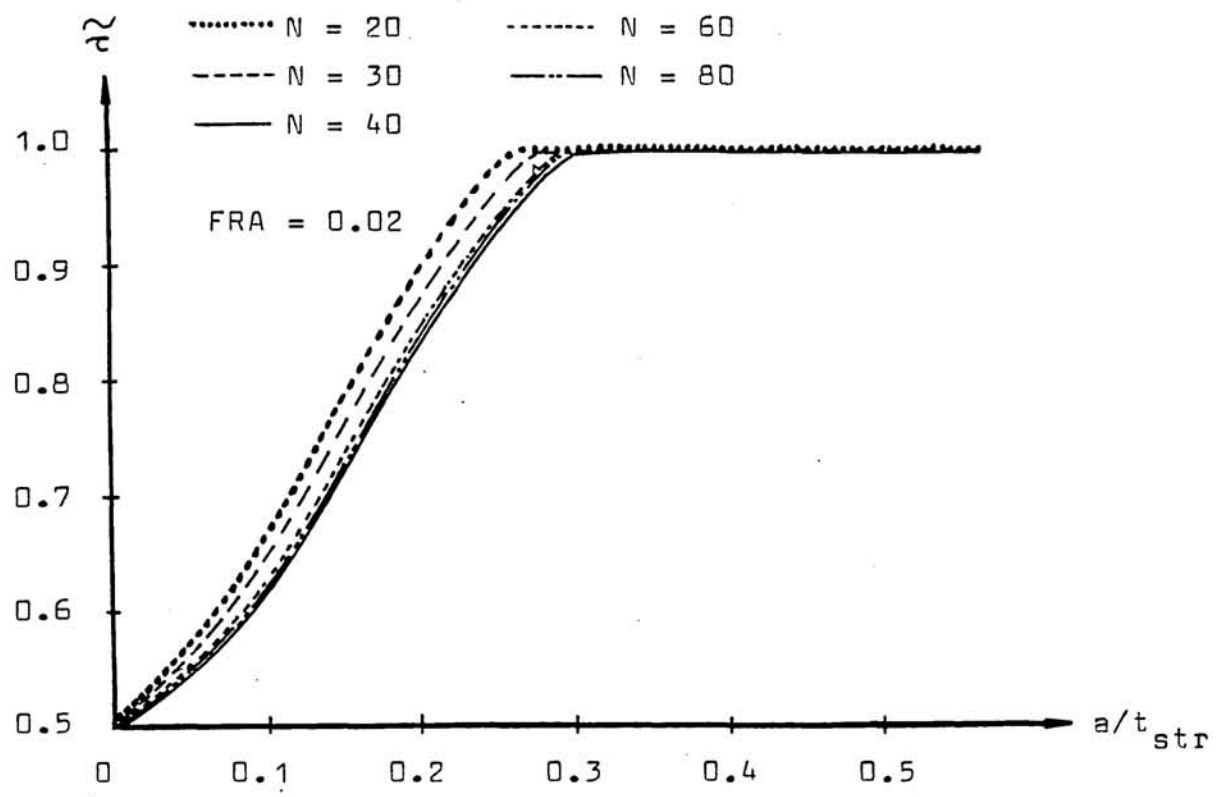

FIGURE 4.2 GRID-INDEPENDENCE TESTS (2)
EFFECT OF THE NUMBER OF GRID NODES.

tests for the above computations. These results are represented by the variation of fold-average reactedness with the dimensionless age, a/t_{str}. It is observed that the criterion of the step independence solution is FRA$\leqslant$0.02.

Effect of the number of grid nodes

A few calculations were made with different numbers of grids to examine the influence of changing the number of cross-fold grid nodes. The results of the test cases are listed in Table 4.3. It should be noted that in each case the incremental factor has been kept constant (FRA=0.02). Figure 4.2 presents the variations of fold-average reactedness with dimensionless age under the influence of the number of grid nodes.

Since the flame-following-grid system is employed, the prediction is not strongly dependent on the cross-fold grid, and grid-independence in this direction was achieved easily. The grid independence can therefore be observed by consideration of Table 4.3 and of Figure 4.2. The calculations described here show that 40 cross-fold grid nodes is considered to be satisfactory.

Factor of step size FRA=0.02, computer used: CDC 6600

Run No.	1	2	3	4	5
Number of cross-grid	20	30	40	60	80
a/t_{str}	0.17	0.17	0.17	0.17	0.17
$\tilde{\tau}$	0.801	0.776	0.772	0.772	0.772
$\tilde{T}$	932	913	911	911	911
$\tilde{H}x10^6$	1.81	2.05	2.08	2.	2.07
$\tilde{O}x10^7$	5.25	5.97	5.8	6.1	6.
$\widetilde{HO_2}x10^5$	2.64	2.99	2.8	3.	2.3
$\widetilde{H_2O}x10^2$	5.64	5.5	5.47	5.47	5.47
$\widetilde{OH}x10^7$	7.09	8.29	7.76	7.5	8.
$\widetilde{O_2}x10^2$	1.27	1.43	1.45	1.45	1.45
$\widetilde{H_2}x10^2$	0.981	1.	1.	1.	1.
Reaction rate					
$\tilde{R}_{H_2}$	-5.31	-4.2	-3.6	-3.65	-3.8
$\tilde{R}_{H_2O}$	5.48	6.1	6.16	6.15	6.2
Computer time (secs)	50.5	75.4	120.	151.5	221.

TABLE 4.3: GRID INDEPENDENCE TESTS - EFFECT OF NUMBER OF CROSS-FOLD GRIDS

4.6 Presentation of Results

All results obtained here are on the basis of 40 cross-fold grid nodes, with the age interval factor, FRA=0.02. These grid independent criteria are:

$$N = 40 \text{ (number of cross-fold grid nodes);}$$

$$\delta a = \text{the least of } \{0.02t_{diff}(\frac{Y}{Y_o})^2, 0.02t_{str}, 0.02t_{react}\}.$$

4.6.1 Burn-out and mixing times of a fold

Various values have been taken for the eddy-stretching represented by, t_{str}; for the chemical reaction, represented by, t_{react}; and for the fold burn-out time, t_b; so as to vary the values of the governing parameters:

$$t_{diff}/t_{react};\ t_{diff}/t_{str} \text{ and } t_b/t_{react}.$$

Table 4.4 contains results of a series of numerical computations, expressed in terms of the burn-out and mixing times, (t_b and t_m) with the burning constant C=0.7754.

The fold burn-out time has been defined in sub-section 4.4.2. The fold unmixedness and the fold mixing time are discussed here. The ratio of the square root of the fold concentration variance to the corresponding

t_{diff}/t_{str}	t_{diff}/t_{react}	10^3	5.718×10^3	10^4	5.718×10^4	10^5	5.718×10^5	10^6
0	t_b/t_{react}	10.93	26.18	34.7	84.2	112.1	263.2	358.2
	t_m/t_{react}	$>t_b$	$>t_b$	$>t_b$	$>t_b$	$>t_b$	$>t_b$	$>t_b$
10^3	t_b/t_{react}	$>t_m$	10.2	15.3	52.6	76.445	217.12	304.43
	t_m/t_{react}	5.01	$>t_b$	$>t_b$	$>t_b$	$>t_b$	$>t_b$	$>t_b$
10^4	t_b/t_{react}	$>t_m$	$>t_m$	$>t_m$	16.21	25.27	100.56	153.5
	t_m/t_{react}	0.58	3.52	6.1	$>t_b$	$>t_b$	$>t_b$	$>t_b$
10^5	t_b/t_{react}	$>t_m$	$>t_m$	$>t_m$	$>t_m$	$>t_m$	19.1	33.7
	t_m/t_{react}	0.063	0.39	0.67	4.1	7.2	$>t_b$	$>t_b$
10^6	t_b/t_{react}	$>t_m$	$>t_m$	$>t_m$	$>t_m$	$>t_m$	$>t_m$	$>t_m$
	t_m/t_{react}	0.007	0.042	0.075	0.44	0.8	4.7	8.4
10^7	t_b/t_{react}	$>t_m$	$>t_m$	$>t_m$	$>t_m$	$>t_m$	$>t_m$	$>t_m$
	t_m/t_{react}	0.00084	0.0047	0.0082	0.048	0.088	0.5	0.9

TABLE 4.4: RESULTS OF FOLD BIOGRAPHIC STUDIES

fold-average quantity is defined as the unmixedness (i.e. $\frac{\sqrt{\widetilde{\phi'^2}}}{\tilde{\phi}}$). This ratio is also regarded as a degree of steam segregation (Brodkey, 1975; Pratt, 1976).

When this index is equal to zero, the two 'parent' gas layers of the fold are fully mixed. In this circumstance, all the gas properties are evened out across the fold.

Since all the cross-fold profiles are supposed to be

step-like at the birthplace, the fold unmixedness index is initially very high. The fold mixing time, t_m, is defined as the time required for the fold unmixedness index becomes zero.

Observation

(i) When the t_{diff}/t_{str} is negligibly small, t_b/t_{react} increases as t_{diff}/t_{react} increases. This can be examined further on the first row of Table 4.4. It is seen that the dimensionless burn-out time, t_b/t_{react}, is nearly proportional to $\sqrt{t_{diff}/t_{react}}$. However, the mixing time, t_m, is much longer than the burn-out time. What would happen is that the non-stretched fold would be completely burnt out before fully mixing is achieved.

(ii) When t_{diff}/t_{str} is moderate and t_{diff}/t_{react} is high, the fold burn-out time is affected, almost, by the stretching time alone; since the burning process is proceeded by way of flame speed propagation and associated with stretching. The burning regime of these folds is classified as the internal flame propagation regime.

(iii) When t_{diff}/t_{str} is appreciably larger than t_{diff}/t_{react}, the two gas 'parent' layers have

rapidly been evened out before significant reactions take place. Under these circumstances, the mixing time is very short. The burning regime is classified as spontaneous ignition.

(iv) In the cases of fast mixing, as shown in the last row of Table 4.4, the mixing time t_m/t_{react} is proportional to t_{diff}/t_{react}. This is because the rapid diffusion can cause the rate of inter-diffusion to increase.

(v) When the reaction rate is low (at small values of t_{diff}/t_{react}), the mixing time t_m/t_{react} becomes very short at high t_{diff}/t_{str}. This is because rapid stretching can cause the stretched-fold properties to be evened-out before the chemical reaction takes place.

(vi) It is also observed that the burn-out time of a fold for the spontaneous ignition regime is much longer than the internal flame propagation ones. The reason will be discussed in turn.

Discussion

Behaviour of the chemically controlled regime

Since the present results are based on a particular mixture ratio with M_o equals 0.5, the spontaneous ignition regime is strongly dependent upon the initial mixture proportion and the reaction time. Since the mixture proportion employed is different from the stochiometric ratio, at small t_{diff}/t_{react} and large t_{diff}/t_{str}, the gases in the fold do not burn to completion at all. However, when the reaction time is appreciably small, more unburned fuel will be consumed in a rapid stretched-fold. These phenomena will be illustrated further in sub-section 4.6.4.

Behaviour of the internal flame propagation regime

When t_{diff}/t_{str} equals zero or moderate values, and t_{diff}/t_{react} is much larger than t_{diff}/t_{str}, the burning process of the fold is classified as an internal flame propagation regime. Under these circumstances, two kinds of burn-out times have been predicted: (a) the linear propagation time, t_f, which is adopted for non-stretched fold cases; and (b) the non-linear flame propagation time, t_b, which is adopted for stretched-fold cases.

The above results show that: (a) t_f is proportional to $\sqrt{t_{diff} t_{react}}$; (b) t_b is generally in agreement with the analytical formula, i.e. $t_b = t_{str} \ln|1+t_f/t_{str}|$ (see Table 4.6); and (c) when the ratio of t_f/t_{str} is appreciably large, t_b will only be proportional to the stretching time, t_{str}.

4.6.2 Flame speed calculations

Under different governing parameters (t_{diff}/t_{react} and t_{diff}/t_{str}) for the internal flame propagation regime different flame propagation speeds, S_u, have been computed numerically in each interval during the fold burning process, in accordance with:

$$S_u = \frac{\psi}{\rho_u} \frac{d\tilde{\tau}}{da} \quad . \qquad (4.6\text{-}1)$$

Since the flame-following-grid system ensures that the calculation domain covers only the thin reaction zone and the number of grid nodes is fine enough, the calculated flame-speed is likely to be grid independent (see Section 4.5).

Results

The influence of t_{diff}/t_{react} on the calculated flame speed for the laminar-speed-control regime is first

illustrated in Figure 4.3. It represents a family of curves of the calculated flame speed versus the age in dimensionless expression. The abscissa is a/t_f and the ordinate is S_u/S_u^*. It is noted that S_u^* is a reference data obtained from hydrogen-oxygen-nitrogen plane flame propagation with the value S_u^*=0.092 m/sec (see Dixon-Lewis 1970b). Many values of t_{diff}/t_{react} are selected to perform computations and each computational case represents the special features of the fold characteristics.

By considering a fixed parameter t_{diff}/t_{react}, the computed flame speed, S_u, is obviously dependent upon the reference reaction time, t_{react}.

Discussion

It is observed that the development of the flame speed which results from computations can be divided into three regions.

The first is defined as the flame speed adjustment region. This region occupies approximately 8% of the fold's life-time. At first, the two gas 'parent' layers are in contact with a thin zone. Since the reaction time is much shorter than the diffusion and stretching times, the thin reaction zone will travel across the fold with a velocity which initially accelerates with

i FLAME SPEED ADJUSTMENT REGION.

ii STEADY FLAME PROPAGATION REGION.

iii COMPLETE BURNED-OUT REGION.

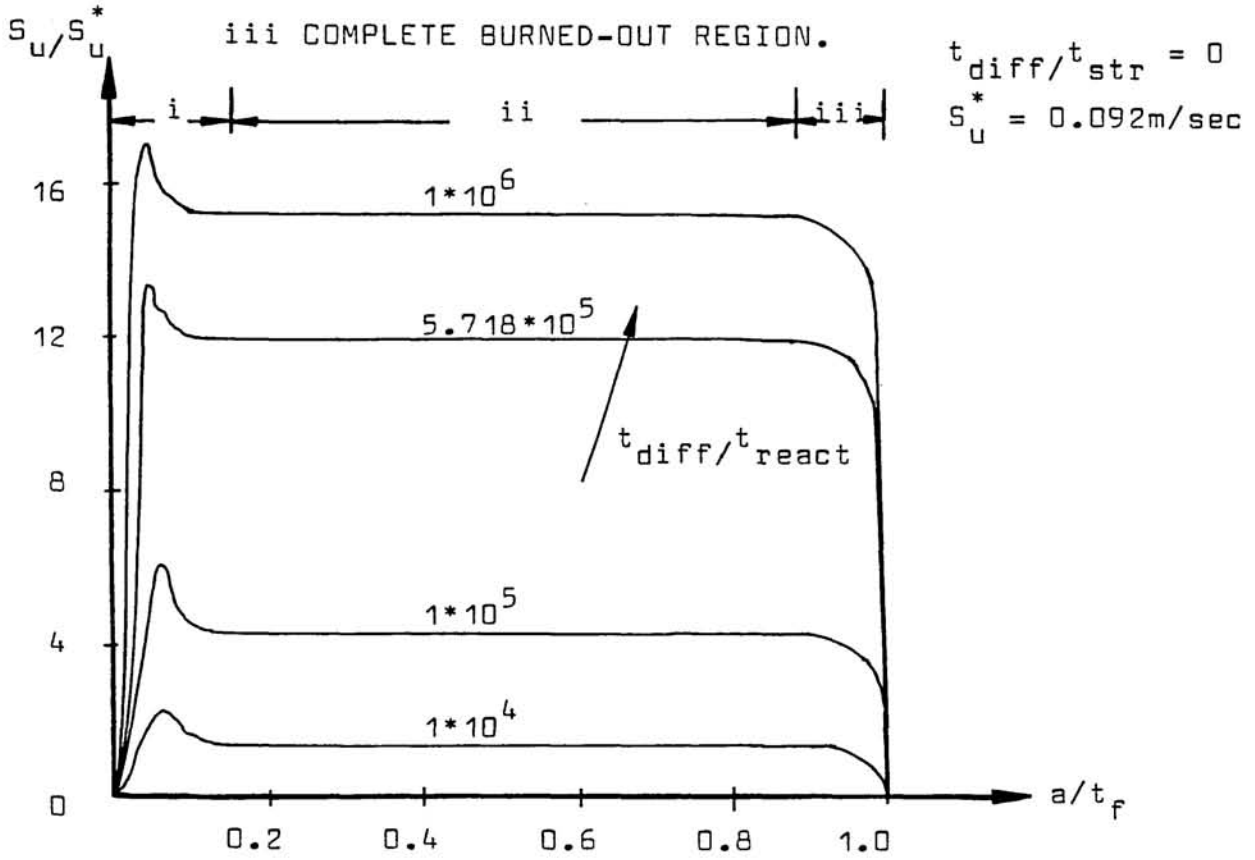

FIGURE 4.3 THE INFLUENCE OF THE REACTION TIME ON THE LAMINAR FLAME SPEED DISTRIBUTION VERSUS DIMENSIONLESS AGE a/t_f UNDER A CONSTANT RATIO OF t_{diff}/t_{str} FOR THE INTERNAL-PROPAGATION CASES.

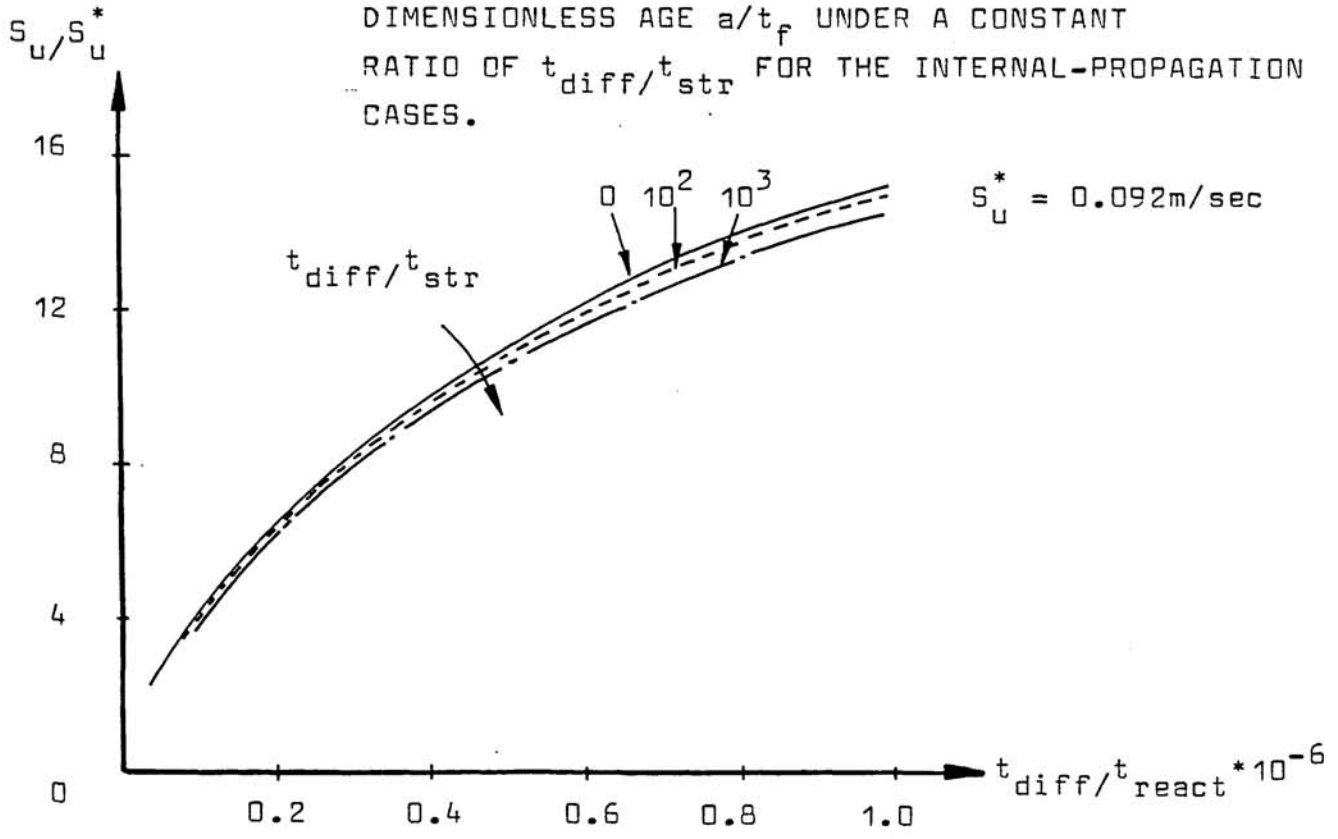

FIGURE 4.4 VARIATION OF FLAME SPEED WITH DIFFERENT PARAMETERS, t_{diff}/t_{str} AND t_{diff}/t_{react}.

age. After an initial adjustment period, the flame speed will be slowed down and will approach a constant value.

The second is defined as the steady flame propagation region. During this period, the flame adjusts itself so that its speed of propagation equals the fixed value. Therefore, the laminar flame speed idealisation is adopted in this region. Since the thin zone travels steadily across the fold, the unburned gases are consumed at a fixed rate, $\frac{d\tilde{\tau}}{da}$.

The third is defined as the fold complete burn-out region. When the thin reaction zone touches the edge of the unburned layer, at least 90% of the gas fuel properties have been consumed. Therefore, the Arrhenius term of reactions become very small. Subsequently, the flame speed decreases.

The above phenomena will be presented further in the diagrams of profiles of concentrations across the fold at various ages.

Relations between flame speed and reaction time

The calculated flame speeds which are associated with different stretching and reaction times are shown in Figure 4.4.

It has been summarised for all the present internal flame propagation cases on this diagram. Each location in the curve represents a predicted flame speed which is characterised by parameters of t_{diff}/t_{str} and t_{diff}/t_{react}.

The above predictions indicate that the calculated flame speed is inversely proportional to the square root of the chemical reaction time. This gives further support for the analytical approach to the flame speed generalisation of the internal flame propagation regime, as already discussed in sub-section 4.4.1. Since values of t_{diff}/t_{react} are larger than t_{diff}/t_{str} ones, the stretching rate has only little effect on the flame speed calculations.

4.6.3 Predictions for comparison with analytical results

The analytical solutions and the numerical calculations of different burning regimes have been discussed in Section 4.4, and the sub-section 4.6.1, respectively.

The task is to present the comparisons between the numerical calculations and the analytical solutions here.

Laminar flame speed

Table 4.5 gives the comparison between the computed flame speeds and the analytical results obtained from equation (4.4-7). It is observed that the discrepancy between the predictions and the analytical ones is about 15%.

t_{diff}/t_{react} →		5.718×10^3	10^4	5.718×10^4	10^5	5.718×10^5	10^6
t_{diff}/t_{str} ↓	(m/sec)	S_u^*	S_u	S_u	S_u	S_u	S_u
0	analytical result	0.092	0.122	0.29	0.385	o.92	1.22
	prediction	0.094	0.126	0.306	0.406	1.1	1.41
10^3	analytical result	0.092	0.122	0.29	0.385	0.92	1.22
	prediction	0.091	0.124	0.287	0.391	0.97	1.38
10^4	analytical result			0.29	0.385	0.92	1.22
	prediction			0.285	0.39	0.91	1.34

TABLE 4.5: THE COMPARISON BETWEEN THE PREDICTED FLAME SPEEDS AND THE ANALYTICAL SOLUTIONS

Fold burn-out time

The comparison between the predicted burn-out time of the fold and the results of the analytical approach is given in Table 4.6 Again, it is observed that the discrepancy between the predictions and the analytical ones is also about 15%.

t_{diff}/t_{str} ↓	t_{diff}/t_{react} →		5.718×10^3	10^4	5.718×10^4	10^5	5.718×10^5	10^6
0	t_b/t_{react}	analytical result	29.32	38.77	92.7	122.6	293.2	387.7
		prediction	26.18	34.7	84.2	112.1	263.2	358.2
10^3	t_b/t_{react}	analytical result	10.37	15.85	55.11	80.03	236.58	327.74
		prediction	10.2	15.3	52.6	76.5	217.12	304.43
10^4	t_b/t_{react}	analytical result			16.27	25.85	103.67	158.51
		prediction			16.21	25.27	100.56	153.5

TABLE 4.6: THE COMPARISONS BETWEEN THE PREDICTED FOLD BURN-OUT TIME AND THE CORRESPONDING ANALYTICAL SOLUTIONS

Discussion

Since the flame speed expression in equation (4.4-7) contains a reference data S_u^*, the accuracy of this data obtained from experiments is usually within $\pm$ 20%

(see Schott, 1959; Edmondson, 1971 and Dixon 1970b). In addition, the flame propagation in a stretched-fold area actually be divided into three regions which have already been illustrated in Figure 4.3.

It is notable that the present numerical calculations of the flame speed and the fold burn-out time are generally in good agreement with the analytical solutions for the internal flame propagation regime. However, it should also be noted that the analytical approach can only give part of the fold-biography results. Further detailed study on the fold-biography can only be done numerically, such as the intermediate species distributions across the fold at various ages and the fold probability-density functions. These, will be discussed in detail in the next section.

4.6.4 Other features of the fold biography

Now, the task is to express the other features of the single-fold computations. These are given below:

(a) The instantaneous profiles across the fold

The instantaneous profiles across the fold, at various ages, are obtained by solving the partial-differential equation (3.2-1) and the necessary auxiliary relations.

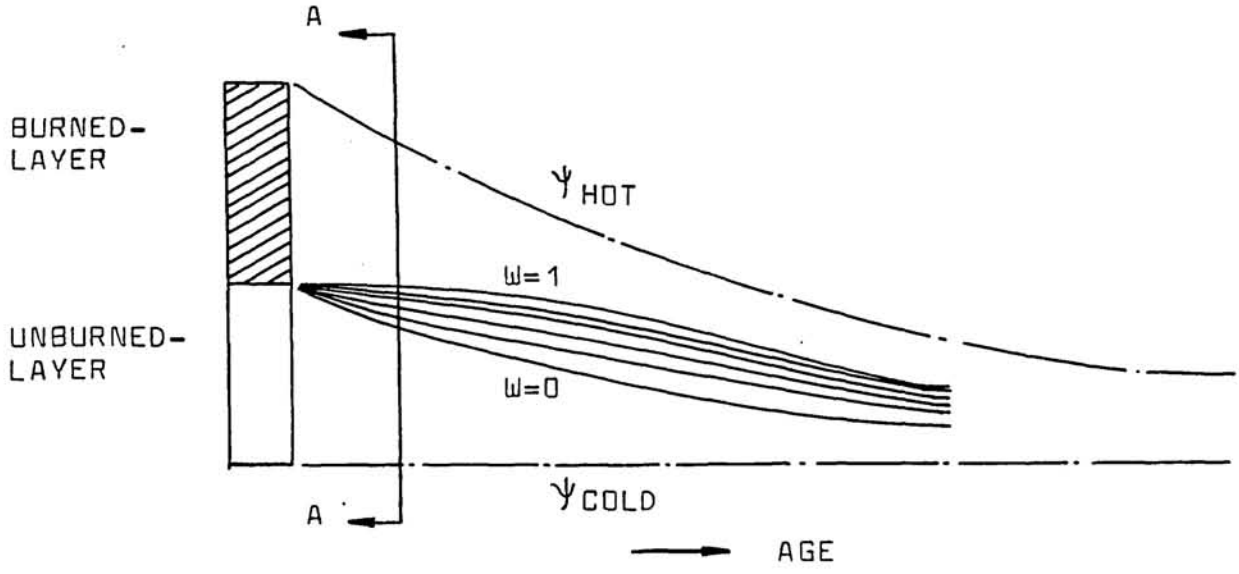

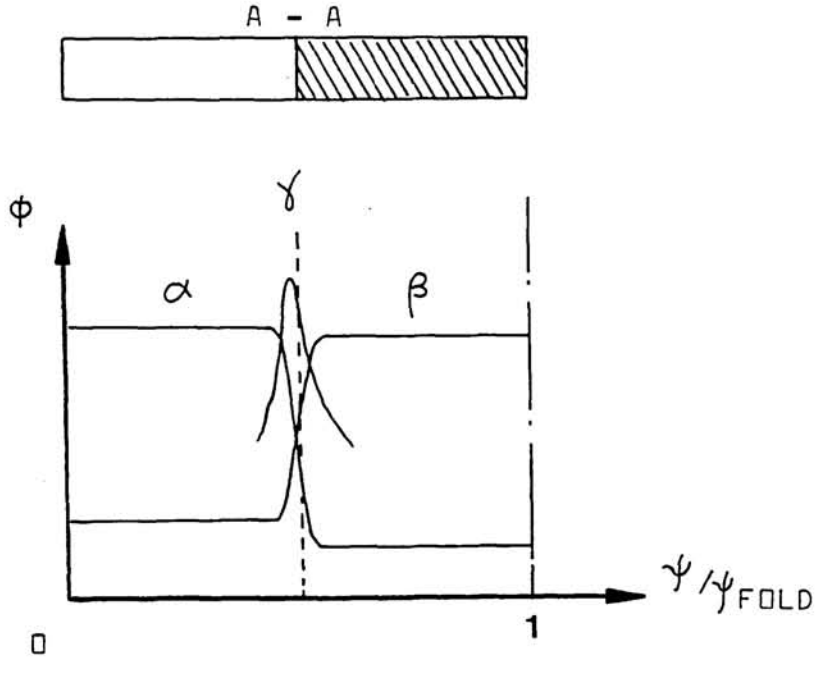

FIGURE 4.5 ILLUSTRATION OF THE RESULTING PROFILES OF SPECIES CONCENTRATIONS ACROSS THE FOLD AT THE BIRTHPLACE.

Typical cross-fold profile, at any successive age, is given by:

$$\phi = \phi\{\psi, a\} \quad , \qquad (4.6\text{-}2)$$

where 'a' is the age, and ψ is a kind of stream function described above.

The sketches on Figure 4.5 illustrate the resulting profiles of species concentrations across the fold at the birthplace. The ordinate is the instantaneous property (concentration or temperature) and the abscissa is the non-dimensional stream function defined as:

$$\psi/\psi_{FOLD} \equiv \frac{\int_o^y \rho dy}{\int_o^Y \rho dy} \quad , \qquad (4.6\text{-}3)$$

where y is the distance normal to the fold; and, Y is the fold thickness at age 'a', at which the stream function is equal to ψ_{FOLD}.

Three typical samples are chosen for the presentations:-

(i) <u>Laminar-speed-control regime</u>

governing parameters	$t_{diff}/t_{str}=0$	$t_{diff}/t_{react}=10^6$	$M_o=0.5$

(FIGURES 4.6 - 4.13)

(ii) Internal flame propagation regime

governing parameters	$t_{diff}/t_{str}=10^3$	$t_{diff}/t_{react}=10^6$	$M_o=0.5$

(FIGURES 4.14 - 4.17)

(iii) Fast mixing associated with chemical-kinetic control regime

governing parameters	$t_{diff}/t_{str}=10^7$	$t_{diff}/t_{react}=10^6$	$M_o=0.5$

(FIGURES 4.18 - 4.21)

It should be mentioned that for the fast mixing regime, after all the gas properties have been evened out by the rapid stretching, the governing equations of species concentrations can be expressed in terms of the ordinary differential ones. This is because the diffusion terms of the corresponding equations can be neglected. Hence, the number of numerical grid nodes can be reduced to one.

(i) Results of laminar-speed-control regime

Variations of temperature and major species concentrations through the flame, at various ages, are shown in Figures 4.6 - 4.9.

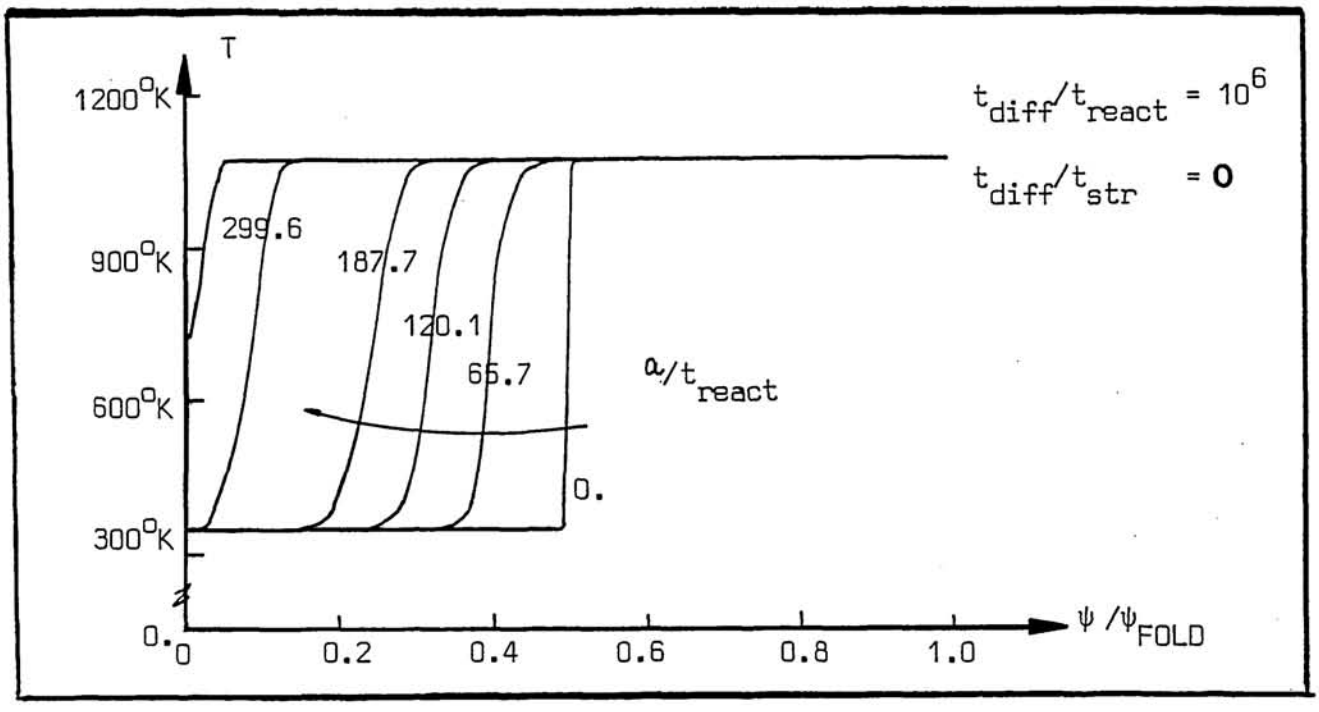

FIGURE 4.6 LAMINAR FLAME SPEED CONTROL REGIME ——— THE TEMPERATURE DISTRIBUTIONS IN THE FOLD.

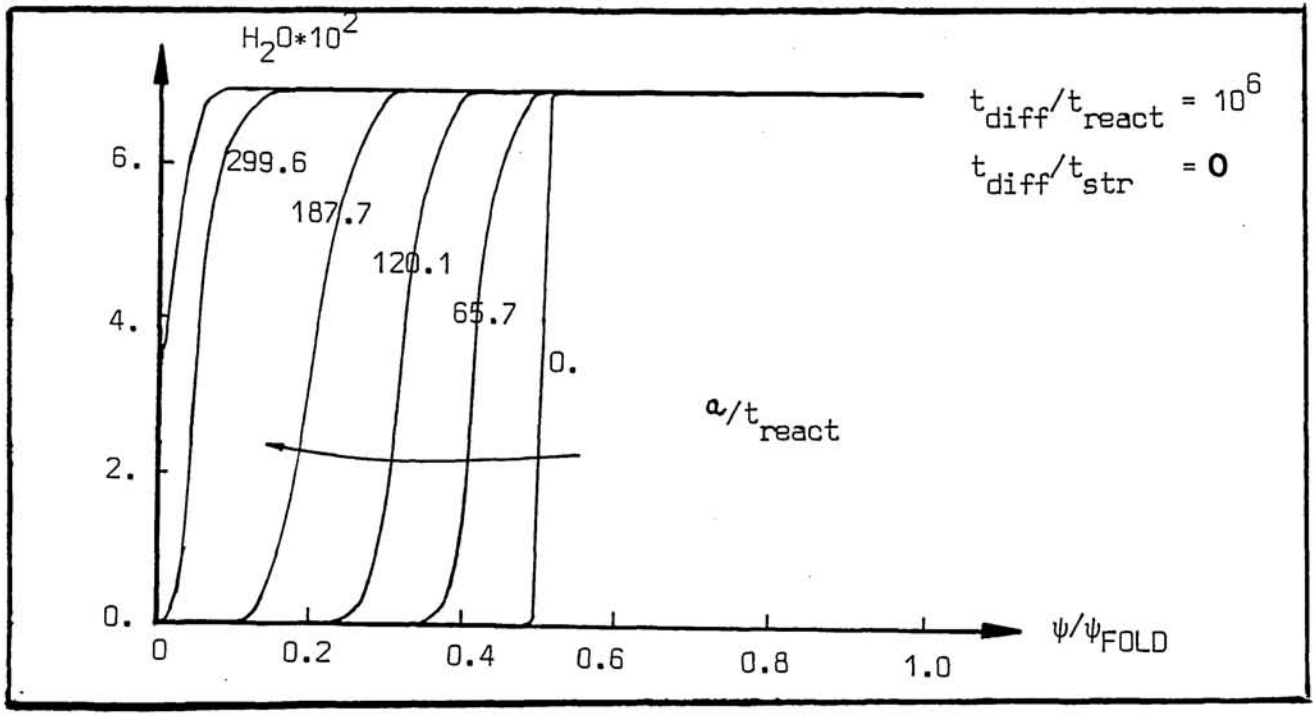

FIGURE 4.7 LAMINAR FLAME SPEED CONTROL REGIME ——— THE H_2O DISTRIBUTIONS IN THE FOLD.

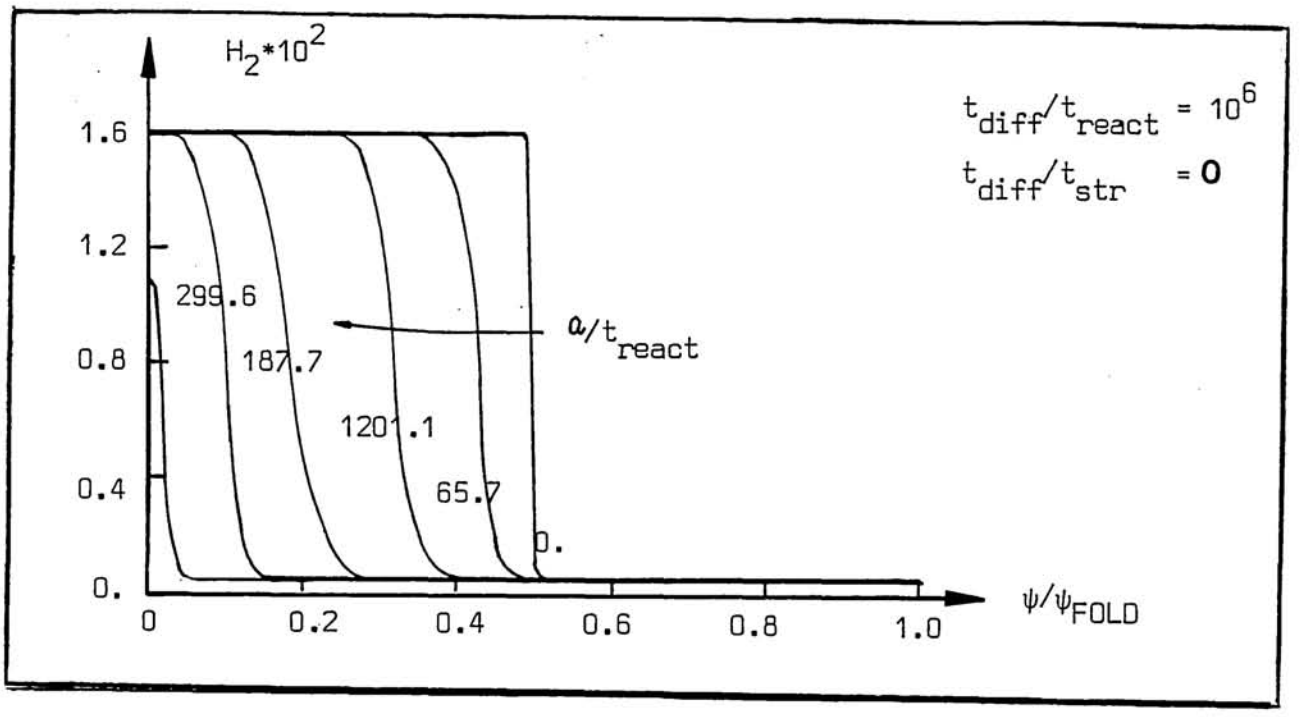

FIGURE 4.8 LAMINAR FLAME SPEED CONTROL REGIME ——
THE H_2 DISTRIBUTIONS IN THE FOLD.

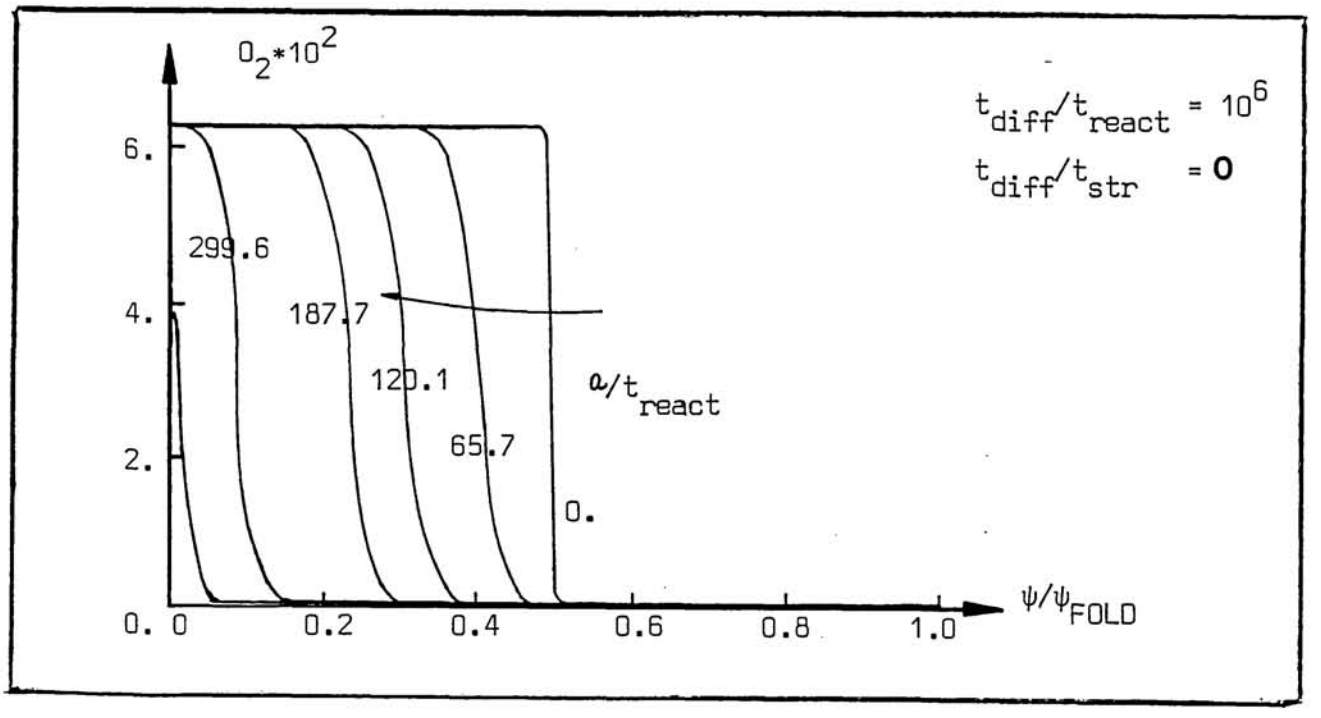

FIGURE 4.9 LAMINAR FLAME SPEED CONTROL REGIME ——
THE O_2 DISTRIBUTIONS IN THE FOLD.

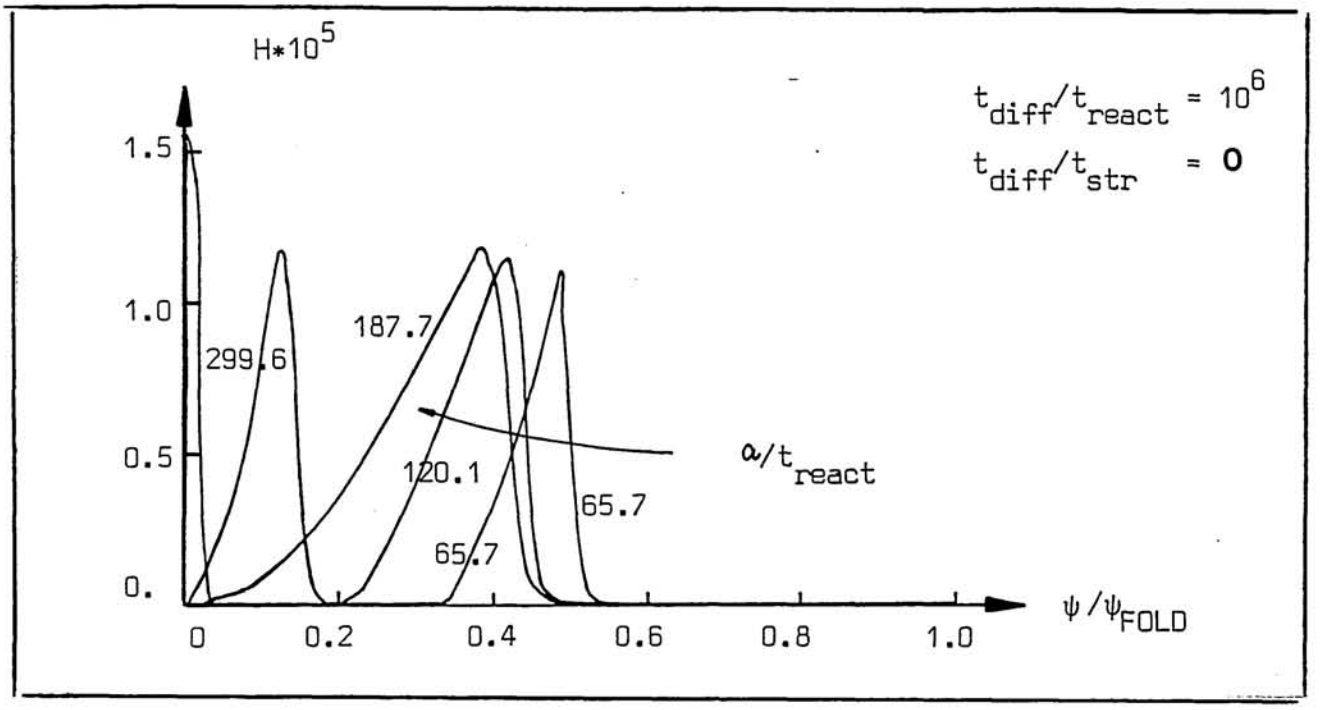

FIGURE 4.10 LAMINAR FLAME SPEED CONTROL REGIME ——
THE H DISTRIBUTIONS IN THE FOLD.

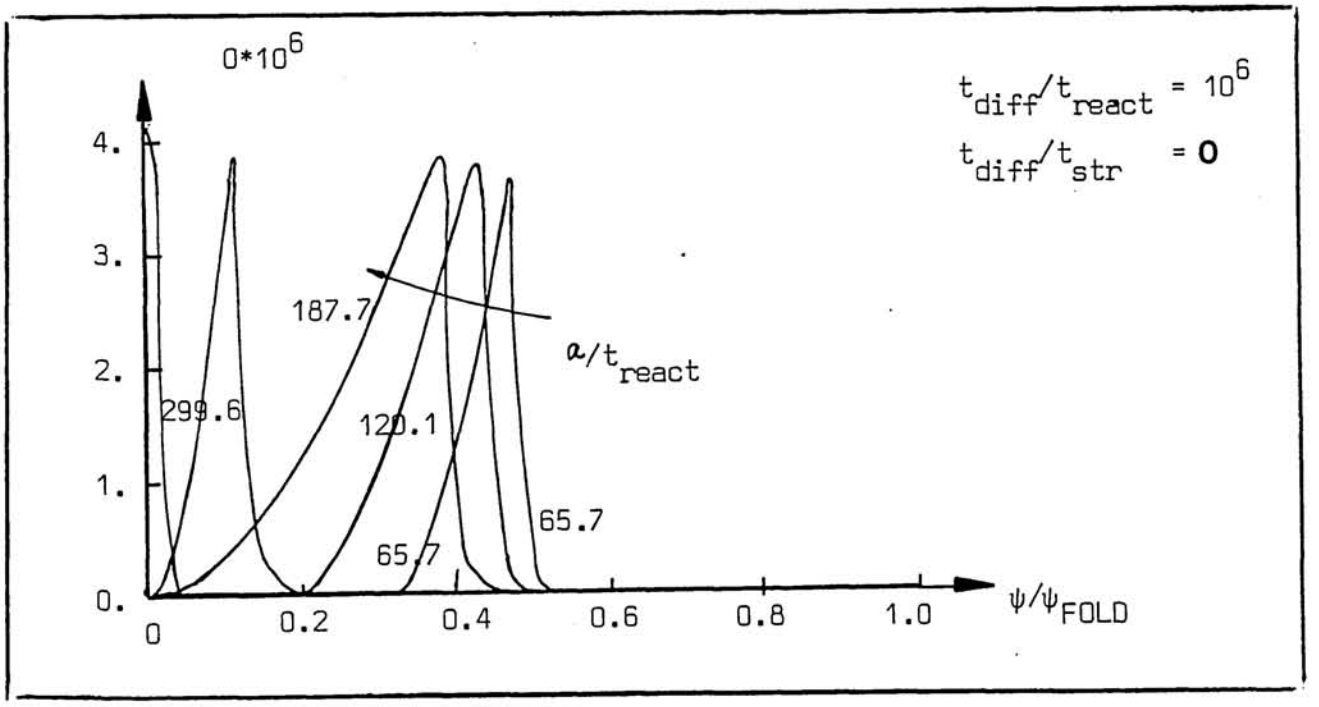

FIGURE 4.11 LAMINAR FLAME SPEED CONTROL REGIME ——
THE O DISTRIBUTIONS IN THE FOLD.

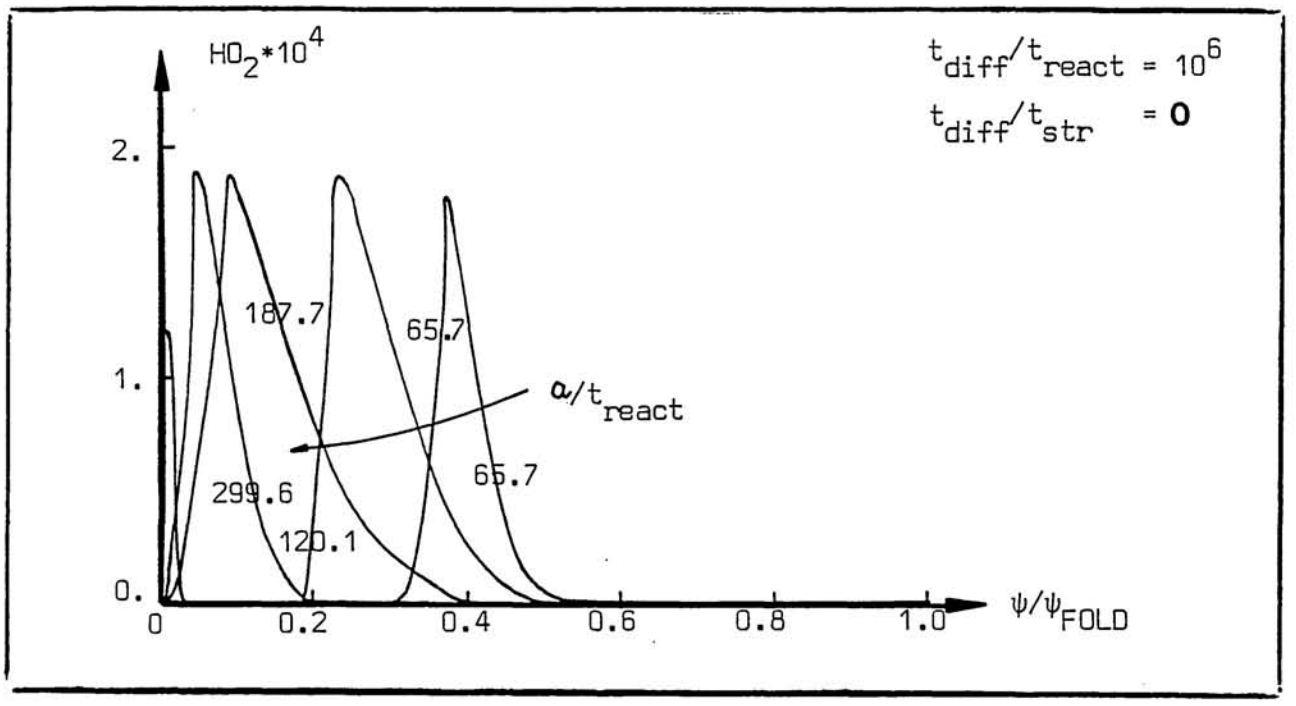

FIGURE 4.12 LAMINAR FLAME SPEED CONTROL REGIME ——— THE HO_2 DISTRIBUTIONS IN THE FOLD.

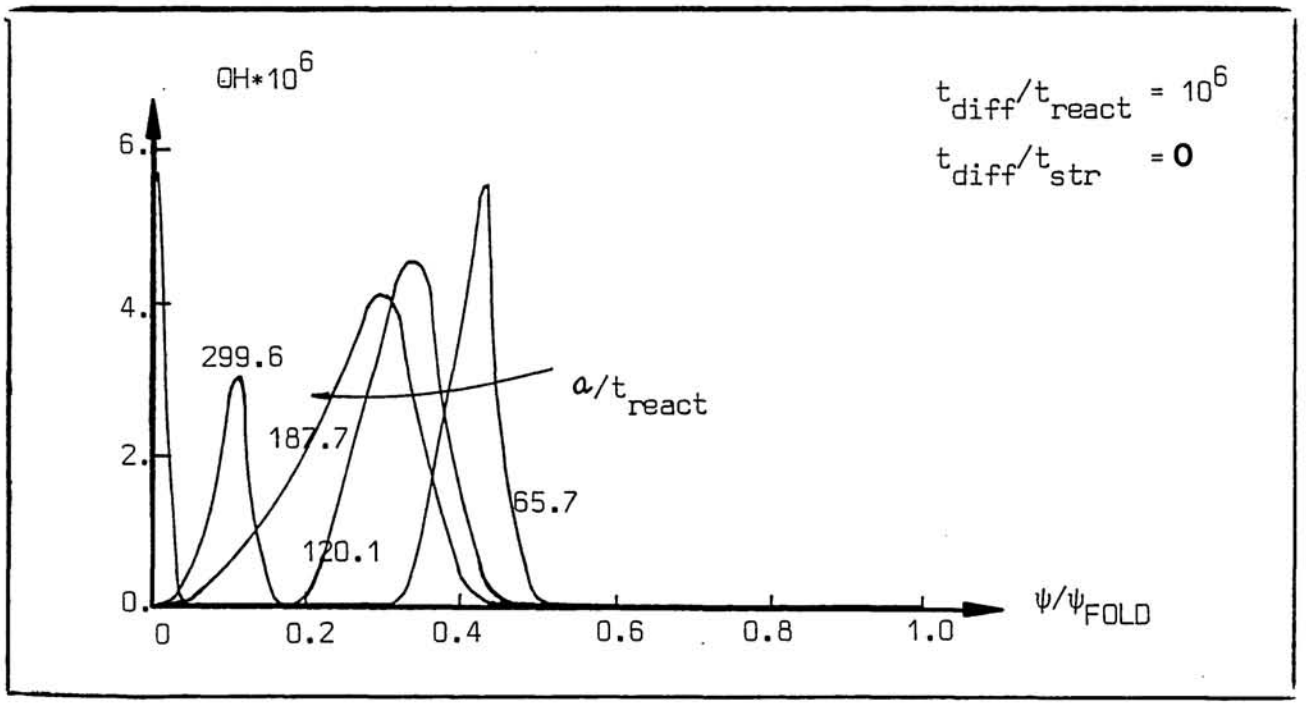

FIGURE 4.13 LAMINAR FLAME SPEED CONTROL REGIME ——— THE OH DISTRIBUTIONS IN THE FOLD.

Inspection of the cross-fold profiles shows that the chemical reaction is confined to a thin zone which separates burned gases from unburned ones; and this thin zone travels at a uniform velocity across the fold from burned part to unburned part. During the burning process, all major species profiles display almost the same shapes and propagate steadily with different successive ages. Until the flame front touches the unburned symmetrical plane, the gradients of species concentrations across the fold become less steep. At the symmetrical unburned-plane, all gradients of the corresponding concentrations are zero.

It should be emphasised that not only the concentrations of the major species are calculated but also of the intermediate ones. The predicted profiles of such radical species through the flame, at various ages, are shown in Figures 4.10 - 4.13. Inspection of the intermediate species distributions shows that the hydroperoxyl concentration exhibits higher values when compared with other minor species. The mass fraction ratio of (HO_2) and (O) is seen to be about 50 at the corresponding peaks (i.e. $(HO_2):(O) \simeq 50$).

(ii) <u>Results of internal flame propagation regime</u>

Figures 4.14 - 4.17 represent the species concentration distributions across the fold which is subjected to stretching.

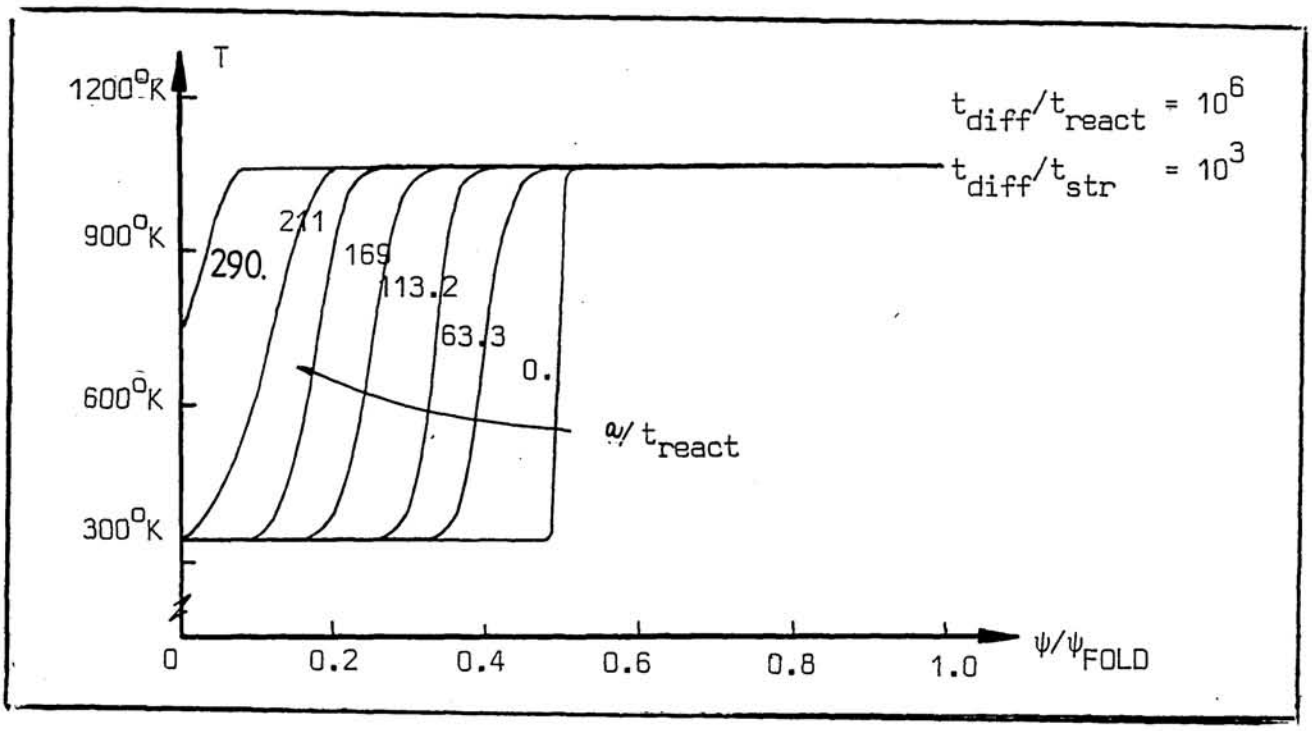

FIGURE 4.14 INTERNAL FLAME PROPAGATION REGIME ——— THE TEMPERATURE DISTRIBUTIONS IN THE FOLD.

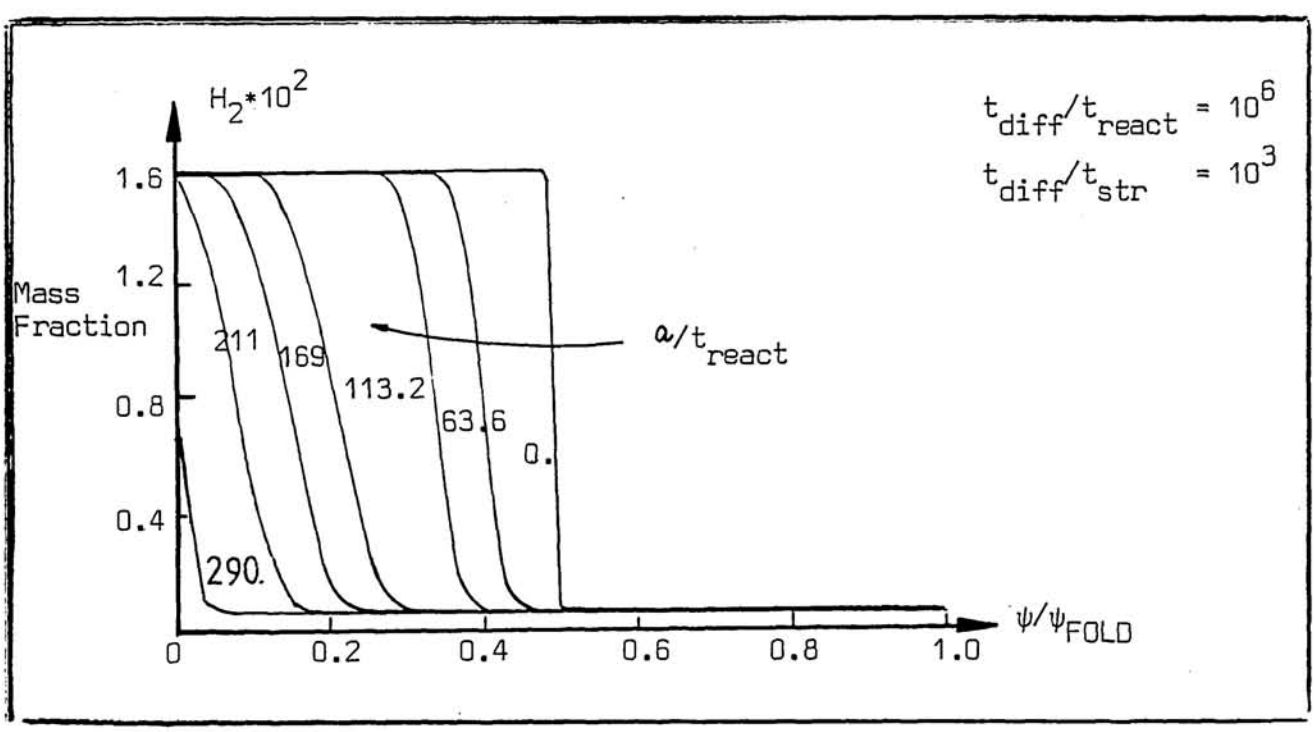

FIGURE 4.15 INTERNAL FLAME PROPAGATION REGIME ——— THE H_2 DISTRIBUTIONS IN THE FOLD.

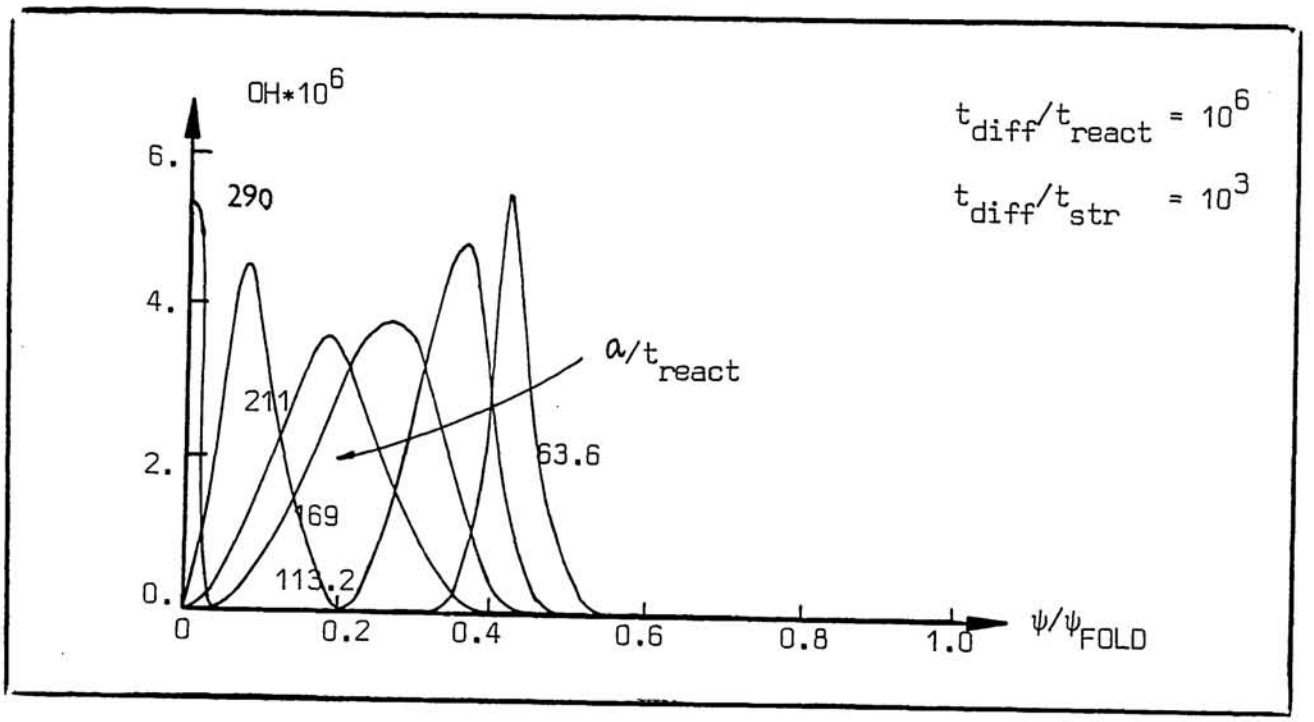

FIGURE 4.16 INTERNAL FLAME PROPAGATION REGIME ——— THE OH DISTRIBUTIONS IN THE FOLD.

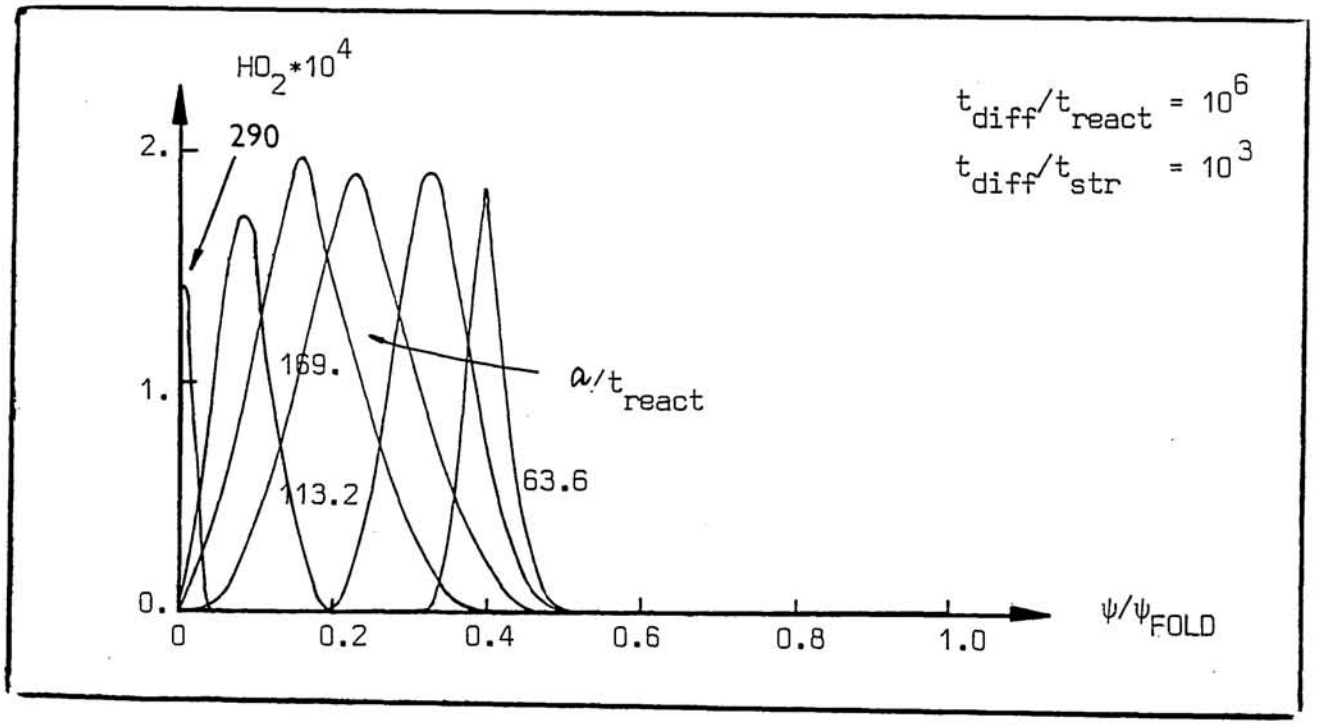

FIGURE 4.17 INTERNAL FLAME PROPAGATION REGIME ——— THE HO_2 DISTRIBUTIONS IN THE FOLD.

Since the reaction time is shorter than the diffusion and stretching times, the cross-fold profiles at different successive ages which have been observed from the laminar-speed-control regime, are still being observed here. However, the fold distance is diminished exponentially as the age increases. It is also seen that the fold burn-out time for the present case is appreciably shorter than the previous regime. For instance, t_b/t_{react}=304.43 for the present case; and t_f/t_{react}=358.2 for the previous case.

The reason is that since the present burning regime is subjected to the stretching process, the fold size is continuously reduced. The reduction in fold size will cause the fold burning rate to increase. Hence, the fold burn-out time has to decrease as the burning rate increases.

(iii) Results of fast mixing associated with chemical-kinetic control

Figures 4.18 - 4.21 represent the fast mixing associated with chemical-kinetic control regimes within a fold. Inspection of Figure 4.18 shows that all the gas properties are evened out by rapid stretching at the dimensionless age a/t_{react}=0.88. Under these circumstances, the burning process is controlled by

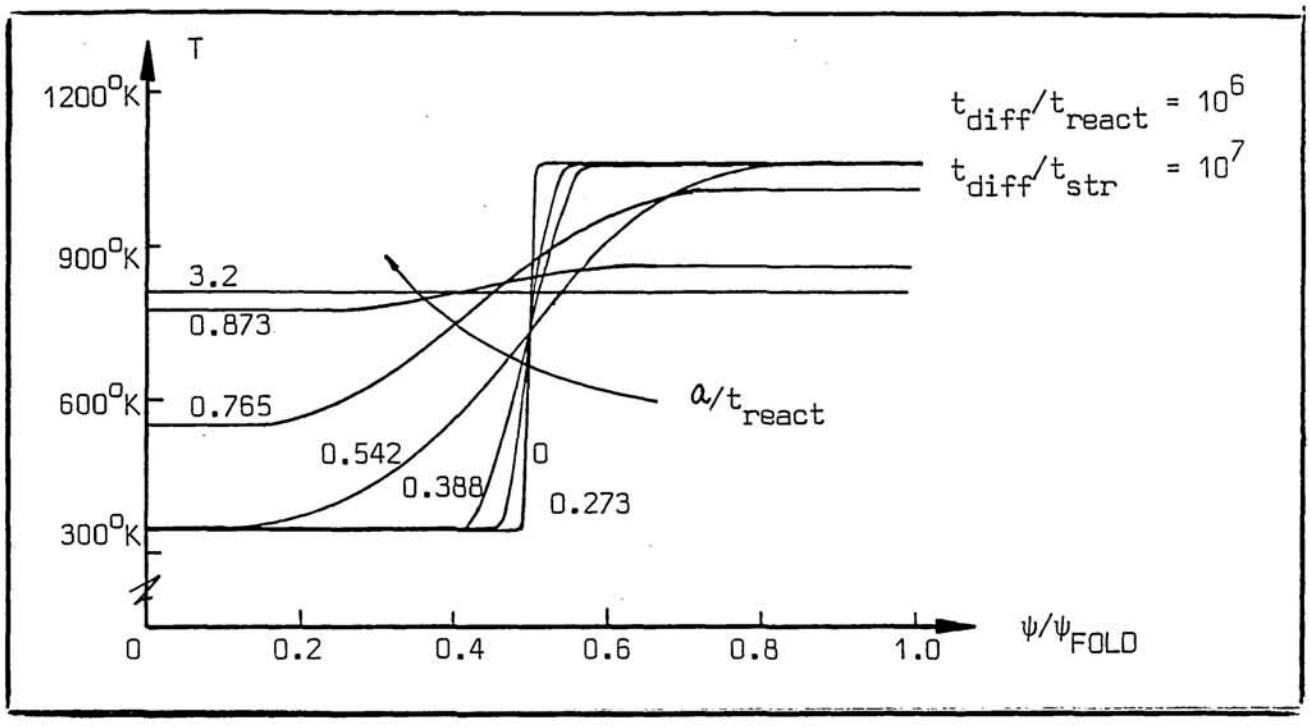

FIGURE 4.18 FAST MIXING —— THE TEMPERATURE DISTRIBUTIONS IN THE FOLD.

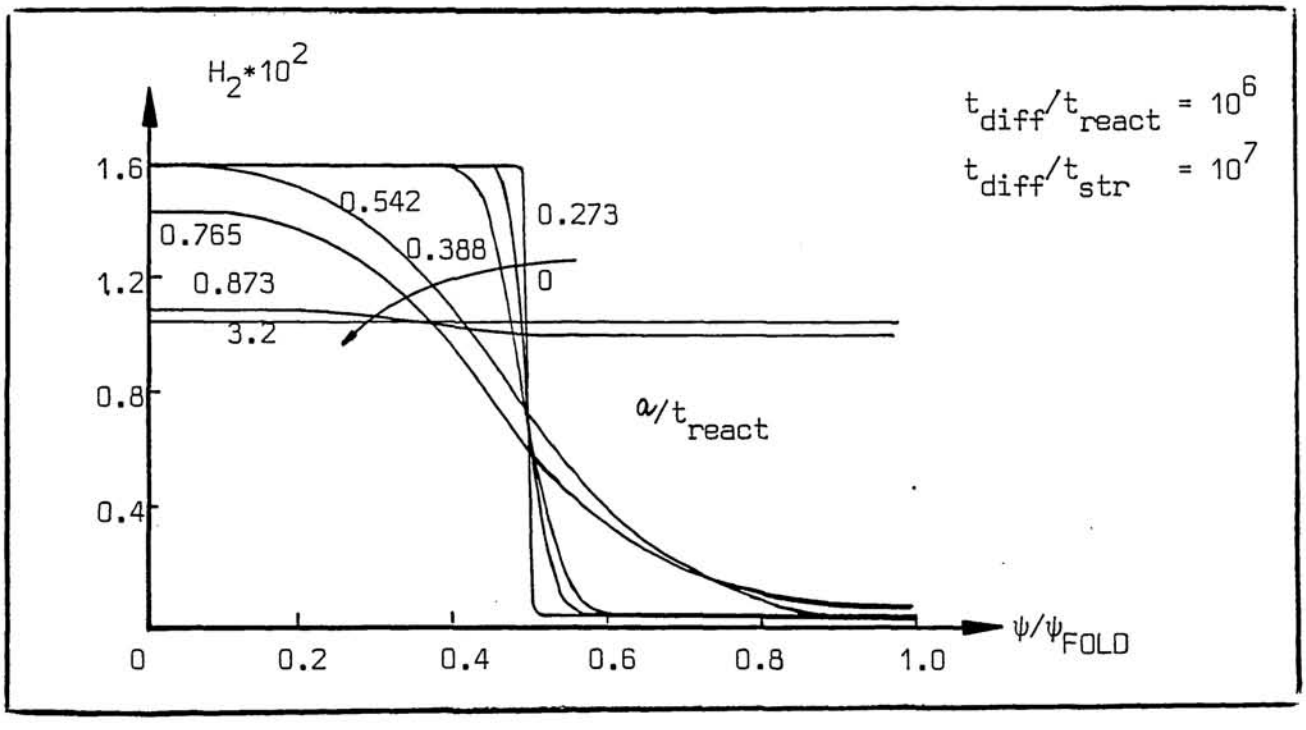

FIGURE 4.19 FAST MIXING —— THE H_2 DISTRIBUTIONS IN THE FOLD.

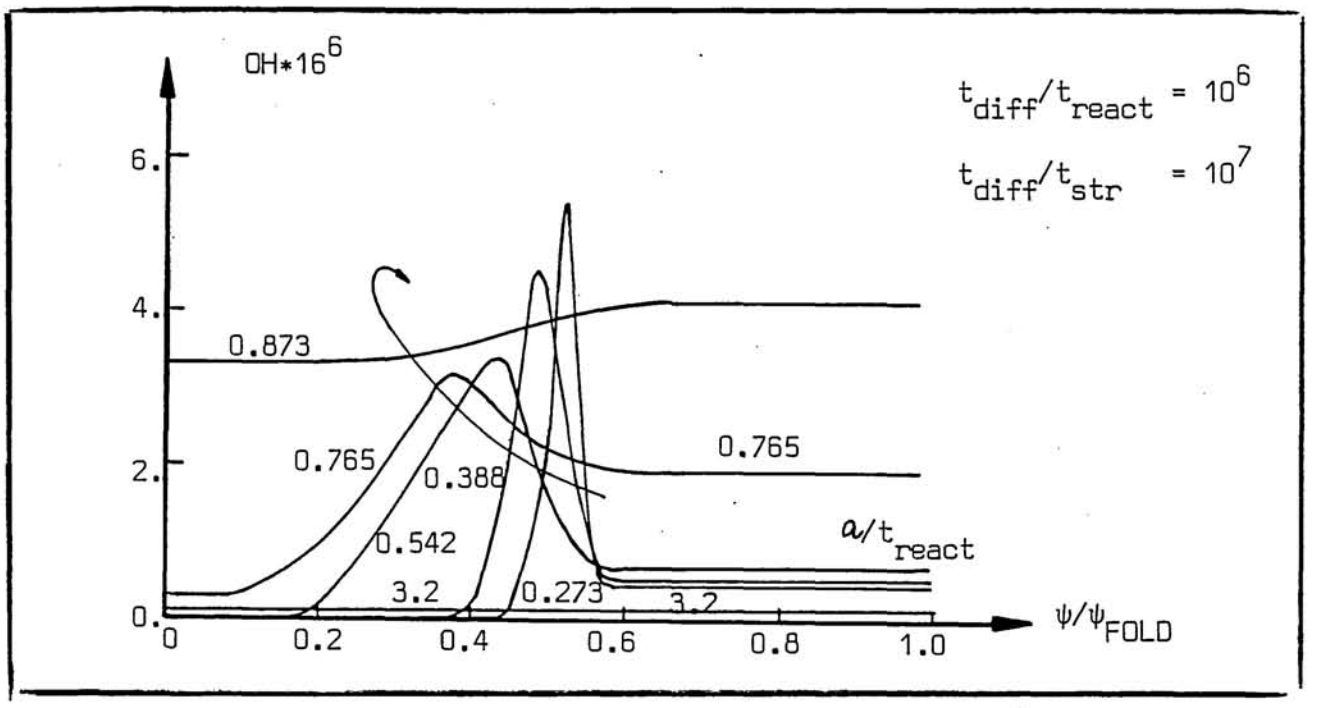

FIGURE 4.20 FAST MIXING —— THE OH DISTRIBUTIONS IN THE FOLD.

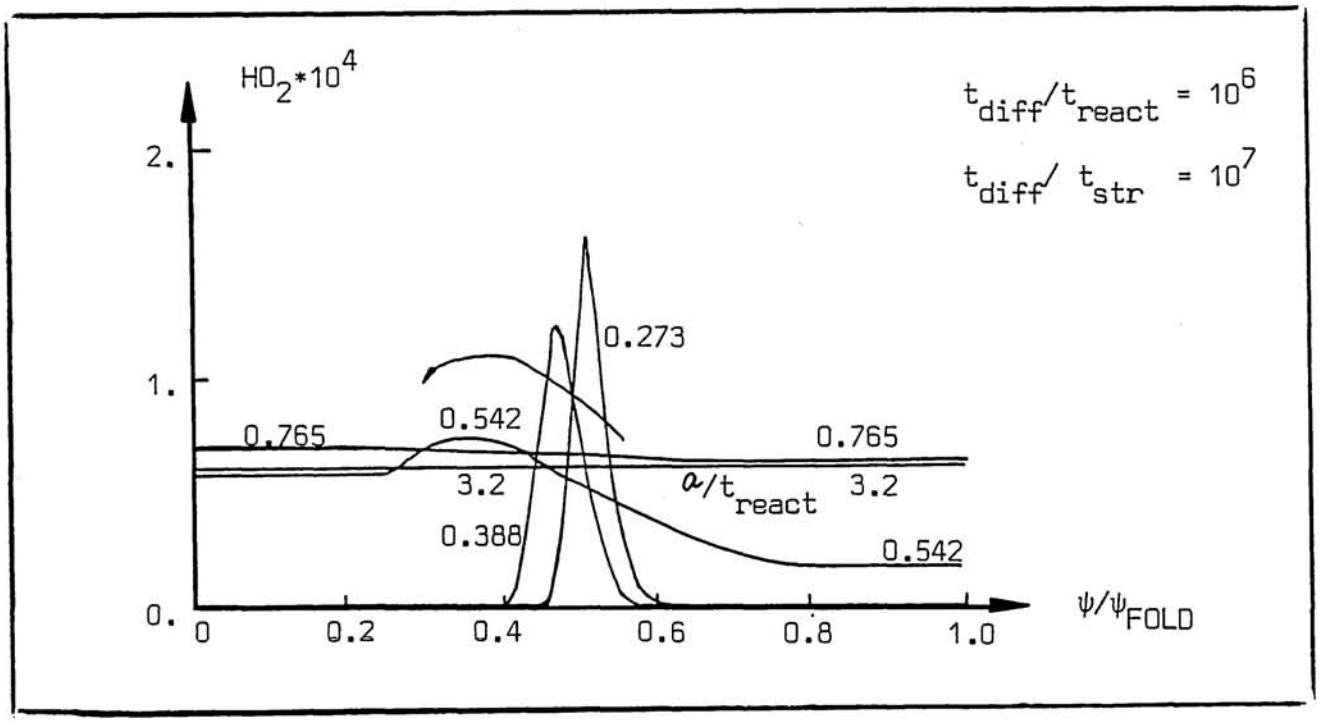

FIGURE 4.21 FAST MIXING —— THE HO_2 DISTRIBUTIONS IN THE FOLD.

chemical kinetics. The phenomenon of the fold is quite similar to those that resulted from the fragment-coalescence approach, as described in Chapter 1.6.2. Since the stretching time is so short in comparison with the diffusion and reaction times, the fresh gases across the fold do not burn to completion.

(b) Probability-density functions of the fold

A probability-density function of the fold, $\tilde{p}d\phi$ is defined as the fraction of mass of gas for which concentration of variable ϕ at the prevailing ω interval, $\delta\omega$, lies between ϕ and $\phi+d\phi$. Hence, at any particular age, the $\tilde{p}$ distribution can be computed, in accordance with:

$$\tilde{p}\langle\phi,a\rangle = \frac{\sum_{\phi}^{\phi+\delta\phi} \frac{d\omega}{\int_{o}^{Y} d\omega}}{\delta\phi} \quad . \qquad (4.6\text{-}4)$$

It should be noted that the above $\tilde{p}$ distributions at various ages are computed directly through the corresponding instantaneous profiles, $\phi\langle\omega,a\rangle$.

The integral probability distribution

In some circumstances, the integral probability distribution, $\tilde{I}$, is more convenient for presentation. It is defined as the fraction of mass for which the sum of

probability finding $\tilde{p}d\phi$ at the prevailing ω interval, $\delta\omega$, lies between ϕ_{min} and ϕ;

$$\tilde{I}\langle\phi,a\rangle = \int_{\phi_{min}}^{\phi} \tilde{p}d\phi \quad . \qquad (4.6\text{-}5)$$

Obviously, the total sum of the $\tilde{p}d\phi$ at any successive age must be equal to unity.

$$\sum_{\phi_{min}}^{\phi_{max}} \tilde{p}d\phi = 1 \quad , \qquad (4.6\text{-}6)$$

where ϕ_{min} and ϕ_{max} are the corresponding minimum and maximum values of $\phi\langle\omega,a\rangle$ at age 'a'.

Method of computation

In order to show how the $\tilde{p}d\phi$ can be computed numerically, imagine a cross-fold profile which is presented in a graphical form as in Figure 4.22. The computation of $\tilde{p}$ distribution has been performed by scanning through the whole ϕ profile domain (from ϕ_{min} to ϕ_{max}). It is supposed that the fraction-interval of ϕ, $\delta\phi$, is equal to $\frac{\phi_{min}-\phi_{max}}{M}$, where M is the total number of the fractional intervals (M=20 is chosen).

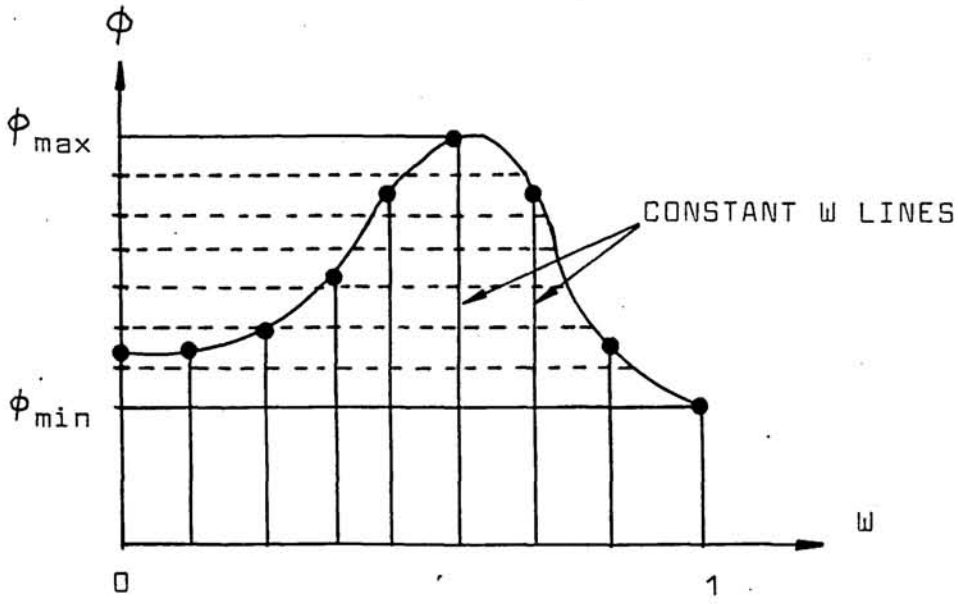

FIGURE 4.22 METHOD OF THE COMPUTATION OF $\tilde{P}$ DISTRIBUTIONS.

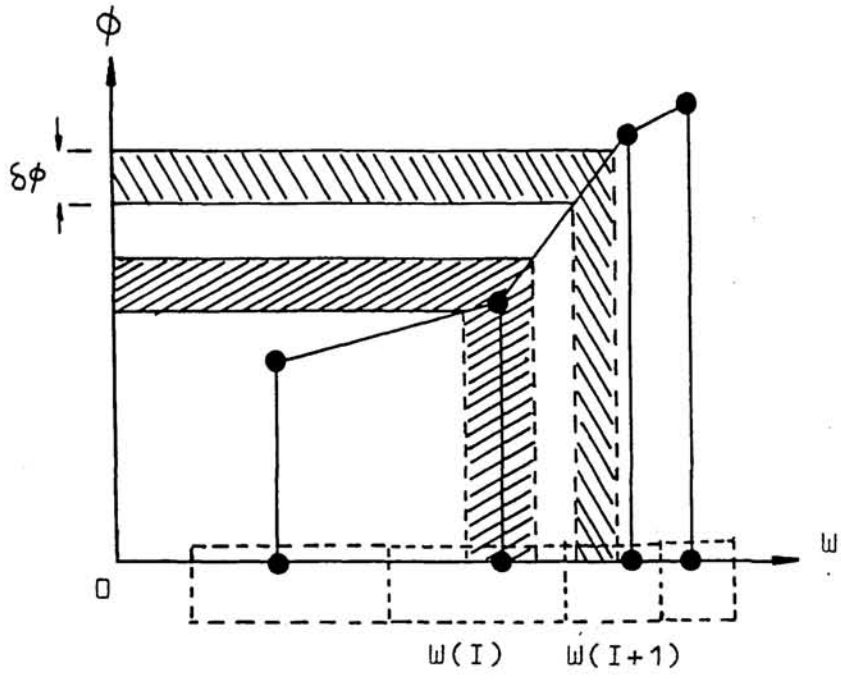

FIGURE 4.23 ILLUSTRATION OF THE LINEAR-INTERPOLATION METHOD.

The method employed here is that of linear interpolation. Once the successive $\delta\phi$ has been scanned in a ω cell, as illustrated in Figure 4.23, the probability-finding of ϕ at the prevailing ω is calculated in accordance with equation 4.6-4.

Results

The fold $\tilde{p}d\phi$ distributions of instantaneous reactedness and concentrations, at any successive instant of age, for two different burning regimes are presented below.

(i) $\tilde{p}$ distributions across the fold which are under the laminar-speed-control

The $\tilde{p}d\tau\sim\tau$ diagram of reactedness is shown in Figure 4.24(a).

It is observed that the shapes of $\tilde{p}d\tau$ exhibit a 'U' shape with two spikes in two ends. Initially, both spikes give equal proportions of burned to unburned masses. During the period of successive progress of the burning process within the fold, the proportion of

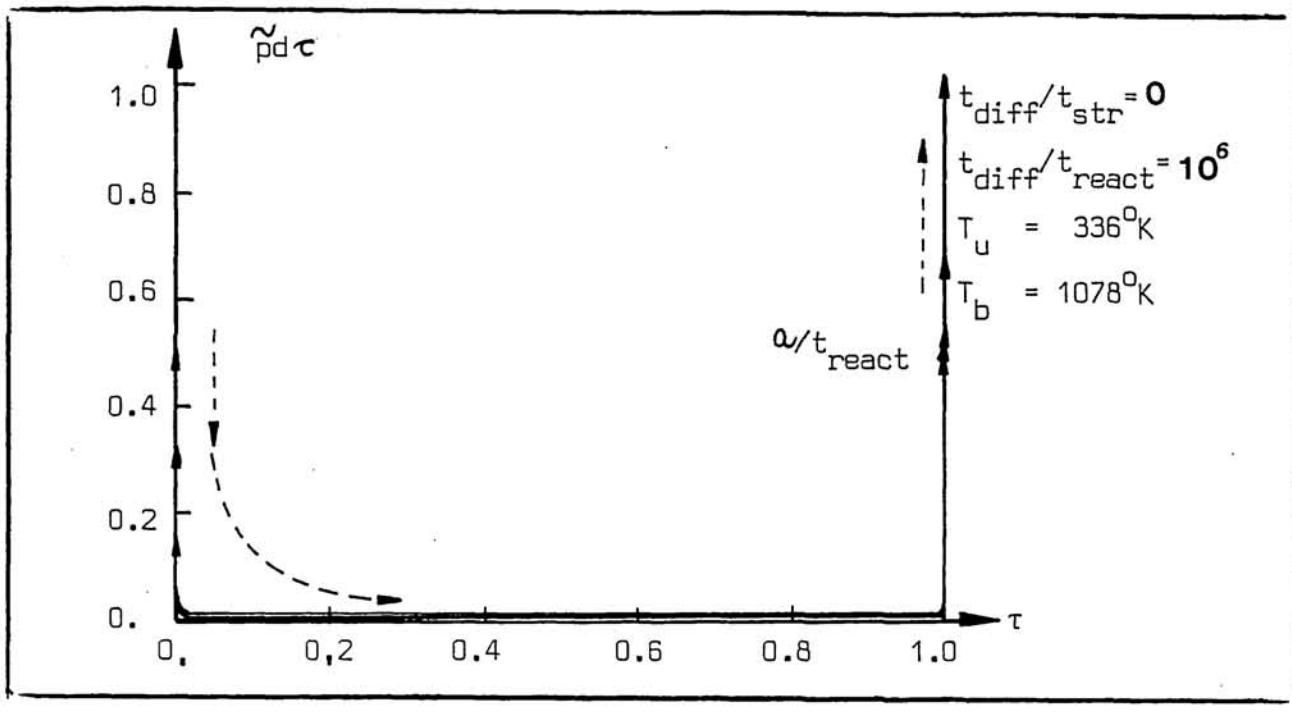

FIGURE 4.24(a) EVOLUTION OF THE FOLD PROBABILITY DENSITY FUNCTION, $\tilde{p}d\tau$, AS AGE PROGRESSES.

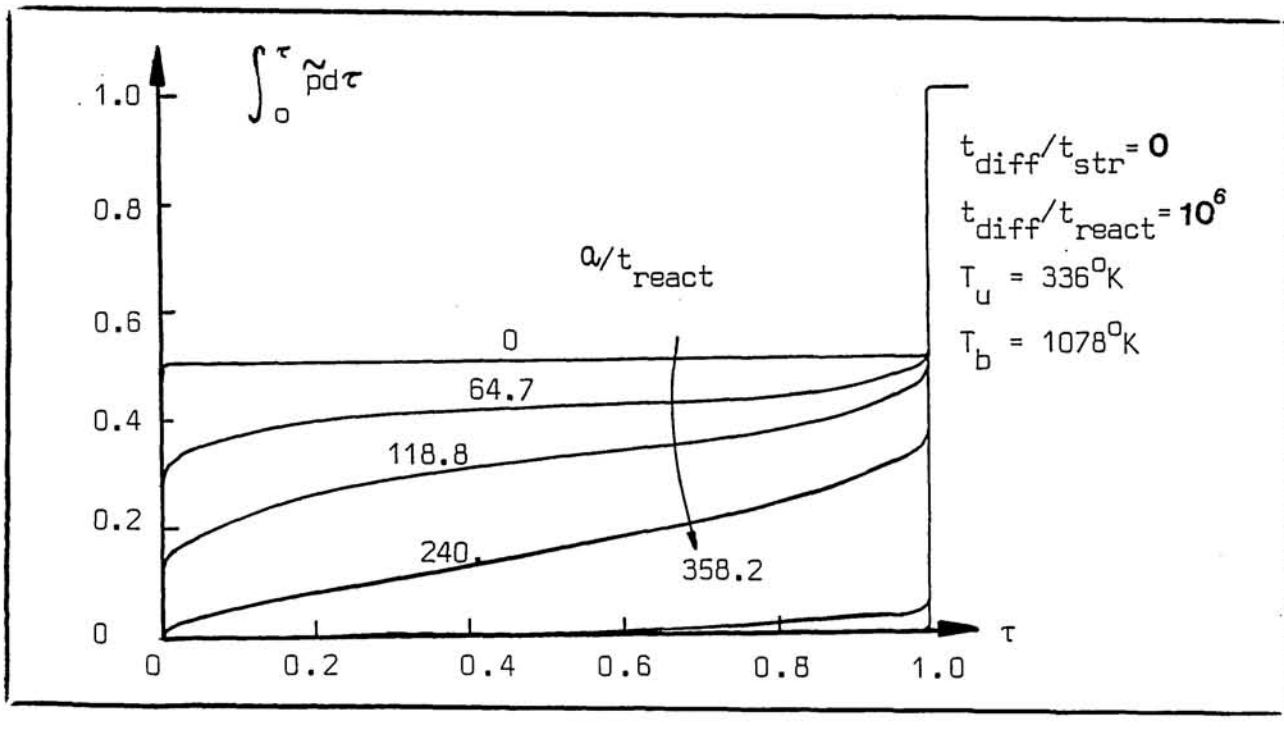

FIGURE 4.24 (b) EVOLUTION OF THE FOLD PROBABILITY DENSITY FUNCTION, $\int_0^\tau \tilde{p}d\tau$, AS AGE PROGRESSES.

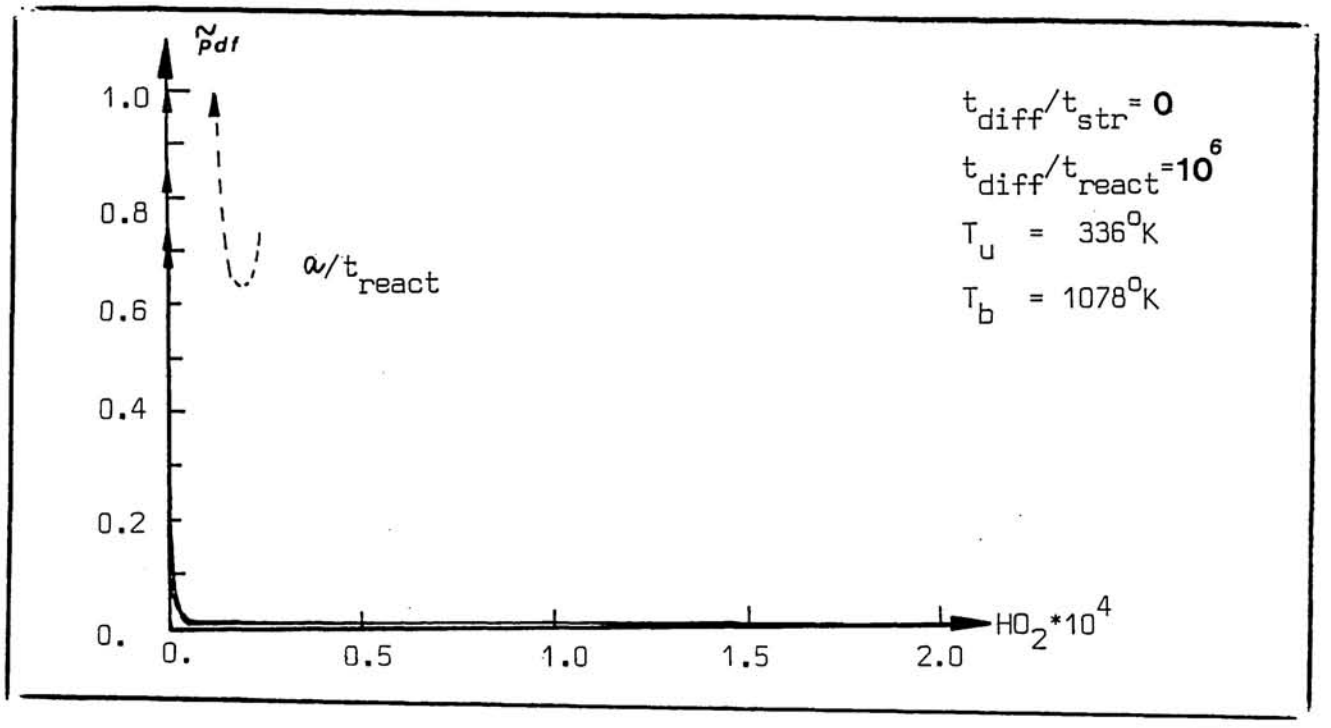

FIGURE 4.25(a) EVOLUTION OF THE FOLD PROBABILITY DENSITY FUNCTION, $\tilde{p}df$, AS AGE PROGRESSES.

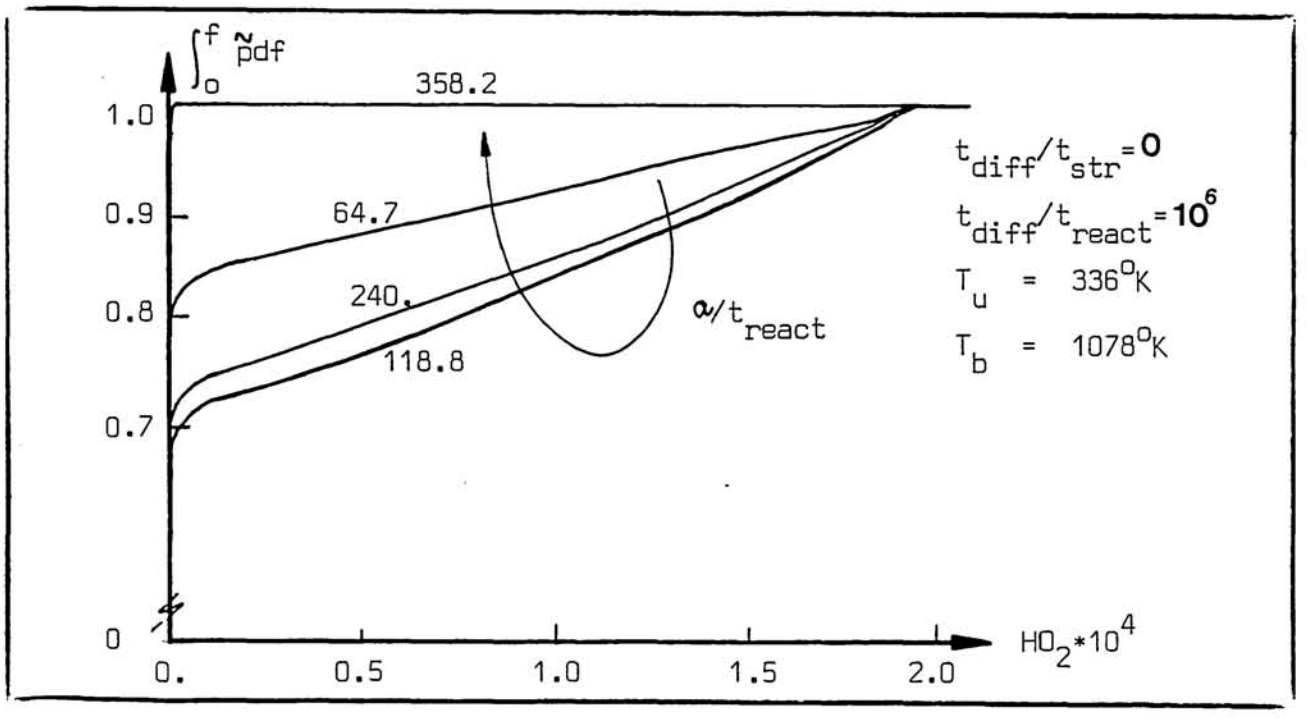

FIGURE 4.25(b) EVOLUTION OF THE FOLD PROBABILITY DENSITY FUNCTION, $\int_0^f \tilde{p}df$, AS AGE PROGRESSES.

unburned spike decreases whilst the burned spike increases. Finally, there is only a single spike located at the burned end.

Attention should now be directed to the $\tilde{p}$ distributions of the intermediate species. These are displayed in Figure 4.25(a). Inspection of Figure 4.25(a) shows that the $\tilde{p}$ distributions of the hydroperoxyl species exhibit a single spike and are connected by a smooth 'tail'. This is because the intermediate species variations are mainly concentrated within the thin zone.

In order to facilitate more understanding of the decay of instantaneous concentrations in the fold, the integral of probability-density functions, $\int_0^{\phi} \tilde{p} d\phi \sim \phi$, at various ages are illustrated on the Figures 4.24(b) and 4.24(b), respectively. Inspection of Figure 4.24(b) shows that the integral $\tilde{p} d\tau$ distributions of the reactedness give a step-like function and move steadily and horizontally towards the burned gases. Finally, there is only a single 'delta-function' which exists at the burned region.

Discussion

The laminar-flame-speed control regime within the fold shows that the burned and unburned gases are separated by a thin flame front. The distributions of $\tilde{p} d\phi$ can be

characterised by two single 'delta'-functions and a 'ridge'. The left-hand spike is specified by a delta function, $P_1 = \int_{\phi_{min}}^{\phi_{min}+\delta\phi} \tilde{p}d\phi$; whilst the right-hand spike is given by another delta function, $P_2 = \int_{\phi_{max-\delta\phi}}^{\phi_{max}} \tilde{p}d\phi$. These two are separated by a 'ridge' which is specified by the width and the depth of the horizontal portion of the $\tilde{p}$ curve with a negligible area of $1-P_1-P_2$ beneath it.

(ii) <u>$\tilde{p}$ distributions across the fold which are under the chemical-kinetic control</u>

Two cases are presented here. The first is an extreme case of chemical-kinetic control regime in which the fast mixing is associated with extinction. As illustrated in Figure 4.26, the $\tilde{p}d\tau$ distribution starts with a 'U' shape which is specified by two spikes and a ridge. Due to the fast mixing, the $\tilde{p}\sim\tau$ profiles are rapidly characterised by a single spike. Since rates of chemical reactions are low and the stretching process is rapid, the variations of $\tilde{p}\sim\tau$ profiles remain unchanged with age after the full mixing has been achieved. This fold is defined as a 'blow-out' fold.

The second case is a typical case of the chemical-kinetic control regime in which the fast mixing is associated

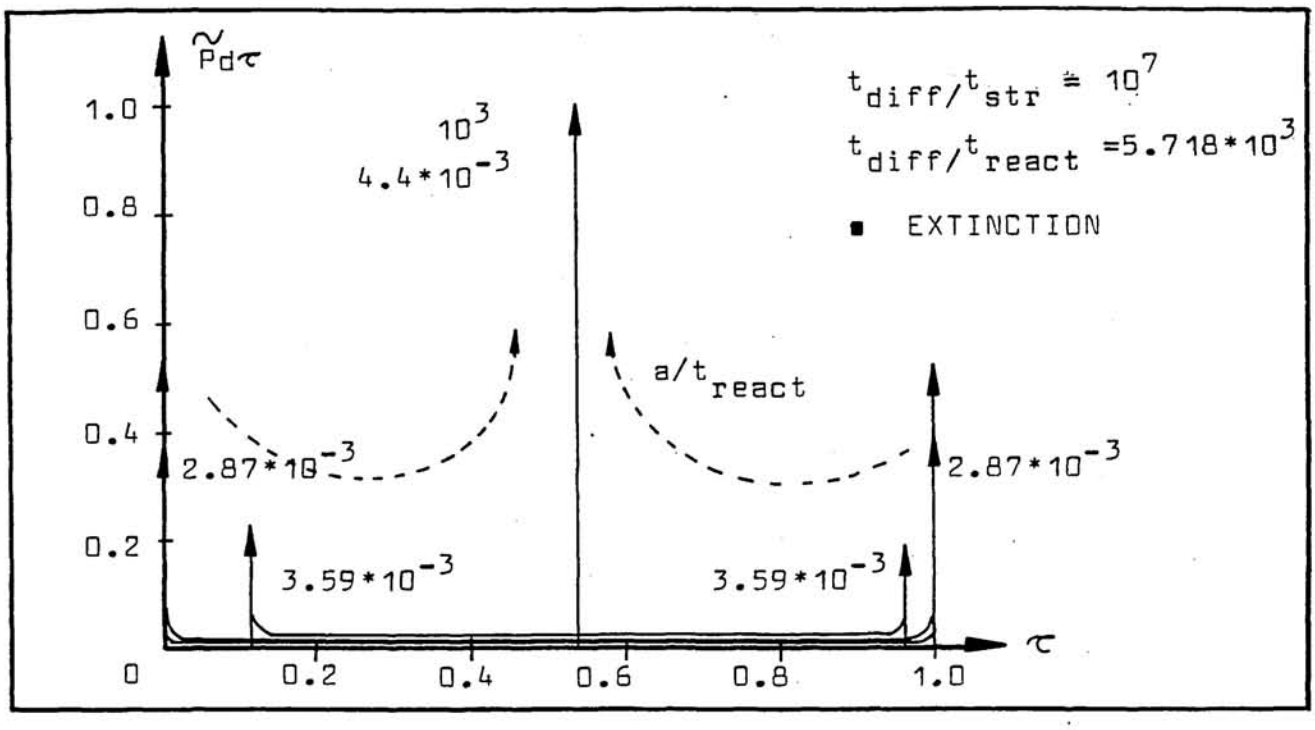

FIGURE 4.26 EVOLUTION OF THE FOLD PROBABILITY DENSITY FUNCTION, $\tilde{P}_\tau$, AS AGE PROGRESSES.

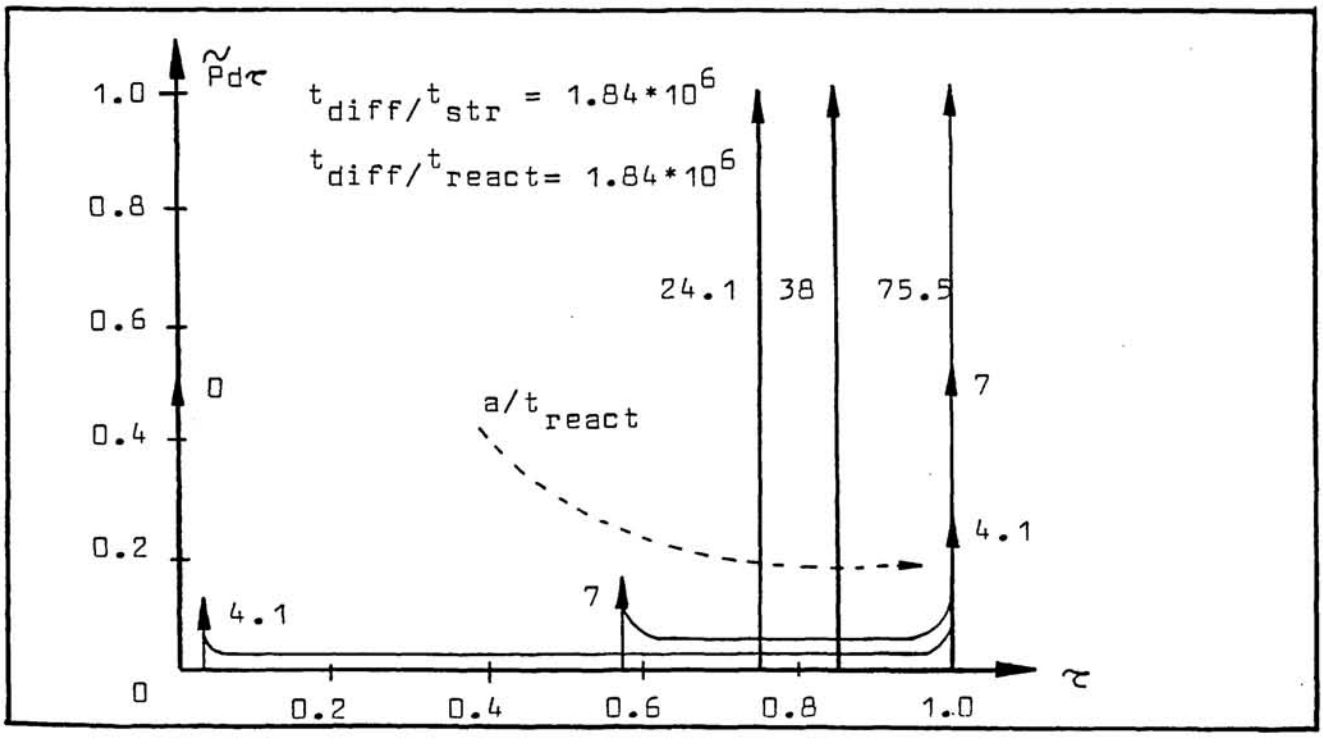

FIGURE 4.27 EVOLUTION OF THE FOLD PROBABILITY DENSITY FUNCTION, $\tilde{P}_\tau$, AS AGE PROGRESSES.

with spontaneous ignition. Since the fresh gases of the newly-formed fold form a highly reactive mixture in comparison with the first case, spontaneous ignition takes place. As illustrated in Figure 4.27, the gas properties across the fold are rapidly evened out by high stretching. Hence, it is observed that the $\tilde{p}$ distribution exhibits a single spike. Since the rates of reactions are very high, it is seen that the single spike of the $\tilde{p}$ distribution gradually moves towards the fully burned end. Finally, there is only a single 'spike' which exists at the fully burned end.

(c) <u>The variations of fold-average properties with age</u>

It should be recalled that values of the burn-out and mixing times have been tabulated in Table 4.4. Now, variations of fold-average properties with age for a single fold are discussed. The fold-average quantity, $\tilde{\phi}$, at age 'a', is defined as:

$$\tilde{\phi}\{a\} = \frac{\int_0^Y \phi\rho dy}{\int_0^Y \rho dy} \quad . \qquad (4.6\text{-}7)$$

The above calculation is based on mass averaging. Two kinds of results are presented, namely, (i) variations of fold-average reactedness with age; and (ii) variations of fold-average species concentration with age. Since

the above quantities are functions of age

and since they are also influenced by the values of the governing parameters t_{diff}/t_{str} and t_{diff}/t_{react}, the presentations will be arranged in terms of these parameters.

(i) Variations of fold-average reactedness with age

The variations of reactedness, $\tilde{\tau}$ with age are displayed in Figures 4.28 - 4.31. In each diagram, the parameter t_{diff}/t_{str} is fixed whilst the parameter t_{diff}/t_{react} is varied. Presentations are therefore of a particular burning regime in which the influence of reaction time parameter on the fold is investigated.

Figure 4.28 shows the characteristics of the laminar-speed-control regime. Each curve displayed on this diagram represents a particular fold behaviour which is governed by t_{diff}/t_{react}. Since stretching is absent, the relationship between $\tilde{\tau}$ and age is linear. It is observed that the progress of $\tilde{\tau}$ is by way of a thin flame zone propagation. The slope of such a curve is proportional to the flame speed. It is also observed that the progress of $\tilde{\tau}$ takes shorter age to achieve completion of the burn-out of the fold in the highly reactive mixture (i.e. $t_{diff}/t_{react}=10^6$) than that of

the fold corresponding to a low reactive mixture (i.e. $t_{diff}/t_{react}=10^3$).

Figures 4.29 - 4.30 show the results of the internal-flame propagation regime in which the fold is subjected to stretching. Since the stretching rate is moderate, the relation of $\tilde{\tau}$~a is no longer linear. If the value of $\frac{\sqrt{t_{diff}t_{react}}}{t_{str}}$ becomes large, the progress of $\tilde{\tau}$ with age is controlled by eddy-stretching. However, if the value is small, the progress of $\tilde{\tau}$ with age is controlled by molecular diffusion, eddy-stretching and chemical kinetics. When both reaction time and stretching time are of the same order, the transition of the burning regime from internal flame propagation to spontaneous ignition takes place.

Figure 4.31 displays the results of chemical kinetic control regime. Since the rate of stretching is extremely high and the rate of reaction is low, it is observed that the spontaneous ignition which is associated with fast mixing of a fold does not burn to completion.

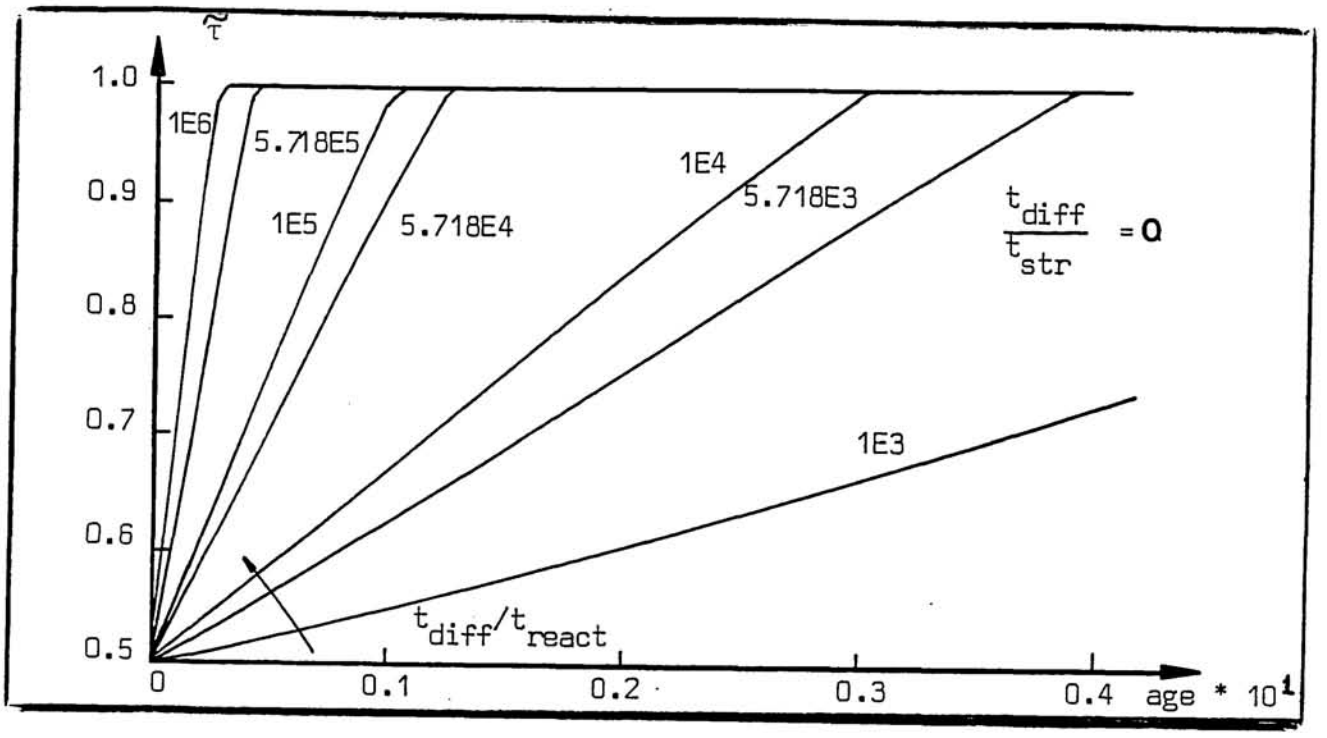

FIGURE 4.28 THE INFLUENCE OF THE REACTION TIME ON THE AVERAGE REACTEDNESS $\tilde{\tau}$ WITHOUT STRETCHING.

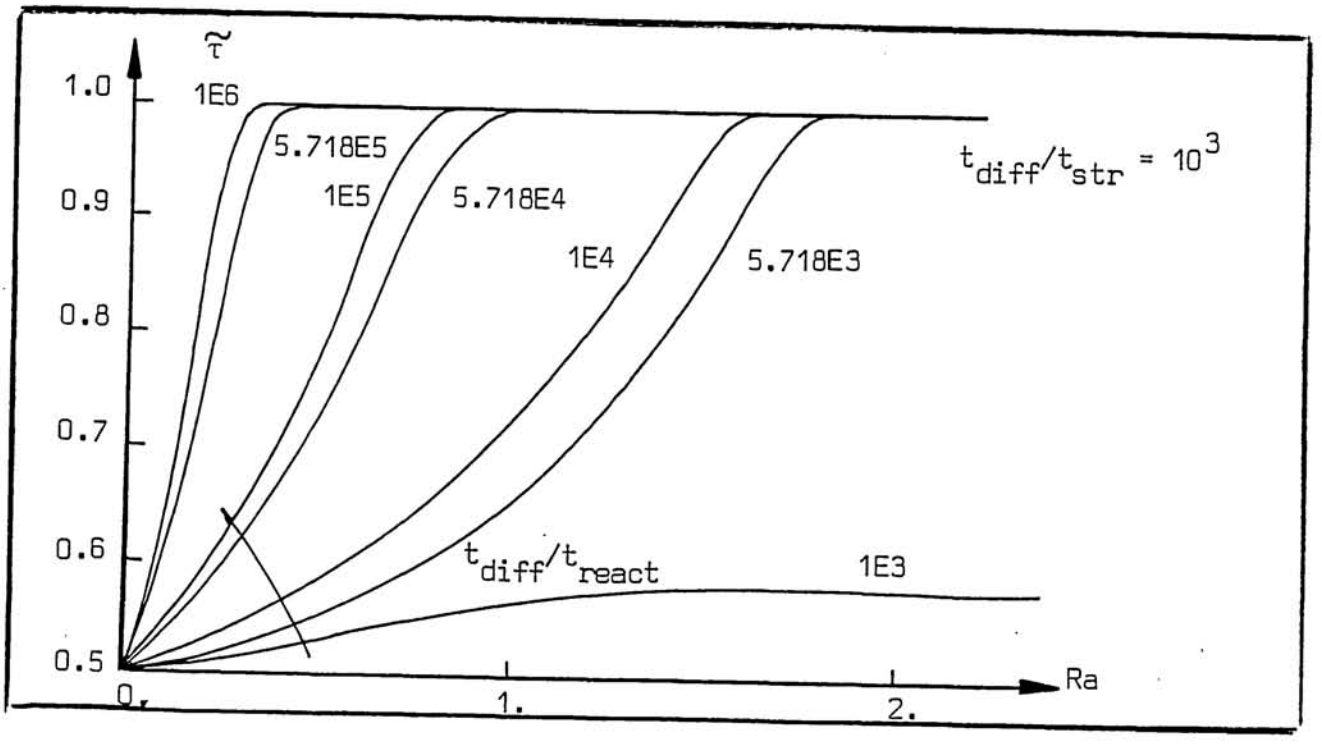

FIGURE 4.29 THE INFLUENCE OF THE REACTION TIME ON THE AVERAGE REACTEDNESS $\tilde{\tau}$ AT $t_{diff}/t_{str} = 10^3$.

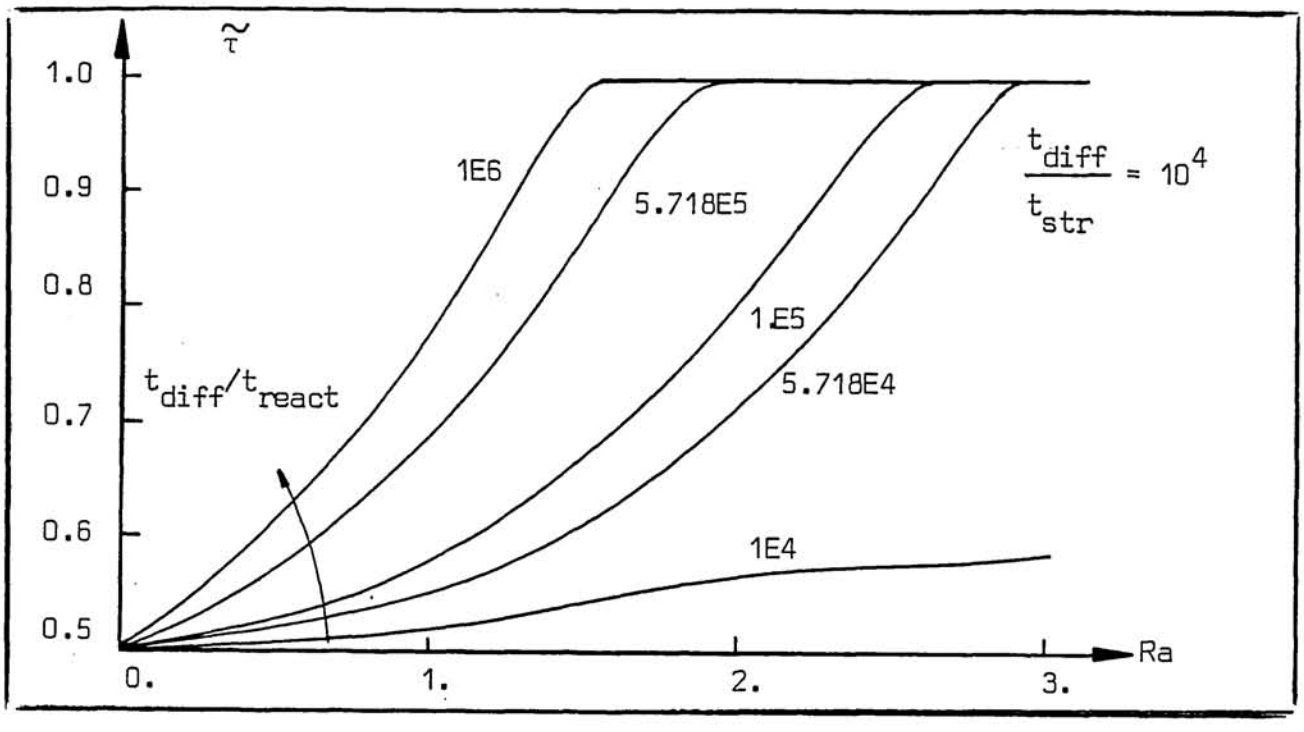

FIGURE 4.30 THE INFLUENCE OF THE REACTION TIME ON THE AVERAGE REACTEDNESS $\tilde{\tau}$ AT $t_{diff}/t_{str} = 10^4$.

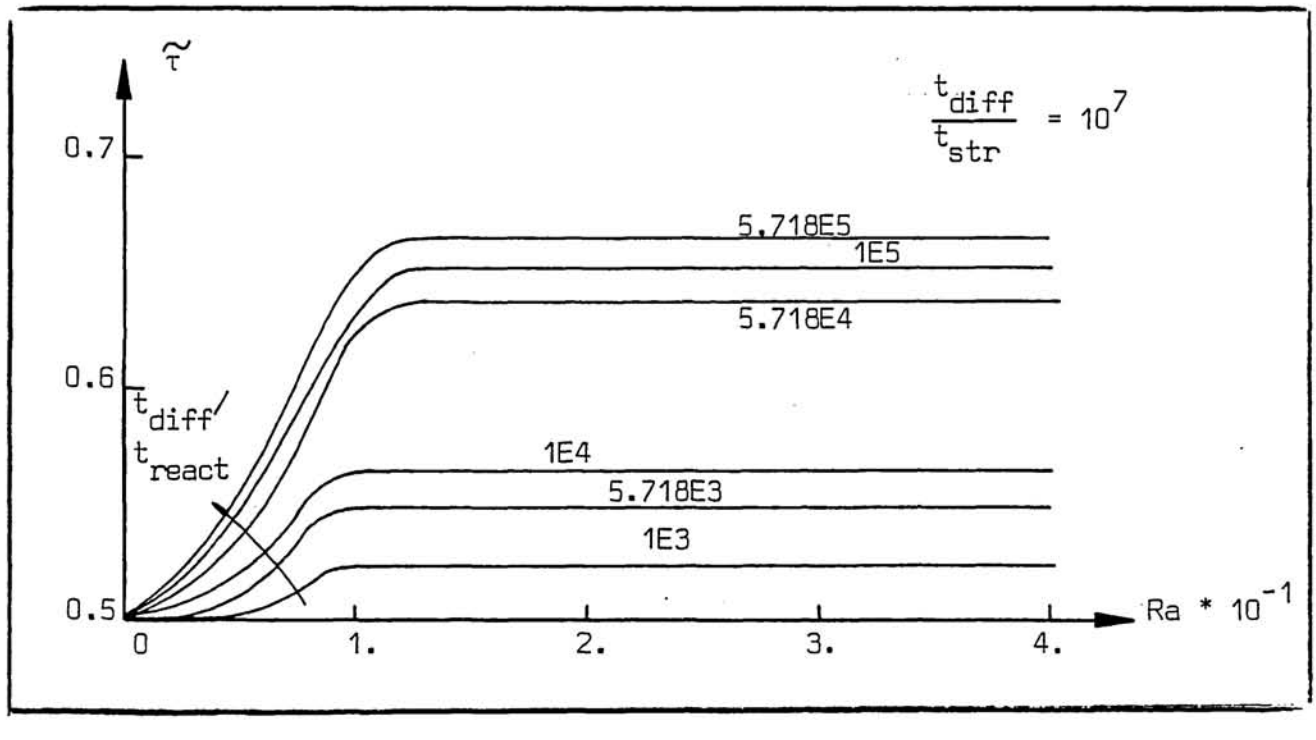

FIGURE 4.31 THE INFLUENCE OF THE REACTION TIME ON THE AVERAGE REACTEDNESS $\tilde{\tau}$ AT $t_{diff}/t_{str} = 10^7$.

(ii) Variations of fold-average species concentration with age

The results are classified into three different regimes, namely, laminar flame speed-control regime (Figures 4.32 - 4.34), internal flame propagation regime (Figures 4.35 - 4.37), and chemical kinetic control regime (Figures 4.38 - 4.40).

Since the parameter t_{diff}/t_{str} is fixed for each particular regime, each diagram represents the variations of fold-average concentration with age under the influence of t_{diff}/t_{react}.

Results of each regime are presented in two parts. The first is concerned with the major species distributions; whilst the second is focussed on the minor ones.

Laminar speed control regime

Figure 4,32 shows the effect of t_{diff}/t_{react} on the $\tilde{H}_2$ distribution. It is observed that high values of t_{diff}/t_{react} lead to short burn-out time and low values to higher ones. Figures 4.33 - 4.34 show the fold-average concentrations of $\tilde{HO}_2$ and $\tilde{H}$ versus age, respectively. Clearly, the non-linearity of Arrhenius terms must have strong effects on the intermediate species calculations. Inspection of Figures 4.32 - 4.34 reveals that the burn-out time of this

regime is proportional to the square-root of the product of diffusion time and reaction time.

Internal flame propagation regime

Figures 4.35 - 4.37 show the fold-average concentration variations of $\tilde{H}_2$, $\widetilde{HO}_2$ and $\tilde{H}$ with the dimensionless age, a/t_{str}. Since the stretching rate is moderate and the reaction rates are high, the features of flame propagation in association with stretching are observed. It is important to note that each curve in each diagram represents a single stretched-fold which is under the influences of hydrodynamics, laminar-transport and chemical kinetics. When the value of $\sqrt{t_{diff}/t_{react}}/t_{str}$ is large, the stretching effect on the fold is more profound.

Chemical kinetic control regime

Figures 4.38 - 4.40 display the results of chemical kinetic control regime. Since the chemical reaction time is long and the stretching time is short, spontaneous ignition can only take place after the gas properties across the fold have been evened out. Figure 4.40 shows that the formation of $\widetilde{HO}_2$ is important when the reaction rate is low. It is seen in Figure 4.38 that the highly reactive mixture leads to much unburned gases burning to completion.

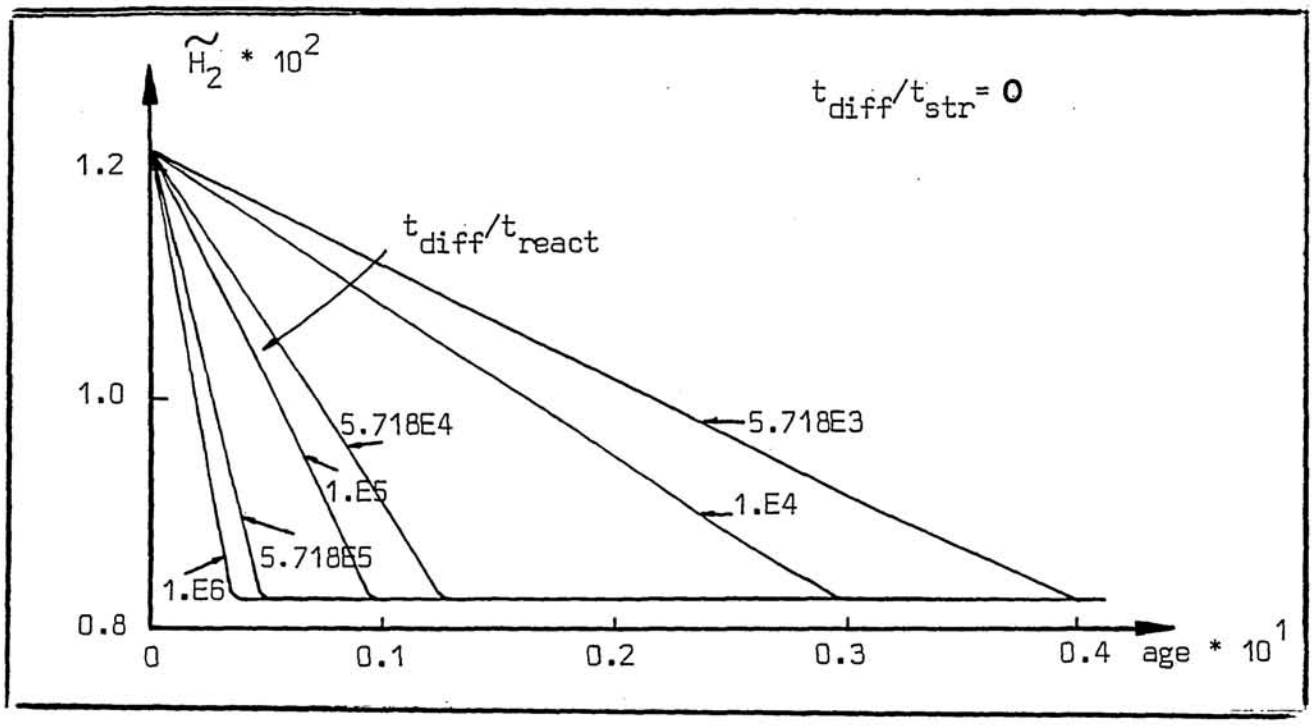

FIGURE 4.32 THE INFLUENCE OF THE REACTION TIME ON THE FOLD-AVERAGE QUANTITY UNDER THE LAMINAR FLAME SPEED CONTROL, REPRESENTED ON $\tilde{H}_2 \sim a$ DIAGRAM.

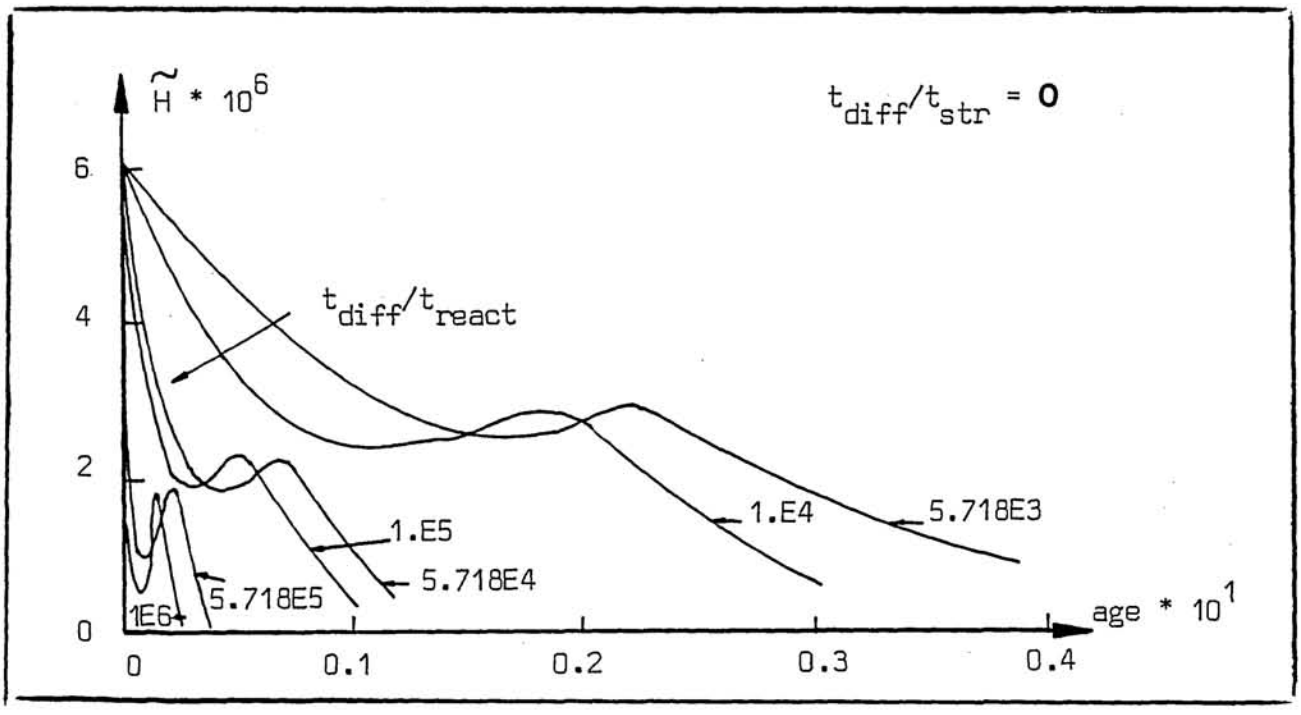

FIGURE 4.33 THE INFLUENCE OF THE REACTION TIME ON THE FOLD-AVERAGE QUANTITY UNDER THE LAMINAR FLAME SPEED CONTROL, REPRESENTED ON $\tilde{H} \sim a$ DIAGRAM.

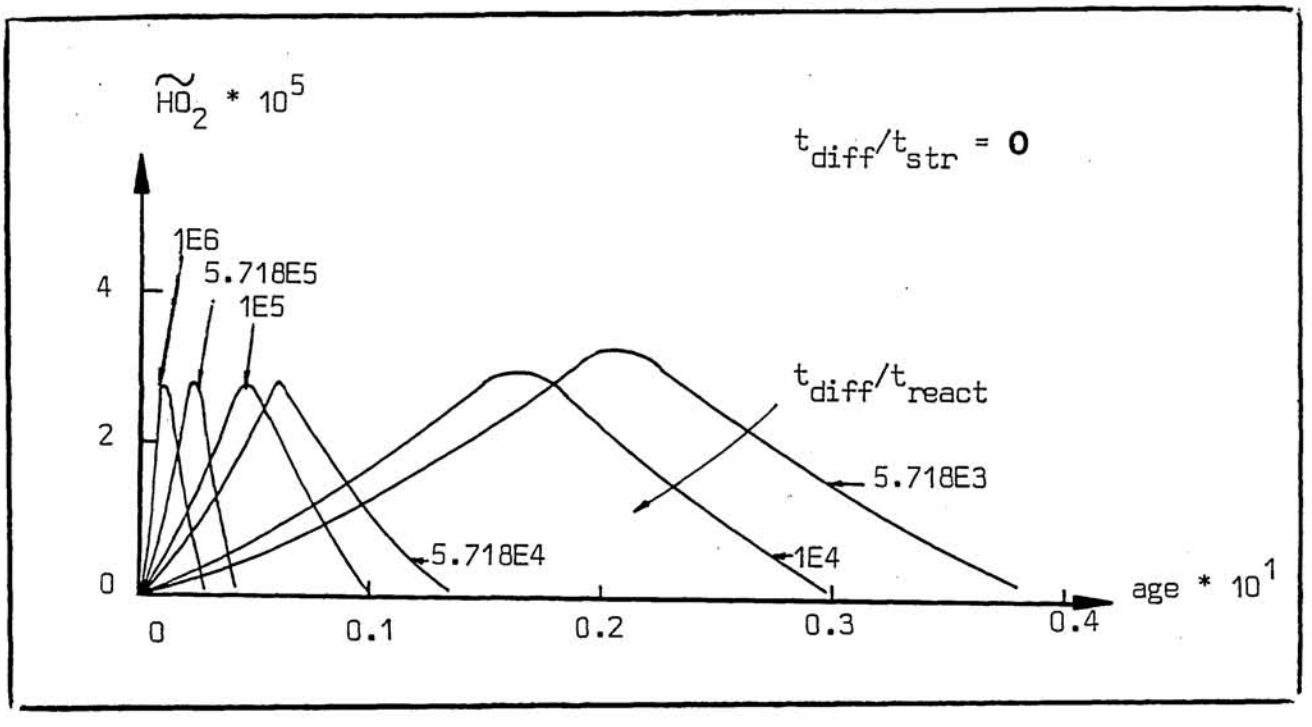

FIGURE 4.34 THE INFLUENCE OF THE REACTION TIME ON THE FOLD-AVERAGE QUANTITY UNDER THE LAMINAR FLAME SPEED CONTROL, REPRESENTED ON $\widetilde{HO}_2 \sim$ a DIAGRAM.

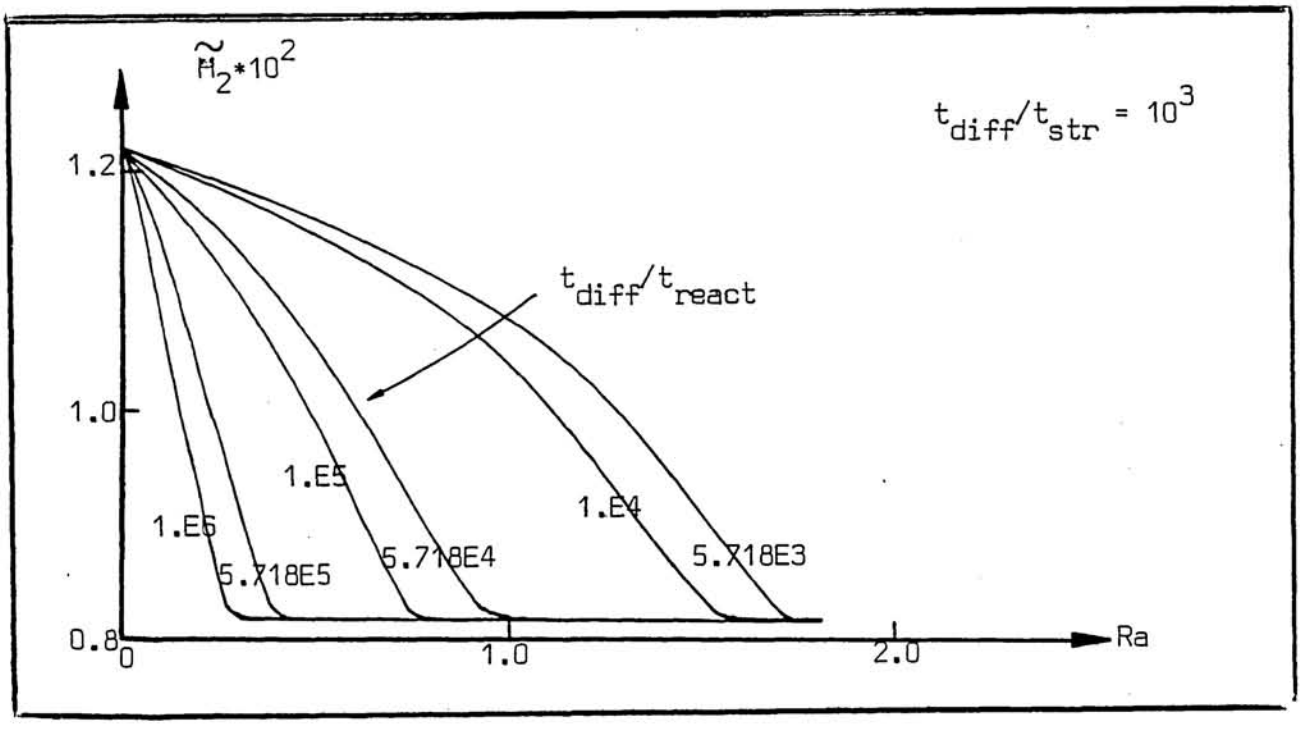

FIGURE 4.35 THE INFLUENCE OF THE REACTION TIME ON THE FOLD-AVERAGE QUANTITY UNDER THE STRETCHING CONTROL, REPRESENTED ON $\widetilde{H}_2 \sim a/t_{str}$ DIAGRAM.

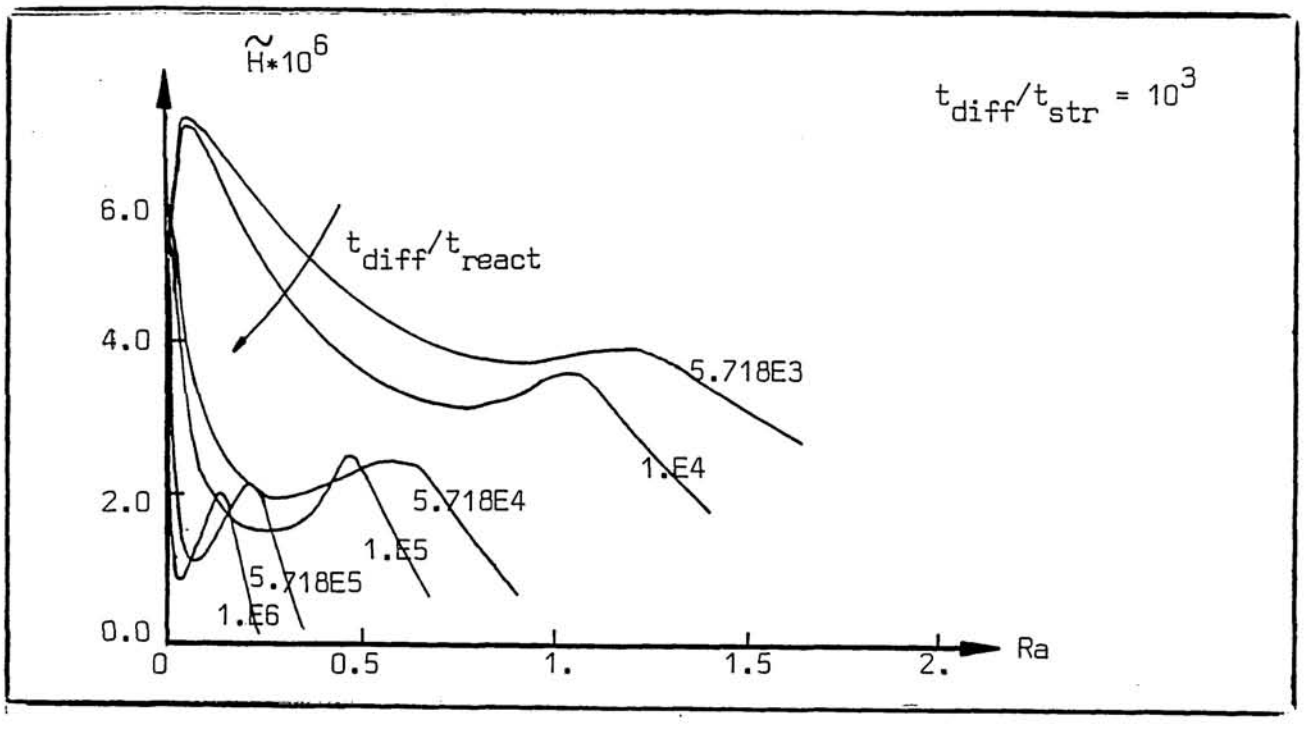

FIGURE 4.36 THE INFLUENCE OF THE REACTION TIME ON THE FOLD-AVERAGE QUANTITY UNDER THE STRETCHING CONTROL, REPRESENTED ON $\widetilde{H} \sim a/t_{str}$ DIAGRAM.

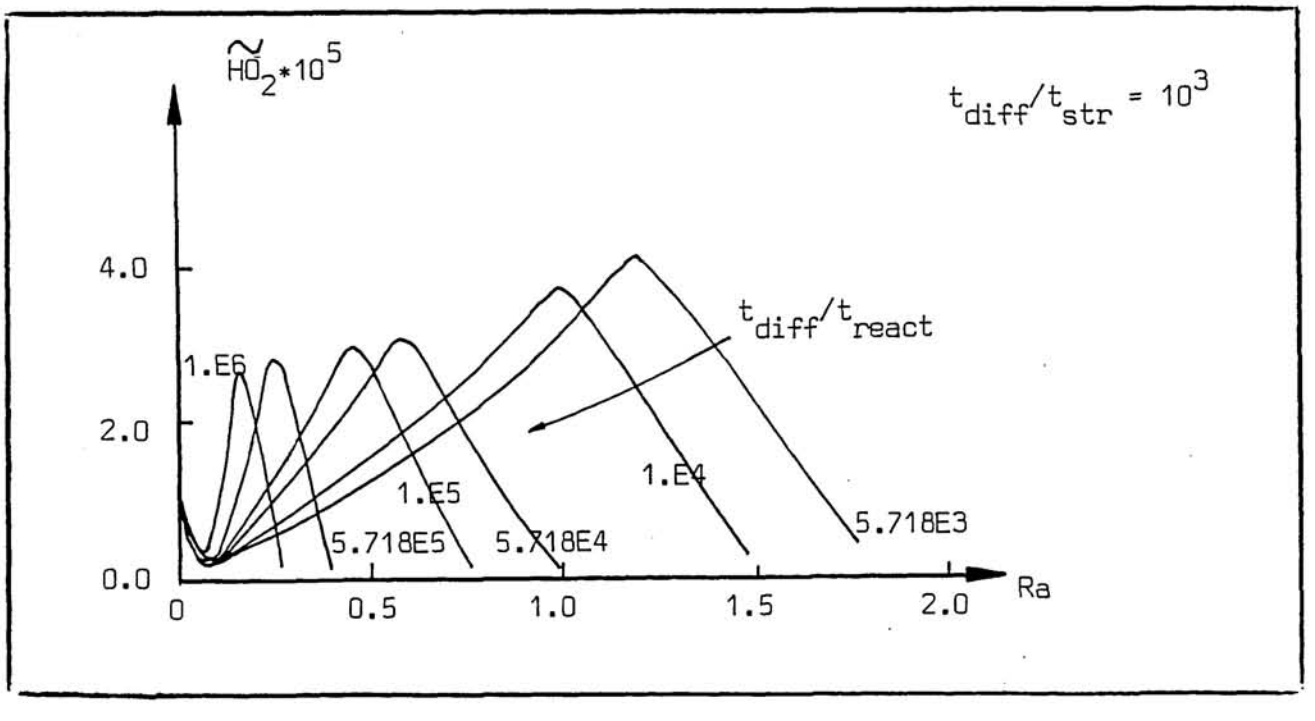

FIGURE 4.37 THE INFLUENCE OF THE REACTION TIME ON THE FOLD-AVERAGE QUANTITY UNDER THE STRETCHING CONTROL, REPRESENTED ON $\widetilde{HO}_2 \sim a/t_{str}$ DIAGRAM.

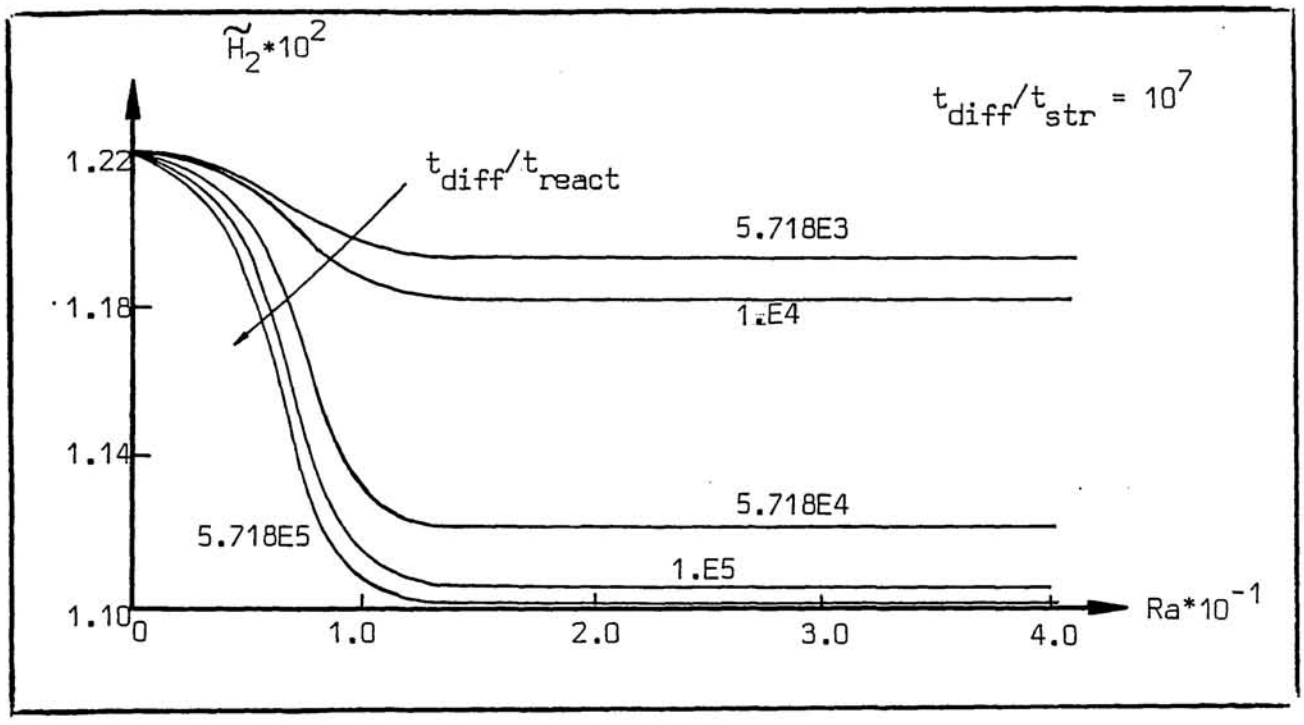

FIGURE 4.38 THE INFLUENCE OF THE REACTION TIME ON THE FOLD-AVERAGE QUANTITY UNDER THE CHEMICAL KINETIC CONTROL, REPRESENTED ON $\tilde{H}_2 \sim a/t_{str}$ DIAGRAM.

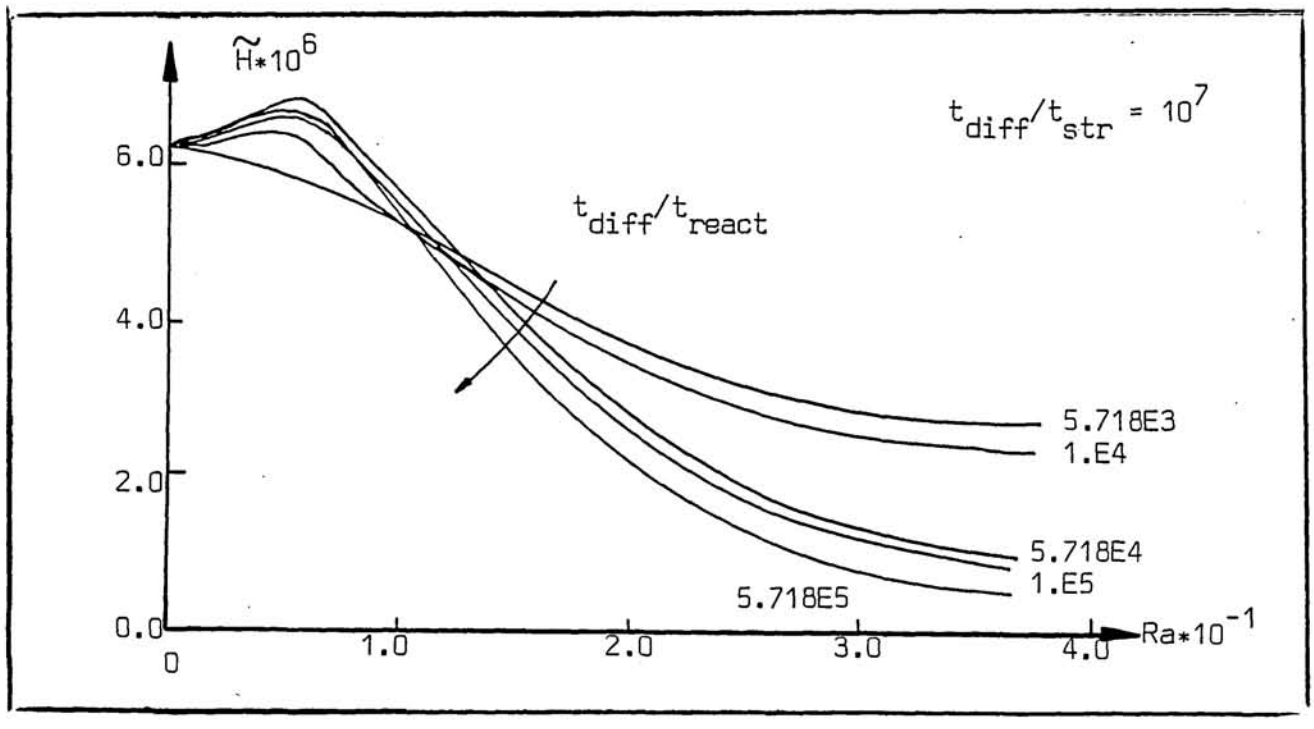

FIGURE 4.39 THE INFLUENCE OF THE REACTION TIME ON THE FOLD-AVERAGE QUANTITY UNDER THE CHEMICAL KINETIC CONTROL, REPRESENTED ON $\tilde{H} \sim a/t_{str}$ DIAGRAM.

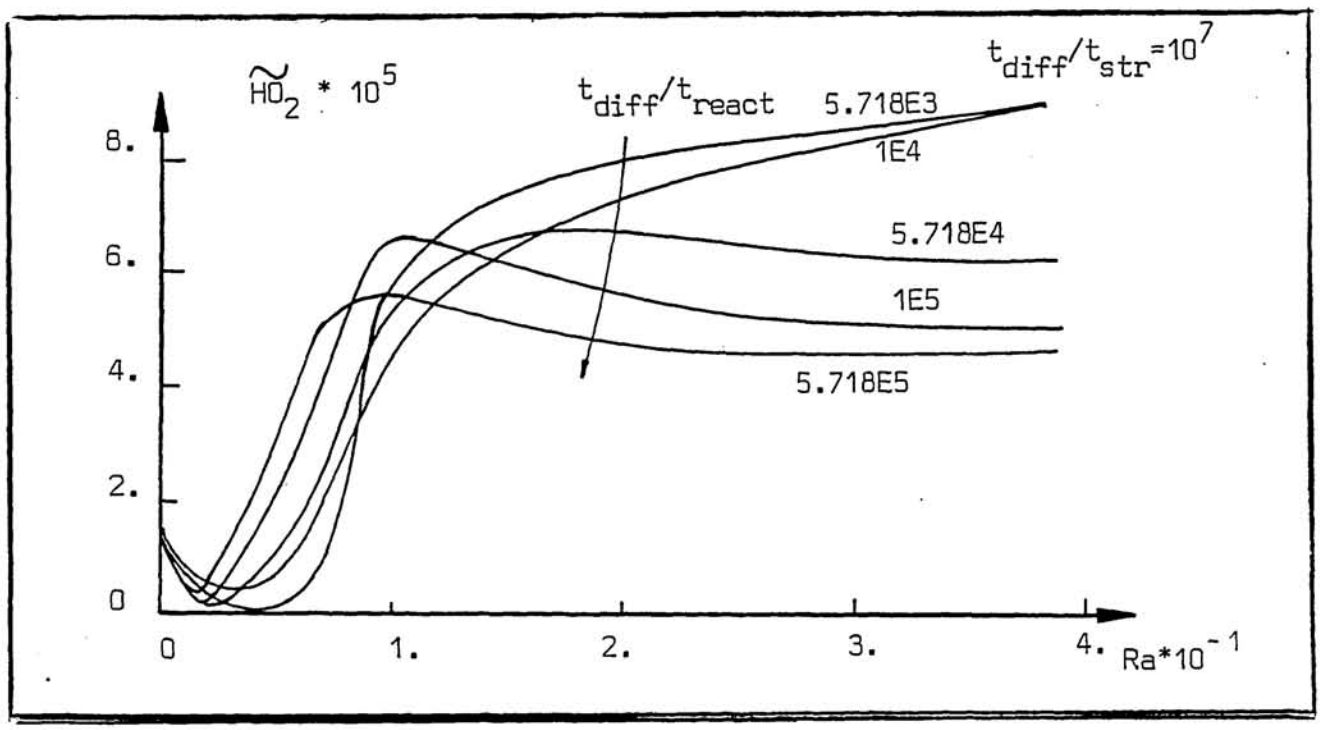

FIGURE 4.40 THE INFLUENCE OF THE REACTION TIME ON THE FOLD-AVERAGE QUANTITY UNDER THE CHEMICAL KINETIC CONTROL, REPRESENTED ON $\widetilde{HO}_2 \sim a/t_{str}$ DIAGRAM.

(iii) The fold-average reaction rate

The cross-fold reaction rate of species concentration at any successive age can be expressed as:

$$r_\phi \{\psi, a\} = \sum_j (\alpha'_{ij} - \alpha''_{ij}) (R_j - R_{-j}) , \qquad (4.6\text{-}8)$$

where α'_{ij} and α''_{ij} are the total stoichiometric coefficients of species i in reaction j as a reactant and as a product, respectively.

The corresponding fold-average reaction rate is therefore calculated from:

$$\tilde{r}_\phi \{a\} = \frac{\int_0^Y r_\phi \rho dy}{\int_0^Y \rho dy} . \qquad (4.6\text{-}9)$$

Results are expressed as a function of fold-average species, in the form: $\tilde{r}_\phi \sim \tilde{\phi}$.

Figures 4.41 - 4.42 show the results of a number of calculated reaction rate curves under a constant value of t_{diff}/t_{react}. Figure 4.41 shows how the rate of stretching can affect the reaction rate variations. It is noted that the larger the rate of stretching, the steeper the dependence of reaction rate upon $\tilde{\phi}$.

In addition, the reaction rate curve is shifted to an unburned region as the rate of stretching increases. The

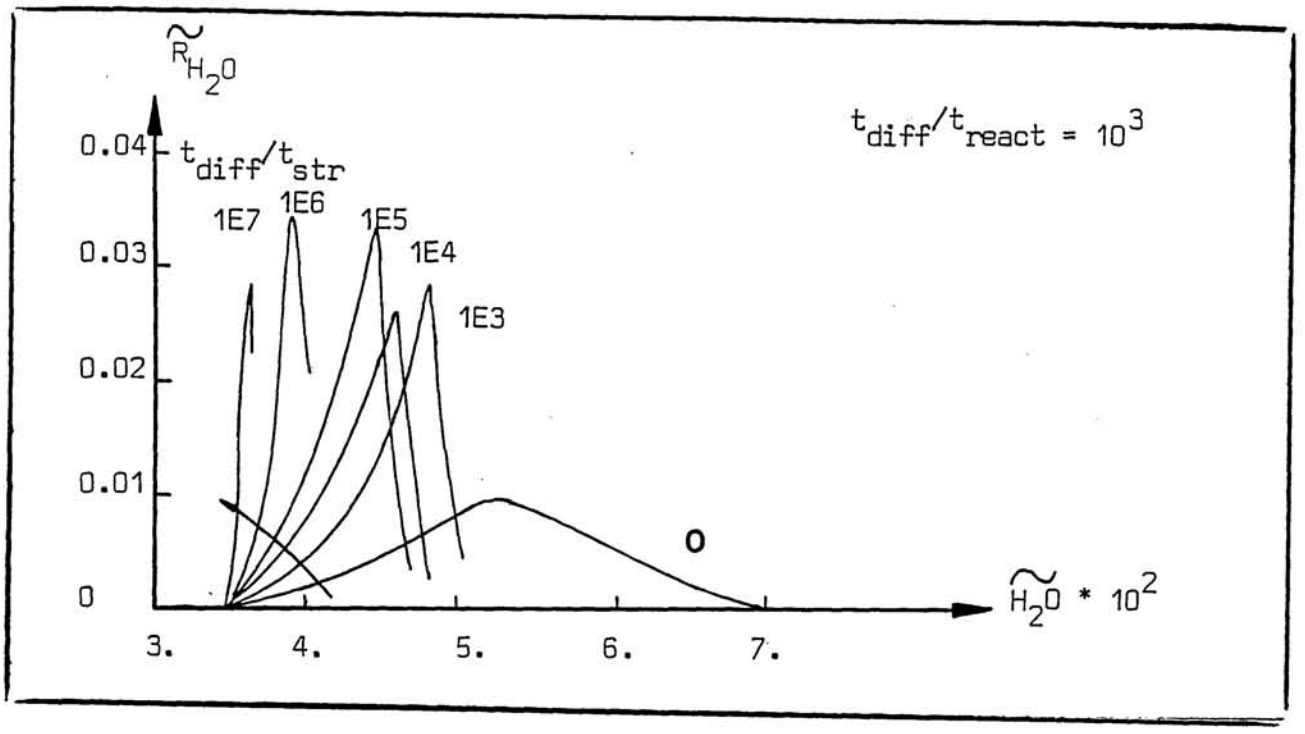

FIGURE 4.41 THE INFLUENCE OF THE STRETCHING TIME ON THE FOLD-AVERAGE REACTION RATE OF H_2O VERSUS ITS FOLD-AVERAGE UNDER A CONSTANT RATIO OF t_{diff}/t_{react}.

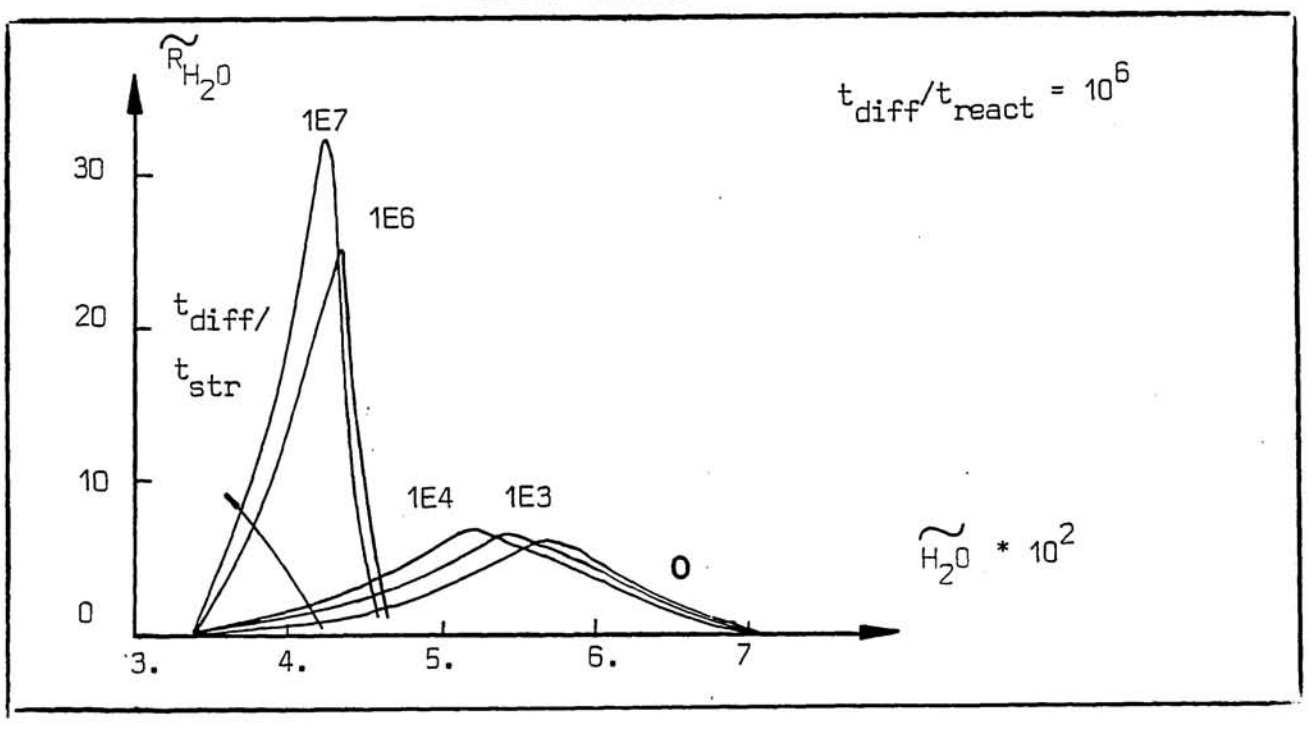

FIGURE 4.42 AS FOR FIGURE 4.41, BUT WITH A MORE REACTIVE MIXTURE.

extreme case is that the rapid stretching (i.e. $t_{diff}/t_{str}=10^7$; $t_{diff}/t_{react}=10^3$) can cause the reaction rate to fall drastically. Consequently, extinction takes place.

(iv) <u>The fold reaction rate correlation</u>

The fold reaction-rate correlation, $\tilde{\tilde{r}}_\phi\{a\}$, at age 'a', is defined as the ratio of the fold-average reaction rate, $\tilde{r}_\phi\{a\}$, to the reaction rate $r_{\phi V}\{a,\tilde{T},\tilde{\sigma}_1,\ldots\ldots,\tilde{\sigma}_N\}$, which would result from inserting fold-average concentrations and temperature into the Arrhenius expression:-

$$\tilde{\tilde{r}}_\phi\{a\} = \frac{\tilde{r}_\phi\{a\}}{r_{\phi V}\{a,\tilde{T},\tilde{\sigma}_1,\ldots\ldots\tilde{\sigma}_n\}} \quad . \qquad (4.6\text{-}10)$$

This correlation term indicates that the exact fold-average reaction rate can be higher or lower than the reaction-rate depending on the fold-average values. Figure 4.43 shows the influence of the reaction time on the reaction-rate correlation, $\tilde{\tilde{r}}_{H_2}$, at various dimensionless ages, a/t_{str}. It is seen that less-than-unity values of $\tilde{\tilde{r}}_{H_2}$ occur when the reaction time is very short, for then the burning process of the fold is controlled by hydrodynamic (stretching). If the burning process is operated in this regime, the results of reaction-rate, depending on fold-average quantities

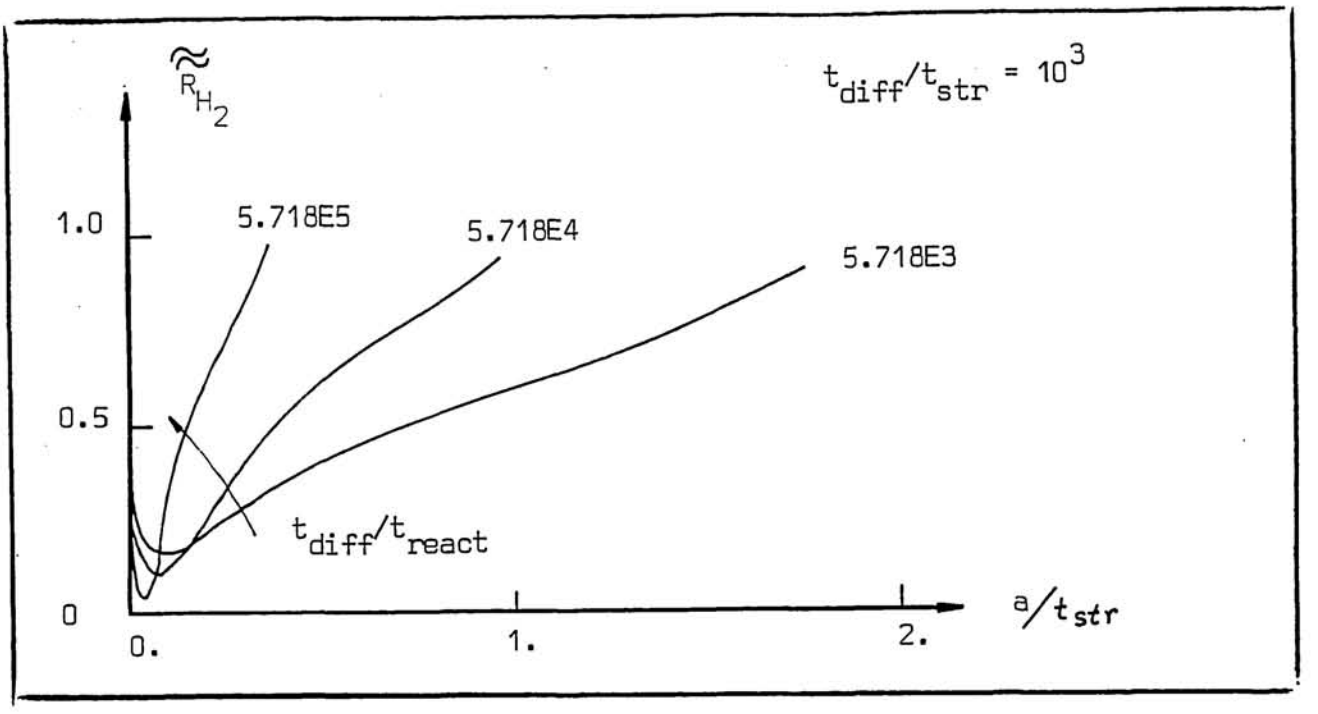

FIGURE 4.43 THE INFLUENCE OF THE REACTION TIME ON THE REACTION-RATE CORRELATION, $\tilde{\tilde{R}}_{H_2}$, AT VARIOUS DIMENSIONLESS AGES a/t_{str}, UNDER A CONSTANT RATIO OF t_{diff}/t_{str}.

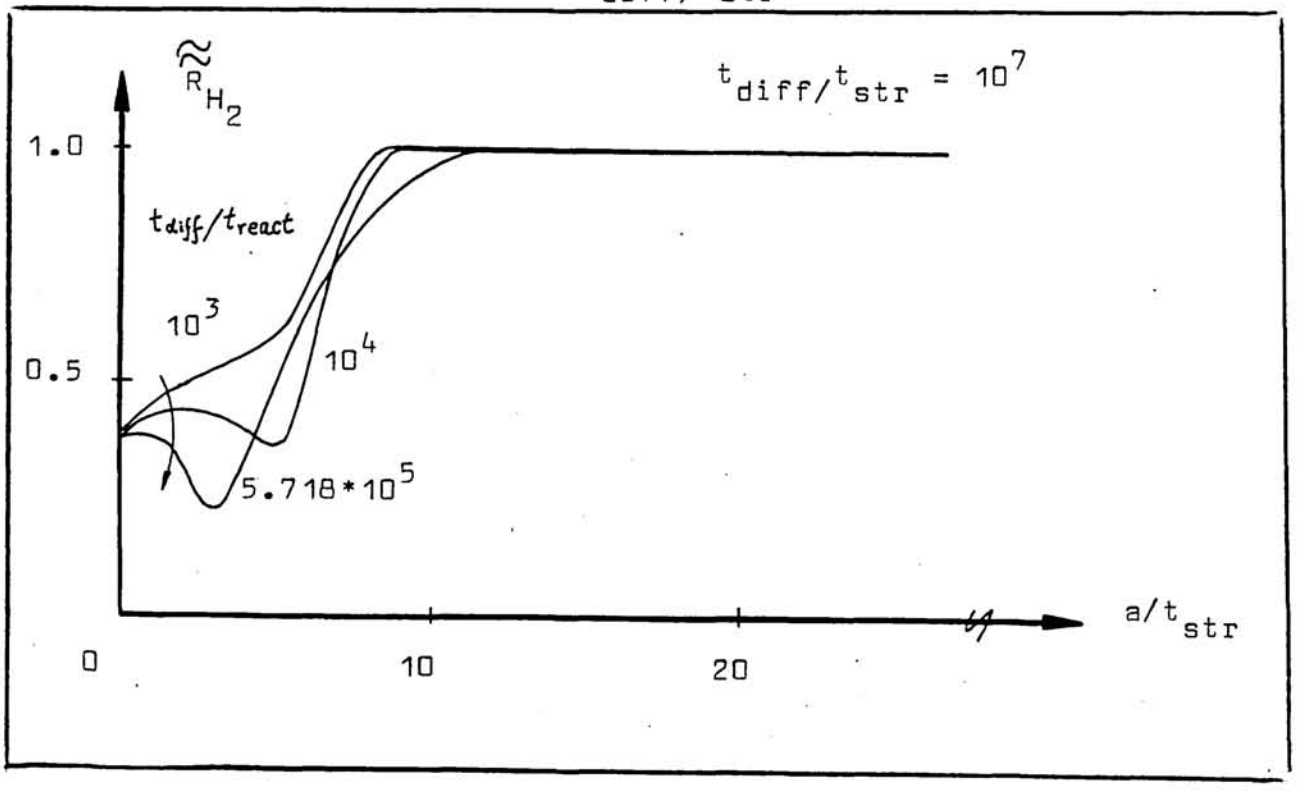

FIGURE 4.44 AS FOR FIGURE 4.43, BUT WITH MORE RAPID STRETCHING.

would display serious errors.

Figure 4.44 shows the influence of the reaction time on $\tilde{\tilde{r}}_{H_2}$ variations under the chemical-kinetic control. Due to the fast mixing, it is observed that the values of $\tilde{\tilde{r}}_{H_2}$ rises rapidly as age increases, until it reaches 1.0, at which value it remains. If the burning regime is operated in this mode, the difference between the fold-average reaction rate and the results of reaction-rate depending on the fold-average quantities can be neglected.

Inspection of Figures 4.43 - 4.44 reveals that the fold biographic analysis does provide a reliable means of computing fold reaction rate correlations.

4.7 Closure

Since the effects of hydrodynamics, laminar-transport and chemical kinetics on a single fold have been described as a set of non-linear differential equations, three different burning regimes within a fold have been demonstrated numerically. These are:

1. Laminar flame propagation across a non-stretched fold;

2. Laminar flame propagation across a fold which is being significantly diminished in thickness by stretching;

3. Chemical reaction within a fold which, at any successive age, has a practically uniform composition.

The method of computing fold biography copes successfully with fully realistic assumptions for thermodynamic properties, with diffusion coefficients that are different for each species and are functions of both temperature and species concentration. In addition, a seven-step reaction mechanism of hydrogen-oxygen system (Dixon-Lewis, 1970b) has been successfully incorporated into the fold biographic theory. The prediction of the intermediate species shows that the formation of hydroperoxyl species is of significance within the reaction zone. This radical species is formed mainly by the association of hydrogen atoms with oxygen, and is removed by its own reaction with hydrogen atoms according to the following steps:

$$H+HO_2 \rightleftharpoons OH+OH$$
$$H+HO_2 \rightleftharpoons H_2+O_2$$

The theoretical approach of the fold biography described in the beginning of the chapter has now been thoroughly validated. The flame-following-grid method has been shown to be able to handle calculations of internal flame propagation regime involving complex assumptions for chemical kinetics, thermodynamic and transport properties,

without requiring excessive accounts of computer time (see Section 4.5).

It is suggested that the ESCIMO approach is capable of predicting the behaviour of stretched folds by means of numerical solution method. The interaction of turbulence and chemistry therefore becomes easily understandable.

CHAPTER 5 - EXPERIMENTAL WORKS

5.1 Introduction

This chapter contains an account of the experiment that provided the data presented and employed in Chapter 6 for verifying the theoretical predictions.

So far, there is only very little available experimental information on the influence of stretching rate on small-scale eddies in turbulent reacting flow (Karlovitz, 1953; Kent and William, 1974). In addition, there has not been a direct comparison between the experimental results and the fold biographic theory as attempted in this work. Furthermore, a combination of experimental method and theoretical analysis provides a clearer picture of the biographical part of the ESCIMO theory. This theory also prompted further experimental studies of the 'unmixed' diffusion model of non-reacting and reacting laminar multiple stretched-folds. These show how the stretching rate, laminar-transport and chemical kinetics can affect the fold biography.

The work is divided into two parts here:

I : Cold flow measurements in which there is no combustion and uniform temperature prevails everywhere.

II : Hot flow measurements involving combustion.

P A R T I

COLD FLOW EXPERIMENT

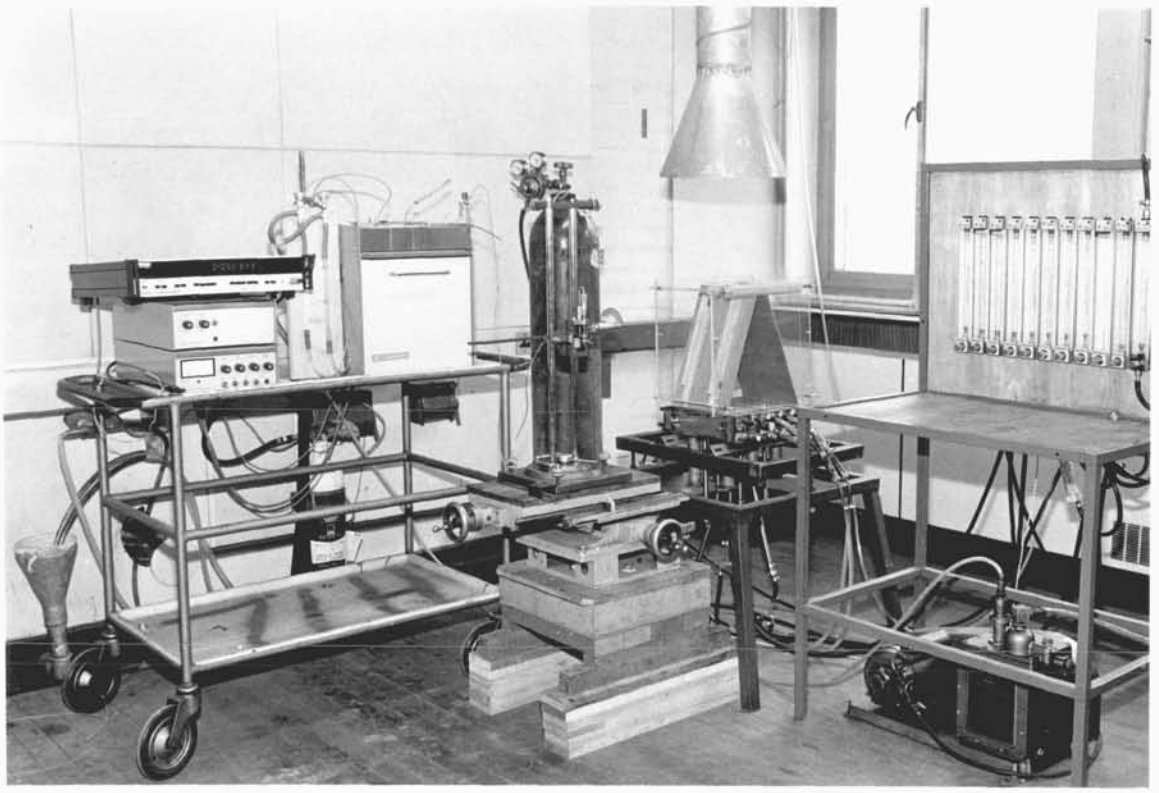

FIGURE 5.1 A PICTORIAL VIEW OF THE COLD FLOW EXPERIMENTAL APPARATUS.

FIGURE 5.2 CLOSE UP VIEW OF THE ISOTHERMAL FLOW RIG.

5.2 Objectives

- To study the stretching, mixing and diffusion processes of any successive multiple-fold.

- To provide some useful experimental data for the verification of the biographic theory.

- To serve as a basis for further work on the laminar diffusion stretched-flame with the aid of the same apparatus.

5.3 Experimental Apparatus

A pictoral view of the cold flow experimental apparatus and the close-up view of the isothermal flow rig are shown in Figures 5.1 and 5.2, respectively.

The layout of the experimental apparatus for the cold flow measurement is shown in Figure 5.3. It consists of the gas supply system, the reactor, the test section and the layout of measuring equipment.

5.3.1 Gas supply system

The gas supply system is contained in Figure 5.3. Air was first discharged from the main air supply unit through the air filter and the two-stage pressure regulators.

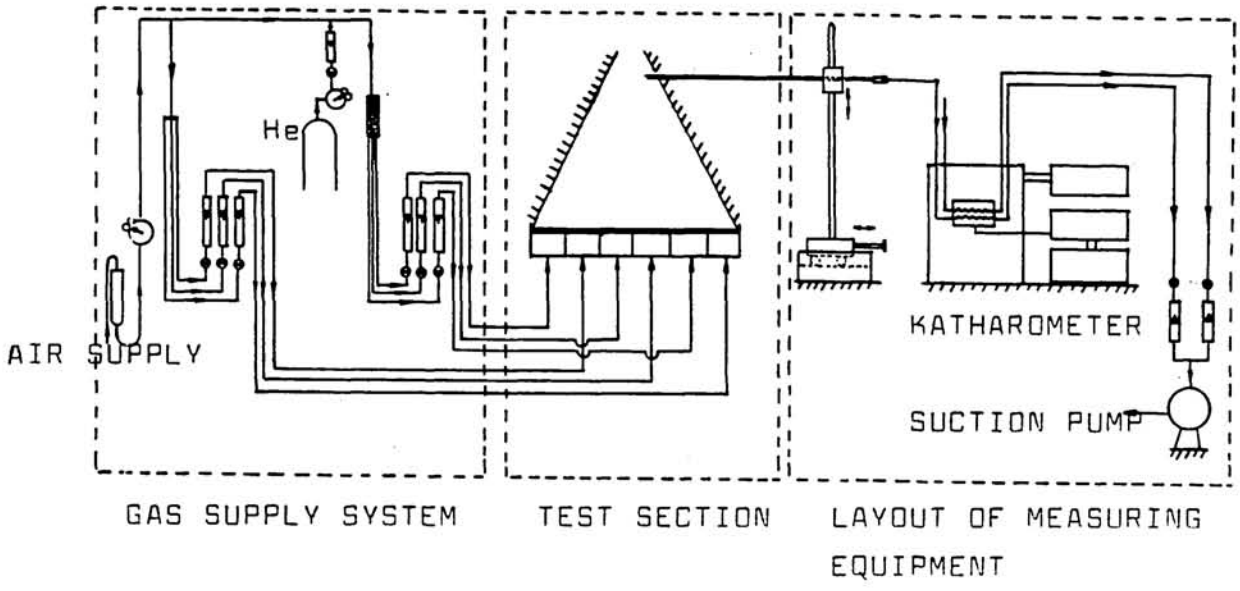

Figure 5.3 EXPERIMENTAL APPARATUS FOR COLD FLOW MEASUREMENT

The flow was carried by a 3/8"ϕ gas supply tubing and diverted into two streams. One was admitted into a manifold and fed into three air supply lines. The other stream was initially mixed with helium tracer in a perspex mixer (1½"ϕ x 6½"ℓ; and filled with 1/8"ϕ glass bead). Then it was diverted into the other three gas supply lines. Finally, the air and helim tracer+air were alternately fed into the reactor chambers. The air flow-rate of each feeding line was directly read off the standard air rotameter (GEC Series 1100) immediately upstream of the reactor. Constant air flow rates were obtained by fixing the readings of the rotameters. Since the helium was employed as a tracer gas, its flow rate was adjusted by means of a small-scale rotameter (60 cc/min was set) so that it was less than 0.2% of the maximum air flow.

5.3.2 The reactor

The reactor consisted of six rectangular chambers, each made of 1/32" thick stainless steel sheets. A 3/8"ϕ, 6" long stainless steel tube was welded to the back of each chamber. This reactor was designed such that the air and the helium tracer+air were alternately and continuously discharged from the chambers.

In order to ensure uniformity of the injected flow, the front surface of the chamber was made of a 0.052" thick sintered stainless steel porous sheet (2" x 9" each, porosity ≡ 12.5μ). Such a small size porosity ensured that the injected flow was uniformly discharged from the porous strips.

Since the reactor would also be used in studying the fold biography with hydrogen-air combustion, water-cooling jackets were provided on both sides of the chamber (see Figure 5.5). However, this cooling system was not in use for the cold flow experiments.

The geometry and dimension of a single rectangular chamber is shown in Figure 5.5.

5.3.3 The test section

The test section of the apparatus was an open convergent channel which was directly connected to the reactor. It composed of two pieces of ¼" thick perspex plane and two pieces of 1/8" thick hard board.

The inclined angle was adjustable but always fixed for each run. This angle was measured by an inclinometer. In addition, a fixed scale further downstream of the test section also served to indicate the accuracy of the measured angle.

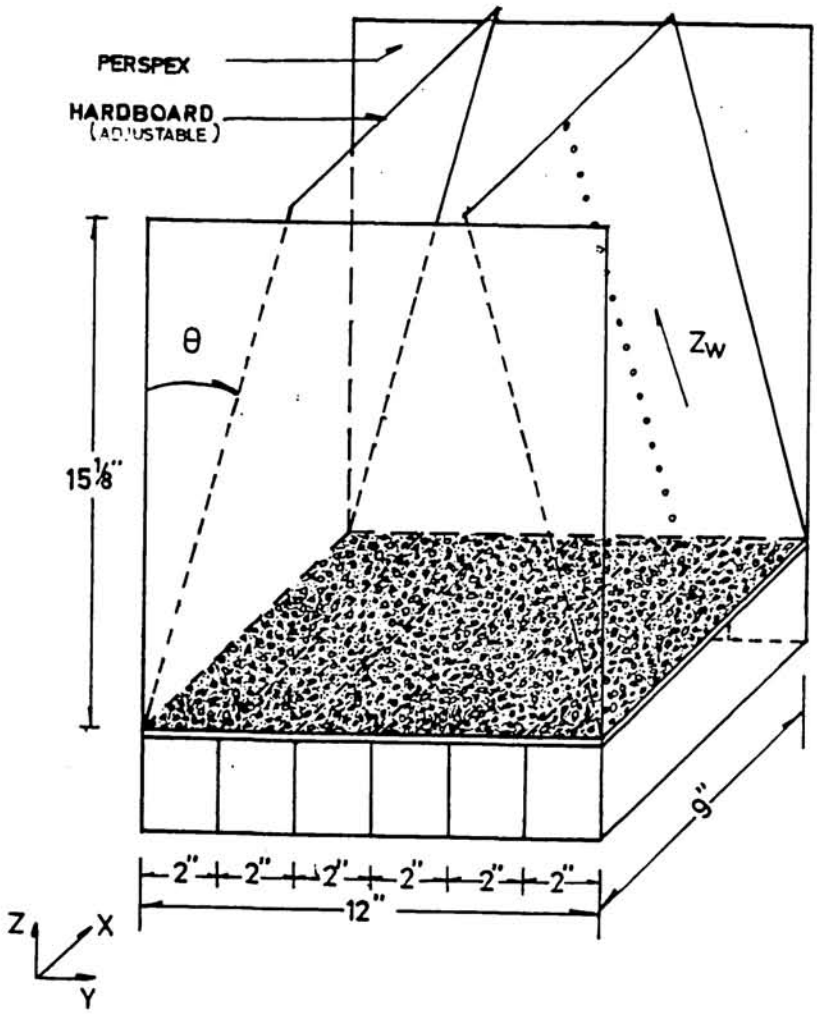

Figure 5.4 DETAILS OF THE TEST SECTION

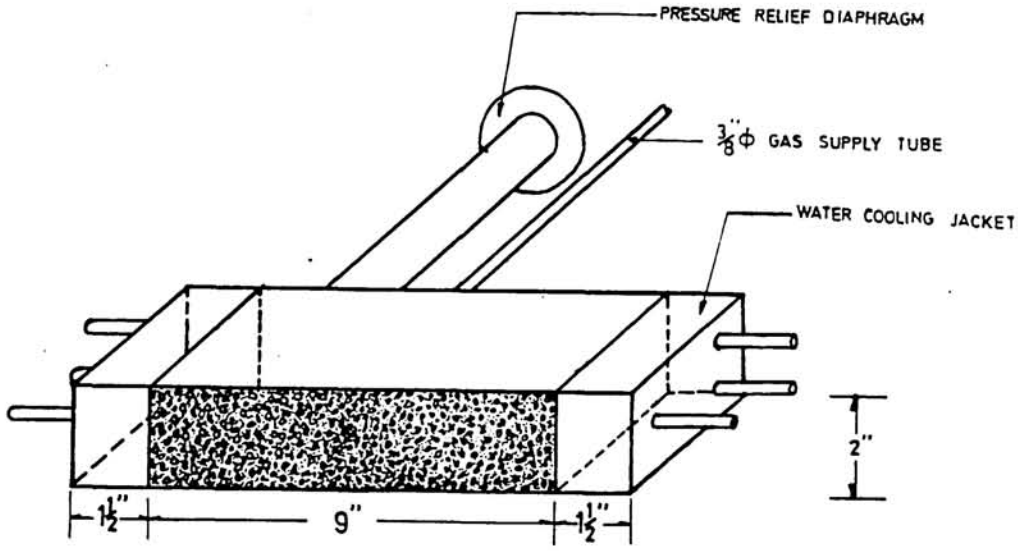

Figure 5.5 THE COMPONENT OF THE REACTOR

The dimensions and geometry of the test section are shown in Figure 5.4. It was designed so as to ensure that the profile of the flow had negligible variation in the x-direction at different measuring sections. Therefore, the flow pattern could be considered as two-dimensional in any arbitrary plane YZ. The centre plane of the test section was chosen for the concentration measurements.

Since five fluid layer-pairs were steadily formed from the reactor, the geometry ensured that the newly-formed folds would be stretched and developed up to the exhaust. The effects of stretching, mixing and diffusion on the folds could then be studied.

5.3.4 The measured quantity

In the experiment, only measurements of helium gas sampled at different locations in the test section were made. The concentrations were measured by means of a Katharometer, the details of which will be discussed in sub-section 5.3.7.

5.3.5 The coordinate and the measuring locations

The origin of the coordinates was set at the porous strips (see Figure 5.4). The coordinates which were parallel to the inclined wall were defined as $x \sim z_w$.

The cross-stream direction was y.

If the inclined angle of the wall was θ, the longitudinal distance z was therefore equal to $z_w \cos\theta$.

A series of 0.5cm diameter probing holes with equal spacing were provided on the centreline of the inclined wall for the helium tracer measurement. The holes were sealed when not in use. The measuring locations are shown in Figure 5.4. To allow the tracer concentration in the test section to be measured, a 1mm I.D. sampling probe was provided. Provision was made for inserting the probe by a slider and guide located in the traversing gear. Movement of the probe was obtained using a micrometer-based traversing gear as described in the next section.

5.3.6 The traversing mechanism

In order to control the three-dimensional motions of the sampling probe, a traversing gear was mounted on the compound table. The sampling probe and its guide were fixed on the slider of the traversing gear. The z-direction movement was provided by moving the slider. When the measurements were carried out, the slider was clamped in the correct position. Movements in the x- and y-directions were provided by adjusting the micrometer of the compound table (accuracy up to $\pm$ 0.00254mm).

5.3.7 The measuring equipment

The layout of concentration measuring equipment is shown systematically in Figure 5.3. It consisted of a sampling probe to record the helium concentration in the test section; a Katharometer to detect the concentration signal; a digital volt-meter to display the signal; and a suction pump to suck and maintain a constant rate of sample and reference-gas streams.

The sampling probe

The sampling probe is sketched in Figure 5.6. It was constructed from a stainless steel tube 480mm long with a 1mm diameter. A 1mm internal diameter flexible tube, approximately 100cm long, was used to connect the sampling probe to the Katharometer head.

The Katharometer

The Katharometer unit was of the "Model 304" type manufactured by PYE. It consisted of a thermal conductivity detector head, an oven controller to maintain a constant oven temperature, and a katharometer power supply. The Katharometer was operated at a Wealtstone bridge current in the thermal conductivity head. The bridge current, the bridge balancing and the output signal polarity reversal were controlled by the Katharometer power supply.

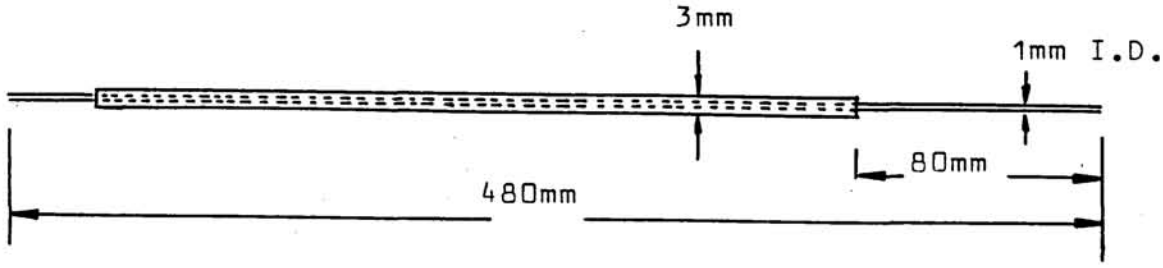

Figure 5.6 THE SAMPLING PROBE

The digital volt-meter

The Katharometer output signal was displayed on a "digital volt-meter" Solarton type 7075 with error about ± 0.025%. The accuracy of the digital volt-meter was up to four figure digits.

The suction pump

The sample was drawn from the test section by a suction pump. The suction pump was manufactured by Edwards High Vacuum, Model 2SC150B.

The sampling rates

The sample rate was regulated and metered by a rotameter fitted with a needle-valve. The sample and the reference flow rates were both maintained at 40 mL/min during the experiments. The range of response shown (0-50MV) correspond to the range of helium concentration used (0-0.2%) at a sample flow rate of 40 mL/min. The resolution time of the concentration measurement was the time required to flush the sample stream from its conduits to the detecting cell of the Katharometer. The value for the above sampling rate was about 50 seconds. These provided sufficient information for data processing.

5.4 Experimental Procedure

The following operation sequences were performed:

(1) The laboratory windows were closed and it was ensured that the drift-blows over the test rig were negligible.

(2) The inclined angle of the test section was adjusted to the specified value.

(3) The edges of the test section were completely sealed.

(4) The maximum and minimum traverse locations of the probe, through each specified hole, were marked. These correspond to the location at the two inclined walls, respectively.

(5) The Katharometer circuit and suction pump motor were switched on.

(6) Checks were made to ensure steady state.

(7) The maximum and minimum helium concentrations were recorded from the DVM readings. These correspond to the helium tracer gas and the pure air stream, respectively, at the injection mouth of the porous strips (1mm above the strips). This provided the variation range of the helium tracer at each specified traverse.

(8) The sampling probe traverses were made. At all specified locations, the DVM readings and the position of the sampling tip were recorded.

(9) The measuring section was changed, and the steps 7 and 8 were repeated until the whole experimental run was finished.

5.5 Experimental Conditions

The influence of stretching on the multiple folds was studied by varying the test sections inclined angle and the initial air flow rate of the porous strips.

Three angles of inclination e.g. 0°, 11.623^{o}, 20.96^{o} and two different air flow rates were investigated. These correspond to no stretching, moderate stretching and high stretching. Consequently, six typical runs were made for presentation and comparison with the numerical results (see Chapter 6). The experimental conditions are tabulated in Table 5.1.

Inspection of the experimental parameters shows that the Reynolds numbers based on the width of reactor and the total flow rate of reactor are Re=358 and 524 respectively, which justify the assumption of laminar flow.

Run No.	1	2	3	4	5	6
Inclined angle	0°	11.623^{o}	20.96^{o}	0°	11.623^{o}	20.96^{o}
Test section height z(m)	0.384	0.384	0.384	0.384	0.384	0.384
Width of reactor mouth Y_o (m)	0.313	0.313	0.313	0.313	0.313	0.313
Number of strips	6	6	6	6	6	6
Width of porous strip W_{in} (m)	0.0508	0.0508	0.0508	0.0508	0.0508	0.0508
Area of porous strip (m^2)	0.2286 x0.0508	0.2286 x0.0508	0.2286 x0.0508	0.2286 x0.0508	0.2286 x0.0508	0.2286 x0.0508
Air flow rate/ strip $\dot{m}_{inj}$ (kg/ sec)	$2.38x10^{-4}$	$2.38x10^{-4}$	$2.38x10^{-4}$	$3.57x10^{-4}$	$3.57x10^{-4}$	$3.57x10^{-4}$
Strip injection velocity U_{in} (cm/sec)	1.727	1.727	1.727	2.59	2.59	2.59
Air temperature	$20^{o}C$	$20^{o}C$	$20^{o}C$	$20^{o}C$	$20^{o}C$	$20^{o}C$
Air pressure	1atm	1atm	1atm	1atm	1atm	1atm
Air density (kg/m^3)	1.19	1.19	1.19	1.19	1.19	1.19
Air viscosity (kg/m-sec)	$1.84x10^{-5}$	$1.84x10^{-5}$	$1.84x10^{-5}$	$1.84x10^{-5}$	$1.84x10^{-5}$	$1.84x10^{-5}$

TABLE 5.1: CONDITIONS IN WHICH EXPERIMENTS WERE PERFORMED

Estimation of the initial velocity

Since the porosity of the porous strips was fine enough (porosity ≡ 12.5 microns) to ensure uniformity of initial profiles, the initial velocity of multiple folds could be estimated from the continuity equation given by:-

$$u_{in} = \frac{\dot{m}_{inj}}{\rho_{air}\, w_{in}\, \ell} \quad , \qquad (5.5\text{-}1)$$

where u_{in} is the initial velocity of the multiple folds;

$\dot{m}_{inj}$ is the air flow rate/strip;

ρ_{air} is the air density;

w_{in} is the width of the porous strip; and

ℓ is the length of the strip.

5.6 Experimental Results

5.6.1 Interpretation of results

The results were presented in the dimensionless form of the helium concentration C for six typical runs.

It was interpreted at the measuring location from the local DVm reading, e, as follows:-

$$C = \frac{e-e_{min}}{e_{max}-e_{min}} \quad , \qquad (5.6\text{-}1)$$

where e_{max} and e_{min} are the DVM readings for the sample at the helium tracer entry point, and at the pure air stream entry point, respectively.

Since the initial helium flow rate was only about 0.2% by volume of air flow rate, the experimental results could be interpreted from equation (5.6-1), as percentage departured from linearity.

5.6.2 Presentation of results

Figures 5.7 and 5.8 give the measured concentration distributions for run no.3. The profile distributions shown are, as appropriate, the measured helium concentration versus the non-dimensional traverse distance Y/Y_N at different level z, where z is the longitudinal distance from the porous strips.

It is observed that the initial multiple-folds are being stretched and developed in the longitudinal direction. In the far downstream region, the high stretching and the fast mixing effects force the concentration profile to become uniform across the folds.

It should be noted that the measured data for other runs are not presented in this section; as the complete experimental data are presented in Chapter 6, where these are compared with the predictions of the numerical calculation. Consequently, the influences of the

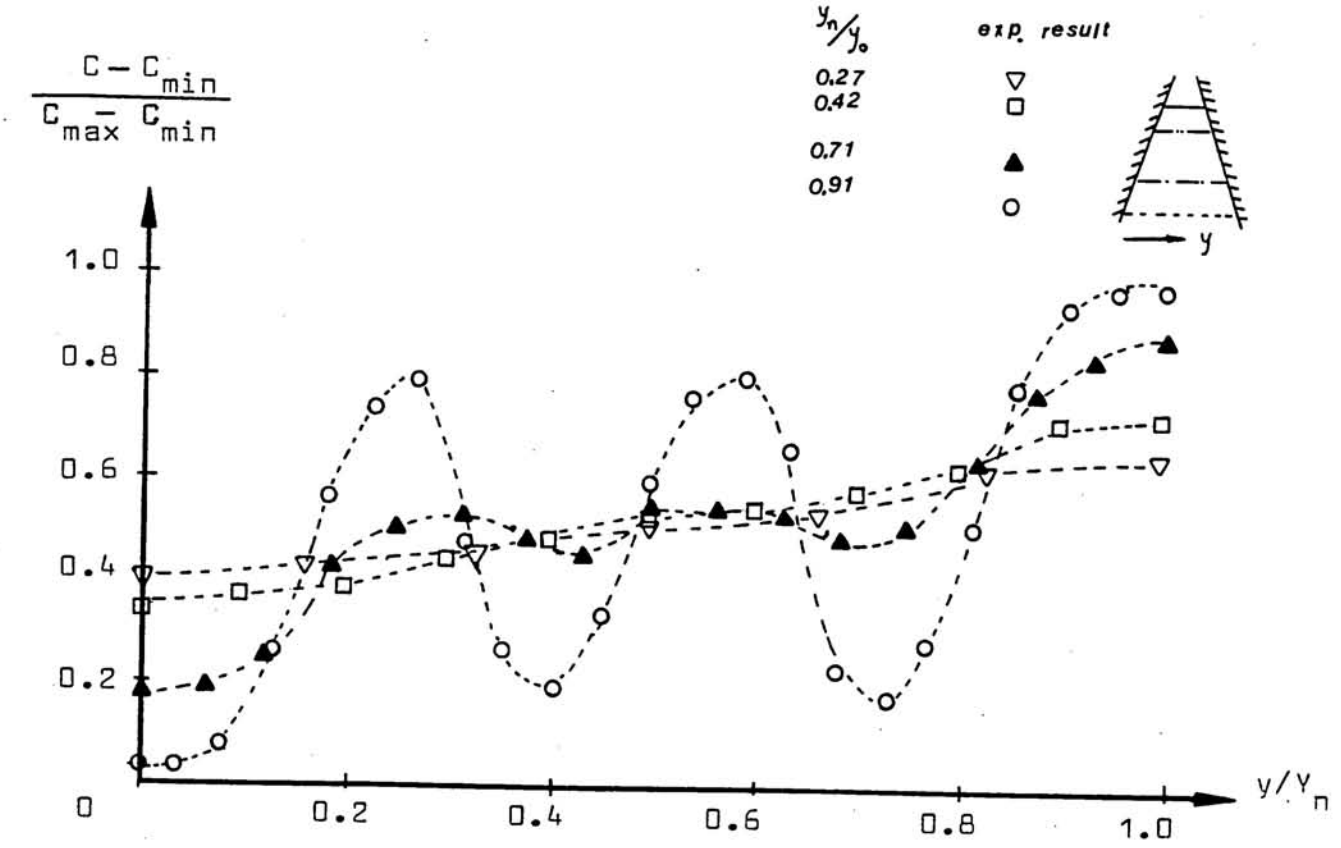

FIGURE 5.7 MEASUREMENTS OF HELIUM CONCENTRATION IN A CONVERGENT CHANNEL WITH 20.96° INCLINED ANGLE.

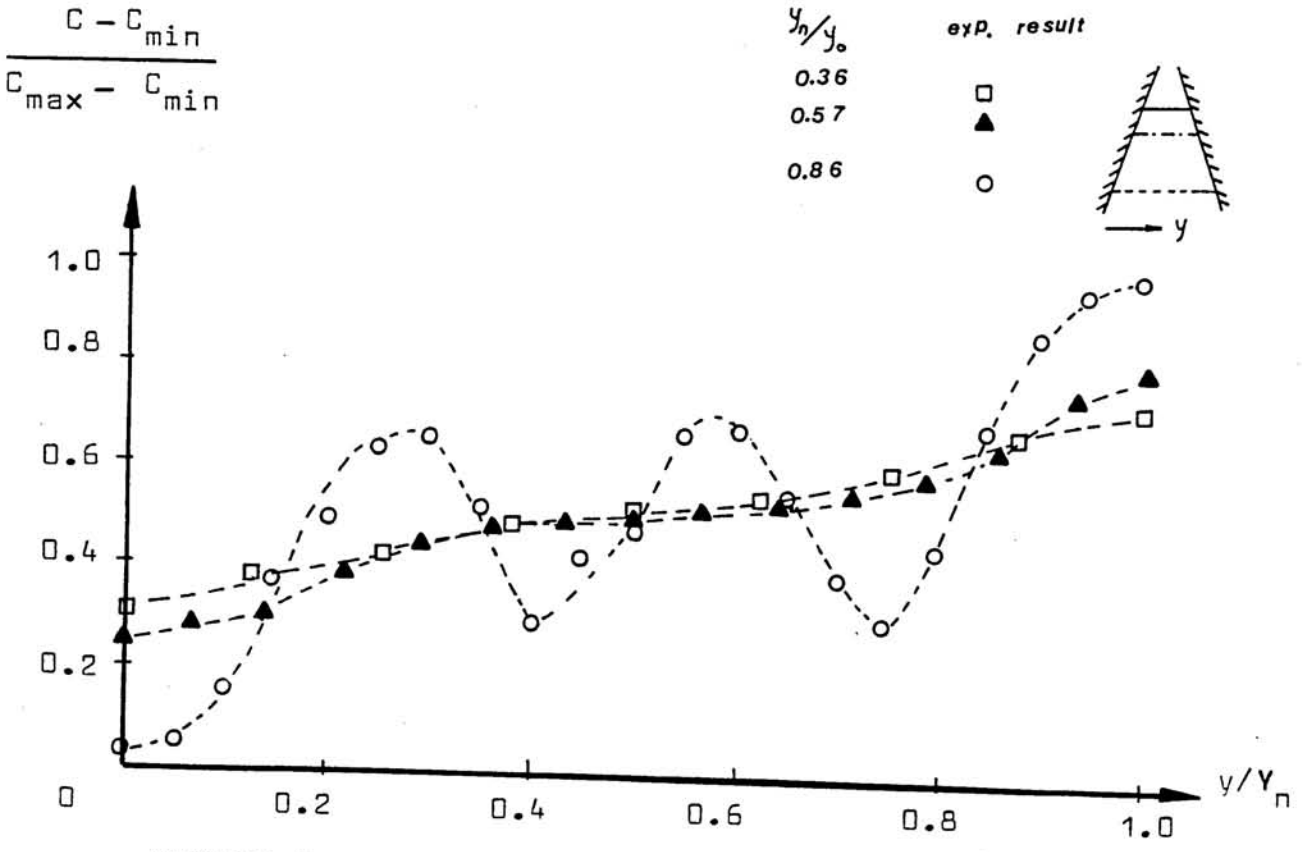

FIGURE 5.8 MEASUREMENTS OF HELIUM CONCENTRATION IN A CONVERGENT CHANNEL WITH 20.96° INCLINED ANGLE.

inclined angle and injection velocity on the stretched folds will be further discussed in Chapter 6.

5.7 Discussion of Results

5.7.1 Error analysis

The maximum experimental errors involved in the various measurements are estimated here.

(1) The inclined angle

The measurements of inclined angle by the inclinometer were likely to be accurate to within $\pm$ 0.2^{o}.

(2) Position of the sampling probe tip

Since the accuracy of traversing gear was up to $\pm$ 1mm, the estimated accuracy with which the probe tip location could be determined was $\pm$ 1mm in the y-direction and $\pm$ 1mm in the z-direction.

(3) Some external factors which influenced the DVM readings

The change of the laboratory temperature and the draught of air would affect the DVM readings. However, these effects were found to be very small. In practice, the e_{max} and e_{min} were measured, before and after each concentration traverse (about 20mins). The latter

quantity should, of course, always be zero, and it was found to be so. Therefore, the error in interpreting the dimensionless concentration was estimated to be within 1%.

(4) Aerodynamic effects

When introducing the sampling probe into the gas flow, the suction rate and the probe geometry would distort the streamline of the flow. Consequently, the sampling measurements would be affected by these factors. Fortunately, the aerodynamic disturbance was proved to be insignificant (as will be given below).

A disk-sink model discussed by Rosener (1962), Fristrom and Westenberg (1965) was adopted for calculating the perturbation of the sampling probe.

As shown in Figure 5.9, a sink of radius r and strength (the volumetric flow rate), Q, distorts the unperturbed velocity v_∞. The theoretical treament from the above authors gave an expression for the fractional flow distortion v_y/v_∞ as a function of the perturbed distance, δ, and the sampling rate ratio, $(\alpha = \frac{Q}{\pi r^2 v_\infty})$.

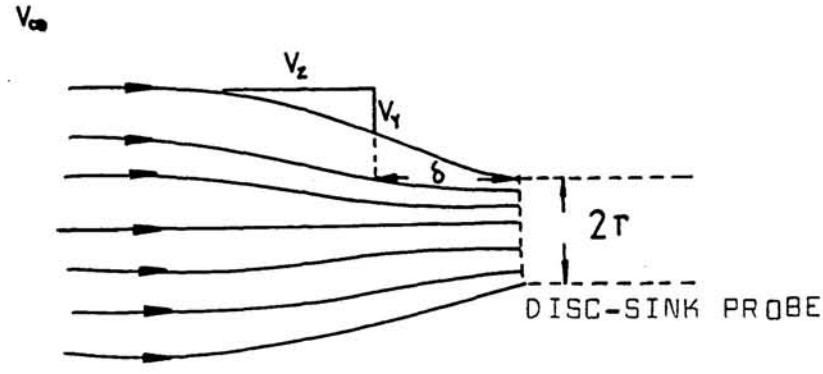

Figure 5.9 SCHEMATIC OF FLOW LINES SHOWING DISTORTION DUE TO SINK.

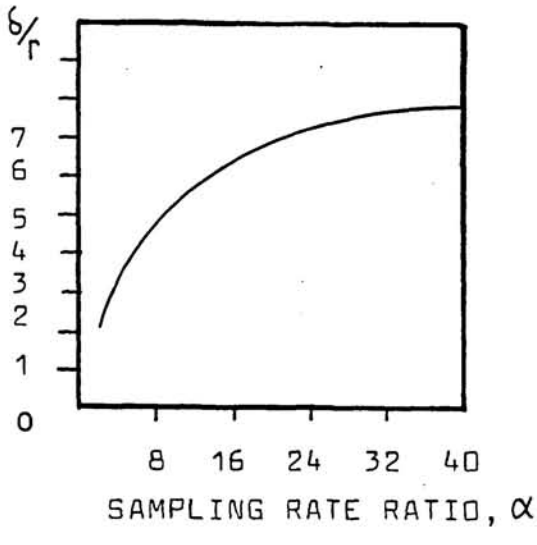

Figure 5.10 DISTANCE (NUMBER OF SINK RADII) AHEAD OF PROBE AT WHICH DISTORTION v_y/v_∞ IS 5%, AS FUNCTION OF SAMPLING RATE RATIO α.

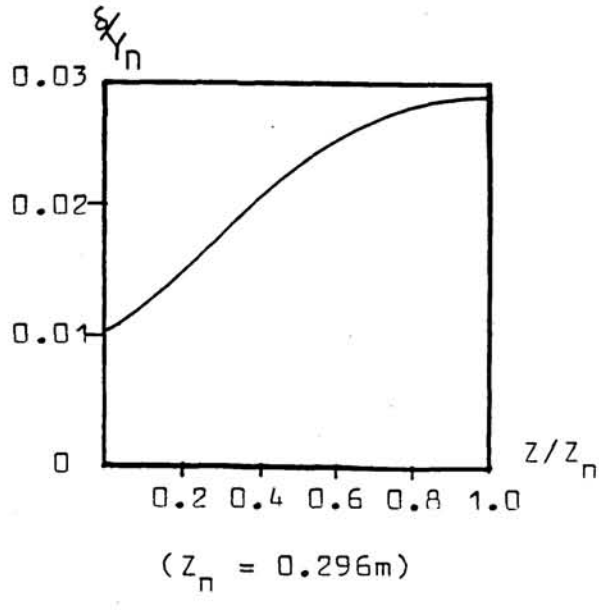

Figure 5.11 THE DISTURBANCE ERROR.

Under these circumstances, the result for a flow distortion is generally less than 5% (i.e. $v_y/v_\infty \leq 5\%$) and the probe sampling rates correspond to a value of α in the range of 4 to 40. Consequently, a 5% distortion will be estimated to occur at 3 to 7 probe radii ($\frac{\delta}{r}$) upstream, as illustrated in Figure 5.10.

Figure 5.11 shows the disturbance error, δ/Y_N, which appeared at the traverse distance as a function of non-dimensional longitudinal distance z/z_N, where Y_N is the dimension of the traverse distance at level z; and z_N is the maximum height of the test section.

Further downstream of the test section, the continuity equation shows that the v_∞ increases rapidly as a result of diminishing Y_N. Hence, for the sampling probe with r=0.5mm, the maximum value of the perturbed distance, δ, should be less than 2mm at the downstream region of the test section.

It is observed that the maximum error is less than 3% when compared to the dimension of the test section. This is not a serious aerodynamic disturbance.

(5) <u>The pressure drop across the porous strips</u>

Since the test section was subjected to atmospheric pressure (1atm), the maximum pressure difference, δp, between the gas supply system and the test section was the pressure drop across the porous strips. The following Darcy's equation recommended by the porosint manufacturer was employed for the estimation of the pressure drop across the porous strips.

$$\delta p = \frac{\dot{v} \ell n}{981 \, A\phi} \quad , \qquad (5.7\text{-}1)$$

where $\dot{v}$ = flow rate of fluid in mL/sec;

A = effective area of porous strips in sq cm;

n = absolute viscosity of fluid in centriposes;

ℓ = thickness of porous material in cms;

ϕ = permeability coefficient; and

δp = pressure drop across porous wall in gms/cm^2.

The technical data for the porous strip is tabulated in Table 5.2.

$\dot{v}$	ℓ	n	A	ϕ	δp
300	0.317	1.78×10^{-2}	116	1.5×10^{-5}	1

TABLE 5.2: THE TECHNICAL DATA FOR THE POROUS STRIP

The above results show that the maximum pressure drop across the porous strip was about $1 gm/cm^2$. The data was used for rotameter calibration.

(6) Flow rate measurement

The air flow rates and the sampling flow rates were measured by the rotameter manufactured by GEC, the Series 1100. Each rotameter was fitted with a needle valve. This valve served the secondary purpose of smoothing out the fluctuations into the flow by the main air supply.

Since the pressure drop across the porous strip had been estimated, the operating pressure of the rotameter was therefore equal to 14.715 lbf/in^2, which was close to 1atm.

The error of the scale reading of the rotameter was therefore likely to be less than ± 1%.

5.7.2 Three-dimensional effect

As already shown in Figure 5.4, the distance between the two channel walls in the x-direction was 9". Since the porosity of the porous strip was fine enough to ensure uniformity of injection, the fluid flow had negligibly small variation along this direction at different traverse sections.

To demonstrate the three-dimensional effect on the measurement, one more test was made. The experimental conditions were exactly the same as Run No.5 (in Table 5.1). The measuring locations were given as follows: Two additional sets of data were obtained from other two parallel YZ planes; ± 1½" apart from the centreline of the inclined wall at two different traverse sections.

Comparisons between those sets of data were made and are shown in Figure 5.13 and 5.14. Again, the results are presented in the dimensionless form of the helium concentration c versus dimensionless distance Y/Y_N.

It is observed that the results generally show that the three-dimensional effect on the flow pattern was negligibly small at the centre region of the test section.

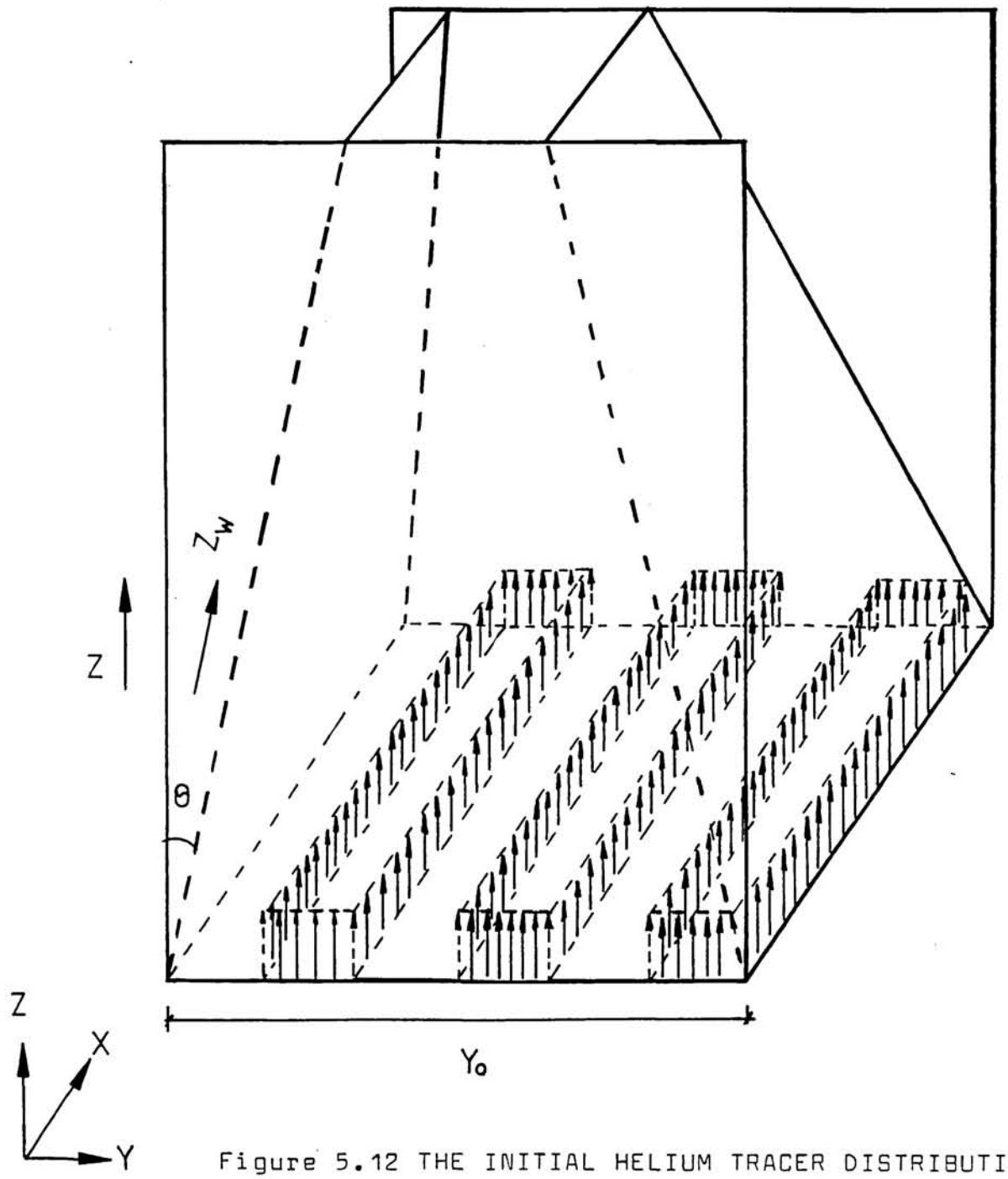

Figure 5.12 THE INITIAL HELIUM TRACER DISTRIBUTION.

EXPERIMENTAL RESULT

RUN NO. 5

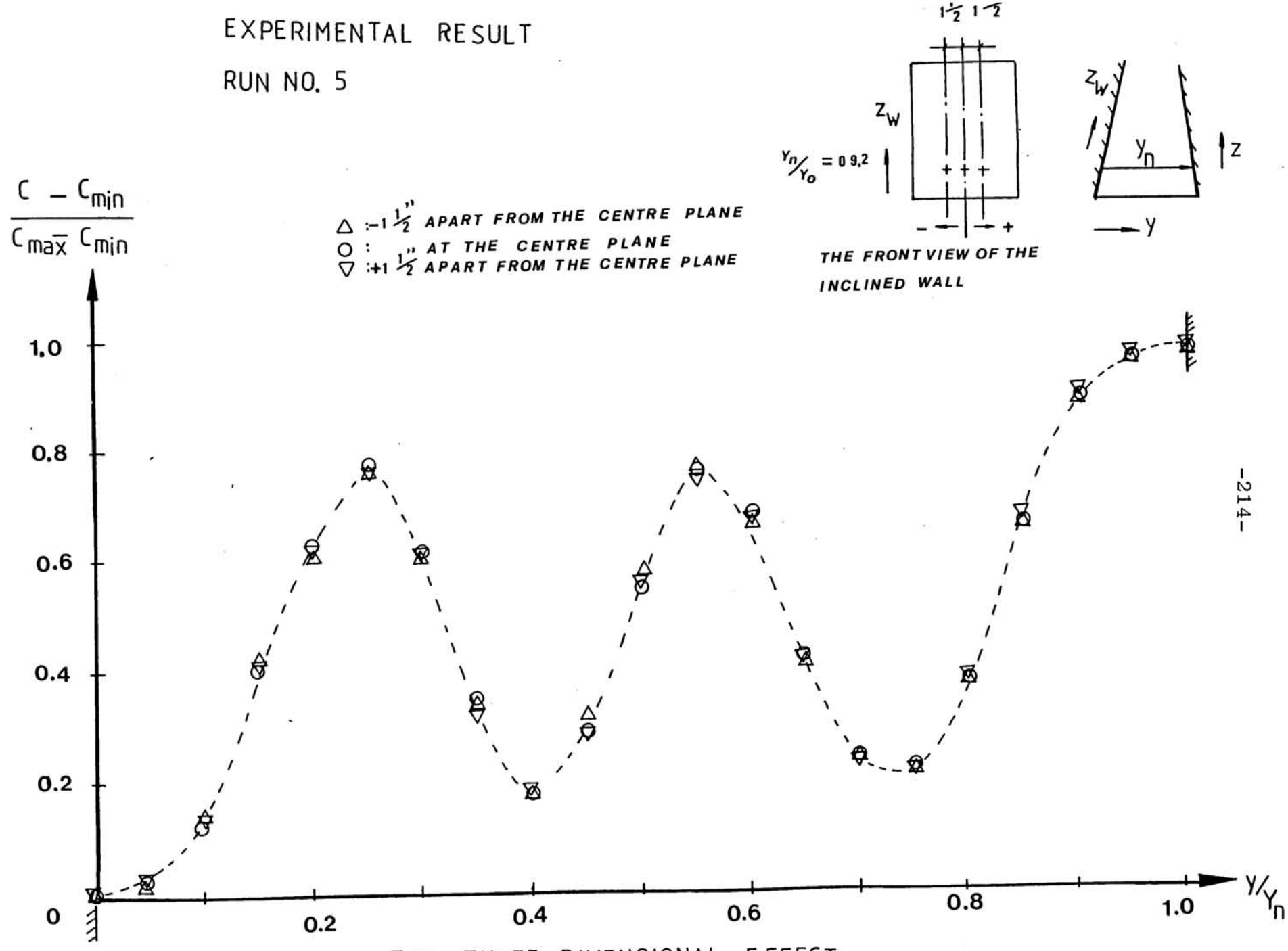

Figure 5.13 THE THREE-DIMENSIONAL EFFECT.

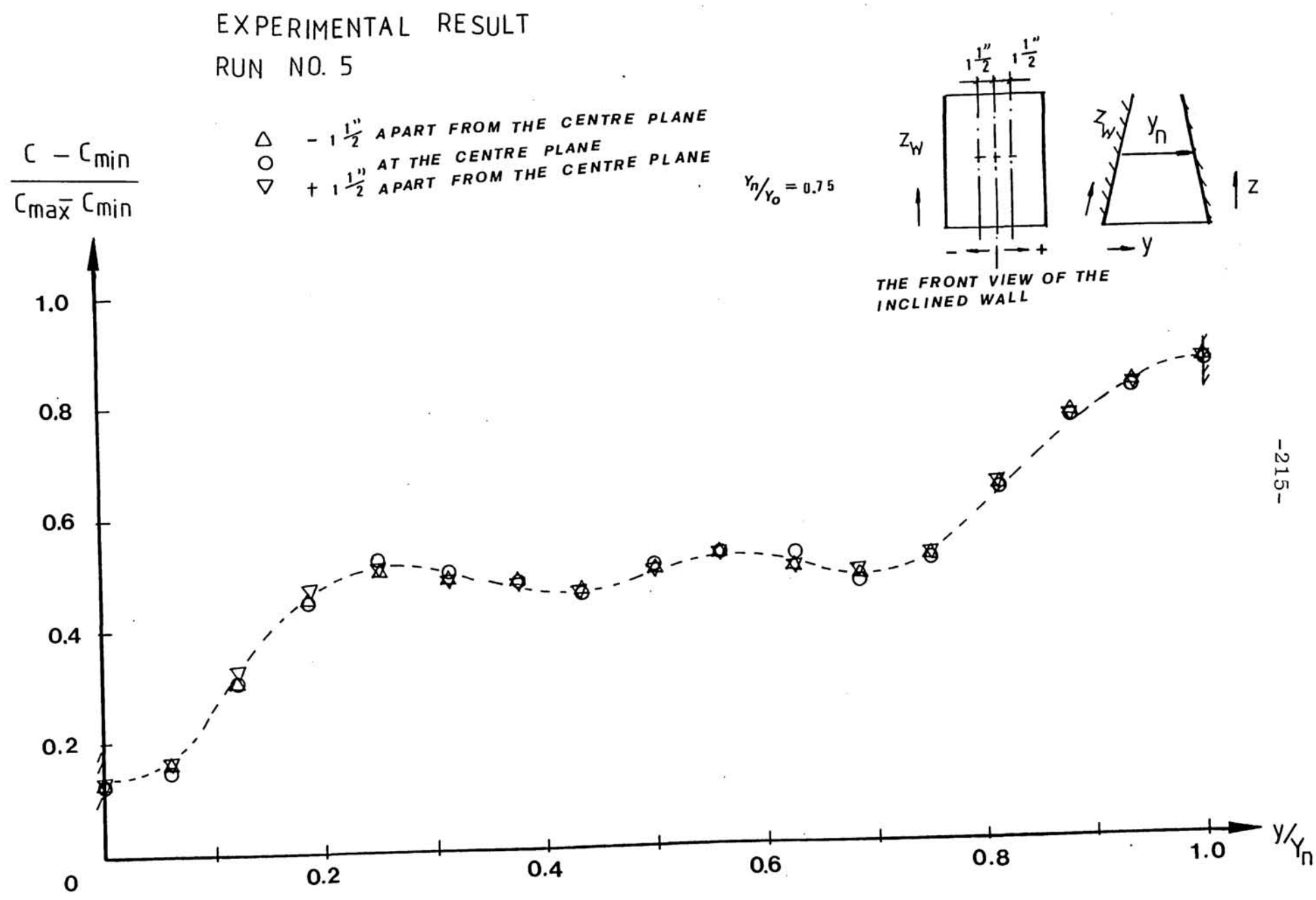

Figure 5.14 THE THREE-DIMENSIONAL EFFECT.

5.7.3 Degree of reproducibility

As a test of the reliability of the results, measurements as described above were repeated a number of times; in most cases the repeated tests were taken on a different day.

Typical results for the repeated run are given in Figures 5.15 and 5.16. These prove that the results are generally reproducible.

5.8 Remarks

The cold flow experiments were conducted with the objective of providing data for the verification of the numerical predictions for the isothermal, non-reacting multiple-folds inside a two-dimensional converging channel.

Since the results of cold flow experiments were shown to be successful, the next task was to further demonstrate the behaviour of the hydrogen-air laminar diffusion stretched flame. This is presented in detail in Part II.

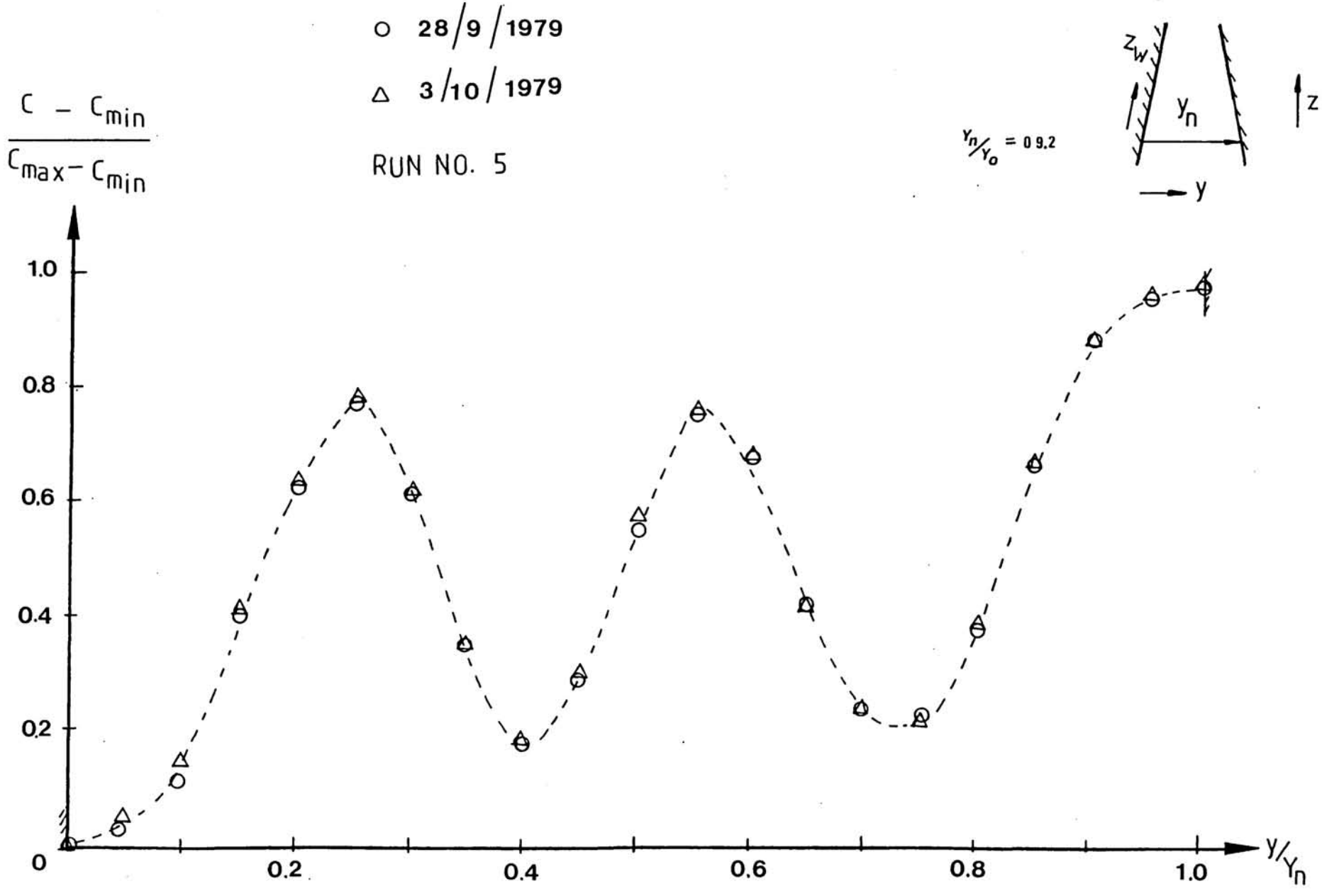

Figure 5.15 REPRODUCIBILITY FOR RUN NO. 5.

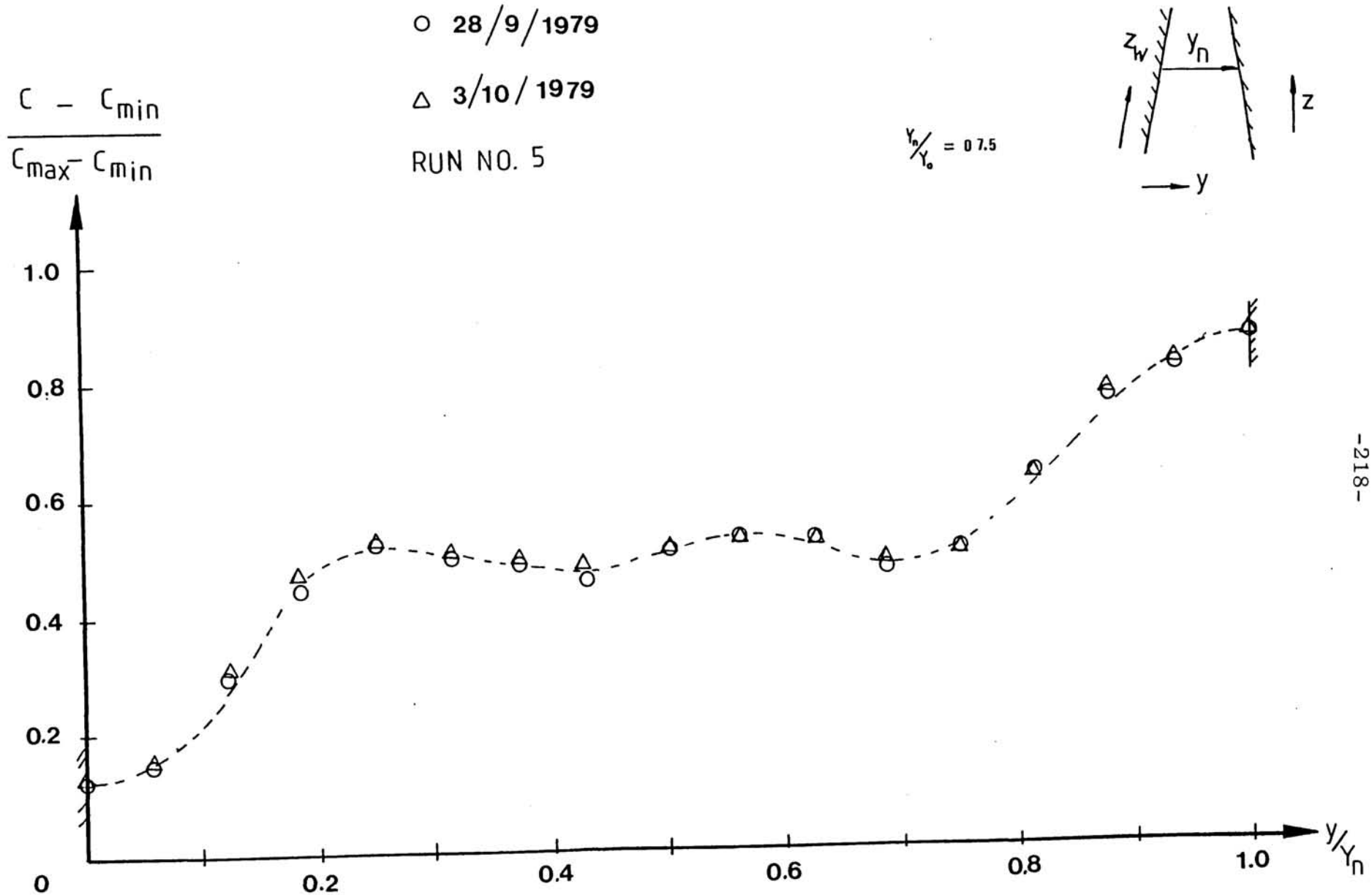

Figure 5.16 REPRODUCIBILITY FOR RUN NO. 5.

P A R T I I

HOT FLOW EXPERIMENT

5.9 Introductory Remarks

5.9.1 The problem considered

The experiment described here is concerned with the fold biographic studies in which combustion occurred. An apparatus was designed for establishing a symmetric plane, laminar diffusion flame under stretching. Hydrogen+ nitrogen and air were alternately and steadily injected into the test section from the porous strips of the reactor (i.e. the birthplace of folds). The flow was confined to a converging duct (the test section) which caused it to contract (i.e. folds were being stretched). Since ignition occurred, the effects of stretching on the laminar diffusion stretched-flame could be observed.

First, the objectives of the experiment are outlined. Then, descriptions of the experimental apparatus and measuring equipment are given. The experimental procedure, experimental conditions and method of interpretation of results are reported.

Finally, an analysis of the error involved in the measurements is discussed.

5.10 Objectives of the Experiment

The fold biographic theory of the isothermal flow has been investigated experimentally in Part I. It was

desirable to employ the same apparatus to study the laminar stretched flame.

The objectives of the experiment were:

- To study a hydrogen-air laminar diffusion stretched flame in a converging duct.
- To provide some experimental data for the verification of the prediction procedure of fold biographic theory with the ESCIMO approach.

5.11 Experimental Apparatus

The test section geometry employed here was, for the most part, the same as that for the cold flow experiments. In addition, some modifications were introduced. These were:

(1) The reactor was reduced to three rectangular chambers. The construction details of each chamber has already been described in the cold flow experiment.

(2) A fuel line was connected to the central chamber.

(3) The test section was made of 1/8" thick asbestos sheets.

(4) An ignition system in conjunction with a safety circuit was used.

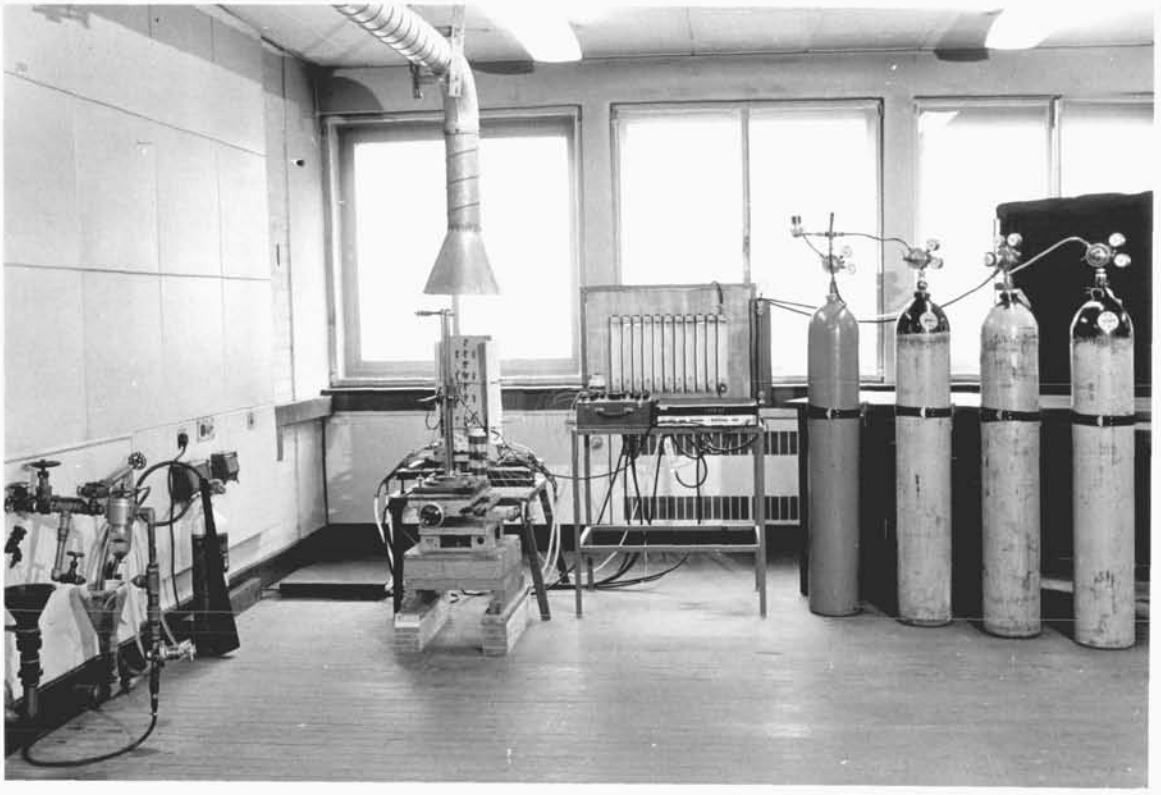

FIGURE 5.17 A PICTORIAL VIEW OF THE HOT FLOW EXPERIMENTAL APPARATUS.

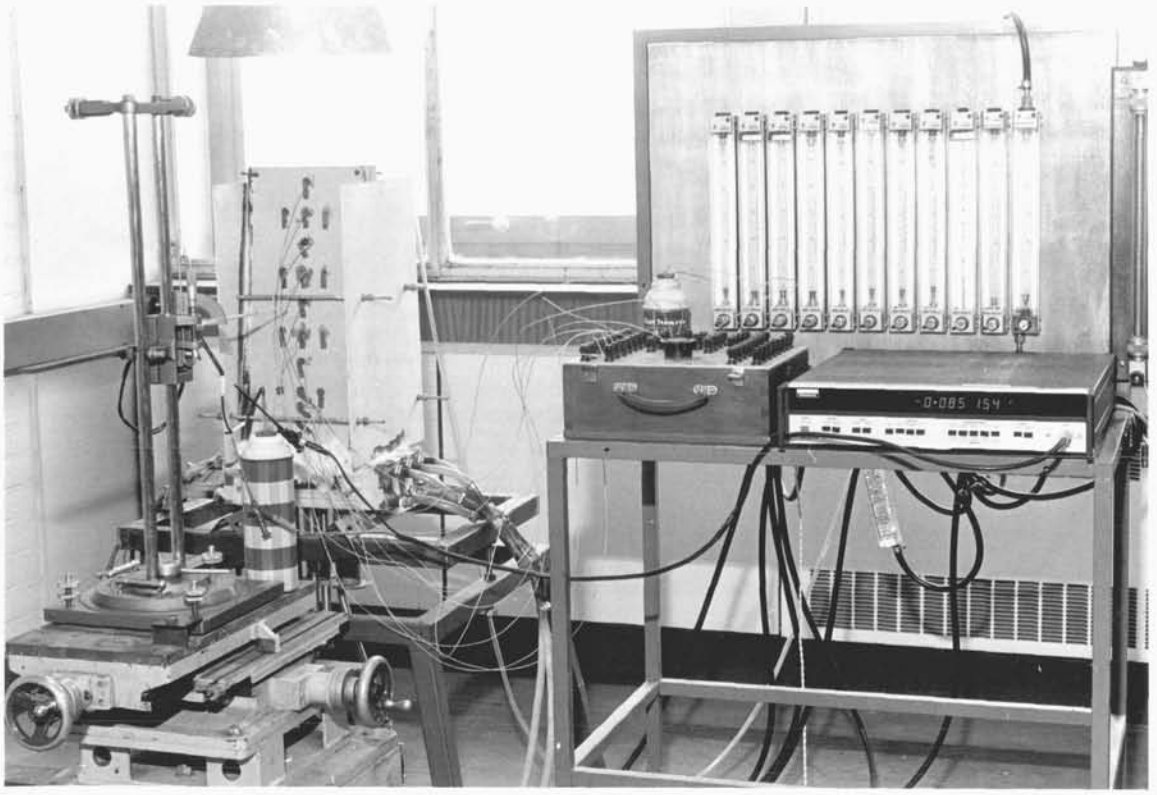

FIGURE 5.18 CLOSE UP VIEW OF THE COMBUSTION RIG.

(5) A symmetrical, laminar plane, stretching diffusion flame was maintained at the entrance of the test section.

(6) The cooling water system and the exhaust gas system were in operation.

(7) The inclined-wall temperature distribution of the test section was measured by the thermocouple embedded in the wall.

A photograph of the experimental facility is shown in Figure 5.17. The close-up view of the hot flow rig is shown in Figure 5.18. Details of the apparatus are given below.

5.11.1 The gas supply system

The air supply line

First, air was steadily discharged from the main air supply unit, and then filtered into the pressure regulator. Then, it was distributed into two lines and fed into the first and the third reactor chambers. In each line, the air flow rate was metered upstream by a rotameter fitted with a needle valve.

The fuel supply line

The fuel supply system consisted of a hydrogen gas line

and a nitrogen line. The gases were supplied from the high pressure cylinders (Supplier: BOC, purity: greater than 99.9%).

First, the ignition system was operated. The hydrogen gas was discharged from the hydrogen cylinder and then passed through an automatic solenoid valve, after the ignition circuit had been activated. The solenoid valve was operated with a flame detector through a safety circuit, described in the next section.

After metering the flow rates by the calibrated rotameters, the hydrogen and nitrogen streams were premixed in a 3/8"ϕ gas supply tubing before entering a mixer. This mixer also served as a flame trap.

Finally, the combustible mixture (hydrogen + nitrogen) was admitted into the central reactor chamber.

5.11.2 The ignition system

Initial ignition of the flame was provided by a Practorol Gas Burner Unit, Series No. 4973A. It consisted of a spark plug, a flame detector, a solenoid valve and a control panel. The spark plug and the flame detector which were mounted on the side wall of the test section were located at 2.54cm downstream of the porous strips. Since the burner control unit was continuously operating during the experiment, the above device was

employed to ignite the gas and detect the flame at the same time. The ignition circuit in conjunction with a safety device is shown in Figure 5.19.

The arrangement ensured that the spark was generated by a 20kV, 23mA ignition transformer. Since the flame was established at a short distance away from the porous strips, the safety circuit was also operated. The safety circuit was such that if the flame detector did not sense the flame in the test section in six seconds, the solenoid valve would shut the hydrogen gas off.

5.11.3 The cooling water system

The reactor was cooled by a cooling water jacket on both sides of the chambers as described in Part I. The cooling water was discharged through a regulating valve and distributed by a manifold to the water jackets. As the flame approached the porous strips, it began to transfer heat to the water jackets. Then, the heat was carried away by the cooling water. The water flow rate was adjusted such that the temperature at the water-out flow did not rise more than a few degrees. The removal of heat by the porous strips to the water jacket was a necessary flame stabilising mechanism (Botha and Spalding, 1954).

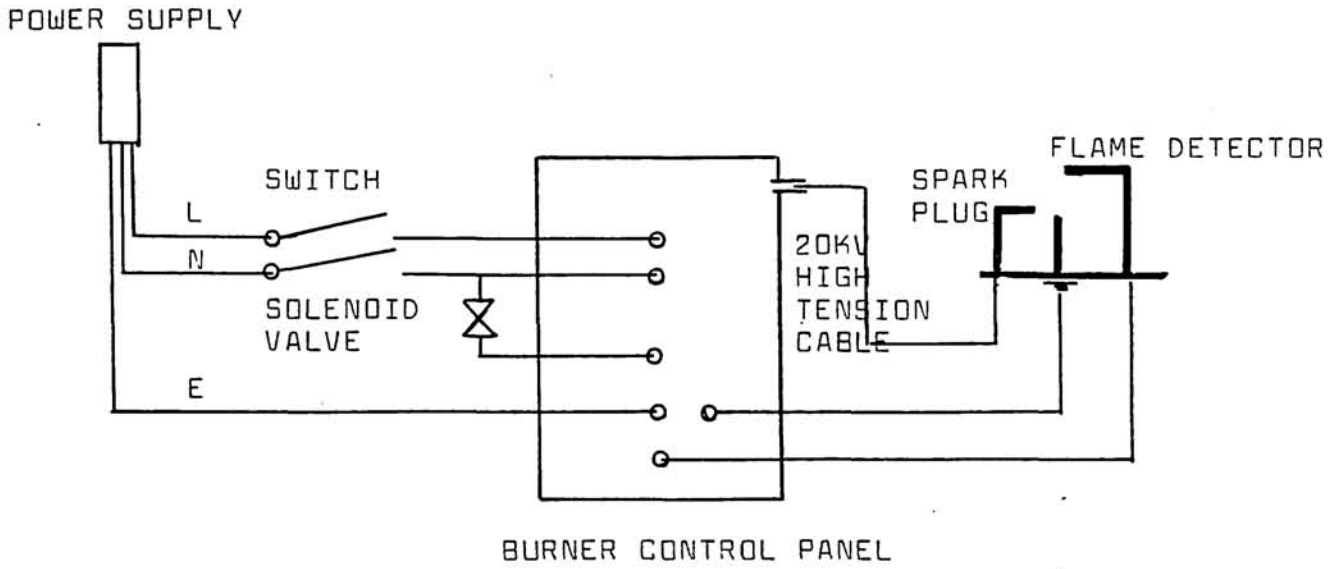

Figure 5.19 THE IGNITION CIRCUIT

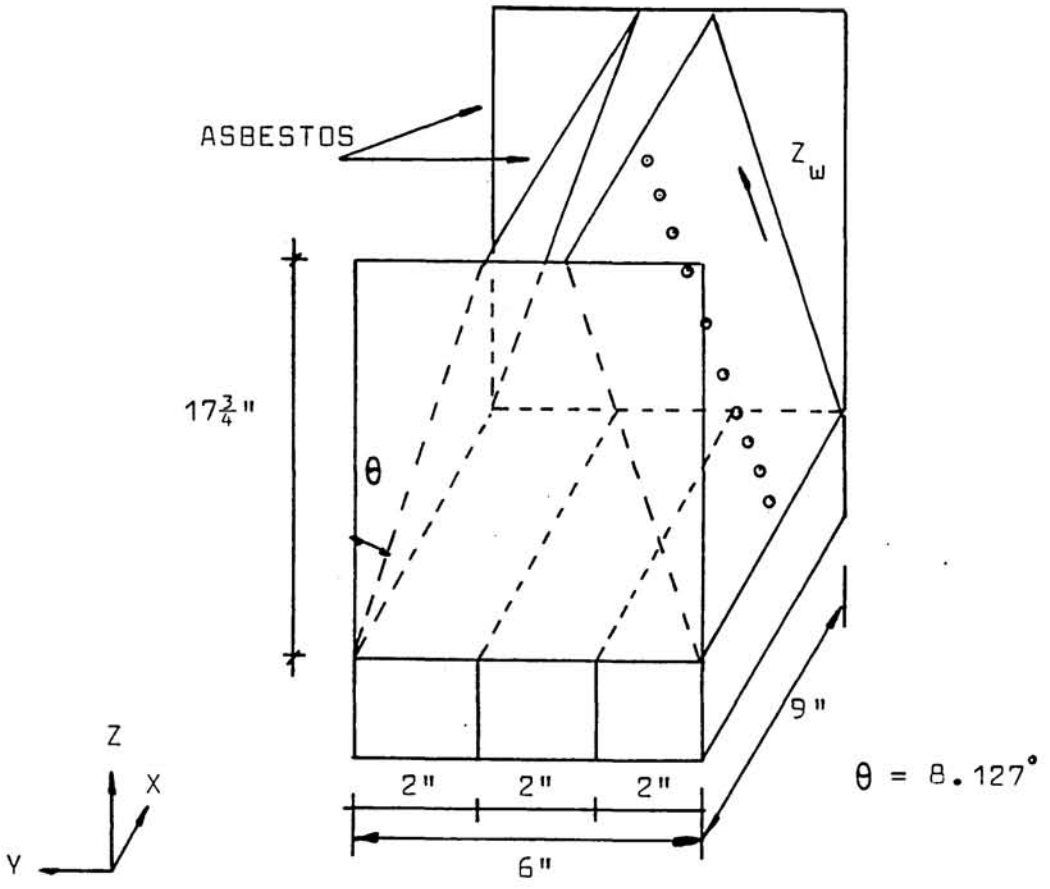

Figure 5.20 THE TEST SECTION

5.11.4 Flame stabilisation

In order to stabilise the diffusion flame, each porous strip was separated by thin stainless steel septums (thickness ≡ 0.3125mm, height = 5mm). The thin septums were mounted at the entrance of the test section. The diffusion flame was therefore maintained at the boundary between each of the two streams of uniform velocity profiles, separated by the thin septums.

5.12 The Configuration of the Test Section

The dimensions of the test section are shown in Figure 5.20. The middle and bottom parts of it were clamped with a ¼"ϕ threaded rod which held the compression spring on the side walls. These threaded rods provided the necessary strain to eliminate the warping of the test section during the experiment. The edges of the test section were sealed by cement after the inclined angle had been fixed.

5.13 The Measured Quantities

The gas temperature was sensitive to detect and easily obtainable by the temperature measurement technique. Thus, only temperature measurement was made, with the aid of 20% R_n-P_t ∿ 40% R_h-P_t thermocouple.

5.14 The Measured Locations

Nineteen probing holes were provided at the test section. Eleven of them were located on the centreline of the inclined-wall, the other eight being 1½" on both sides of the centreline.

Gas temperatures in the test section were measured with the probing holes on the centreline of the inclined-wall at the following locations: 1", 2", 3", 4", 8" and 12" from the bottom of the inclined-wall.

5.15 The Wall Temperature

The temperature distribution along the inclined wall was measured by means of ½mm diameter chromium-aluminium thermocouple wires. Eleven hot junctions of chromium-aluminium thermocouples were stuck along the centreline of the inclined wall, as shown in Figure 5.18.

The wires were well insulated by the twin bore insulator and were connected through a selector switch to a DVM.

5.16 Temperature Measuring Equipment

The temperature measuring equipment consisted of a thermocouple wire, a thermocouple probe and a DVM.

The thermocouple wire

The thermocouple wire material was chosen to be of 0.075mm diameter 20% R_h-R_t∿40% R_h-R_t because:

(1) The wire could be used over a range of 0^oC to 1800^oC. The manufacturer guaranteed this type of thermocouple to conform to the following tolerance.

Temperature range	up to 1100^oC	1100^oC-1550^oC	above 1550^oC
tolerance	$\pm$ 3^oC	$\pm$ 4^oC	$\pm$ 8^oC

This provided accurate, reliable and reproducible temperature measurements.

(2) Such fine wires were of low thermal capacity. It could therefore respond rapidly in detecting temperatures.

(3) The effects of thermal conduction along the elements from the measuring junction to other parts of the thermocouple system and the effects of radiation could be greatly reduced.

(4) The material was less subject to oxidation. The life span was consequently increased.

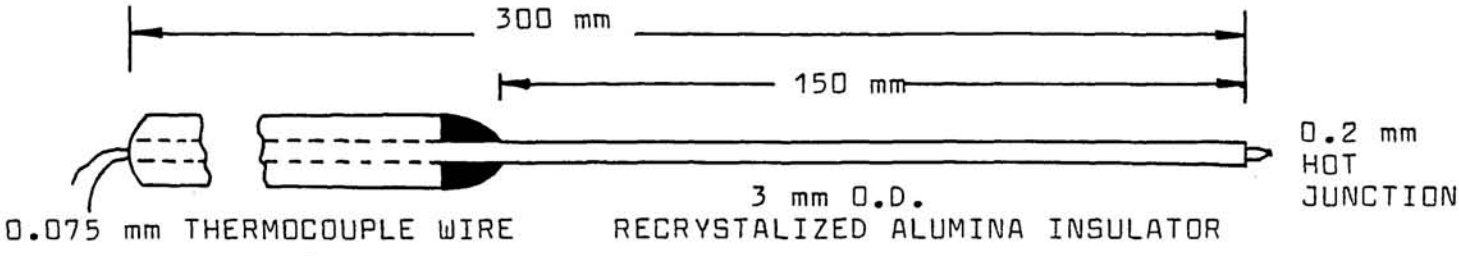

Figure 5.21 THE THERMOCOUPLE PROBE

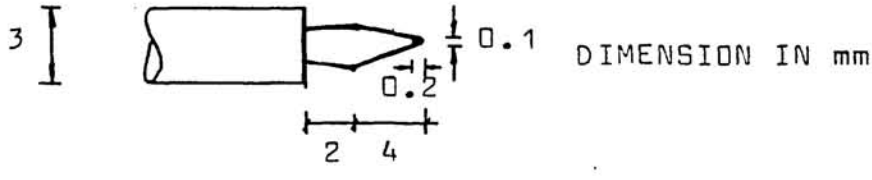

Figure 5.22 THE HOT JUNCTION

The hot junction

A diagram of the thermocouple hot junction is shown in Figure 5.22. The 20% R_h-P_t 40% R_h-P_t wires were butt-welded together. The diameter of the bead was 0.2mm. The thermocouple bead was coated with the noncataclytic oil (silicon oil, Fristrom and Westenberg, 1965). Consequently, this wire was particularly good in resisting oxidation and corrosion, and was also homogeneous.

The cold junction

The temperature reading indicated by the instrument was a temperature difference. The actual temperature of the hot junction was therefore equal to the instrument reading plus that of the cold junction reading. However, the cold junction was immersed in an ice bath. This ensured that the cold junction reading was always zero. In order to prevent the introduction of extraneous emf from such junctions, the extension wire employed was of the same material as the measuring junction itself.

The probe

A diagram of the thermocouple probe is sketched in Figure 5.21. The body of the probe consisted of a 3mm twin bore insulator with a short piece of copper tube cemented to it at the clamping end. The insulator was

made of "recrystalised aluminium" manufactured by "Thermal Syndicate Limited".

The properties of the insulating material as provided by the manufacturer were:

Material	: recrystalised aluminium.
Thermal conductivity	: 0.014 Cal/msec^{o}C at 1000°C.
Maximum working temperature	: 1900°C.
Thermal expansion	: 8 x 10^{-6} m/C^{o}.

The advantage of using the insulator was that it did not require any sheathing.

5.17 Experimental Conditions

The experimental conditions are tabulated in Table 5.3. Due to the narrow range of stability of the flame and for reasons of safety, only the lean hydrogen-air mixture of laminar diffusion combustion was observed in the test section under the inclined-angle 8.127^{o}. Hence, one flame (denoted by Flame A) was investigated.

5.18 Experimental Procedure

The experimental sequence was as follows:

(1) The inclined-wall angle was adjusted and the edges of the test section were sealed.

	Flame A
Dimension of the test section (width x height) m^2.	0.1524x0.45
Inclined angle θ.	8.127^{o}
Dimension of porous strip m^2.	0.0508x0.2286
Width of the strip m.	0.0508
Number of supply air strips.	2
Supply air flow rate/strip kg/sec	1.373×10^{-3}
Fuel used.	Hydrogen
Number of supply fuel strips	1
Supply fuel flow rate/strip kg/sec (Hydrogen + Nitrogen)	4.06145×10^{-4}
Hydrogen flow rate kg/sec	4.5045×10^{-5}
Nitrogen flow rate kg/sec	3.611×10^{-4}
Overall hydrogen/air ratio	0.0164
Total number of strips (folds)	3
Reynolds number (based on inlet condition, test section width, and total flow rate).	524
Supply air temperature.	$30^{o}C$
Supply fuel temperature.	$30^{o}C$

TABLE 5.3: THE EXPERIMENTAL CONDITIONS

(2) The extraction fan motor was switched on.

(3) The cooling water was set at a suitable value.

(4) The supply air flow rate was set at the desired value.

(5) The burner control unit was switched on to create a 20KV spark to ignite a stable diffusion flame.

(6) The air, hydrogen and nitrogen flow rates were adjusted to suitable experimental conditions.

(7) Time was allowed for steady-state to be reached.

(8) The wall temperature distribution was recorded.

(9) The thermocouple traverses were performed and the DVM readings and thermocouple hot junction position were recorded.

(10) The wall temperature was recorded again.

5.19 Measurement Details

1. Igniting the fuel and air

The diffusion mixture of the hydrogen + nitrogen and air stream entering the test section was ignited by means of spark (which was operated by the burner control unit). The spark plug and the flame detector were located 2.54cm downstream of the side wall. Therefore, the flow pattern at the centre region of the test section, which was far away from the side walls, was not affected by the introduction of the spark plug.

2. Adjusting the individual flow rates

When the flame was stable, the individual flow rates of hydrogen, nitrogen and air were simultaneously, and gradually adjusted to their desired values. Hence, the possibility of blow-out of the flame could be eliminated.

3. Attaining steady-states

Steady-state was obtained by detecting the invariance of the inclined-wall temperature distribution over a period of about half-an-hour.

4. The thermocouple probe traverses

The thermocouple probe traverses were made inside the test section in the same way as in the cold flow experiment. However, the present traverses were only confined to the first half of the temperature profile because of the symmetry of the test section. The other half of the temperature profile was assumed to be symmetric with the theoretical symmetrical axis. The actual axis of symmetry was further checked by the full traverses of the probing holes near the upstream region of the test section. The reasons for performing a half traverse of the temperature measurements were:-

(1) Since the cold flow experiments had shown that the results were in good agreement with predicted ones (as will be seen in Chapter 6), and the three-dimensional effect on the centre region of the test section was negligibly small (Figures 5.13 - 5.14), the symmetrical flow pattern was supposedly adopted in the present combustion experiment.

(2) Since a standard hydrogen cylinder ($255ft^3$) could only be used to perform the present experiment in 3 hours duration, the extra operation might complicate safety design.

5.20 Calculation of the gas temperature from the emf readings

The thermocouple wire had a hot and a cold junction. This latter was immersed in an ice bath. The ice bath temperature was measured by means of a Hg thermometer and was kept at $0^{o}C$ during the experiment. Hence, it was not necessary to make any correction for the cold junction. The hot junction temperature could directly be interpreted from the calibration table (Table 5.4).

However, it would differ from the adjacent gas temperature. The reasons were:

(1) Due to the radiation heat loss from the

	0°C	100°C	200°C	300°C	400°C	500°C	600°C	700°C	800°C
0°	0	0·041	0·093	0·161	0·250	0·363	0·505	0·678	0·885
	·004	·004	·006	·008	·010	·013	·016	·019	·023
10°C	0·004	0·045	0·099	0·169	0·260	0·376	0·521	0·697	0·908
	·003	·005	·006	·008	·010	·013	·016	·020	·023
20°C	0·007	0·050	0·105	0·177	0·270	0·389	0·537	0·717	0·931
	·004	·005	·006	·008	·011	·013	·016	·020	·023
30°C	0·011	0·055	0·111	0·185	0·281	0·402	0·553	0·737	0·954
	·004	·005	·007	·008	·011	·014	·017	·020	·023
40°C	0·015	0·060	0·118	0·193	0·292	0·416	0·570	0·757	0·977
	·004	·005	·007	·009	·011	·014	·017	·020	·024
50°C	0·019	0·065	0·125	0·202	0·303	0·430	0·587	0·777	1·001
	·004	·005	·007	·009	·011	·014	·018	·021	·025
60°C	0·023	0·070	0·132	0·211	0·314	0·444	0·605	0·798	1·026
	·004	·005	·007	·009	·012	·015	·018	·021	·024
70°C	0·027	0·075	0·139	0·220	0·326	0·459	0·623	0·819	1·050
	·004	·006	·007	·010	·012	·015	·018	·022	·025
80°C	0·031	0·081	0·146	0·230	0·338	0·474	0·641	0·841	1·075
	·005	·006	·007	·010	·012	·015	·018	·022	·025
90°C	0·036	0·087	0·153	0·240	0·350	0·489	0·659	0·863	1·100
	·005	·006	·008	·010	·013	·016	·019	·022	·026

	900°C	1000°C	1100°C	1200°C	1300°C	1400°C	1500°C	1600°C	1700°C	1800°C
0°	1·126	1·401	1·707	2·046	2·416	2·814	3·237	3·678	4·130	4·585
	·026	·029	·033	·036	·039	·041	·043	·045	·046	·045
10°C	1·152	1·430	1·740	2·082	2·455	2·855	3·280	3·723	4·176	4·630
	·027	·030	·033	·036	·039	·042	·044	·045	·045	·045
20°C	1·179	1·460	1·773	2·118	2·494	2·897	3·324	3·768	4·221	4·675
	·026	·030	·033	·036	·039	·042	·044	·045	·046	·045
30°C	1·205	1·490	1·806	2·154	2·533	2·939	3·368	3·813	4·267	4·720
	·027	·030	·033	·036	·039	·042	·044	·045	·045	·045
40°C	1·232	1·520	1·839	2·190	2·572	2·981	3·412	3·858	4·312	4·765
	·027	·030	·034	·037	·040	·042	·044	·045	·046	·045
50°C	1·259	1·550	1·873	2·227	2·612	3·023	3·456	3·903	4·358	4·810
	·028	·031	·034	·037	·040	·042	·044	·046	·045	·045
60°C	1·287	1·581	1·907	2·264	2·652	3·065	3·500	3·949	4·403	4·855
	·028	·031	·034	·038	·040	·043	·044	·045	·046	·044
70°C	1·315	1·612	1·941	2·302	2·692	3·108	3·544	3·994	4·449	4·899
	·028	·031	·035	·038	·040	·043	·044	·045	·045	·044
80°C	1·343	1·643	1·976	2·340	2·732	3·151	3·588	4·039	4·494	4·943
	·029	·032	·035	·038	·041	·043	·045	·045	·046	
90°C	1·372	1·675	2·011	2·378	2·773	3·194	3·633	4·084	4·540	
	·029	·032	·035	·038	·041	·043	·045	·046	·045	

TABLE 5.4 STANDARD CALIBRATION TABLE FOR JMM 20% RHODIUM-PLATINUM: 40% RHODIUM-PLATINUM THERMOCOUPLES.

E.m.f. values are given in millivolts and temperature in degrees C. Cold junction is at 0° C.

To assist in interpolating between two given values, the difference between successive e.m.f. readings is shown in smaller type.

thermocouple bead to the test section walls at high gas temperatures.

(2) Due to the conduction heat loss in the wire.

The corrections made were as follows:

(1) Radiation correction

The temperature of the thermocouple bead was below the actual gas temperature because the thermocouple bead lost heat by radiation to the wall. Under steady-state conditions, the rate of heat flow by radiation from the thermocouple bead to the wall was equal to the rate of heat flow by convection from the gas to the thermocouple bead.

The heat balance equation is:

$$h_c A_j \ (T_g - T_j) = A_j \ \sigma\varepsilon \ (T_j^{\ 4} - T_w^{\ 4}) \ , \qquad (5.20\text{-}1)$$

where $A_j \equiv$ surface area of the thermocouple bead in cm^2;

$h_c \equiv$ convective heat transfer coefficient between bead and hot gas in erg cm^{-2} sec^{-1} $^oK^{-1}$;

$T_g \equiv$ gas temperature in ^oK;

$T_j \equiv$ hot junction temperature in ^oK;

$T_w \equiv$ inclined wall temperature in ^oK;

$\sigma \equiv$ Steffan-Boltzmann constant = 5.67×10^{-5} erg cm^{-2} $^oK^{-4}$ sec^{-1}; and

$\varepsilon \equiv$ emissivity of the thermocouple junction.

The value of the h_c could be calculated from the Nusselt number. Since the thermocouple bead was supposed to be a perfect sphere, the Nusselt number, which was based on the bead diameter, could be expressed as a function of the Reynolds number and the Prandtl number. Moreover, the present thermocouple wire was fine and the exhaust gas was relatively clean. It was supposed that no fuel droplet of the carbon particles could be deposited on the bead. Consequently, a value of $\varepsilon = 0.3$ was expected (Glawe and Shepard, 1954; Serag El Din, 1977).

The value of h_c was calculated as follows: The equation recommended by Moffat (1962) for wires normal to the flow was used:

$$Nu = \frac{h_c d}{k} = 1.122\ (0.44 \pm 0.06)\ Re^{0.5}\ Pr^{0.31}\ , \qquad (5.20\text{-}2)$$

where $k \equiv$ the conductivity of the hot gas = 5.2×10^4 $erg^{-1} sec^{-1}\ {}^{o}K^{-1} cm^{-1}$;

$d \equiv$ estimated junction bead diameter = 0.02cm;

$v \equiv$ typical gas velocity = 150 cm/sec;

$\nu \equiv$ kinetic viscosity at $1650^{0}K$, which corresponds roughly to the highest junction temperature where the correction is maximum = $2cm^2/sec$; and

$$Re = \frac{vd}{\nu} = 1.5.$$

The above results gave Nu = 0.63;

$$h_c = 1.6\text{x}10^6 \text{ erg.cm}^{-2}.\text{sec}^{-1}.{}^{o}\text{K}^{-1}.$$

Substituting these values into the heat balance equation permitted the evaluation of the gas temperature.

$$T_g = T_j + 1.06\text{x}10^{-11} (T_j{}^4 - T_w{}^4) \ {}^{o}\text{K}. \qquad (5.20\text{-}3)$$

The above equation shows that the maximum radiation heat loss was less than 50°K.

(2) Conduction correction

When the thermocouple was inserted into the test section and supported at the inclined wall, the wall would, in general, be colder than the hot gas; thus there would be heat transfer, and this would lead to a probe temperature different from that of the gas temperature.

For a steady-state situation, when the thermocouple bead extended a distance L from the wall, the following conduction correction equation was used (Doebelin, 1966).

$$T_j - T_g = \frac{T_w - T_g}{\cosh \sqrt{\frac{h}{k} \frac{2}{r}}\ L} \quad , \qquad (5.20\text{-}4)$$

where r ≡ radius of the probe = 0.15cm;

h ≡ film coefficient of heat transfer = 2×10^5 erg.sec^{-1}.^{o}K^{-1}.cm^{-2} at 1000°K;

$k \equiv$ thermal conductivity of the probe = 6×10^4 $erg.sec^{-1}.{}^{o}K^{-1}.cm^{-1}$; and

$L \equiv$ the distance between the thermocouple bead and the wall = 10mm (estimated).

Hence, $T_j - T_g = 2.5 \times 10^{-3} (T_w - T_g)$, (5.20-5)

The above equation shows that the maximum conduction error for the present experiment was less than $4^{o}C$.

5.21 Experimental Results

For all experimental parameters, the measurements were repeated at least once, to ensure the reproducibility of the experiments. The experimental results of Flame A are displayed in Figures 5.23-28.

It was observed that:

(a) The non-adiabatic laminar diffusion flame was under the influence of buoyancy and stretching.

(b) The temperature profile at upstream region is shown in Figure 5.23. This profile shows that the flame front was located at about 10% nearer the centreline. The maximum measured temperature was about $1650^{o}K$.

(c) The measured temperature profiles showed that the temperature gradients became less steep as the

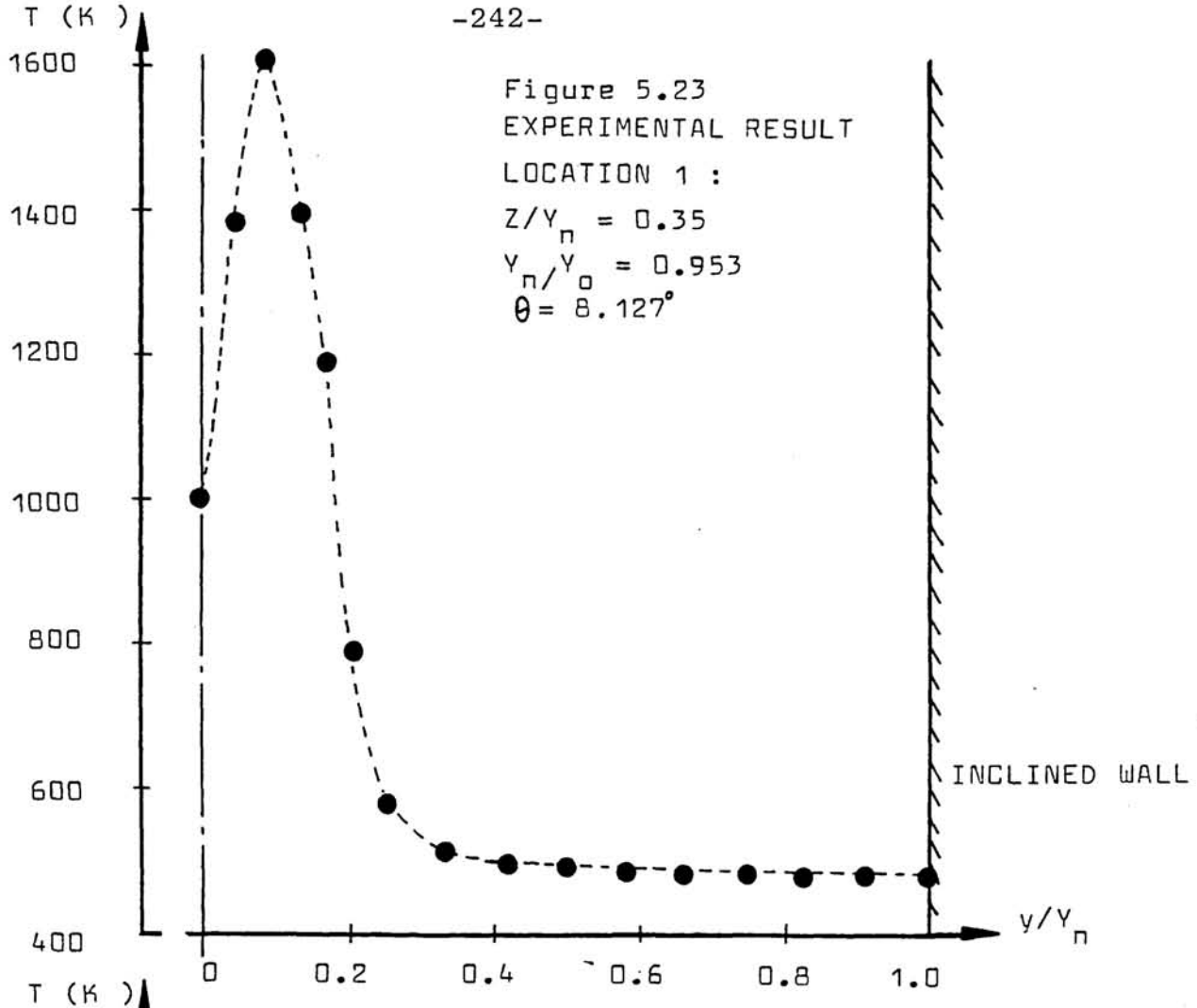

Figure 5.23
EXPERIMENTAL RESULT
LOCATION 1 :
$Z/Y_n = 0.35$
$Y_n/Y_o = 0.953$
$\theta = 8.127^\circ$

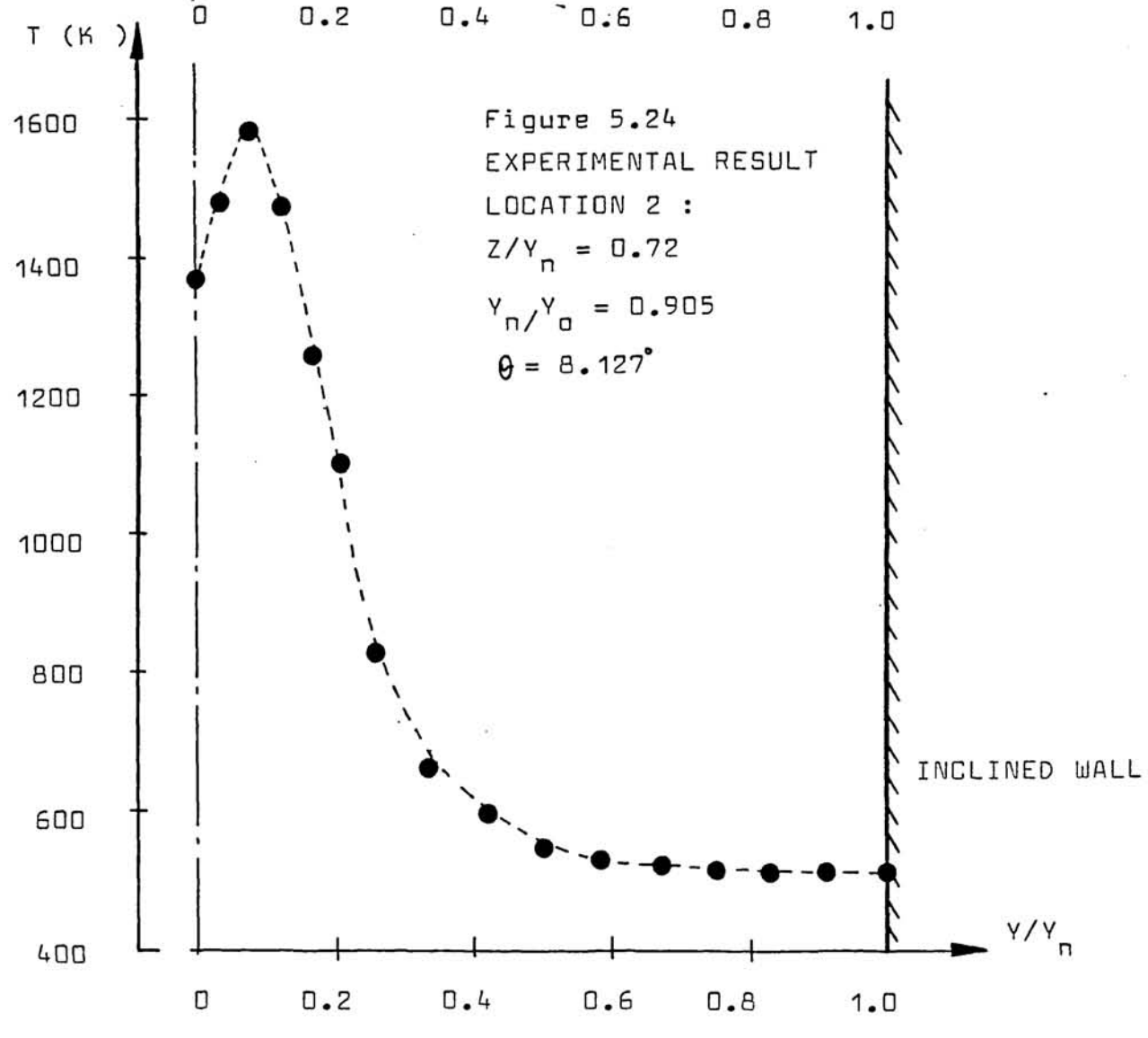

Figure 5.24
EXPERIMENTAL RESULT
LOCATION 2 :
$Z/Y_n = 0.72$
$Y_n/Y_o = 0.905$
$\theta = 8.127^\circ$

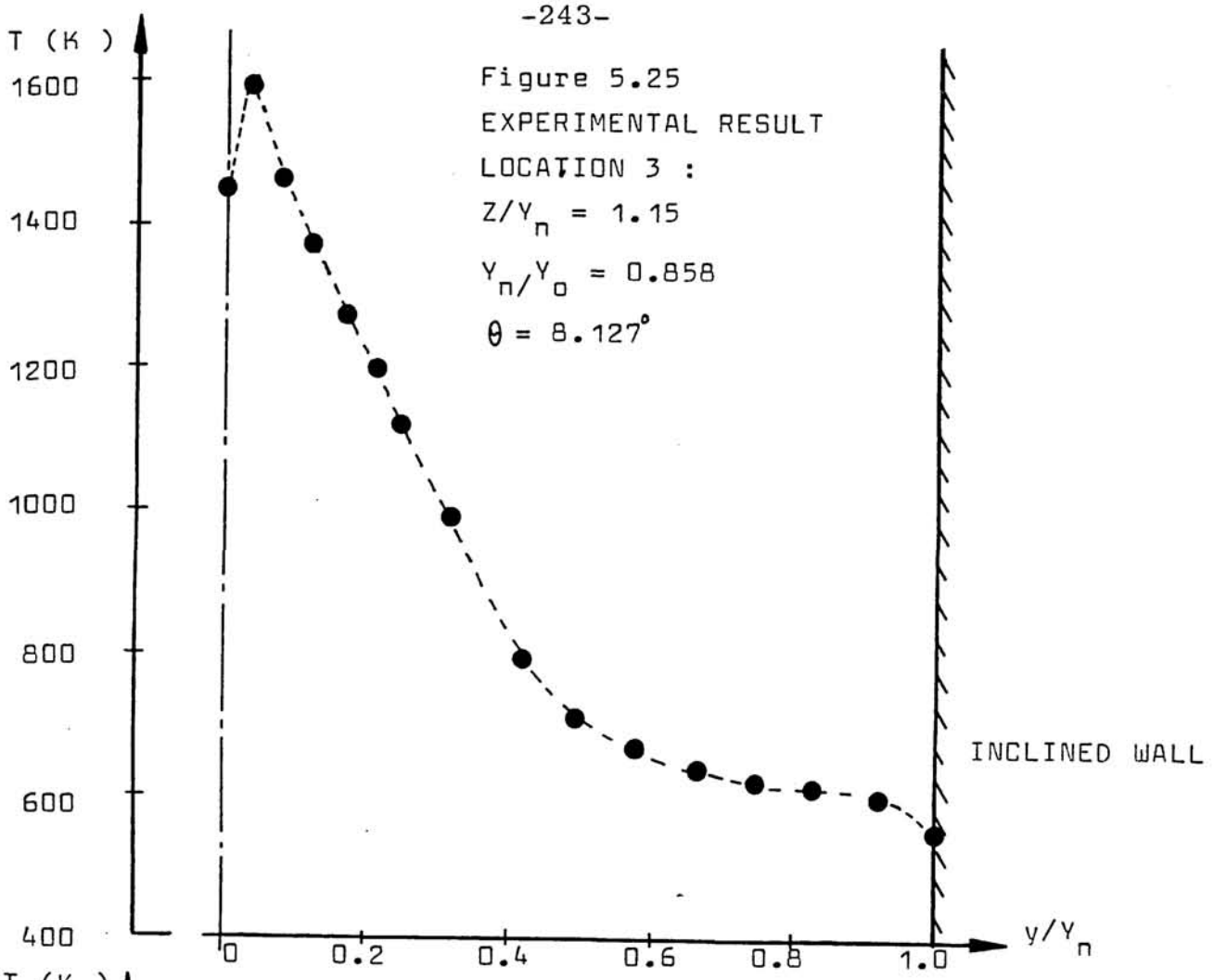

Figure 5.25
EXPERIMENTAL RESULT
LOCATION 3 :
$Z/Y_n = 1.15$
$Y_n/Y_o = 0.858$
$\theta = 8.127°$

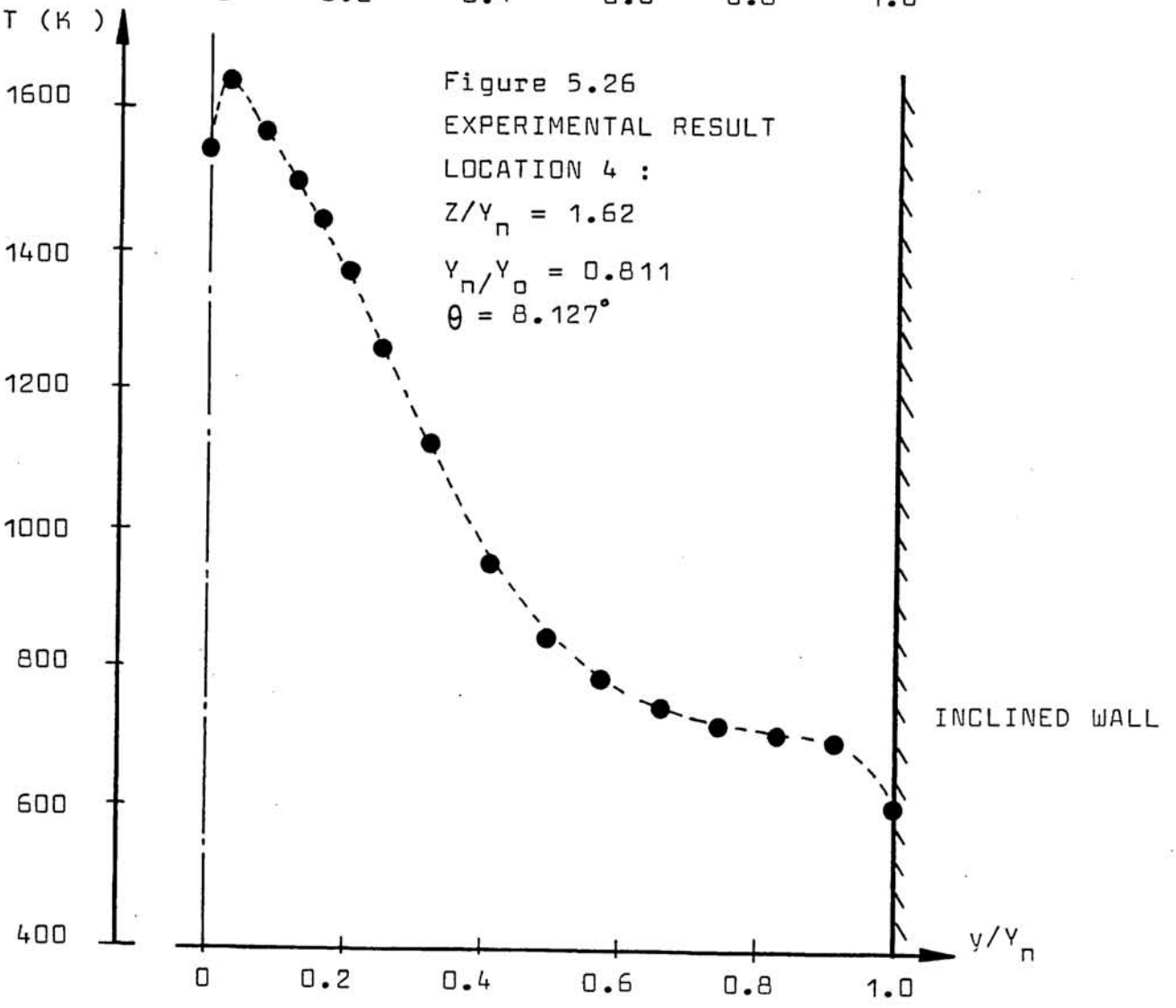

Figure 5.26
EXPERIMENTAL RESULT
LOCATION 4 :
$Z/Y_n = 1.62$
$Y_n/Y_o = 0.811$
$\theta = 8.127°$

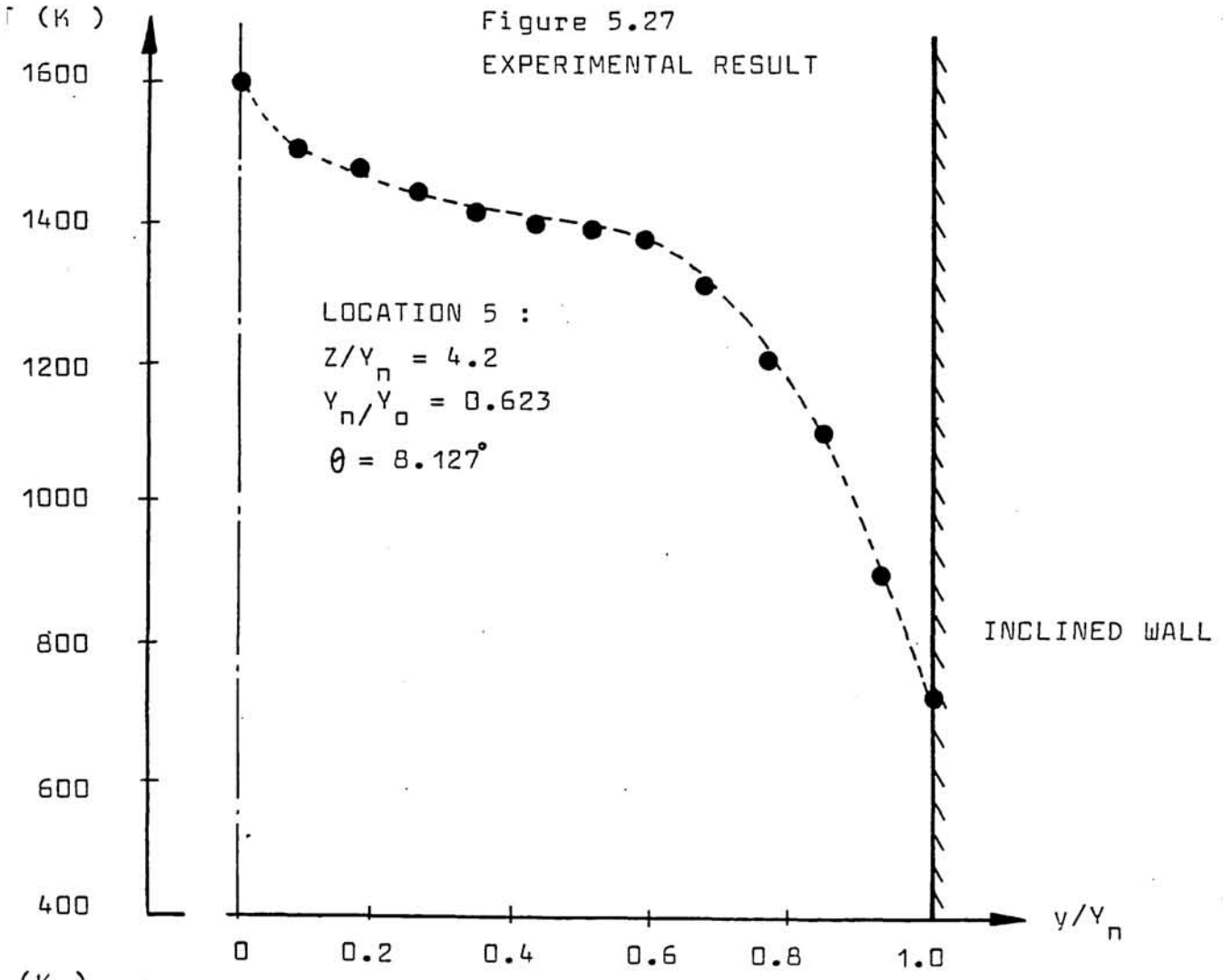

Figure 5.27
EXPERIMENTAL RESULT

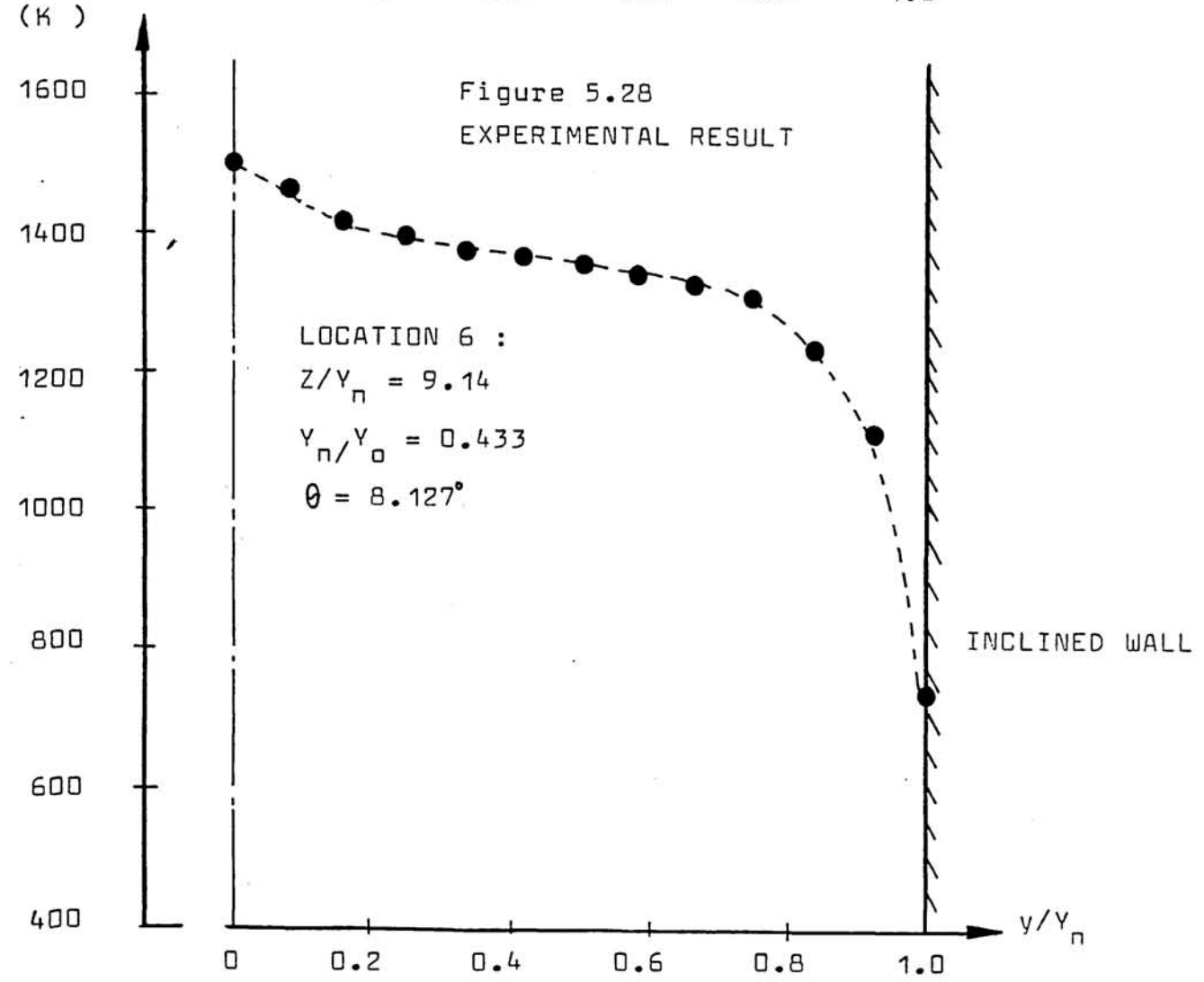

Figure 5.28
EXPERIMENTAL RESULT

flame developed downstream. This can further be examined from Figures 5.25-26.

(d) Figure 5.27 shows that the cross-fold temperature profile was nearly uniform.

(e) The combustion was complete further downstream. Thus, only the diffusion, mixing and heat transfer were observed in Figure 5.28.

5.22 Discussion

5.22.1 Error analysis

1. The gas temperature measurements

The measurement of the temperature of reacting gas by means of a thermocouple is subject to two major sources of error. (a) The effect of the probe on the flame;and (b) the temperature measurement technique. The perturbation caused by the presence of the probe can be classified as aerodynamic, thermal and chemical.

Aerodynamic effect

The principal aerodynamic effect of the probe is the velocity-deficient wake behind it, which can be visualised as resulting in a local propagation of the flame closer to the probe. The wake displacement has

been estimated to be roughly six or seven bead diameters downstream of the thermocouple bead employed (0.2mm diameter), the wake displacement error is of the order of 1.5mm which is relatively small when compared to the dimension of the test section.

The thermal effect

The thermal effect of a probe as a hot sink is a function of the temperature difference between the stream and the probe. However, it must be recalled that the rate of heat transfer by radiation from the thermocouple bead to the wall and the rate of heat transfer by conduction from the bead to the wall along the support has already been estimated in Section 5.20. The quantitative correctness of these calculations (maximum error of $50^{o}K$ in the radiation heat loss, and $4^{o}K$ in conduction heat loss) indicates that the disturbance introduced by such a thermocouple on the temperature field could also be negligible.

The chemical disturbance

The principal chemical disturbance of the thermocouple is the promotion of catalytic reactions on the thermocouple surface. Since the thermocouple wire employed is highly resistant to oxidation corrosion,

the effect is negligible. Below 1200°F, the presence of unburned hydrogen caused a platinum shielded thermocouple to read higher by as much as 25°F (Moffat 1962).

2. Wall temperature measurement

In measuring the wall temperature, as mentioned in Section 5.15, a wire length of 2000 times its diameter was kept at almost isothermal conditions with the junction. In this case, the conduction error is very small and can be neglected.

3. Flow rate measurement

The same errors are involved here as in the cold flow experiment; a maximum error of $\pm$ 1% is also expected.

4. Inclined-wall angle

The inclined wall angle adjustment is likely to be accurate to within $\pm$ 0.2 degree.

5. Error in determining the position of the thermocouple hot junction

Again, the estimated accuracy with which the thermocouple probe location could be determined is similar to the cold flow experiment, which is $\pm$ 1mm in the

traverse direction, and ± 1mm in the z-direction.

6. "Symmetry" of temperature profiles

Theoretically, the experimental conditions and the geometry of the test section ensure that the laminar diffusion stretched-flame is symmetric across the folds. In practice, the difference between the measured local axis of symmetry and the theoretical axis of symmetry required further testing. To examine the "symmetry" of the temperature profiles, several full traverses of the cross-section for the experimental conditions of Flame A at the following locations were made.

z_w = 1", 2" and 8".

The measured profiles are displayed in Figures 5.29-31.

The above results show some discrepancies in temperature between the two corresponding temperature profiles.

As shown in Figure 5.29, the profile on the right half of the centreline exhibits less steepness than the left ones. The maximum difference is about 8%.

5.22.2 Degree of reproducibility of the measurements

Figures 5.32-34 show the profiles of temperature measurement obtained on two different days for the same

Figure 5.29 "SYMMETRY" OF TEMPERATURE PROFILE
LOCATION 1

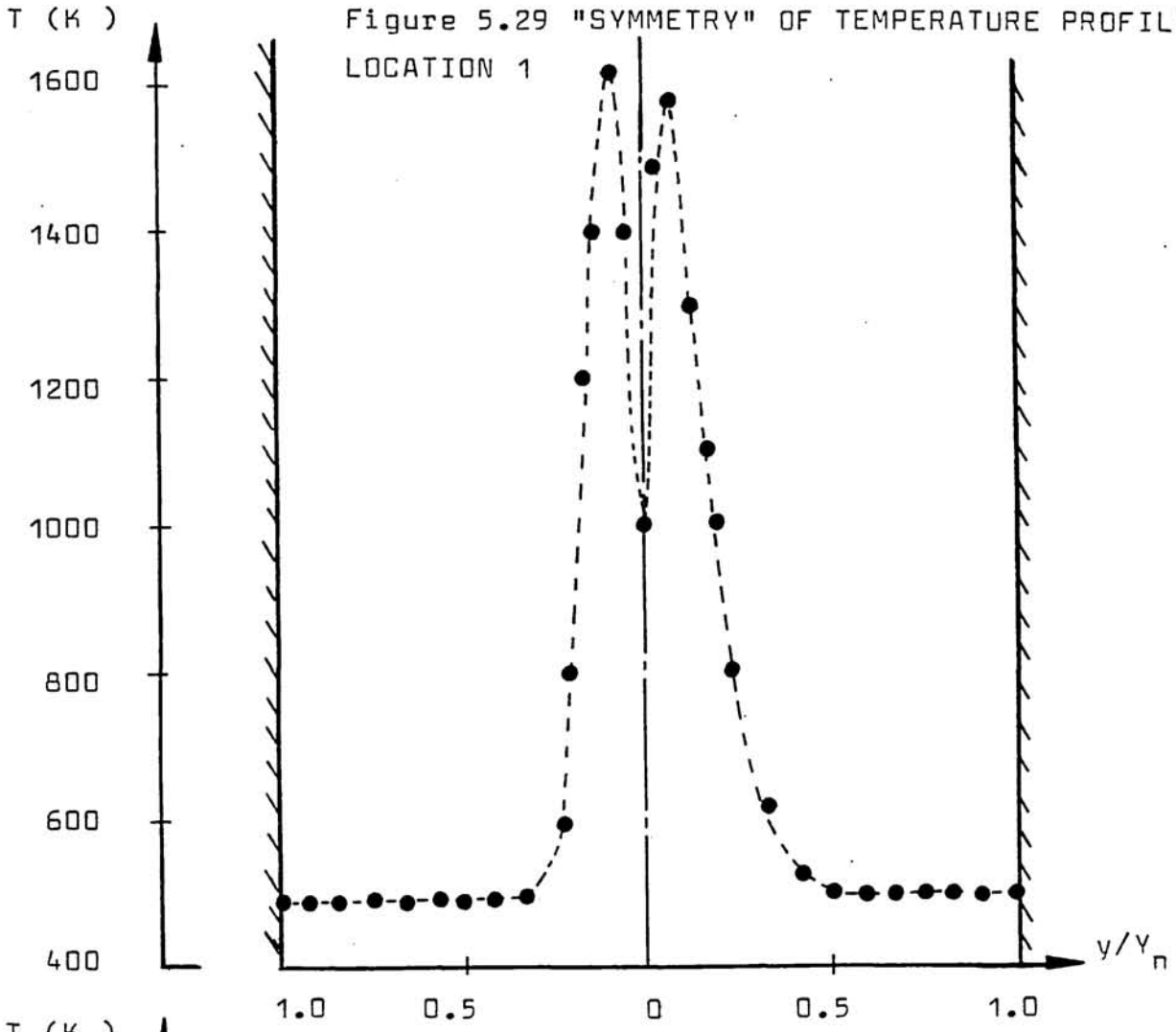

Figure 5.30 "SYMMETRY" OF TEMPERATURE PROFILE
LOCATION 2

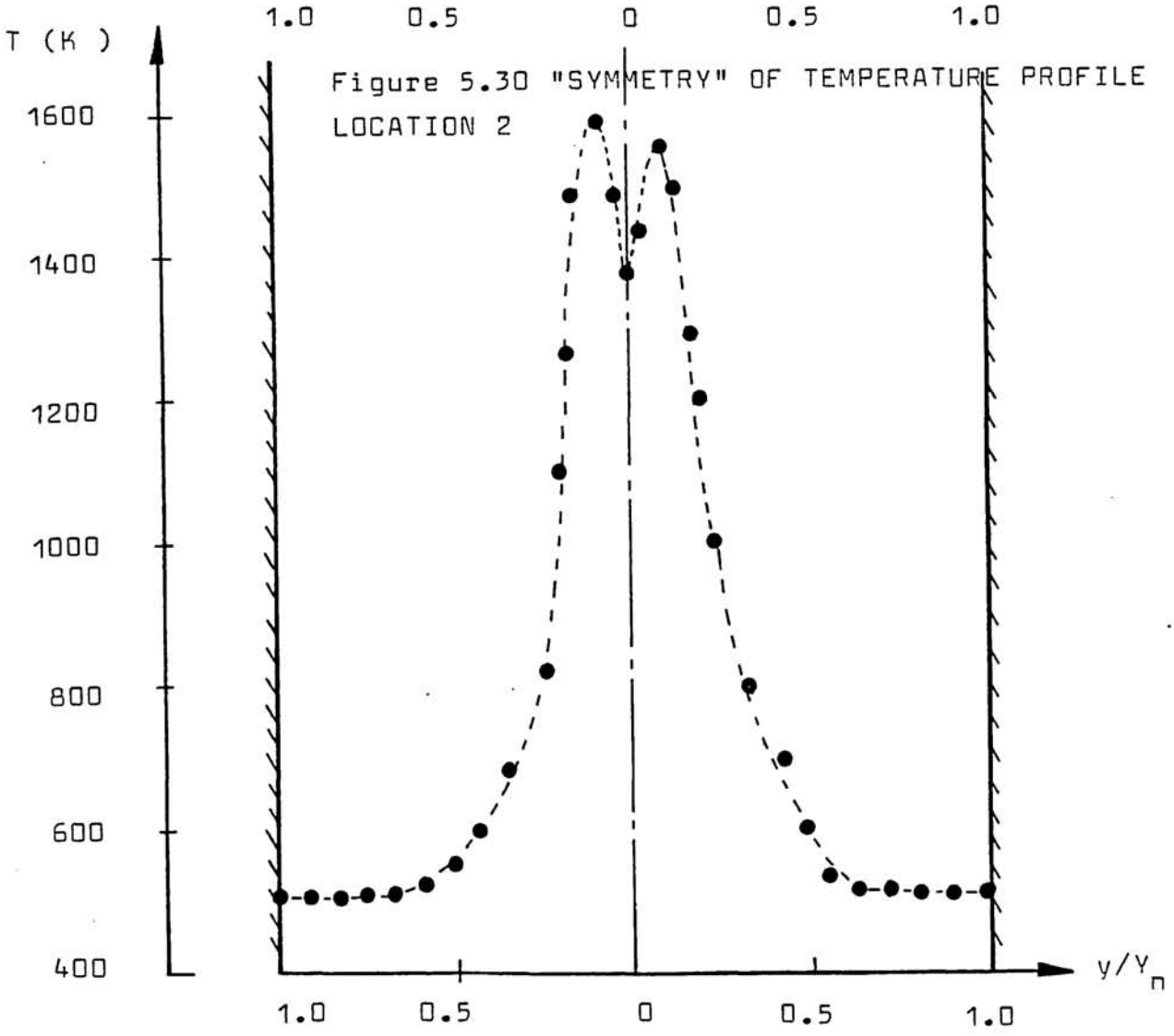

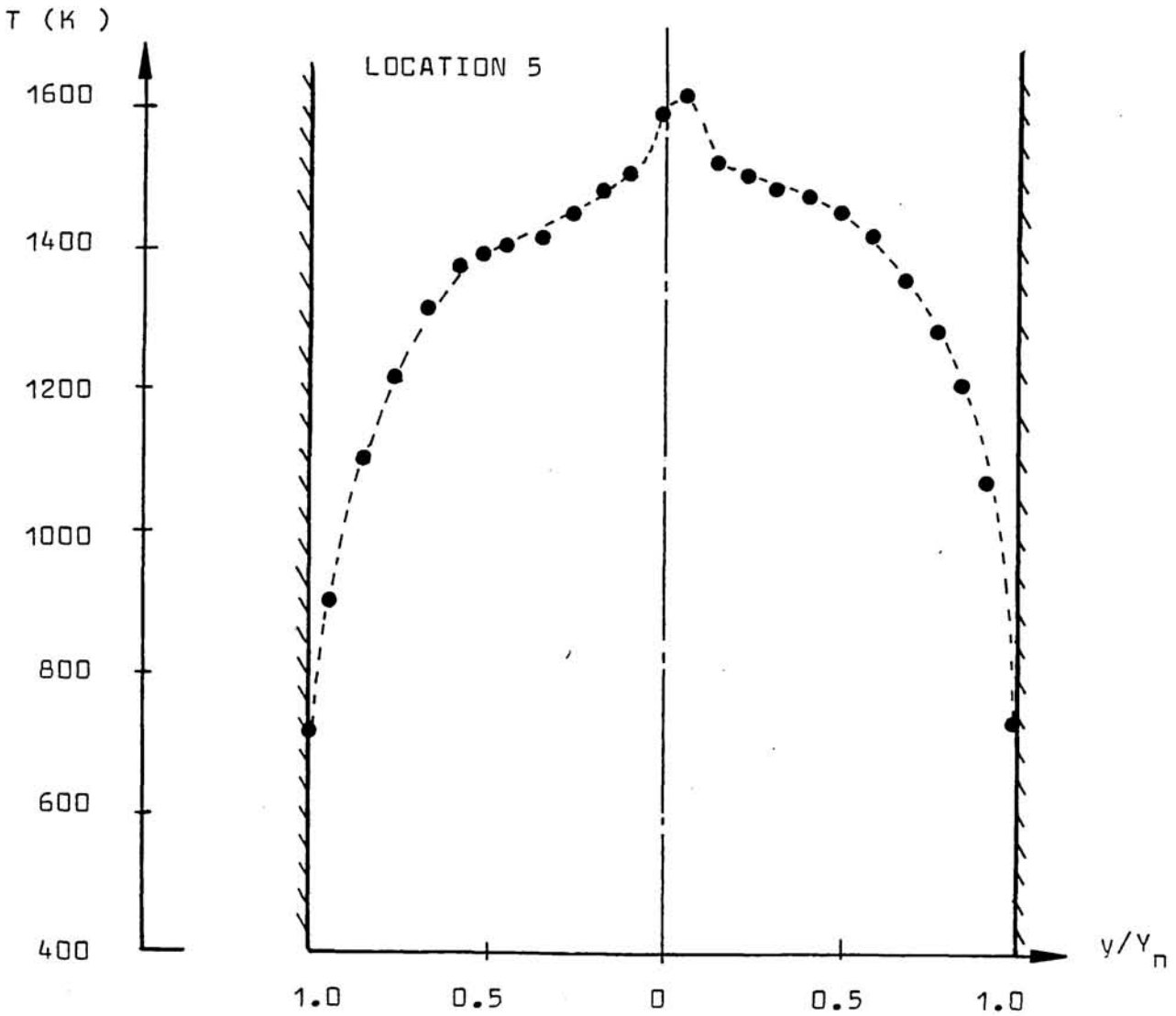

Figure 5.31 "SYMMETRY" OF TEMPERATURE PROFILE

Figure 5.32 DEGREE OF REPRODUCIBILITY

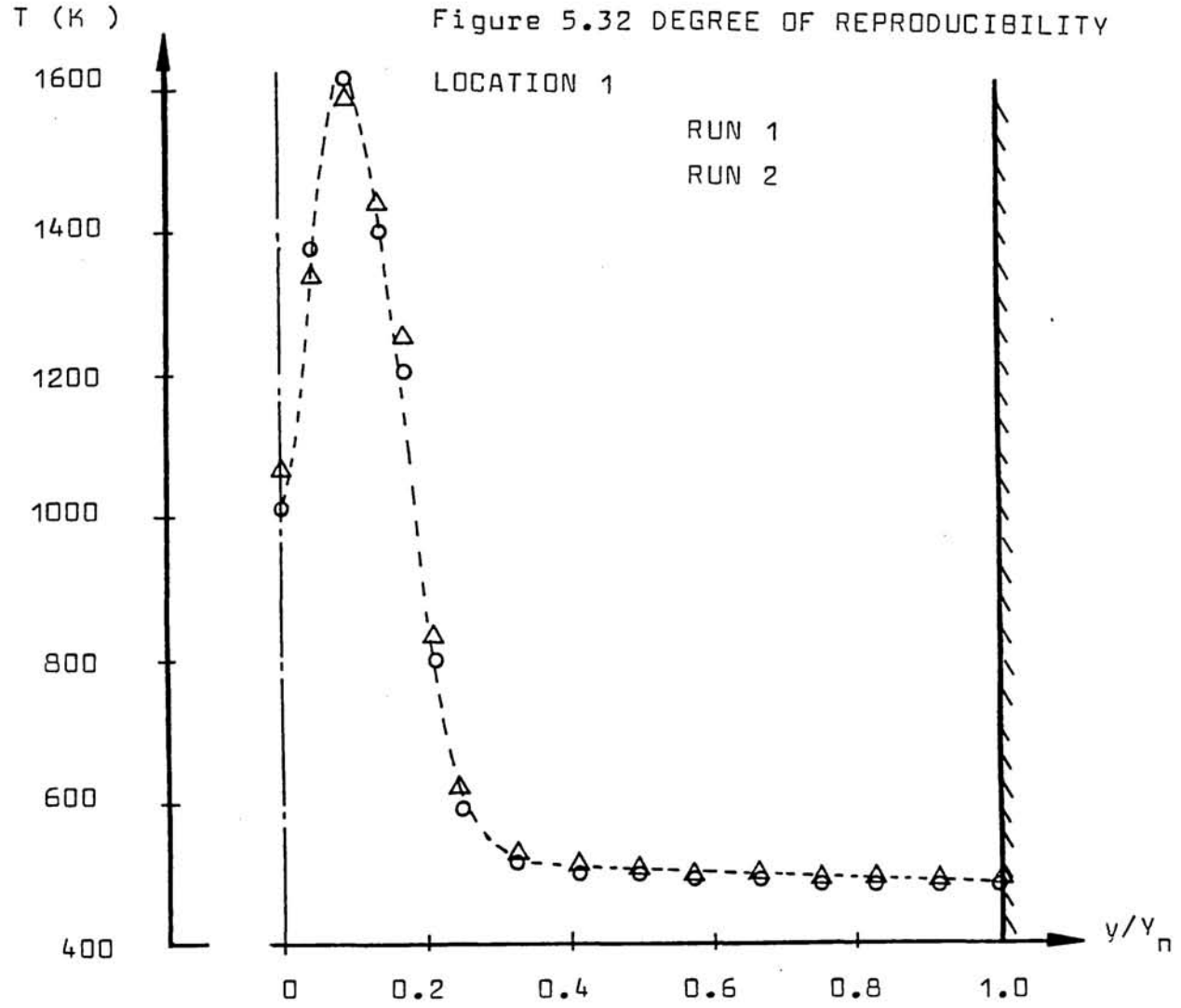

Figure 5.33 DEGREE OF REPRODUCIBILITY

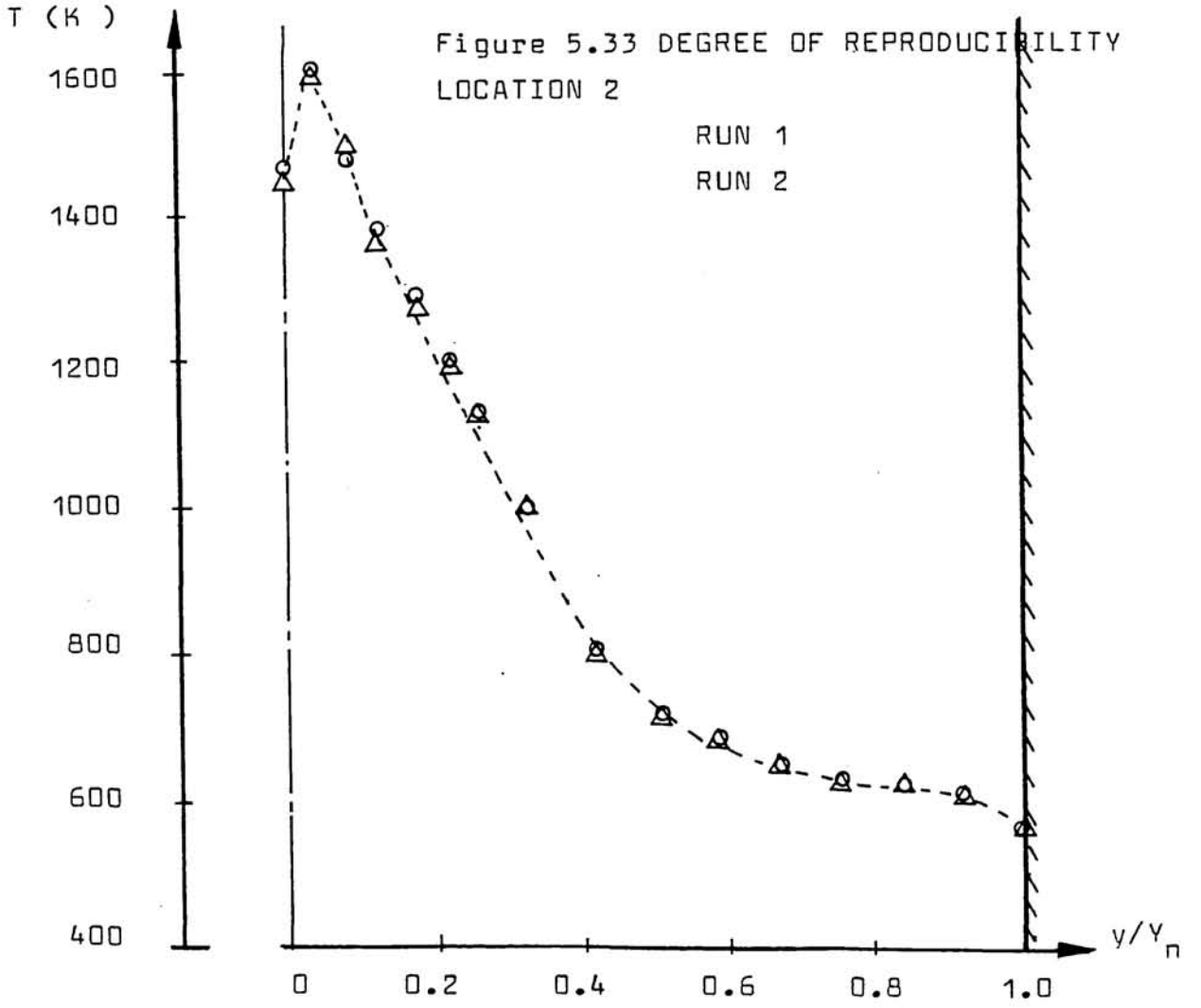

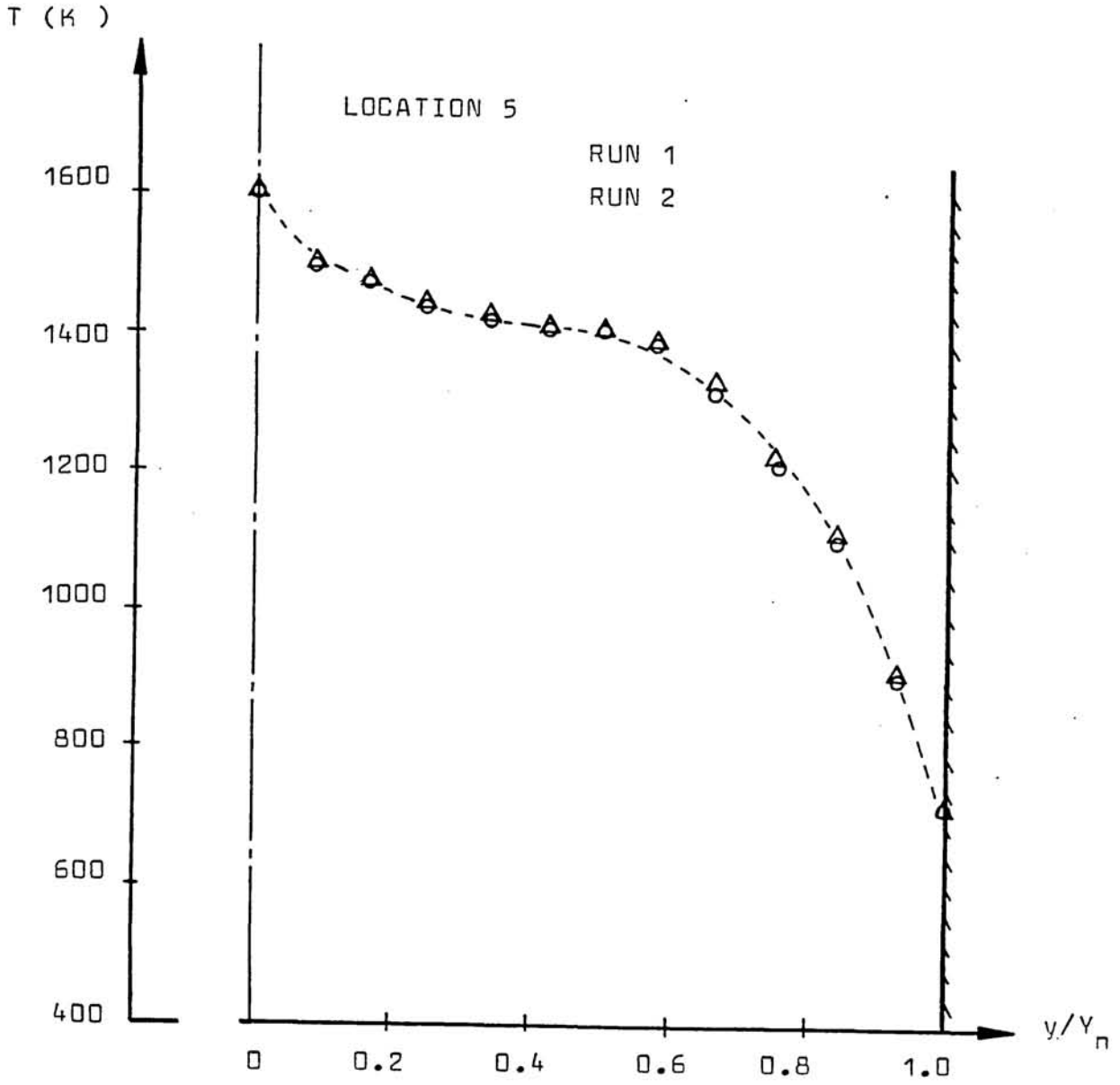

Figure 5.34 DEGREE OF REPRODUCIBILITY

experimental conditions of Flame A. The results for these repeated runs are displayed at three measuring sections only.

It is seen that the degree of reproducibility is generally good.

5.23 Concluding Remarks

Temperatures have been measured under combustion in the two-dimensional converging duct.

It is found that the buoyancy effect will increase the entrainment of air to the flame zone and reduce the flame length. Consequently, the stretching rate of the cross-stream folds has to increase. However, it should further be examined by the prediction procedure, as given in Chapter 6.

5.24 Closure

Two types of experiments have been performed, namely (a) a cold-flow experiment, in which distributions of concentrations of a tracer-gas across the stretched-folds have been measured; and (b) a combustion experiment, in which the temperature profiles across the laminar diffusion hydrogen-air stretched flame have been measured.

The objective of developing experimental methods for the verification of the fold biographic theory has been achieved.

CHAPTER 6 - COMPARISON OF PREDICTIONS WITH EXPERIMENTAL RESULTS

6.1 Introduction

The work described in this chapter comprises the author's experimental contribution to the study of fold biography presented in Chapter 5.

The main objective is to validate the "non-mixed" model of the fold biographic theory by comparing the predictions with the author's measurements. In addition, an extension of the fold biographic study is also presented.

6.2 Outline of the Chapter

(i) The cold flow predictions are presented in Section 6.3. These include:

- Description of the problem.
- Comparison of predictions with experimental results.

An extension of the fold biographic study:

- A theoretical treatment for the results of cold flow experiments (Lagrangian approach).
- Probability-density functions of stretched-folds in which combustion does not take place.

(ii) The hot flow predictions are presented in

Section 6.4 embracing:

- The problem considered.
- Numerical solution procedure in which buoyancy effect is taken into consideration in the confined flame.
- Comparison of predictions with experimental results.
- Probability-density functions of stretched-folds in which combustion occurs.

Finally, Section 6.5 contains the closing remarks on the work covered in this chapter.

6.3 The Cold-Flow Prediction

6.3.1 Description of the problem

As described in Chapter 5, five new folds are continuously and steadily formed from the six strips of the reactor. The configuration of the test section ensures that the folds become progressively thinner upwards. In this circumstance, the stretching rate of the folds is being controlled and the thickness of the folds across the test section is diminishing linearly with the longitudinal distance. Obviously, the fold stretching rate increases with the inclined

angle. It is therefore necessary to compute, for every location of the folds, (a) the relationship between the rate of stretching and the age path; and (b) the fold probability-density function, $\tilde{p}d\phi$. The latter represents the variation of $\tilde{p}$ with ϕ at different ages under the stretching effects, ϕ being the dimensionless concentration of helium.

This is most conveniently done with the aid of the Moving Observer. However, here, the coordinate system of the experimental apparatus is first stated, and then, the Lagrangian approach is described in detail (Section 6.3.9).

6.3.2 Experimental coordinate system

The processes which are considered in the cold-flow experiments are steady flows in which five new folds are continuously formed from the porous strips. The task here is to formulate (1) the thickness of the multiple-folds; and (2) the fold-average velocity. The results will be expressed as functions of the inclined angle, θ, and the longitudinal distance, z. Hence the effect of stretching is allowed for.

(1) The thickness of the multiple-folds

The geometry of the test section shows that the thickness

of cross-folds, Y_N, decreases as z increases in accordance with (Figure 6.1),

$$Y_N = Y_o - 2 \tan\theta \, z \ , \qquad (6.3\text{-}1)$$

where Y_o is initial thickness of cross-folds;

θ is the inclined angle;

and, z is the longitudinal distance.

The validity of the above equation is restricted by the dimensions of the test section. The maximum path of the folds, z_{max}, is:

$$z_{max} = \frac{Y_o}{2\tan\theta} \quad . \qquad (6.3\text{-}2)$$

With this limitation (equation 6.3-2), the cross-fold thickness approaches zero in the location (z_{max}). Finally, folds lose their identities by being removed from the system by outflow.

(2) <u>The fold-average velocity</u>

The fold-average velocity, $\tilde{u}$, at location z is given by:

$$\tilde{u} = \frac{\int_o^{Y_N} \rho u \, dy}{\int_o^{Y_N} \rho \, dy} \quad . \qquad (6.3\text{-}3)$$

Since the flow is isothermal and the density of the fluid medium is constant, the continuity equation gives:

$$\tilde{u}\, Y_N = u_o\, Y_o \quad , \qquad (6.3\text{-}4)$$

where u_o, Y_o are the initial velocity and the initial cross fold thickness, respectively.

Substitution of equation (6.3-1) into equation (6.3-4) yields:

$$\tilde{u} = \frac{u_o}{1 - \frac{2\tan\theta}{Y_o} z} \quad . \qquad (6.3\text{-}5)$$

The thickness of the multiple-folds and the fold-average velocity have been described. The remaining task is to verify the effect of the rate of stretching on the folds. First, the mathematical statement of the fold-flow prediction is given below. Then, comparisons of the predicted with measured quantities are made. Thereby, an extension of the fold biographic study can be presented.

6.3.3 Mathematical statement

The geometry and the flow conditions employed for the predictions are the same as those for the experimental study given in Chapter 5. The initial profile of the helium tracer and domain of the experiment are illustrated in Figure 6.1.

Assumptions

- The flow is two-dimensional, parabolic, plane, steady and laminar.
- The flow field is isothermal and uniform temperature ($293^{o}K$) prevails everywhere.
- The initial helium concentration is only 0.1% in air. Consequently, the concentration distribution of tracer gas has no bearing on the hydrodynamic field.
- The lip thickness between the strips is negligible.
- The walls are smooth and impervious.

Property data

- Air density : $1.19\ kg/m^3$.
- Air viscosity : 1.84×10^{-5} kg/msec.
- Prandtl number of helium : 0.22.

$$Y_n = Y_o - 2\tan\theta\, Z$$

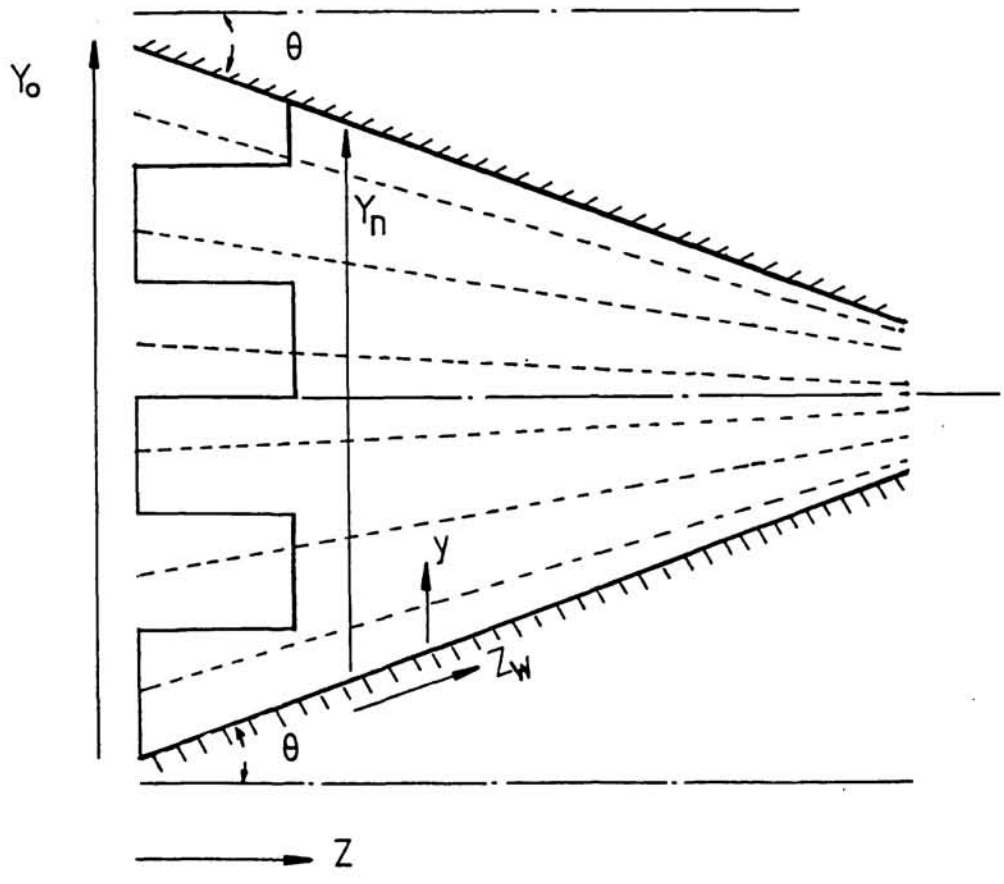

Figure 6.1 THE INITIAL HELIUM TRACER DISTRIBUTION

6.3.4 Governing differential equations

Equation of momentum

$$\frac{\partial u}{\partial z} = \frac{\partial}{\partial \xi} (\tau r) + \frac{1}{\rho u} (- \frac{\partial p}{\partial z}) \quad , \qquad (6.3\text{-}6)$$

where τ $\equiv$ is the shear stress;

ξ $\equiv$ the stream function, defined by:

$\xi \equiv \int_{o}^{y} \rho u \, dy$; and

$\frac{\partial p}{\partial z}$ is the longitudinal pressure gradient.

Equation of helium concentration

$$\frac{\partial \phi}{\partial z} = \frac{\partial}{\partial \xi} (\rho u \frac{\mu}{\sigma} \frac{\partial \phi}{\partial \xi}) \quad . \qquad (6.3\text{-}7)$$

Initial conditions

- Strip width : 0.0508m.
- Number of strips : 6.
- Velocity profile: u_o is uniform, and is given in Table 5.1.
- Helium concentration distribution: Battlement (see Figure 6.1).

Boundary conditions

- At the I, E boundaries, the inclined walls are

impervious, and the velocity is zero.

$$u_I = 0 \ ,$$

$$u_E = 0 \ .$$

- The flux of helium tracer at the wall is zero, $\frac{\partial \phi}{\partial y} = 0$, where y represents the direction normal to the wall.

6.3.5 Computational details

Details of the conditions have been tabulated in Table 5.1 (Chapter 5). Typical information for a particular computational run is given below:

Prediction of isothermal stretching for multiple-folds	Pertinent Data
Configuration	2D convergent channel
Number of cross-stream grid nodes	60
Number of forward steps	400
Computer time used on CDC 6400	13 secs

TABLE 5

6.3.6 Comparison of the predicted with measured quantities

Comparisons of the predictions with the experimental results for three different inclined angles are displayed

in Figures 6.2-13. The results are presented in the form of dimensionless concentration $\frac{C-C_{min}}{C_{max}-C_{min}}$ versus dimensionless distance Y/Y_N at different cross-stream sections.

6.3.7 Results

The 0° inclined angle

In this case, the rate of stretching is zero. Only the mixing and diffusion processes in the folds can be observed. Two different injected air flow rates have been investigated. The corresponding results are shown in Figures 6.2-3 and Figures 6.4-5.

The following remarks are made:

- In the upstream region, the mixing for the experimental results is somewhat faster than the predicted one.
- It is observed that discrepancy between the measurement and prediction exists near the wall regions.
- Further downstream of the test section, the agreement between the prediction and the measurement is generally satisfactory.

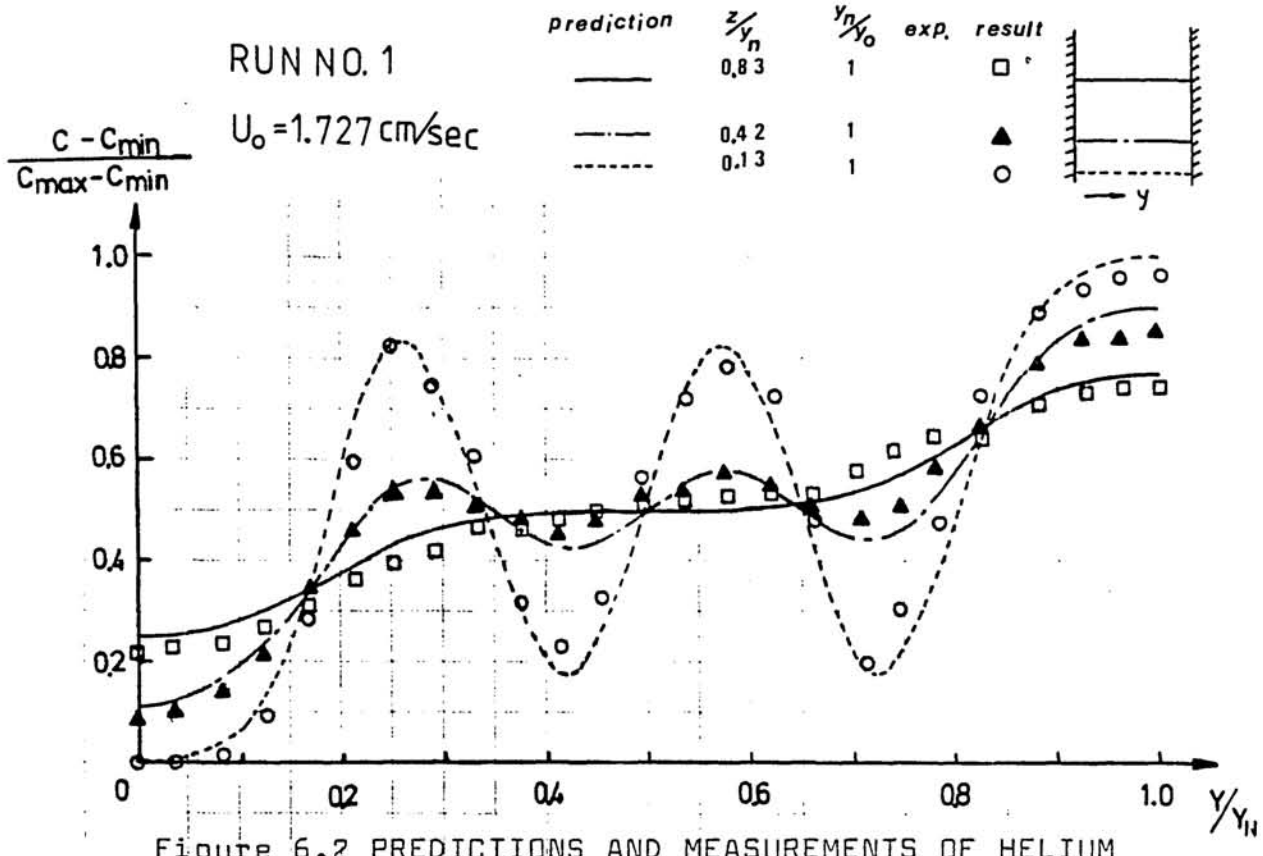

Figure 6.2 PREDICTIONS AND MEASUREMENTS OF HELIUM CONCENTRATION IN A CONVERGENT CHANNEL WITH 0° INCLINED ANGLE.

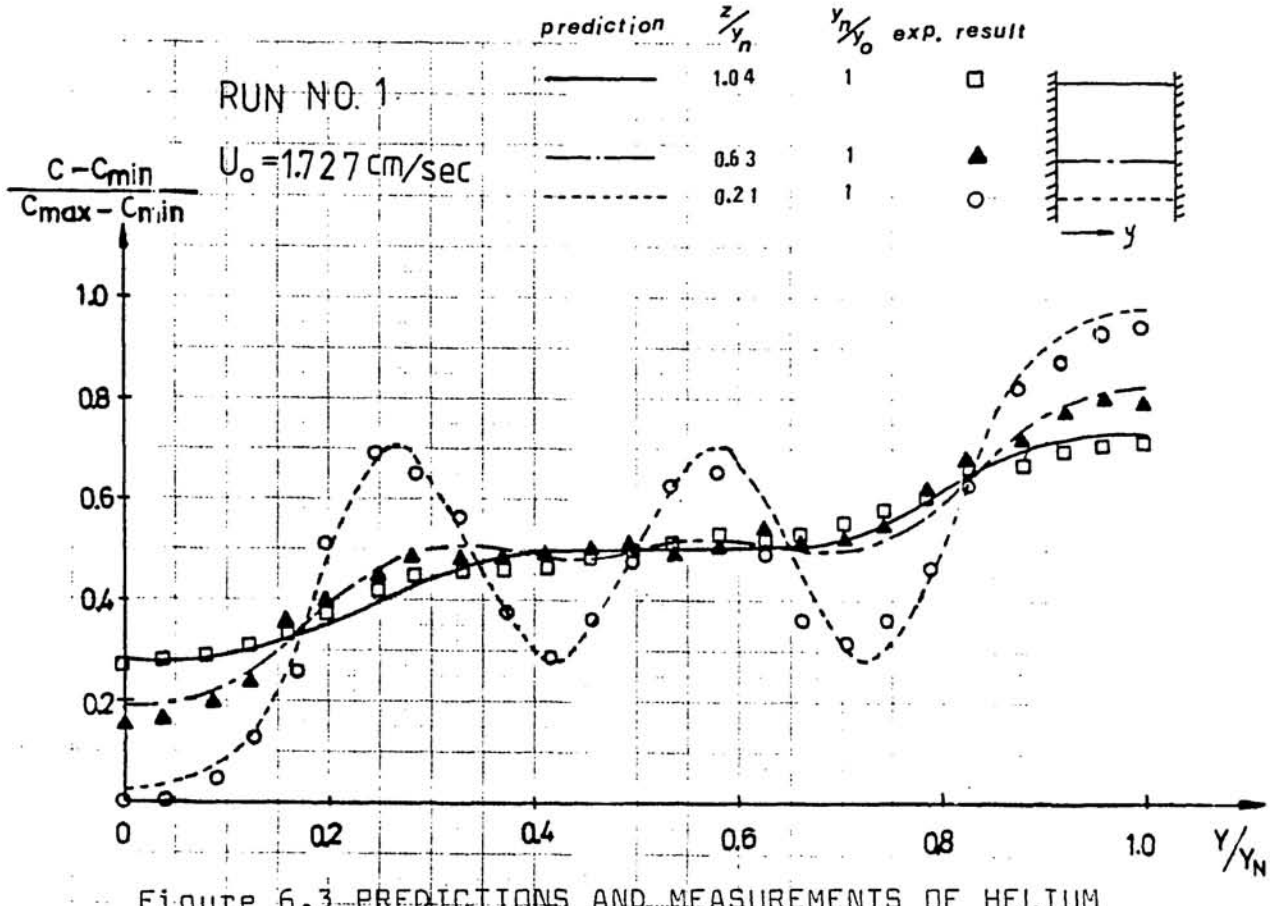

Figure 6.3 PREDICTIONS AND MEASUREMENTS OF HELIUM CONCENTRATION IN A CONVERGENT CHANNEL WITH 0° INCLINED ANGLE.

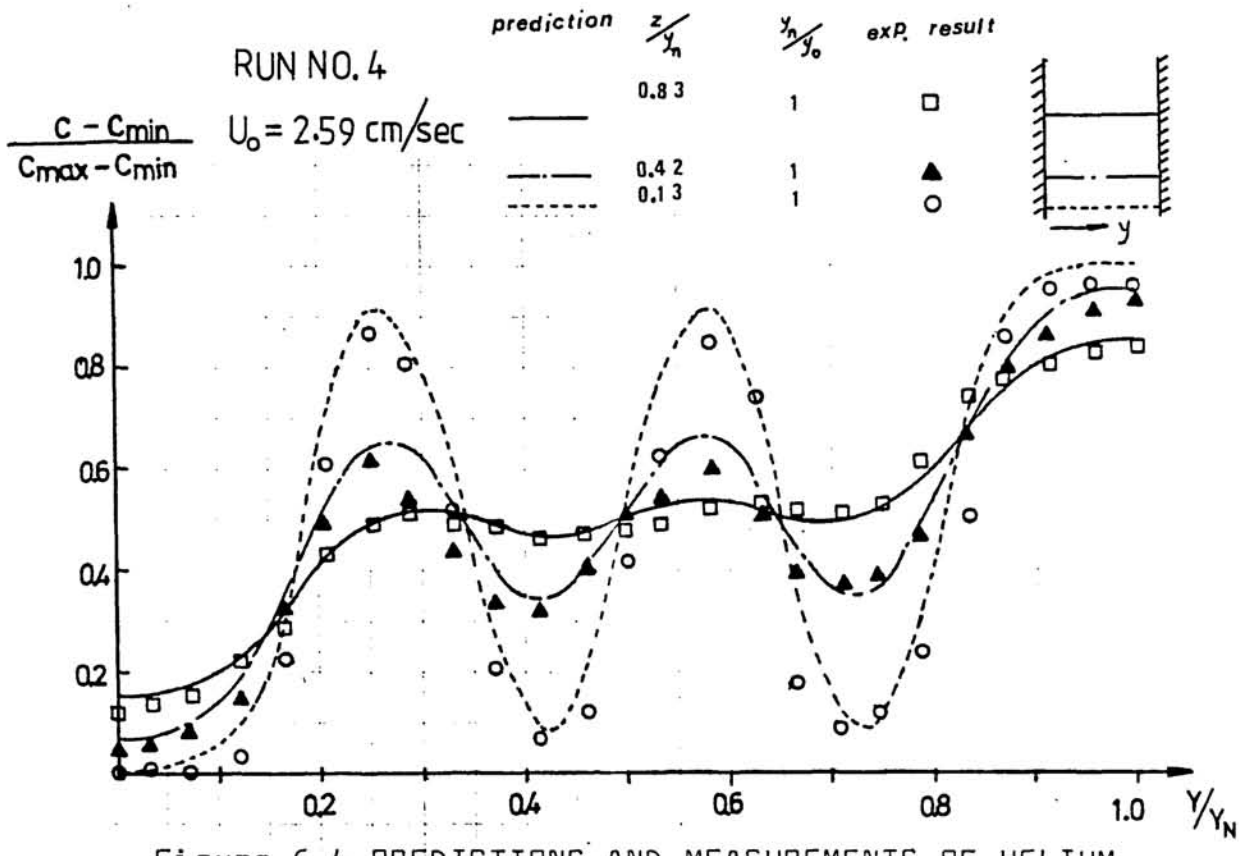

Figure 6.4 PREDICTIONS AND MEASUREMENTS OF HELIUM CONCENTRATION IN A CONVERGENT CHANNEL WITH 0° INCLINED ANGLE.

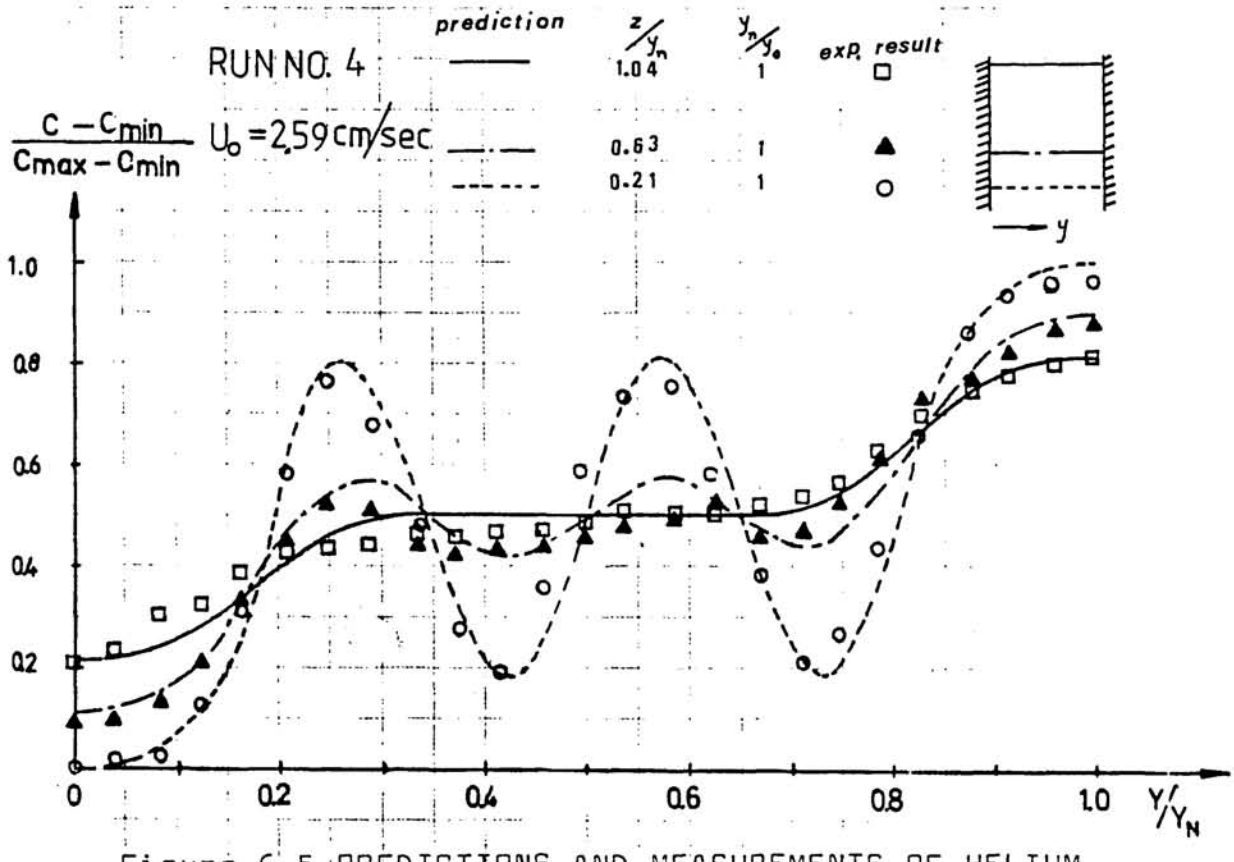

Figure 6.5 PREDICTIONS AND MEASUREMENTS OF HELIUM CONCENTRATION IN A CONVERGENT CHANNEL WITH 0° INCLINED ANGLE.

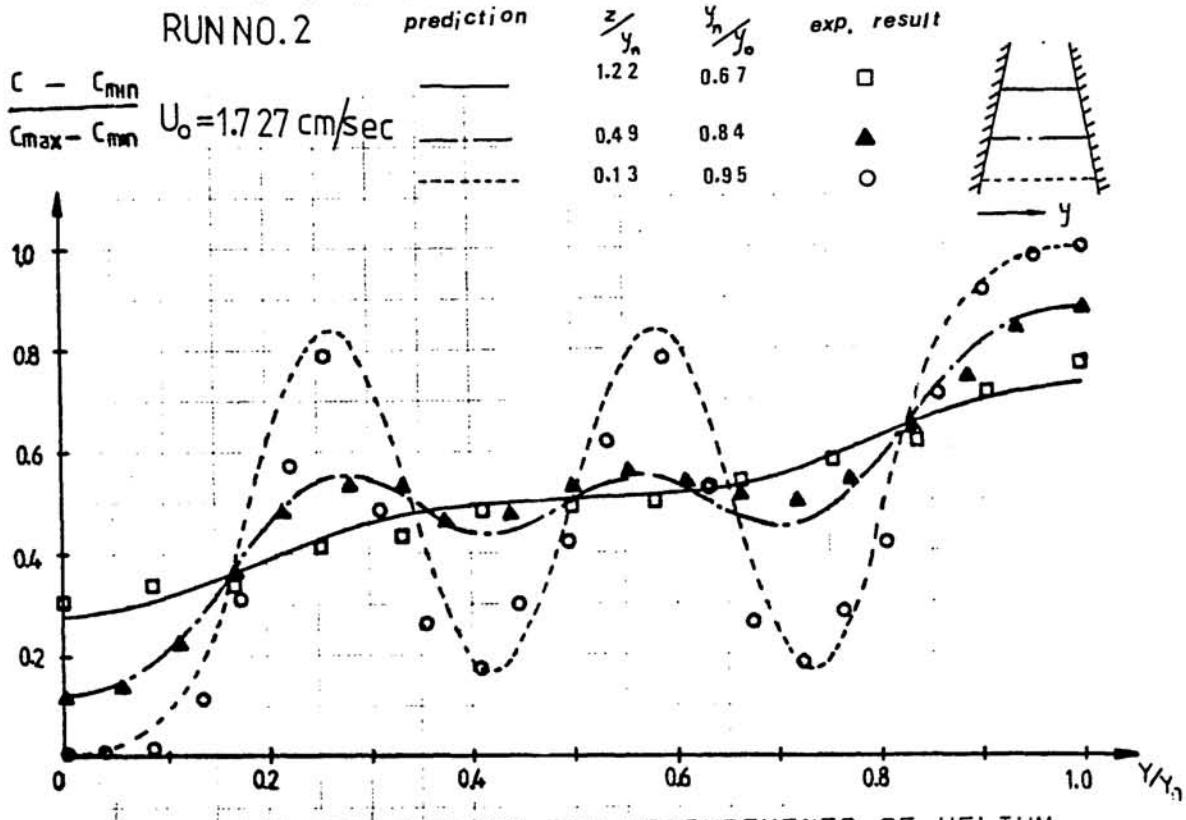

Figure 6.6 PREDICTIONS AND MEASUREMENTS OF HELIUM CONCENTRATION IN A CONVERGENT CHANNEL WITH 11.623° INCLINED ANGLE.

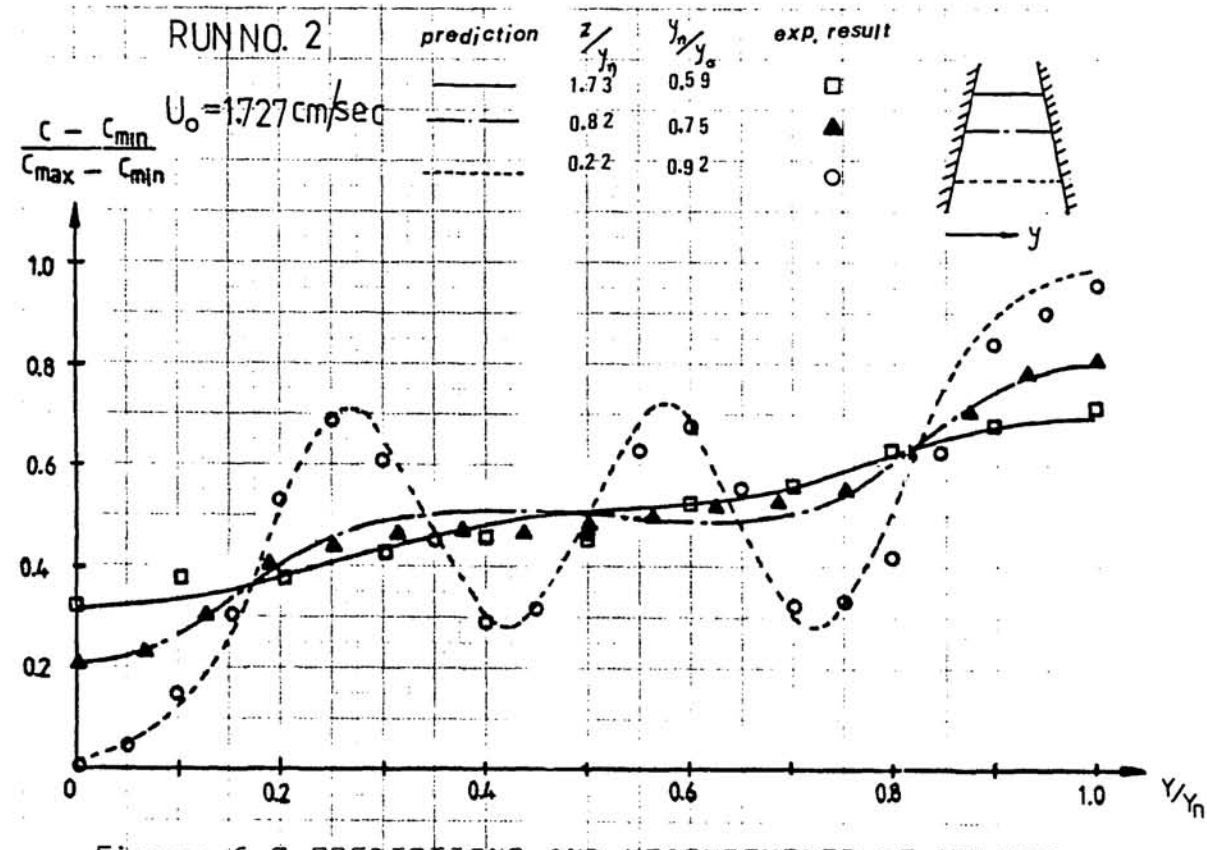

Figure 6.7 PREDICTIONS AND MEASUREMENTS OF HELIUM CONCENTRATION IN A CONVERGENT CHANNEL WITH 11.623° INCLINED ANGLE.

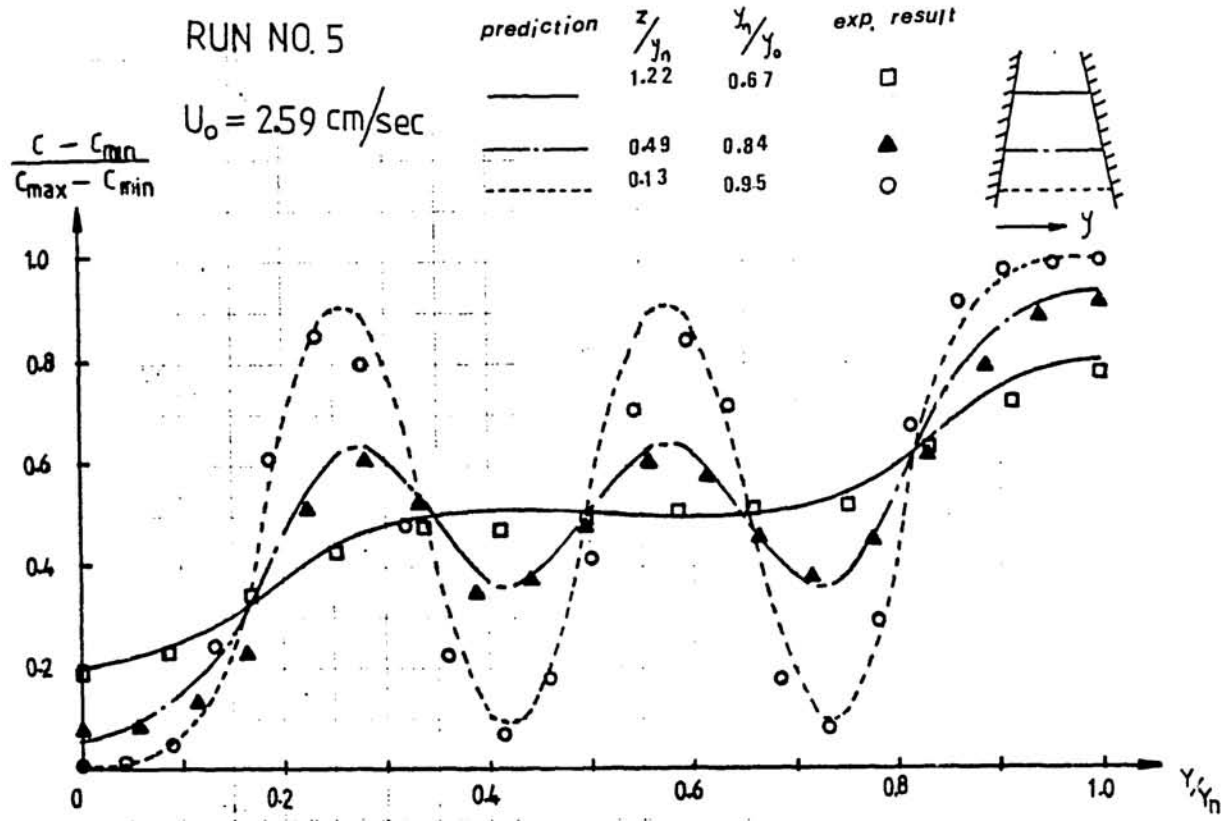

Figure 6.8 PREDICTIONS AND MEASUREMENTS OF HELIUM CONCENTRATION IN A CONVERGENT CHANNEL WITH 11.623° INCLINED ANGLE.

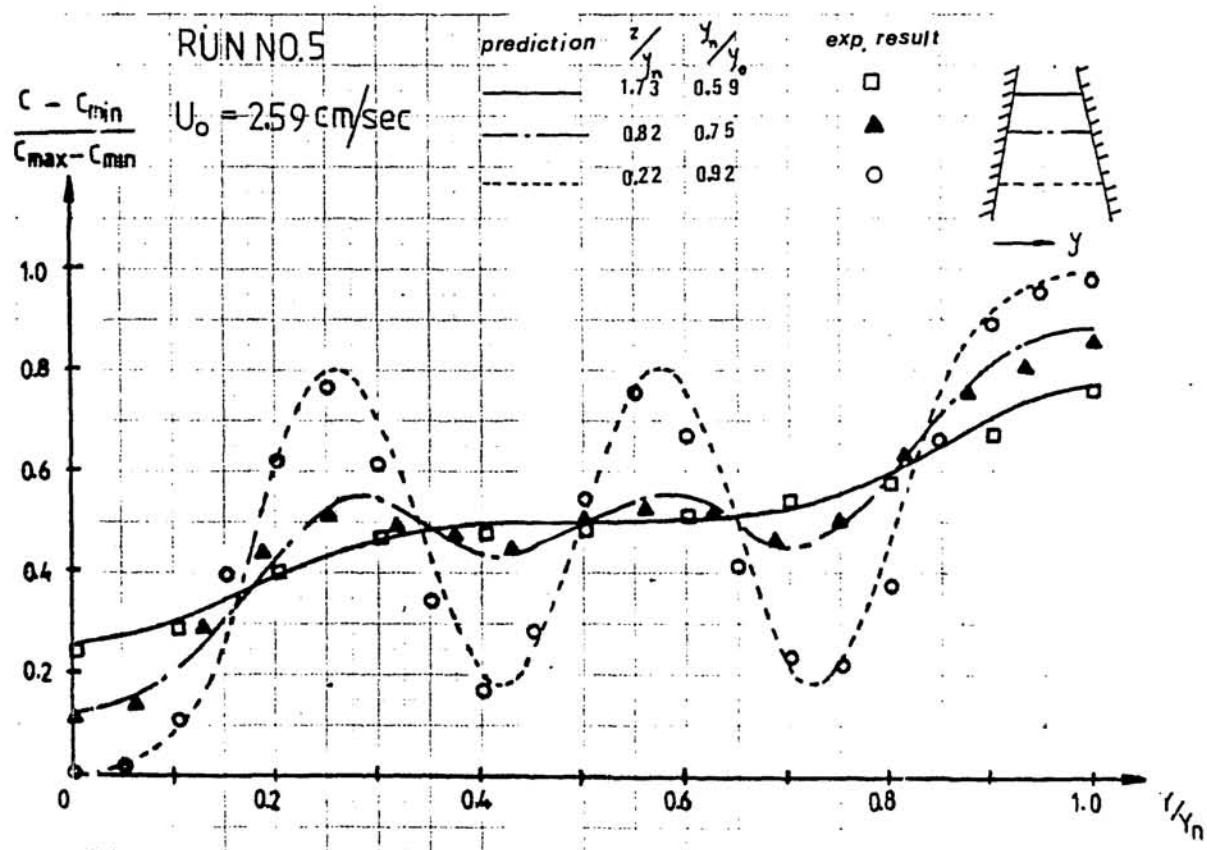

Figure.6.9 PREDICTIONS AND MEASUREMENTS OF HELIUM CONCENTRATION IN A CONVERGENT CHANNEL WITH 11.623° INCLINED ANGLE.

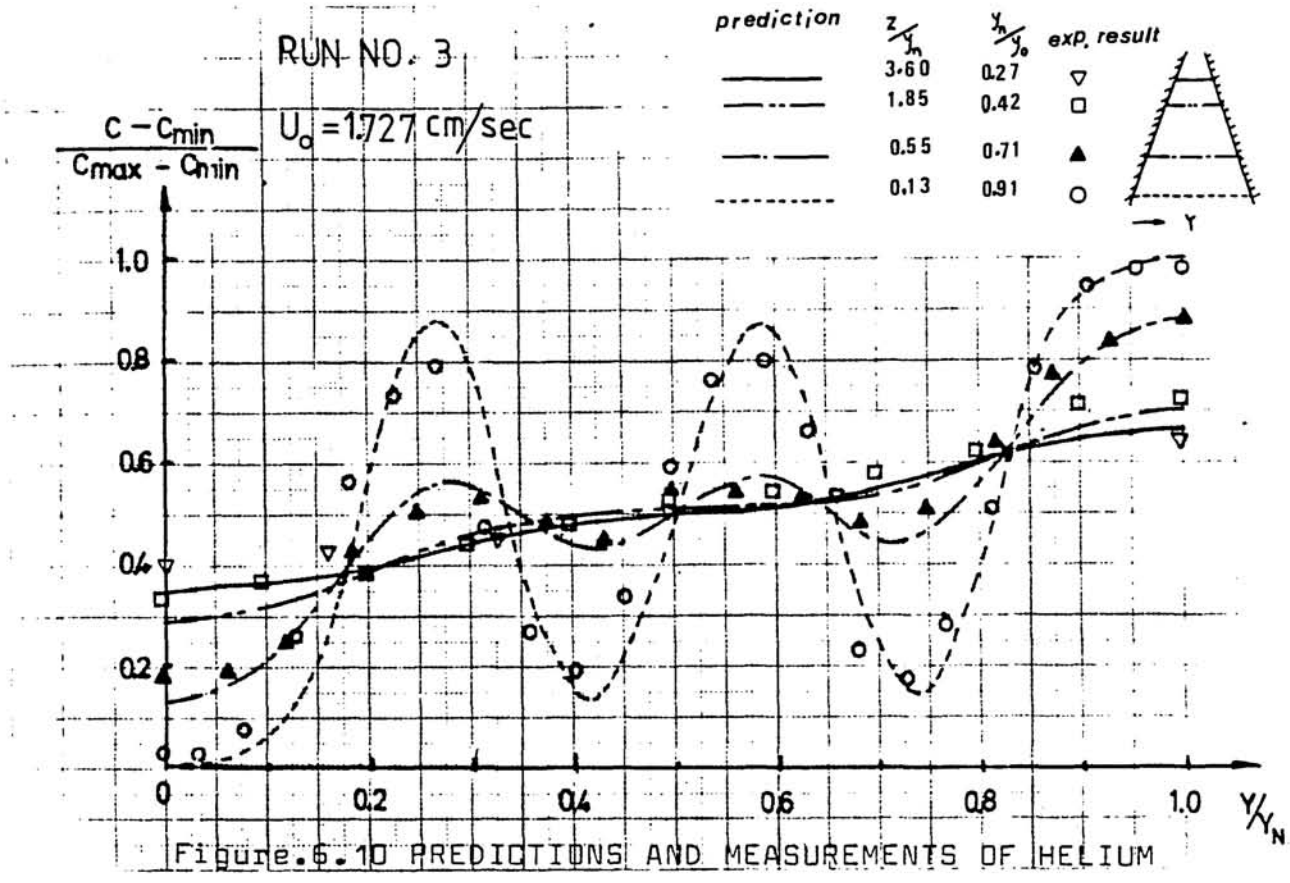

Figure.6.10 PREDICTIONS AND MEASUREMENTS OF HELIUM CONCENTRATION IN A CONVERGENT CHANNEL WITH 20.96° INCLINED ANGLE.

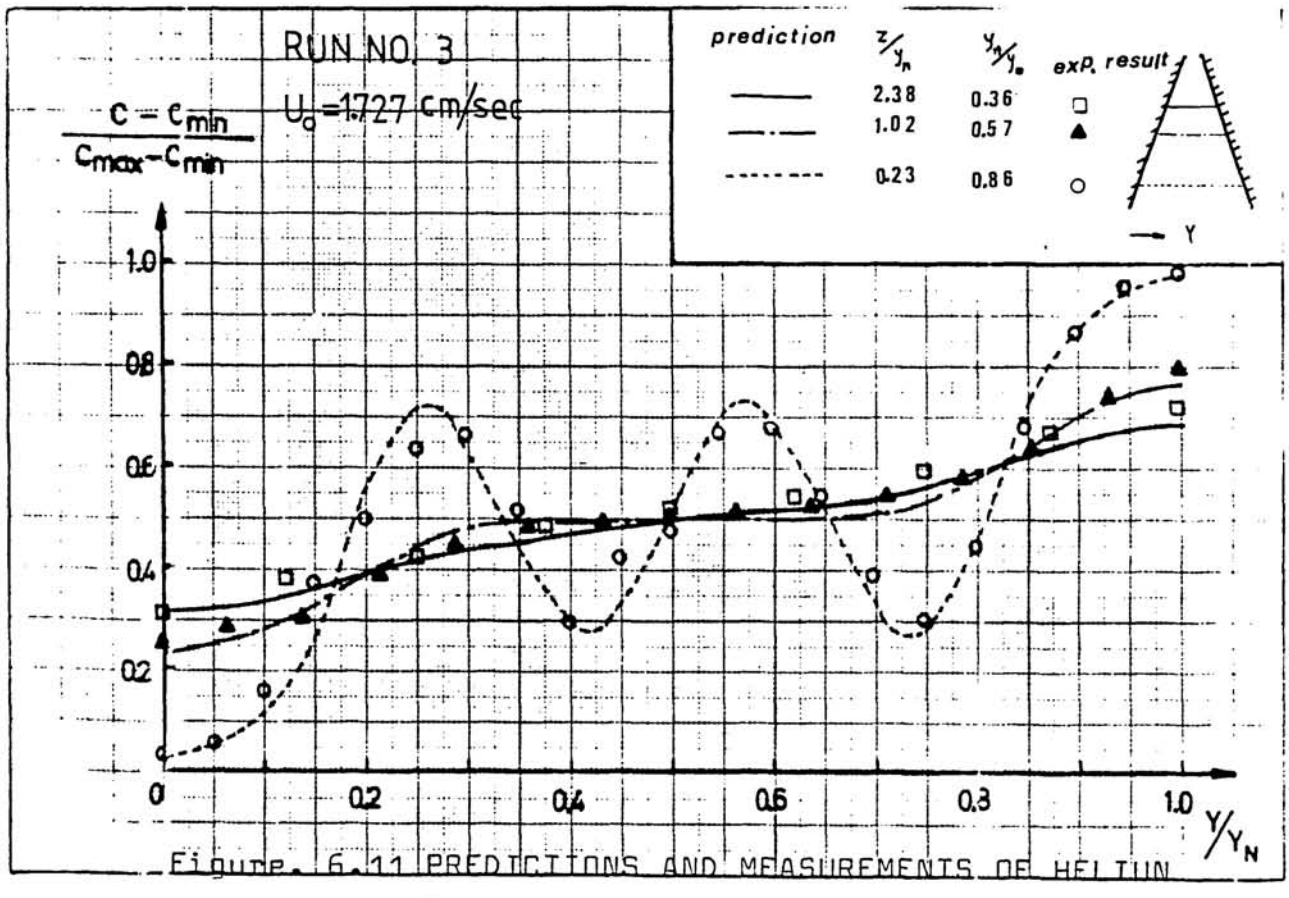

Figure. 6.11 PREDICTIONS AND MEASUREMENTS OF HELIUM CONCENTRATION IN A CONVERGENT CHANNEL WITH 20.96° INCLINED ANGLE.

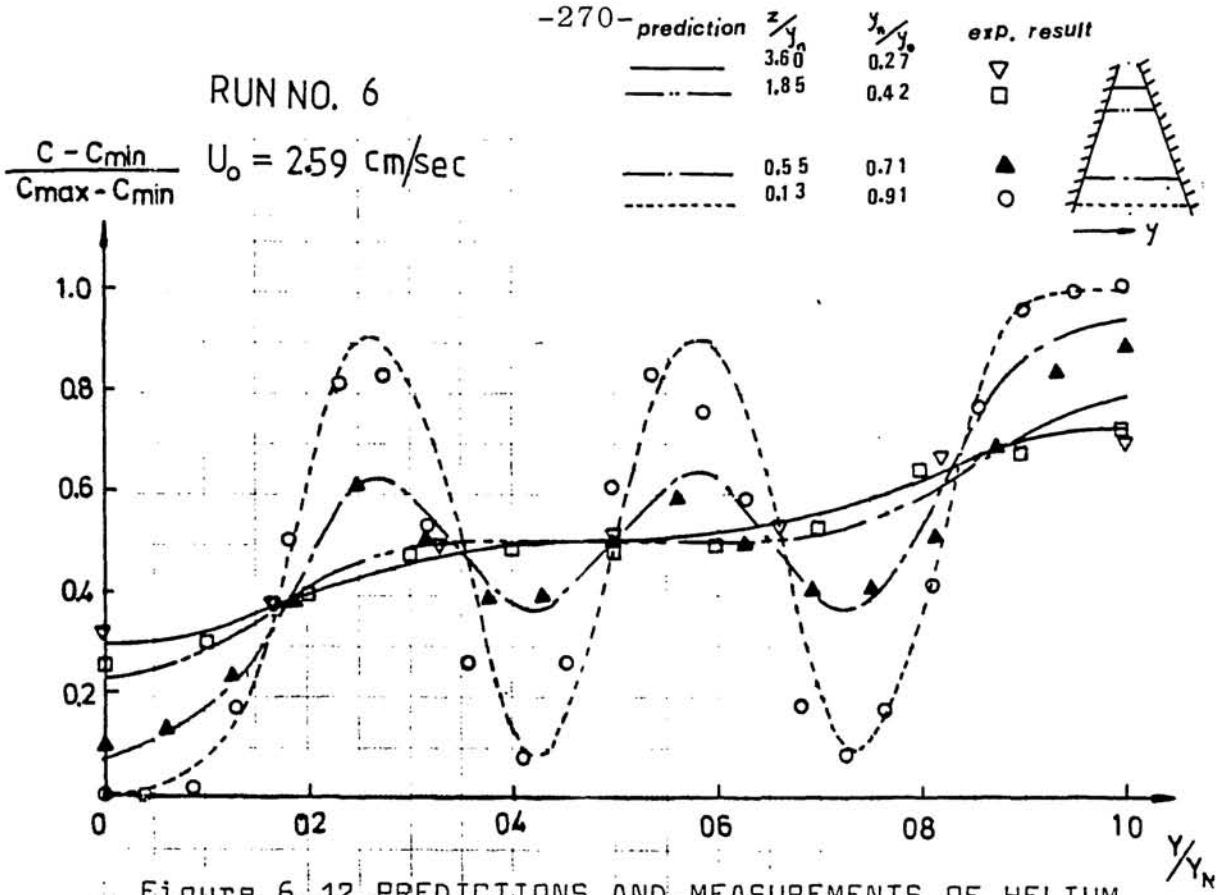

Figure 6.12 PREDICTIONS AND MEASUREMENTS OF HELIUM CONCENTRATION IN A CONVERGENT CHANNEL WITH 20.96° INCLINED ANGLE.

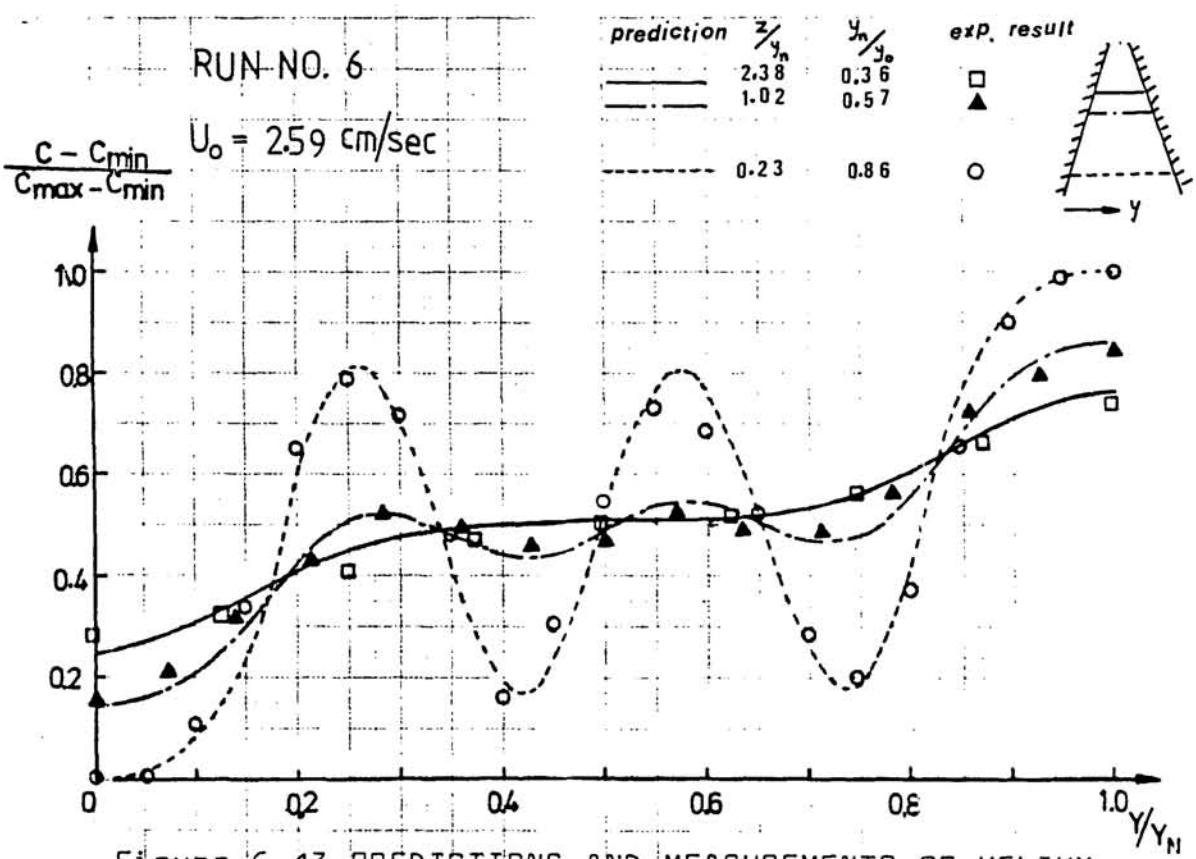

Figure 6.13 PREDICTIONS AND MEASUREMENTS OF HELIUM CONCENTRATION IN A CONVERGENT CHANNEL WITH 20.96° INCLINED ANGLE.

The 11.623^{o} inclined angle

In this case, the influence of stretching on the folds is moderate. The results of the comparisons made are shown in Figures 6.6-7 and Figures 6.8-9.

The following remarks can be made:

- It is observed that discrepancy between the measurement and the prediction also exists near the wall regions.
- The results (prediction and experiment) show that the concentration distribution is steeper than the 0° case in upstream regions.
- Since the folds are diminished continuously, the concentration distribution profiles becomes less steep than the 0° case downstream.

The 20.96^{o} inclined angle

In this case, the effect of the stretching rate is more profound. The corresponding results are shown in Figures 6.10-11 and Figures 6.12-13 respectively.

The following phenomena are observed:

- In the upstream region, the mixing for the experiment is faster than the prediction and the

concentration distribution profiles is steep.

- In the downstream region, the high stretching rate forces the concentration across the multiple-folds to become uniform.

The velocity distribution

For a typical prediction (θ=20.96^{o}), the velocity profiles at different longitudinal locations of the convergent channel are shown in Figure 6.14. Since the fluid flow is still in the developing region, the variation of velocity across the folds is only affected by the viscous action near the inclined walls. It can be seen that the velocity distribution across the folds is quite uniform.

6.3.8 Discussion

Inspection of the above results (Figures 6.2-13) reveals that the predictions obtained from different cases are generally in good agreement with the measurements. In order to make use of the Lagrangian approach for the verification of the experimental results (the influence of the stretching rate on the stretched-folds), it is necessary to perform some coordinate transformations. This will provide the useful information for refining the fold biographic theory (see Sections 6.3.9-13).

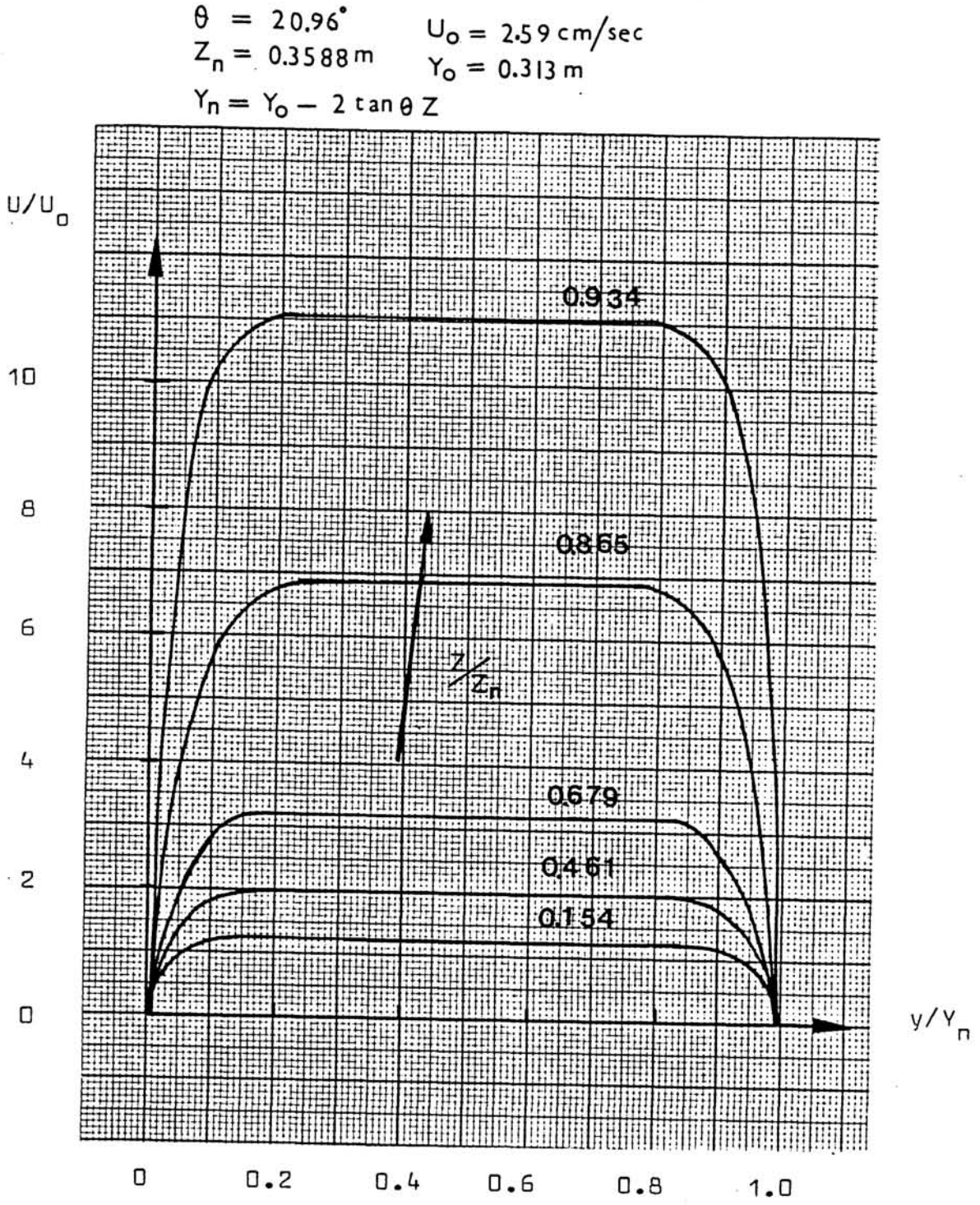

FIGURE 6.14 PREDICTIONS OF VELOCITY DISTRIBUTION IN A CONVERGENT CHANNEL WITH 20.96° INCLINED ANGLE.

6.3.9 Lagrangian approach

Consider any successive multiple-fold which has already been formed from the reactor strips with the initial thickness Y_o. Suppose an observer moves with the mean path of the folds (the age path). The history of the folds is as a one-dimensional transient problem. The results can therefore be expressed as functions of age. The concentration distribution of helium across the folds at age 'a' is thus given by $\phi\{a,y\}$, where y is the cross-fold distance.

The age

The relations between the age and the longitudinal distance is linked with the fold-average velocity, i.e.

$$\frac{dz}{da} = \tilde{u} \quad . \qquad (6.3\text{-}8)$$

Substitution of equation (6.3-5) into equation (6.3-8) and integrating the resulting equation yields:

$$a = \frac{z}{2}\left(\frac{1}{u_o} + \frac{1}{\tilde{u}}\right) \quad . \qquad (6.3\text{-}9)$$

The $\tilde{u}$~a relations

Eliminating z between equations (6.3-5) and (6.3-9) gives:

$$a = \frac{\left(1 - \frac{u_o}{\tilde{u}}\right)\left(1 + \frac{u_o}{\tilde{u}}\right)}{4 \frac{\tan\theta}{Y_o} u_o} \quad . \qquad (6.3\text{-}10)$$

Hence,

$$\tilde{u} = \frac{u_o}{\sqrt{1 - \frac{4 \tan\theta \, u_o}{Y_o} a}} \quad . \qquad (6.3\text{-}11)$$

The above equation shows that the fold-average velocity, $\tilde{u}$, is a function of age only.

6.3.10 The extension of fold biographic study

It is of interest to perform numerical calculations of the isothermal stretched-folds under the experimental conditions given above. First, the characteristic times are specified, then, results of the numerical calculations are presented.

The stretching time

In the Lagrangian approach, the stretching time of the folds, t_{str}, is described as a function of age, as:

$$\frac{da}{t_{str}} = - \frac{d\,Y_N}{Y_N} \quad ; \qquad (6.3\text{-}12)$$

where Y_N is the cross-fold thickness.

Substitution of the continuity equation into equation (6.3-12) gives:

$$1/t_{str} = \frac{d\,\ell n\,\tilde{u}}{da} \quad . \qquad (6.3\text{-}13)$$

Hence,

$$t_{str} = \frac{Y_o}{2\,\tan\theta\,u_o} - 2a \quad . \qquad (6.3\text{-}14)$$

The result is that the stretching time decreases linearly with age. This implies that the rate of stretching is no longer constant but increases linearly with age.

The diffusion time

The diffusion time of the folds is defined as:

$$t_{diff} = \frac{\rho_{air} Y_o^2}{\Gamma_{H_e}} \quad , \qquad (6.3\text{-}15)$$

where ρ_{air} is the density of air;

Γ_{H_e} is the exchange coefficient of helium;

and Y_o is the initial thickness of the folds.

The thickness of folds

The thickness of the folds at age, 'a' is given by:

$$Y_N = Y_o \, \mathrm{Exp} \left(- \int_o^a \frac{dt}{t_{str}}\right) \quad . \qquad (6.3\text{-}16)$$

6.3.11 Presentation of results

The above theoretical approach provides extensive information on stretching effects on the cold-flow experiments.

The effects of stretching, mixing and diffusion on the multiple-fold under different stretching conditions are tabulated in Tables 6.1-3. They contain results from the cold-flow experiments. The results are expressed in terms of dimensionless ratios:

$$\frac{\tilde{u}}{u_o}, \frac{Y_N}{Y_o}, t_{diff}/t_{str} \text{ and } a/t_{diff}.$$

Dimensionless longitudinal location	z/z_{max}	0	0.103	0.345	0.69	1.0
Dimensionless cross-fold distance	$\frac{Y_N}{Y_o}$	1	1	1	1	1
Dimensionless velocity	$\frac{\tilde{u}}{u_o}$	1	1	1	1	1
Stretching parameter	$\frac{t_{diff}}{t_{str}}$	0	0	0	0	0
Dimensionless age	$a/t_{diff} x10^3$	0	1.05	3.52	7.03	10.2

$\theta=0^o$, u_o=2.59cm/sec, z_{max}=0.368m.

TABLE 6.1: INFLUENCES OF DIFFUSION AND MIXING ON THE MULTIPLE-FOLDS (CASE 1) - NON-STRETCHING

Dimensionless longitudinal location	z/z_{max}	0	0.103	0.344	0.689	1.0
Dimensionless cross-fold distance	$\frac{Y_N}{Y_o}$	1	0.95	0.84	0.67	0.527
Dimensionless velocity	$\frac{\tilde{u}}{u_o}$	1	1.05	1.19	1.49	1.89
Stretching parameter	$\frac{t_{diff}}{t_{str}}$	47.3	52.27	67.18	103.5	168.6
Dimensionless age	$a/t_{diff} x10^3$	0	1	3.13	5.74	7.6

$\theta=11.623^o$, $u_o=2.59$cm/sec, $z_{max}=0.36$m.

TABLE 6.2: INFLUENCES OF DIFFUSION AND MIXING ON THE MULTIPLE-FOLDS (CASE 2) - MODERATE STRETCHING

Dimensionless longitudinal location	z/z_{max}	0	0.118	0.20	0.40	0.60	0.80	0.882	1.0
Dimensionless cross-fold distance	$\frac{Y_N}{Y_o}$	1	0.91	0.86	0.71	0.57	0.42	0.361	0.27
Dimensionless velocity	$\frac{\tilde{u}}{u_o}$	1	1.1	1.16	1.41	1.75	2.38	2.77	3.7
Stretching parameter	$\frac{t_{diff}}{t_{str}}$	88.45	105.44	121.44	173.4	277.7	497.8	682.3	1124.2
Dimensionless age	$a/t_{diff} x10^3$	0	0.911	1.54	2.77	3.85	4.65	4.92	5.2

$\theta=20.96^o$, $u_o=2.59$cm/sec, $z_{max}=0.296$m.

TABLE 6.3: INFLUENCES OF DIFFUSION AND MIXING ON THE MULTIPLE-FOLDS (CASE 3) - HIGH STRETCHING

6.3.12 Discussion

For the zero inclined angle case (Table 6.1), the time required for the concentration profile to become fully uniform across the multiple folds is longer than that of the large inclined angle (Table 6.3), as shown in Tables 6.1 and 6.3.

Inspection of Table 6.3 shows that the stretching parameter, $\frac{t_{diff}}{t_{str}}$, rapidly increases with age. It is evident that the helium concentration is evened out by the high stretching rate.

6.3.13 Probability-density function

In order to show the influence of stretching on the multiple-folds, the results of Table 6.3 are illustrated by the $\tilde{p}d\phi$ diagram shown in Figure 6.15. The results are presented in form of the fold probability-density findings of the helium concentration, $\tilde{p}$, versus the non-dimensional helium concentration, ϕ, at various ages.

It is observed that $\tilde{p}$ is symmetric about (ϕ=0.5). During the stretching and mixing processes, the $\tilde{p}$ distribution shifts nearer the symmetry axis.

The shape of $\tilde{p}$ then becomes very steep. It subsequently exhibits a spike at which the helium concentration is equal to half (0.5).

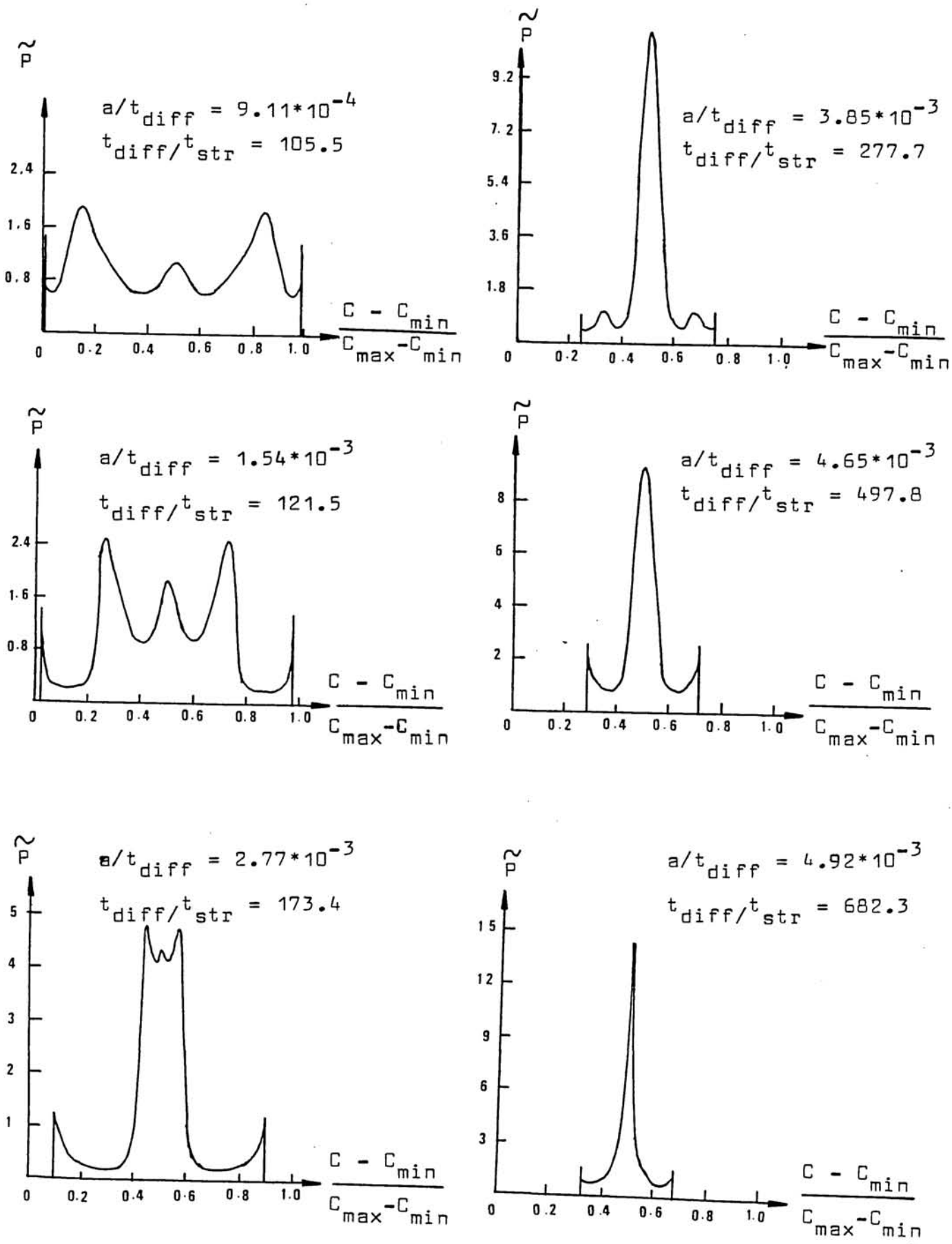

Figure 6.15 THE INFLUENCES OF DIFFUSION TIME AND STRETCHING TIME ON THE PROBABILITY DENSITY DISTRIBUTION OF HELIUM TRACER AT DIFFERENT AGES.

6.3.14 Summary

- Comparison between the experimental results and the predictions have been made. It has been shown that the predicted results are generally in good agreement with the experimental data.

- An extensive study of fold biography has been conducted and presented above.

- It has been found that the stretching time of the multiple-folds, for the cold flow experiment, is a linear function of age. Obviously, the age of the multiple-folds is restricted by the experimental apparatus.

- The shape of the probability-density function of the multiple-folds is seen to be symmetric. This is a special feature of the isothermal, uniform density, laminar, stretched-folds.

6.4 The hot-flow prediction

6.4.1 Introduction

This section describes the results of computations made for a two-dimensional steady laminar diffusion flame developed inside a vertical open converging

channel for which experimental data is available. The latter are the results of the author's combustion experiments (see Chapter 5).

6.4.2 The problem

Figure 6.16 shows the progress of the combustion and mixing processes between the hydrogen fuel and air from the entrance to test section to the exhaust.

The hydrogen+nitrogen and air are initially separated by a thin septum. Since the flame is stabilised near the porous strips, the reaction zone can build up. The latter expands and becomes thicker downstream of the jets on each side of the separating reactants. Due to the fact that the diffusion flame is considered only in the fuel-lean mixture range, large quantities of excess air are admitted (Burke and Schumann, 1928; Wolfhard and Parker, 1949). Hence, the reactions are governed by the finite rates at which oxygen and hydrogen can diffuse into the reaction zone.

The effect of the laminar transport, stretching and chemical kinetics on this flame can be predicted by the present solution procedure.

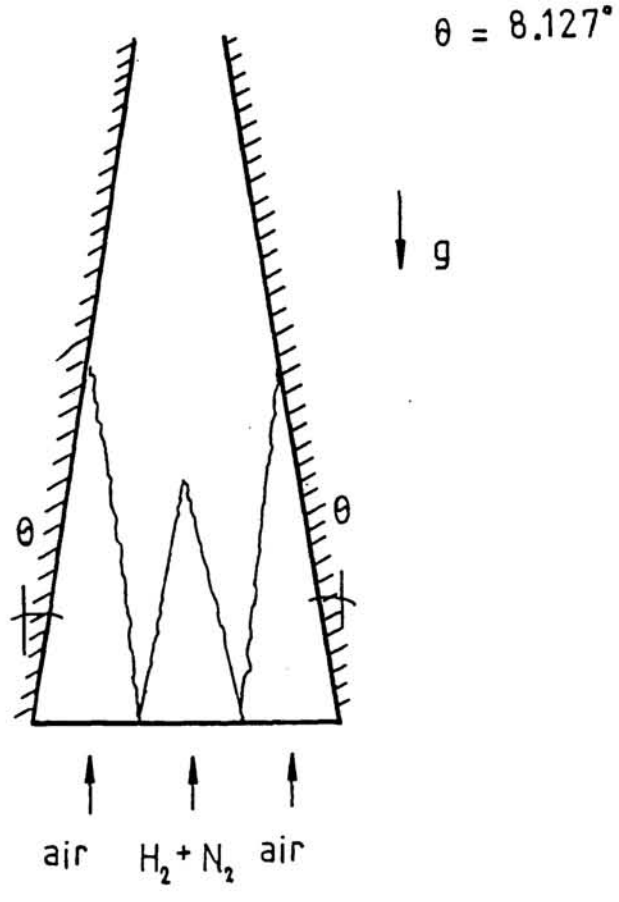

FIGURE 6.16 THE PROGRESS OF THE COMBUSTION AND MIXING PROCESSES BETWEEN THE HYDROGEN FUEL AND AIR IN A CONVERGING CHANNEL.

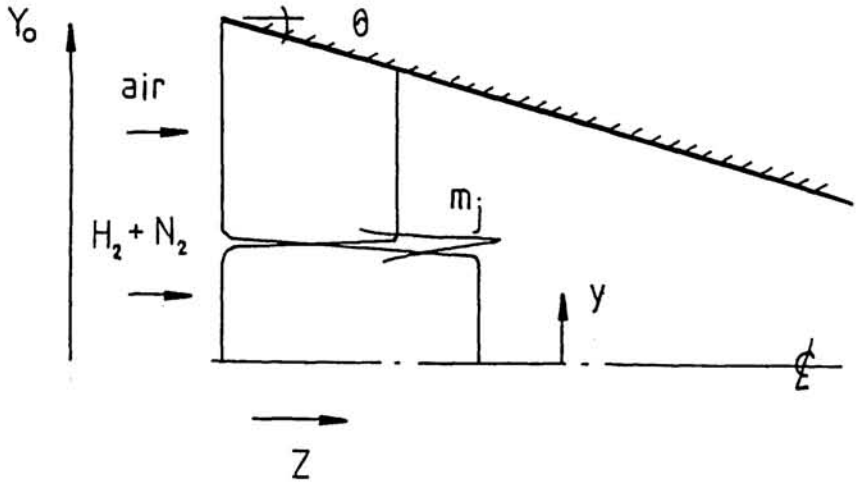

FIGURE 6.17 ILLUSTRATION OF THE FLOW SITUATIONS AND THE TYPICAL DISTRIBUTION OF SPECIES CONCENTRATIONS ON THE CALCULATION DOMAIN.

6.4.3 Objectives

The objectives of this section are:

- To establish a prediction procedure for a plane, laminar diffusion flame which is subjected to stretching in a converging channel, under the influence of buoyancy.
- To incorporate a hydrogen-air lean mixture of the complex chemical kinetic scheme into the prediction procedure.
- To show that the numerical solution procedure (TDMA + SENECKS) does not require excessive computer time.
- To compare the results of prediction with the combustion experiments made in Chapter 5.
- To present the results of the calculated $\tilde{p}d\tau$ of stretched-folds in which combustion occurs.

6.4.4 Mathematical statement

Assumptions

- The flow is two-dimensional, incompressible, steady, parabolic, plane symmetric and laminar. Thus, the three-dimensional effect on the side walls is negligible.
- The lateral momentum equation is not taken into consideration.

- The molecular transport and thermodynamic properties employed are the same as in Chapter 2.
- A 9 step gas-phase reaction mechanism of H_2-air diffusion flame for fuel-lean mixture cases reported by Dixon-Lewis (1970b) is employed here and is tabulated in Table 6.4.
- The flame is non-adiabatic.
- The radiative transfer of heat is absent.
- The inclined walls are smooth, impervious to mass transfer, entirely inert chemically and the roughness at the walls is neglected.

6.4.5 The governing equations

Conservation of longitudinal momentum

$$\frac{\partial u}{\partial z} = \frac{\partial}{\partial \xi} (\tau r) + \frac{1}{\rho u} \{g (\rho_{ref} - \rho) - \frac{\partial P}{\partial z}\} , \quad (6.4\text{-}1)$$

where ξ is a kind of stream-function defined by

$$\xi \equiv \int_0^y \rho u \, dy;$$

g is the gravitational acceleration;

z is the longitudinal distance; and

ρ_{ref} is a function of z alone.

J	Elementary reactions	A_j	B_j	T_j	A_{-j}	B_{-j}	T_{-j}
1	$OH+H_2 \rightleftharpoons H_2O+H$	3.02×10^{10}	0	2500	9.3×10^{10}	0	0
2	$H+O_2 \rightleftharpoons OH+O$	2.24×10^{11}	0	8000	1.301×10^{10}	0	0
3	$O+H_2 \rightleftharpoons OH+H$	1.742×10^{10}	0	4100	8.3×10^{6}	1	3500
4	$M+H+O_2 \rightleftharpoons HO_2+M$	1.5×10^{9}	0	-400	2.143×10^{12}	0	23140
5	$H+HO_2 \rightleftharpoons OH+OH$	1.995×10^{11}	0	950	1.191×10^{10}	0	20280
6	$M+H+H \rightleftharpoons H_2+M$	6.397×10^{11}	-1	0	5×10^{10}	0	51640
7	$M+H+OH \rightleftharpoons H_2O+M$	2.301×10^{16}	-2	0	2.228×10^{11}	0	48300
8	$OH+HO_2 \rightleftharpoons H_2O+O_2$	5.012×10^{10}	0	500	5.343×10^{11}	0	36950
9	$O+HO_2 \rightleftharpoons OH+O_2$	5.012×10^{10}	0	503	5.146×10^{10}	0	28270

TABLE 6.4: STANDARD VALUES OF A_j, B_j and T_j FOR FORWARD AND REVERSE REACTIONS

P is defined by:

$$P \equiv p + \int \rho_{ref}\, g\, dz \quad . \qquad (6.4\text{-}2)$$

Conservation of atomic elements

$$\frac{\partial m_{el}}{\partial z} = \frac{\partial}{\partial \xi}\left(\rho^2 D_{el} u \frac{\partial m_{el}}{\partial \xi}\right) \quad . \qquad (6.4\text{-}3)$$

Conservation of species

$$\frac{\partial \phi_j}{\partial z} = \frac{\partial}{\partial \xi}\left(\rho^2 D_j u \frac{\partial \phi_j}{\partial \xi}\right) + \frac{S_{\phi_j}}{\rho u} \quad . \qquad (6.4\text{-}4)$$

Conservation of stagnation enthalpy

$$\frac{\partial \tilde{h}}{\partial z} = \frac{\partial}{\partial \xi} \left(\rho u \frac{\lambda}{C_p} \frac{\partial \tilde{h}}{\partial \xi}\right) + \frac{\partial}{\partial \xi} \left\{\sum_j \left(\rho D_j - \frac{\lambda}{C_p}\right) \rho u h_j \frac{\partial \phi_j}{\partial \xi}\right\}$$

↑ convection ↑ diffusion ↑ multiple diffusional flux

$$+ \frac{\partial}{\partial \xi} \left\{\left(\mu - \frac{\lambda}{C_p}\right) \rho u \frac{\partial \frac{u^2}{2}}{\partial \xi}\right\} \quad . \qquad (6.4\text{-}5)$$

↑ kinetic heating

Equation of state

For a perfect gas, the equation of state is given by:

$$p = \rho \frac{R}{\overline{w}} T \quad , \qquad (6.4\text{-}6)$$

where R is the Universal gas constant, $\overline{w}$ is the molecular weight of mixture; T and p are the absolute temperature and pressure, respectively.

6.4.6 Solution procedure

A numerical solution procedure for solving the buoyant-confined flame is described here. An important feature of the problem considered is that the chemistry and the

hydrodynamics can change very rapidly during each marching step.

When the buoyancy term is included, the high acceleration of the flow creates a very steep diffusion flux gradient across the layer. Hence, more air entrains near the base of the flame. In this circumstance, a special treatment is required for the hydrodynamics in order to satisfy both continuity and momentum equations in each step. This implies that while the numerical method for solving the chemical species and enthalpy remains unchanged (as described in Chapter 3), the momentum equation should be iterated further in order to include the variation of area change with pressure, body force and shear stress.

Usually, this correction is applied to the longitudinal pressure gradient when solving confined flow to ensure that the calculated duct area, at any cross-section, matches the width of the converging duct. The correction-procedure is given below.

Block correction

Suppose the area of the converging duct is D and the sum of calculated cell area, $\Sigma\Delta y$, is given by:

$$\Sigma\Delta y = \int_{I}^{E} \frac{d\xi}{\rho u} \quad . \qquad (6.4\text{-}7)$$

The error in calculating the total cell area, $d\Sigma\Delta y$ is: $d\Sigma\Delta y = D - \Sigma\Delta y$, (6.4-8)

It is required to find what pressure change should be applied to the whole flow at a cross-section to make $d\Sigma\Delta y=0$.

Differentiating equation (6.4-7) with respect to pressure gives:

$$\frac{d\Sigma\Delta y}{dp} = \int_1^2 - (\rho u)^{-2} \left(\rho \frac{du}{dp} + u \frac{d\rho}{dp}\right) d\xi \ . \quad (6.4\text{-}9)$$

The truncated momentum equation gives:

$$\frac{du}{dp} = - \frac{1}{\rho u} \quad . \quad (6.4\text{-}10)$$

Since the flow is incompressible, $\frac{d\rho}{dp} = 0$.

Thus, equation (6.4-9) may be expressed as:

$$\frac{d\Sigma\Delta y}{dp} = \int_I^E \frac{1}{\rho^2 u^3} d\xi \quad . \quad (6.4\text{-}11)$$

Hence, the pressure change becomes:

$$dp = \frac{d\Sigma\Delta y}{\int_I^E \frac{1}{\rho^2 u^3} d\xi} \quad . \quad (6.4\text{-}12)$$

Finite-difference form of the momentum equation

The numerical form of momentum equation is given by:

$$D_i u_i^{(k+1)} = A_i u_{i+1}^{(k+1)} + B_i u_{i-1}^{(k+1)} + S_u^{(k)} + u_{i,u} \delta\omega_i \ , \qquad (6.4\text{-}13)$$

where A_i, B_i, D_i are the numerical coefficients; $S_u^{(k)}$ is the source term, defined by:

$$S_u^{(k)} \equiv \frac{1}{(\rho_i u_i)^{(k)}} \{g(\rho_{ref} - \rho_i)^{(k)} - \frac{dp}{dz}^{(k)}\} dz \ .$$

The superscript 'k' indicates the iteration number.

The pressure gradient (equation 6.4-12) is substituted into the momentum equation (equation 6.4-13) and the resulting equation is iterated until satisfactory convergence is achieved (described below).

Relaxation factor

In order to avoid instability which could lead to the calculated duct area oscillating about the true value at each marching step, under-relaxation of the pressure gradient is required. Thus,

$$dp = \eta \ dp^{(k-1)} + (1-\eta) \ dp^{(k)} \ , \qquad (6.4\text{-}14)$$

where η is the under-relaxation factor (η=0.1 is chosen).

Convergence

The iteration is terminated when the calculated duct area error, $d\Sigma\Delta y$, falls within a specified tolerance (i.e. $\frac{d\Sigma\Delta y}{D} = 10^{-3}$).

6.4.7 Computational details

The grid distribution and forward step size

The flame exhibits a very steep diffusion flux gradient near the porous strips at the entrance of the test section. Hence, the number of grid points, and the grid spacing in this region should be fine enough for adequate prediction of the chemical reactions.

In the present calculations, 60 non-uniform grid nodes are used in the cross-stream direction. The grids are distributed more densely in the steep gradient region as well as near the wall. Preliminary calculations showed that the longitudinal velocity changed rapidly near the inlet region, but more gradually downstream thus a very fine equally-space grid is also employed in the longitudinal direction. Details of these will be discussed in sub-section 6.4.8.

Domain of calculation

Since the geometry is symmetric, only one half of the calculation domain needs to be considered. Figure 6.17 illustrates the flow situations and the typical distribution of species concentrations on the calculation domain.

Initial conditions

In order to predict the flame, it is necessary to specify the cross-stream variations of all the dependent variables at a short distance above the porous strips with the assumption of the boundary layer profiles in question.

The following compositions in the fuel and air layers are respectively determined by the upstream flow-rate measurement. The velocity profile is determined by the continuity equation.

Conditions in the fuel layer

Length of the layer	: ℓ = 0.2286m.
Thickness of the layer	: δ_1 = 0.0244m.
Mass flow rate of hydrogen	: $\dot{m}_{H_2}$ = 2.252×10^{-5} kg/sec
Mass flow rate of nitrogen	: $\dot{m}_{N_2}$ = 1.8055×10^{-4} kg/sec.
Total mass flow rate	: $\dot{m}_{tol}$ = 2.03×10^{-4} kg/sec

Mass fraction	: $H_2 = 0.11.$
	$N_2 = 0.89.$
Measured temperature	: $473^{o}K.$
Pressure	: 1 atom.
Velocity	: $u = \frac{\dot{m}_{tol}}{\rho\delta_1\ell} = 0.127\ msec^{-1}.$
Stagnation enthalpy	: $\tilde{h} = \sum_j \sigma_j h_j + \frac{u^2}{2}$.

Conditions in the air layer

Length of the layer	: $\ell = 0.2286m.$
Thickness of the layer	: $\delta_2 = 0.0508m.$
Mass flow rate of air	: $\dot{m}_{air} = 1.373x10^{-3}$ kg/sec.
Mass fraction	: $O_2 = 0.232.$
	$N_2 = 0.768.$
Measured temperature	: $473^{o}K.$
Pressure	: 1 atom
Velocity	: $u = \frac{\dot{m}_{air}}{\rho\delta_2\ell} = 0.162m.$
Stagnation enthalpy	: $\tilde{h} = \sum_j \sigma_j h_j + \frac{u^2}{2}$.

Conditions in the initial reaction zone

The reaction zone thickness, δ_3, is assumed to be 2% of the initial fold thickness. The fuel and air are supposed to be mixed over this narrow region. The concentration profiles are in the form of cosine

functions. The temperature is prescribed high enough for combustion to take place.

Initial fold thickness

$$Y_o = \delta_1 + \delta_2 + \delta_3 = 0.0762\text{m}.$$

Boundary conditions

Velocity

At the I, E boundaries, the inclined walls are impervious, and the velocity is zero.

$$U_I = 0 \ ,$$

$$U_E = 0 \ .$$

Species concentration

The fluxes of species concentrations at wall are zero, $\frac{\partial \phi}{\partial y} = 0$, where y represents the direction normal to the wall.

Wall temperature

At the wall surfaces, boundary conditions are provided by specifying temperatures. The values of the corresponding temperatures have been obtained from experimental data (see Chapter 5). With the aid of the

least-square linear regression analysis, the result of the temperature distribution along the inclined wall is further expressed as a 5th order polynomial function:-

$$T=A_o+A_1z+A_2z^2+A_3z^3+A_4z^4+A_5z^5 \ {}^oK \quad , \qquad (6.4\text{-}15)$$

where A_i's are the polynomial coefficients (given below) and z is the longitudinal distance.

A_o	A_1	A_2	A_3	A_4	A_5
473.	1457.	-1278.	-2439.	-1251.	3262

Heat flux

Since the wall temperature is specified, the heat flux is deduced from the temperature of the near-wall grid node and the heat-transfer coefficient (Stanton number for stagnation enthalpy) prevailing at the fluid-solid interface.

The near-wall grid temperature is computed from the equation of state; while the heat-transfer coefficient is calculated by employing the following wall function (Spalding 1978a):-

- shear stress coefficient:

$$s = \frac{1}{R} - \tfrac{1}{2}F \quad , \qquad (6.4\text{-}16)$$

- Stanton number for stagnation enthalpy:

$$S_R = \frac{1}{R\sigma} \quad , \qquad (6.4\text{-}17)$$

where R is the Reynolds number, defined by, $R \equiv (\frac{\rho u y}{\mu})_C$;

F is pressure gradient number, defined by,

$F \equiv (\frac{y}{\rho u^2})_C \frac{dp}{dx}$; and

σ is the Prandtl number, defined by, $\sigma \equiv (\frac{\mu}{\Gamma_h})_C$.

The subscript 'c' indicates the outer limit of the Couette-flow.

6.4.8 Grid-independence tests

Grid-independence tests are carried out in the present case by varying the number of grid nodes and the forward step size.

Figures 6.18-6.21 show the predicted u-velocity variations and the cross-stream temperature distributions, using various grid sizes.

The above tests showed that no change occurred in the results for the 60 and 80 grid nodes. Therefore, for the present

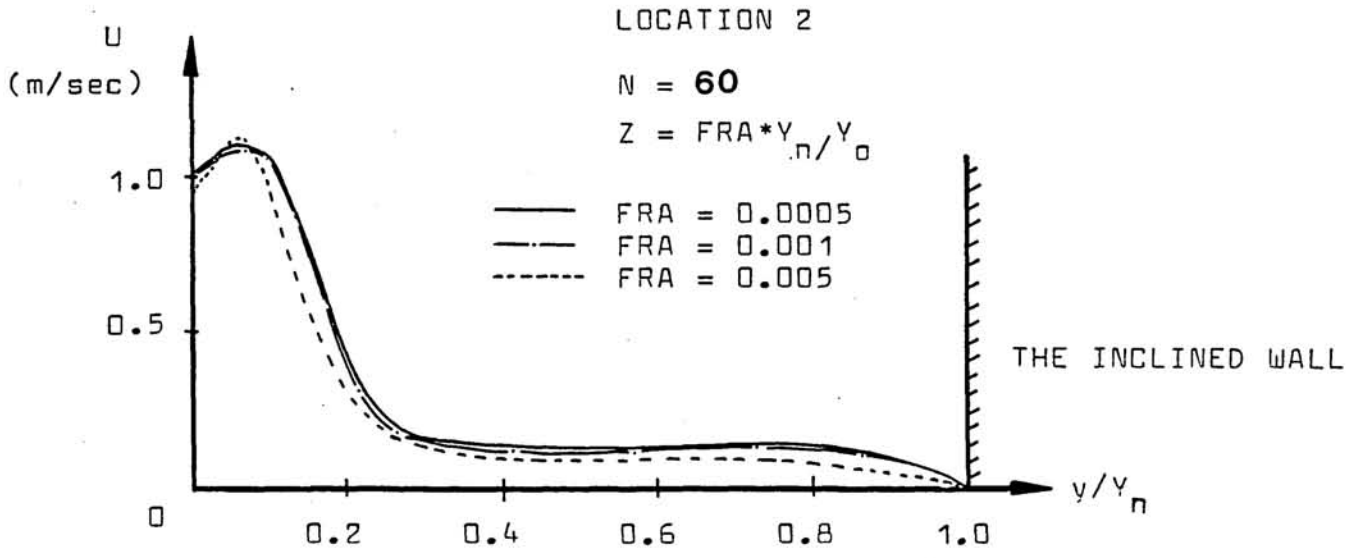

FIGURE 6.20 GRID-INDEPENDENCE TESTS(2)
EFFECT OF THE FRA.

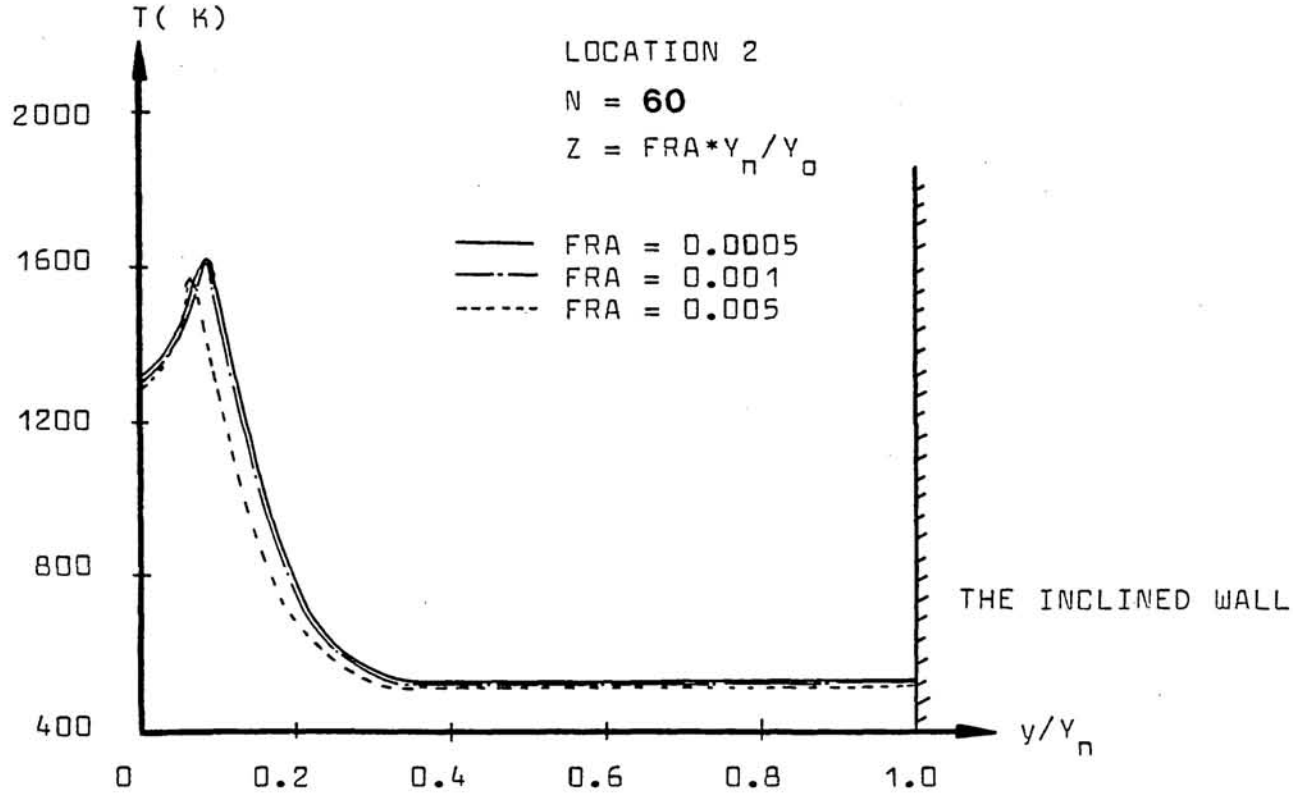

FIGURE 6.21 GRID-INDEPENDENCE TESTS(2)
EFFECT OF THE FRA.

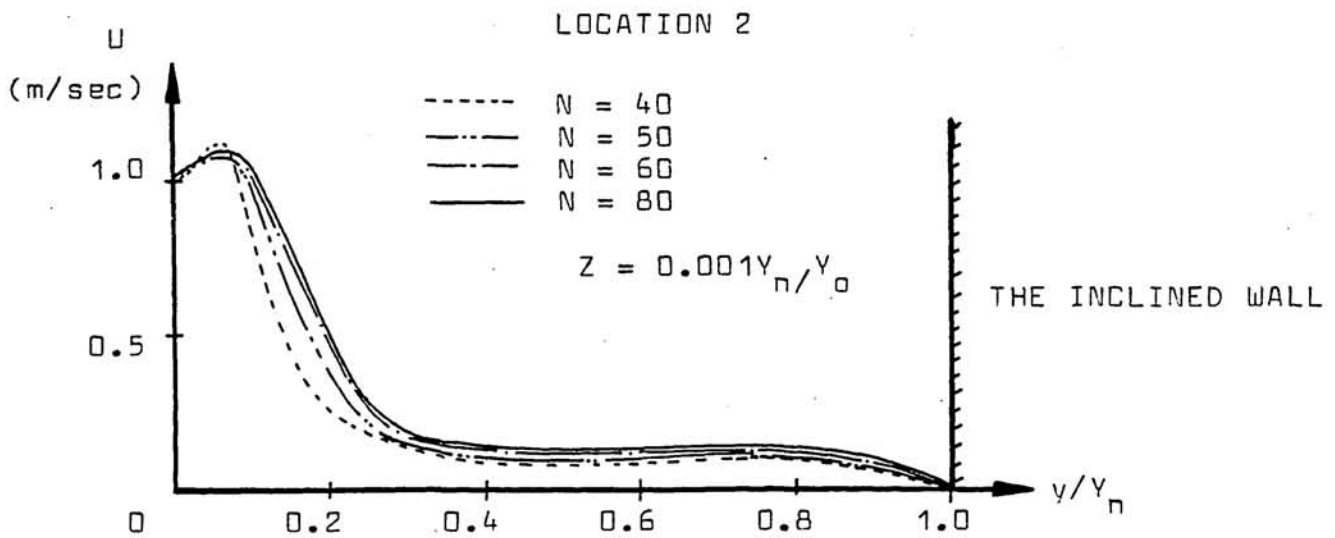

FIGURE 6.18 GRID-INDEPENDENCE TESTS(1)
EFFECT OF THE NUMBER OF GRID NODES.

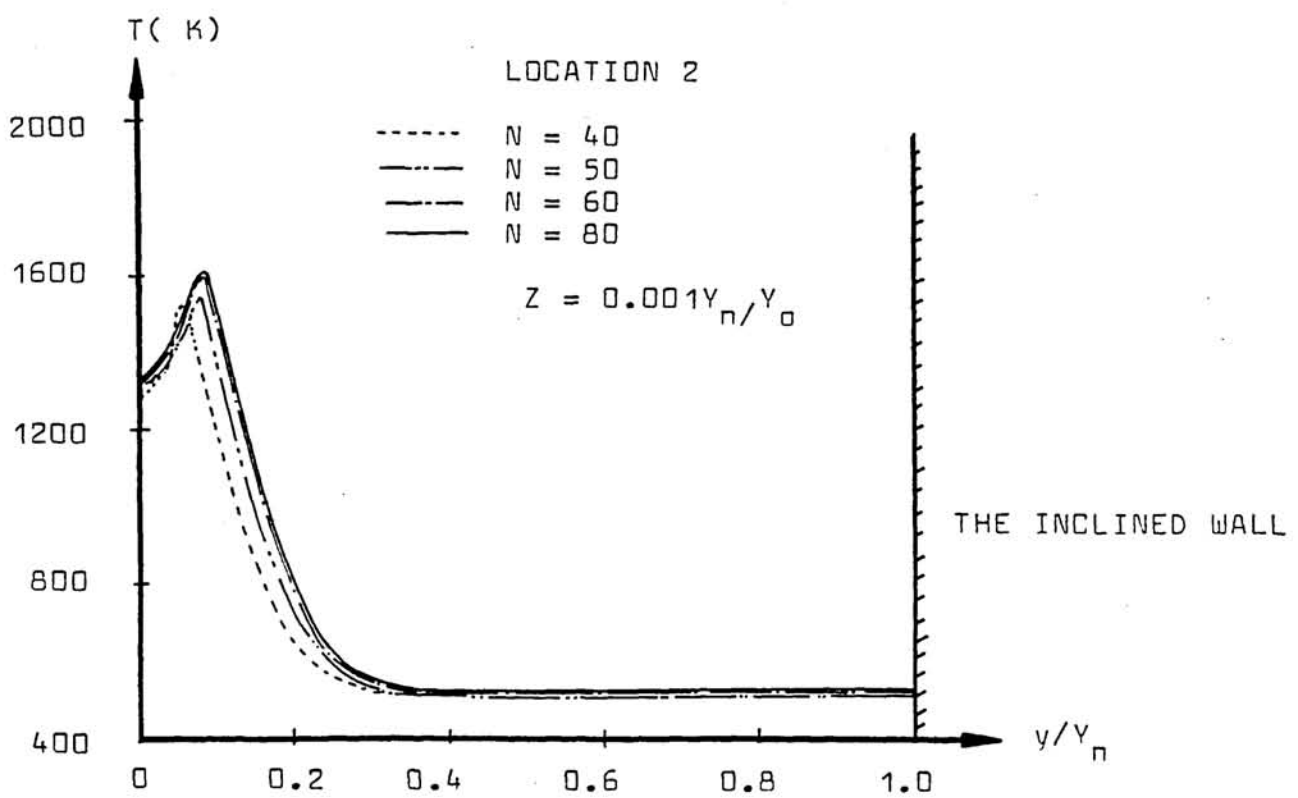

FIGURE 6.19 GRID-INDEPENDENCE TESTS(1)
EFFECT OF THE NUMBER OF GRID NODES.

calculations, 60 grid nodes (non-uniformly distributed) are used.

Typical information for a computational run is given below.

Prediction of laminar diffusion hydrogen air stretched-flame	Pertinent Data
Configuration	2D convergent channel
Grid distribution	Non-uniform
Number of cross-stream grid nodes	60
Step size δz	$0.001Y_N/Y_o$
Number for forward steps	1000
Iteration (hydrodynamic step) maximum number of iterations/ step	15
Iteration (chemistry step) maximum number of iterations/ point (point-by-point adjustment)	20
Computer time in CDC 6600 used	317 secs
Storage	32K

6.4.9 Comparison between the predicted and measured quantities

Figures 6.22-6.27 show the comparison between the predicted and measured cross-fold temperature distribution in the y-direction (i.e. the direction parallel to the porous strips at the entrance of the test

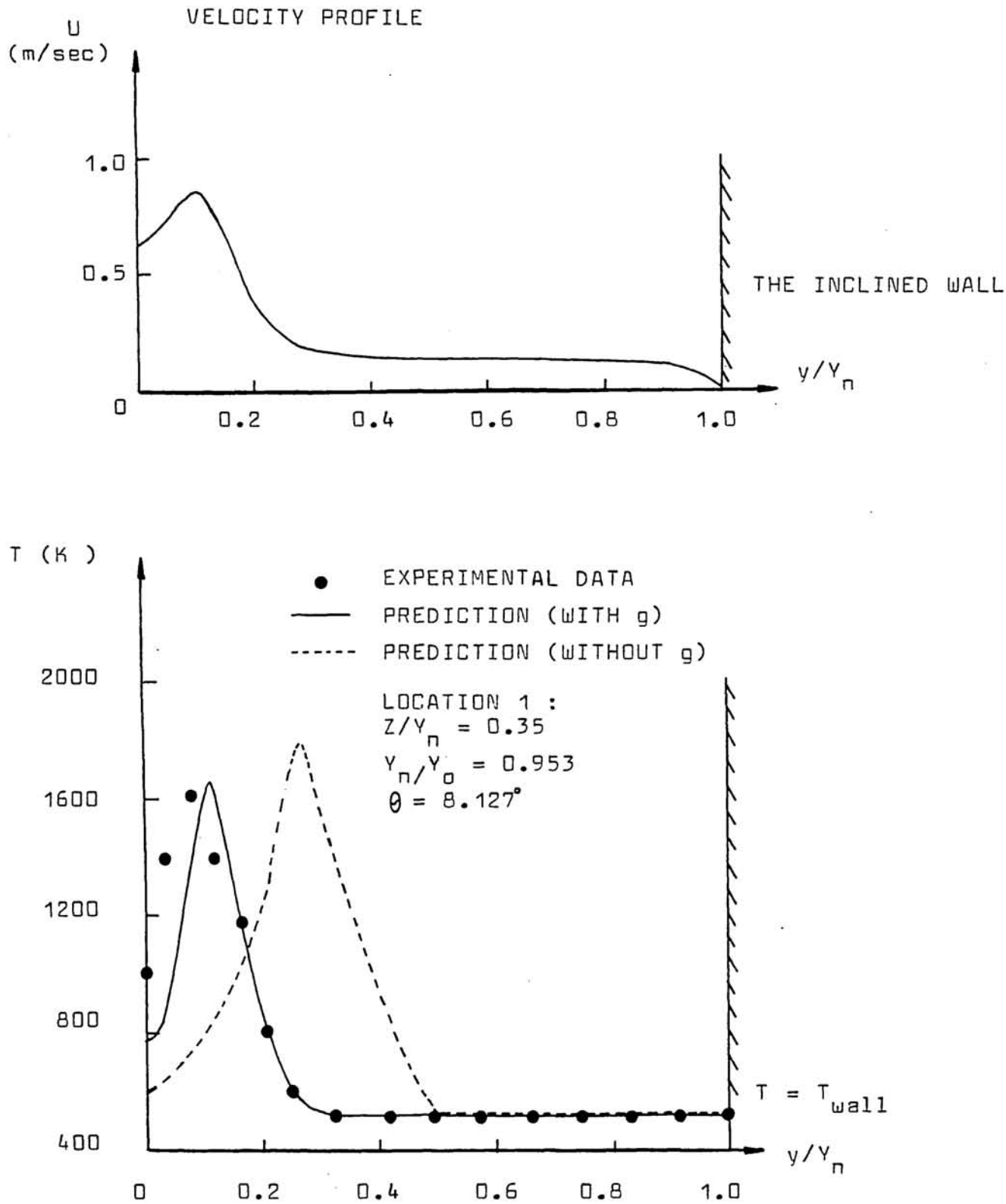

Figure 6.22 THE COMPARISON OF PREDICTED AND EXPERIMENTAL TEMPERATURE PROFILE.

section) at several downstream locations corresponding to fixed values of normalised $z(z/Y_N)$. 'z' is the longitudinal distance of the vertical converging jet, and Y_N is the half width of confined walls at location z.

Two sets of predictions are displayed on each diagram. These correspond to the solutions obtained with and without the buoyancy effect.

(Location 1) Figure 6.22 shows that:

1. When the buoyancy effect is excluded in the solution procedure, the predicted flame front differs markedly from the measured one.

2. When the buoyancy effect is included, the predicted temperature rises from a minimum value near the wall to a maximum at about 0.11 Y_N away from the centreline and then subsequently decreases significantly in the centreline region. The predicted flame front agrees with the measured one.

3. The predicted temperature profile generally agrees satisfactorily with the experimental

data. However, near the centreline of the converging jet, the temperature is somewhat under-predicted.

(Location 2) Figure 6.23 shows that:

1. When the buoyancy effect is excluded, the predicted temperature profile is incorrect.

2. When the buoyancy effect is included, the temperature peak is correctly predicted. The peak occurs at about 0.09 Y_N away from the centreline as a result of the shifted flame front due to buoyancy.

3. The predicted and the measured temperatures of the centreline of the converging jet show significant increase compared with the results of Location 1.

4. The predicted and the measured temperature show some discrepancies at the mixing region (i.e. from $Y=0.1Y_N$ to 0.4 Y_N). The calculated temperature profiles shows a greater gradient than the experimental data indicates.

VELOCITY PROFILE

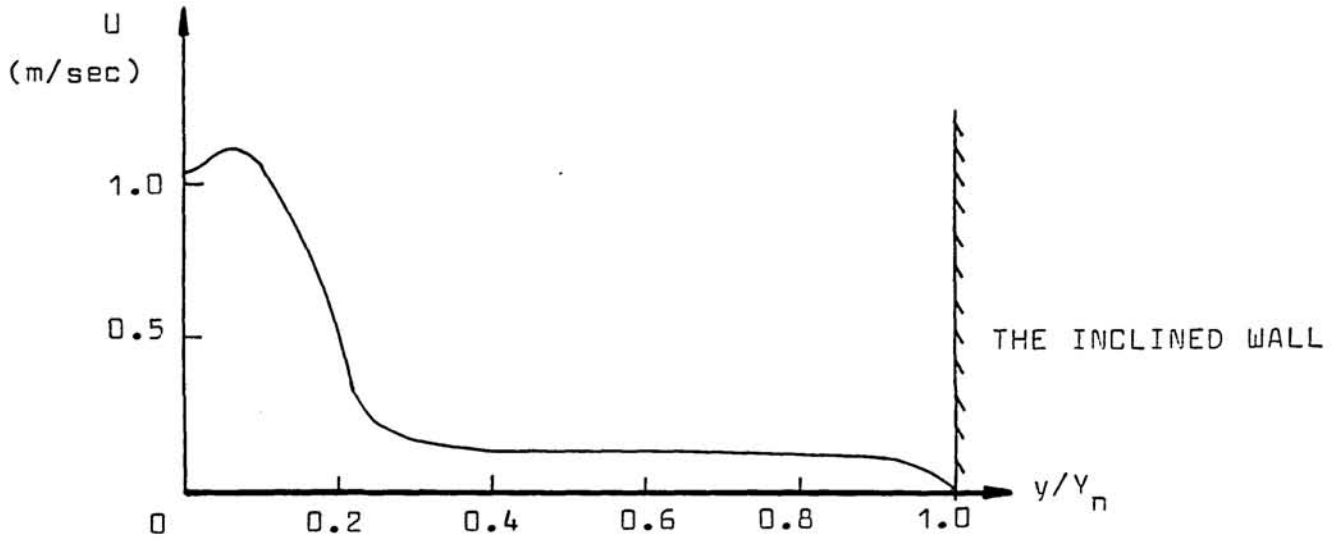

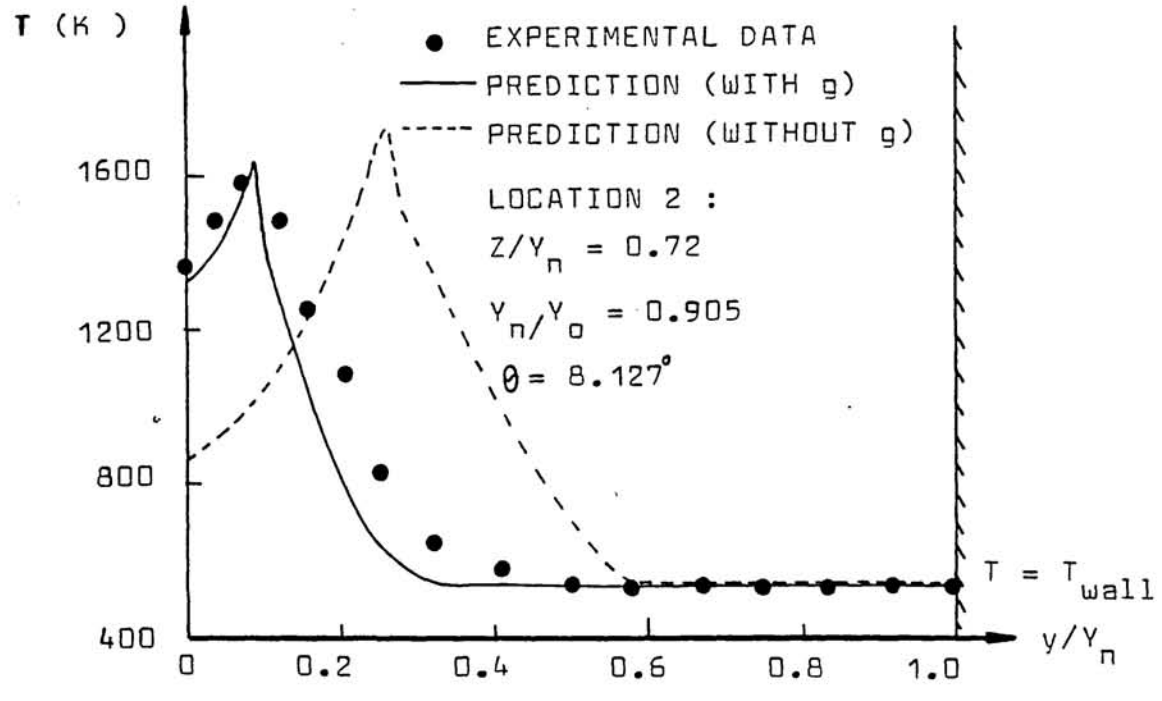

Figure 6.23 THE COMPARISON OF PREDICTED AND EXPERIMENTAL TEMPERATURE PROFILE.

(Location 3)

The trend of the cross-fold temperature profile which is similar to those of Location 2 is observed in Figure 6.24.

It is seen that the predicted temperature profile gives a steeper gradient than the measured one. Despite the experimental data not being perfectly symmetrical about the centre-axis as they should ideally be, the predicted data exhibits a slightly higher temperature at the centreline of the converging jet.

(Location 4)

Some discrepancies between predicted and measured behaviour of the temperature profile are shown in Figure 6.25. It is observed that the predicted flame-front is shifted to the central-axis; while the measured one is located at about 0.04 Y_N away from it.

In the region between 0.1 Y_N and 0.35 Y_N, it can be seen that the predicted temperature profile is more uniform and then decreases smoothly towards the wall. As a consequence of the cooling effect of the entrained air from the outer jets, the temperatures are minimum at the outer region which is far away from the central

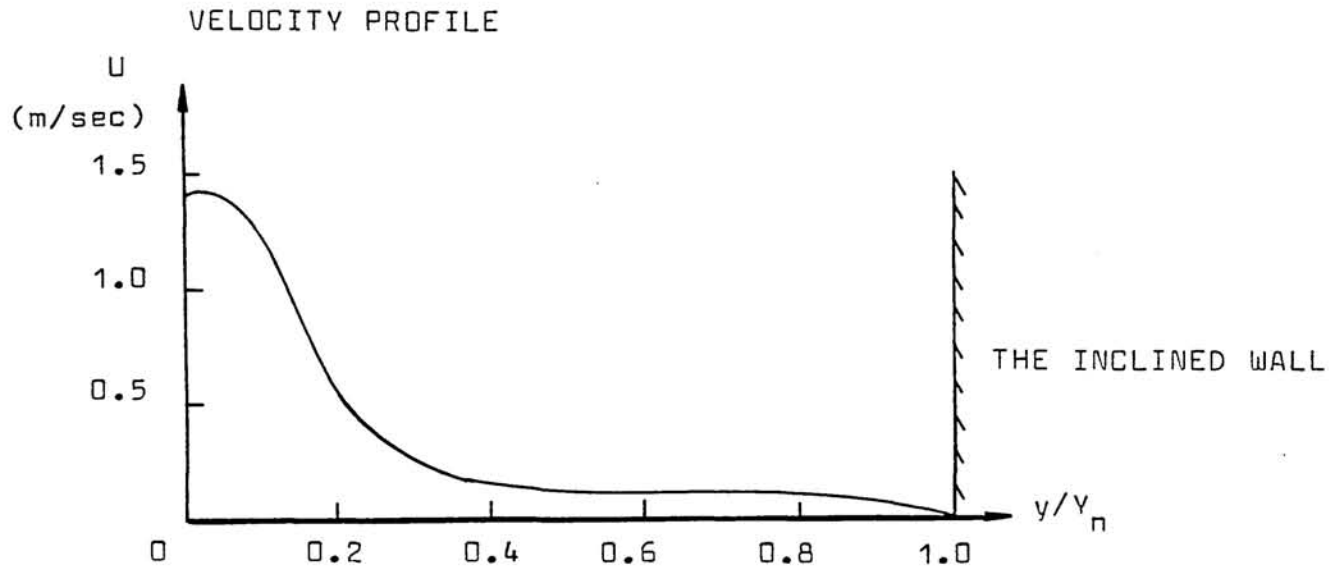

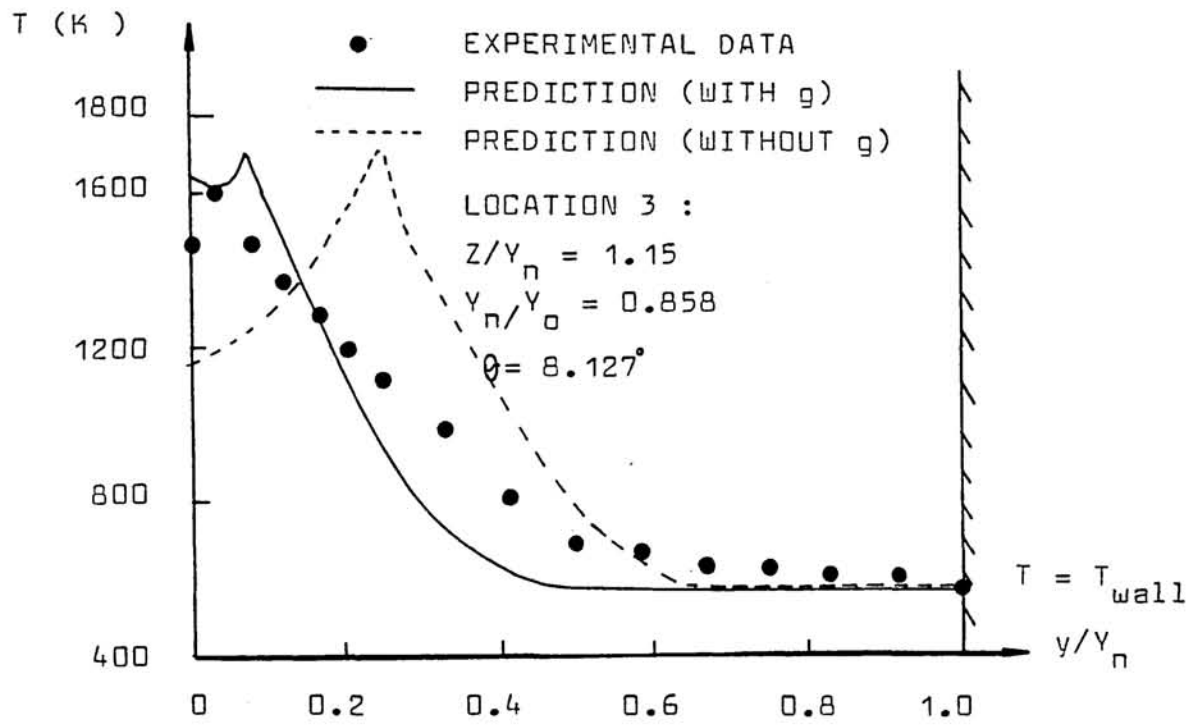

Figure 6.24 THE COMPARISON OF PREDICTED AND EXPERIMENTAL TEMPERATURE PROFILE.

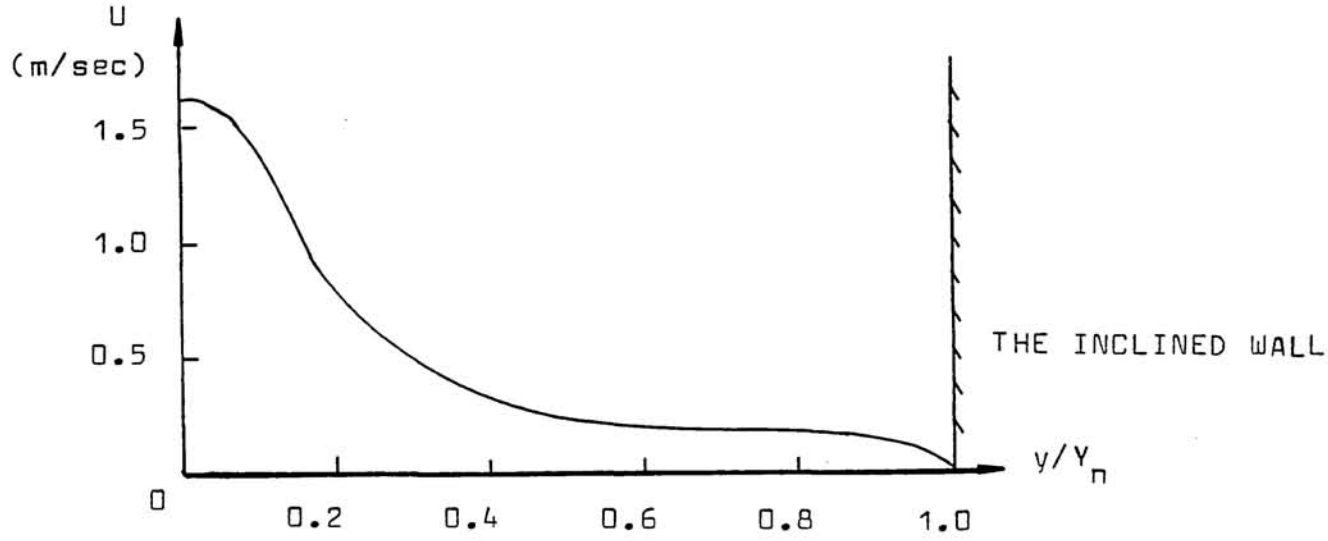

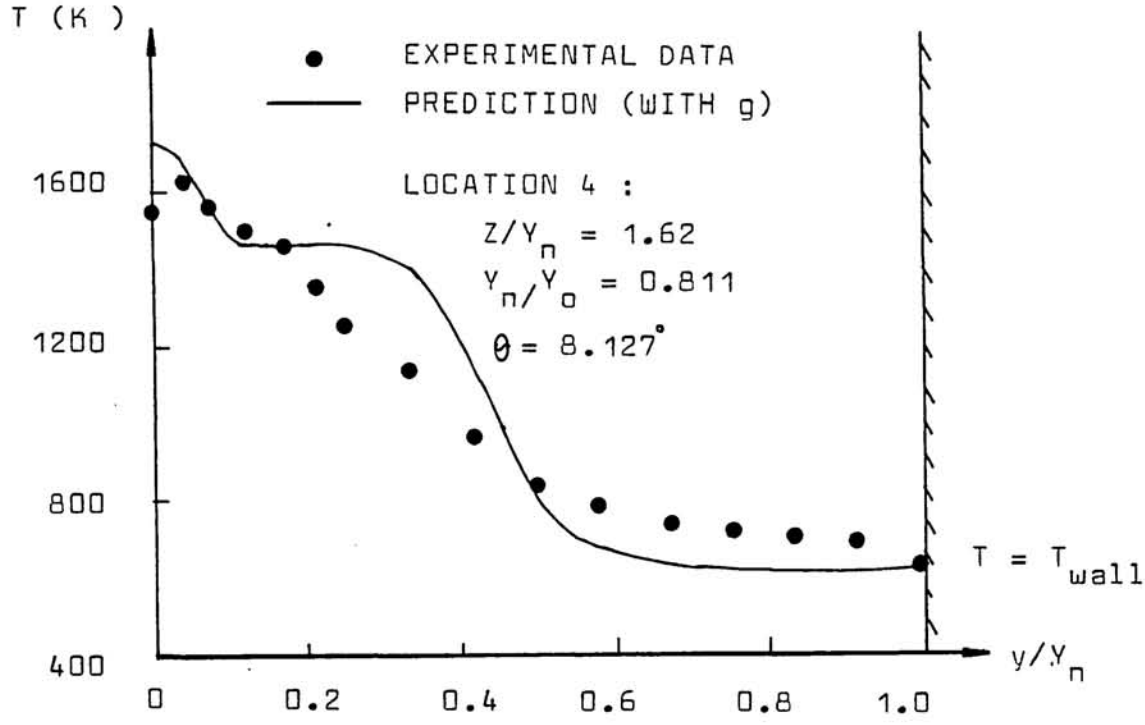

Figure 6.25 THE COMPARISON OF PREDICTED AND EXPERIMENTAL TEMPERATURE PROFILE.

axis of the converging jet. In this region, the predicted results show better agreement with the experimental ones.

(Location 5)

Figure 6.26 shows that the predicted temperature distribution is somewhat higher than the measured profile.

(Location 6) Figure 6.27 shows that:

1. The predicted temperature profile shows fair agreement with measurement when buoyancy effect is included in the solution procedure.

2. The temperature profile becomes smoother and its gradient across the fold is less than that at the upstream. This suggests that the combustion is complete.

6.4.10 Further predictions

Structure of the diffusion stretched-flame

So far, the cross-fold profiles give only the variation of temperature distributions. It is useful to have a greater insight of the flame structure from the present predictions.

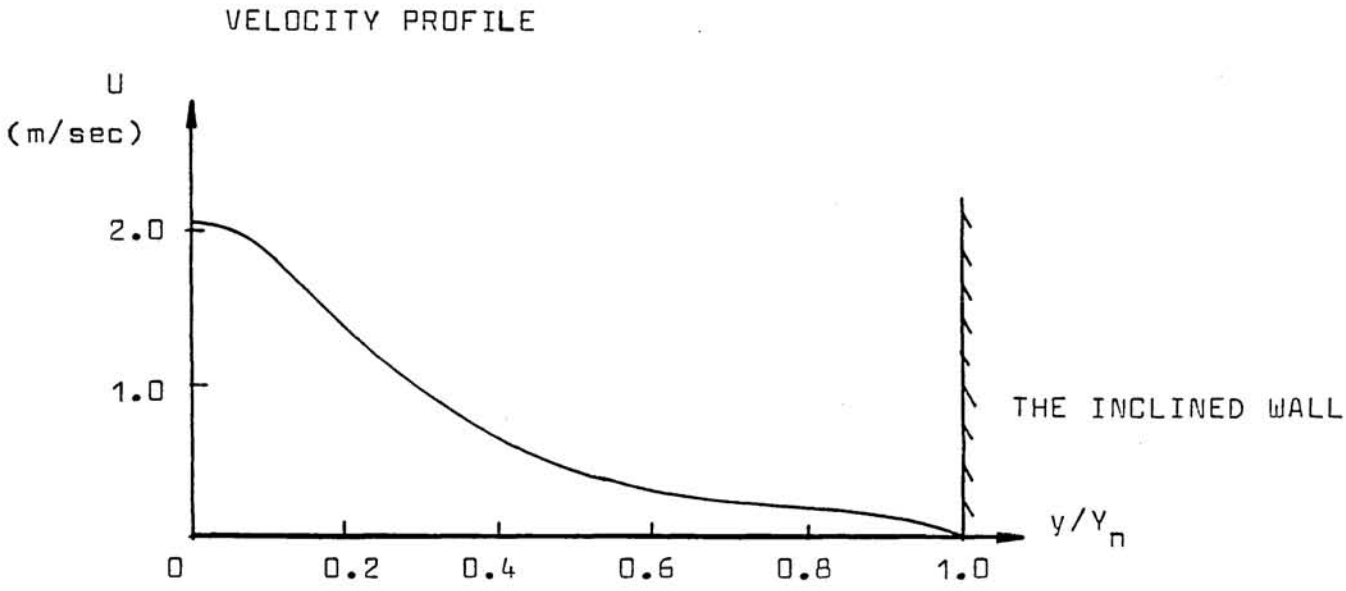

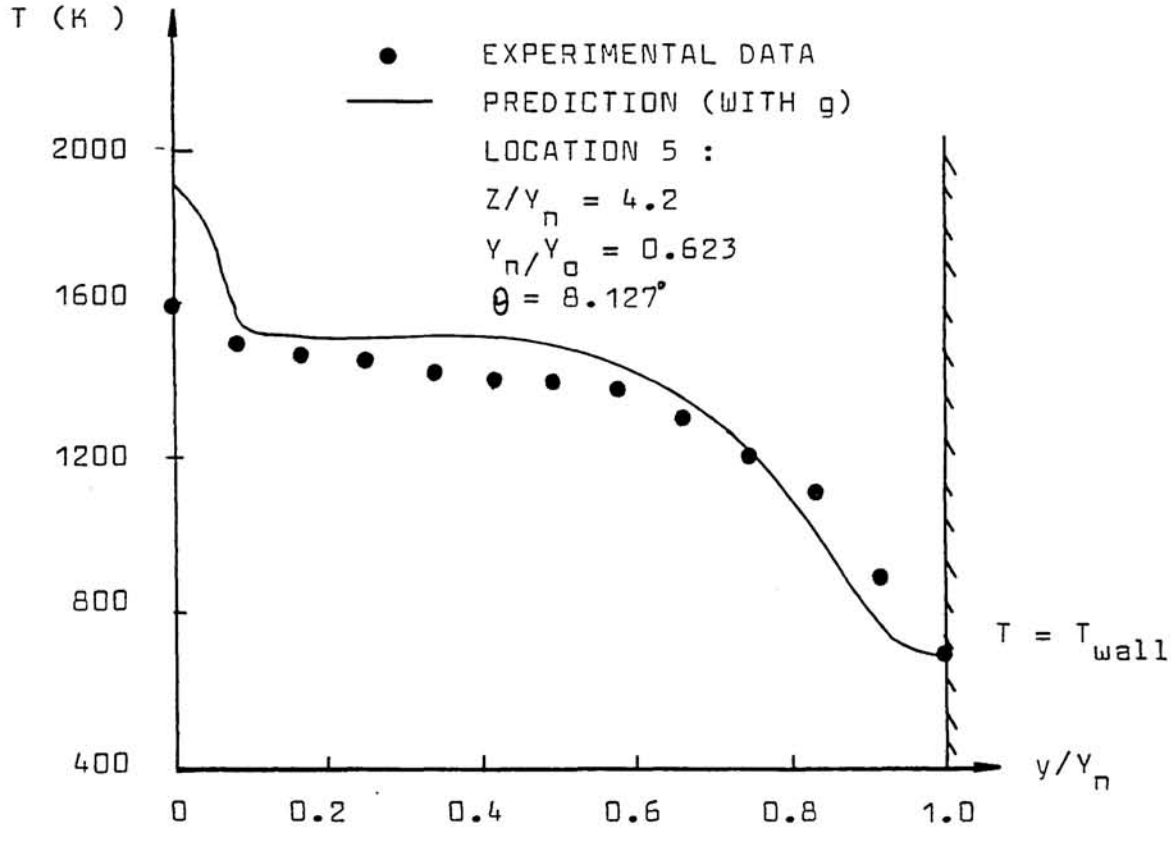

Figure 6.26 THE COMPARISON OF PREDICTED AND EXPERIMENTAL TEMPERATURE PROFILE.

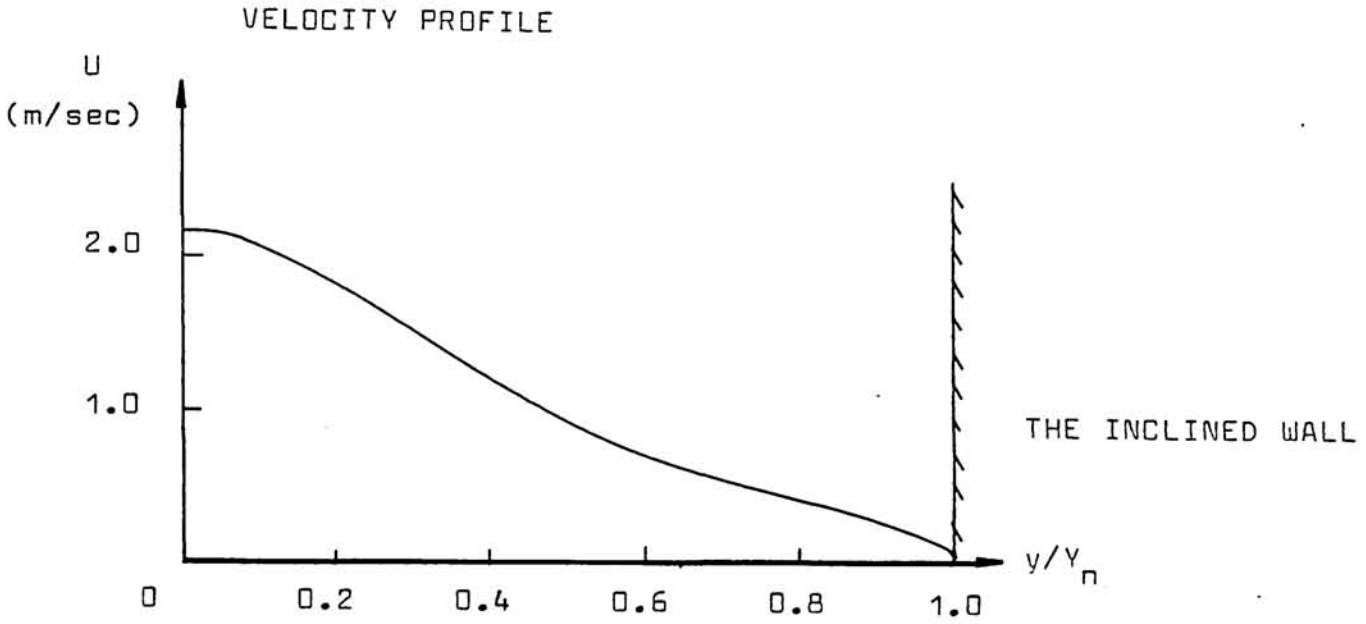

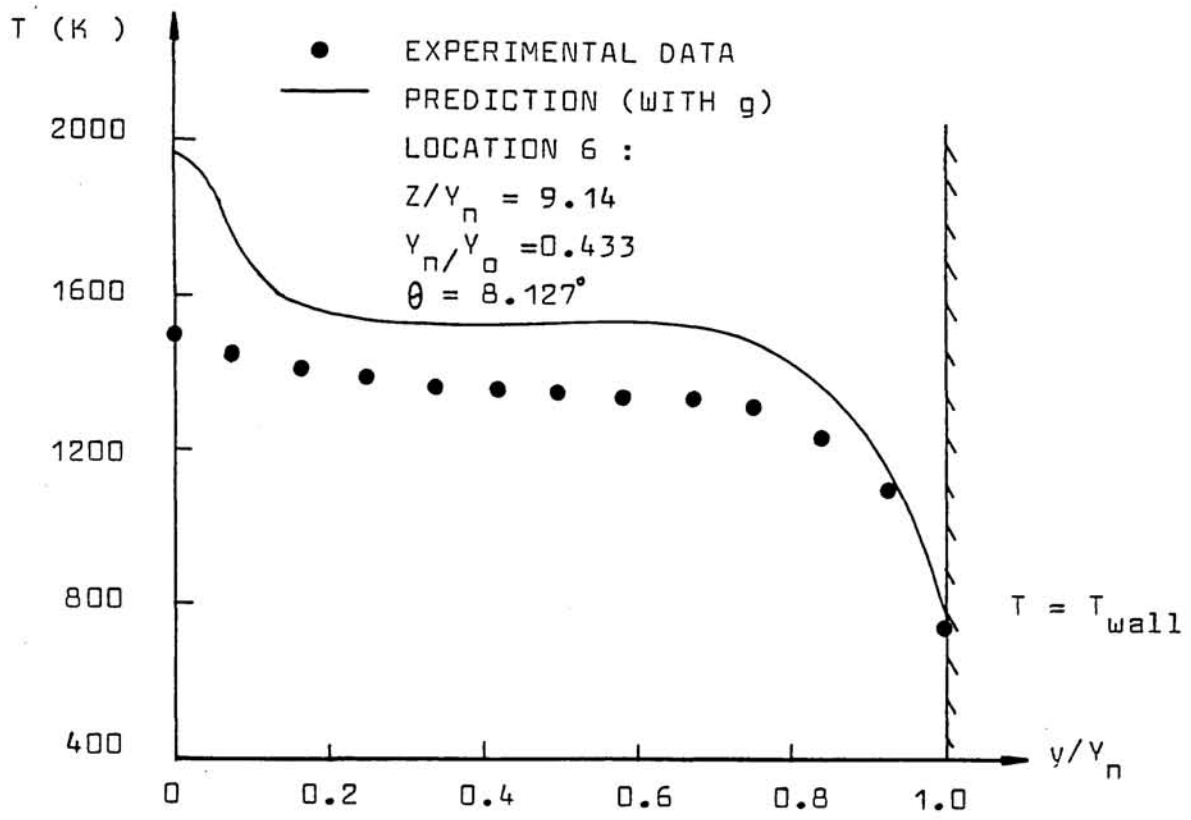

Figure 6.27 THE COMPARISON OF PREDICTED AND EXPERIMENTAL TEMPERATURE PROFILE.

The results are illustrated in Figures 6.28-6.33 These show the cross-fold profiles of species concentrations as functions of longitudinal distance.

The interaction between the laminar transport, stretching and chemical kinetics of the fold is described below.

Observation

1. The overlapping of the concentrations of H_2 and O_2 is seen to change from a small to a large amount as the stretched-fold develops upwards. It is suggested that the combustion proceeds in a thick reaction zone.

2. As illustrated in Figure 6.28-6.30, all intermediate species have zero mass fraction away from the reaction zone, reach a peak within the flame zone and then fall abruptly. It is of interest to note that peaks of the radical species (i.e. H,O and OH) are located near the flame-front while the peak of the hydroperoxyl radical, HO_2, is located away from the front and at a lower temperature region.

3. Figure 6.32 indicates that the majority of the hydrogen fuel has already been consumed while the rest of the variations of major species

concentrations are nearly evened out. These show that interdiffusion has a greater effect than the chemical reaction. Under these circumstances, the stretched-fold is burned in diffusion/premixed fashion.

4. Figure 6.33 shows the hydrogen fuel has been consumed. It is also observed that all the major species concentrations are uniformly distributed across the fold. The gradients of intermediate species become less steep than those in the upstream region. It is believed that the combustion is complete.

6.4.11 Discussion

Effect of buoyancy

If the buoyancy effect is neglected, it is observed that flame lengths are larger than the measured ones. The effect of buoyancy is to shorten the flame.

As a consequence of the effect of buoyancy force on the stretched-flame, the entrainment of air into the flame from the outer air jet is accelerated.

Effect of stretching

An increase of the entrainment rate from the outer

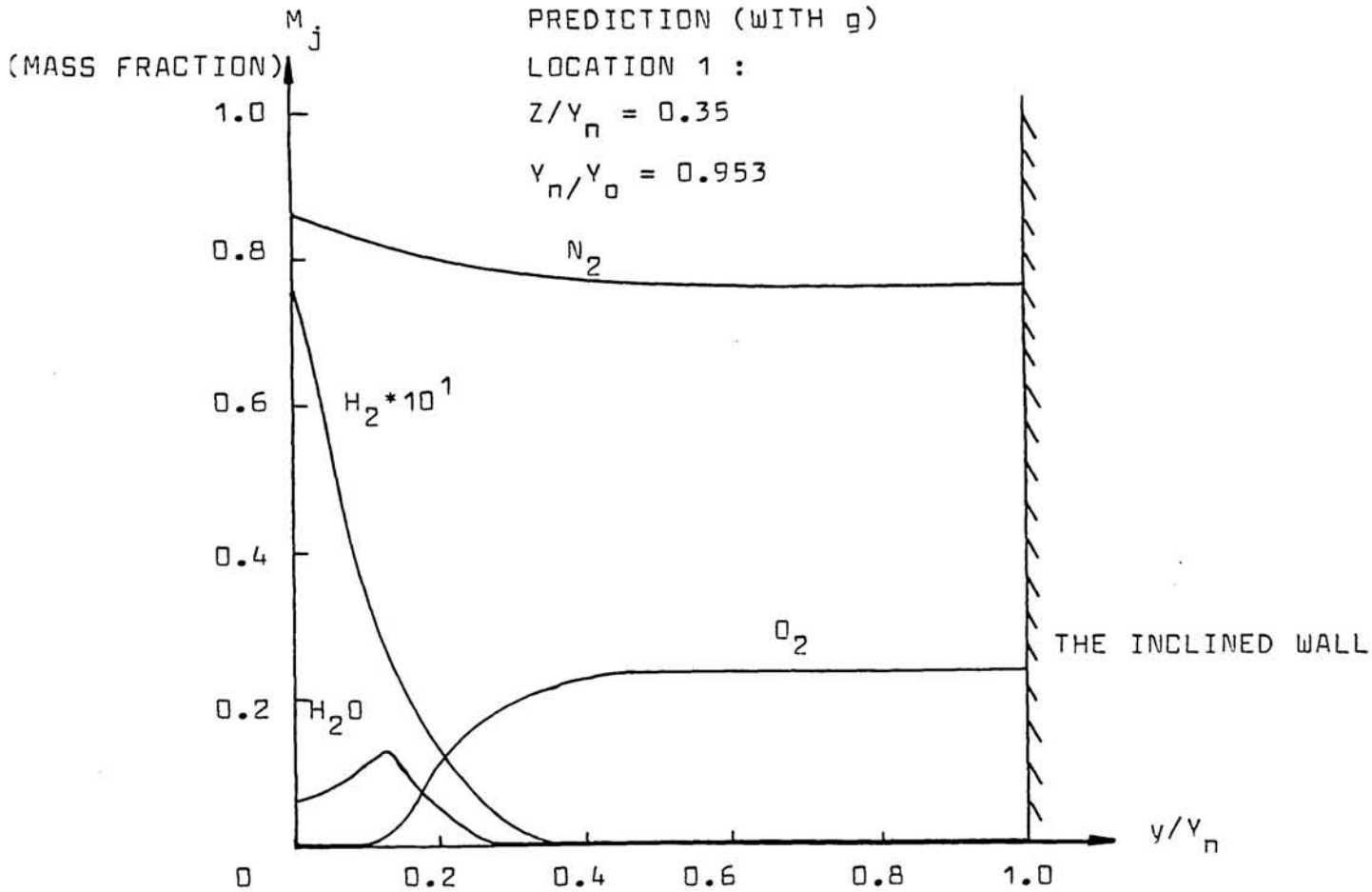

(a) MAJOR COMPONENTS

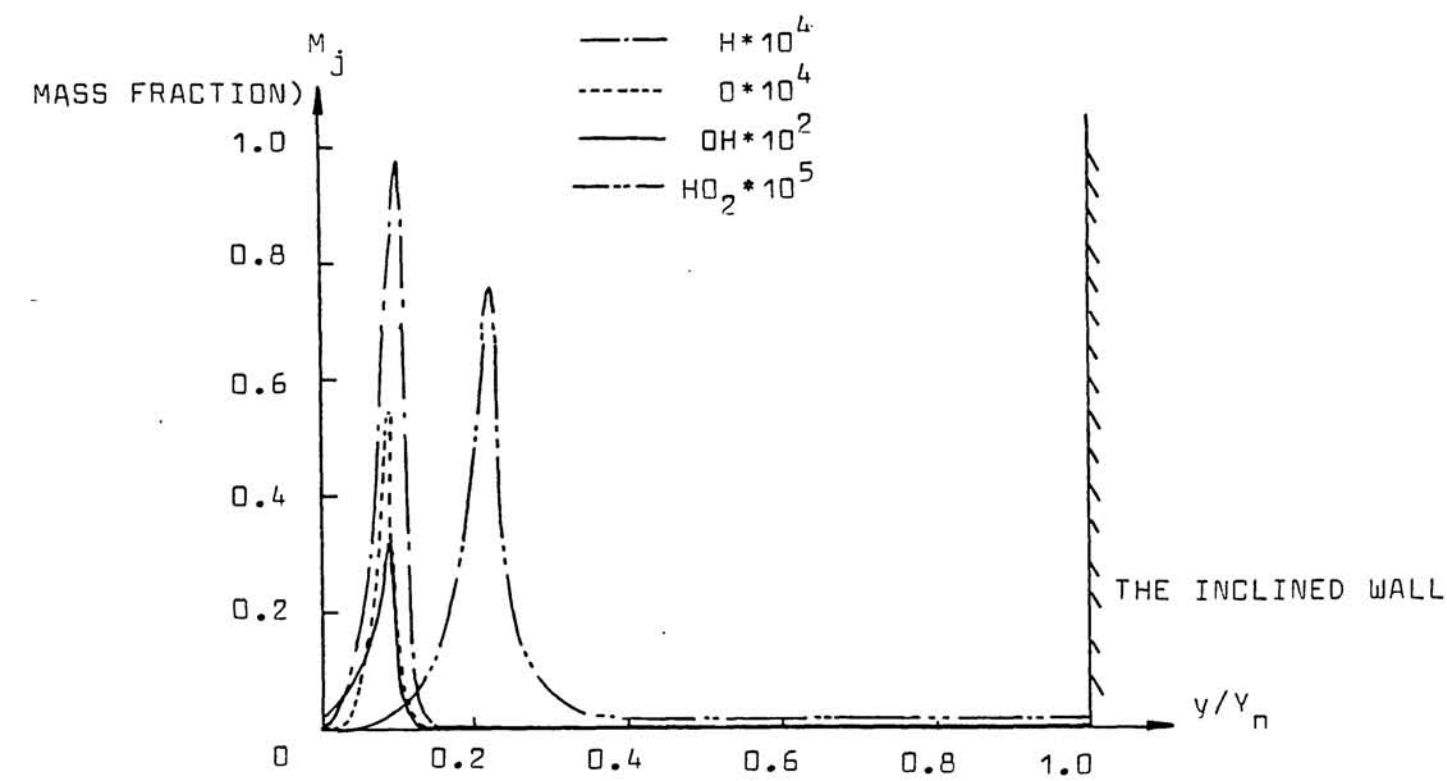

(b) MINOR COMPONENTS

Figure 6.28 SPECIES CONCENTRATIONS VERSUS DIMENSIONLESS DISTANCE IN COMPOSITION PROFILES.

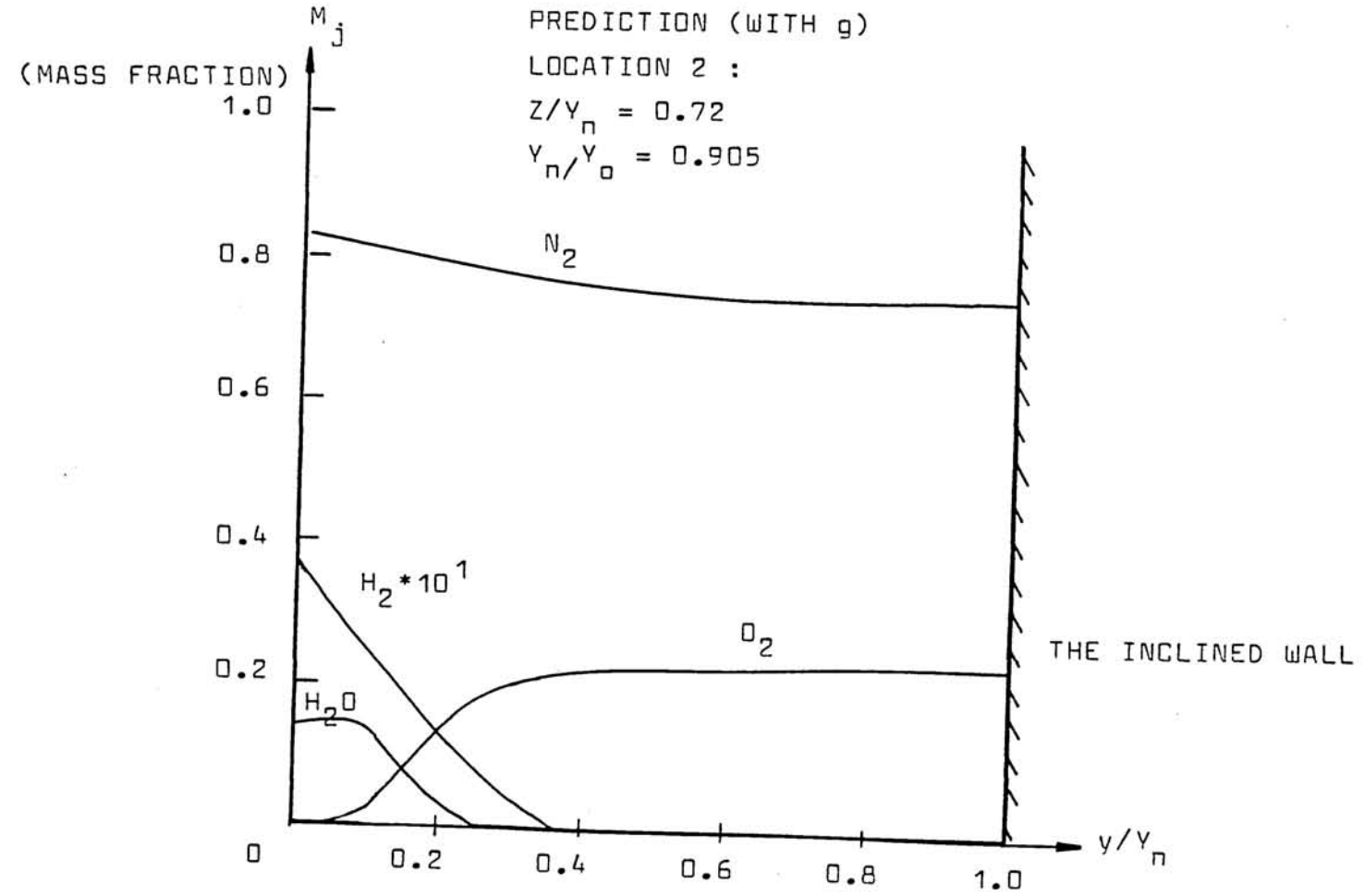

(a) MAJOR COMPONENTS

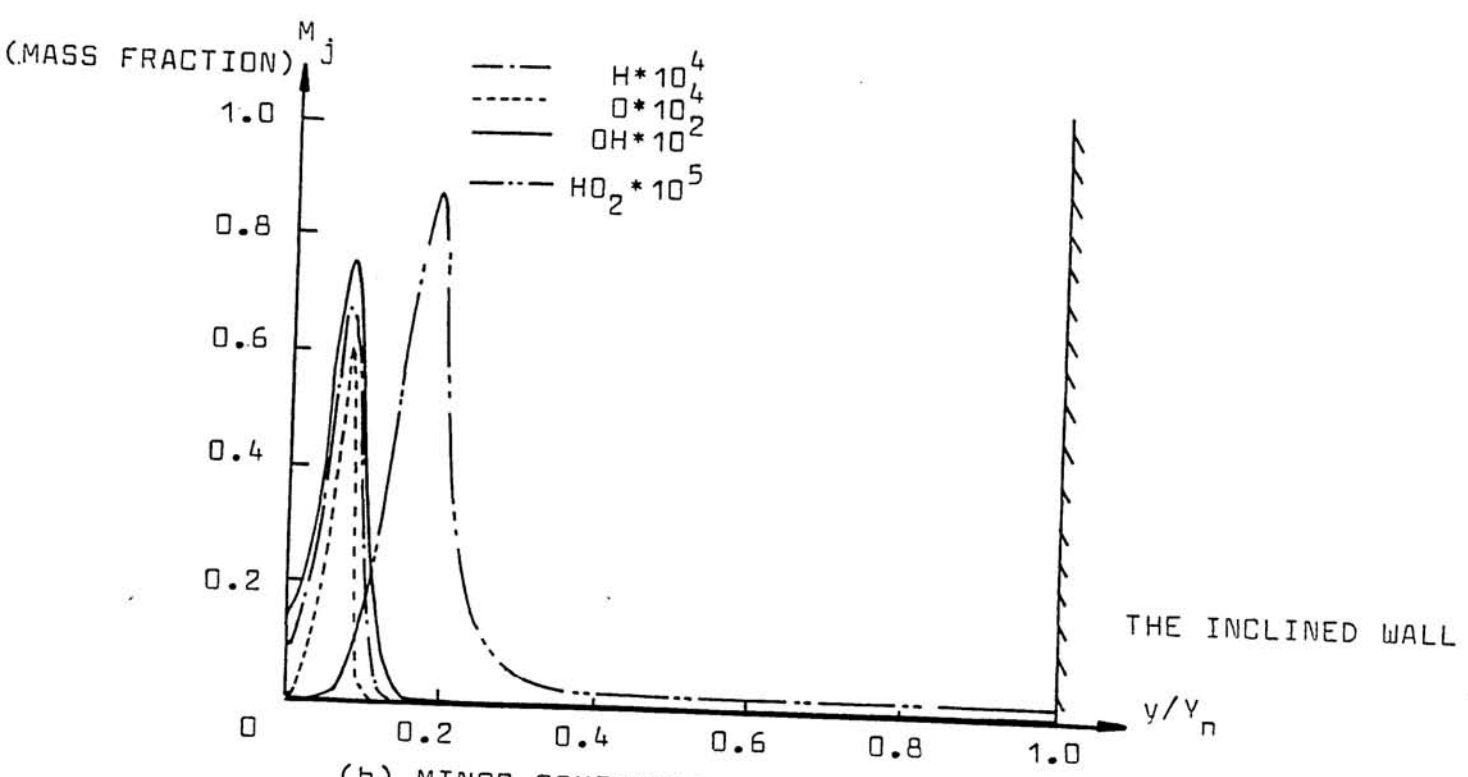

(b) MINOR COMPONENTS

Figure 6.29 SPECIES CONCENTRATIONS VERSUS DIMENSIONLESS DISTANCE IN COMPOSITION PROFILES.

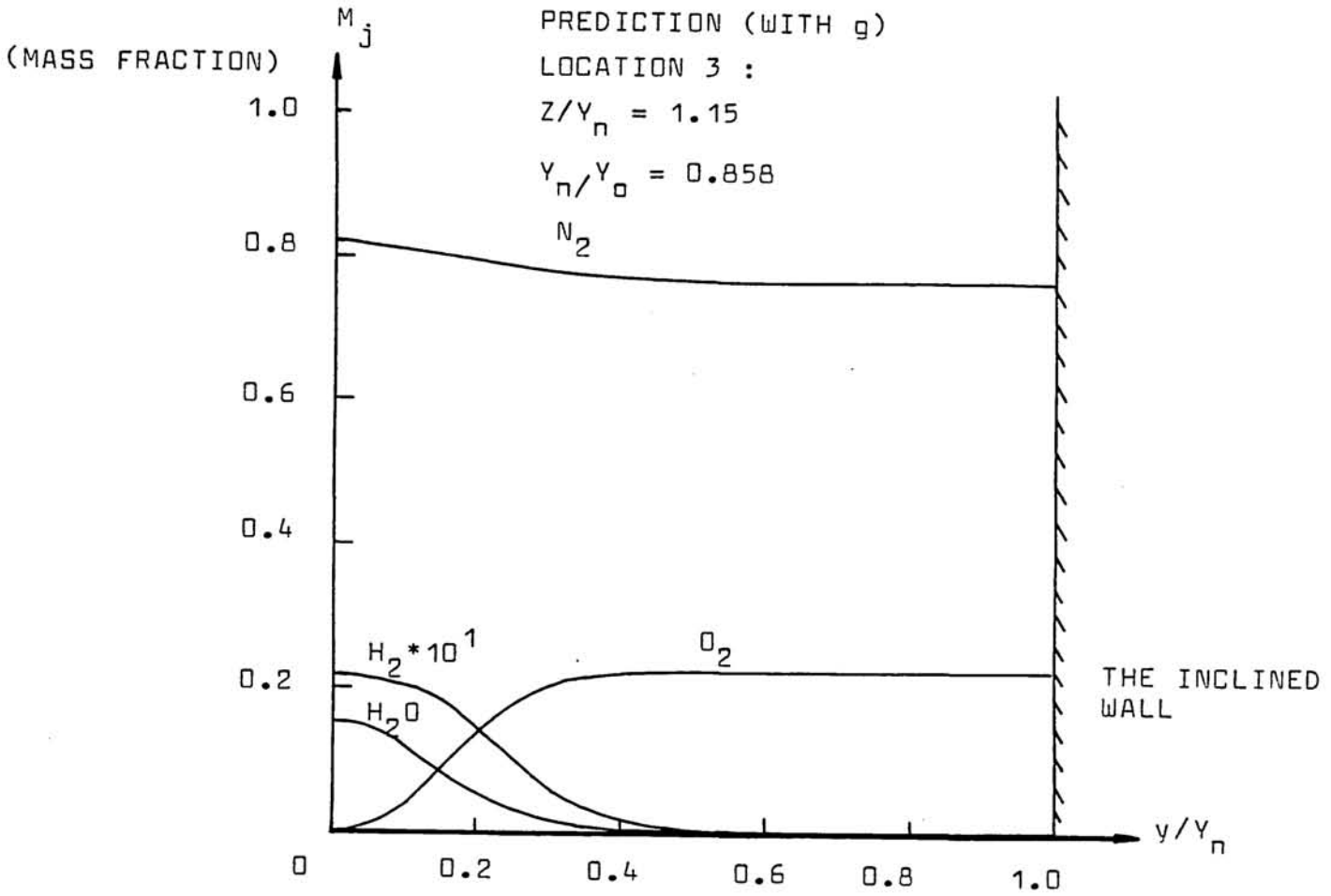

(a) MAJOR COMPONENTS

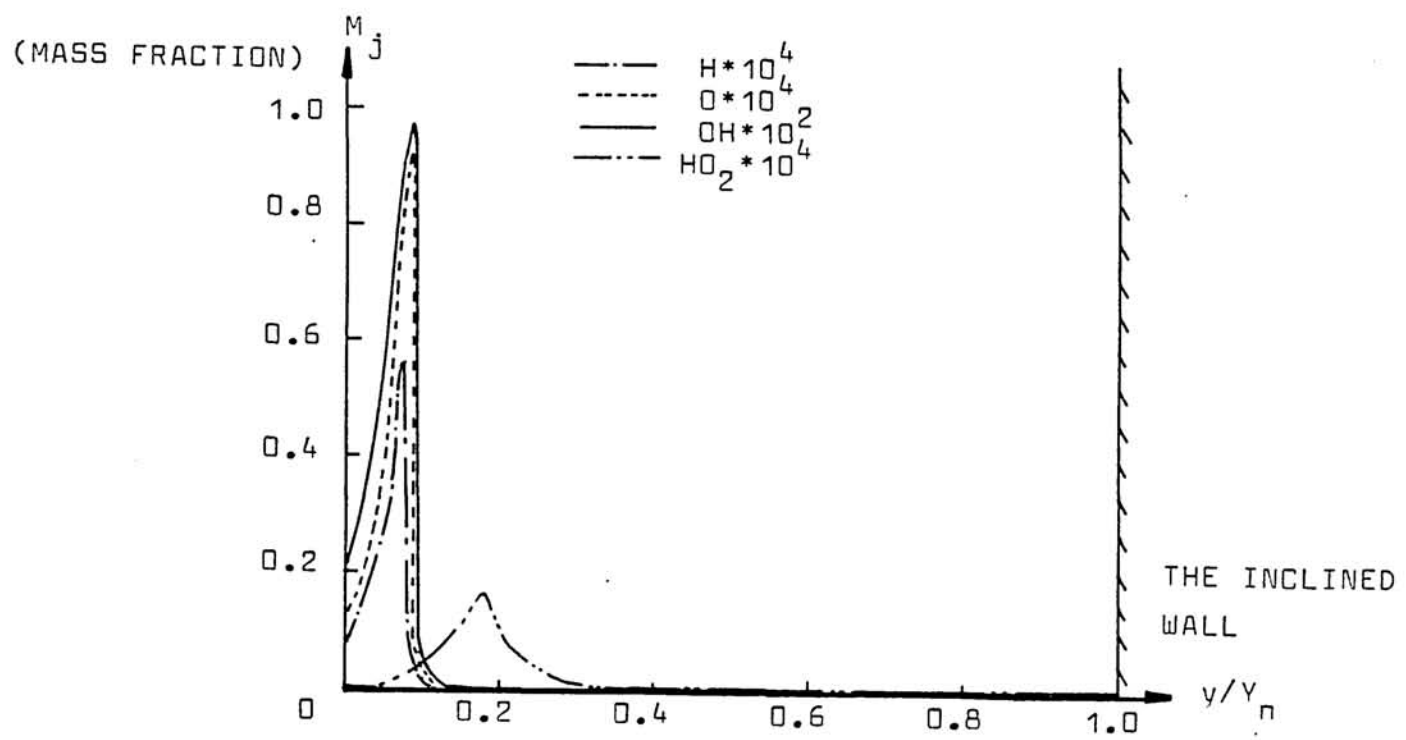

(b) MINOR COMPONENTS

Figure 6.30 SPECIES CONCENTRATIONS VERSUS DIMENSIONLESS DISTANCE IN COMPOSITION PROFILES.

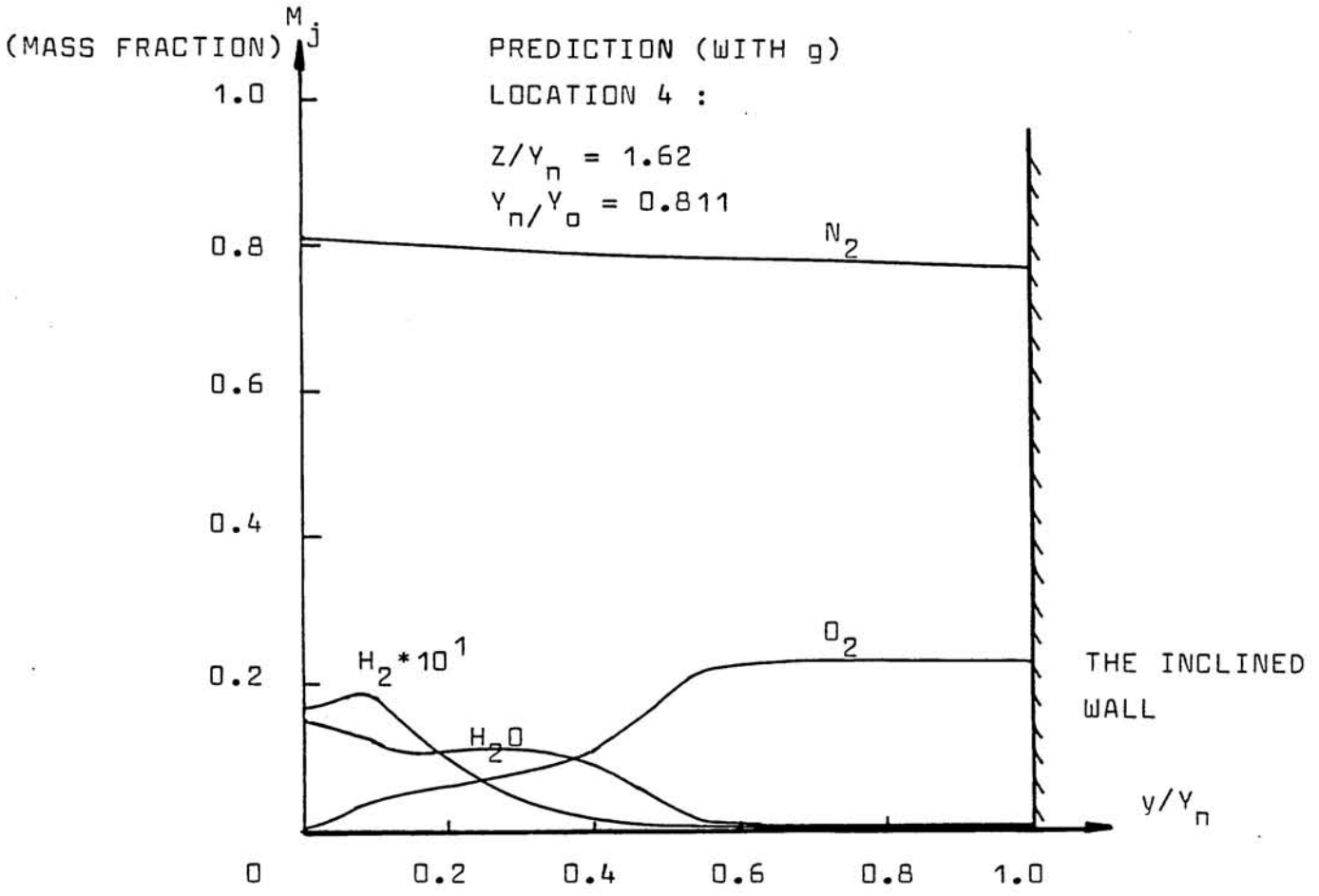

(a) MAJOR COMPONENTS

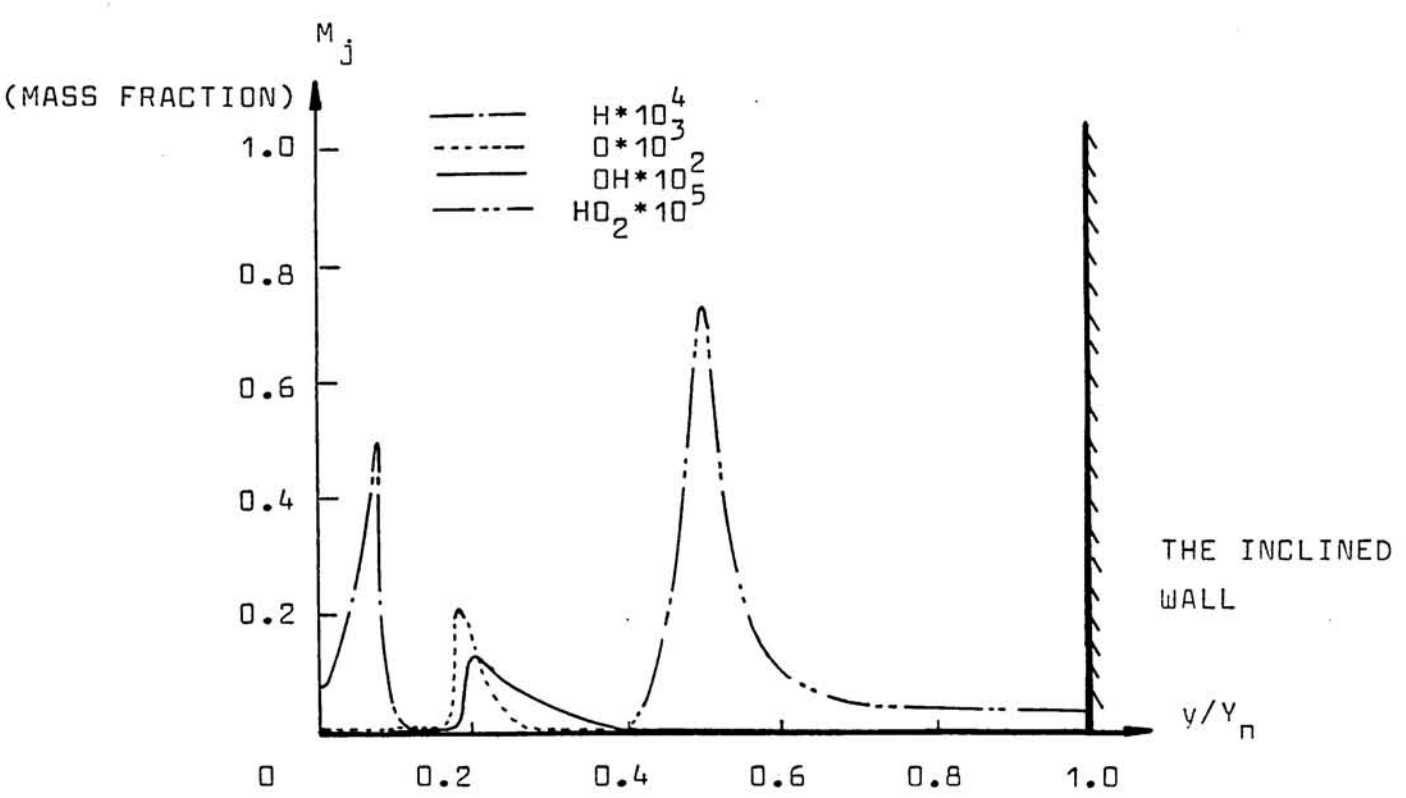

(b) MINOR COMPONENTS

Figure 6.31 SPECIES CONCENTRATIONS VERSUS DIMENSIONLESS DISTANCE IN COMPOSITION PROFILES.

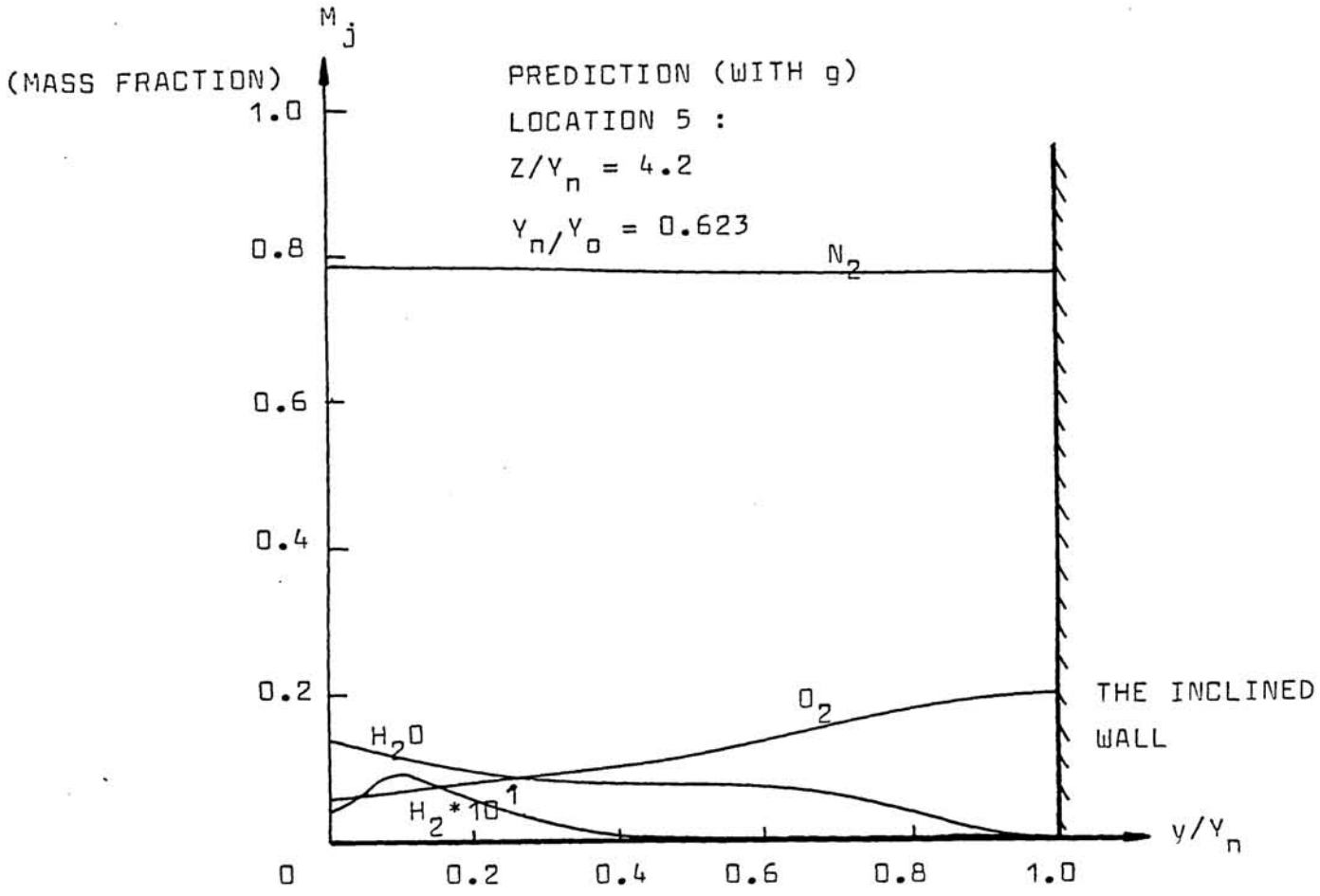

(a) MAJOR COMPONENTS

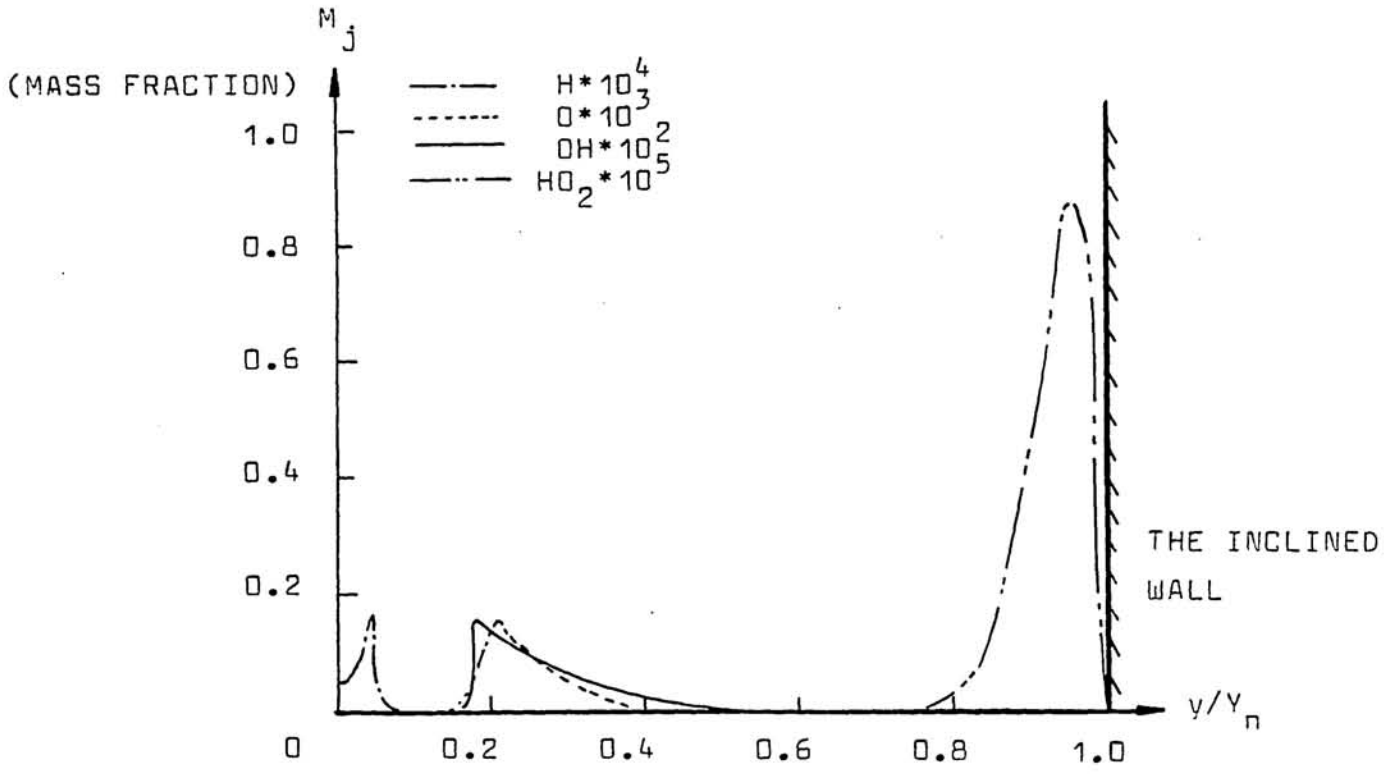

(b) MINOR COMPONENTS

Figure 6.32 SPECIES CONCENTRATIONS VERSUS DIMENSIONLESS DISTANCE IN COMPOSITION PROFILES.

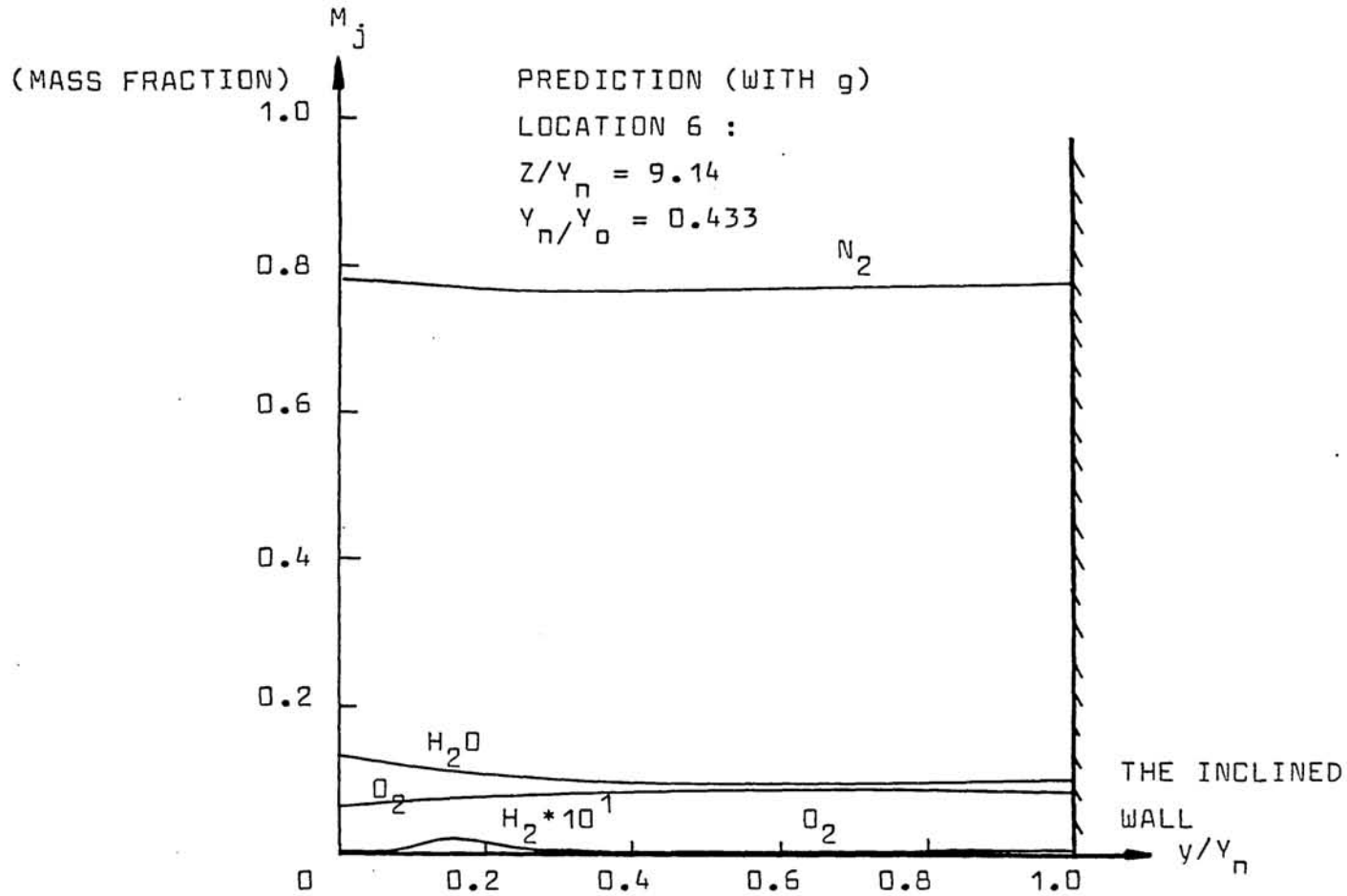

(a) MAJOR COMPONENTS

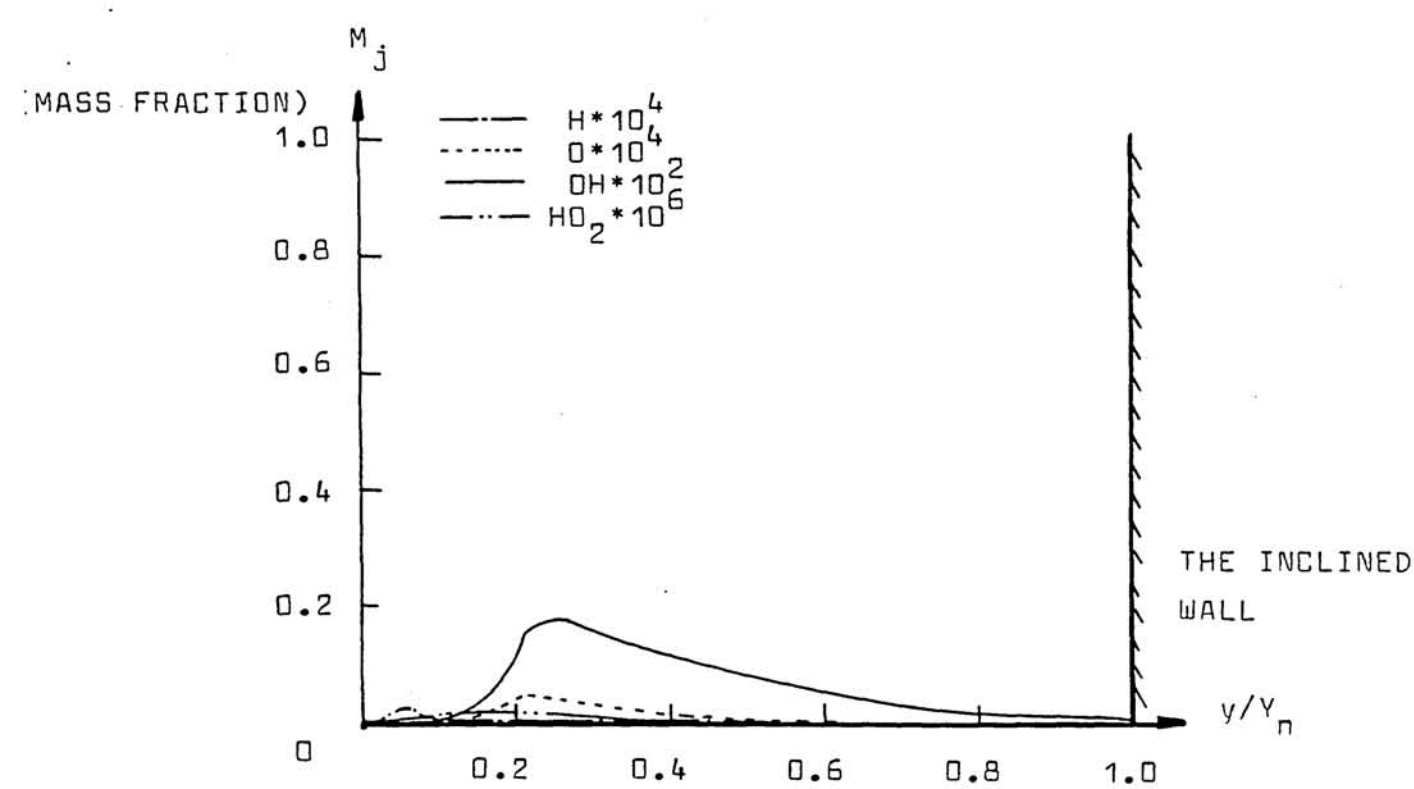

(b) MINOR COMPONENTS

Figure 6.33 SPECIES CONCENTRATIONS VERSUS DIMENSIONLESS DISTANCE IN COMPOSITION PROFILES.

air jets to the centre stretched-flame produces an increase in the rate of stretching.

The gradient of the diffusional flux becomes very steep as a results of cross-fold thickness (Y_N) diminution and entrainment rate increase by buoyancy. The steep gradients increase the rates of inter-diffusion.

It should be recalled that the analytical solution of the isothermal stretched-folds (as shown in Section 6.3) indicates that the stretching rate is increasing linearly with the age path. Since the geometry of the test section for the diffusion converging jet remains unchanged, the stretching rates of the present stretched-flame must be even higher than the isothermal stretched-fold ones.

Effect of chemical kinetics

The choice of the mechanism scheme

A nine-step reaction mechanism of a hydrogen-lean mixture has been applied to the present prediction procedure, because different elementary reactions are only important in different mixture regimes. In view of fuel-lean mixture, reaction steps 8 and 9 (Table 6.4, see Fenimore and Jones, 1959) are particularly useful for describing the rates of radical recombination and

heat evolution in the hydrogen-lean flames. For this reason, steps 8 and 9 have been incorporated into the hydrogen-oxygen mechanism in addition (see Table 6.4), e.g.

$$OH+HO_2 \rightleftharpoons H_2O+O_2$$

$$O+HO_2 \rightleftharpoons OH+O_2$$

Formation of the free radical species

Since combustion proceeds by way of a number of intermediate reactions, each reaction step involving at least one radical species, it is of importance to consider the formation of the free radicals (such as H, OH, O and HO_2). In the present predictions the chemical reaction is dominated by the slow branching reaction:-

$$H+O_2 \longrightarrow OH+O.$$

During the combustion process, the hydroperoxyl radicals are formed mainly by the following steps:-

$$M+H+O_2 \rightleftharpoons HO_2+M$$

and $$H+HO_2 \rightleftharpoons OH+OH$$

(Hastie, 1975; Fristom and Westernberg, 1965; and Dixon, 1970b).

From the results of the predictions, it can be seen that the formation of hydroperoxyl radical, HO_2, is of significance for the lean-hydrogen stretched flame.

Interaction between laminar transport, stretching and chemical kinetics

The initial condition of the fuel layer has been set to a fuel lean mixture. Since the fuel-lean mixture is far from stoichiometry, the chemical reaction rate of the flame is low. The lower flame temperature also descreases the reaction rate for the slow-branching reaction.

When the buoyancy effect is taken into consideration and the cross-fold thickness is diminished continuously, the flame is subjected to fast mixing than chemical reaction. When the operative chemical reaction rates are small compared with the rate of stretching, the Damköhler number ($N_D=t_{str}/t_{react}$) becomes very small. Under these circumstances, the rate of inter-diffusion becomes greater than the reaction. Therefore, the fuel and oxygen can diffuse into the reaction zone. Consequently, the reaction zone could be very thick at the downstream. Thus, the stretched-fold is burned in diffusion/premixed fashion.

6.4.12 Probability-density function of the fold

Cross-fold temperature profiles of the diffusion stretched flame have been interpreted from fold $\tilde{p}d\tau$ distributions ($\tau \equiv$reactedness) as illustrated in Figures 6.34-6.39.

Figure 6.34 shows that a strong spike appears at $\tau=0$ and is connected by an almost horizontal shallow from $\tau=0$ to 1. The result is correspondingly predicted near the initial station.

Figure 6.35 shows that the $\tilde{p}$ distribution starts to increase the mass of the probability-density findings at $\tau=0.8$. This is due to the cross-fold thickness being diminished and the combustion taking place by way of interaction between inter-diffusion and chemical reaction.

Figures 6.36-6.37 show similar trends;that the $\tilde{p}$ distribution continuously increases on the flame temperature region and decreases on the lower temperature region.

Figure 6.38 shows the $\tilde{p}d\tau$ shape is somewhat close to the Gaussian distribution at which the flame is fully burned.

Figure 6.39 shows similar trends as Figure 6.38. In addition, the $\tilde{p}d\tau$ is shifted towards

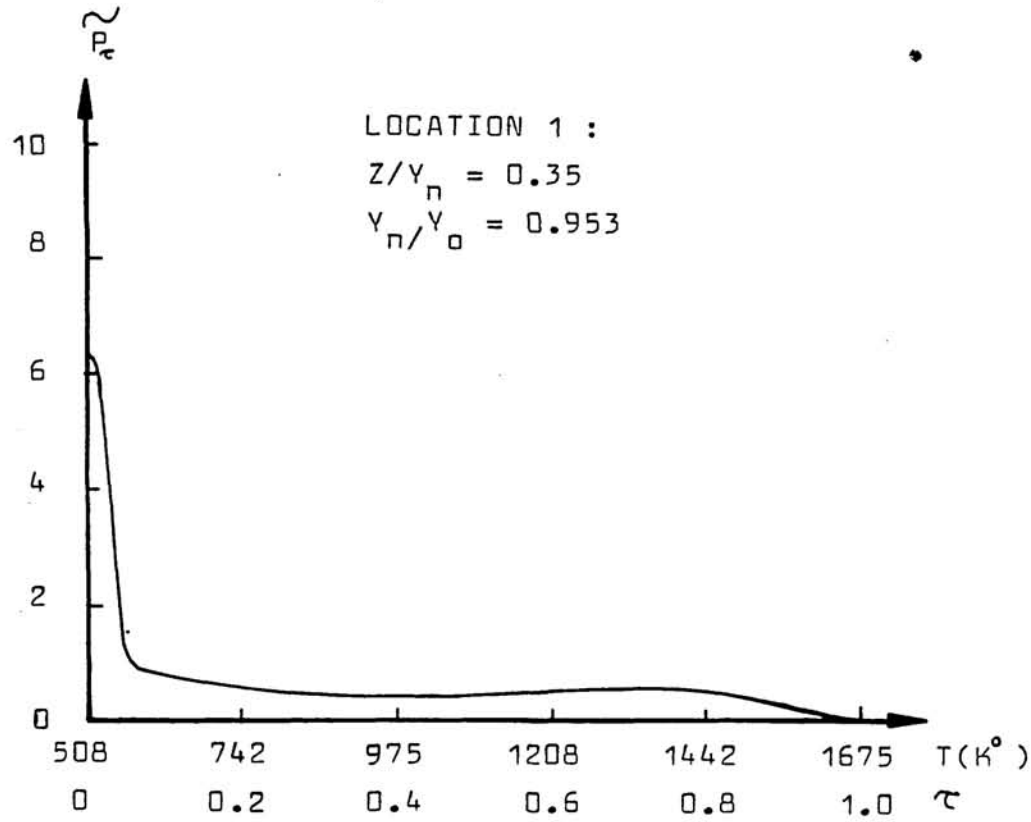

Figure 6.34 PROBABILITY-DENSITY FUNCTION DISTRIBUTION OF REACTEDNESS.

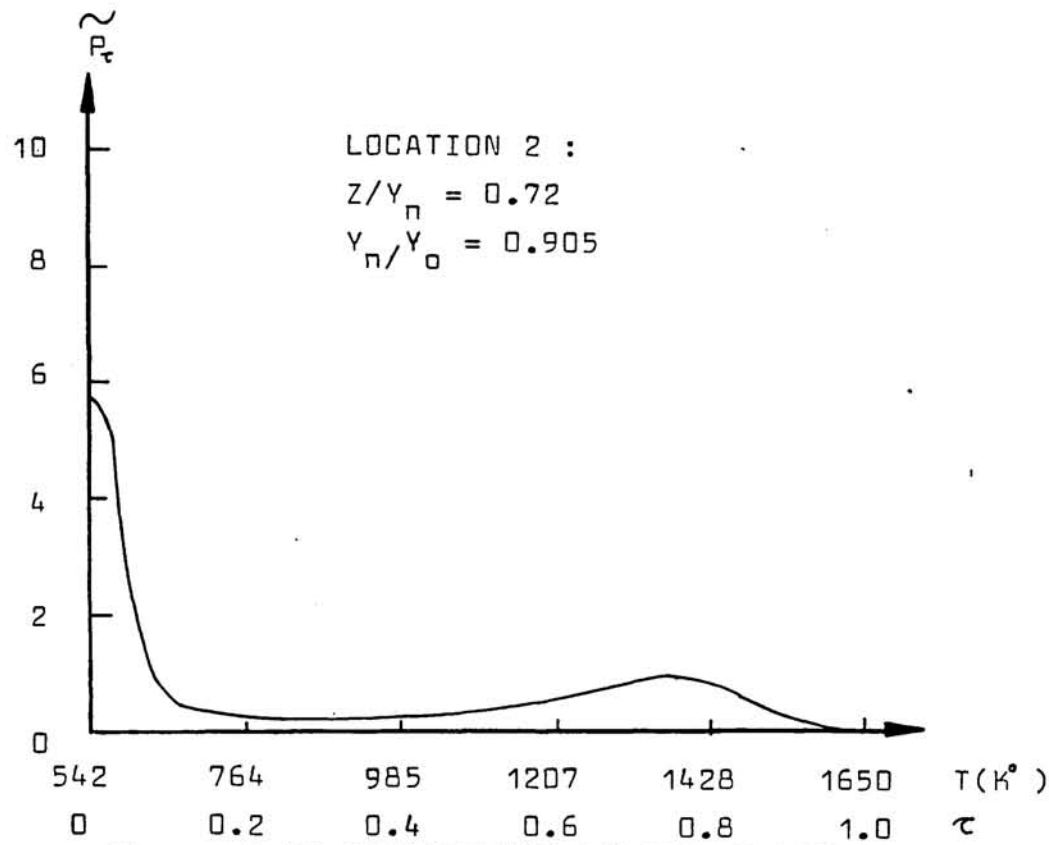

Figure 6.35 PROBABILITY-DENSITY FUNCTION DISTRIBUTION OF REACTEDNESS.

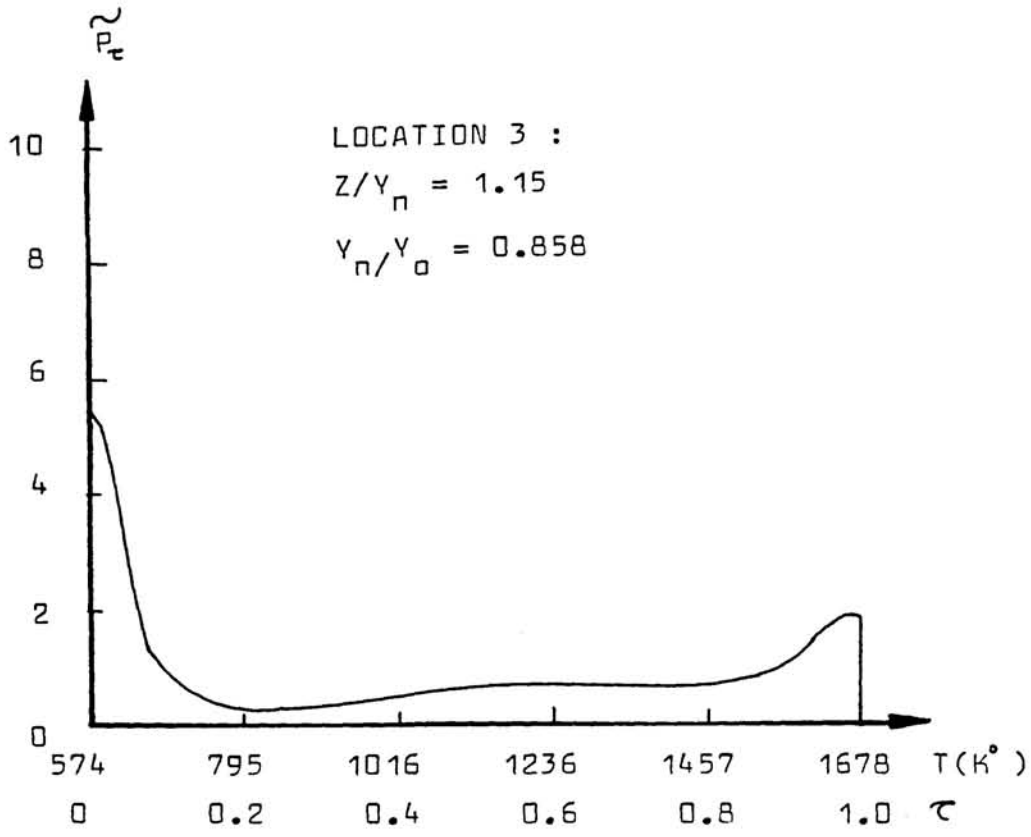

Figure 6.36 PROBABILITY-DENSITY FUNCTION DISTRIBUTION OF REACTEDNESS.

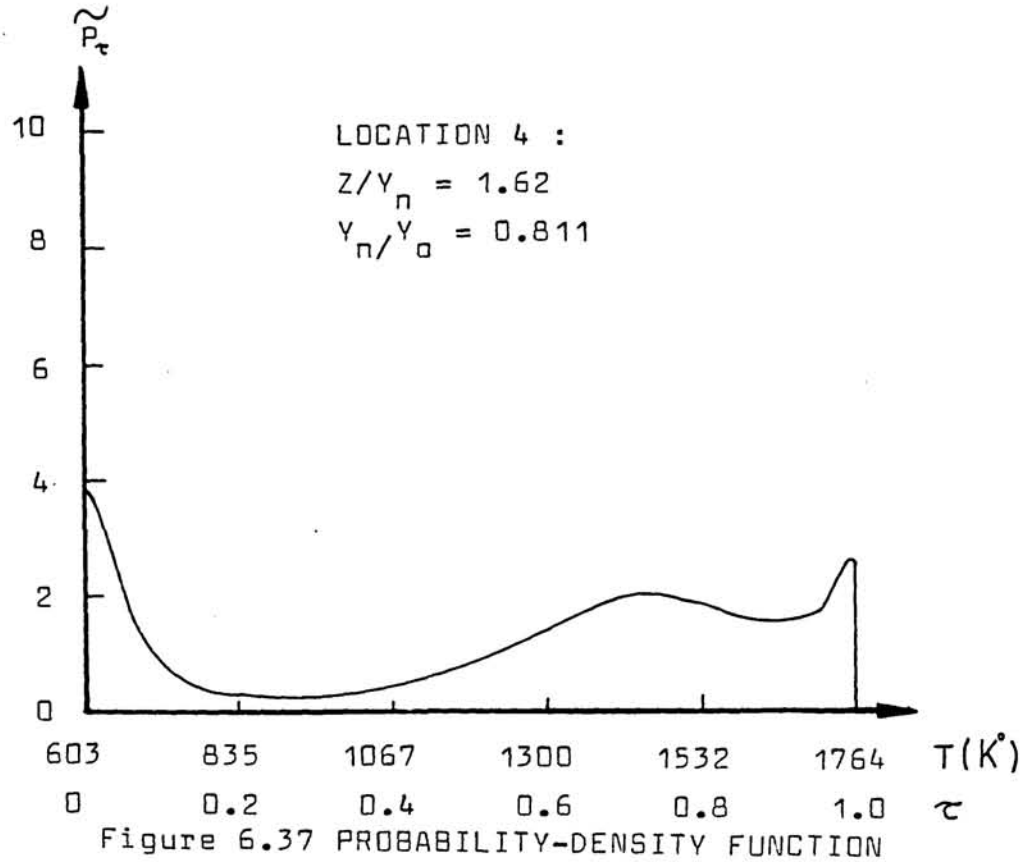

Figure 6.37 PROBABILITY-DENSITY FUNCTION DISTRIBUTION OF REACTEDNESS

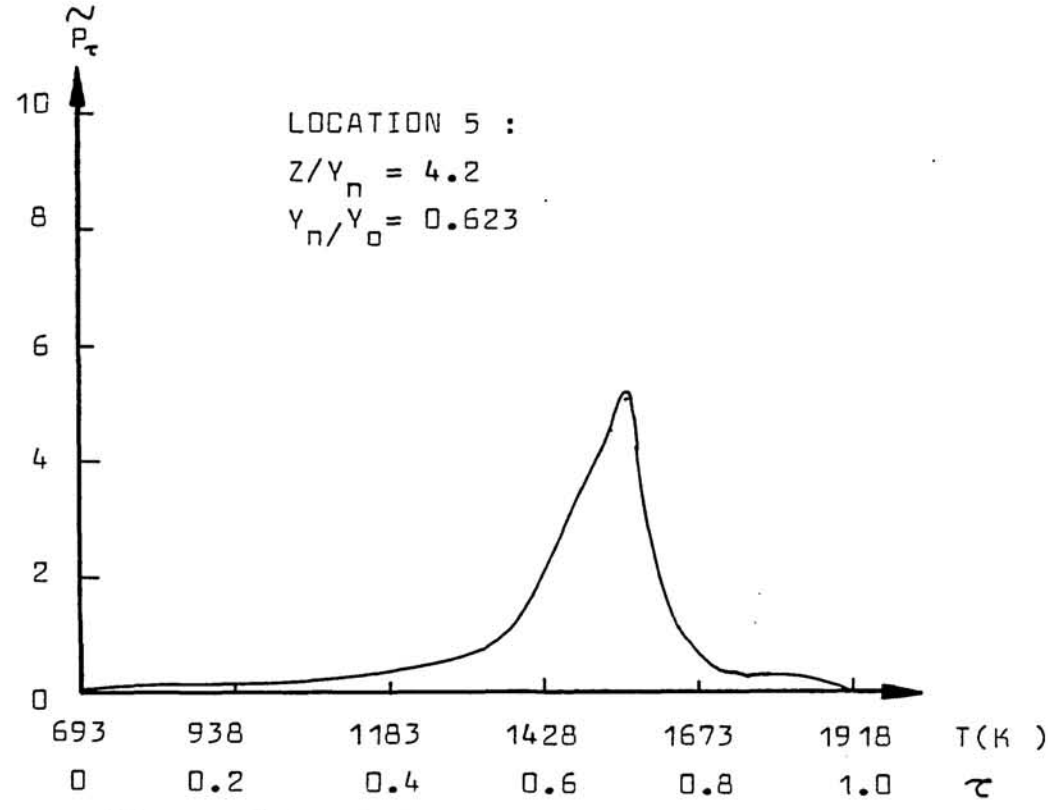

Figure 6.38 PROBABILITY-DENSITY FUNCTION DISTRIBUTION OF REACTEDNESS.

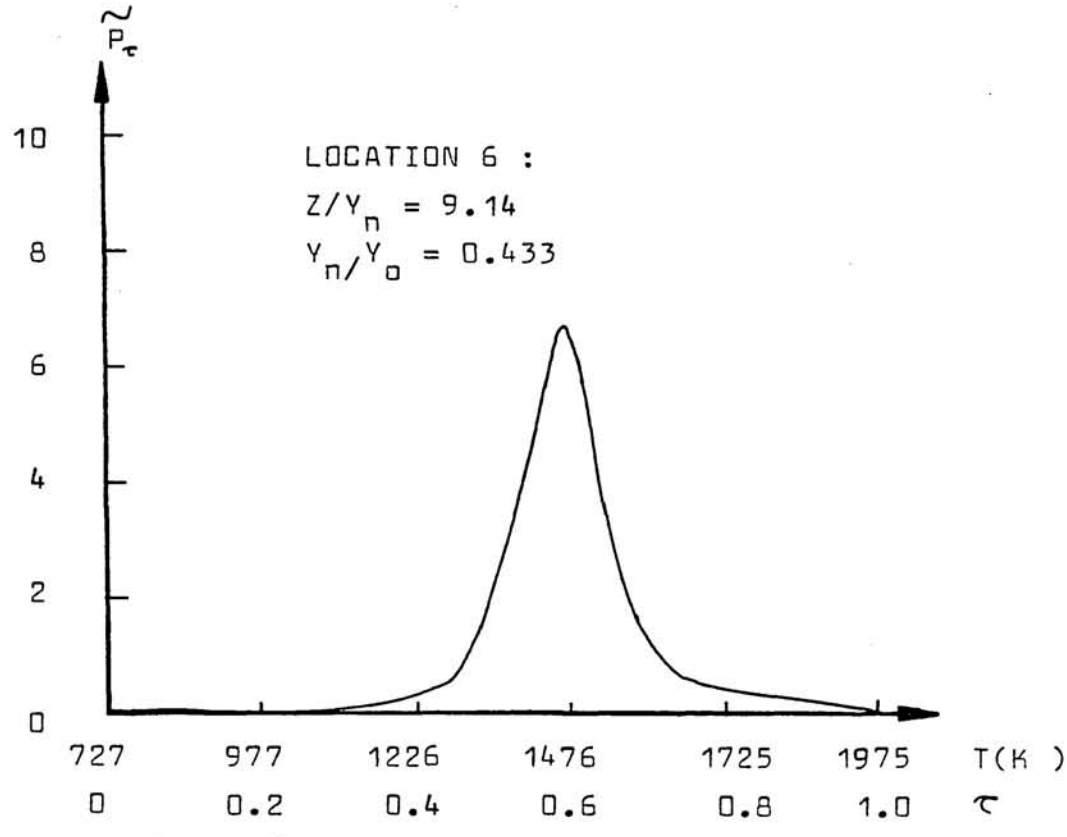

Figure 6.39 PROBABILITY-DENSITY FUNCTION DISTRIBUTION OF REACTEDNESS.

the lower temperature region. This suggests that the combustion has finished and only that mixing and diffusion can be observed.

6.5 Closure

In this chapter, results have been predicted for laminar diffusion stretched-folds. The predictions have been compared extensively with experimental data. The data show that, for the isothermal flow studied, the comparisons are generally in good agreement with the experimental data. For the hydrogen-air combustion results of the comparison are fair.

The present solution procedure (TDMA+SENECKS) shows that the computer time requirement is about 50 times faster than the two-operators splitting method (Kee and Miller, 1978) and about 10 times faster than the CREK code (Wormeck and Pratt, 1976). The numerical solution procedure for solving chemical kinetic equations described in Chapter 3 has been validated that it does not require excessive computer time for comparable accuracy.

In isothermal flow experiments, some examples of the probability-density functions in multiple stretched-folds have been studied theoretically (Section 6.3). It has been observed that the shapes of $\tilde{p}d\phi$ are fairly

symmetric. However, in the combustion experiment, it can be seen that the shapes of $\tilde{p}$ are unsymmetrical. In general, the non-equilibrium structure of this laminar diffusion hydrogen-air stretched-flame shows that the $\tilde{p}$ distributions are far from Gaussian except when the combustion has finished. It is evident that the probability-density function is strongly dependent on the nature of the flow field.

In view of this it is reasonable to conclude that, only the ESCIMO approach has the potential to calculate the $\tilde{p}$df in a realistic way. In Chapter 7, the complete ESCIMO theory will be applied to the study of a well-stirred reactor.

CHAPTER 7 - APPLICATION OF ESCIMO TO THE WELL-STIRRED REACTOR

7.1 Introduction

7.1.1 The problem considered

In this chapter, the ESCIMO theory of turbulent combustion is applied to seven-step chemical reactions between pre-mixed hydrogen fuel and air in a steady-flow well-stirred reactor. A typical spherical stirred reactor is shown in Figure 7.1. The Longwell's spherical reactor usually consists of two concentric spheres with some perforations on the outer sphere for the exhaust of combustion products; the inner spherical surface is also perforated and connected to a tube supplied with the inflowing fresh mixture. If the injection holes have small enough diameters, the high-velocity jets of the supply mixture will induce recirculation and random turbulence. However, the stirring action is so great that the time-average statistical properties of the mixture are independent of position in the reactor.

7.1.2 Previous work

The "kinetic-only theory" approach

The "kinetic-only" procedure was first applied to the theory of ideal stirred-reactor by Longwell (1955). The major assumption of this procedure is that the turbulent

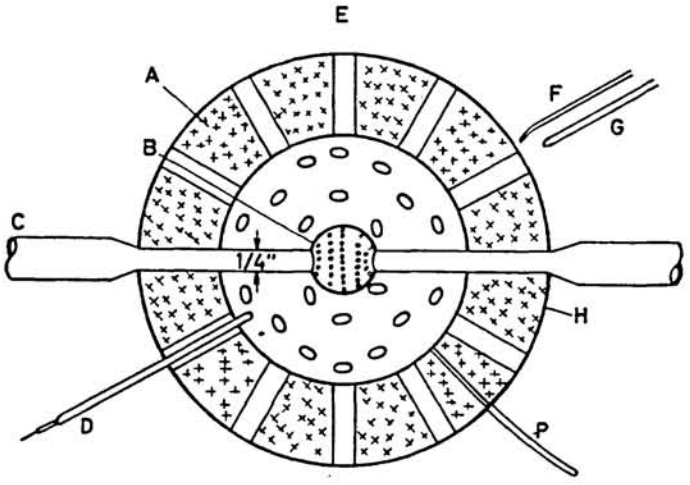

FIGURE 7.1 A TYPICAL SPHERICAL STIRRED REACTOR
(LONGWELL AND WEISS, 1955)

A: INSULATING FIREBRICK, INTERNAL DIAM. 3 IN.

B: INJECTOR SPHERE, STAINLESS STEEL, OUTSIDE DIAM. $\frac{3}{4}$ IN., INSIDE, IN.; 68 HOLES, 0.047 IN. DIAM.

C: INLET TUBE, STAINLESS STEEL, OUTSIDE DIAM. $\frac{1}{2}$ IN.

D: GAS SAMPLE PROBE, STAINLESS STEEL.

E: EXIT HOLE (ONE OF 60), $\frac{1}{4}$ IN. DIAM.

F: SPARK WIRE.

G: HYDROGEN IGNITION JET.

H: NICKEL SHELL, OUTSIDE DIAM. 5 IN., 0.038 IN. THICK.

P: PRESSURE TAP.

fluctuation is negligible. Consequently, the time-average reaction rate is the same function of the time-average concentration and temperature as that of the instantaneous rate of instantaneous combustion and temperature. Hence, full knowledge of chemical kinetics can be incorporated.

Longwell and Weiss (1955) first investigated the combustion of a well-stirred reactor with various fuels. As a result of increasing the mass inflow rate, decreasing the pressure or departing from the reactive mixture ratio, they found that the flame was extinguished. They reported that the blow-out limit for a given equivalence ratio was determined by the loading factor G/VP^n, where G is the molar feed rate of fuel; V is the reactor volume; P is the absolute pressure in the reactor; and n is the overall reaction order.

The effects of the geometry of the reactor and the optimum number of feed holes were investigated by Blichner (1962), Hottel, William and Miles et al (1967). Blichner employed propane as a fuel by varying the equivalence ratio to observe the blow-out limit. Hottel and Miles (1967) employed the scattered-light technique which was originally developed by Rosensweig (1961) and improved by Becker et al (1963) to investigate similar phenomena. A hydrocarbon-fog tracer was

chosen for this investigation, hence, the mixing phenomena can be studied experimentally and the difficulty of combustion in the well-stirred reactor can be avoided. A postulated second-order reaction rate based on this cold-air model was expressed in an Arrhenius form and the kinetic constants were thus obtained (Miles, 1964).

Pratt and Starkman (1970) applied a one-step reaction scheme to ammonia-air in an adiabatic, well-stirred reactor. The equivalence ratio and the temperature were measured with the mass spectrometer, and the Chr/Al thermocouple, respectively. The experimental results were plotted in a stability map which is represented as the equivalence ratio versus the air-loading diagram. The best 'fit' kinetic constants were therefore found.

Jenkins and Spalding (1967) employed a 9-step hydrogen-oxygen mechanism to investigate a steady-flow adiabatic stirred-reactor. Measurement of temperature in the reactor was made under a wide range of conditions for different initial composition, temperature and mass inflow rate. A plausible set of elementary reactions was postulated and the values of the rate constants were determined which gave the best agreement with the experimental data.

Results of the above studies are usually expressed in terms of the maximum volumetric reaction rate for the

aggregate of the participating reactions, and of the corresponding blow-out limit. These quantities are found to be related to the kinetic constants.

The "hydrodynamic+kinetic theory" approach

Since the concentration fluctuation in the turbulent combustion can never be ignored, any theory related to turbulent combustion should be capable of predicting the behaviour of turbulent reacting flow correctly. Hence, the theory of a well-stirred reactor has been revised by Evangilista (1969) and Pratt (1976) using the fragment-coalescence procedure. Borghi et al (1974) employed the presumed-pdf procedure in which the influences of hydrodynamic and chemical kinetics can be taken into account. However, there are at least two defects in these procedures. First, by using the fragment-coalescence approach, the molecular transport is regarded as being so rapid as to allow the fragments to coalesce and to mix instantly; hence, the influence of the laminar transport terms on the turbulent flame prediction is absent. Secondly, the root-mean-square fluctuations are determined by the presumed-pdf procedure which is questionable, and the results are found to be dependent

strongly upon the presumed-pdf shape (see Section 7.4).

7.1.3 Review of earlier results by ESCIMO approach

The ESCIMO approach can be regarded as the "hydrodynamics+ transport+kinetic" theory of turbulent reacting flows (Spalding 1979e). The distribution function of the fold population with respect to age in a well-stirred reactor was given by Spalding (1978b). The application of the ESCIMO theory to a one-step exothermic chemical reaction between pre-mixed fuel and air in a steady-flow well -stirred reactor was investigated by Spalding (1979a, 1979e). The influences of mass fraction of fresh gas in a newly formed fold and the residence time on the well-stirred reactor with the aid of one-step exothermic chemical reaction between pre-mixed fuel and air were investigated by Ma, Spalding and Sun (1980). All the above results were characterised in three dimensionless time ratios. These time ratios will also be used for the present investigation.

7.1.4 Purposes of the present study

The purposes of the present study are:

- To show that the influences of hydrodynamics, Laminar-transport and chemical kinetics on the performance of a well-stirred reactor can be taken into consideration by the established theory.

- To extend the ESCIMO approach to multiple chemical reactions in the hydrogen-oxygen-nitrogen system.
- To show that it is possible to compute the root-mean-square values of concentration fluctuations from the knowledge of probability-density functions.
- To present some quantitative results, and to explain the various phenomena which arise in the well-stirred reactor.

7.2 Mathematical Description

7.2.1 Method of analysis

The ESCIMO theory is applied in the present study. The method of analysis discussed by Spalding (1979a) is employed. The complete ESCIMO theory combines the two elements, namely, the micro-aspect and the macro-aspect which will be described as below.

7.2.2 Assumptions for macro-scale aspect

The system considered is that of the ideal well-stirred reactor in which:

- the pre-mixed mixture of N_2-H_2-O_2 is continuously, and steadily injected;

- the time-average statistical properties of the mixture are independent of position in the reactor;
- the properties of the mixture in the steady exit stream are the same as those in the reactor;
- the pressure is uniform in the reactor; and
- the reactor walls are impervious to heat and inert chemically.

7.2.3 Demographic analysis

The residence time

The residence time of the well-stirred reactor is defined as:

$$t_{res} = \frac{\rho_o V}{\dot{m}} \quad , \qquad (7.2\text{-}1)$$

where ρ_o is the density of outlet gases;

V is the reactor volume;

and $\dot{m}$ is the mass flow rate through the well-stirred reactor.

This time scale is very significant. A low value of $\frac{\dot{m}}{V}$ implies the residence time is long, a zero value corresponds to equilibrium and a high value implies short residence time. When the residence time diminishes sufficiently,

extinction takes place.

Engulfment (fold formation)

The injected gases, through the feed holes, engulf their own mass of recirculating hot gases from the reactor. Folds having initial fold-sizes are formed by the interleaves of unburned and burned layers with the initial mass fraction of unburned material M_o. The fold formation rate, $\dot{R}$, is therefore given by:

$$\dot{R} = \frac{\dot{m}}{M_o \rho_o V} \quad . \qquad (7.2\text{-}2)$$

Re-engulfment

Folds leave the recirculation zone ("death") in two ways: they may disappear through the outlet orifices, or they may be re-engulfed into new folds. Since the rate of the inflow and the rate of outflow should be the same, the rate of re-engulfment is deducible from the rate of inflow and the mass fraction of fresh gas in a newly-formed fold, as already given in equation (7.2-2).

Population distribution function

Let m'da be the mass of material in the reactor having ages between a and a+da, the total mass of gas in the

reactor is given by:

$$\rho_o V = \int_o^\infty m'da \quad . \qquad (7.2\text{-}3)$$

Substituting equation (7.2-3) into equation (7.2-1) yields:

$$\frac{\dot{m}}{\int_o^\infty m'da} = \frac{1}{t_{res}} \quad . \qquad (7.2\text{-}4)$$

If $p_a da$ represents the probability-density function of fold material m'da which lies between ages a and a+da, then p_a is written as:

$$p_a = \frac{m'(a)}{\int_o^\infty m'da} \quad . \qquad (7.2\text{-}5)$$

Since the rate of fold formation, $\dot{R}$, is supposed to be uniform throughout the reactor, and since the time-average statistical properties of the mixture are independent of position in the reactor, the turbulent transport equation of fold population distribution function can be simplified as:

$$\dot{p}_a = 0 \quad . \qquad (7.2\text{-}6)$$

Hence, the variation of p_a with time must be given by (Spalding (1978b):

$$\frac{\partial p_a}{\partial t} = - \frac{\partial p_a}{\partial a} - \dot{R}\, p_a = 0 \quad . \qquad (7.2\text{-}7)$$

The first term on the right represents the movement of material m' as a result of aging. The second term represents the m' decreases as a result of outflow and re-engulfment.

In the steady-state, $\frac{\partial p_a}{\partial t}$ must be equal to zero. By integration and insertion of an integration constant- ($p_a\{0\} = \frac{\dot{m}}{M_o\ \rho_o\ V}$), the $p_a\{a\}$ function is:

$$p_a = \frac{1}{M_o\ t_{res}} \mathrm{Exp}(- \frac{a}{M_o\ t_{res}}) \quad . \qquad (7.2\text{-}8)$$

7.2.4 Assumptions for micro-aspect

Fold at the birthplace

It is supposed that all fold sizes at the birthplaces have the same initial fold thickness Y_o and the same mass fraction of unburned material M_o. The initial fold thickness Y_o is supposed to be of the order of the hole diameter through which the gas is injected. The value of M_o is specified in accordance with the assumption of the initial burned-to-unburnedmasses ratio. Effects of M_o will be investigated.

Stretching rate

In view of the macro-scale aspect, the time-average properties in the reactor are uniform and the stretching rate is one. The stretching rate due to the time-average mean motion is supposed to be uniform throughout the fold biographic investigation and of the order of the injection velocity divided by the hole diameter.

During the stretching process, the fold thickness is continuously diminished in accordance with:

$$\frac{d}{da} \ln \int_{o}^{Y} \rho dy = - \frac{1}{t_{str}} \quad , \qquad (7.2\text{-}9)$$

where the stretching time, t_{str}, is the reciprocal of the stretching rate.

Extension of the ESCIMO approach to multiple reactions

The main advantage of the ESCIMO approach is that the analysis of the biographical part can be separated from the demographical one, hence, the most advanced knowledge of chemical kinetics and of molecular transport can be incorporated.

Chemical kinetic

The 7-step of the reaction mechanism of hydrogen-oxygen-

nitrogen system described in Chapter 2 is used in the present study.

Molecular transport

Again, the diffusion model of calculating the laminar transport properties described in Chapter 2 is also employed here.

7.2.5 Biographic analysis

It has been shown in Chapter 2, from which the following results are obtained, that variations of fold-average quantities with age are analysed with the aid of a moving observer. Hence, the governing equations employed are the same as in Section 2.4.

7.2.6 The coupling of demography and biography

The problem

The gases in the stirred-reactor contain folds of all ages, in accordance with distribution function of equation (7.2-8). Since folds of all ages are considered, the space-average property, $\overline{\phi}$, must be written as:

$$\overline{\phi} = \int_0^\infty \tilde{\phi}(a)\, p_a \, da \quad . \qquad (7.2\text{-}10)$$

Since all fold-average properties at the old age (i.e. $a \geq t_b$) must be the same as the corresponding fold-average value at the burn-out time, equation (7.2-10) is expressed as follows:

$$\overline{\phi} = \int_o^{t_b} \tilde{\phi}\langle a \rangle \, p_a \, da + \tilde{\phi}\langle t_b \rangle \int_{t_b}^{\infty} p_a \, da \, . \qquad (7.2\text{-}11)$$

The final expression of $\overline{\phi}$ is given by:

$$\overline{\phi} = \int_o^{t_b} \tilde{\phi}\langle a \rangle \, p_a \, da + \tilde{\phi}\langle t_b \rangle \left| 1 - \int_o^{t_b} p_a \, da \right| . \qquad (7.2\text{-}12)$$

However, the $\tilde{\phi}\langle a \rangle$~a relation depends upon $\overline{\phi}_{b,o}$ (i.e. space-average of ϕ from the reactor which enters the freshly-formed fold). Hence, the computation is iterative in nature.

Iterative procedure

The following guess-and-correct procedure which was first introduced by Spalding (1979a) is employed.

1. All the population-average quantities are assumed to be at equilibrium.* Hence, the composition of species concentrations in the hot stream can be determined initially by the method of mini-

---

* If the chemical-kinetic scheme is finite, the iterative procedure will lead the solution from equilibrium to kinetic state.

misation of Gibbs free-energy, as described in Chapter 3.

2. The fold biography of the ESCIMO approach is analysed according to Chapter 3. Thereby, the variations of fold-average quantities with age are obtained.

3. The overall population-average quantities are calculated by being multipled by the population-distribution function and then added in proportion to the contributions of each age interval as already expressed in equation (7.2-12).

4. Employ this as a new guess for $\overline{\phi}_{b,o}$ and repeat steps 2 and 3.

5. Continue until no appreciable change in $\overline{\phi}_{b,o}$ occurs.

The sample computations

All the computations have been performed for a hydrogen-oxygen-nitrogen mixture, having the inlet conditions:

MASS FRACTION								Temperature	Equivalence Ratio
N_2	O_2	H_2	H_2O	O	H	OH	HO_2		
0.71725	0.217898	0.0648508	0	0	0	0	0	298^oK	2.38

The chemical-kinetic data and the transport properties have been given in Chapter 2, and the gases are ideal.

Computational details

As already discussed in Section 4.5, all results obtained here are based on 40 cross-fold grid nodes, with the age interval factor, FRA=0.02. The grid-independent criteria are: N=40 (number of cross-fold grid nodes); and δa = the least of $(0.02 t_{diff}(\frac{Y}{Y_o})^2$, $0.02\ t_{str}$, $0.02\ t_{react})$.

Normally, the iterative procedure described in the previous section requires three iterations for satisfactory convergence. Therefore, the computational requirements for a typical run are about 30K words of storage space, and about 300 seconds execution time on the CDC 6600 computer.

7.2-7 Dimensional analysis

The performance of a well-stirred reactor can be characterised by the dimensionless quantities:
(1) the chemical loading; (2) the Reynolds number; (3) the mixing rate; and (4) M_o. These appear respectively as (Spalding, 1979e):

Chemical loading $C_1 \equiv \frac{\dot{m}}{\rho_o \; V \; r_{ref}}$; (7.2-14)

Reynolds number $C_2 \equiv \frac{\dot{m} \; V^{1/3}}{n \; A \; \mu_o}$; (7.2-15)

Mixing rate $C_3 \equiv \frac{n \; A}{V^{2/3}}$; (7.2-16)

and $\tilde{\tau}_o = (1-M_o)\bar{\tau}$; (7.2-17)

where $\dot{m}$, ρ_o, V, r_{ref} have been described above;

n is the number of injection holes;

A is the area of an injection hole;

and μ_o is the turbulent viscosity of the outflowing gas.

In practice, the hydrodynamic behaviour of the reactor shows that the number of injection holes, n; the ratio of the size of the reactor to the feed-hole diameter, $\frac{V^{1/3}}{Y_o}$; and the ratio of the turbulent viscosity to the laminar viscosity, $\frac{\mu_o}{\mu}$ are of the order of 10^2 (Blichner, 1962; Hottel, Williams and Miles, 1967).

Controlling parameters

According to Spalding (1979e), the performance is computed as a function of the three independent dimensionless time ratios corresponding to the chemical loading, the Reynolds number, and the mixing rate:

$$C_1 \alpha \frac{t_{react}}{t_{res}} \quad ;(7.2\text{-}18)$$

$$C_2 \alpha \frac{t_{diff}}{t_{res}} \quad ;(7.2\text{-}19)$$

$$C_3 \alpha \frac{t_{str}}{t_{res}} \quad .(7.2\text{-}20)$$

Inspection of equations (7.2-14 - 7.2.16) reveals that the corresponding proportionality constants are: 1, 10^4 and 10^2. Therefore the results are expressed in terms of three dimensionless groups:

$$C_1 = \frac{t_{react}}{t_{res}} \quad ;(7.2\text{-}21)$$

$$C_2 = \frac{t_{diff}}{t_{res}} \times 10^4 \quad ;(7.2\text{-}22)$$

$$C_3 = \frac{t_{str}}{t_{res}} \times 10^2 \quad .(7.2\text{-}23)$$

7.3 Presentation of Results

It should be recalled that the behaviour of a single stretched-fold which initially consists of equal masses of burned and unburned layers has been studied in Chapter 4. The task here is mainly focussed on studying the performance of a well-stirred reactor which consists of various folds at different ages. First, the influence of M_o on the fold biography of the reactor is highlighted.

The performance of the well-stirred reactor, which is characterised by dimensionless time ratios and M_o is discussed in detail in sub-section 7.3.2.

7.3.1 Typical results of fold biography

In this section, the model approach is supposed to be applied to an ideal, perfectly-stirred reactor. Therefore, the chemical loading and the mixing rate are very low and the residence time of the reactor is sufficiently long in comparison with stretching, diffusion and reaction times. The results described here can be regarded as extreme cases of the well-stirred reactor system.

Effects of M_o

The influence of the initial fresh mass fraction of the 'parent' layers on the fold biography were investigated by varying M_o in the range from 0.25 to 0.9. The results are presented in two parts; fold burn-out and mixing times, and fold-average reaction rate. Each part which consists of two typical burning regimes will now be described.

(1) Fold burn-out and mixing times

Table (7.1) contains results of a typical internal flame propagation regime, expressed in terms of the

Internal flame propagation p=1atm, t_{diff}/t_{str}=100, t_{diff}/t_{react}=1.84x10^6				
M_o	0.25	0.5	0.75	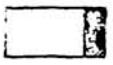 0.9
Burning constant C	0.322	0.435	0.662	extinction
Fold burn-out time t_b/t_{react} prediction	130	330	680	extinction
Analytical result (equation 7.3-1)	110	292.7	666.	extinction
Predicted flame speed S_u (m/sec)	3.05	3.02	3.	extinction
Analytical solution of $S_u=S_u^* \sqrt{\frac{t^*_{react}}{t_{react}}}$	2.98	2.98	2.98	extinction

TABLE 7.1: RESULTS OF FOLD BURN-OUT TIME AND FLAME SPEED CALCULATION

Spontaneous ignition p=1atm, t_{diff}/t_{str}=1.84x10^6 t_{diff}/t_{react}=1.84x10^6				
M_o	0.25	0.5	0.75	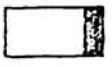 0.9
Mixing time (prediction) t_m/t_{react}	7.14	7.43	7.91	extinction
Burn-out time t_b/t_{react} (prediction)	70.	75.5	84.9	extinction

TABLE 7.2: RESULT OF FOLD MIXING AND BURN-OUT TIMES

predicted burn-out time and the corresponding flame speed. The comparison between the numerical calculations and the analytical solutions are also given.

Table (7.2) contains results of a spontaneous ignition regime. expressed in terms of the predicted burn-out time and mixing time.

Observation

It is observed that in both regimes the assumption of low vaue of M_o will cause the fold burn-out time to be very short. However, when M_o is high (as already shown in the cases of M_o=0.75), the time required for completion of the reaction is longer than the low M_o ones.

Discussion

(i) Internal flame propagation regime

The behaviour of the stretched-fold which has been discussed in Chapter 4 is also observed here. It shows that the fold is burned to completion in accordance with the analytical formula:

$$t_b = t_{str} \ln \left| 1+(1-\tilde{\tau}_o)\, C \sqrt{t_{diff}\, t_{react}}/t_{str} \right|$$

, (7.3-1)

The comparison between the prediction and analytical solution of the burn-out time shows the discrepancy is about 18% (see Table 7.1).

(ii) Spontaneous ignition regime

Since the initial composition of the fold is highly reactive, the reaction and stretching times are so short that the fold proceeds by way of spontaneous ignition. For the present cases, the result shows the burn-out time of the spontaneous ignition regime is shorter than that of the internal flame propagation ones.

(iii) Extinction

Since the newly-formed fold has the value of fold-average reactedness $\tilde{\tau}_o$, the relevant equation between $\tilde{\tau}_o$ and M_o is: $1-\tilde{\tau}_o=M_o$. The implication of this is that extinction may take place as M_o increases over the critical value. This has already been shown in Tables 7.1 and 7.2 (extinction takes place at $M_o=0.9$). The fact is that the reactedness of the engulfed burned gas diminishes below the critical value. Consequently, the stretched-fold cannot burn.

(2) Fold-average reaction rate

The influence of M_o on the fold-average reaction rate is investigated by studying the $\tilde{r}_\phi \sim \tilde{\phi}$ relations.

Two burning regimes are observed. The results are shown in Figures 7.2 and 7.3, respectively. In each case, the abscissa is the fold-average concentration, and the ordinate is the corresponding fold-average reaction rate.

It is observed that when M_o is low, the fold-average rate decreases. On the other hand, high M_o shifts the reaction rate curve to the unburned end. An extreme case is that extinction takes place.

It is also observed that the fold-average reaction rate of the spontaneous ignition regime is higher than that of the internal flame propagation.

Discussion

When M_o is low, the newly-formed fold engulfs much more burned fluid than the unburned one. Consequently, the Arrhenius reaction source will decrease (because the mass of the fresh fold is small). In this circumstance, the fold burn-out time is short because only a small proportion of fresh mixture is consumed.

Since the fold-average reaction rate of the spontaneous regime is higher than the internal flame propagation one, the fold burn-out time of the spontaneous ignition regime is short compared with the internal flame propagation one (as already tabulated in Tables 7.1 and 7.2).

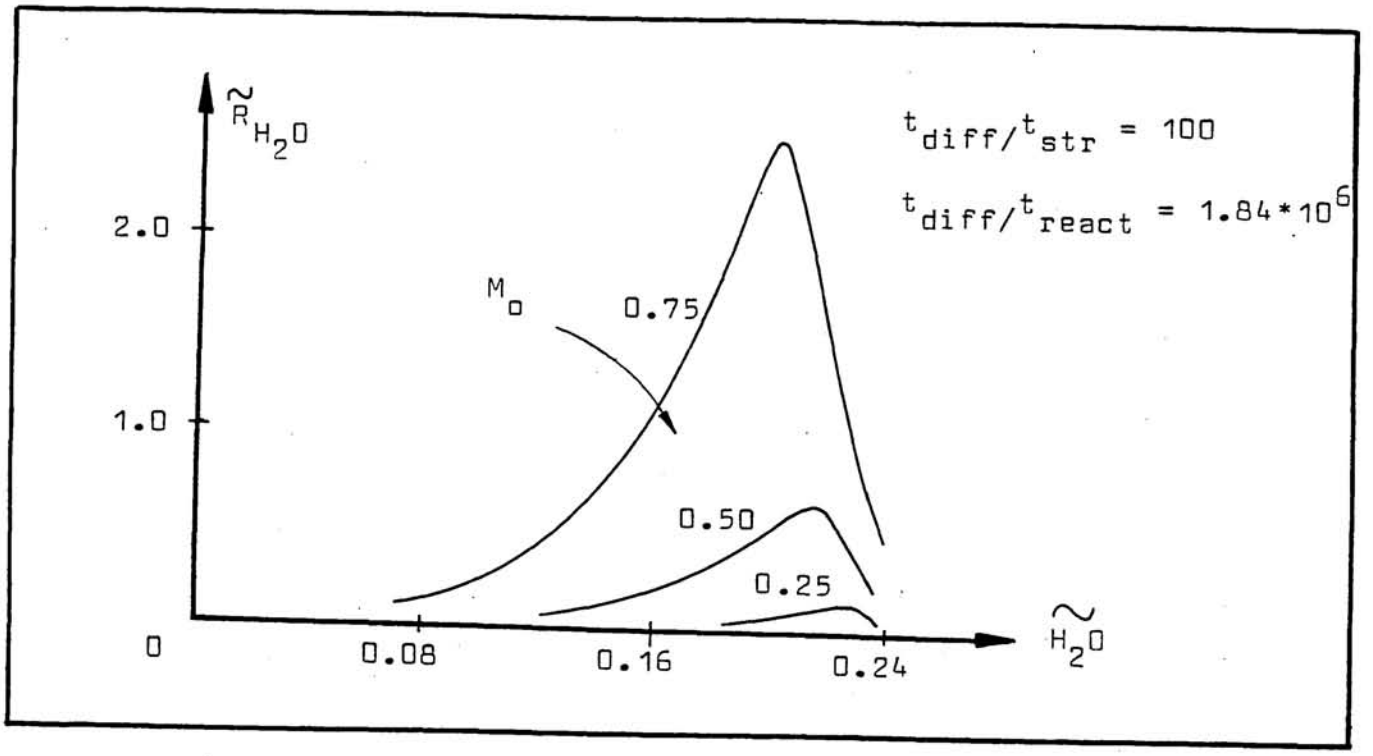

FIGURE 7.2 THE INFLUENCE OF M_o ON THE FOLD-AVERAGE REACTION RATE.

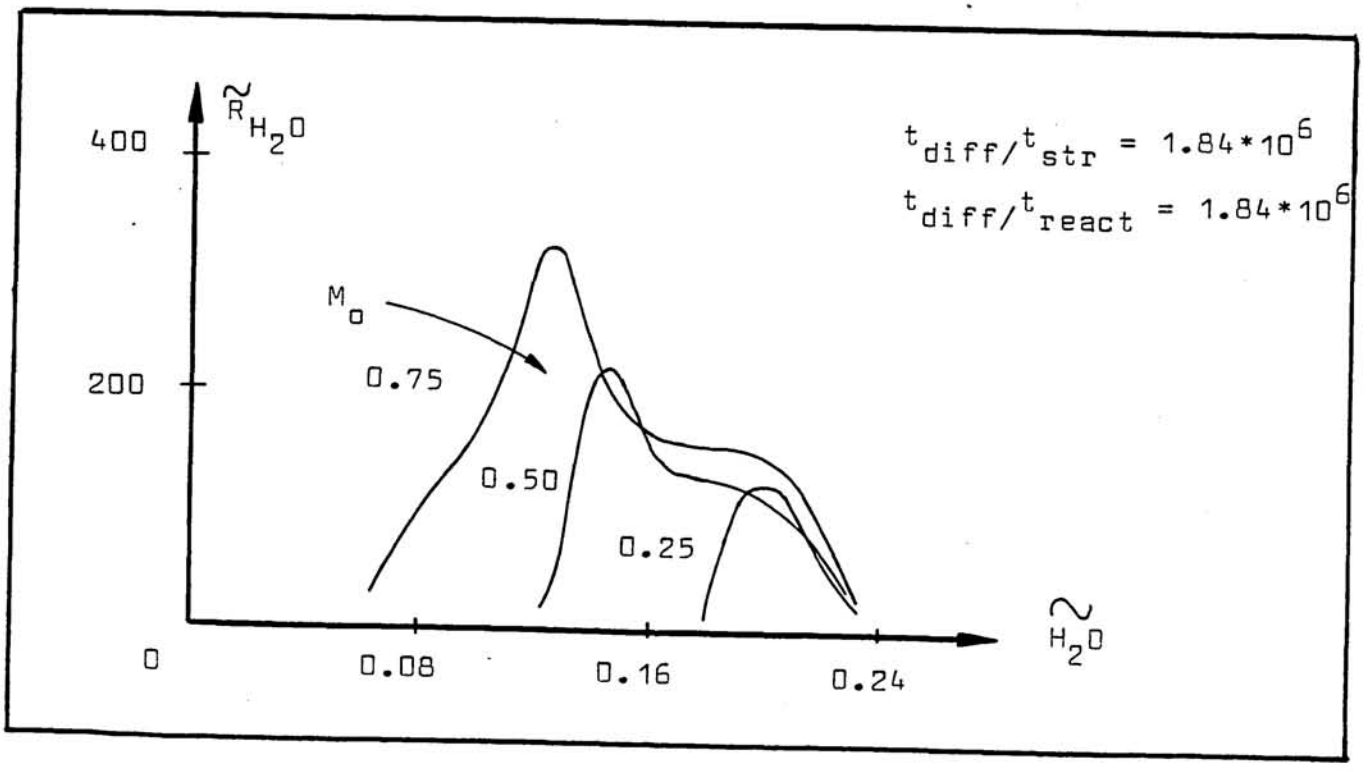

FIGURE 7.3 THE INFLUENCE OF M_o ON THE FOLD-AVERAGE REACTION RATE.

7.3.2 The performance of a well-stirred reactor

Various values have been taken for the reaction time, t_{react}; the stretching time, t_{str}; the diffusion time, t_{diff}; and the residence time, t_{res}, so as to vary the values of three governing parameters:

chemical loading, C_1 $(\frac{t_{react}}{t_{res}})$;

Reynolds number, C_2 $(\frac{t_{diff}}{t_{res}} \times 10^4)$;

mixing rate, C_3 $(\frac{t_{str}}{t_{res}} \times 10^2)$,

and of the mass rate M_o.

The major interest is to study the most influential factors, namely, mixing rate and chemical loading on the reactor performance. The results of computations are presented and discussed. First, attention is focussed on studying the parameter of mixing rate.

The effect of mixing rate

(a) Computational results

Table 7.3 contains the results of a series of computations for 27 distinct conditions in which the mixing rate is varied from 5×10^{-1} to 5×10^{5} while M_o is varied from 0.25 to 0.75. In addition, the Reynolds number

and chemical loading are fixed (C_2=9.2x10^6, C_1=10^{-3}).

The high Reynolds number characterises fully turbulent flow and the present chemical loading is low. Therefore, the reactor performance is likely to be influenced only by the mixing rate and M_o. The results which are shown in Table 7.3 are presented in terms of the space-average reactedness, $\bar{\tau}$.

Chemical loading C_1 = 10^{-3}; Reynolds number C_2 = 9.2x10^6										
M_o ↓	$\frac{t_{str}}{t_{res}}$ →	5x10^{-3}	10^{-2}	10^{-1}	1.84x10^{-1}	1.84	1.84x10^1	9.2x10^1	9.2x10^2	5x10^3
0.75	$\bar{\tau}$	0.995	0.92	BLOW OUT 0.3	BLOW OUT 0.25	BLOW OUT 0.25	BLOW OUT 0.25	BLOW OUT 0.25	BLOW OUT 0.25	BLOW OUT 0.25
0.5	$\bar{\tau}$	0.995	0.995	0.995	0.995	0.88	0.75	BLOW OUT 0.6	BLOW OUT 0.5	BLOW OUT 0.5
0.25	$\bar{\tau}$	0.995	0.995	0.995	0.995	0.995	0.995	0.96	0.9	BLOW OUT 0.75

TABLE 7.3: POPULATION-AVERAGE REACTEDNESS, $\bar{\tau}$, AT VARIOUS MIXING RATES

(b) Space-average reactedness

Figure 7.4 displays results of such computations. The space-average reactedness, $\bar{\tau}$, is shown as a function of mixing rate. The abscissa is $\frac{t_{str}}{t_{res}}$ in logarithmic scale, while the ordinate is $\bar{\tau}$ in linear scale.

Observation

(i) If $\tilde{\tau}_o$ is not very small, all $\bar{\tau}$ values will be equal to unity when the mixing rate is very low.

(ii) As the mixing rate increase, $\bar{\tau}$ will diminish. When this loading is sufficiently large, $\bar{\tau}$ will exhibit sudden fall. This is one kind of blow-out.

(iii) When the presumption of M_o is high, $\bar{\tau}$ will drop abruptly even though the mixing rate is moderate. This phenomenon is another kind of blow-out.

Discussion

When the stretching time is considerably longer than the reaction time, the micro burning process is essentially controlled by internal flame propagation. It has been observed that blow-out can occur in two different way. The explanations of both observations are given below:-

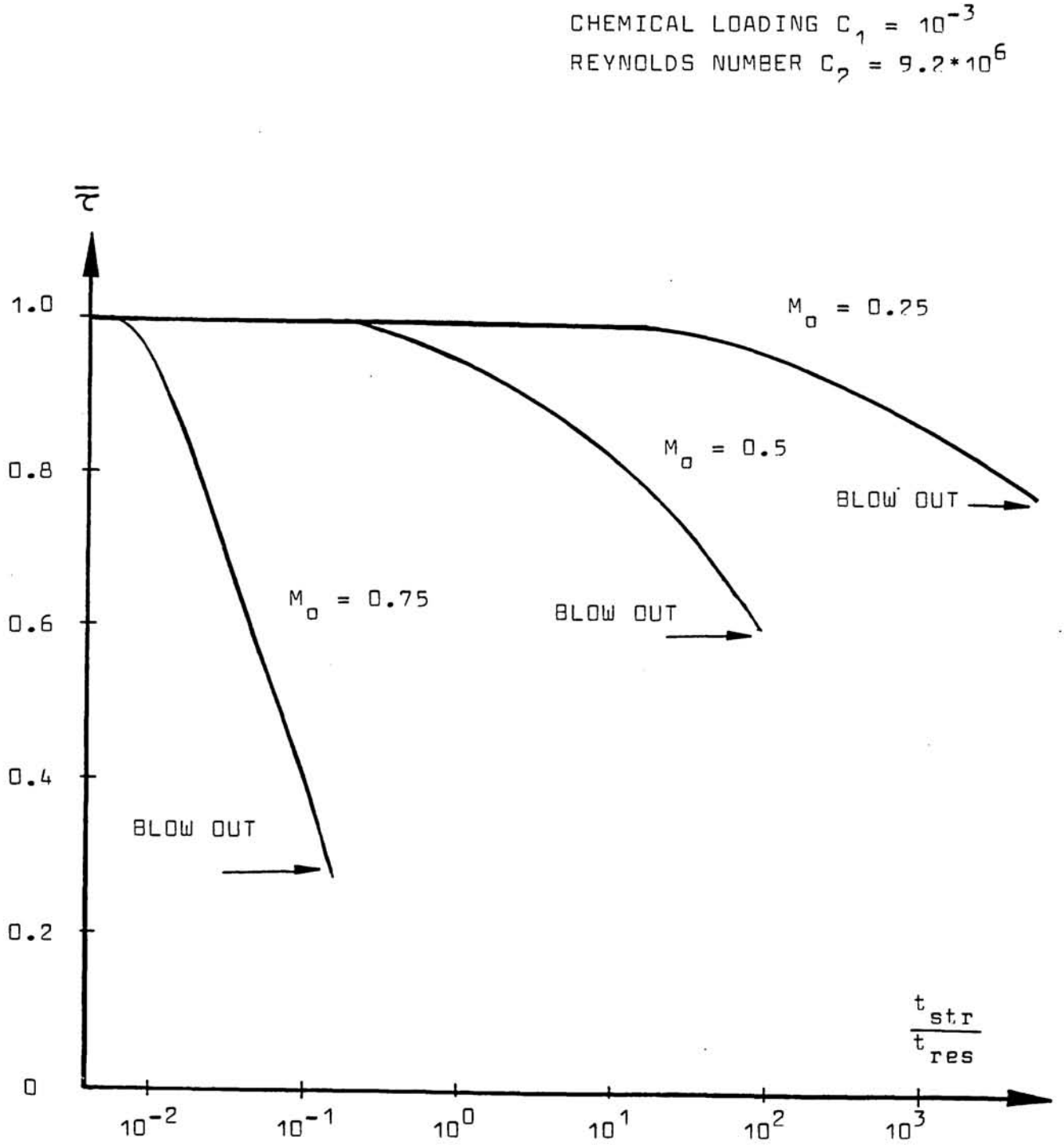

Figure 7.4 POPULATION-AVERAGE REACTEDNESS, $\bar{\tau}$, AT VARIOUS MIXING RATE.

- As mixing rate increases, the high fluctuation folds at different ages in the reactor ensure that the reaction rate∿temperature curves broaden somewhat and shift down toward the inlet stream, thus reducing the activation energy term and eventually ceasing the reaction.

- If M_o is large, the newly-formed fold engulfs too much unburned gases. Consequently, the gases in the fold do not burn to completion at all. Therefor, $\bar{\tau}$ decreases.

The effect of chemical loading

(a) Computational results

The influence of chemical loading on the performance of reactor is shown in Table 7.4. It contains the results of predictions for 24 distinct cases in which the chemical loading varies from 10^{-5} to 1.84×10^{-1} and M_o varies from 0.25 to 0.75. In addition, the Reynolds number and mixing rate are fixed ($C_2=1.84 \times 10^5$, $C_3=10^{-3}$). The results are presented in terms of the space-average reactedness, $\bar{\tau}$.

Reynolds number $C_2=1.84\times10^5$; Mixing rate $C_3=10^{-3}$									
M_o ↓	C_1 →	10^{-5}	5×10^{-5}	7×10^{-5}	10^{-4}	5×10^{-3}	3×10^{-2}	10^{-1}	1.84×10^{-1}
0.75	$\bar{\tau}$ →	0.995	0.995	0.55	BLOW OUT 0.25	BLOW OUT 0.25	BLOW OUT 0.25	BLOW OUT 0.25	BLOW OUT 0.25
0.5	$\bar{\tau}$ →	0.995	0.995	0.995	0.995	0.91	0.75	BLOW OUT 0.5	BLOW OUT 0.5
0.25	$\bar{\tau}$ →	0.995	0.995	0.995	0.995	0.982	0.91	0.77	BLOW OUT 0.75

TABLE 7.4: POPULATION-AVERAGE REACTEDNESS, $\bar{\tau}$, AT VARIOUS CHEMICAL LOADINGS

(b) Space-average reactedness curves

Figure 7.5 presents results of such calculations. The space-average reactedness, $\bar{\tau}$, is shown as a function of chemical loading.

Discussion

When t_{str}/t_{react} is small in comparison with t_{diff}/t_{str}, the micro burning process is essential to that of spontaneous ignition. The performance of the reactor

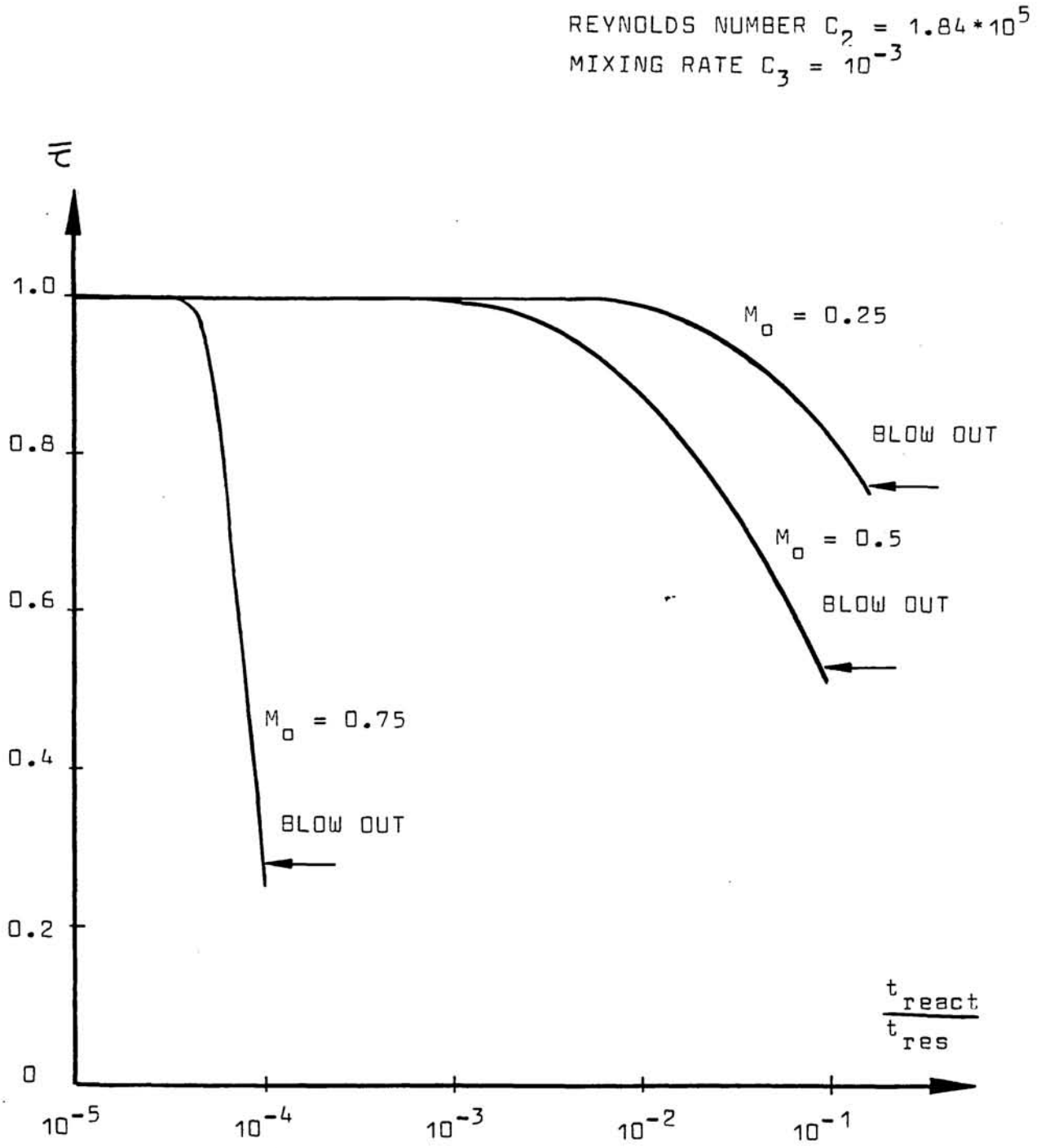

Figure 7.5 POPULATION-AVERAGE REACTEDNESS, $\bar{\tau}$, AT VARIOUS CHEMICAL LOADING.

is governed by the reaction and residence times.

As illustrated in Figure 7.5, when the chemical loading increases, the space-average reactedness decreases. An extreme is that the blow-out will take place at a critical loading. This is because when the residence time diminishes sufficiently, the non-linearity of the $\bar{r}_\phi \sim \bar{\phi}$ relation ensures that the reactor conditions are very close to those of the inlet conditions. Therefore, the blow-out can be detected by varying the chemical loading from very low values to high loading until the flame extinction occurs.

It is also observed that the space-average reactedness diminishes as M_o becomes large. Since the burned gases in all newly-formed folds depend upon the corresponding space-average composition in the reactor, the link betweem initial fold-average reactedness, $\tilde{\tau}_o$, and the space-average reactedness, $\bar{\tau}$, is given by the relevant equation (Spalding 1979e):

$$\tilde{\tau}_o = (1-M_o)\bar{\tau} \quad . \qquad (7.3\text{-}2)$$

Inspection of equation (7.3-2) shows that the blow-out is obtained at large values of M_o.

7.3.3 Population-average quantities

The population-average reactedness presented in the previous section represents the reactor characteristics. When $\tilde{\phi}$ and $\tilde{P}$ are known for individual folds as functions of age, it is possible to employ the population distribution function to yield population-average quantities. Thus, other features of the well-stirred reactor like the population-average species concentrations and reaction rates are easy to compute with the ESCIMO approach.

(a) Population-average species concentrations

Results of a number of calculated concentrations based on the fixed parameters C_1 and C_2 over a range of different values of mixing rate are presented in Figures 7.6-12. The abscissa is t_{str}/t_{res} in logarithmic scale while the ordinate is ϕ in linear scale. Each location on the calculated curve represents the corresponding population-average concentration which is characterised by a set of controlling parameters.

Results of the calculated concentrations are also expressed as functions of chemical loading, as illustrated in Figures 7.13 - 19.

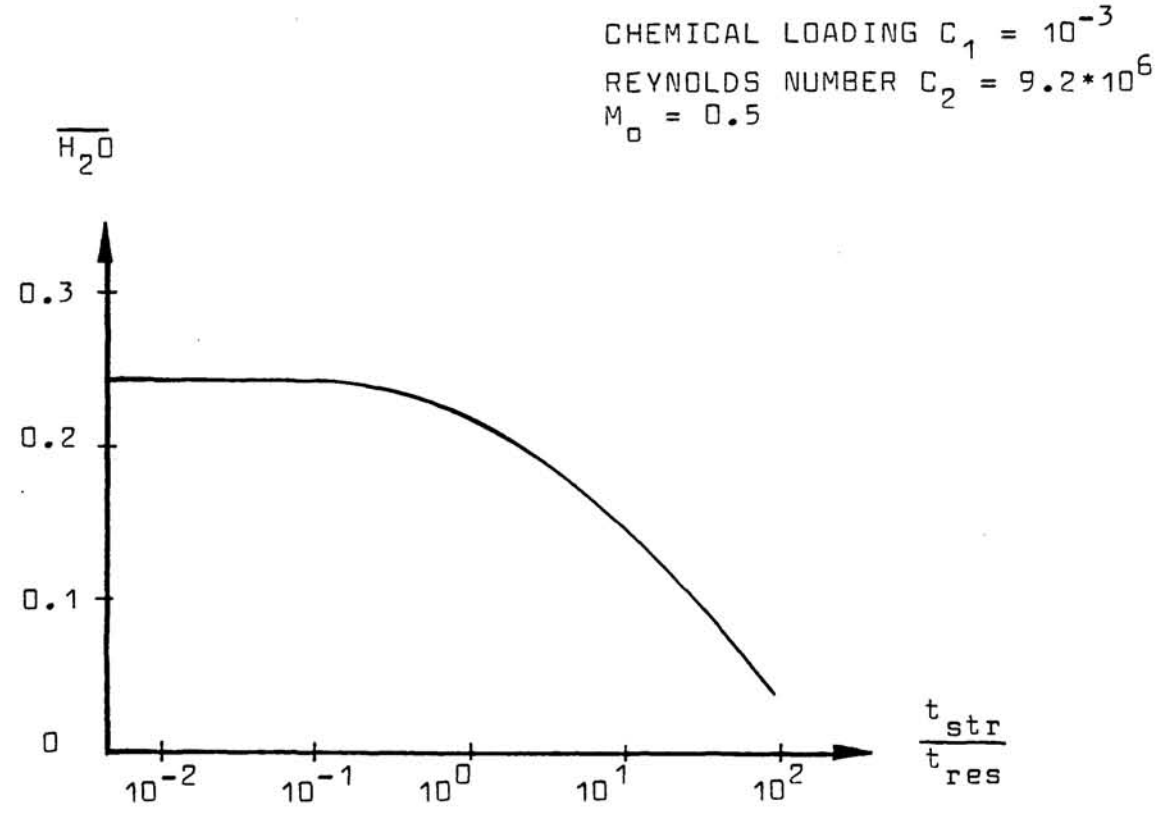

Figure 7.6 POPULATION-AVERAGE SPECIES CONCENTRATION AT VARIOUS MIXING RATE.

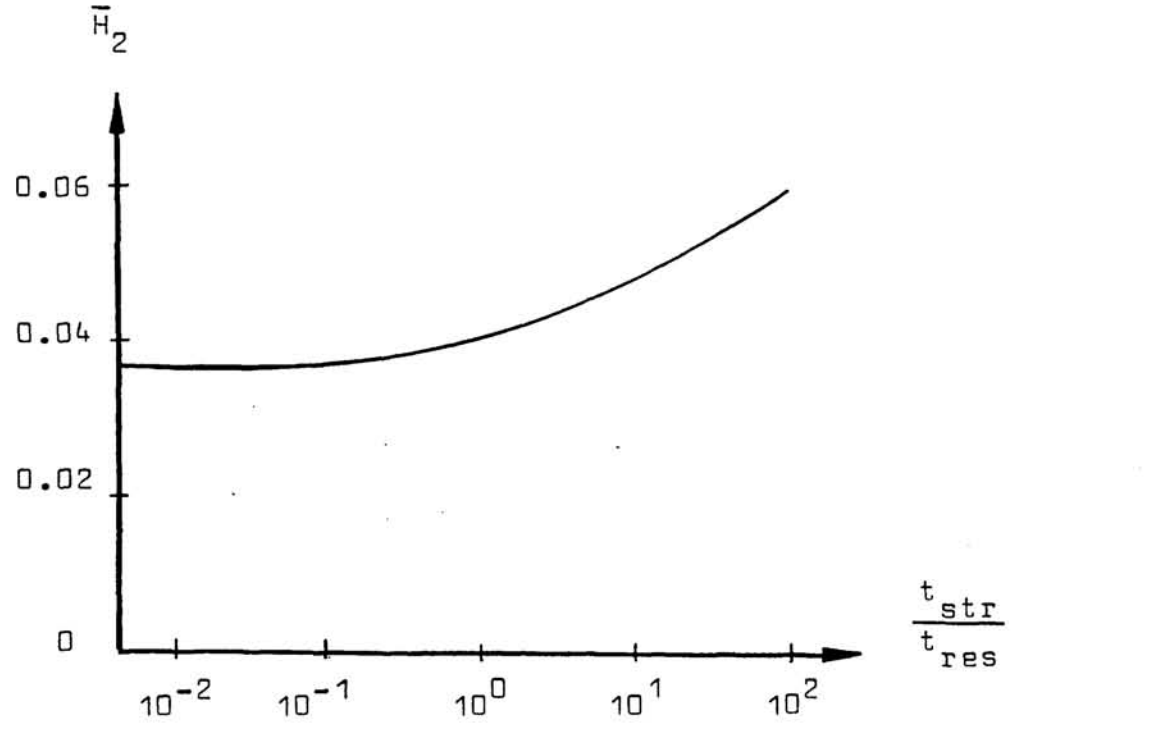

Figure 7.7 POPULATION-AVERAGE SPECIES CONCENTRATION AT VARIOUS MIXING RATE.

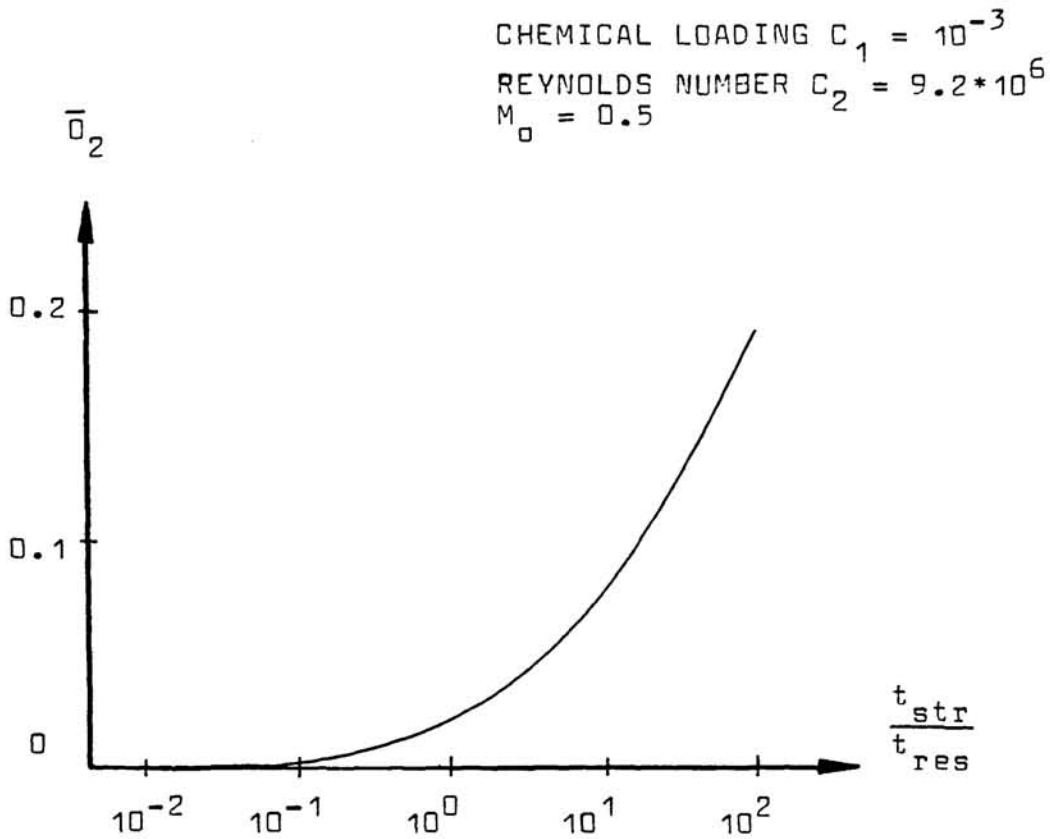

Figure 7.8 POPULATION-AVERAGE SPECIES CONCENTRATION AT VARIOUS MIXING RATE.

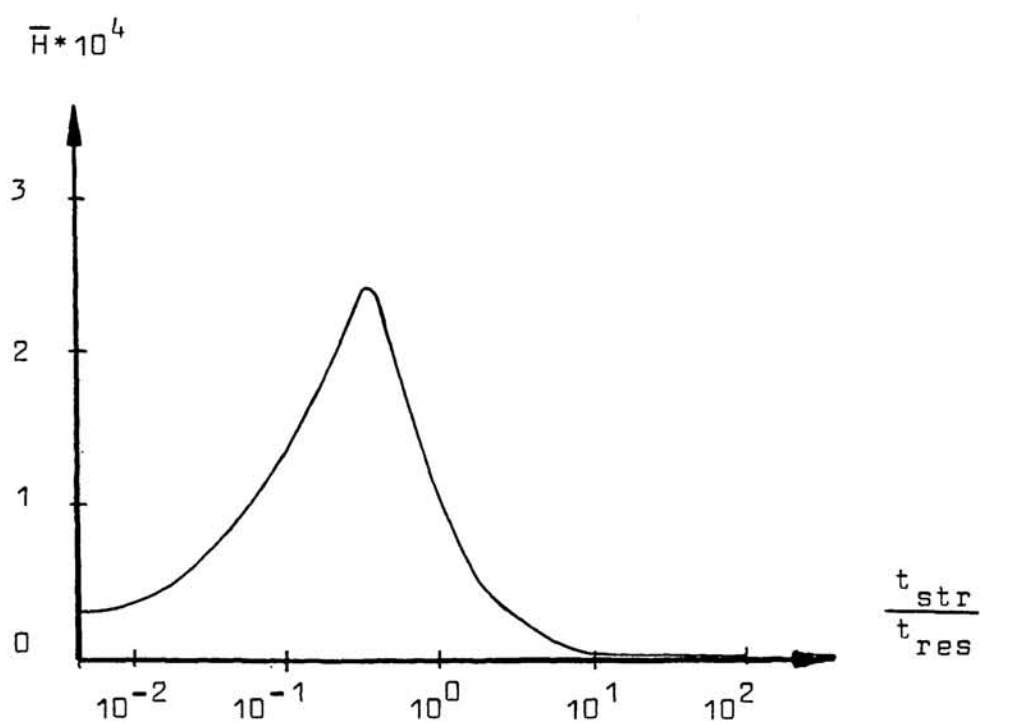

Figure 7.9 POPULATION-AVERAGE SPECIES CONCENTRATION AT VARIOUS MIXING RATE.

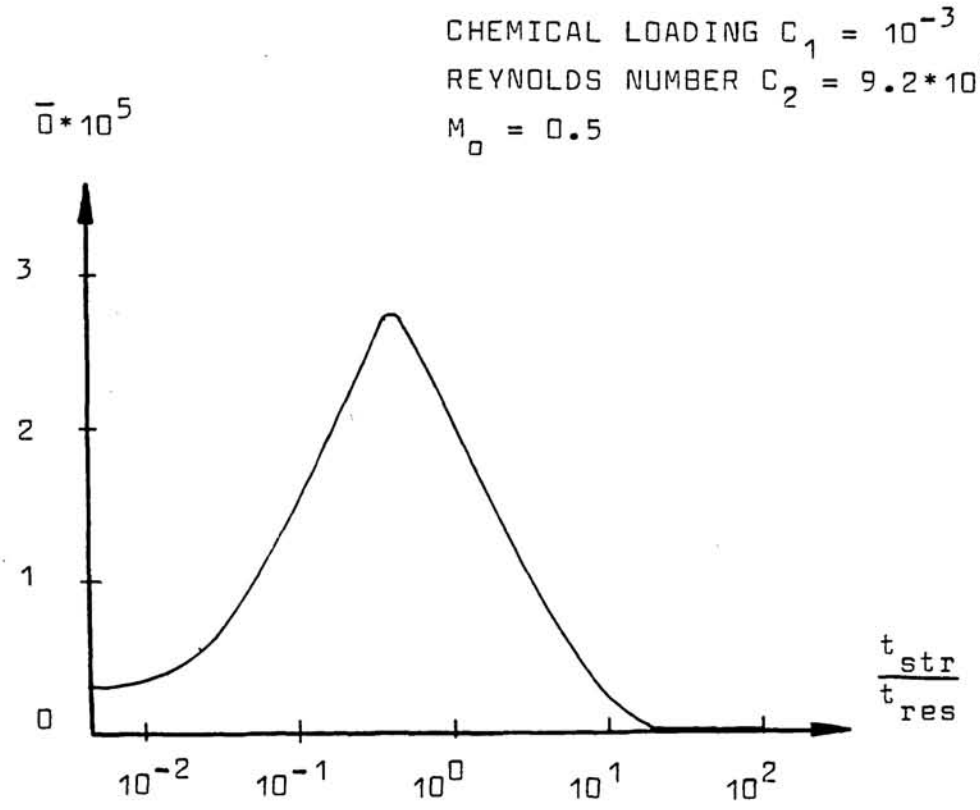

Figure 7.10 POPULATION-AVERAGE SPECIES CONCENTRATION AT VARIOUS MIXING RATE.

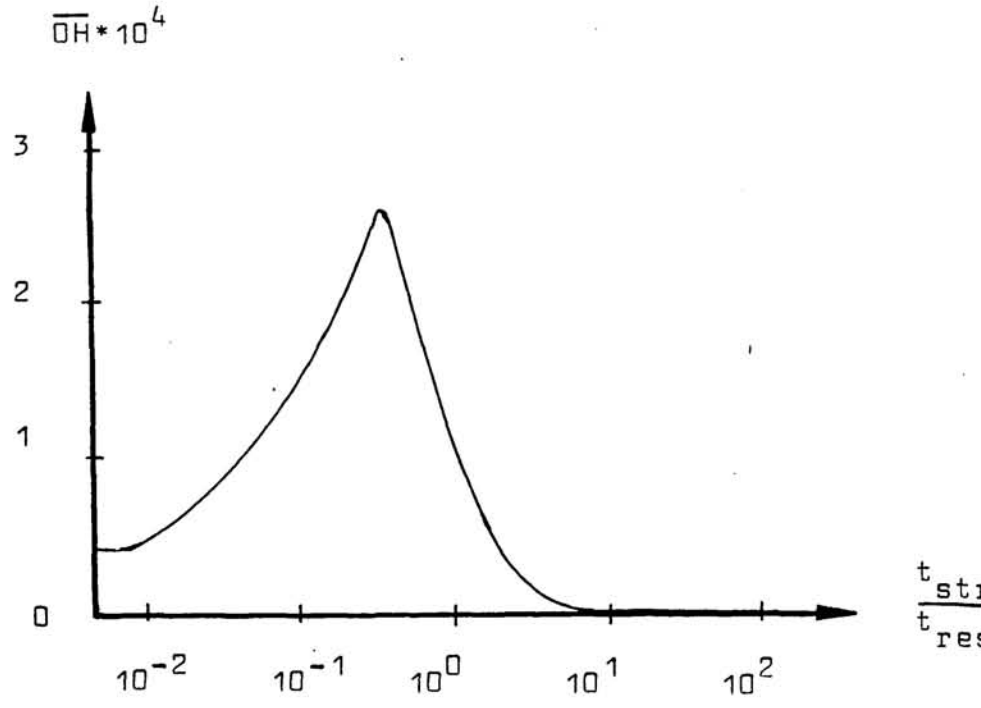

Figure 7.11 POPULATION-AVERAGE SPECIES CONCENTRATION AT VARIOUS MIXING RATE.

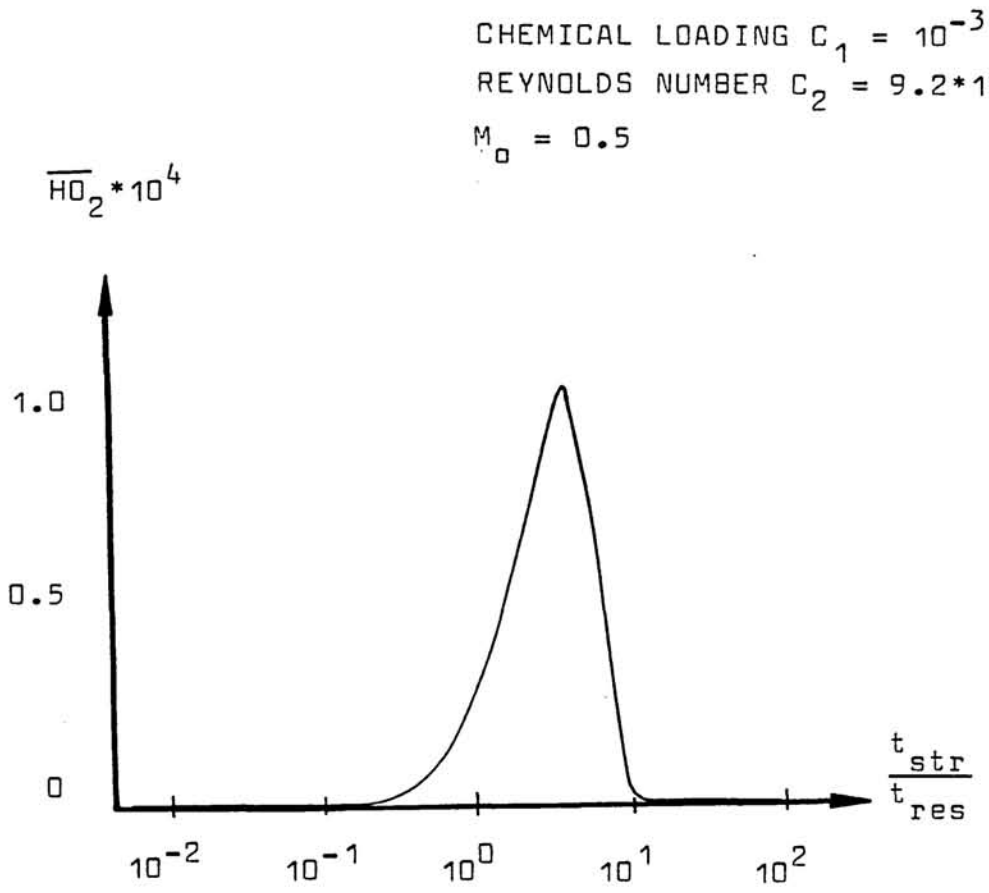

Figure 7.12 POPULATION-AVERAGE SPECIES CONCENTRATION AT VARIOUS MIXING RATE.

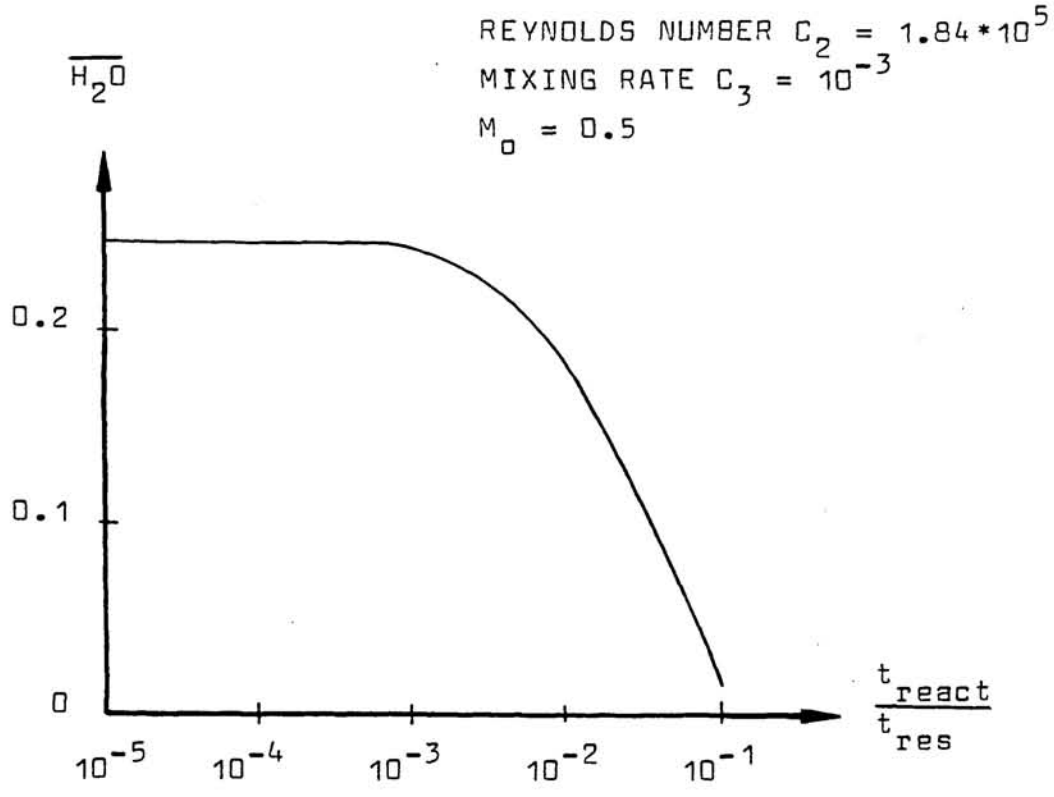

Figure 7.13 POPULATION-AVERAGE SPECIES CONCENTRATION AT VARIOUS CHEMICAL LOADING.

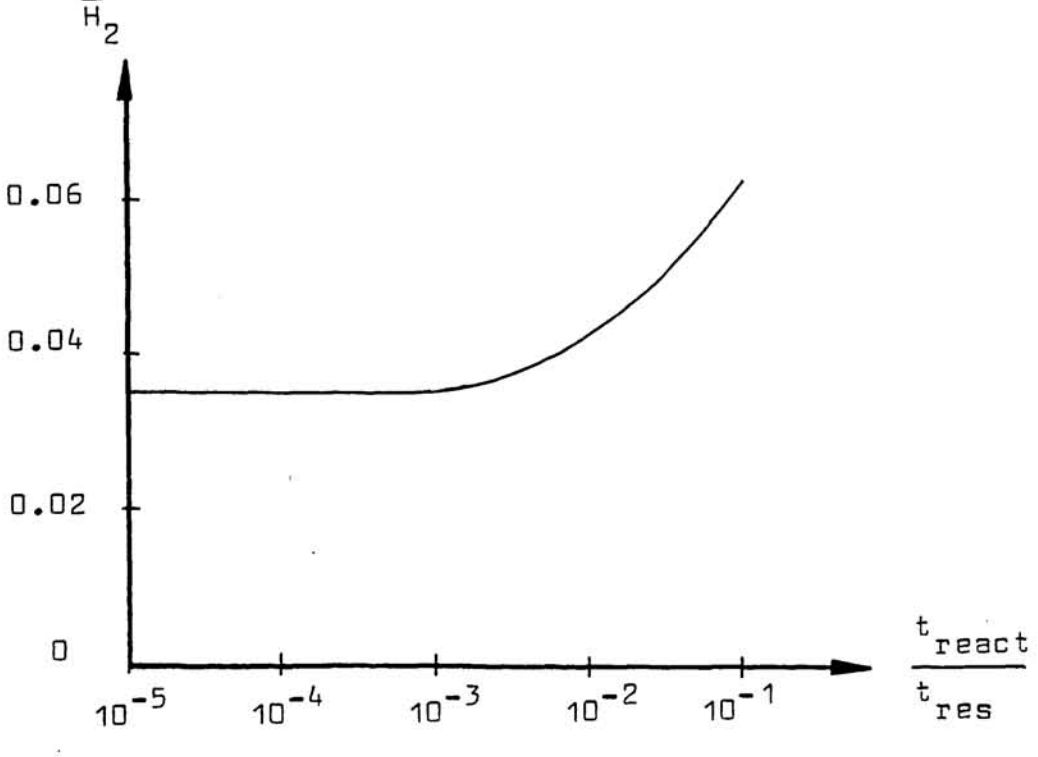

Figure 7.14 POPULATION-AVERAGE SPECIES CONCENTRATION AT VARIOUS CHEMICAL LOADING.

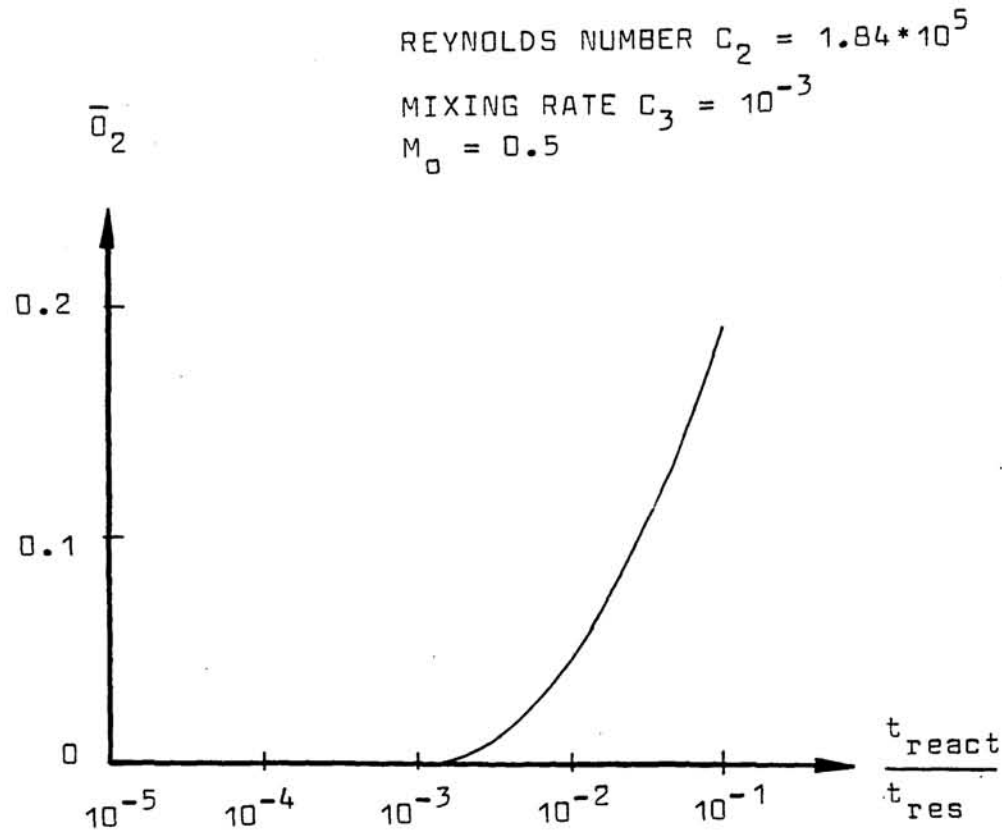

Figure 7.15 POPULATION-AVERAGE SPECIES CONCENTRATION AT VARIOUS CHEMICAL LOADING.

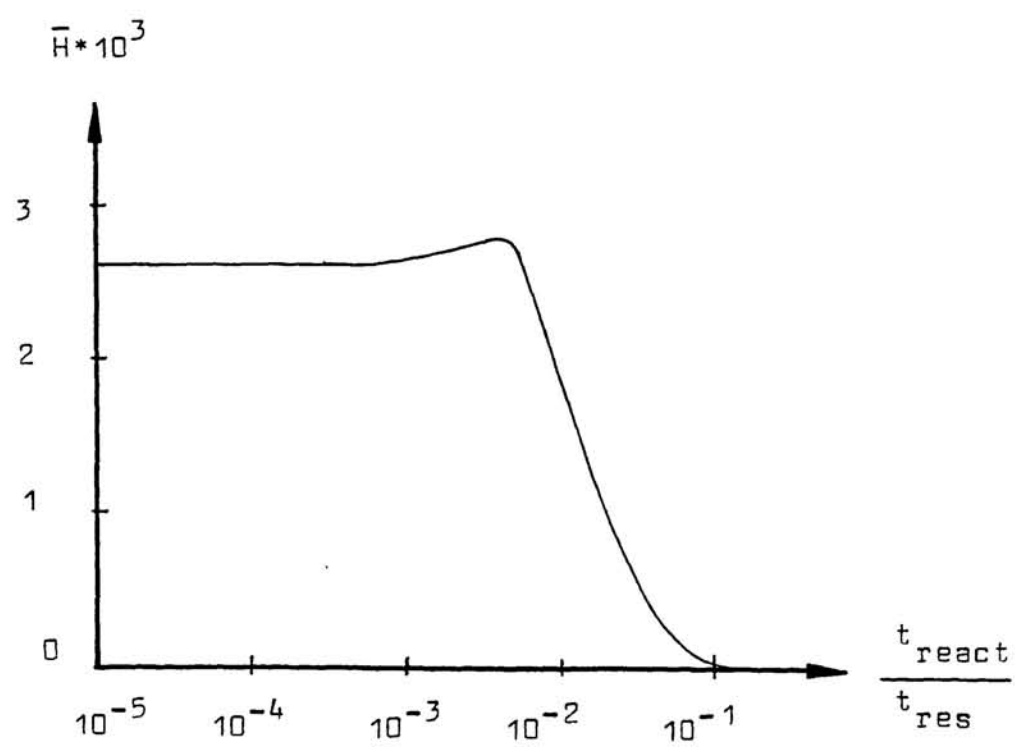

Figure 7.16 POPULATION-AVERAGE SPECIES CONCENTRATION AT VARIOUS CHEMICAL LOADING.

REYNOLDS NUMBER $C_2 = 1.84*10^5$
MIXING RATE $C_3 = 10^{-3}$
$M_o = 0.5$

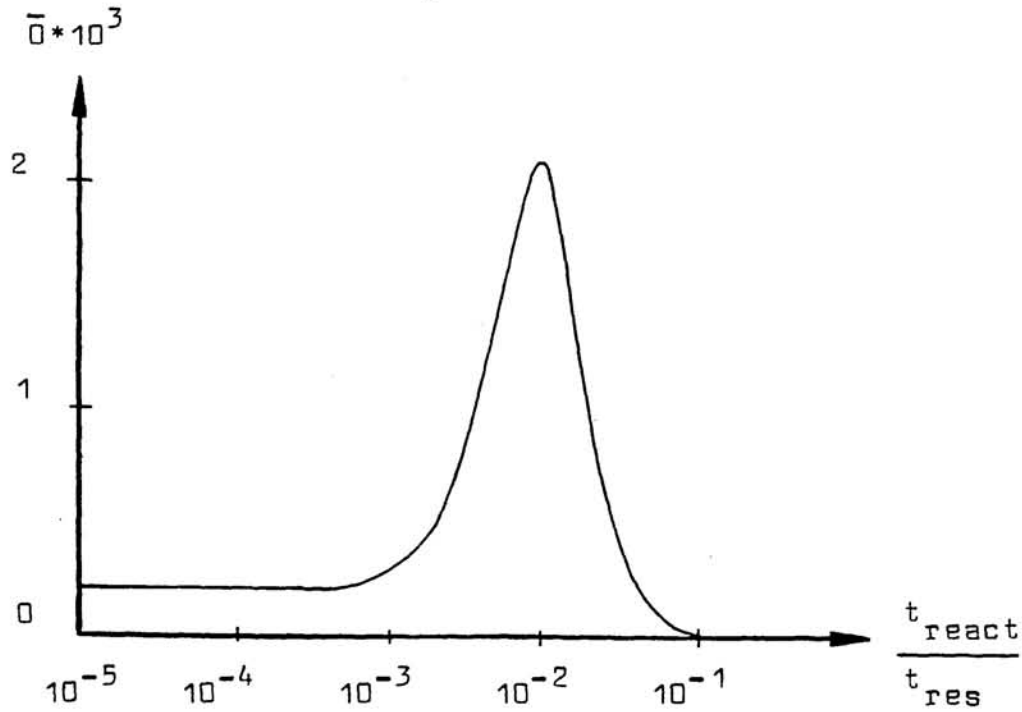

Figure 7.17 POPULATION-AVERAGE SPECIES CONCENTRATION AT VARIOUS CHEMICAL LOADING.

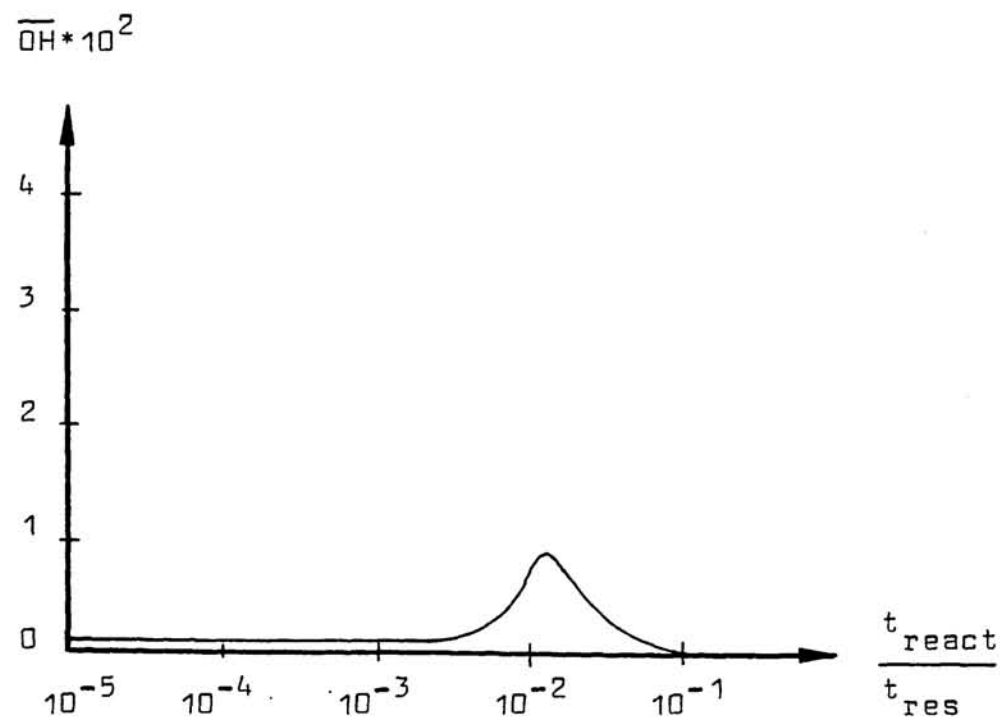

Figure 7.18 POPULATION-AVERAGE SPECIES CONCENTRATION AT VARIOUS CHEMICAL LOADING.

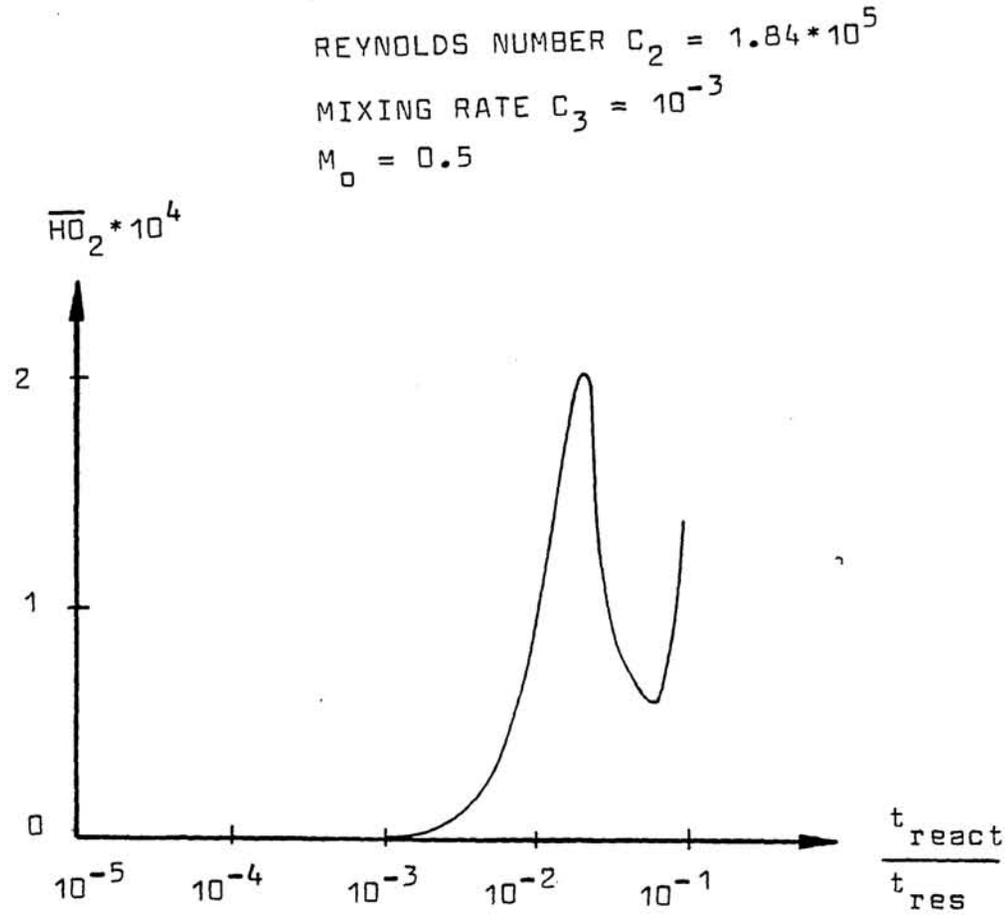

Figure 7.19 POPULATION-AVERAGE SPECIES CONCENTRATION AT VARIOUS CHEMICAL LOADING.

Discussion

It is observed that the predicted curves of the major species have the same characteristics as those of the population-average reactedness. However, the predicted curves of the minor species exhibit quite different features. When the mixing rate and/or the chemical loading are moderate, the minor species distribution will increase with C_1 and C_3. However, further increase of the mixing rate or chemical loading will result in the combustion being terminated. Under these circumstances, the characteristic curves of the minor species will decrease. Finally, blow-out occurs.

(b) Population-average reaction rate

It would be recalled that the characteristics of the fold-average reaction rates have been studied (sub-section 7.3.1). It is important to discuss the relationship of the fold-average reaction rates with the population-distribution function. Since the time-average statistical properties of the mixture are independent of position in the reactor, the space-average reaction rate of the corresponding species is one which is characterised by a set of controlling parameters. The space-average reaction rate of species ϕ is given by:

$$\bar{r}_\phi = \int_0^\infty \tilde{r}_\phi \, P_a \, da \qquad , \qquad (7.3\text{-}3)$$

Since the chain reactions of hydrogen-oxygen system are present, calculation of $\bar{r}_\phi$ can only be performed numerically.

Results

The characteristic curves of $\bar{r}_\phi \sim C_1$ and $\bar{r}_\phi \sim C_3$ are shown in Figures 7.20-26 and 7.27-33 respectively. The positive value of $\bar{r}_\phi$ denotes the rate of creation and the negative the rate of destruction.

As illustrated in Figure 7.20, three branches on the performance curve can be observed. The lower branch (from A to B) corresponds to equilibrium operation and represents stable combustion in the reactor. Increase in either the mixing rate or the chemical loading (middle region, from B to C) leads to the reaction rate finally reaching a maximum value (at point C). A decrease in the residence time (i.e. by increasing the fuel-injection rate), or lowering of the reactive mixture will cease the reaction. It is seen that the upper branch of the curve (from C to D) is an unstable operating condition. Since the maximum reaction rate at C is a critical point, a slight change in the controlling parameters will cause the reaction to shift to either the upper branch or the lower one.

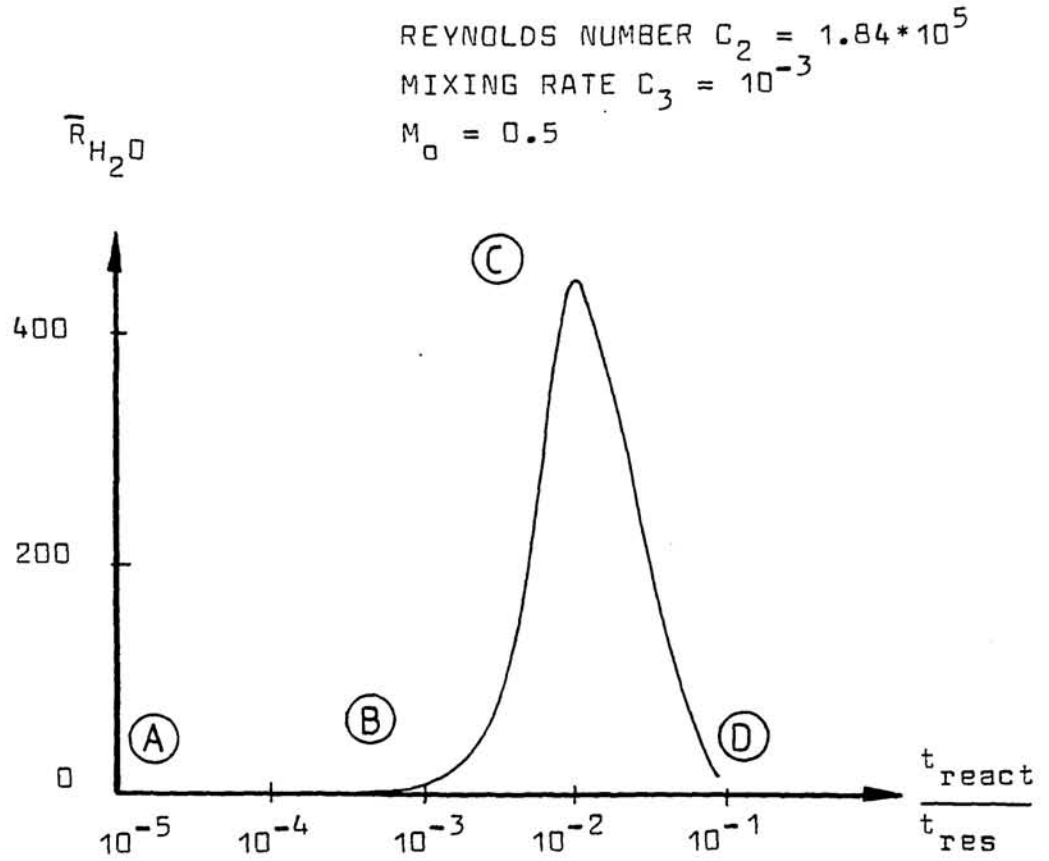

Figure 7.20 POPULATION-AVERAGE REACTION RATE AT VARIOUS CHEMICAL LOADING.

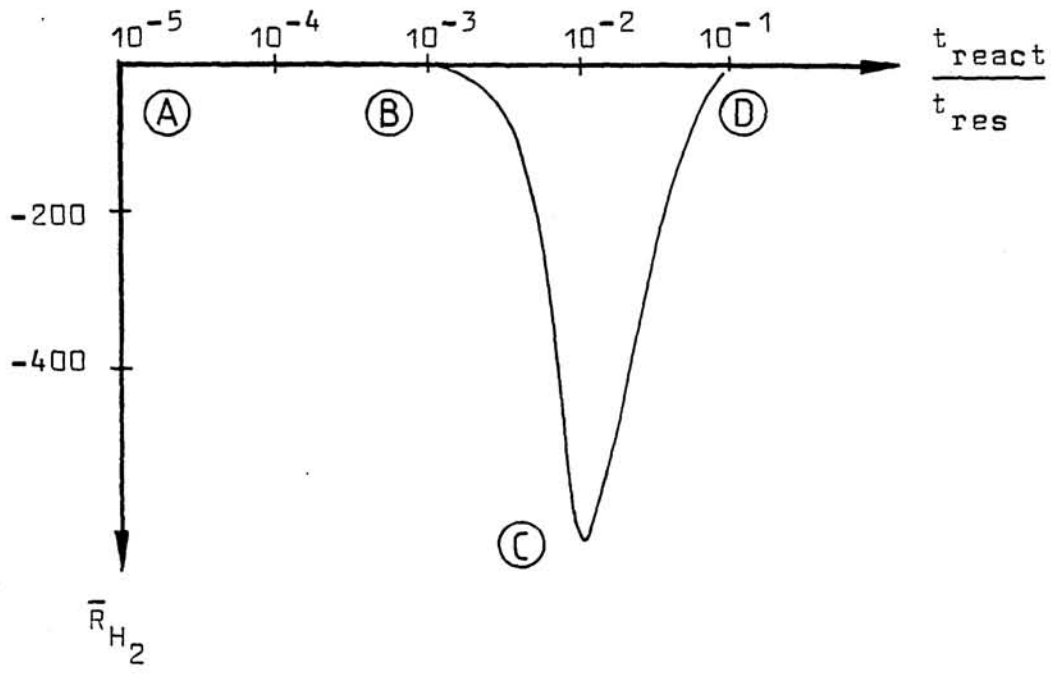

Figure 7.21 POPULATION-AVERAGE REACTION RATE AT VARIOUS CHEMICAL LOADING.

REYNOLDS NUMBER $C_2 = 1.84*10^5$
MIXING RATE $C_3 = 10^{-3}$
$M_o = 0.5$

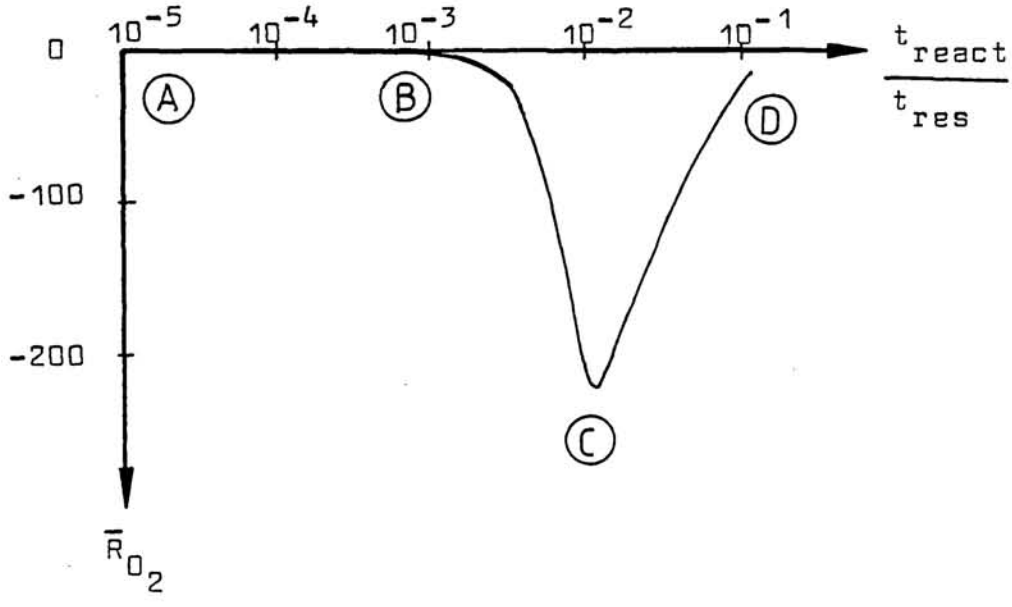

Figure 7.22 POPULATION-AVERAGE REACTION RATE AT VARIOUS CHEMICAL LOADING.

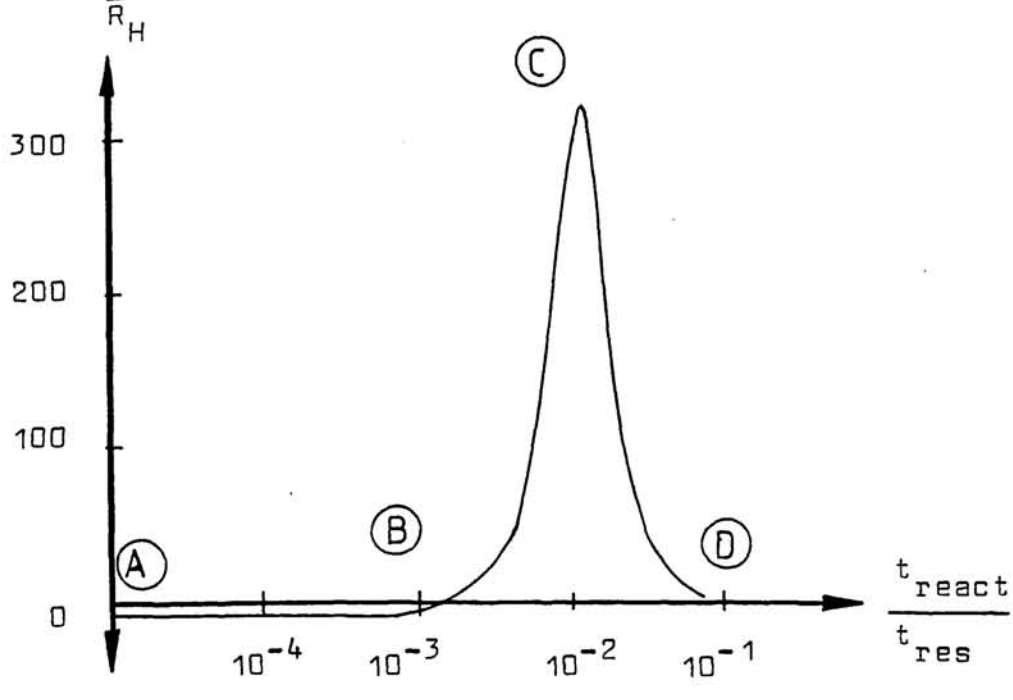

Figure 7.23 POPULATION-AVERAGE REACTION RATE AT VARIOUS CHEMICAL LOADING.

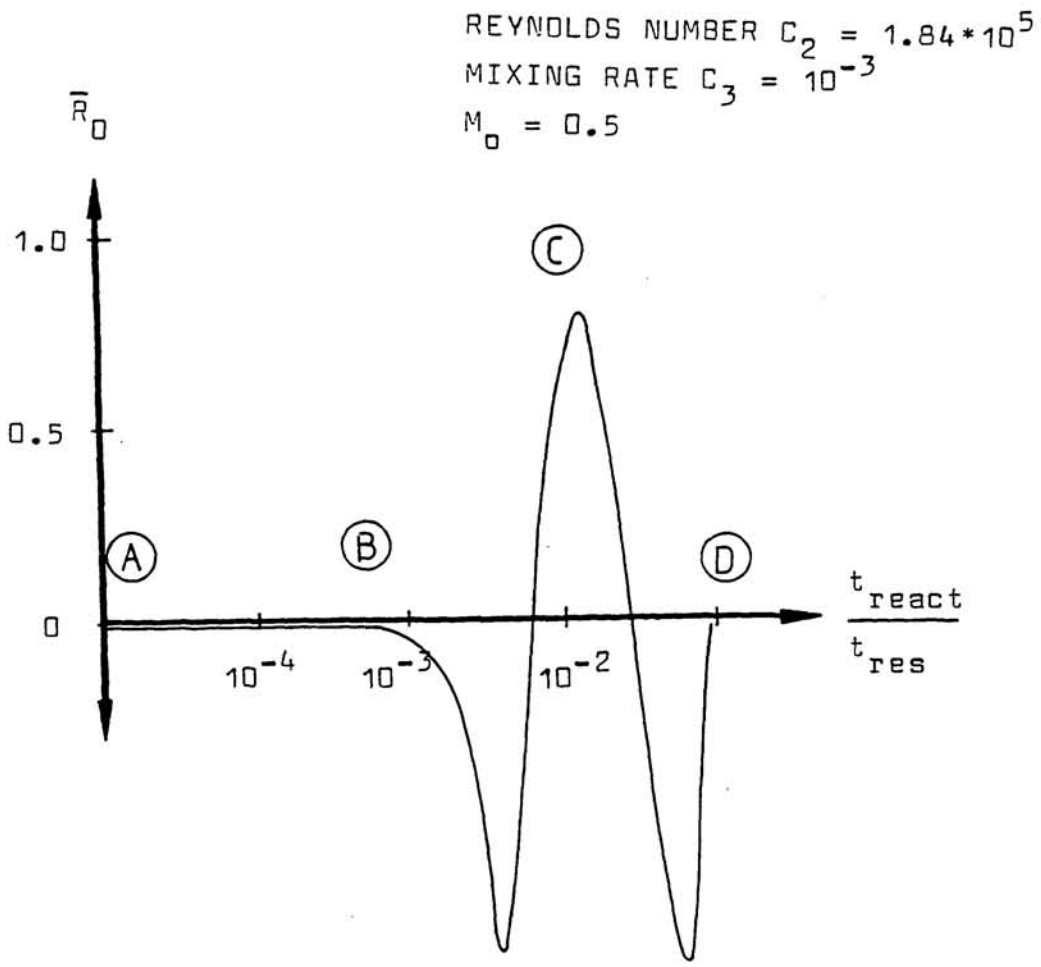

Figure 7.24 POPULATION-AVERAGE REACTION RATE AT VARIOUS CHEMICAL LOADING.

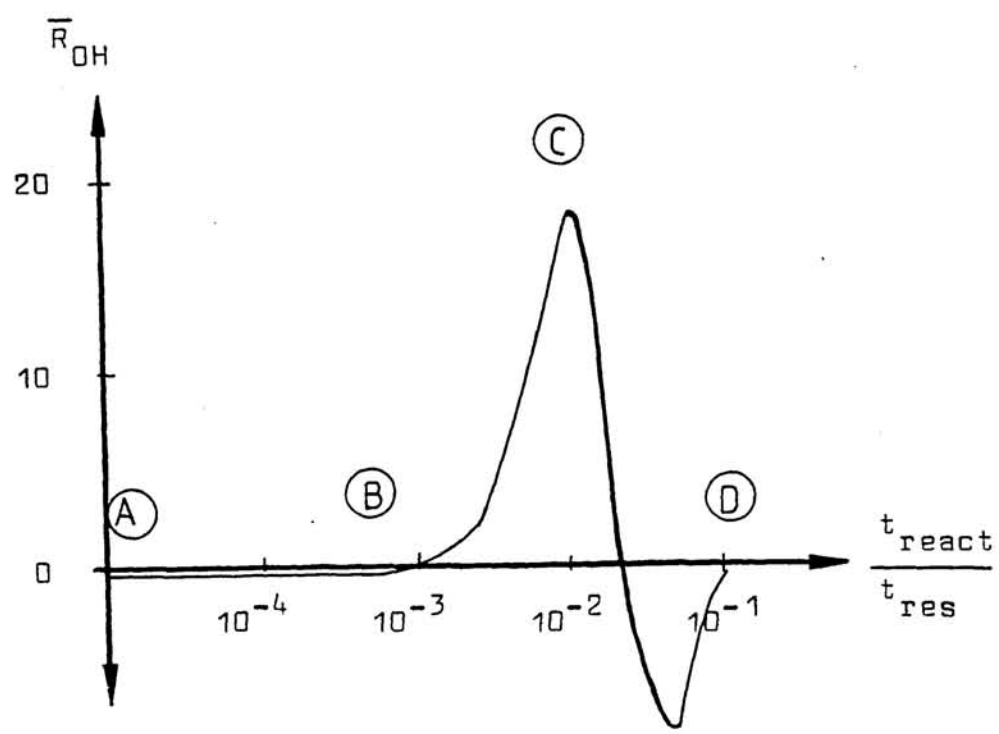

Figure 7.25 POPULATION-AVERAGE REACTION RATE AT VARIOUS CHEMICAL LOADING.

REYNOLDS NUMBER $C_2 = 1.84*10^5$

MIXING RATE $C_3 = 10^{-3}$

$M_o = 0.5$

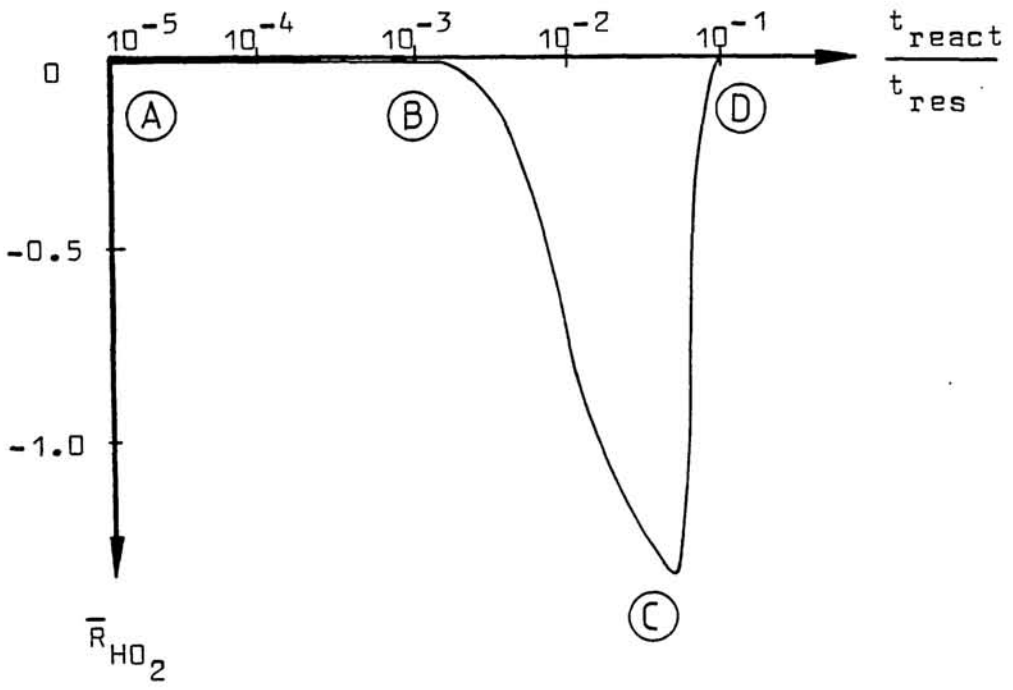

Figure 7.26 POPULATION-AVERAGE REACTION RATE AT VARIOUS CHEMICAL LOADING.

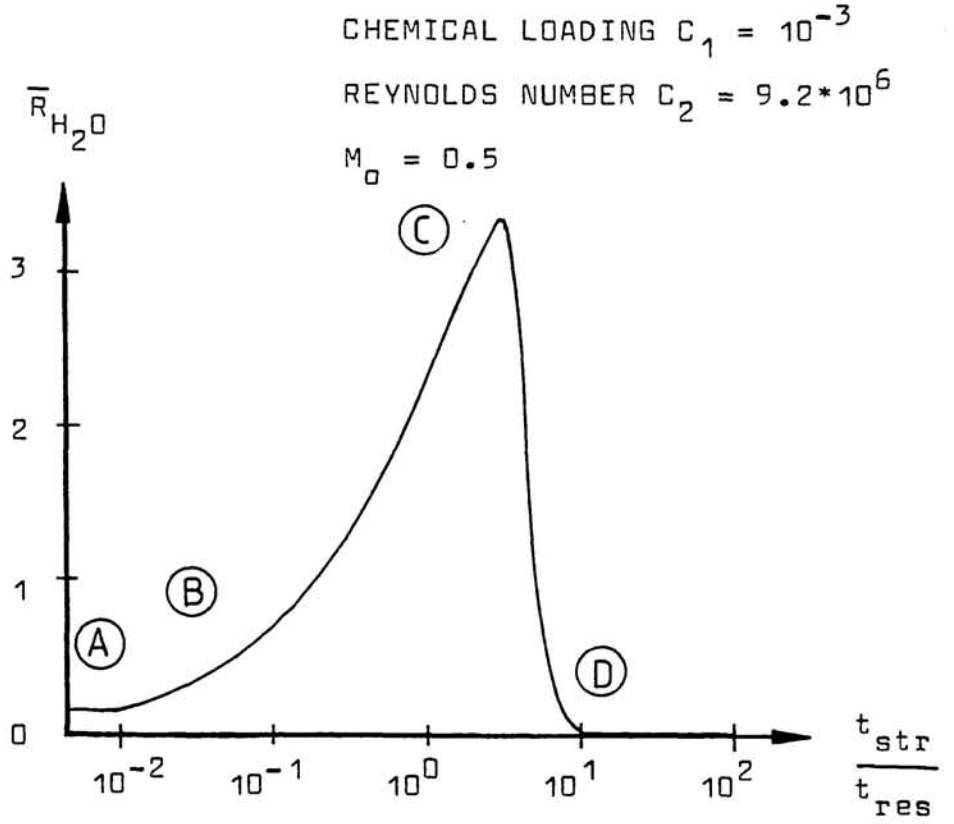

Figure 7.27 POPULATION-AVERAGE REACTION RATE AT VARIOUS MIXING RATE.

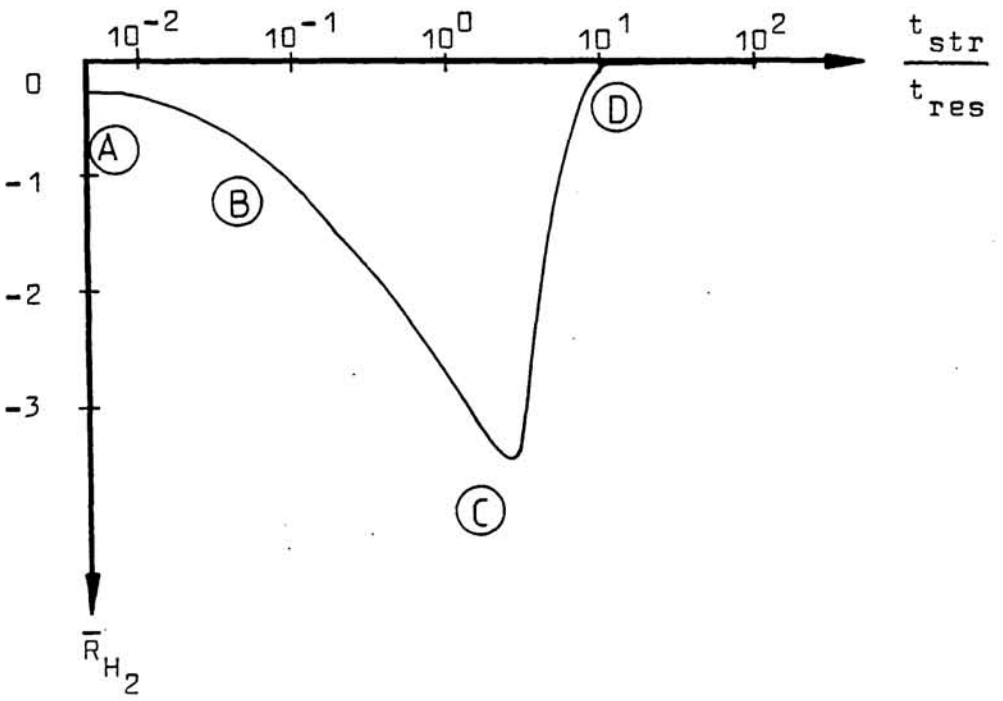

Figure 7.28 POPULATION-AVERAGE REACTION RATE AT VARIOUS MIXING RATE.

CHEMICAL LOADING $C_1 = 10^{-3}$
REYNOLDS NUMBER $C_2 = 9.2*10^6$
$M_o = 0.5$

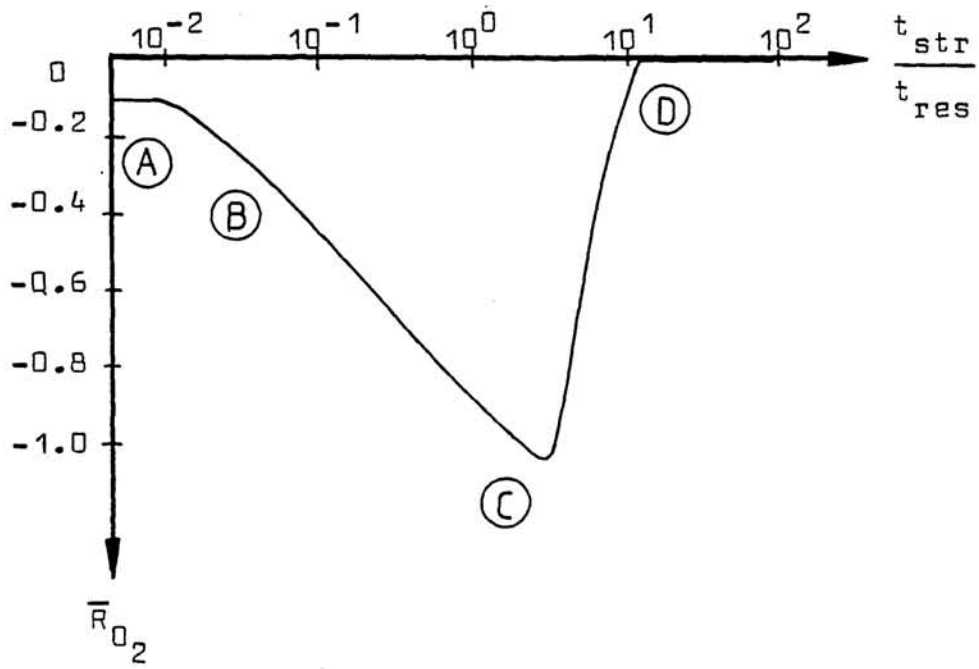

Figure 7.29 POPULATION-AVERAGE REACTION RATE AT VARIOUS MIXING RATE.

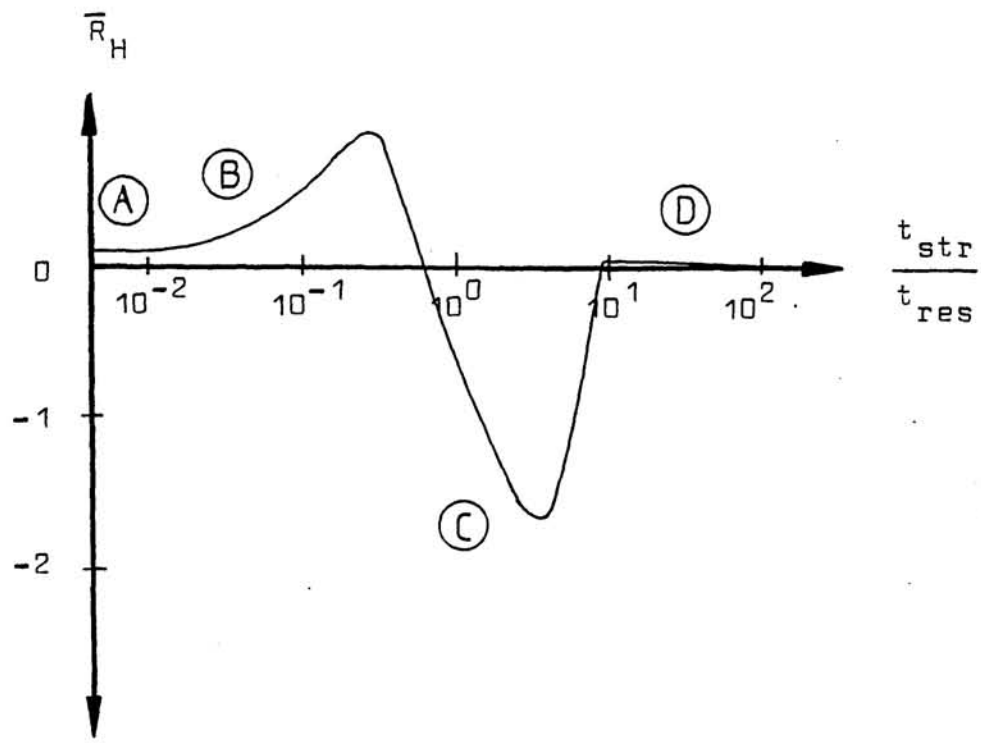

Figure 7.30 POPULATION-AVERAGE REACTION RATE AT VARIOUS MIXING RATE.

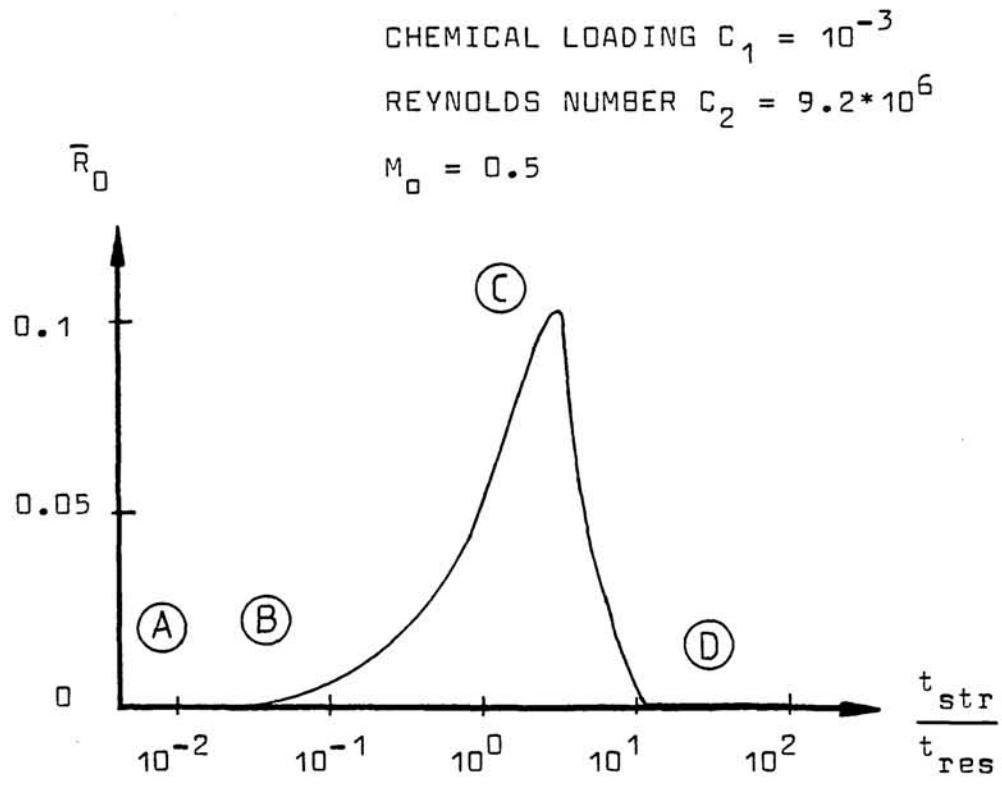

Figure 7.31 POPULATION-AVERAGE REACTION RATE AT VARIOUS MIXING RATE.

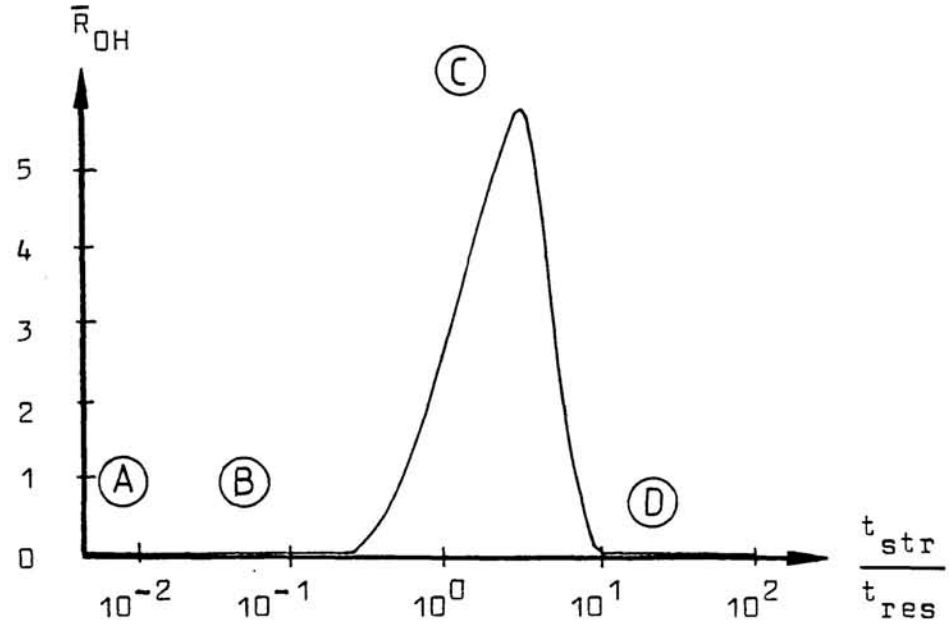

Figure 7.32 POPULATION-AVERAGE REACTION RATE AT VARIOUS MIXING RATE.

CHEMICAL LOADING $C_1 = 10^{-3}$
REYNOLDS NUMBER $C_2 = 9.2*10^6$
$M_o = 0.5$

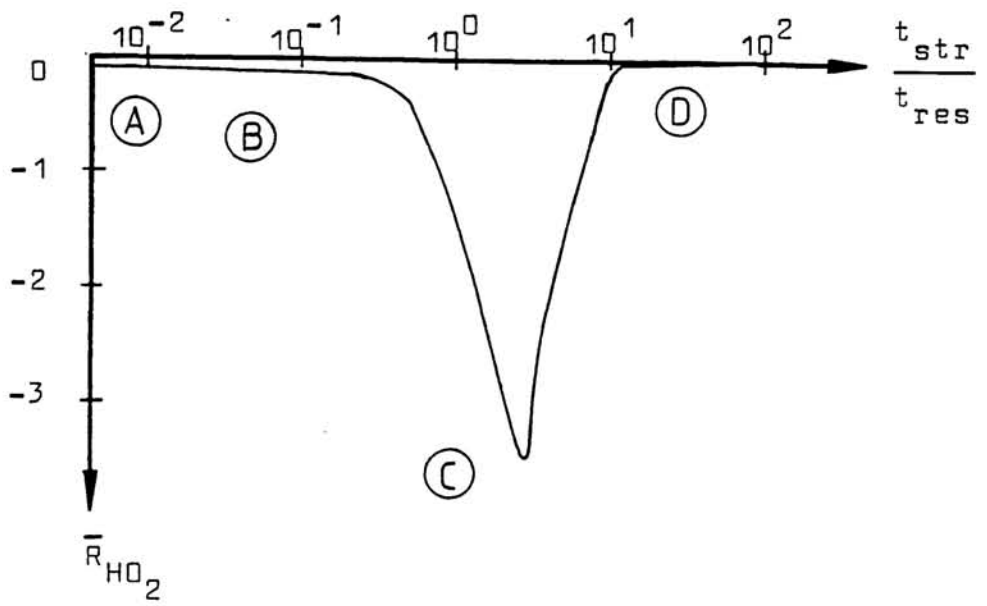

Figure 7.33 POPULATION-AVERAGE REACTION RATE AT VARIOUS MIXING RATE.

Discussion

The above results imply that $\bar{r}_\phi$ has the form $\bar{r}_\phi(t_{react}, t_{diff}, t_{str}, t_{res})$ expressing the influences of hydrodynamics, laminar transport and chemical kinetics on the population-average reaction rate. Understandably, the reaction rate characteristics cannot have unique relations since chain reactions are present. However, similarities of the population-average burning rate (equation 7.3-4) and the population-average reaction rate do exist. It is therefore worthwhile to discuss the behaviour of the former in the reactor under three different burning regimes. The population-average burning rate is given by:-

$$\dot{\bar{\tau}} = \int_0^\infty \frac{d\tilde{\tau}}{da} P_a \, da \quad . \qquad (7.3\text{-}4)$$

The following important remarks can be made.

(i) Spontaneous ignition regime

When t_{react} is of the same order as either t_{diff} or t_{str}, the non-uniformity of the fold properties across the fold would be evened out before the significant reactions takes place. Under these circumstances, $\dot{\bar{\tau}}$ is governed only by the reaction and residence times. The fragment-

coalescence approach belongs to this operating mode.

(ii) Laminar flame speed control regime

When the value of t_{diff}/t_{react} is large and the stretching rate is negligibly small, the burning regime is that of laminar-speed-control.

The fold-average burning rate $\frac{d\tilde{\tau}}{da}$ is uniform up to the linear flame burn-out time t_f and zero beyond it, so that the population-average burning rate is simply:

$$\dot{\bar{\tau}} = \int_o^{t_f} \frac{1-\tilde{\tau}_o}{t_f} \frac{1}{M_o\ t_{res}} \mathrm{Exp}\left(-\frac{a}{M_o\ t_{res}}\right) da \quad ,(7.3\text{-}5)$$

i.e. $$\dot{\bar{\tau}} = \frac{1-\tilde{\tau}_o}{t_f} \left| 1 - \mathrm{Exp}\left(-\frac{t_f}{M_o\ t_{res}}\right) \right| \quad . \qquad (7.3\text{-}6)$$

The exponential term expresses the non-linearity relations between $\dot{\bar{\tau}}$ and the ratio of the linear flame burn-out time to the residence time of the well-stirred reactor.

(iii) Internal flame propagation regime

When t_{diff}/t_{react} is large and t_{diff}/t_{str} is moderate, the population-average burning rate of this regime is given by:

$$\dot{\bar{\tau}} = \int_{o}^{t_b} \frac{1-\tilde{\tau}_o}{t_f} \operatorname{Exp}\,(a/t_{str}) \frac{1}{M_o\, t_{res}}$$

$$\operatorname{Exp}\left(-\frac{a}{M_o\, t_{res}}\right) da \quad , \qquad (7.3\text{-}7)$$

Hence,

$$\dot{\bar{\tau}} = \frac{1-\tilde{\tau}_o}{t_f} \frac{1}{1-\dfrac{M_o\, t_{res}}{t_{str}}} \; 1-\operatorname{Exp}\left(\frac{t_b}{t_{str}} - \frac{t_b}{M_o\, t_{res}}\right) \quad . \qquad (7.3\text{-}8)$$

When t_{diff}/t_{str} is considerably smaller than t_{diff}/t_{react}, the flame front of the micro burning process within the fold starts (see Chapter 4).

In fragment-coalescence approach, the influences of laminar transport on the time-mean reaction rate calculation are absent. Therefore, the models employed by Evangelista (1969) and Borghi (1974) fail to predict $\dot{\bar{\tau}}$ in the internal flame propagation regime.

On the other hand, the ESCIMO approach does account for the influences of hydrodynamic, laminar-transport and chemical kinetics on $\dot{\bar{\tau}}$, as already demonstrated in this section.

7.4 Connexion with the "presumed-pdf" procedure

7.4.1 Purpose

The purpose of this section is to demonstrate the ability of the ESCIMO theory by being extended to multiple-reactions. In order to show the advantage of the theory, the probability-density functions calculated for a well-stirred reactor to which it is applied will be given. Some other earlier approaches from selected works of Borghi (1974) and Evangelista et al (1969) are highlighted and the superiority of the present theory is discussed. For this purpose, the performance of the well-stirred reactor is expressed in terms of the first and second moments of probability-density functions which are useful and interesting not only to practitioners of the ESCIMO approach, but also to those who guess 'probability-density functions' and the law which governs them.

7.4.2 Criticism of the "presumed-pdf" procedure

As illustrated in Figure (7.34), three possible pdf shapes are assumed at different locations within the flame. The 'guess' values of the probability-density functions of species concentrations and temperature have been used as "closure assumptions" for calculating the time-average reaction rates in premixed flame. However,

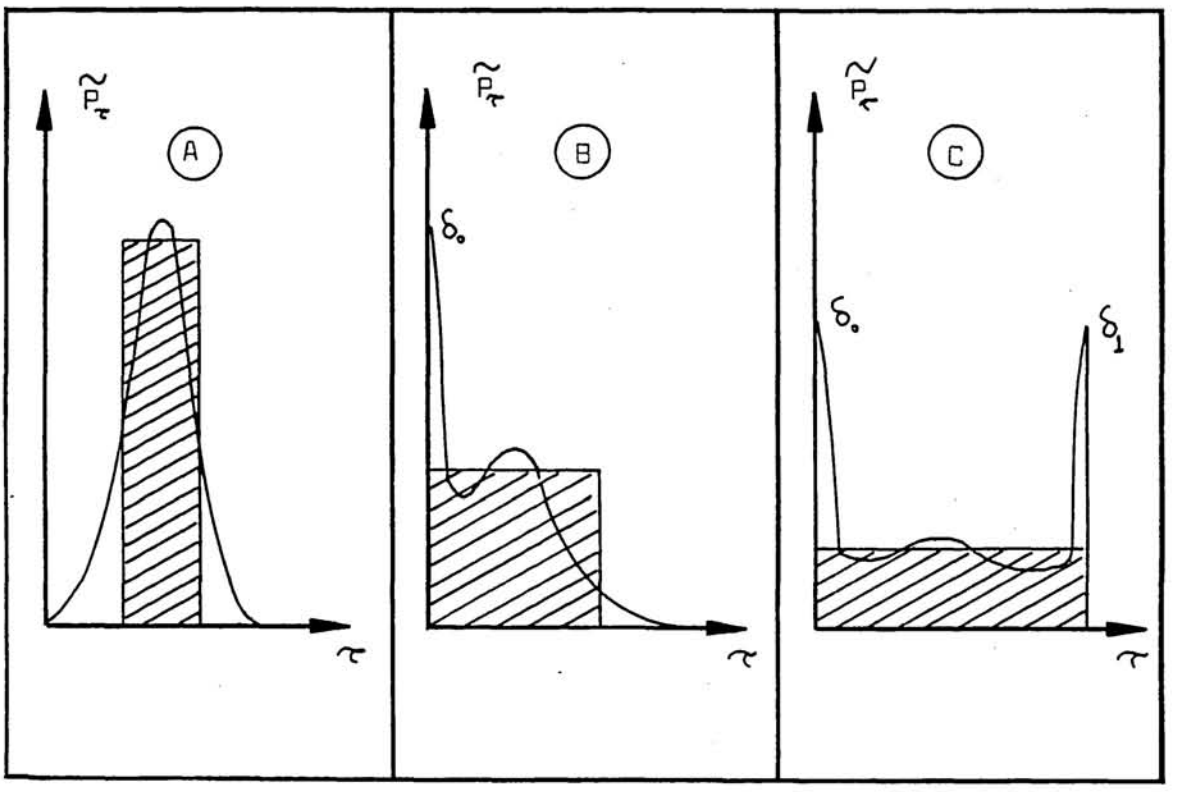

FIGURE 7.34 TYPICAL PRESCRIPTIONS FOR PROBABILITY DENSITY FUNCTION (BORGHI AND MOREAN, 1977)

the predictions have been shown to be very sensitive to the pdf presumption (Borghi, 1974). In addition, these "closure assumptions" do not give realistic time-average reaction rates. In complex chemical reactions, the pdf must vary widely in shape. Thus, the "presumed-pdf" procedure is inadequate to calculate the turbulent reacting flow satisfactorily.

7.4.3 Criticism of the fragment-coalescence procedure

As already mentioned in sub-section 7.1.2, the model is of the "hydrodynamic+kinetic" type. Three particular defects, which result from the "closure assumptions", the presumed-pdf and absence of effect of laminar-transport, are shown in their predictions (Evangelista, 1969). Since they take no account of the laminar-transport term on the time-average reaction rate, their approach fails to predict the finite-rate reactions when the flame front exists in the fragments.

In view of the above reasons, the need for a different approach cannot be over emphasised.

7.4.4 The alternative

In the ESCIMO approach, three different pdf's should be distinguished: (1) the fold $\tilde{p}d\phi,\tilde{p}$; (2) the population-

distribution function, P_a; and (3) the probability-density function, $\bar{P}$ for concentration fluctuations. The first two are regarded as the special features of the ESCIMO output while the last is the $\bar{p}d\phi$ of the material-finding in the space which is connected directly with the probability space of turbulent fluctuations.

Since $\tilde{p}$ is known for individual folds, as functions of age, the $\bar{p}d\phi$ of the material ϕ, which lies in the interval of ϕ to $\phi+d\phi$, in the reactor on space-average is given by:

$$\bar{p}\langle\phi\rangle = \int_0^\infty \tilde{p}\langle\phi,a\rangle\, P_a\, da \quad . \qquad (7.4\text{-}1)$$

Definitions of the probability-density function

The mathematical description will now be on the space-average values and other fluctuating quantities. These include: (1) the $\bar{p}$ function, and (2) its first and second moments.

Consider a dependent variable ϕ. If the probability-density finding of ϕ between ϕ and $\phi+d\phi$ is $\bar{p}\langle\phi\rangle d\phi$, then,

$$\int_{\phi_{min}}^{\phi_{max}} \bar{p}\langle\phi\rangle d\phi = 1 \quad . \qquad (7.4\text{-}2)$$

The first and second moments can be calculated from the knowledge of $\bar{p}$ in the turbulent reacting flows. The former is simply $\bar{\phi}$, while the latter can easily be related to $\sqrt{\overline{\phi'^2}}$, the root-mean-square value of the ϕ fluctuations.

In other words, the first moment is given by:

$$\bar{\phi} = \int_{\phi_{min}}^{\phi_{max}} \bar{p}\langle\phi\rangle\phi d\phi \quad . \qquad (7.4\text{-}3)$$

The corresponding variance, $\overline{\phi'^2}$ is defined as the mean-square departure of the instantaneous quantity from its population-average value:

$$\overline{\phi'^2} = \int_{\phi_{min}}^{\phi_{max}} (\phi-\bar{\phi})^2 \bar{p}d\phi$$

$$= \int_{\phi_{min}}^{\phi_{max}} \phi^2 \bar{p}\langle\phi\rangle d\phi - \bar{\phi}^2 \quad . \qquad (7.4\text{-}4)$$

Numerical calculation

Since the fold $\tilde{p}d\phi$ has been calculated by way of the linear-interpolation method given in Chapter 4, all moments of variable ϕ defined in the $\bar{p}d\phi$ space are easily evaluated.

The $\bar{p}$ distribution

The probability-density function of ϕ in the space is calculated from:

$$\bar{p}\langle\phi\rangle = \sum_{o}^{\infty} \tilde{p}\, P_a\, da$$

$$= \sum_{o}^{t_b} \tilde{p}\, P_a\, \delta a + \tilde{p}\langle t_b, \phi\rangle \left| 1 - \sum_{o}^{t_b} P_a\, \delta a \right| \quad . \qquad (7.4\text{-}5)$$

Population-average quantity

$$\bar{\phi} = \sum_{o}^{t_b} \tilde{\phi} P_a \delta a + \tilde{\phi}\langle t_b\rangle \left| 1 - \sum_{o}^{t_b} P_a \delta a \right| \quad . \qquad (7.4\text{-}6)$$

Root-mean-square quantity

Since the $\bar{p}$'s and $\bar{\phi}$'s have been calculated, the root-mean-square value of ϕ can be expressed as:

$$\sqrt{\overline{\phi'^2}} = \sqrt{\sum_{\phi_{min}}^{\phi_{max}} \phi^2\, \bar{p}\delta\phi - \bar{\phi}^2} \quad . \qquad (7.4\text{-}7)$$

The fluctuation intensity

The fluctuation intensity of ϕ is defined as the root-mean-square value of ϕ divided by its population-average value $\bar{\phi}$, i.e.

$$I = \frac{\sqrt{\overline{\phi'^2}}}{\bar{\phi}} \quad . \qquad (7.4\text{-}8)$$

The above value indicates the degree of fluctuation.

7.4.5 Results of the ESCIMO approach

Results of the concentration fluctuations are given as functions of the chemical loading and mixing rate. The corresponding shapes of $\bar{p}$df's under four different sets of controlling parameters (indicated by boxes in Tables 7.3 and 7.4) are also presented.

(i) The effect of chemical loading

In Figures (7.35 - 7.39), the concentration fluctuations are shown as functions of chemical loading. It is observed that at low range of loading (A to B), the fluctuation is small. For higher values (C to D), the fluctuation increases rapidly. At the blow-out region (point D), the fluctuation is so high that the combustion is terminated.

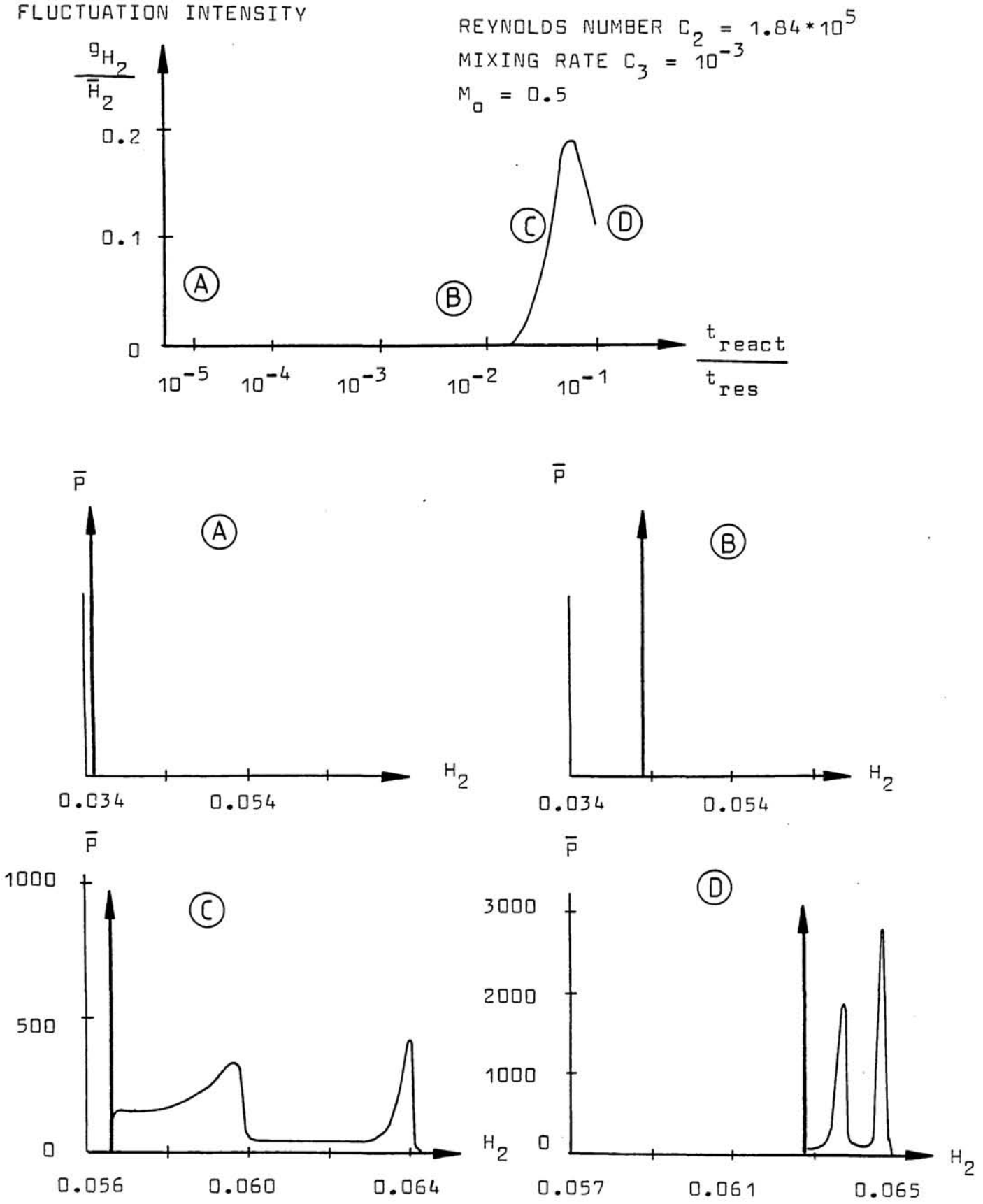

Figure 7.35 SHAPES OF PROBABILITY-DENSITY FUNCTION, THE (A)-(D) SHAPES CORRESPOND TO AN INCREASE OF THE CHEMICAL LOADING.

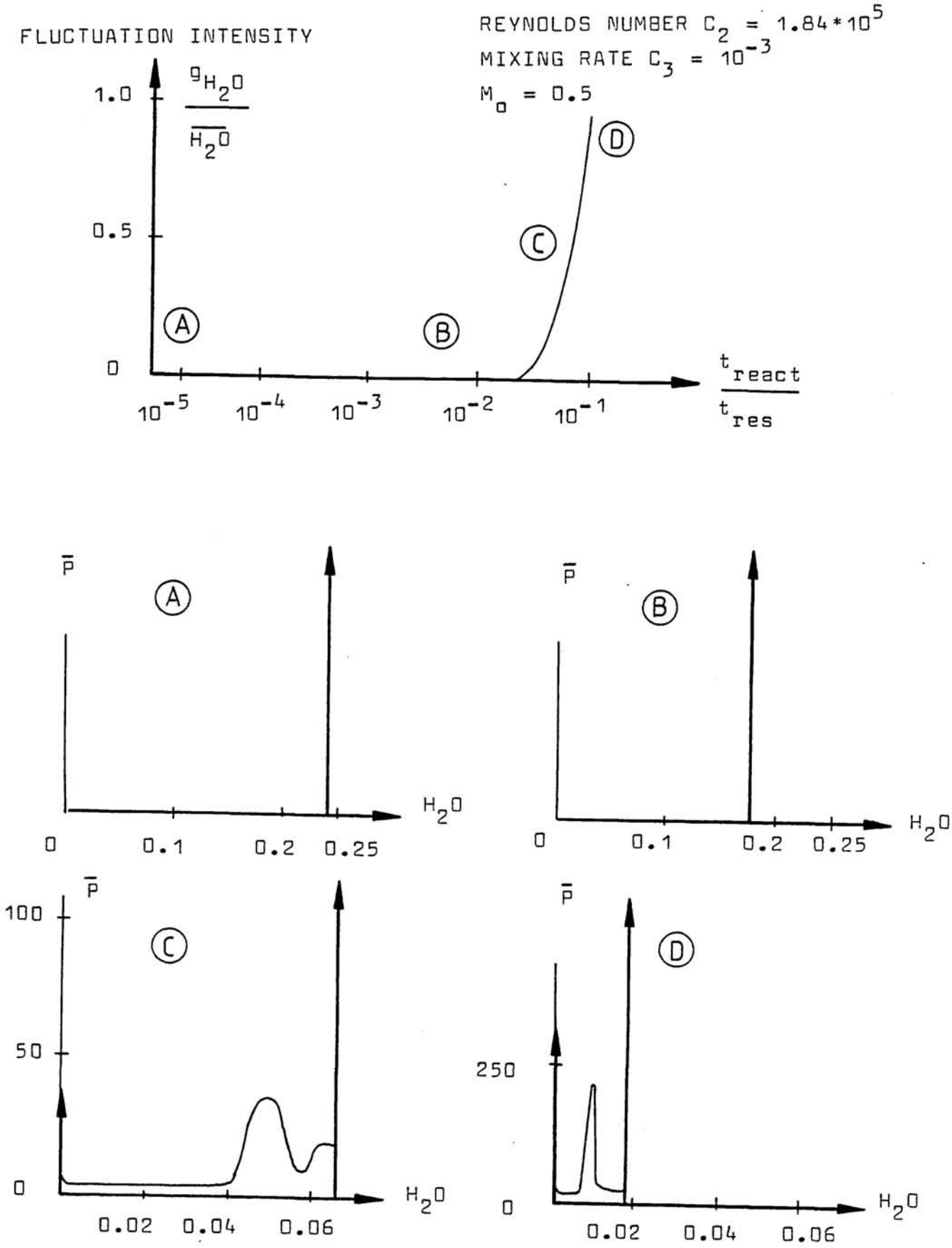

Figure 7.36 SHAPES OF PROBABILITY-DENSITY FUNCTION, THE (A)-(D) SHAPES CORRESPOND TO AN INCREASE OF THE CHEMICAL LOADING.

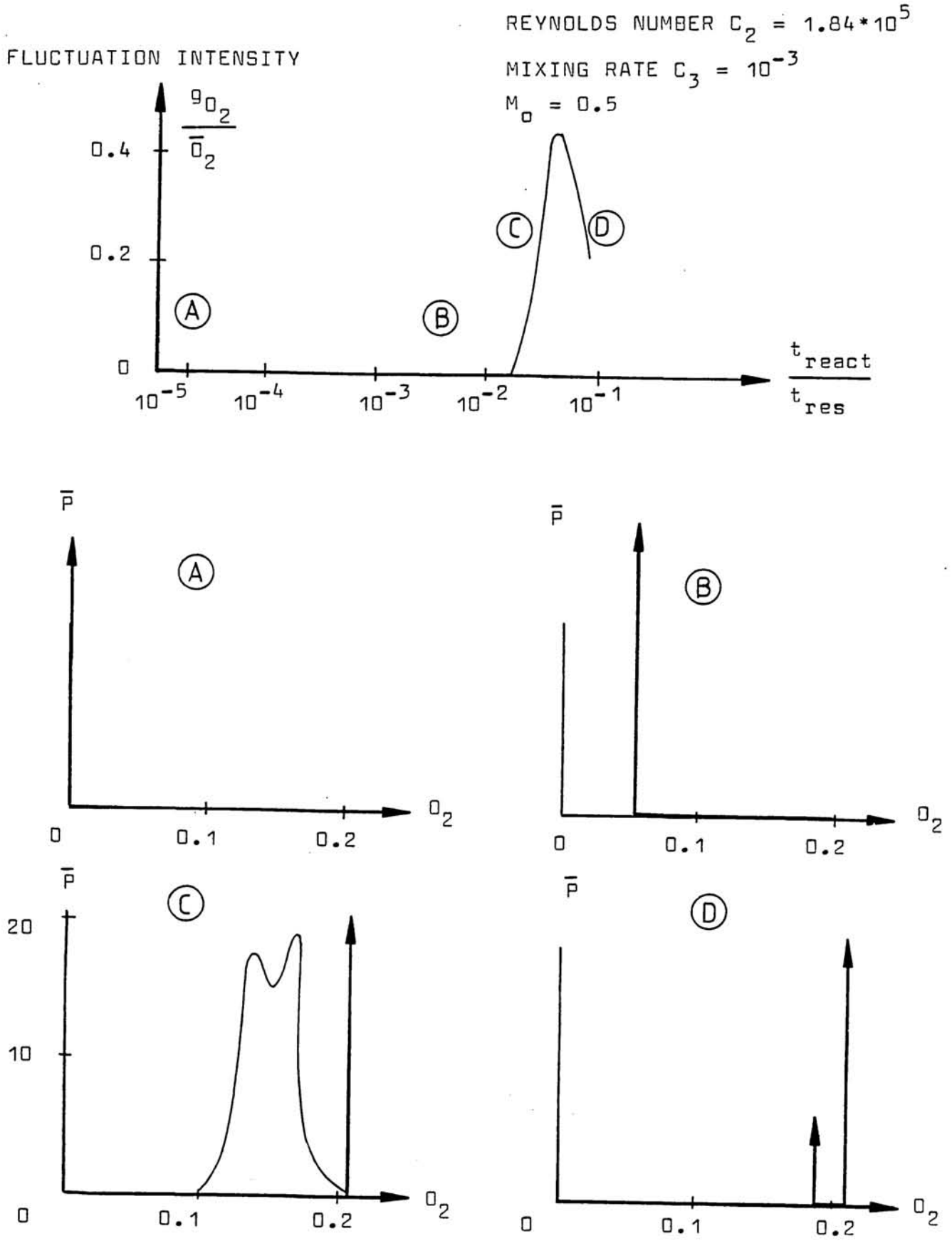

Figure 7.37 SHAPES OF PROBABILITY-DENSITY FUNCTION, THE (A)-(D) SHAPES CORRESPOND TO AN INCREASE OF THE CHEMICAL LOADING.

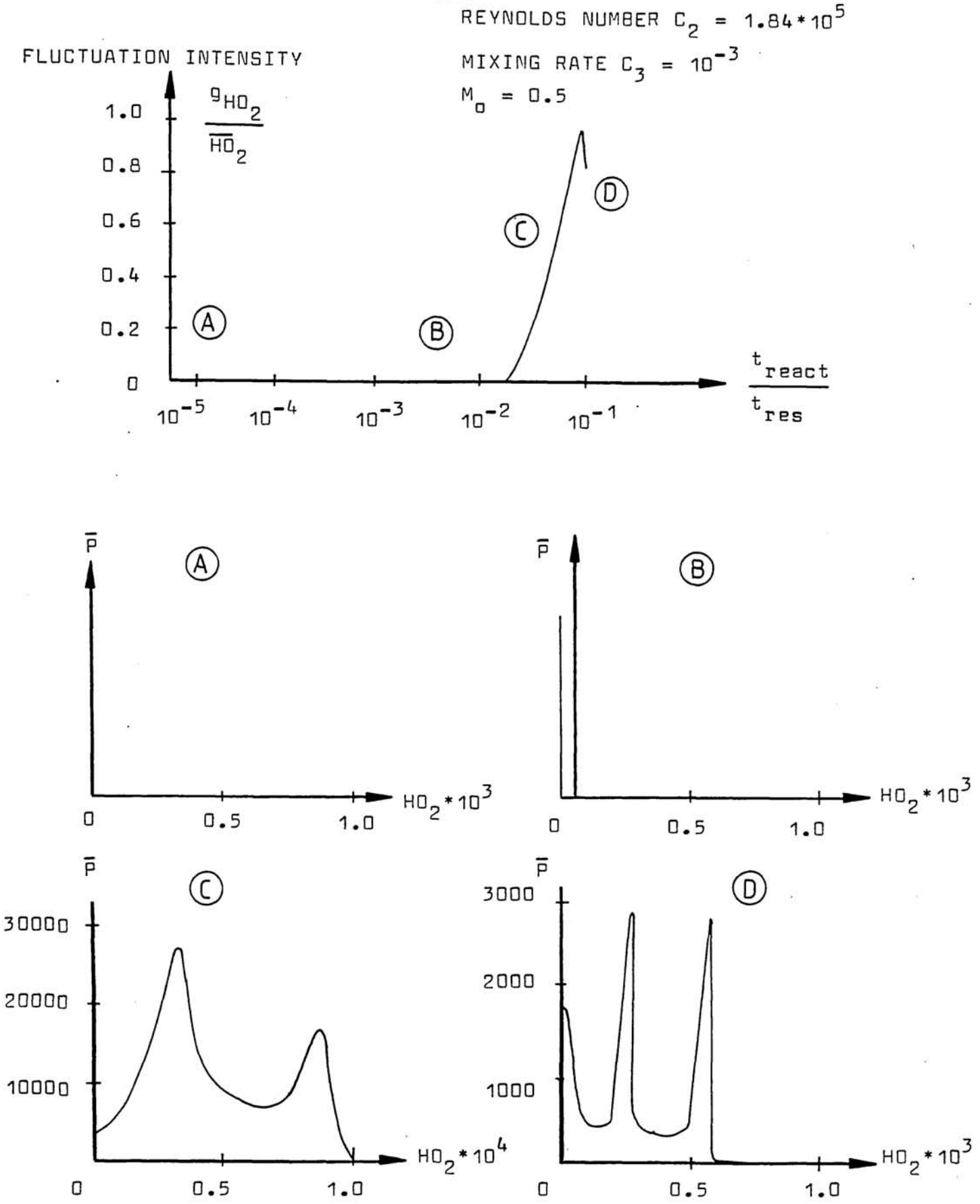

Figure 7.38 SHAPES OF PROBABILITY-DENSITY FUNCTION, THE (A)-(D) SHAPES CORRESPOND TO AN INCREASE OF THE CHEMICAL LOADING.

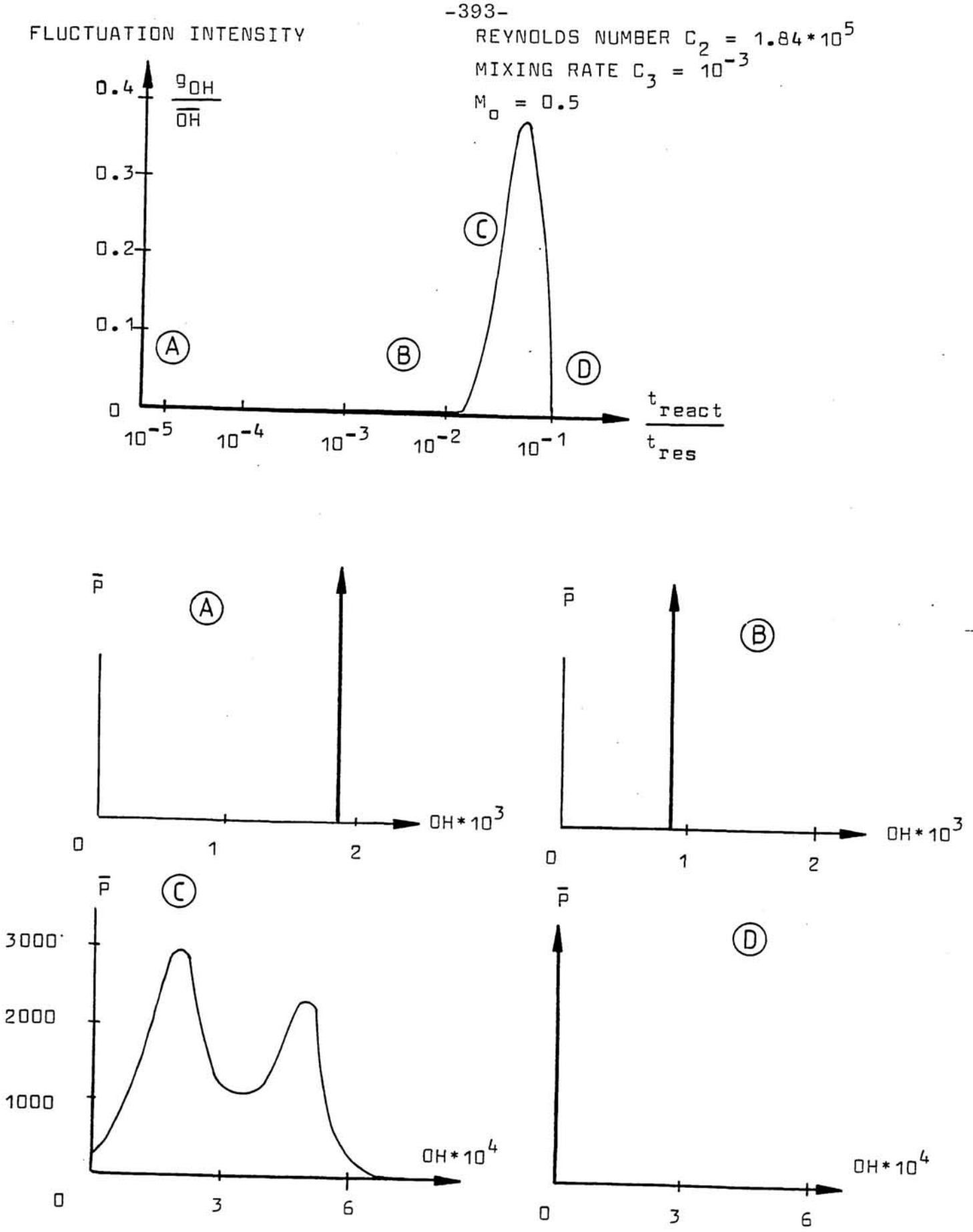

Figure 7.39 SHAPES OF PROBABILITY-DENSITY FUNCTION, THE (A)-(D) SHAPES CORRESPOND TO AN INCREASE OF THE CHEMICAL LOADING.

The real shapes of the $\bar{p}$df

It has been demonstrated that in the performance of a reactor, the concentration fluctuation must depend on the controlling parameters, consequently, so will the shapes of the $\bar{p}$df. As illustrated in Figures (7.35 - 7.39), shapes of $\bar{p}$df are very sensitive to the chemical loading. The results are described as follows.

Region A

As t_{react}/t_{res} approaches zero, the performance is close to that of ideal perfectly-stirred reactors. Hence, only a single 'spike' can be observed.

Region B

As t_{react}/t_{res} increases, the combustion process is that of finite-rate combustion. It is seen that the $\bar{p}$ distribution has finite value from $\phi=\phi_{min}$ to $\bar{\phi}$, and has a single 'spike' at the latter position.

Region C

When t_{react}/t_{res} increases beyond the lower range, the $\bar{p}$ starts to exhibit two spikes at $\phi=\phi_{min}$ and ϕ_{max} and linked by a wide distribution area. In this circumstance, the micro-burning regime is that of spontaneous ignition.

It is for this situation that the fragment-coalescence model is intended.

Region D

Near the blow-out point, t_{react}/t_{res} is so high that the fluctuation is extremely large. Therefore, the $\bar{p}$ distribution is shifted towards the inlet-steam condition. As the consequences of high fluctuation and low activation energy, the flame is extinguished.

(ii) The effect of mixing rate

Figures (7.40 - 7.44) show results of concentration fluctuations as functions of mixing rate. Since the reaction time is considerably shorter than both the stretching and diffusion times ($C_1=10^{-3}$, $C_2=9.2\times10^{6}$), the micro-burning regime is that of internal flame propagation. It is seen that for small (but finite) values of t_{str}/t_{res} (from A to B), concentration fluctuations become so small that the reactor is close to being perfect. For larger values of t_{str}/t_{res} (from C to D), the fluctuation increases. It is observed that a sufficiently large mixing rate will precipitate flame extinction.

The most significant implication of these results are that the influences of hydrodynamics, laminar transport and chemical kinetics on the reactor performance can be observed. More profound results of shapes of $\bar{p}$ obtained from four different regions are discussed in turn.

Region A

Both the mixing rate and chemical loading are very low and the combustion process is thus close to equilibrium. Hence, only a single spike is observed.

Region B

In this region, the mixing rate tends to increase while the chemical loading remains finite. It is observed that the $\bar{p}$ distribution is characterised by two spikes at ϕ_{min} and ϕ_{max}. In addition, the $\bar{p}$ distribution on the ϕ_{max} is more profound.

Region C

This corresponds to a further increase in the mixing rate. It shows that the $\bar{p}$df shapes tend to consist mainly of two spikes at ϕ_{min} and ϕ_{max}. It is for this situation that the eddy-break-up model is intended.

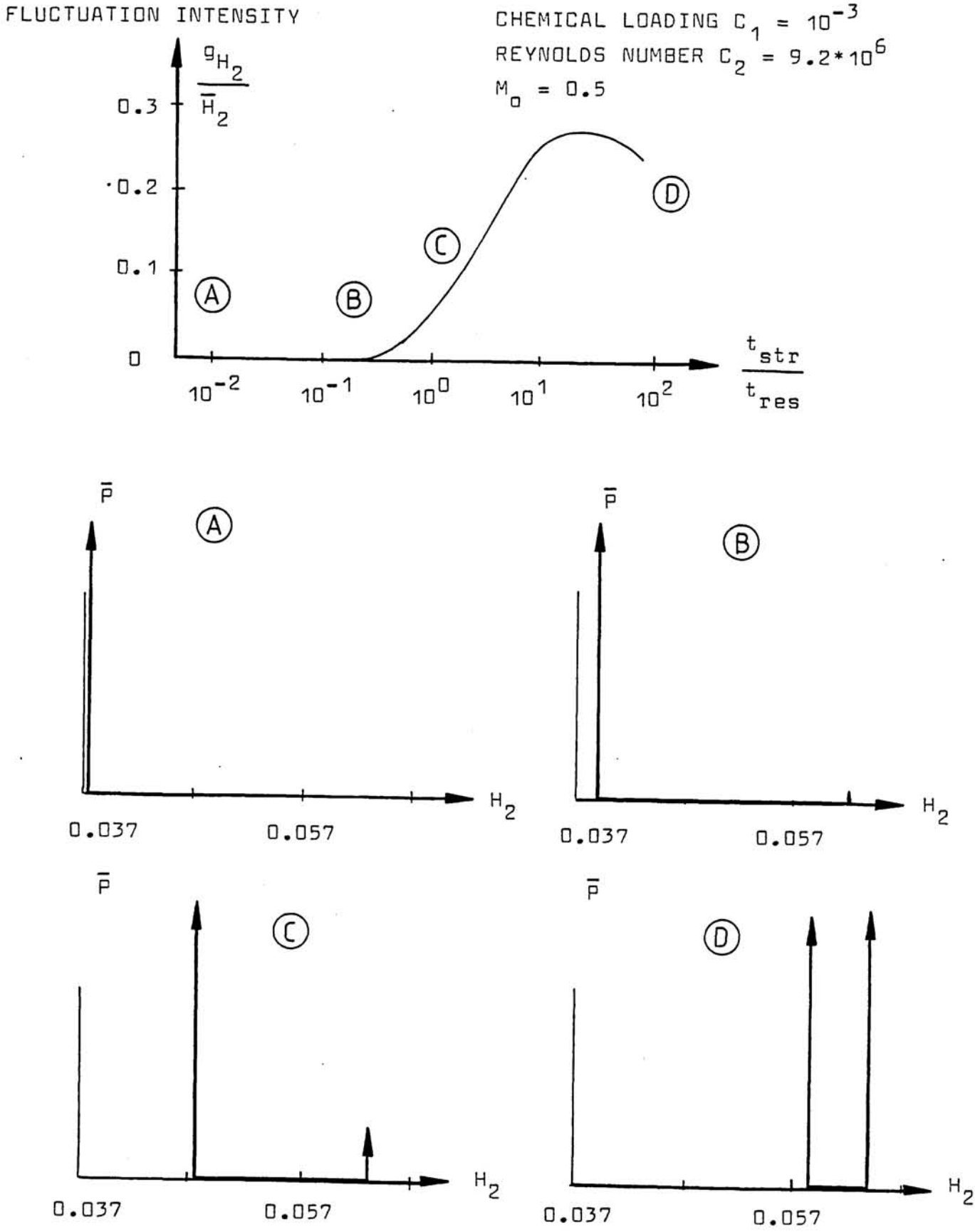

Figure 7.40 SHAPES OF PROBABILITY-DENSITY FUNCTION, THE (A)-(D) SHAPES CORRESPOND TO AN INCREASE OF THE MIXING RATE.

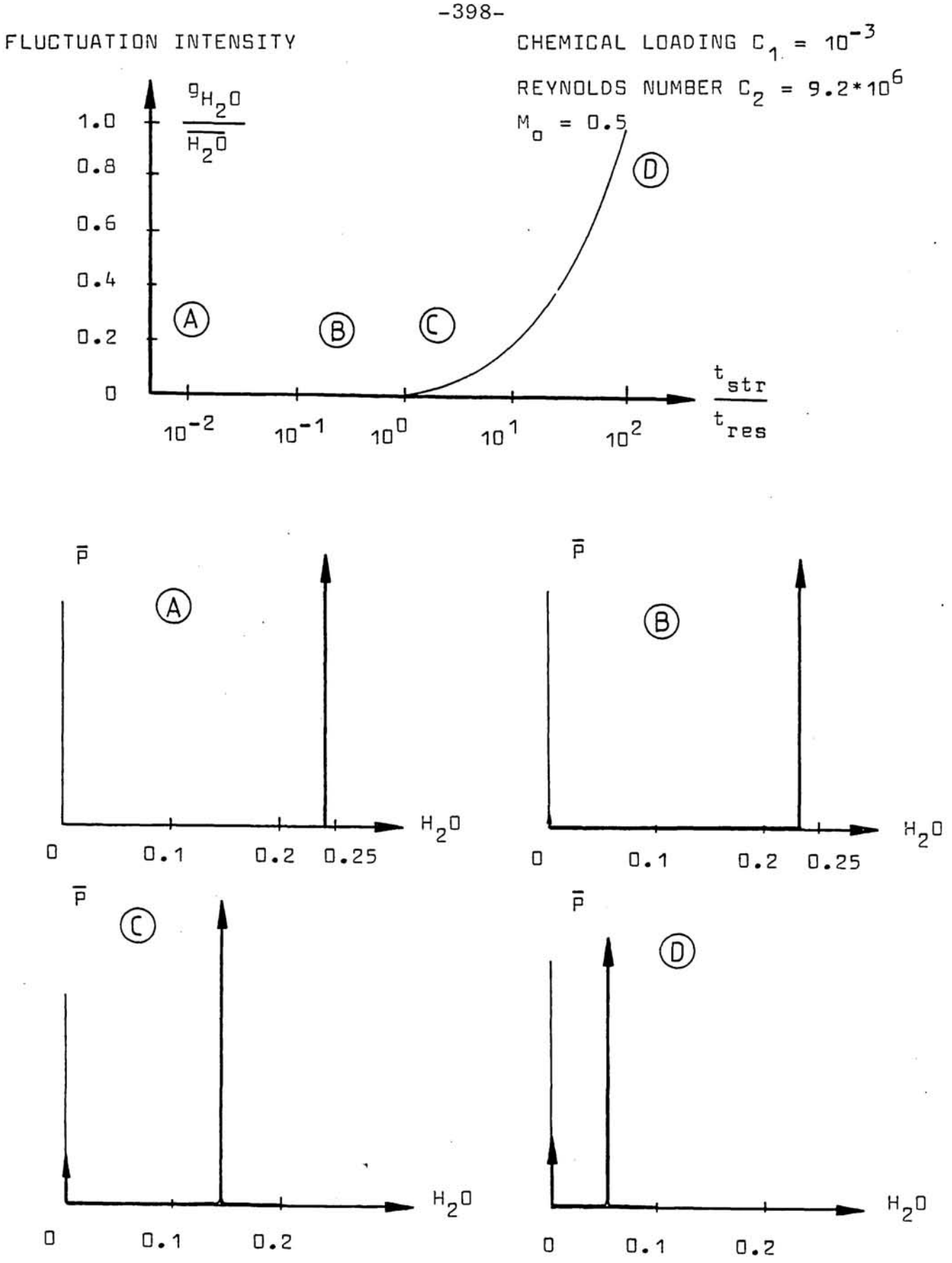

Figure 7.41 SHAPES OF PROBABILITY-DENSITY FUNCTION, THE (A)-(D) SHAPES CORRESPOND TO AN INCREASE OF THE MIXING RATE.

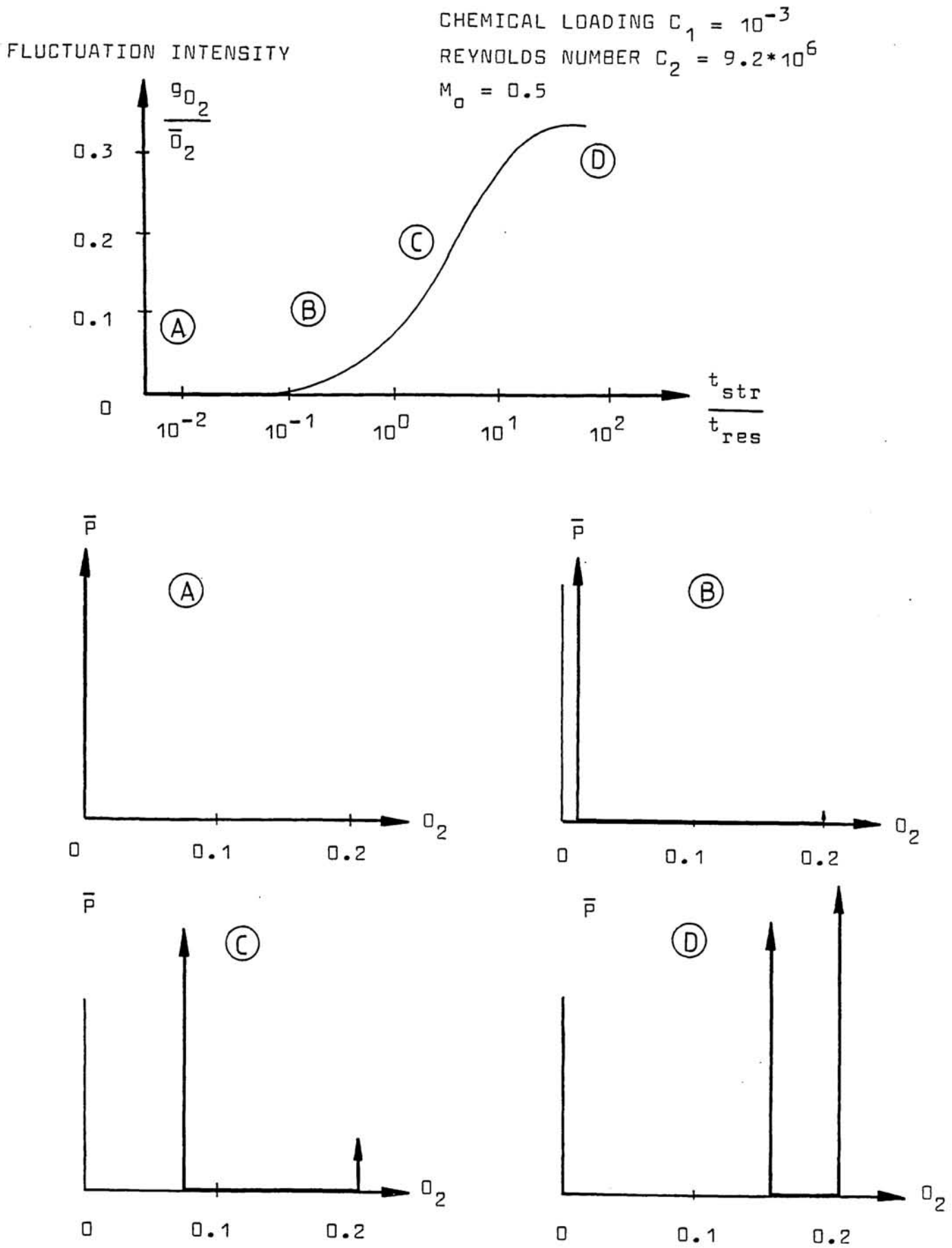

Figure 7.42 SHAPES OF PROBABILITY-DENSITY FUNCTION, . THE (A)-(D) SHAPES CORRESPOND TO AN INCREASE OF THE MIXING RATE.

FLUCTUATION INTENSITY

CHEMICAL LOADING $C_1 = 10^{-3}$

REYNOLDS NUMBER $C_2 = 9.2*10^6$

$M_o = 0.5$

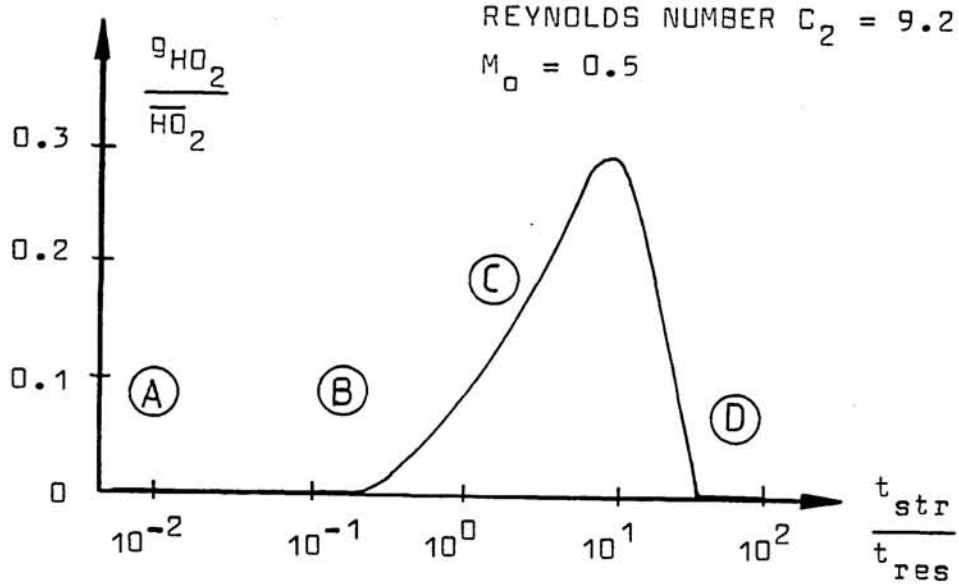

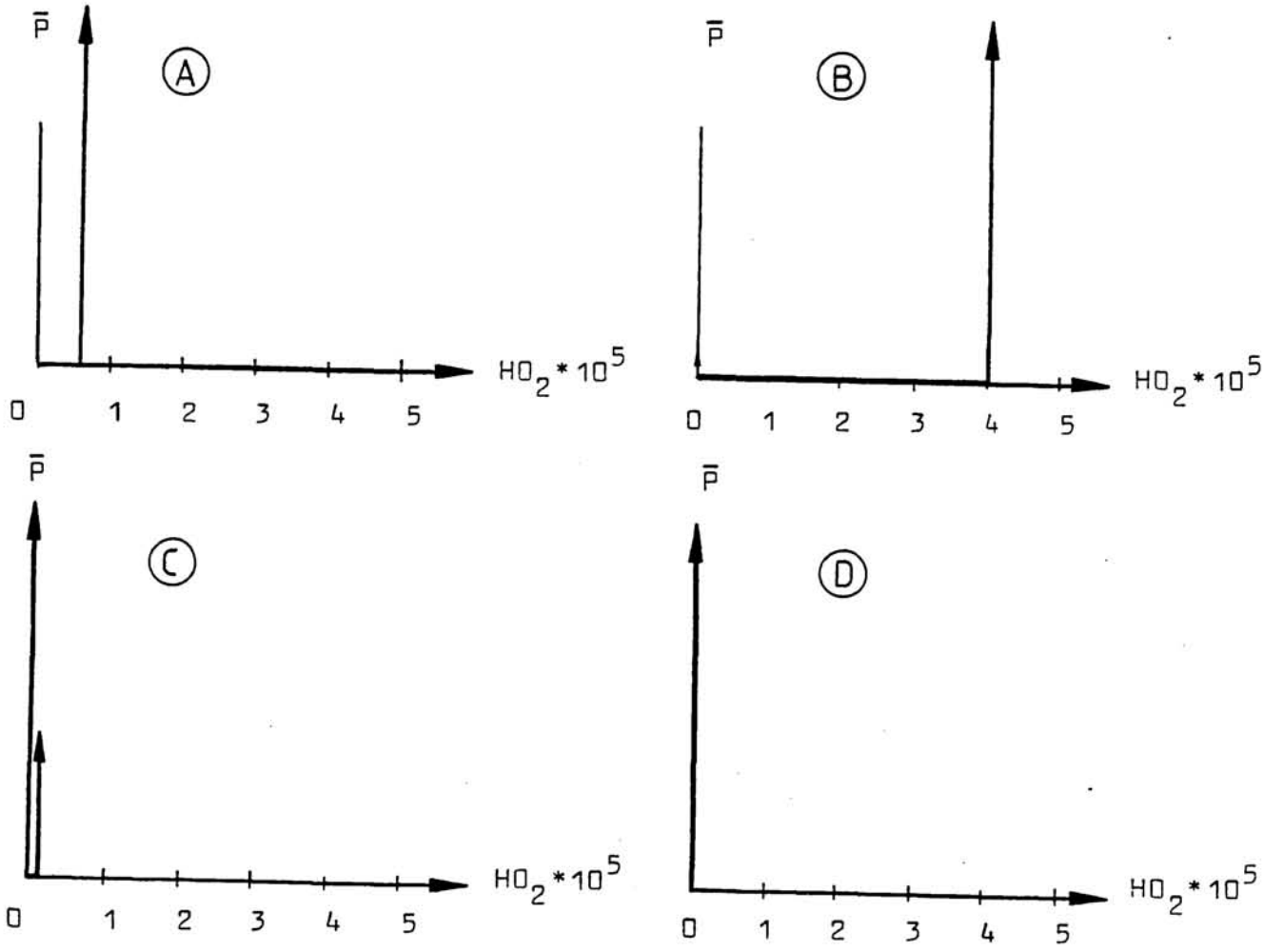

Figure 7.43 SHAPES OF PROBABILITY-DENSITY FUNCTION, THE (A)-(D) SHAPES CORRESPOND TO AN INCREASE OF THE MIXING RATE.

FLUCTUATION INTENSITY

CHEMICAL LOADING $C_1 = 10^{-3}$

REYNOLDS NUMBER $C_2 = 9.2*10^6$

$M_o = 0.5$

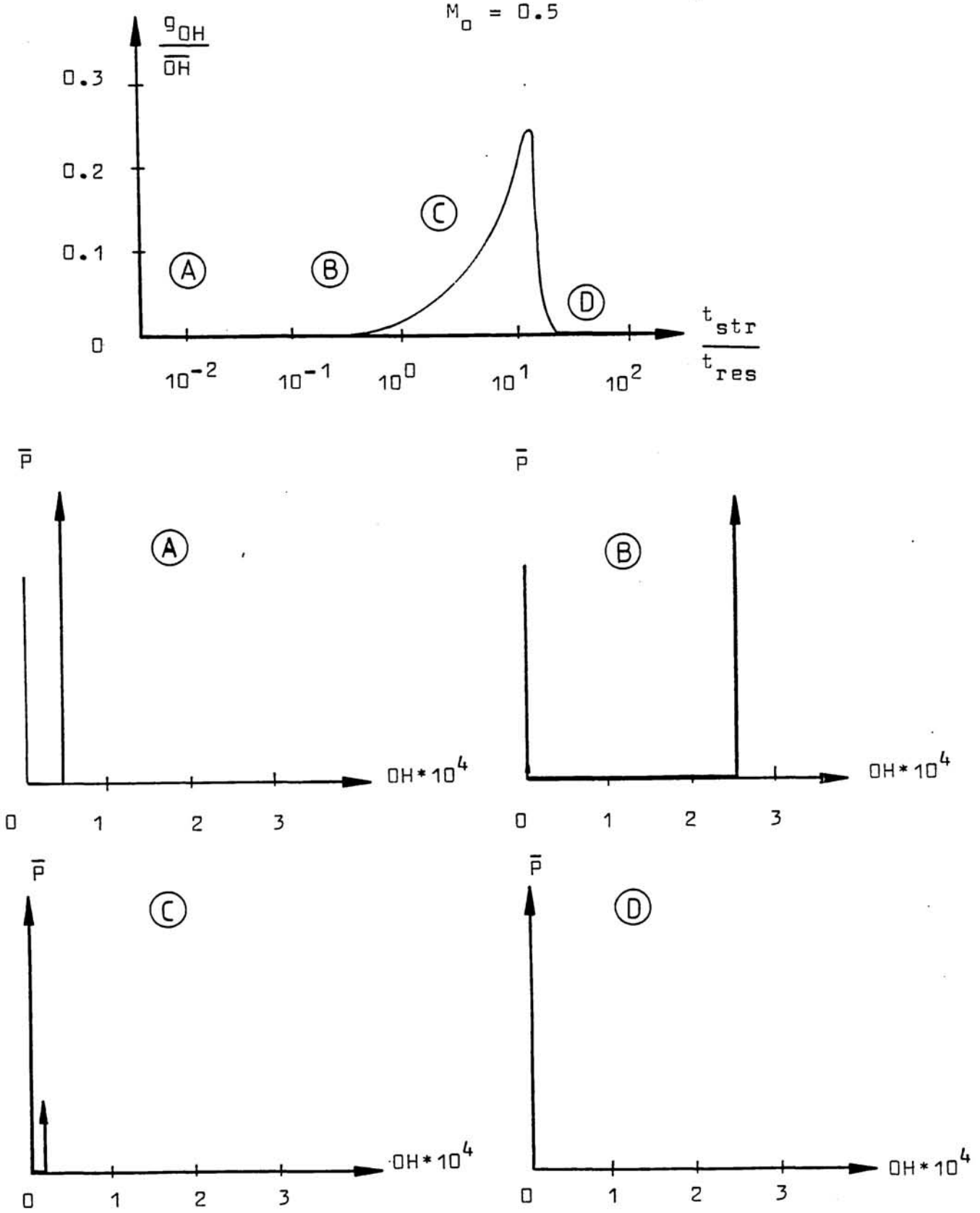

Figure 7.44 SHAPES OF PROBABILITY-DENSITY FUNCTION, THE (A)-(D) SHAPES CORRESPOND TO AN INCREASE OF THE MIXING RATE.

Region D

Here, the mixing rate is sufficiently high. It is observed that the $\bar{p}$ distributions are shifted to the inlet-stream conditions.

Discussion

The above results have two important aspects. First, it is shown that the predicted concentration fluctuations can be explained by the shapes of the corresponding $\bar{p}$df. In the absence of experimental data the ESCIMO approach does provide the quantitative results. Secondly, it is evident from Figures 7.35 - 7.39 that the Borghi's presumption of the $\bar{p}$df shape is never observed. Since the probability-density functions are governed by the physical laws (hydrodynamics, laminar-transport and chemical kinetics), it is argued that the $\bar{p}$df of concentration fluctuations must be calculated from the theory rather than the 'presumed-pdf' procedure.

7.5 Closure

This chapter has been concerned with the application of the ESCIMO theory (biographic and demographic aspects) to the well-stirred reactor. The following conclusions can be drawn regarding the work reported therein.

1. The ESCIMO approach has been extended to multiple chemical reactions.

2. The complete solution procedure of the ESCIMO approach has been shown to yield realistic solution of the performance of the reactor. Since the high Reynolds number employed characterises fully turbulent flow, the performance has been shows to be influenced by the mixing rate and chemical loading. Thus when the mixing rate or the chemical loading increases sufficiently, blow out occurs.

3. Results of concentration fluctuations have been expressed as first and second moments of the corresponding probability-density functions. It has been shown that shapes of $\bar{p}$df vary widely and are governed by the physical laws. The ESCIMO approach has been proved to provide the potential advantage of calculating the $\bar{p}$df directly. The objective of extending the ESCIMO approach incorporating the effects of hydrodynamics, laminar-transport and chemical kinetics on the time-average reaction rate has been achieved.

CHAPTER 8 - CONCLUDING REMARKS

8.1 Achievements of the Present Work

The main achievements of the present study and the conclusions are summarised as follows:

8.1.1 Theoretical achievements

(1) Numerical achievement

A solution procedure which combined the advantages of two numerical algorithms for solving complex chemical kinetic equations has been developed, applied and validated.

It has been shown that the present procedure provides a rapid solution to problems associated with turbulent reacting flows.

(2) Fold-biographic study

The present work has been devoted to the presentation of the fold-biographic study within a stretched-fold. The inter-diffusion model chosen is appropriate to the pre-mixed combustible hydrogen-oxygen gases. The chemical reaction mechanism employed is that of the 7-step elementary reactions of hydrogen-oxygen system. A wide range of conditions which are associated with molecular diffusion, eddy stretching and chemical kinetics has been investigated.

It has been shown that the analytical approach cannot handle the intermediate conditions. Subsequently, three burning regimes have been demonstrated numerically.

These are:

(a) Laminar flame propagation across a non-stretching fold;

(b) Laminar flame propagation across a fold which is being significantly diminished in thickness by stretching; and

(c) spontaneous iginition within a fold which, at any instance, has a practically uniform composition.

These provide a qualitative and quantitative understanding of the interaction of turbulence∿chemistry within a small scale fold.

(3) Application of the ESCIMO theory to the well-stirred reactor

In order to demonstrate the potential of the ESCIMO approach, the complete theory has been applied to the well-stirred reactor. The performance has been computed as a function of three independent dimensionless ratios, corresponding to the chemical

loading, the Reynolds number and the mixing rate. It is of importance that the space probability-density function distributions have been calculated from the theory rather than using any presumed-pdf procedure. In addition, the root-mean-square values of concentration fluctuations have been deduced directly from the first and second moments of the corresponding $\bar{p}$df's.

The objective of demonstrating the ESCIMO approach which incorporates the full knowledge of multiple reactions has therefore been achieved.

8.1.2 Experimental achievements

With the aim of verifying the fold-biographic theory, two types of experiments have been performed, namely: (a) a cold flow experiment, in which distributions of concentrations of a tracer gas across the stretched-folds have been measured; and (b) a combustion experiment, in which temperature variations across the laminar diffusion hydrogen-air stretched flame have been measured.

The experimental measurements of multiple laminar stretched folds in open converging channels, carried out in the present study, showed the correct trends. In addition, a numerical solution procedure which adopted the present laminar stretched flame under the influence of buoyancy has been developed and employed.

The computational requirements are about 32K words of storage space, and about 317 seconds execution time on a CDC 6600 computer.

The comparisons of predictions with experimental results are generally fair.

8.2 Suggestions for Future Work

The present investigation disclosed some areas where further research is required in order to raise the abilities of the theory. These include:

(1) Extension to pollutant-forming reactions

The main exothermic reaction scheme which oxidises a hydrogen-oxygen system by way of many intermediates has successfullly been applied in the present study. The task should be extended to those of pollutant-forming reaction schemes, resulting in the formation of nitrogen oxide in turbulent flames.

(2) Extension to non-premixed reactions in a well-stirred reactor

The ESCIMO theory of turbulent combustion has been applied to the pre-mixed, steady-flow well-stirred reactor. The task should also be extended to formulate the fold population distribution function into two groups. The first group comprises folds formed from reactor-average gases

engulfed by fresh fuel. The second comprises folds in which the reactor-average gases are engulfed by fresh oxidant. The computational time is therefore about twice as much as for pre-mixed gases.

(3) Extension to complex flows

In order to apply the ESCIMO approach to more complex flow situations, it is of importance to develop the demographic theory. The most straightforward method is to solve fold-transport equations which describe how folds are formed at any birthplace in the flow field; having the initial size, age and composition within a given range, and how folds are transported to any other place.

The coupling of the fold biographic and demographic theories will become a major task after the general demographic theory has been developed.

(4) Experimental investigation of birth-rate statistics

It would be useful to perform the fold size, fold formation rate statistics measurements at different birthplaces in a simple turbulent flow field.

REFERENCES

1. ARRHENIUS S (1889)
"Uber die Reaktiongeschwindigkeit bei der Inversion von Rohrzucken Durch Savren". Z. Phys. Chem. 4, 226, 1889.

2. BALDWIN R R AND COWE D W (1962)
"The Inhibition of Hydrogen and Oxygen Reaction by Formaldehyde". Trans. Faraday Soc., 58, 1768.

3. BARR J AND MULLINS B P (1954)
"Combustion in Vitiated Atmospheres".
I - Combustion Process in Vitiated Air.
II - Some Preliminary Studies of Diffusion Flames.
III - Effect of Oxygen Concentration on Ignition Induction Period.
IV - Performance of a Typical Combustion Chamber.
V - Application of Results.
Fuel 33, 181, 200, 205 and 225.

4. BAULCH D L, DRYSDALE D D AND HORNE D G (1968-1970)
"High Temperature Reaction Rate Data". Univ. of Leeds, Report Nos. 1-5.

5. BECKER H A, HOTTEL H C AND WILLIAMS G C (1963)
"Mixing and Flow in ducted Turbulent Jets". Ninth Symp. (Int) on Combustion, pp.7-20.

6. BECKER H A, HOTTEL H C AND WILLIAMS G C (1968) "Characterisation of Concentration Fluctuations in a Turbulent Jet by the Scattered Light Technique". Paper No. 17d, 56th Annual Meeting of the AIChE.

7. BEVILAQUA P M (1975) "Some Observations on the Mechanism of Entrain ment"in"Turbulent Mixing in Non-Reactive and Reactive Flows". SNB Murthy (Ed), Plenum Press, New York.

8. BILGER R W AND KENT J H (1972) "Concentration Fluctuation in Turbulent Jet Diffusion Flames". Sydney Univ Dept of Mech. Eng., Report F46.

9. BILGER R W (1975) "Turbulent Jet Diffusion Flames". Proc. Progress in Energy and Combustion Science I.

10. BILGER R W (1976a) "The Structure of Diffusion Flames". Combustion Science and Technology, Vol 13, pp 155-170.

11. BILGER R W (1976b)
"Reaction Zone Thickness and Formation of Nitric Oxide in Turbulent Diffusion Flames". Combustion and Flame, 26, pp. 115-123.

12. BLICHNER O E (1972)
"A Fluid Dynamic Study of a Spherical and a Cylindrical Stirred Reactor". Eighth Symp. (Int) on Combustion, pp. 995-1002.

13. BONNOIR C, BORGHI R AND MAGRE P (1977)
"Turbulent Combustion in a Stirred Combustor". Turbulent Combustion, edited by L A Kennedy AIAA, New York, NY, pp. 331-349.

14. BORGHI R (1974)
"Computational Studies of Turbulent Flows with Chemical Reaction" in "Turbulent Mixing in Non-Reactive and Reactive Flows". Edited by S N B Murthy Plenum Press, New York.

15. BORGHI R AND MOREAN P (1977)
"Turbulent Combustion in a Premixed Flow". Acta Astronautica, Vol 4, pp. 321-341.

16. BOTHA J P AND SPALDING D BRIAN (1954)
"The Laminar Flame Speed of Propane/Air Mixtures with Heat-Extraction from the Flame". Proc. of the Royal Society A, Vol. 229, pp. 71-96.

17. BOWMAN C T (1973)
"Kinetics of Nitric Oxide Formation in Combustion Processes".
Fourteenth Symposium (Int) on Combustion, p.729, The Combustion Institute, Pittsburgh, Penn.

18. BOWMAN B R, PRATT D T AND CROWE C T (1973)
"Effects of Turbulent Mixing and Chemical Kinetics on Nitric Oxide Production in a Jet-Stirred Reactor". Fourteenth Symposium (Int) on Combustion, p. 805, The Combustion Institute, Pittsburgh, Penn.

19. BRAY K N C AND LIBBY P A (1976)
"Interaction Effects in Turbulent Premixed Flames". Physics of Fluids,, Vol. 19, pp. 1687-1701.

20. BRODKEY R S (1975)
"Turbulent Mixing Studies in a Chemical Reactor" in "Turbulent Mixing in Non-Reactive and Reactive Flows". S N B Murthy (Ed), Plenum Press, New York.

21. BROWN G L AND ROSHKO A (1974)
"On Density Effects and Large Structures in Turbulent Mixing Layers". J. Fluid Mech., Vol. 64, Part 4, pp. 775-816.

22. BULEWICZ E M AND SUGDEN T M (1958)
"The Recombination of Hydrogen Atoms and Hydroperoxyl Radical in Hydrogen Flame Gas". Trans. Faraday Soc., 54. 1855.

23. BURKE S P AND SCHUMANN T E W (1928)
"Diffusion Flames".
Idustr. Engng Chem., 20, 998.

24. CARETTO L S (1976)
"Mathematical Modelling of Pollutant Formation". Prog. Energy Combustion Sci. Vol 1, pp. 47-71, Pergamon Press.

25. CASE P L AND PRATT D T (1977)
"A New Integration Algorithm for Chemical Kinetics". 1977 Spring Meeting of the Western States Section/The Combustion Institute WSS/CI 77-23.

26. CHAMPION M, BRAY K N C AND MOSS J B (1977)
"The Turbulent Combustion of a Propane-Air Mixture". Acta Astronautica, Vol 5, pp. 1063-1077.

27. CLYNE M A A AND THRUSH B A (1963)
"Rates of Elementary Processes in the Chain Reaction Between Hydrogen and Oxygen - I. Reaction of Oxygen Atoms". Proc. Roy. Soc (Lond), A275, J44.

28. COCHRAN T H (1972)
"Experimental Investigation of Laminar Gas Jet Diffusion Flames in Zero Gravity". TN D-6523, NASA.

29. CROOM B H AND LEYHE E W (1966)
"Thermodynamic, Transport and Flow Properties for the Products of Methane Burned in Oxygen-Enriched Air". NASA SP-3035.

30. CURL R L (1963)
"Dispersed phase mixing, I: Theory and Effects in Simple Reaction".
AICheJ, Vol. 9, p.175.

31. DAMKOHLER G (1940)
A, Elektrochem, 46, pp. 601-626

32. DAMKOHLER G (1947)
"The Effect of Turbulence on the Flame Velocity in Gas Mixtures". NACA Tech. Memo, No. 1112.

33. DAVIES P O A L (1975)
"Coherent Structures in Turbulence" in "Turbulent Mixing in Non-Reactive and Reactive Flows". Edited by S N B Murthy Plenum Press.

34. DIXON-LEWIS G (1967)
"Flame Structure and Flame Reaction Kinetics: I. Solution of Conservation Equations and Application to Rich Hydrogen-Oxygen Flames". Proc., Roy. Soc., A298, pp. 495-512.

35. DIXON-LEWIS G (1968)
"Flame Structure and Flame Reaction Kinetics: II. Transport Phenomena in Multicomponent Systems". Proc. Roy. Soc., A307, pp. 111-135.

36. DIXON-LEWIS G, SUTTON M M AND WILLIAMS A (1970a)
"Flame Structure and Flame Reaction Kinetics: IV. Experimental Investigations of a Fuel-Rich Hydrogen+Oxygen+Nitrogen Flame at Atmospheric Pressure". Proc. Roy. Soc., A317, pp. 227-234.

37. DIXON-LEWIS G (1970b)
"Flame Structure and Flame Reaction Kinetics: V. Investigation of Reaction Mechanism in a Rich Hydrogen+Nitrogen+Oxygen Flame by Solution of Conservation Equations". Proc. Roy. Soc., (Lond) A317, pp. 235-263.

38. DOEBELIN E O (1966)
"Measurement Systems, Application and Design".
McGraw-Hill.

39. DONALDSON C DUP AND HILST G R (1972)
"Chemical Reactions in Inhomogeneous Mixtures,
The Effect of the Scale on Turbulent Mixing".
Presented Proc. Heat Transfer and Fluid Mechanics
Institute.

40. DONALDSON C DUP AND VARMA A K (1976)
"Remarks on the Construction of a Second-Order
Closure Description of Turbulent Reacting Flows".
Combustion Science and Technology, Vol 13,
pp. 55-78.

41. DOPAZO C AND O'BRIEN E E (1976)
"Statistical Treatment of Non-Isothermal Chemical
Reactions in Turbulence". Comb. Sci. and Tech.,
Vol 13, pp. 99-122.

42. EDELMAN R B, FORTUNE O H, WEILERSTEIN, GERTRUDE,
COCHRAN, THOMAS H AND HAGGARD J B (1973)
"An Analytical and Experimental Investigation of
Gravity Effects upon Laminar Gas Jet Diffusion
Flames". Fourteenth Symp. (Int) on Combustion,
pp. 399-412, The Combustion Institute, Pittsburgh,
Penn.

43. EDELMAN R B AND HARSHA P T (1977)
"Some Observations on Turbulent Mixing with Chemical Reactions". Presented as Paper 77-142 at the AIAA 15th Aerospace Sciences Meeting, Los Angeles, Calif., January 24-26, 1977.

44. EDMONDSON H AND MICHAEL P H (1971)
"The Burning Velocity of Hydrogen-Air Flames". Combuston and Flame, 16, pp. 161-165.

45. ELAINE S O AND JAY P B (1979)
"Theoretical and Computational Approach to Modelling Flame Ignition". Laboratory for Computational Physics, Naval Research Laboratory Washington, DC, December 1979.

46. ELGHOBASHI S E (1974)
"Characteristics of Gaseous Turbulent Diffusion Flames in Cylindrical Chambers - A Theoretical and Experimental Investigation".
PhD Thesis, University of London.

47. ELGHOBASHI S E, PUN W M AND SPALDING D BRIAN (1975)
"Concentration Fluctuations in Isothermal Turbulent Confined Coaxial Jets". Imperial College, Dept of Mech. Eng., London Report HTS/75/23.

48. ELGHOBASHI S E, SPALDING D BRIAN AND SRIVATSA S K (1977)
"Prediction of Hydrodynamics and Chemistry of Confined Turbulent Methane-Air Flame with Attention to Formation of Oxides of Nitrogen".
NASA CR-135179.

49. EVANGELISTA J J, SHINNER R AND KATZ S (1969)
"The Effect of Imperfect Mixing on Stirred Combustion Reactors". Twelfth Symp. (Int) on Combustion, the Combustion Institute, pp. 901-912.

50. FAY J A (1954)
"The Distribution of Concentration and Temperature in a Laminar Jet Diffusion Flame".
J. Aero. Sci., 21, pp.681.

51. FENIMORE C P AND JONES G W (1959)
"Consumption of Oxygen Molecules in Hydrocarbon Flames Chiefly by Reaction with Hydrogen Atoms".
J. Phys. Chem., 63, 1834.

52. FRISTROM R M AND WESTERNBERG A A (1965)
"Flame Structure". McGraw-Hill Book Co., New York.

53. FRISTROM R M
"Radial Concentrations and Reactions in a Methane Oxygen Flame". Proc. 9th Symp. (Int) on Combustion, 560, the Combustion Institute, USA.

54. GANJI A T AND SAWYER R F (1980)
"Turbulence, Combustion, Pollutant and Stability Characterisation of a Premixed Step Combustor". NASA CR/3230.

55. GAYDON A G AND WOLFHARD H G (1979)
"Flames, Their Structure, Radiation and Temperature". John Wiley and Sons, New York.

56. GEANHOPLIS C J (1971)
"Mass Transport Phenomena". Holt, Rinehart and Winston Inc.

57. GLAWE G E AND SHEPARD C E (1954)
"Some Effects of Exposure to Exhaust-Gas Streams on Emittance and Thermoelectric Power of Bare Wire Platinum Rhodium-Platinum Thermocouples". NACA, TN 3253.

58. GOLOVICHEV V I, PREOBRAZHENSKY N G AND YASAKOV V A (1976)
"Numerical Study of Non-Equilibrium Processes in Two-Dimensional Turbulent Reactive Gas Flows". Archives of Mechanics 28, 5-6, pp.733-758, Warszawa.

59. GORDON S AND MCBRIDE B (1971)
"Computer Program for Calculation of Complex Chemical Equilibrium Compositions". NASA SP-273.

60. GOSMAN A D (1969)
"Prediction of the Hydrodynamic and Combustion Properties of the Conical Stirred Reactor". Imperial College, Dept of Mech Eng., EF/TN/A/20.

61. HARLOW F H AND NAKAYAMA P I (1967)
"Turbulent Transport Equations". Phys. Fluids, 10, pp 323.

62. HARLOW F H (1973)
"Turbulence Transport Modelling". AIAA Selected Reprint Series, Vol XIV, AIAA New York.

63. HASTIE J W (1975)
"High Temperature Vapours". Academic Press.

64. HINDMARSH A C (1972)
"Linear Multistep Methods for Ordinary Differential Equations: Method Formulations, Stability and the Methods of Nordsieck and Gear". Lawrence Livermore Lab., UCRL-51186.

65. HIRSCHFELDER J O, CURTISS C F AND BIRD R B (1954) "The Molecular Theory of Gases and Liquids". John Wiley and Sons Inc., New York.

66. HOTTEL H C AND HAWTHORNE W R (1949) "Diffusion in Laminar Flame Jets". 3rd Symposium, p.254.

67. HOTTEL H C, WILLIAMS G C AND MILES G A (1967) "Mixedness in the Well-Stirred Reactor" Eleventh Symposium (Int) on Combustion, p.771, The Combustion Institute, Pittsburgh, Pennsylvania.

68. HOWE N M AND SHIPMAN C W (1965) "A Tentative Model for Rates of Combustion in Confined Turbulent Flames". Tenth Symposium (Int) on Combustion, The Combustion Institute, p.1139.

69. ISSA R, SPALDING D BRIAN AND TATCHELL D G (1974) "Guide to the Computer Program REP3". CHAM Project Report 631/2.

70. JAIN V K AND SPALDING D BRIAN (1965) "Combustion and Flame", 9, p.37.

71. JANAF, THERMOCHEMICAL TABLES (1971) National Bureau of Standards, USA, NSRDS 37, COM-71, 50363.

72 JENKINS D R, SPALDING D BRIAN AND YUMLU V S (1967) "Combustion of Hydrogen and Oxygen in a Steady-Flow Adiabatic Stirred Reactor". Eleventh Symp. (Int) on Combustion, The Combustion Institute, Pittsburgh, Penn., pp. 779-790.

73. JONES A AND PROTHERO A (1968) "The Solution of the Steady-State Equations for an Adiabatic Stirred Reactor". Combustion and Flame 12, pp.457.

74. KARLOVITZ B (1953) "Open Turbulent Flames". 4th Symp. (Int) on Combustion, p.60.

75. KARLOVITZ B, DENNISTON D W, KNAPSCHAEFER D W AND WELLS F E (1953) "Studies on Turbulent Flames". 4th Symp. (Int) on Combustion, pp. 613-620.

76. KAUFMAN F AND GRECO F P DEL (1963) "Fast Reaction of OH Radicals". Ninth Symp. (Int) on Combustion, Academic Press Inc., New York (1963), p. 659.

77. KEE R J AND MILLER J A (1978)
"A Split-Operator, Finite-Difference Solution for Axisymmetric Laminar-Jet Diffusion Flame". AIAA Vol 16, No. 2.

78. KENT J H AND WILLIAMS F A
"Extinction of Laminar Diffusion Flames for Liquid Fuels". Fifteenth Symp. (Int) on Combustion.

79. KOLOMOGOROV A N (1942)
"Equation of Turbulent Motion of an Incompressible Fluid". IZV Akad. Nawk USSR., Ser. Phys., Vol.6, No. 1/2, pp. 56-58. (Translated into English at Imperial College, Mech Eng. Dept. Report No. ON/6, 1968).

80. KUMAGAI S AND ISODA H (1956)
Sixth Symp. (Int) on Combustion p.726. Williams and Wilkins, Baltimore.

81. LAPIDUS L AND SEINFELD J H (1971)
"Numerical Solution of Ordinary Differential Equations". Academic Press.

82. LAUNDER B E AND SPALDING D BRIAN (1972)
"Mathematical Models of Turbulence". Academic Press.

83. LEWIS AND ELBE V (1961)
"Combustion, Flames and Explosions of Gases". Academic Press.

84. LIBBY P A (1976)
"On Turbulent Flows with Fast Chemical Reactions. Part III: Two-Dimensional Mixing with Highly Dilute Reactants". Combustion Science and Technology, Special Issue on Turb. Reactive Flows, Vol 13, Nos. 1-6. pp.79-98.

85. LINIGER W AND WILLOUGHBY R A (1967)
"Efficient Numerical Integration of Stiff Systems of Ordinary Differential Equations". IBM Research Report RL-1970.

86. LOCKWOOD F C AND ODIDI A O (1974)
"Measurement of Mean and Fluctuating Temperature and of Ion Generation in Round Free-Jet Turbulent Diffusion and Premixed Flames". Apr (1974) HTS/74/17 Mech. Eng. Dept., Imperial College.

87. LOCKWOOD F C AND NOGUIB A S (1975)
"The Prediction of the Fluctuations in the Properties of Free Round-Jet, Turbulent Diffusion Flames". Combustion and Flame, Vol. 24, p.109.

88. LOCKWOOD F C (1977)
"The Modelling of Turbulent Premixed and Diffusion Combustion in the Computation of Engineering Flows". Combustion and Flame 29, pp. 111-122.

89. LONGWELL J P AND WEISS M A (1955)
"High Temperature Reaction Rates in Hydrocarbon Combustion". Ind. Eng., Chem., 47, pp.1637-43.

90. MA A S C, SPALDING D BRIAN AND SUN R L T (1980)
"Application of the ESCIMO Theory to Combustion in a Well-Stirred Reactor". HMT Series, Vol.4, Pergamon Press (to be published).

91. MA A S C, NOSEIR M A AND SPALDING D BRIAN (1980)
"An Application of the ESCIMO Theory of Turbulent Combustion". Paper presented at the AIAA Meeting in January 1980, Pasadena, California, USA.

92. MARBLE F E AND BROADWELL J E (1977)
"The Coherent Flame Model for Turbulent Chemical Reactions". Project SQUID Technical Report TRW-9-PU.

93. MASON E A (1954)
"Transport Properties of Gases Obeying a Modified Buckingham (exp-six) Potential". J. Chem. Phys., 22, p.169.

94. MASON H B & SPALDING D BRIAN (1973)
"Prediction of Reaction Rates in Turbulent Premixed Boundary Layer Flows". Combustion Institute European Symp. pp. 601-606.

95. MCLAIN A G, JACHIMOWSKI C J AND WILSON C H (1979)
"Chemical Kinetics Modelling of Benzine and Toluene Oxidation Behind Shock Waves". NASA Technical Paper 1472.

96. MILES G A (1964)
"Performance Analysis of the Exothermic, Adiabatic Well-Stirred Reactor". Sc. D. Thesis MIT, Chem. Eng. Dept.

97. MOFFAT R J (1962)
"Gas Temperature Measurement". In Temperature Measurement and Control in Science and Industry, Vol. III, Ed., C M Herzfield. pp. 553-572. Rheinhold Publishing Corp., New York.

98. MONCHICK L (1959)
"Collision Integrals for the Exponential Repulsive Potential". Phys. Fluids, 2, p.695.

99. MONCHICK L, MUNN R J AND MASON E A (1966)
"Thermal Diffusion in Polyatomic Gases; A Generalised Stefan-Maxwell Diffusion Equation". J. Chem. Phys. 45, pp. 3051-3058.

100. NAGUIB A S (1975)
"The Prediction of Axisymmetrical Free-Jet, Turbulent Reacting Flows". PhD Thesis, Univ of London.

101. PENNER S S AND MULLINS B P (1959)
"Explosions, Detonation, Flammability and Ignition". AGARD, Pergamon Press, p. 224.

102. POPE S B (1976)
"The Probability Approach to the Modelling of Turbulent Reacting Flows". Combustion and Flame, Vol. 27, p. 299.

103. PRANDTL L (1945)
"Uber eir neves Formal-System fur die Ausgebildete Turbulenz". Nachrichten von der Akad. der Wissenschaft in Gottingen.

104. PRATT D T AND STORKMAN E S (1969)
"High Temperature Kinetics of Ammonia-Air Combustion".
Twelfth Symp. (Int) on Combustion, the Combustion Institute, pp. 891-900.

105. PRATT D T (1976)
"Mixing and Chemical Reaction in Continuous Combustion". Progress in Energy and Combustion Science, Vol. 1, pp. 73-86.

106. RHODES R P, HARSHA P T AND PETERS C E (1974)
"Turbulent Kinetic Energy Analysis of Hydrogen-Air Diffusion Flames". Acta. Astronautica, 1, p.443.

107. RIZZI A W AND BAILEY H E (1975)
"A Generalised Hyperbolic Marching Method for Chemically Reacting Three-Dimensional Supersonic Flow Using a Splitting Technique". Proceedings AIAA Second Computational Fluid Dynamics Conf., Hartford, Conn. June 1975, pp. 38-46.

108. ROSENSWEIG R E (1960)
"Measurement and Characterisation of Turbulent Mixing". Sc.D Thesis Dept of Chem Eng., MIT.

109. ROSENWEIG R E, HOTTEL H C AND WILLIAMS G C (1961) "Smoke-Scattered Light Measurement of Turbulent Concentration Fluctuation". Chem.Eng.Sci. 15, p.111.

110. ROSHKO A (1975) "Progress and Problems in Understanding Turbulent Shear Flows" in "Turbulent Mixing in Non-Reactive and Reactive Flows". S N B Murthy (Ed), Plenum Press, New York.

111. ROSHKO A (1976) "Structure of Turbulent Shear Flow: A New Look". AIAA 14th Aerospace Meeting, Washington, DC, Jan 26-28, 1976.

112. ROSNER D E (1962) "The Theory of Differential Catalytic Probes for the Determination of Atom Concentrations in High Speed, Non-Equilibrium Streams of Partially Dissociated Gases". ARS, J., 32, p.1065.

113. SCHOTT G L AND KINSEY J L (1958) "Kinetic Studies of Hydroxyl Radicals in Shock Waves. II: Induction Times in the Hydrogen-Oxygen Reaction". J. Chem. Phys., 29, p.1177.

114. SCHOLTE T G AND VAAGS P B (1959) "The Burning Velocity of Hydrogen-Air Flames". Combustion and Flame, 3, p. 495.

115. SERAG-ELDIN M A (1977)
"The Numerical Prediction of the Flow and Combustion Processes in a Three-Dimensional Can Combustor". PhD Thesis, Univ of London.

116. SHCHELKIN K I (1943)
"On Combustion in a Turbulent Flow". Zhur. Tekhn. Fiz. (USSR), 13, pp. 520-530, English Translation, NACA Tech. Memo No. 1110.

117. SPALDING D BRIAN (1957a)
"Predicting the Laminar Flame Speed in Gases with Temperature-Explicit Reaction Rates - I". Combustion and Flame, 1, p. 287.

118. SPALDING D BRIAN (1957b)
"One-Dimensional Laminar Flame Theory for Temperature-Explicit Reaction Rates - II". Combustion and Flame, 1, p. 296.

119. SPALDING D BRIAN (1957c)
"Transport Processes Between Fluids and Clouds of Suspended Particles: Some Exact Solutions". Proceedings of the Royal Society, A. Vol. 242, pp. 430-443.

120. SPALDING D BRIAN (1958)
"Approximate Solutions of Transient and Two-Dimensional Flame Phenomena: Constant Enthalpy Flames". Proc. Royal Soc A, Vol. 245, pp. 352-372.

121. SPALDING D BRIAN (1959)
"Theory of the Rate of Spread of Confined Turbulent Premixed Flames". Seventh Symp. (Int) on Combustion, Butterworth's Scientific Publications, London, pp. 595-603.

122. SPALDING D BRIAN (1967)
"The Spread of Turbulent Flames Confined in Ducts". Eleventh Symp (Int) on Combustion, the Combustion Institute, pp. 807-815.

123. SPALDING D BRIAN AND STEPHENSON P L (1971a)
"Laminar Flame Propagation in Hydrogen+Bromine Mixtures". Proceedings Roy. Soc. A, Vol 324, pp. 315-337.

124. SPALDING D BRIAN (1971b)
"Concentration Fluctuations in a Round Turbulent Free-Jet". Chem. Eng. Sci., Pergamon Press, Vol 26, pp. 95-107.

125. SPALDING D BRIAN (1971c)
"Mixing and Chemical Reaction in Steady Confined Turbulent Flames". 13th Symp. on Combustion, The Combustion Inst., Pittsburgh, p. 649.

126. SPALDING D BRIAN (1976a)
"A New Model of Turbulent Combustion". Imp. Coll. Mech. Eng. Report HTS/76/10.

127. SPALDING D BRIAN (1976b)
"Development of the Eddy-Break-Up Model of Turbulent Combustion". Imp. Coll. Mech. Eng. Report HTS/76/1, and 16th Int Combustion Symp. MIT.

128. SPALDING D BRIAN (1976c)
"Mathematical Models of Turbulent Flames: A Review". Combustion Science and Technology, Special Issue on Turb. Reactive Flames, Vol 13, Nos. 1-6, pp. 1-25.

129. SPALDING D BRIAN (1976d)
"The ESCIMO Theory of Turbulent Combustion". Imp. Coll. Mech. Eng. Report HTS/76/13.

130. SPALDING D BRIAN (1977a)
"Chemical Reactions in Turbulent Fluids". Imp. Coll. Mech. Eng. Dept., Report HTS/77/11. Also in Levich 60th Birthday Conference on Physico-chemical Hydrodynamics, Advance Publications, London, p. 321.

131. SPALDING D BRIAN (1977b)
"The PAM2 Computer Code: An Introduction". CHAM TR/40.

132. SPALDING D BRIAN (1978a)
"GENMIX; A General Computer Program for Two-Dimensional Parabolic Phenomena". HMT Series, Vol 1, Pergamon Press, Oxford.

133. SPALDING D BRIAN (1978b)
"A General Theory of Turbulent Combustion". Journal of Energy Vol. 2, No. 1, pp. 18-23, (Jan/Feb 1978).

134. SPALDING D BRIAN (1978c)
"Progress in Developing the ESCIMO Model of Turbulent Combustion". Imp. Coll. Mech. Eng. Report HTS/78/6.

135. SPALDING D BRIAN (1979a)
"The Influences of Laminar Transport and Chemical Kinetics on the Time-Mean Reaction Rate in a Turbulent Flame". 17th Symp (Int) on Combustion.

136. SPALDING D BRIAN (1979b)
"Secondary Combustion in Rocket Plumes - A Theoretical Approach". Paper Presented at XII International Symp. on Shock Tubes and Waves, Jerusalem, July 16-19, 1979.

137. SPALDING D BRIAN (1979c)
"Prediction of Turbulent Combustion in Practical Systems". Paper presented at the International Gas-Turbine Congress-Exhibition, Haifa, Israel, July 1979.

138. SPALDING D BRIAN (1979d)
"The Modelling of Complex Flows". Chapter 6 of Turbulent Reacting Flows edited by P A Libby and F A Williams, to be published by Springer Verlag.

139. SPALDING D BRIAN (1979e)
"Theories of Turbulent Reacting Flows". AIAA Conference, New Orleans.

140. SRIVATSA S K AND TAM L T (1979)
"Chemical Kinetics Solution Method Incorporated in the PAM 2 Code". CHAM Limited, Report TR/41, 1978.

141. STAMBULEANU A (1976)
"Flame Combustion Processes in Industry". Abacus Press.

142. SUMMEFIELD N, REITER S H, KEBELY V AND MASCOLO R W (1955)
"The Structure and Propagation Mechanism of Turbulent Flames in High Speed Flow". Jet Propulsion, Vol 25, p.377.

143. SUMMERFIELD M (1956)
"Turbulent Flames in Gases". Jet Propulsion, Vol 26, p.485.

144. SWITHENBANK J, TURAN A, FELTON P G AND SPALDING D BRIAN (1979)
"Fundamental Modelling of Mixing, Evaporation and Kinetics in Gas-Turbine Combustors". Dept of Chem. Eng. and Fuel Tech., Univ of Sheffield, Report No. HIC 320.

145. THOMAS P D AND WILSON K H (1975)
"Efficient Computation of 'Stiff' Chemically Reacting Flow in Turbulent Free Jets". Proc.

AIAA Second Computational Fluid Dynamics Conf., Hartford, Conn., June (1975) pp. 124-132.

146. TSATSARONIS G (1978)
"Prediction of Propagating Laminar Flames in Methane, Oxygen, Nitrogen Mixtures". Combustion and Flame 33, pp. 217-239.

147. TSIEN H S (1951)
"Influence of Flame Front on the Flow Field". Trans. Am. Soc. Mech. Engrs., Series E, J. Appl. Mech., Vol 18, p. 188.

148. VARMA A K, FISHBURNE E S AND DONALDSON C (1977)
"Aspects of Turbulent Combustion". Presented as paper 77-100 at the AIAA 15th Aerospace Science Meeting, Los Angeles, Calif., Jan 24-26.

149. WANG CHANG C S, UHLENBECK G E AND DE BOER J (1964)
"Studies in Statistical Mechanics (J. de Boer and G E Uhlenbeck, eds), Wiley and Sons, Amsterdam, New York 1964, Vol 2.

150. WORMECK J J AND PRATT D T (1976)
"CREK: Computer Program for Calculation of Combustion Reaction Equilibrium and Kinetics in Laminar or Turbulent Flow". Washington State Univ, Dept of Mech. Eng. Report No. WSU-ME-TEL-76-1.

151. WORMECK J J (1976)
"Computer Modelling of Turbulent Combustion in a Longwell Jet-Stirred Reactor". PhD Thesis Washington State University.

152. WILLIAMS F A (1965)
"Combustion Theory". Addison-Wesley Publishing Co., Mass., Reading.

153. WILLIAMS G C, HOTTEL H C AND MORGAN A C (1969)
"The Combustion of Methane in a Jet-Mixed Reactor". 12th Symp. (Int) on Combustion, p.913, The Combustion Institute, Pittsburgh, Penn.

154. WILLIAMS F A (1974)
"Recent Advances in Theoretical Descriptions of Turbulent Diffusion Flames" in "Turbulent Mixing in Non-Reactive and Reactive Flows". Edited by S N B Murthy, Plenum Press, New York.

155. WILLIAMS F A AND LIBBY P A (1980)
"Some Implications of Recent Theoretical Studies in Turbulent Combustion". AIAA 18th Aerospace Sciences Meeting. January 14-16 1980 Pasadena, California.

156. WITTE A B ET AL (1975)
TRW Final Report, AFWL-TR-75-266.

157. WOHL K, GAZLEY C AND KAPP N (1949)
"Diffusion Flames". 3rd Symposium on Combustion, pp. 288.

158. WOLFHARD H G AND PARKER W G (1949)
"A New Technique for the Spectroscopic Examination of Flames at Normal Pressure". Proc. Phys. Soc. (London), A62, p.722.

159. YANENKO N N (1971)
"The Method of Fractional Steps". Springer-Verlag, New York, USA.

APPENDIX A - THE LEAST-SQUARE LINEAR REGRESSION ANALYSIS

All the binary diffusion coefficients D_{ij}'s and species viscosities μ_j's described in equations 2.5-7 - 2.5-9 are expressed in the form of AT^B. Values of A's and B's for various diffusion coefficients and species viscosities are obtained by the method of least-square linear regression analysis.

The following procedure is adopted:

1. Let D_{ij} and μ_j have the form:

$$f = AT^B \qquad ;(A.1)$$

$$A_1 = \log A \qquad ;(A.2)$$

$$A_2 = \log B \qquad ;(A.3)$$

Hence, $\log f = A_1 + A_2 \log T$.(A.4)

where A and B are the coefficients, T is the absolute temperature in ^oK.

2. From the principle of least-square linear regression, values of A_1 and A_2 are respectively obtained from equations A.5 - A.6:

$$\frac{\partial J}{\partial A_1} = 0 \quad , \qquad (A.5)$$

$$\frac{\partial J}{\partial A_2} = 0 \qquad , \qquad (A.6)$$

where, $J \equiv \sum_{i=0}^{n} (\log\mu_j - \log f)_i^2$;

$n = 220.$

3. The solution of equations (A.5-A.6) gives:

$$A_1 = \frac{(\Sigma\log T_i)\ (\Sigma\mu_j) - (n+1)\ \Sigma\log T_i\mu_j}{(\Sigma\log T_i)^2 - (n+1)\ (\Sigma\log T_i)^2} \ , \qquad (A.7)$$

$$A_2 = \frac{(\Sigma\mu_j) - (\Sigma\log T_i)\ A_1}{(n+1)} \qquad ; \qquad (A.8)$$

where T_i's are the interval temperature with 10^oK increment, starting from $T_o=300^oK$ to $T_{220}=2500^oK$; data of μ_j's or D_{ij}'s are given by equations 2.5-7 - 2.5-9.

4. Hence, μ_j's and D_{ij}'s are further expressed in the form: AT^B where $A = \mathrm{Exp}\ (A_1)$ and $B = A_2$.

Values of A's and B's for various species viscosities are given below:

Species	$Ax10^7$	B
N_2	5.066	0.632
H	2.111	0.6283
O	5.558	0.6281
HO_2	1.785	0.7281
H_2O	0.5871	0.9215
OH	5.562	0.6305
O_2	6.072	0.6307
H_2	2.084	0.6553

TABLE A.1: COEFFICIENTS OF SPECIES VISCOSITIES

kT/ϵ	Ω	kT/ϵ	Ω	kT/ϵ	Ω	kT/ϵ	Ω	kT/ϵ	Ω
0.30	2.785	1.15	1.482	1.95	1.186	3.5	0.9999	6.0	0.8963
.35	2.628	1.20	1.452	2.0	1.175	3.6	.9932	7.0	.8727
.40	2.492	1.25	1.424	2.1	1.156	3.7	.9870	8.0	.8538
.45	2.368	1.30	1.399	2.2	1.138	3.8	.9811	9.0	.8379
.50	2.257	1.35	1.375	2.3	1.122	3.9	.9755	10.0	.8242
.55	2.156	1.40	1.353	2.4	1.107	4.0	.9700	20.0	.7432
.60	2.065	1.45	1.333	2.5	1.093	4.1	.9649	30.0	.7005
.65	1.982	1.50	1.314	2.6	1.081	4.2	.9600	40.0	.6718
.70	1.908	1.55	1.296	2.7	1.069	4.3	.9553	50.0	.6504
.75	1.841	1.60	1.279	2.8	1.058	4.4	.9507	60.0	.6335
.80	1.780	1.65	1.264	2.9	1.048	4.5	.9464	70.0	.6194
.85	1.725	1.70	1.248	3.0	1.039	4.6	.9422	80.0	.6076
.90	1.675	1.75	1.234	3.1	1.030	4.7	.9382	90.0	.5973
.95	1.629	1.80	1.221	3.2	1.022	4.8	.9343	100.0	.5882
1.00	1.587	1.85	1.209	3.3	1.014	4.9	.9305	200.0	.5320
1.05	1.549	1.90	1.197	3.4	1.007	5.0	.9269	400.0	.4811
1.10	1.514								

TABLE A.2 : VALUES OF kT/ϵ and Ω

APPENDIX B - LINEARISATION OF THE CHEMICAL REACTION SCHEMES

Three types of reactions are considered.

TYPE 1:

$$\sigma_1 + \sigma_2 \underset{K_{-j}}{\overset{K_j}{\rightleftharpoons}} \sigma_3 + \sigma_4$$

Forward reaction rate $R_j = K_j \rho^2 \sigma_1 \sigma_2$;
reverse reaction rate $R_{-j} = K_{-j} \rho^2 \sigma_3 \sigma_4$.

The total reaction sources of species σ_1, σ_2, σ_3, σ_4 are respectively given by:

$$S_{\sigma_1} = S_{\sigma_2} = -S_{\sigma_3} = -S_{\sigma_4}$$

$$= - \rho^2 K_j \sigma_1 \sigma_2 + \rho^2 K_{-j} \sigma_3 \sigma_4 .$$

The positive sign indicates the creation source while the negative sign indicates the destruction source. The $\frac{\partial S_\sigma}{\partial \sigma}$ term is obtained by first differentiating the total S_σ term with respect to the reacting species σ, then taking the total derivative over the elementary reaction step in which σ is involved. In other words, $\frac{\partial S_\sigma}{\partial \sigma}$ is given by:

$$\frac{\partial S_\sigma}{\partial \sigma} = - \rho^2 K_j(\sigma_1+\sigma_2) - \rho^2 K_{-j}(\sigma_3+\sigma_4)$$

TYPE 2:

$$M + \sigma_1 \underset{K_{-j}}{\overset{K_j}{\rightleftharpoons}} \sigma_3 + \sigma_4 + M$$

$$R_j = \frac{K_j \rho^2 \sigma_1}{\overline{W}} \quad ;$$

$$R_{-j} = \frac{K_{-j} \rho^3 \sigma_3 \sigma_4}{\overline{W}} \quad .$$

$$S_{\sigma_1} = -S_{\sigma_3} = -S_{\sigma_4} = - \frac{\rho^2}{\overline{W}} K_j \sigma_1 + \frac{\rho^3}{\overline{W}} K_{-j} \sigma_3 \sigma_4 .$$

$$\frac{\partial S_\sigma}{\partial \sigma} = - \frac{\rho^2}{\overline{W}} K_j - \frac{\rho^3}{\overline{W}} K_{-j} (\sigma_3+\sigma_4) \quad .$$

TYPE 3:

$$M + \sigma_1 + \sigma_2 \underset{K_{-j}}{\overset{K_j}{\rightleftharpoons}} \sigma_3 + M$$

$$R_j = \frac{K_j \rho^3 \sigma_1 \sigma_2}{\overline{W}} \quad ; \quad R_{-j} = \frac{K_{-j} \rho^2 \sigma_3}{\overline{W}}$$

$$S_{\sigma_1} = S_{\sigma_2} = -S_{\sigma_3} = \frac{\rho^2}{\overline{W}} K_{-j} \sigma_3 - \frac{\rho^3}{\overline{W}} K_j \sigma_1 \sigma_2$$

$$\frac{\partial S_\sigma}{\partial \sigma} = - \frac{\rho^2}{\overline{W}} K_{-j} - \frac{\rho^3}{\overline{W}} K_j \ (\sigma_1 + \sigma_2).$$

Finally, all reaction sources are linearised in accordance with:

$$S_\sigma = S_\sigma^* + \frac{\partial S_\sigma}{\partial \sigma} (\sigma - \sigma^*)$$

$$S_\sigma = (S_\sigma^* - \frac{\partial S_\sigma}{\partial \sigma} \sigma^*) + \frac{\partial S_\sigma}{\partial \sigma} \sigma$$

$$= Su + Sp.\sigma \quad ;$$

the superscript * denotes the value at 'early' time.